MAX PLANCK INSTITUTE FOR CHEMISTRY

Max Planck Graduate Center mit der Johannes Gutenberg-Universität

JOHANNES GUTENBERG UNIVERSITÄT MAINZ

Understanding production, interconversion and effects of reactive oxygen species in atmospheric aerosols and the epithelial lining fluid using numerical modelling techniques

Ashmi Mishra

Born on 17.01.1998 in Kathmandu, Nepal

Dissertation

for the award of the academic degree of

'Doctor rerum naturalium '(Dr. rer. nat.) of the faculties:

08 - Physics, Mathematics and Computer Science

09 - Chemistry, Pharmaceutical Sciences, Geography and Geosciences

10 - Biology

University Medicine

Mainz, November 2025

Supervisor:

Second supervisor:

Day of the oral examination: 20 January 2026

For my parents

I hereby declare that I wrote the dissertation submitted without any unauthorized external assistance and used only sources acknowledged in the work. All textual passages which are appropriated verbatim or paraphrased from published and unpublished texts as well as all information obtained from oral sources are duly indicated and listed in accordance with bibliographical rules. In carrying out this research, I complied with the rules of standard scientific practice as formulated in the statutes of Johannes Gutenberg-University Mainz to insure standard scientific practice.

Ashmi Mishra
Mainz, 10 November 2025

Painting by S. Mishra

Abstract

Atmospheric aerosols impact climate, air quality, and public health. During atmospheric transport, aerosols can undergo complex physical and chemical transformation through interactions with atmospheric oxidants. Oxidation reactions are ubiquitous in atmospheric and physiological chemistry, with reactive oxygen species (ROS) being central to atmospheric chemical processing and the health effects of aerosols. To unravel the multiphase chemical kinetics during oxidative processing of atmospherically relevant chemical species, kinetic multi-layer models of aerosol surface and bulk chemistry (KM-SUB) were developed and applied. In the context of human health, new chemical reaction mechanisms have been developed and applied to kinetic models of oxidative potential assays (KM-OP) and of the human epithelial lining fluid (KM-SUB-ELF) to quantify the amount of oxidants that are formed or consumed. The highlights of this thesis are outlined below:

1. Determination of reaction pathways in the ozonolysis of oleic acid. Different reaction mechanisms, with differing levels of complexity, were tested and the mechanism with Criegee intermediates was required to explain the discrepancies observed in previous research. Kinetic multilayer model and Monte Carlo-based global optimization tools were used to reconcile several experimental data sets of oleic acid ozonolysis from multiple studies in the literature at vastly different experimental conditions. The majority of the experimental data was successfully reproduced by the model using an ensemble of kinetic parameter sets. A model analysis revealed that a unique determination of these parameters requires further experimental data at distinct experimental conditions. The range of properties of the individual parameter set provided the error associated with the fit.

   In a related further study, the kinetic model was used to explore the validity of the oxidant exposure metric, i.e., oxidant concentration multiplied by time.

2. Elucidation of the reaction pathways and kinetic parameters of the photochemical processing of mixed organic-inorganic particles across different phase states including liquid, semi-solid, and solid. A kinetic multilayer model was developed to analyze an extensive dataset from a coated-wall flow-tube experiment, which investigated the photochemical processing of citric acid, a secondary organic aerosol (SOA) surrogate, in the presence of iron. The model results showed that following a rapid initial reaction, the reoxidation of Fe(II) limited the photooxidation. Two different kinetic regimes were established: at low humidity (RH < 65%), the bulk diffusion of O_2 limited the reoxidation of Fe(II), while at high humidity (RH > 85%), O_2 was fully saturated in the bulk, and photooxidation was limited by the slow reoxidation of Fe(II). HO_2 and H_2O_2 were major sinks for Fe(II) and therefore played a major role in sustaining photooxidation chemistry.

3. Development and application of a kinetic model that estimates aerosol oxidative potential (OP) based on the composition of particulate matter (PM) to improve the mechanistic, process-level understanding of air pollution health effects. The kinetic model consolidates a large set of laboratory data of ROS production, dithiothreitol, and ascorbic acid depletion, as well as dehydroascorbic acid formation in the presence of the following PM components: SOA, metals, and quinones. The resulting chemical reaction mechanism entails kinetic rate coefficients for the most important reaction pathways. The model was applied to data from field measurements of PM composition and a good agreement between the model and field data in three different sites across Europe was found. The model analysis revealed that OP in the field is predominantly driven by organic molecules and copper. As a predictive OP model, KM-OP is able to estimate the possible health effects of particulate matter solely when chemical composition data are available. Moreover, as a mechanistic model, KM-OP showed not only what PM constituents contribute most to OP but also what specific chemical interactions drive the OP.

4. Determination of the impact of chemical modification to proteins by air pollutants and endogenous biological sources of ROS. The KM-SUB-ELF model was further developed and extended for this purpose. Fine particulate matter (PM2.5) can produce ROS in the respiratory tract in two ways: either directly via chemical reactions or indirectly through stimulation of cells such as neutrophils or macrophages. Model analysis revealed that ROS formed from PM2.5 and nitrogen dioxide showed synergistic effects in the production of nitrotyrosine (Ntyr), an oxidative stress biomarker. Despite being a burden on antioxidants, ozone did not significantly affect the formation of Ntyr.

   In a related study, the KM-SUB-ELF model was used to quantify the chemical production of ROS from PM2.5 and compare it to the production of H_2O_2 via ambient and endogenous sources. The model results show that the chemical production of ROS from PM2.5 was negligible compared to ambient and endogenous sources, rather, PM2.5 played a key role in the conversion of peroxides to the highly reactive OH radical.

Zusammenfassung

Atmosphärische Aerosole beeinflussen Klima, Luftqualität und öffentliche Gesundheit. Während des atmosphärischen Transports können Aerosole durch Wechselwirkungen mit atmosphärischen Oxidationsmitteln komplexe physikalische und chemische Umwandlungen erfahren. Oxidationsreaktionen sind in der atmosphärischen und physiologischen Chemie allgegenwärtig, wobei reaktive Sauerstoffspezies (ROS) eine zentrale Rolle bei der chemischen Verarbeitung in der Atmosphäre und den gesundheitlichen Auswirkungen von Aerosolen spielen. Um die mehrphasige chemische Kinetik während der oxidativen Verarbeitung atmosphärisch relevanter chemischer Spezies zu entschlüsseln, wurden kinetische Mehrschichtmodelle der Aerosoloberflächen- und Volumenchemie (KM-SUB) entwickelt und angewendet. Im Kontext der menschlichen Gesundheit wurden neue chemische Reaktionsmechanismen entwickelt und auf kinetische Modelle von Oxidationspotenzialtests (KM-OP) und der menschlichen Epithelflüssigkeit (KM-SUB-ELF) angewendet, um die Menge der gebildeten oder verbrauchten Oxidationsmittel zu quantifizieren. Die wichtigsten Ergebnisse dieser Arbeit sind im Folgenden zusammengefasst:

1. Aufklärung der Reaktionswege bei der Ozonolyse von Ölsäure. Verschiedene Reaktionsmechanismen mit unterschiedlichem Komplexitätsgrad wurden getestet. Der Mechanismus mit Criegee-Intermediaten war erforderlich, um die in früheren Untersuchungen beobachteten Diskrepanzen zu erklären. Ein kinetisches Mehrschichtmodell und Monte-Carlo-basierte globale Optimierungsmethoden wurden eingesetzt, um eine große Menge experimenteller Daten zur Ölsäure-Ozonolyse aus verschiedenen Studien unter sehr unterschiedlichen Versuchsbedingungen zu reproduzieren. Der Großteil der experimentellen Daten konnte durch das Modell mit einem Ensemble kinetischer Parametersätze erfolgreich reproduziert werden. Eine Modellanalyse zeigte, dass eine eindeutige Bestimmung dieser Parameter weitere experimentelle Daten unter verschiedenen Versuchsbedingungen erfordert. Der Wertebereich der einzelnen Parametersätze lieferte den mit der Anpassung verbundenen Fehler.

   In einer verwandten Anschlussstudie wurde das kinetische Modell verwendet, um die Reaktion schwebender Ölsäuretröpfchen mit Ozon zu simulieren und die Validität der Oxidationsmittel-Exposition, d. h. der Oxidationsmittel-konzentration multipliziert mit der Zeit, als Metrik zu untersuchen.

2. Aufklärung der Reaktionswege und kinetischen Parameter der photochemischen Prozessierung gemischter organisch-anorganischer Partikel in verschiedenen Phasenzuständen zwischen flüssig, halbfest und fest. Zur Analyse umfangreicher Daten aus einem Strömungsrohrexperiment mit beschichteter Wand wurde ein kinetisches Mehrschichtmodell entwickelt. In diesem Experiment wurde die photochemische Prozessierung von Zitronensäure, einem Surrogat für sekundäre

organische Aerosole (SOA), in Gegenwart von Eisen untersucht. Die Modellergebnisse zeigten, dass nach einer schnellen Anfangsreaktion die Reoxidation von Fe(II) die Photooxidation begrenzte. Es wurden zwei verschiedene kinetische Regime etabliert: Bei niedriger relativer Luftfeuchtigkeit (< 65% rel. Luftfeuchte) begrenzte die Diffusion von O_2 die Reoxidation von Fe(II), während bei hoher relativer Luftfeuchtigkeit (> 85% rel. Luftfeuchte) O_2 in der Masse vollständig gesättigt war und die Photooxidation durch die langsame Reoxidation von Fe(II) begrenzt wurde. HO_2 und H_2O_2 waren wichtige Senken für Fe(II) und spielten daher eine wichtige Rolle bei der Aufrechterhaltung der Photooxidationschemie.

3. Entwicklung und Anwendung eines kinetischen Modells, das das oxidative Potenzial (OP) von Aerosolen auf der Grundlage der Zusammensetzung von Feinstaub (PM) schätzt, um das mechanistische, prozessbasierte Verständnis der gesundheitlichen Auswirkungen von Luftverschmutzung zu verbessern. Das kinetische Modell fasst eine große Menge an Labordaten zur ROS-Produktion, zum Dithiothreitol- und Ascorbinsäureverbrauch sowie zur Dehydroascorbinsäurebildung in Gegenwart von SOA, Metallen und Chinonen zusammen. Der resultierende chemische Reaktionsmechanismus beinhaltet kinetische Geschwindigkeitskoeffizienten für die wichtigsten Reaktionswege. Das Modell wurde auf Daten aus Feldmessungen der PM-Zusammensetzung angewendet. Es wurde eine gute Übereinstimmung zwischen Modell und Felddaten an drei verschiedenen Standorten in Europa festgestellt. Die Modellanalyse ergab, dass die OP im Feld überwiegend durch organische Moleküle und Kupfer getrieben wird. Als prädiktives OP-Modell kann KM-OP die möglichen gesundheitlichen Auswirkungen von Feinstaub nur dann abschätzen, wenn Daten zur chemischen Zusammensetzung vorliegen. Darüber hinaus zeigt KM-OP als mechanistisches Modell nicht nur, welche PM-Bestandteile für die OP verantwortlich sind, sondern auch, welche spezifischen chemischen Reaktionen die OP antreiben.

4. Bestimmung des Einflusses chemischer Modifikationen von Proteinen durch Luftschadstoffe und endogene biologische ROS-Quellen. Das KM-SUB-ELF-Modell wurde zu diesem Zweck weiterentwickelt und erweitert. Feinstaub (PM2,5) kann ROS in den Atemwegen auf zwei Arten produzieren: entweder direkt durch chemische Reaktionen oder indirekt durch Stimulation von Zellen wie Neutrophilen oder Makrophagen. Modellanalysen ergaben, dass aus PM2,5 und Stickstoffdioxid gebildete ROS synergistische Effekte bei der Produktion von Nitrotyrosin (Ntyr), einem Biomarker für oxidativen Stress, zeigten. Obwohl Ozon eine Belastung für Antioxidantien darstellt, hatte es keinen signifikanten Einfluss auf die Bildung von Ntyr.

   In einer verwandten Studie wurde das KM-SUB-ELF-Modell verwendet, um die chemische ROS-Produktion aus PM2,5 zu quantifizieren und mit der Produktion von H_2O_2 aus Umgebungs- und endogenen Quellen zu vergleichen. Die Modellergebnisse zeigen, dass die chemische Produktion von ROS aus PM2,5

im Vergleich zu Umgebungs- und endogenen Quellen vernachlässigbar war; vielmehr spielte PM2,5 eine Schlüsselrolle bei der Umwandlung von Peroxiden in das hochreaktive OH-Radikal.

List of Abbreviations

CI	Criegee intermediate
ELF	Epithelial lining fluid
Fe(III) Cit	Iron(III) citrate
H_2O_2	Hydrogen peroxide
HO_2	Hydroperoxyl radical
KM-SUB	Kinetic multi-layer model of aerosol surface and bulk chemistry
KM-GAP	Kinetic multi-layer model of gas-particle interactions in aerosols and clouds
KM-OP	Kinetic model of oxidative potential
Ntyr	Nitrotyrosine
NO_2	Nitrogen dioxide
NO_3	Nitrate radical
OP	Oxidative potential
O_2	Oxygen
O_2^-	Superoxide
O_3	Ozone
OH	Hydroxyl radical
PAH	Polycyclic aromatic hydrocarbons
PM	Particulate matter
PRAD	Photochemical reaction and diffusion
RH	Relative humidity
ROS	Reactive oxygen species
SOA	Secondary organic aerosol
VOC	Volatile organic compounds

Contents

1. Introduction **1**
1.1. Multiphase chemistry 1
1.2. Atmospheric aerosols 1
1.3. Oxidative processing of organic aerosol 2
1.4. Photochemical processing of iron carboxylates 3
1.5. Health effects of air pollution 4
1.6. Numerical kinetic modeling of multiphase chemistry 5
1.7. Research objectives 6

2. Results **8**
2.1. Overview 8
2.2. Kinetic modeling of oleic acid decay during ozonolysis 10
2.3. Kinetic modeling of product formation in the ozonolysis of oleic acid . . 22
2.4. Kinetic modeling of photochemical degradation of iron carboxylates . . 42
2.5. Kinetic modeling of aerosol oxidative potential (KM-OP) 53
2.6. Kinetic modeling of protein modification due to oxidative stress by air pollution in the epithelial lining fluid 86
2.7. Kinetic modeling of ambient and endogenous hydrogen peroxide production in the epithelial lining fluid 99

3. Conclusions and outlook **109**

4. Bibliography **111**

A. Personal List of Publications **127**

B. Supplement **130**

1. Introduction

1.1. Multiphase chemistry

Multiphase chemistry involves interactions of chemical species present in two or more phases (Ravishankara, 1997; Pöschl, 2005; Abbatt and Ravishankara, 2023). These interactions encompass chemical reactions and transport processes (Pöschl and Shiraiwa, 2015; Abbatt and Ravishankara, 2023), and are omnipresent in the Earth system, climate, and life sciences (Pöschl and Shiraiwa, 2015). In the life sciences, the metabolism of many organisms involves the interplay of gases, liquids, and solids (Pöschl and Shiraiwa, 2015). Although the Earth's atmosphere is made up mostly of gases, chemical reactions do not occur solely in the gas phase; they also take place on the surfaces of particles and within liquid droplets (Ravishankara, 1997; Abbatt and Ravishankara, 2023). Multiphase chemical reactions can influence and significantly alter the composition and gas-particle partitioning of atmospheric aerosols (George and Abbatt, 2010; Shiraiwa et al., 2013).

1.2. Atmospheric aerosols

Aerosols are defined as solid or liquid particles suspended in gas (Prospero et al., 1983; Seinfeld and Pandis, 2016). Atmospheric aerosols influence climate, visibility, air quality, and therefore human health (Lohmann and Feichter, 2005; Andreae and Rosenfeld, 2008; Pöschl and Shiraiwa, 2015; Shiraiwa et al., 2017; Lelieveld et al., 2019). Aerosols can scatter and absorb solar and terrestrial radiation, which has direct implications on the climate (Calvin et al., 2023). Furthermore, aerosols act as nuclei for the formation of cloud water droplets and ice crystals (Twomey, 1974, 1977; Rosenfeld et al., 2008; Andreae and Rosenfeld, 2008). The impact of aerosols on climate represents one of the greatest uncertainties in understanding Earth's climate and predicting future climate change (Calvin et al., 2023). Aerosols can cause serious health effects, but how the chemical composition of aerosols plays a role in these effects is unclear (Lelieveld et al., 2015, 2019).

Size is a widely used metric to classify aerosols (Seinfeld and Pandis, 2016). It is an important metric for health effects of aerosols because it affects how deeply the aerosols can penetrate into the lungs (Pope III et al., 2006; Li et al., 2016; Kwon et al., 2020). PM10 refers to particles with aerodynamic diameters that are 10 µm and smaller. Particles below an aerodynamic diameter of 2.5 µm is referred to as PM2.5 (Pope III et al., 2006). Ultrafine particles have an aerodynamic diameter less than 0.1 µm (Pope III et al., 2006; Li et al., 2016). Particles larger than 10 µm can affect the upper airways.

PM2.5 can penetrate deep into the lung alveoli, while ultrafine particles can even reach the bloodstream, which can have adverse effects on other organs of the body (Nemmar et al., 2002; Oberdörster et al., 2002; Schraufnagel et al., 2019). The samplers used in collecting size-selective samples of PM cannot differentiate sizes precisely; thus, particle size is often defined relative to a 50% cut-off at a specific aerodynamic diameter (Chow, 1995).

In the pre-industrial era, aerosol particles originated mostly from natural sources (Andreae, 2007; Hamilton, 2015). In the Anthropocene, human activities dominate the production of PM in urban areas (Boucher, 2015). Aerosol particles persist in the atmosphere for weeks and can reach even the most pristine regions of the planet through large-scale atmospheric circulation. (Andreae, 2007; Eleftheriadis et al., 2009). Aerosols can be categorized into primary and secondary particles (Pöschl, 2005; Boucher, 2015): primary particles are emitted directly from the Earth's surface into the atmosphere and include natural sources, such as bacteria, fungal spores, pollen, viruses (Pöschl, 2005; Després et al., 2012; Fröhlich-Nowoisky et al., 2016), biogenic salts (Elbert et al., 2007; Pöhlker et al., 2012), sea spray, (Quinn et al., 2015) or mineral dust (Choobari et al., 2014; Adebiyi et al., 2023), as well as anthropogenic sources such as cooking or combustion processes (Bond et al., 2013). Secondary particles, such as secondary organic aerosol (SOA), are formed via oxidation reactions of volatile organic compounds (VOCs) by reactive species such as ozone (O_3), nitrate radicals (NO_3), and hydroxyl radicals (OH) (Atkinson and Arey, 2003; Houle et al., 2015; Pöschl and Shiraiwa, 2015; Palm et al., 2017). Generally, OH radicals react by abstracting hydrogen or by adding to C=C double bonds (Atkinson and Arey, 2003; Houle et al., 2015). NO_3 can also abstract hydrogen and can add to C=C double bonds (Palm et al., 2017), while O_3 tends to react through ozonolysis of unsaturated hydrocarbons, among other pathways (Palm et al., 2017). These reactions tend to form products that are low enough in volatility to partition into the condensed phase (Hallquist et al., 2009; Jimenez et al., 2009; Seinfeld and Pandis, 2016). SOA accounts for a large fraction of the organic particulate matter (PM) (Kanakidou et al., 2005; Kroll and Seinfeld, 2008). Organic aerosols consist of thousands of compounds making this fraction chemically very diverse (Goldstein and Galbally, 2007).

Inorganic compounds make up approximately 40-60% of the total aerosol mass (Heintzenberg, 1989; Zappoli et al., 1999; Jimenez et al., 2009). At ambient levels, sulfate, nitrate, ammonium, transition metals, and elemental black carbon (soot) make up the majority of inorganic aerosols (Heintzenberg, 1989; Zappoli et al., 1999; Pryor et al., 2015).

1.3. Oxidative processing of organic aerosol

During atmospheric transport, aerosols undergo complex physical and chemical transformation through interactions with solar radiation and other atmospheric constituents (Song and Carmichael, 1999; Kroll and Seinfeld, 2008; George and Abbatt, 2010; Shiraiwa

et al., 2011). Chemical transformations can be driven by the heterogeneous uptake of gas-phase oxidants. Depending on the phase state, chemical reactions may occur both at the surface and in the bulk of the particles. The uptake of gas phase oxidants can be classified into a reaction-diffusion regime and a mass transfer regime (Berkemeier et al., 2013). The heterogeneous oxidation of organic aerosols can lead to fragmentation, functionalization, and oligomerization (Jimenez et al., 2009; Kroll et al., 2009). Fragmentation tends to produce more volatile species and reduce the particle mass (Jimenez et al., 2009; Kroll et al., 2015). In contrast, oligomerization and functionalization can reduce the volatility as well as O:C ratio (Jimenez et al., 2009; Kroll et al., 2011), which in turn can affect the hygroscopicity, and thus the cloud activation properties (Hemming and Seinfeld, 2001). Hence, these chemical aging processes can significantly alter a particle's physical properties (Pöschl, 2005).

Several experimental techniques are used to investigate the uptake of gas-phase oxidants such as monitoring the loss or production of a trace molecule from the gas-phase, or monitoring the changes in the condensed phase (Abbatt et al., 2012). Multiple experimental and modeling studies have been conducted on the ozonolysis of oleic acid, which serves as a model system for atmospheric multiphase chemistry (Morris et al., 2002b; Hearn and Smith, 2004; King et al., 2004; Morris et al., 2002a; Knopf et al., 2005; Hearn et al., 2005; Ziemann, 2005; Hung and Ariya, 2007; Lee and Chan, 2007; Zahardis and Petrucci, 2007; Vesna et al., 2009; Carslaw et al., 2010; Pfrang et al., 2010; Shiraiwa et al., 2010; Dennis-Smither et al., 2012; Mendez et al., 2014; Al-Kindi et al., 2016; Gallimore et al., 2017; King et al., 2020). Oleic acid is a mono-unsaturated fatty acid and is often used as a tracer for cooking aerosols (Schauer et al., 1996). When ozone reacts with the double bond of the oleic acid, carbonyl compounds and a reactive zwitterion, termed the Criegee intermediate (CI), are formed. The CI can rearrange to form other C9 products or react with other functional groups, leading to formation of high-molecular-weight products (Ziemann, 2005; Zahardis and Petrucci, 2007; Gallimore et al., 2017).

1.4. Photochemical processing of iron carboxylates

Photochemistry is central to many aging processes in the atmosphere. When a molecule absorbs a photon, it can result in bond cleavage, a process referred to as photolysis (George et al., 2015). In contrast to the uptake of oxidants (e.g., OH, O_3, NO_3) from the gas phase, which may react at or near the surface, photochemically active radiation can penetrate the entirety of organic aerosol particles (Alpert et al., 2021; Dou et al., 2021).

Iron can reach the atmosphere from dust, biomass burning, industrial activities, and railway emissions, among other sources (Deguillaume et al., 2005; Harrison et al., 2012; Ito, 2015; Lopez et al., 2023; Al-Abadleh, 2024). Factors such as temperature, pH value, and ionic strength can influence the ability of iron to form complexes (Deguillaume et al., 2005; Faust and Hoigné, 1990). Organic compounds, in particular, have gained increasing attention as potential ligands for Fe(III) complexation, with many carboxy-

lates being identified as important ligands (Chebbi and Carlier, 1996; Weller et al., 2013, 2014).

Fe(III) carboxylate complexes have been recognized as photoactive compounds (Weller et al., 2013, 2014; Alpert et al., 2021; Wang et al., 2023). They can be excited by light in the UV-VIS range, triggering a ligand-to-metal charge transfer (LMCT) (Dou et al., 2021). During photolysis, Fe(III) carboxylates can undergo decarboxylation and organic radicals are formed. In presence of oxygen, reactive oxygen species (ROS, such as the hydroxyl radial (OH), superoxide (O_2^-), hydroperoxyl radical (HO_2) and hydrogen peroxide (H_2O_2)) are generated, and their presence can lead to further decarboxylation, resulting in the breakdown of organic matter (Pozdnyakov et al., 2014; Wang et al., 2023). This photodegradation process may be an important sink of carboxylate groups in the troposphere (Weller et al., 2014; Alpert et al., 2021) and may also affect organic aerosol mass.

1.5. Health effects of air pollution

Air pollution leads to millions of premature deaths every year (Burnett et al., 2018; Turner et al., 2016; Faustini et al., 2014; Lelieveld et al., 2020; Landrigan et al., 2018). Epidemiological research has demonstrated that increased exposure to ambient PM is associated with an increase in hospital admissions, and overall mortality from cardiovascular and respiratory diseases (Burnett et al., 2014; Apte et al., 2015; Cohen et al., 2017; Pope et al., 2019; Brauer et al., 2024). Despite the epidemiological evidence, the molecular-level understanding of the interactions of air pollutants with the human body remains poor.

Air pollutants that are most closely associated with adverse health effects are PM2.5, O_3, and NO_2 (Pope et al., 2019; Landrigan et al., 2018). NO_2 and PM2.5 are often co-emitted from traffic-related sources (Burnett et al., 2004; Achakulwisut et al., 2019). O_3 and NO_2 are oxidants themselves, and the redox-active components of PM2.5 are known to produce oxidants (Lakey et al., 2016; Lelieveld et al., 2021). The ability to induce oxidative stress is a leading hypothesis for the health effects associated with PM2.5.

Recently, oxidative potential (OP) has appeared as an alternative metric to assess the toxicity alongside the more traditional PM2.5 mass concentration (Borm et al., 2007; Bates et al., 2015; Abrams et al., 2017; Weichenthal et al., 2016). OP assays can be categorized into those that quantify the production of oxidants (Charrier and Anastasio, 2011; Charrier et al., 2014; Tong et al., 2016, 2018) and those that evaluate the depletion of typical lung antioxidants or other reducing agents (Charrier and Anastasio, 2012; Fang et al., 2015; Tuet et al., 2017; Utinger et al., 2023; Campbell et al., 2023, 2024, 2025). Therefore, OP is related to the redox activity of air pollutants (Bates et al., 2019). In recent years, a large number of acellular assays have been developed to assess OP of PM (Cho et al., 2005; Ayres et al., 2008; Charrier and Anastasio, 2012; Fang et al., 2015; Tong et al., 2016; Calas et al., 2017; Tuet et al., 2017; Bates et al., 2019; Campbell et al., 2019;

Lin and Yu, 2019; Utinger et al., 2023; Campbell et al., 2023, 2024, 2025) although the exact methodology for the OP assays varies across different studies (Calas et al., 2017; Frezzini et al., 2022; Dominutti et al., 2025; Campbell et al., 2025). Correlation analysis and positive matrix factorization have been used to examine the relationship between OP assays and the sources of PM, as well as to identify the specific PM components that are driving OP activities (Camman et al., 2024; Shahpoury et al., 2024; Liu et al., 2025). There is, however, no clear understanding of what chemical reaction is responsible for the observed effects of PM on OP assays.

The lungs are the primary entry point for air pollution into the human body. Air pollutants can trigger and perpetuate ROS production in the epithelial lining fluid (ELF) (Gurgueira et al., 2002; Lakey et al., 2016; Shiraiwa et al., 2017). The ELF extends from the nasal cavity to the pulmonary alveoli (Mudway and Kelly, 2000) and contains a surfactant monolayer and an aqueous bulk which contains a variety of antioxidants, enzymes, and proteins (van der Vliet et al., 1999; Lakey et al., 2016).

Within the ELF, reactive oxidants can interact with biological molecules, including lipids, proteins, and antioxidants (Bachi et al., 2013). Air pollutants can chemically modify proteins in the human body and trigger oxidative stress and inflammation (Reinmuth-Selzle et al., 2017). Nitrotyrosine (Ntyr) is a type of modified amino acid that has been associated with many severe acute and chronic diseases and serves as an important biomarker of inflammation and oxidative stress (Ischiropoulos, 1998; Bandookwala et al., 2020). Ntyr is produced when tyrosine reacts with ROS/RNS forming long-lived reactive intermediates, such as the tyrosyl radical, which in turn reacts with nitrogen dioxide (Sharma and Graham, 2010; Bachi et al., 2013; Liu et al., 2017; Backes et al., 2021). The tyrosyl radical can also react with another tyrosyl radical and form dityrosine cross-links (Franze et al., 2005; Reinmuth-Selzle et al., 2014, 2017; Backes et al., 2021).

1.6. Numerical kinetic modeling of multiphase chemistry

A kinetic model framework with universally applicable rate equations and parameters for mass transport and chemical reactions was developed by Pöschl, Rudich, and Ammann (PRA framework; Pöschl et al., 2007) to achieve a detailed molecular description of interfacial processes in aerosol kinetics. Using this framework, a variety of kinetic multilayer models have been developed to describe the surface and bulk chemistry in multiphase reaction systems relevant to atmospheric aerosols. Examples include the condensation of water droplets, the formation SOA, the ozonolysis of oleic acid, the degradation of polycyclic aromatic hydrocarbons (PAH) exposed to ozone, and the photochemistry of iron-carboxylates (K2-SURF (Shiraiwa et al., 2009); KM-SUB (Shiraiwa et al., 2010; Berkemeier et al., 2016); KM-GAP (Shiraiwa et al., 2012; Berkemeier et al., 2020); PRAD (Dou et al., 2021); MultilayerPy (Milsom et al., 2022)). Kinetic models have also been used to investigate the health effects associated with aerosol particles (KM-SUB-ELF; Lakey et al., 2016). The KM-SUB-ELF model, based on the KM-SUB

model (Shiraiwa et al., 2010), accounts for the geometry of the lung and explicitly treats mass transport and chemical reactions involving air pollutants, ROS, antioxidants, and surfactants. Time-resolved adsorption and desorption of gaseous molecules into and from the ELF (e.g., O_3, NO_2, H_2O_2), diffusion, and chemical reactions within the lung has been used to estimate ROS production due to air pollution in the presence of antioxidants and enzymes (Lakey et al., 2016).

The kinetic flux models often need a large set of input parameters which are difficult to constrain by experiment (Berkemeier et al., 2017). Thus, global optimization algorithms may be necessary to infer multiple unknown kinetic parameters from experimental data sets; a process known as inverse modeling (Berkemeier et al., 2017; Milsom et al., 2022). In many inverse modeling studies, often a single parameter set from the global optimization algorithm has been presented (Lakey et al., 2016; Dou et al., 2021), although an array of diverse solutions may also exist (Berkemeier et al., 2016, 2017).

1.7. Research objectives

This PhD project spans the fields of atmospheric and physiological chemistry and makes use of the commonalities in the different fields. Oxidation reactions are important in both fields, with reactive oxygen species contributing to health effects and atmospheric chemical processing of aerosols. In order to understand the production, interconversion, and fate of oxidants, it is essential to develop an accurate description of the multiphase reaction kinetics in the atmosphere and the body. Thus, the research goal of this PhD project was to understand the complex reactions mechanism involved in the interconversion and fate of reactive oxygen species within the fields of atmospheric and physiological chemistry using kinetic models.

The specific objectives of the PhD work are summarized below:

1. Reconcile several experimental data sets of oleic acid-ozonolysis from the literature under varying experimental conditions such as reactant concentration and aerosol particle size using a single kinetic model. Investigate the uniqueness of the kinetic parameter sets and quantify the uncertainty.

2. Elucidate the interplay between phase transitions, mass transport, and chemical reaction in the photochemical system of iron carboxylate compounds. Identify mechanisms that describe this system using a common set of kinetic parameters applicable across a broad range of relative humidity in collaboration with Prof. Dr. Markus Ammann.

3. Develop a kinetic model of aerosol oxidative potential to estimate the OP based on the composition of PM for a mechanistic, process-level understanding of air pollution health effects.

4. Investigate and develop a chemical mechanism for modification of proteins in the epithelial lining fluid by reactive species formed from air pollution (PM2.5, O_3,

and NO_2) and endogenous biological sources. Quantify protein modification in the epithelial lining fluid using a chemical kinetic model.

2. Results

2.1. Overview

In the course of my dissertation, I studied oxidative processing and the health effects of atmospheric aerosols. The findings are detailed in a total of 11 manuscripts for publication in peer-reviewed scientific journals. The primary results of the PhD project are outlined in six manuscripts (three first-author and three co-author), which are included in the following sections of this chapter. Five of the papers have already been published in internationally leading journals of environmental science and physical chemistry. Additional results from this PhD project have been published in five other papers. Figure 2.1 provides an overview of the different studies and the connections between them. A summary of the main findings and conclusions of each study is provided at the beginning of each section.

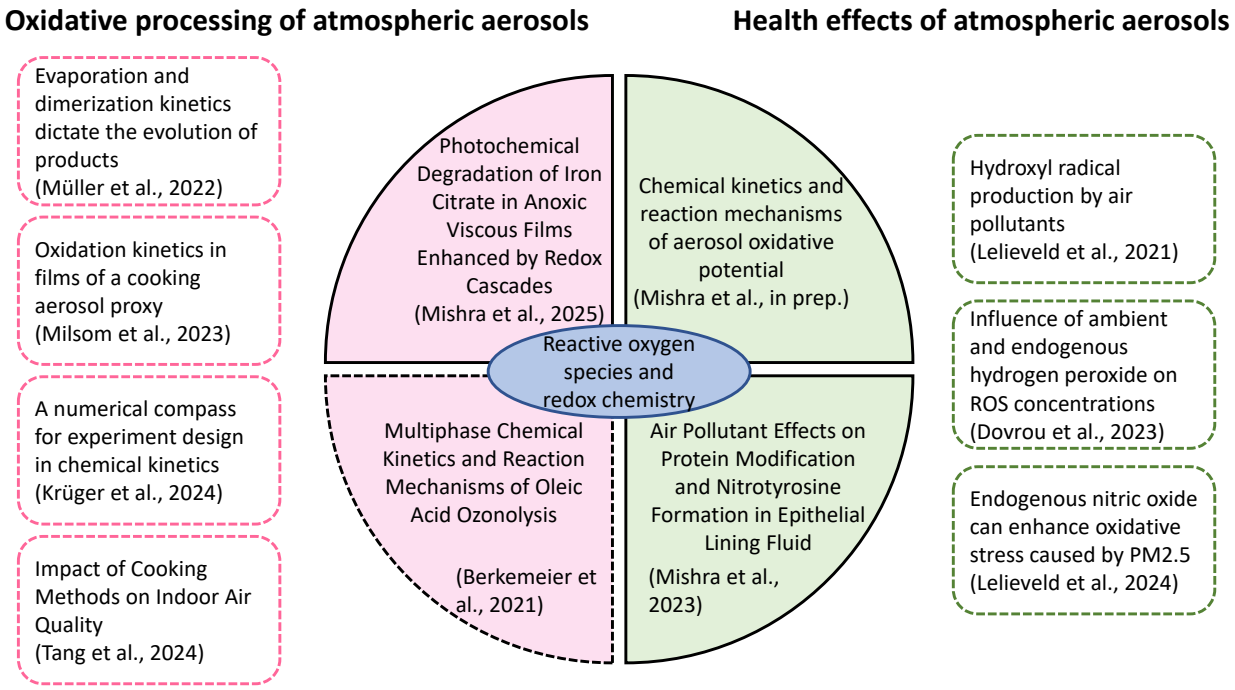

Figure 2.1.: *Overview of the results from the PhD project. Each box corresponds to a project associated with a manuscript. Solid boxes denote first-authored papers and dotted boxes represent co-authored papers.*

The studies from this work quantify the production of reactive species in atmospheric aerosols and in the epithelial lining fluid. All of the presented work involves numerical simulations, with a particular focus on chemical kinetic modeling of multiphase systems. An outline of the thesis is shown below:

Section 2.2 presents a chemical reaction mechanism to reconcile several experimental data sets of the ozonolysis of oleic acid. In this study, inverse modeling technique using kinetic multilayer models and global optimization was developed to determine the underlying kinetic parameters and a technique to quantify the uncertainty associated with the inverse modeling process using ensemble fits was presented.

Section 2.3 builds upon the kinetic model presented in section 2.2 and considers product formation during the ozonolysis of oleic acid to assess the validity of the oxidant exposure metric.

Section 2.4 investigates the impact of humidity on photochemical processing of iron carboxylates using a kinetic model. The inverse modeling technique presented in section 2.2 is used to reconcile the experimental data.

Section 2.5 presents a kinetic model that can estimate the oxidative potential based on the chemical composition of particulate matter. The inverse modeling technique discussed in section 2.2 is applied to a large set of laboratory data of reactive oxygen species (ROS) production, dithiothreitol, and ascorbic acid depletion, as well as dehydroascorbic acid formation.

Section 2.6 estimates the protein modification due to air pollutants and endogenous biological sources of ROS. This is done by developing and extending a kinetic model of the epithelial lining fluid (ELF).

Section 2.7 assesses the influence of H_2O_2 production in the ELF via ambient and endogenous sources. This study also uses the kinetic model of the ELF that was discussed in Section 2.6.

A summary of the key conclusions is presented in the final chapter, along with an outlook for future research.

2.2. Kinetic modeling of oleic acid decay during ozonolysis

The paper in this chapter has been published as a research article in the journal ACS Earth and Space Chemistry. I am the second author of this paper. I developed and optimized the kinetic model, performed the kinetic model simulations, and analyzed the model results together with Thomas Berkemeier. I also contributed to the production of the figures and to the writing of the paper. The supplement to this work can be found in Appendix B.1.

Berkemeier, T., Mishra, A., Mattei, C., Huisman, A. J., Krieger, U. K., and Pöschl, U.: Ozonolysis of Oleic Acid Aerosol Revisited: Multiphase Chemical Kinetics and Reaction Mechanisms. ***ACS. Earth. Space. Chem.*** **5, 3313-3323 (2021).**

In this study, a large set of experimental data on the ozonolysis of oleic acid was analyzed using different reaction mechanisms, with various levels of complexity. The experimental data covered an extensive range of particle sizes and ozone concentrations and were obtained with diverse experimental techniques. Mass spectrometry and Raman spectroscopy were used as detection methods. Inverse modeling using Monte Carlo methods was implemented to reconcile all available experimental data and determine the underlying kinetic parameters. A unique determination of kinetic parameters was not possible when only considering the decay of oleic acid alone. A technique to quantify the uncertainty of the inverse modeling process using ensemble fits was presented.

ACS EARTH AND SPACE CHEMISTRY

http://pubs.acs.org/journal/aesccq

Article

Ozonolysis of Oleic Acid Aerosol Revisited: Multiphase Chemical Kinetics and Reaction Mechanisms

Thomas Berkemeier,* Ashmi Mishra, Coraline Mattei, Andrew J. Huisman, Ulrich K. Krieger, and Ulrich Pöschl*

Cite This: *ACS Earth Space Chem.* 2021, 5, 3313−3323

Read Online

ACCESS | Metrics & More | Article Recommendations | Supporting Information

ABSTRACT: The chemical processing of organic aerosol particles is important for atmospheric chemistry, climate, and public health. The heterogeneous oxidation of oleic acid particles by ozone is one of the most frequently investigated model systems. The available kinetic data span a wide range of particle size and ozone concentration and are obtained with different experimental techniques including electrodynamic balance (EDB), optical tweezers, environmental chamber, and aerosol flow tube reactors using mass spectrometry and Raman spectroscopy as detection methods. Existing kinetic and mechanistic analyses, however, reveal systematic differences and inconsistencies that are a matter of ongoing debate. We developed and applied an inverse modeling approach using a kinetic multilayer model (KM-SUB) and Monte Carlo-based global optimization algorithms to 11 literature data sets and an additional new set of EDB data. We were able to reconcile most experimental data with consistent sets of multiphase chemical kinetic parameters. For a unique determination of these parameters, however, further experiments with simultaneous measurement of multiple observables at specific, insightful reaction conditions are required. We tested three different reaction mechanisms and conclude that secondary chemistry involving Criegee intermediates appears crucial to resolve the discrepancies found in earlier studies. Primary ozone chemistry occurs close to the particle surface and secondary reactions seem to dominate in the particle bulk, involving OH formation and radical chain reactions.

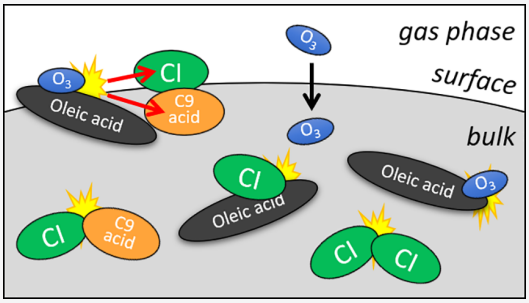

KEYWORDS: *Heterogeneous Chemistry, Aerosol, Reaction kinetics, Ozonolysis, Lipids, Inverse modeling, Criegee Intermediate, Monte Carlo*

INTRODUCTION

Atmospheric particles have an important effect on climate.[1,2] These particles influence Earth's radiative budget by scattering incoming and outgoing radiation and serve as cloud condensation nuclei.[3,4] Further, they also negatively impact human health as they can cause cardiovascular diseases upon inhalation.[5,6] Organic matter makes up a large fraction of fine particulate matter in the atmosphere and originates from biogenic and anthropogenic sources.[7,8]

Oleic acid (OL) is a monounsaturated fatty acid that is present in meat, vegetable oils, fossil fuels, and marine aerosols.[9,10] Fatty acids are a notable fraction of atmospheric aerosols in many environments.[11] Heterogenous oxidation of oleic acid by the reaction with ozone has been subject to multiple experimental and modeling studies and is considered a benchmark system for atmospheric multiphase chemistry.[12−22]

Oleic acid-ozonolysis has been investigated on liquid films[23,24] and monolayers[25] by single particle techniques such as electrodynamic balance[26] and through aerosol ensemble techniques such as environmental chamber[15] or flow tube studies.[22,27,28] In the former, a single particle is levitated and the amount of oleic acid that remains in the particle is commonly studied using Raman spectroscopy, while in the latter, the decay of oleic acid is studied by mass spectrometry.[29]

Many previous studies on heterogeneous aerosol chemistry use so-called resistor models[28,30] to investigate reactions and multiphase processes. Although these models are not computationally cumbersome, many simplifying assumptions have to be made regarding steady-state conditions and mixing. In the past decade, depth-resolved models have been developed to overcome such problems.[18,19,31−34] Deduction of input parameters such as reaction rate coefficients is often challenging as there are many parallel reactions in a system in which transport and chemical reaction are inherently coupled. In recent years, inverse modeling techniques have

Special Issue: Mario Molina Memorial

Received: June 29, 2021
Revised: November 10, 2021
Accepted: November 10, 2021
Published: November 19, 2021

been developed and applied in order to infer and constrain input parameters for kinetic models in the atmospheric sciences.[35−39] Inverse modeling is the process by which model parameters are inferred by fitting a model to experimental data. This is especially useful in order to infer model parameters that are poorly constrained through theory and experiment.

Several studies have investigated the chemical mechanism and product formation from the ozonolysis of oleic acid.[15,17,40] Besides primary oxidation of the double bond in oleic acid with ozone, secondary reactions including Criegee intermediates and hydroxyl radicals are found to not only affect the product spectrum but also to impact reaction kinetics.[28,41−43] However, reconciling the kinetics of this system using numerical models has not been achieved. Pfrang et al.,[44] Shiraiwa et al.,[18] Berkemeier et al.,[20] and Gallimore et al.[22] have previously used kinetic modeling on this system and reported kinetic parameters. However, to our knowledge there are no studies that provide a single kinetic parameter set that can be used to reconcile multiple experimental studies.

In this study, we apply a kinetic multilayer model coupled with a global optimization method[38] to find an optimal correlation between model and experiment that is able to reconcile 12 experimental data sets that have varying experimental conditions such as oxidant concentration and particle size.

METHODS

EDB Measurements. The EDB apparatus consists of a three-wall temperature-controlled glass environmental chamber containing a levitated charged particle held in place through applied electric AC and DC fields. Its operation has been described in detail elsewhere.[45,46] Briefly, a constant flow (typically 25 sccm) of ultrazero dry air with a set mixing ratio of ozone was applied to the particle; a motorized needle valve was used to maintain a pressure of 600 Torr in the chamber. Ozone was generated using a UV photometric ozone calibrator (M401, Advanced Pollution Instrumentation, Inc.). An ozone monitor (Dasibi 1008) at the outflow of the chamber was used to measure ozone concentration under high flow conditions. Such data with various flows let us conclude that with a setting of nominal 500 ppb of the ozone calibrator at most 30 ppb of ozone was lost before the outlet of the environmental chamber. As the levitated particles sits close to the inlet, however, we did not correct for any ozone loss. The cell and all tubing were flushed with ozone (1000 ppb) for 1 h before injection of the particle to passivate the surface of the apparatus. Before injection, the ozone concentration was reduced to nominal 0 ppb, and a single particle of oleic acid was injected and held in the trap for typically a few hours before switching the gas flow to a fixed ozone concentration.

Before and throughout the reaction, the particle was monitored spectroscopically to identify changes in its size and chemical composition. Raman spectroscopy was performed using an Ar-ion laser for excitation (500 mW, 488.0 nm, 240 s integration time) in a 90° scattering geometry. A holographic notch filter was used to reject the elastically scattered light and an optical fiber was employed to deliver the Raman shifted light to a 150 mm spectrograph with a slow scan backilluminated, Peltier cooled, CCD-array detector (DV420, Andor Technology). The extent of the reaction was inferred by the loss of peak area of the C = C bond stretching character at 1655 cm^{-1} normalized to the peak area of the C−H bond character at 1455 cm^{-1}. The size of the particle was monitored by Mie resonance spectroscopy,[47] which provides nanometer resolution to changes in particle size. For the particular experiment shown in Figure 2 (panel EDB1), we applied a nominal ozone mixing ratio of 500 ppb and the particle radius of particle prior to ozone exposure was measured as 9.8 ± 0.3 μm.

Kinetic Model. The kinetic modeling was performed using the kinetic multilayer model of aerosol surface and bulk chemistry KM-SUB.[18] The model compartments include a gas phase, a near-surface gas phase, a sorption layer, a quasi-static surface layer, and a number of bulk layers. The following processes were explicitly resolved for the trace gas ozone: gas-phase diffusion, adsorption, and desorption to and from the sorption layer, surface-bulk exchange, bulk diffusion as well as chemical reaction at the surface and in the bulk of the particle. Nonvolatile condensed phase chemical species, such as oleic acid, are restricted to the processes in the quasi-static surface layer and bulk of the particle. The numerical model autogenerates a script based on an input chemical mechanism and geometry and consists of a system of differential equations, representing the flux-based mass balance to and from each layer. An autogenerated Jacobian matrix is used to accelerate and increase numerical stability of the model calculations. Near the surface, narrowly spaced layers ensured a smooth concentration gradient of ozone. The thickness of these layers was determined by estimating the reacto-diffusive length of ozone in pure oleic acid (l_{rd}), where 15 layers were used to cover a spherical shell of thickness 5 times l_{rd}. Layer numbers for the remaining bulk were chosen large enough to ensure convergence of the numerical modeling result.

Global Optimization. The Monte Carlo genetic algorithm (MCGA),[38] a global optimization tool, is applied for the inverse modeling of the oleic acid−ozone multiphase kinetic system. In the process of inverse modeling, model input parameters are inferred by fitting the kinetic model to experimental observations and results. This is usually achieved by sampling the input parameter space with the model until the model output closely matches the experimental data (Figure 1). MCGA is a two-step algorithm. The first step is a Monte Carlo search where the parameters are randomly sampled from a predefined boundary range. These sampled kinetic parameter sets are evaluated by determining the residual R (as root mean squared error, RMSE, eq 1) between the model results, Y_{model}, and the experimental data, $Y_{experiment}$. All M = 12 experimental data sets and within each set, their m_j data points, are weighted equally in this study.

$$R = \sum_{j=1}^{M} \sqrt{\frac{1}{m_j} \sum_{i=1}^{m_j} \left(\frac{Y_{model}(i) - Y_{experiment}(i)}{\max(Y_{experiment})} \right)^2} \quad (1)$$

The parameter sets with lowest residual are fed into the starting population of a genetic algorithm (GA, Matlab Global Optimization Toolbox) in which they are optimized by processes mimicking survival, recombination, and mutation in evolutionary biology. The optimization is stopped when the population is homogeneous and thus the increase in correlation with the experimental data ceases. After completion of the global optimization, local optimization using golden section search is performed to ensure that the algorithm fully converged into the optimization minimum. This method is applied for model scenario A in this work.

https://doi.org/10.1021/acsearthspacechem.1c00232
ACS Earth Space Chem. 2021, 5, 3313−3323

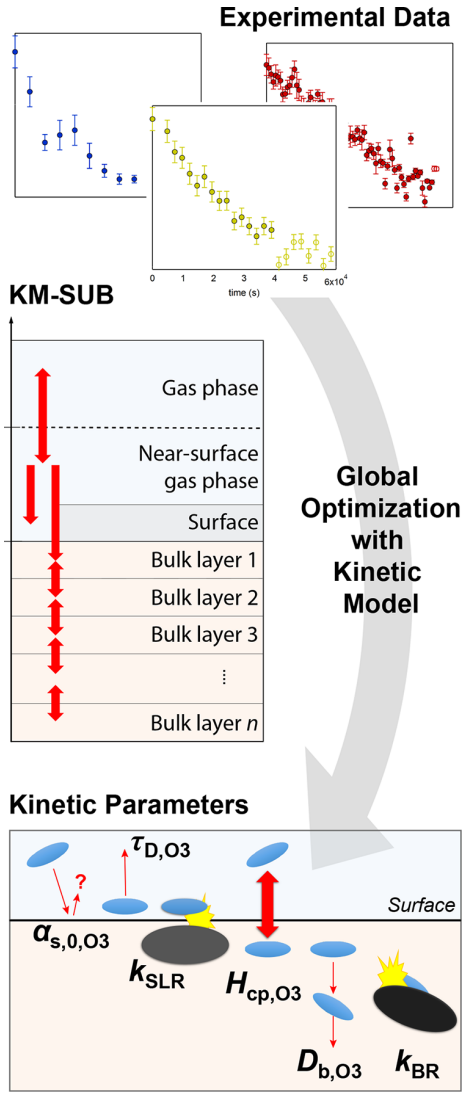

Figure 1. Inverse modeling approach employed in this study. Experimental data sets are used in conjunction with the kinetic model KM-SUB[18] and a global optimization algorithm (Monte Carlo Genetic Algorithm, MCGA,[38] or Markov Chain Monte Carlo, MCMC). Unknown kinetic parameters are sampled and improved within boundaries until a good correlation between the model output and experimental data points is achieved. Adapted from Berkemeier et al.[48] CC-BY-3.0 [2016] Royal Society of Chemistry.

Ideally, a unique fit, that is, a parameter set invariant upon repetition of the fitting process, would be obtained during optimization. However, in underdetermined optimization problems, that is, when not enough data are provided or the model contains too many or nonorthogonal parameters, a unique fit cannot be obtained.[48] In this case, it is less desirable to find a kinetic parameter set that represents a best-possible fit to data. Instead, it is valuable to determine an ensemble of sufficiently well-fitting parameter sets and extract information from the corresponding range of kinetic model solutions. "Best-possible fit" is used here for the parameter set with the lowest residual after multiple executions of the fitting algorithm. We use the term "sufficiently well-fitting" for parameter sets with a residual within a few percent of the best-possible fit. The exact number can be chosen according to the experimental error so that uncertainty in model parameters will also reflect experimental uncertainty. MCGA is not an efficient tool to explore the solution space since only few inverse modeling results can be obtained during the lengthy optimization method. In this case, Markov chain Monte Carlo (MCMC) methods deliver a higher throughput to obtain numerous sufficiently well-fitting solutions, albeit with reduced capability of finding best-possible solutions. The Metropolis–Hastings (MH) algorithm, for example, performs a random walk across the multidimensional input parameter space.[49,50] Individual steps of the random walk are accepted or rejected based on a simple rule of acceptance. In this work, we use the residual between model results and experimental data to determine the acceptance ratio. A decrease in residual always leads to acceptance, whereas an increase in residual from R_1 to R_2 (i.e., $R_2 > R_1$) will be rejected in $100 \times \left(1 - \frac{R_1}{R_2}\right)$ percent of all cases. This method is applied for model scenario B in this work.

RESULTS AND DISCUSSION

The kinetic model multilayer model KM-SUB is applied to a compilation of 12 experimental data of the oleic acid–ozone heterogeneous reaction system, including a new study of oleic acid ozonolysis using the EDB. Of these 12, 7 data sets use single-particle methods and were analyzed using Raman spectroscopy (SP-R), while five data sets use aerosol-ensemble methods that were analyzed using mass spectrometry (AE-MS). An overview over all data sets is given in Table 1.

In the inverse modeling approach, correlation between model and experimental data is achieved using the Monte Carlo genetic algorithm (MCGA) or the Metropolis-Hastings (MH) algorithm. However, in none of the simulations presented in this study is a unique fit to the experimental data achieved. Thus, instead of using single optimized parameter sets, a range of sufficiently well-fitting parameter sets is obtained by repeated execution of the MCGA or MH algorithms. Model output is then analyzed using the ensemble of parameter sets that the kinetic model allows, given the experimental constraints. The optimized "best fit" parameter sets from MCGA are used as a guideline for the best-possible model-experiment correlation. In general, model-experiment correlation increases with the complexity and hence the number of flexible parameters of the kinetic model, while the uniqueness of the determined kinetic parameter set decreases. For this purpose, we use three different chemical mechanisms of increasing complexity and discuss what information can be inferred from each inverse modeling scenario. The modeling scenarios include a simple mechanism (scenario A), a mechanism including the secondary chemistry of Criegee intermediates (scenario B), and a mechanism including radical-chain autoxidation chemistry (scenario C).

Scenario A: Simple Mechanism. In scenario A, oleic acid ozonolysis is treated as one concerted bimolecular reaction step at the surface or in the bulk of the aerosol particle forming unreactive product

$$O_3 + OL \rightarrow \text{product} \quad \text{(R1)}$$

Most of the mass transport properties of oleic acid and ozone remain fixed during the global optimization, as only the desorption lifetime of ozone at the particle surface ($\tau_{D,03}$) is used as fitting parameter. Together with the accommodation coefficient $\alpha_{s,0,03}$ and the effective surface cross-section of an

https://doi.org/10.1021/acsearthspacechem.1c00232
ACS Earth Space Chem. 2021, 5, 3313–3323

Table 1. Environmental Input Parameters for KM-SUB Used with the 12 Experimental Data Sets[a]

	r_{out} (cm)	r_{in} (cm)	T (K)	$[O_3]_g$ (cm^{-3})	method	reference
EDB1	1.0×10^{-3}		290.5	1×10^{13}	SP-R	this study
EDB2	$2.0-3.5 \times 10^{-3}$		296	6.4×10^{12}	SP-R	Lee and Chan[26]
EDB3	$2.0-3.5 \times 10^{-3}$		296	6.4×10^{12}	SP-R	Lee and Chan[26]
EC1	2.0×10^{-5}		296	7.0×10^{13}	AE-MS	Ziemann[15]
OT1	5.6×10^{-4}	2.1×10^{-4}	298	1.5×10^{13}	SP-R	Dennis-Smither et al.[51]
OT2	5.9×10^{-4}	2.2×10^{-4}	298	4.1×10^{13}	SP-R	Dennis-Smither et al.[51]
OT3	4.9×10^{-4}	1.8×10^{-4}	304	1.4×10^{14}	SP-R	Dennis-Smither et al.[51]
OT4	6.0×10^{-4}	2.1×10^{-4}	297	5.1×10^{14}	SP-R	Dennis-Smither et al.[51]
FT1	4.0×10^{-5}		298	2.5×10^{15}	AE-MS	Hearn and Smith[27]
FT2	2.5×10^{-5}		293	2.0×10^{14}	AE-MS	Gallimore et al.[27]
FT3	2.5×10^{-5}		293	3.25×10^{14}	AE-MS	Gallimore et al.[22]
FT4	2.5×10^{-5}		293	5.51×10^{14}	AE-MS	Gallimore et al.[22]

[a]Outer particle radius r_{out}, inner particle radius of coated particles r_{in}, temperature T, and ozone gas phase concentration $[O_3]_g$. Short names for the experimental data sets indicate the experimental apparatus: electrodynamic balance (EDB), optical tweezers (OT), environmental chamber (EC), or aerosol flow tube (FT). The data sets are grouped into single particle−Raman-based techniques (SP-R) and aerosol ensemble−mass spectrometry techniques (AE-MS). As particle radii r_{out} were not determined in Lee and Chan,[26] they have been used as fitting parameter within the given constraints. All other environmental input parameters remained fixed during the model optimization process.

Table 2. Kinetic Input Parameters for KM-SUB and Their Optimization Boundaries to Fit 12 Available Experimental Data Sets According to Scenario A and B[a]

	parameter range		
parameter	scenario A	scenario B	description
k_{SLR1} ($cm^2\ s^{-1}$)	$10^{-15}-10^{-9}$	$10^{-15}-10^{-9}$	surface reaction rate coefficient (R1, R6)
k_{SLR2} (s^{-1})		$10^{-5}-10^{1}$	surface reaction rate coefficient (R2)
k_{SLR3} ($cm^2\ s^{-1}$)		$10^{-15}-10^{-9}$	surface reaction rate coefficient (R3)
k_{SLR4} ($cm^2\ s^{-1}$)		$10^{-15}-10^{-9}$	surface reaction rate coefficient (R4, R5)
k_{BR1} ($cm^3\ s^{-1}$)	$10^{-18}-10^{-12}$	$10^{-18}-10^{-12}$	bulk reaction rate coefficient (R1, R6)
k_{BR2} (s^{-1})		$10^{-5}-10^{1}$	bulk reaction rate coefficient (R2)
k_{BR3} ($cm^3\ s^{-1}$)		$10^{-18}-10^{-12}$	bulk reaction rate coefficient (R3)
k_{BR4} ($cm^3\ s^{-1}$)		$10^{-18}-10^{-12}$	bulk reaction rate coefficient (R4, R5)
$\alpha_{s,\ 0,O3}$	[0.1]	$10^{-3}-1$	surface accommodation coefficient of O_3
$D_{b,O3}$ ($cm^2\ s^{-1}$)	$[1 \times 10^{-6}]$	$[1 \times 10^{-6}]$	bulk diffusion coefficient of O_3 in OL
$D_{b,OL}$ ($cm^2\ s^{-1}$)	$[1.9 \times 10^{-7}]$	$[1.9 \times 10^{-7}]$	self-diffusion coefficient of OL
$H_{cp,O3}$ (mol cm^{-3} atm^{-1})	$[4.8 \times 10^{-4}]$	$[4.8 \times 10^{-4}]$	Henry's law solubility coeff. of O_3 in OL
$\tau_{D,O3}$ (s^{-1})	$10^{-9}-10^{-3}$	$10^{-9}-10^{-3}$	desorption lifetime of O_3
$r_{out,EDB2}$ (μm)	20−35	20−35	particle radius for EDB2
$r_{out,EDB3}$ (μm)	20−35	20−35	particle radius for EDB3

[a]Values that were fixed during the fitting procedures are marked with square brackets.

O_3 molecule σ_{O3}, the desorption lifetime determines the equilibrium surface concentration of ozone in KM-SUB. Further parameters that remained fixed during the global optimization include the diffusion coefficients of ozone ($D_{b,O3}$) and oleic acid ($D_{b,OL}$) as well as the Henry's law solubility coefficient of ozone, $H_{cp,O3}$. A list of all model input parameters used in this study is given in Table 2.

Thus, including the surface and bulk reaction rate coefficients, only three kinetic parameters and two environmental parameters (particle radii for EDB2 and EDB3 experiments) were used as fitting parameters in scenario A. Note that opening ranges of other mass-transport parameters within physical limits did not improve model-experiment correlation significantly.

Even with this simple mechanism and narrow constraints, the model shows a good correlation with many experimental data sets (black dashed lines in Figure 2). Multiple executions of the MCGA yield kinetic parameter sets with near-identical model-experiment correlations (residual ∼0.114). In general, model-experiment correlation is higher for the flow-tube studies (FT1−4) as the initial decay of oleic acid is overestimated for many of the experiments employing single-particle techniques (EDB1,3, OT1−3). The good correlation for experiment EDB2 is likely achieved due to fitting of the particle radius. We see that the model underestimates the loss of oleic acid for experimental data set EC1. This environmental chamber data combines a comparatively low ozone concentration (200 ppb) with comparatively small particle radii (mean radius 200 nm). Note however, that this data set was measured using polydisperse particles with an unknown width and shape of the particle size distribution. KM-SUB operates with a single particle size, which was set to the particle radius reported in the original publication. Shadings in Figure S1 indicate the sensitivity of the model to this effective mean diameter (100−200 nm).

Note that additional experimental data of OL ozonolysis was available from literature, but after consultation with the original authors it was omitted from the global optimization. These data sets deviated from the remaining pool of data and could not be reconciled with the kinetic model. The data sets are

https://doi.org/10.1021/acsearthspacechem.1c00232
ACS Earth Space Chem. 2021, 5, 3313−3323

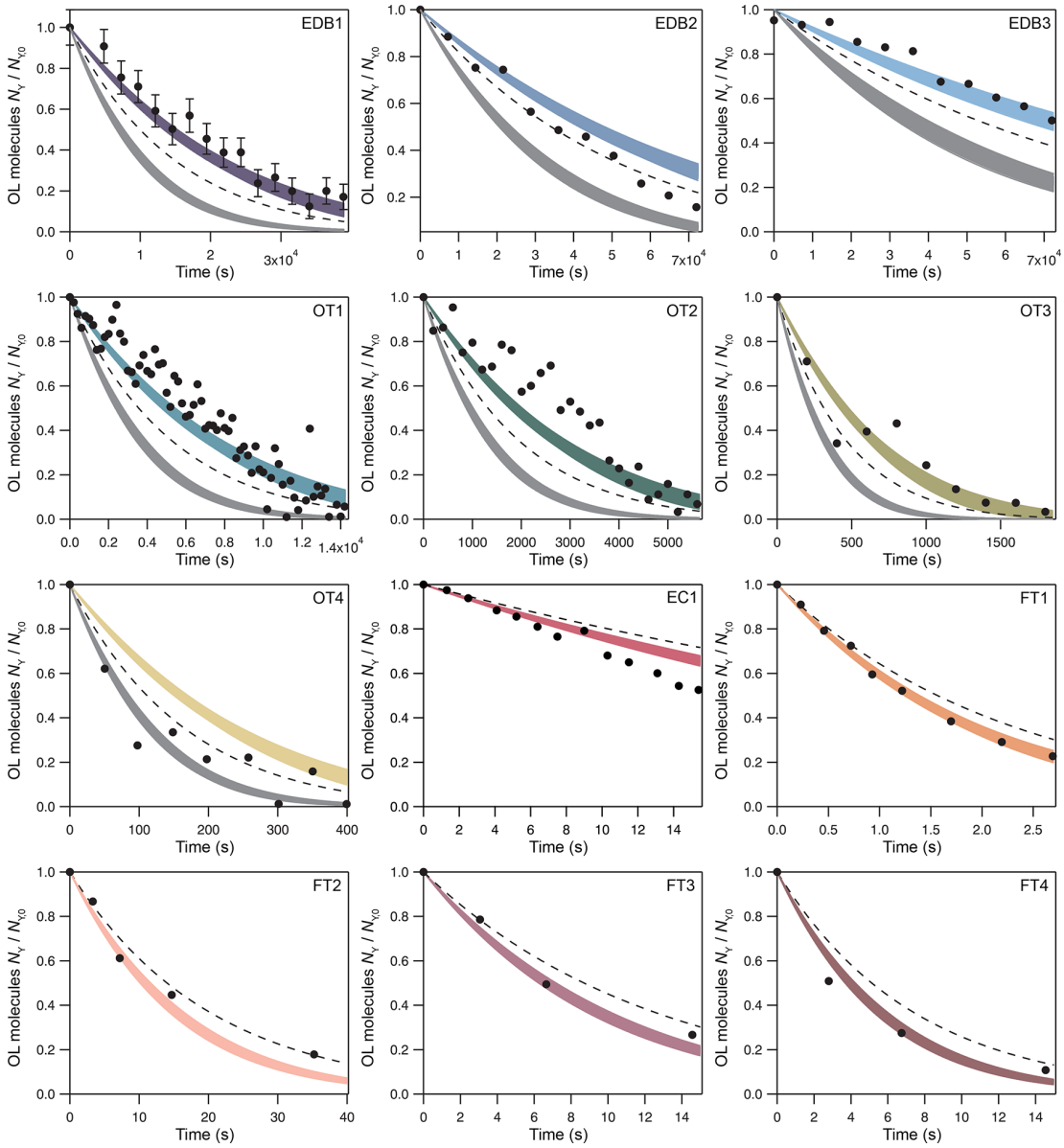

Figure 2. KM-SUB modeling results obtained from fitting to 12 different experimental data sets (markers). Short names for the experimental data sets indicate the experimental apparatus: electrodynamic balance (EDB), optical tweezers (OT), environmental chamber (EC), or aerosol flow tube (FT). Black dashed lines indicates the model output for modeling scenario A. Colored lines show the model results for an ensemble of $N = 167$ fits under modeling scenario B. Gray lines show the model results without consideration of the oleic acid-CI adduct, OL* in experimental data using Raman spectroscopy.

shown together with the model result in Figure S2. At this point, we can only speculate whether a shortcoming of the model or uncertainty in the experiment causes this deviation.

For modeling scenario A, all model simulations fall within the S_{rx} regime, that is, reactive turnover is achieved through surface reaction and limited by chemical reaction rates.[20] This is in agreement with Hearn et al.,[28] who proposed a (near)-surface reaction mechanism. Note that the definition of a surface reaction may deviate from study to study. Here, only a chemical reaction of surface-adsorbed ozone with the (quasi-static) oleic acid surface monolayer is classified as surface reaction. It was not possible to obtain a similar model-experiment correlation with a significant contribution of bulk chemistry. This can be understood with the surface-to-volume ratio of particles in the investigated experimental data sets. A larger contribution of bulk chemistry would, relatively, accelerate oleic acid loss in large particles (with low surface-to-volume-ratio) while decreasing oleic acid loss in the smaller particles. Since oleic acid decay in the larger particles is already overestimated by the model, a stronger contribution of bulk chemistry would hence only decrease model-experiment correlation.

The diversity of kinetic parameter sets obtained in the global optimization of scenario A ($N = 30$) is displayed in Figure 3. Only for one out of three kinetic parameters, k_{BR1}, is a unique solution obtained. In addition, this parameter adopts a value at the very edge of its lower optimization boundary. As discussed above, the best fit is obtained when k_{BR1} is minimal, causing

https://doi.org/10.1021/acsearthspacechem.1c00232
ACS Earth Space Chem. 2021, 5, 3313−3323

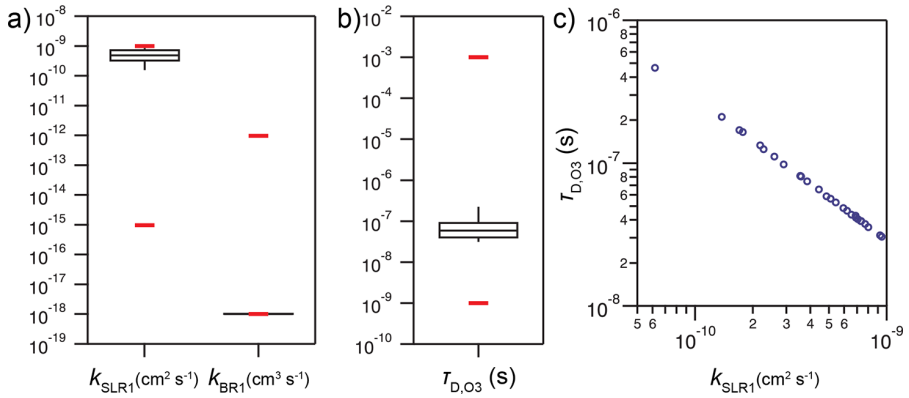

Figure 3. Parameters determined using the MCGA from fitting to experimental data under modeling scenario A (N = 30 fits). (a) Surface and bulk reaction rate coefficients of R1 (OL + O_3 → product), (b) surface desorption lifetime of O_3. The box-whisker plots display the 10, 25, 50, 75, 90 percentiles for each parameter. (c) Interdependence between OL + O_3 surface reaction rate coefficient and desorption lifetime of ozone. The red lines show the upper and lower fitting boundaries.

oleic acid loss to almost exclusively occur at the particle surface. This stands in contrast to common estimates of the bulk reaction rate coefficient, which is reported in the range of 1×10^{-15} cm^3 s^{-1} from bulk liquid experiments.[52] The other two fit parameters show a codependence as detailed in Figure 3c, where an increase in k_{SLR1} can be compensated with a decreases in $\tau_{D,03}$.

In the following, we will investigate how inclusion of secondary chemistry is able to increase model−experiment correlation and resolve inconsistencies in the obtained kinetic model results.

Scenario B: Secondary Chemistry. Quantum-mechanical calculations in the gas phase[53] and product formation studies of the heterogeneous oleic acid−ozone system[15,17,22] have stated that Criegee intermediates (CI) are able to react with a carboxylic acid functional group and loss of OL to CI has been inferred to account for 36% of primary oleic acid loss.[28] For scenario B, we employ an explicit chemical reaction mechanism detailing secondary chemistry with Criegee intermediates at the surface and in the bulk of oleic acid particles

$$O_3 + OL \rightarrow CI + \frac{1}{2}C9\text{-acid} + \frac{1}{2}NN \quad (R1b)$$

$$CI \rightarrow C9\text{-acid} \quad (R2)$$

$$CI + CI \rightarrow \text{diperoxide} \quad (R3)$$

$$CI + C9\text{-acid} \rightarrow AAHP \quad (R4)$$

$$CI + OL \rightarrow OL^* \quad (R5)$$

$$O_3 + OL^* \rightarrow CI + \frac{1}{2}C9\text{-acid} + \frac{1}{2}NN \quad (R6)$$

Here, ozonolysis of OL forms a CI, a stable C9-acid molecule (e.g., oxo-nonanoic acid) and nonanal (NN, R1). NN is assumed to evaporate instantaneously. CI can either isomerize to C9-acid (e.g., nonanoic acid, azelaic acid, R2), react with another CI to diperoxide (R3), or react with C9-acid forming an α-acyloxyalkyl hydroperoxide (AAHP) (R4). Both peroxides are treated as unreactive products in this study. Reaction of CI with the acid moiety of OL forms OL* (R5), an AAHP that still retains the double bond. This substituted alkene reacts similarly to OL with ozone but will likely not be detected as OL in a mass spectrometer. The experimental data sets use two different detection techniques: mass spectrometry (EC1, FT1−4) and Raman spectroscopy (EDB1−3, OT1−4). In the Raman-based experiments, the vibrational mode of the OL* double bond will still be detected and count OL* as OL. This difference in experimental techniques is taken into account in calculating model output by adding the concentrations of OL and OL* for analysis of Raman-based experimental data.

The rate coefficients of reactions R1−R4 are used as model fitting parameters for both surface and bulk reaction (Table 2). R6 is assumed to have the same rate coefficient as R1; similarly, reactions R4 and R5 are assumed to occur with the same rate coefficient. Wide parameter boundaries were chosen for the reaction rate coefficients to allow for a free fit. Compared to scenario A, the increased number of fit parameters in scenario B causes a much greater degeneracy of kinetic parameter sets that fit the experimental data within experimental uncertainty. Hence, instead of determining few optimally fitting parameter sets, we find an ensemble of parameter sets yielding sufficiently good correlation (N = 167, residual <0.108) with the Metropolis−Hastings algorithm. Figure 2 shows these model results for scenario B in the colored solid lines. The degeneracy of model fits can be observed by the spread in model result. Note that although for singular experimental data sets a model fit might appear strictly worse than others, this fit likely scores better for other experimental conditions. Figure S3a shows the kinetic parameters of model fits with residual <0.112 (N = 3995) in a scatter matrix. While some weak relationships between parameters can be identified, no parameter can be uniquely determined. The most pronounced relationship between parameters is found for k_{SLR1} and $\tau_{D,O3}$, as already seen in modeling scenario A.

The bulk reaction rate coefficient of O_3 with OL, k_{BR1}, shows a pronounced peak at 3×10^{-17} cm^3 s^{-1} and no parameter set exceeds $k_{BR1} = 4 \times 10^{-17}$ cm^3 s^{-1}. This value is much smaller than previously reported for the bulk liquid[52] or used in model calculations[9,18,22] but in line with values obtained previously in kinetic model fits to single experimental data sets.[20] Note that the peak vanishes when filtering for better model-experiment correlation (<0.108, N = 167, Figure S3b). We interpret this finding in the following way: on the optimization hypersurface,

https://doi.org/10.1021/acsearthspacechem.1c00232
ACS Earth Space Chem. 2021, 5, 3313−3323

there are larger shallow areas around the local minimum for bulk reaction cases because the primary oxidation chemistry in the bulk is only determined by a single parameter. In contrast, the primary oxidation chemistry on the surface is dependent on two parameters, k_{SLR1} and $\tau_{D,O3}$, which makes the optimization minimum more difficult to find in an MC search.

In order to understand why most kinetic parameters cannot be uniquely determined, we perform a systematic sensitivity study on the ensemble of parameter sets. For all 167 parameter sets, normalized sensitivity coefficients S_i^n are determined using small, local variations of parameter i.[20,54] As the objective function for the sensitivity study, we use the time to reach 10% loss of oleic acid, t_{90}.

$$S_i^n = \frac{\log \Delta t_{90}}{\log \Delta i} \quad (2)$$

Figure 4 reveals the results of the sensitivity analysis. Parameters associated with primary surface reaction, k_{SLR1}, $\tau_{D,O3}$, and $\alpha_{s,0,O3}$ are most sensitive. Parameters associated with primary bulk reaction, k_{BR1}, $D_{b,O3}$, and $H_{cp,O3}$ have a smaller, but nonzero influence on the model result. Remarkably, parameters associated with secondary chemistry, that is, k_{BR2-4} and k_{SLR2-4}, have a negligible influence on oleic acid loss. The latter result is surprising but can be explained with a dominant reaction of CI with acid moieties (C9-acid, OL; R4, R5) compared to unimolecular or bimolecular decomposition of the CI (R2, R3), see discussion below.

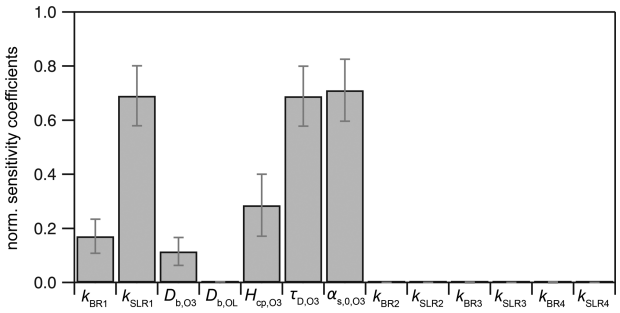

Figure 4. Sensitivity study on KM-SUB input parameters under modeling scenario B. Sensitivities are calculated according to eq 2 using the time to reach 10% reaction progress, averaged over all 12 experimental scenarios. Error bars correspond to standard deviations of sensitivity coefficients among N = 167 kinetic parameter sets. Note that parameters $D_{b,O3}$, $D_{b,OL}$, and $H_{cp,O3}$ were fixed during optimization in this study.

The diversity of the four kinetic parameters with the highest sensitivity coefficients in the global optimization of scenario B (N = 167) is displayed in Figure 5. The surface and bulk reaction rate coefficients of the primary OL oxidation, k_{SLR1} and k_{BR1}, assume values toward the ceiling and floor of their fitting boundaries, respectively (Figure 5a). The surface desorption lifetime and surface accommodation coefficient of O_3, $\tau_{D,O3}$, and $\alpha_{s,0,O3}$, appear to follow no clear trend within their fitting boundaries (Figure 5b,c). However, it is possible to obtain an empirical relationship between these four fitting parameters (Figure 5d), which suffice the following equation as verified in Figure 5d

$$k_{SLR1} \cdot k_{BR1}^{0.396} \cdot \tau_{D,O3} \cdot \alpha_{s,0,O3} = 1.8 \times 10^{-25} \quad (3)$$

Despite the low sensitivity of kinetic parameters of secondary chemistry, the overall model-experiment correlation is improved compared to modeling scenario A with the incorporation of secondary chemistry in modeling scenario B. Most notably, for the single particle-Raman data sets (EDB1−3, OT1−4), all experiments except OT4 show an improved fit when OL* is also attributed to the signal. The effect of not attributing OL* to the Raman signal is shown in the ensemble of gray solid lines in Figure 2 for which OL decay is significantly too fast. Compared to model scenario A, the relative acceleration of the MS-based data sets in model scenario B causes a shift in the share of the surface reaction in total OL loss ($L_{s,OL,R1}/(L_{s,OL,R1} + L_{b,OL,R1})$), which indicates the dominant location of primary OL loss and is shown for all experimental data sets in Figure 6a using box-whisker plots. While in the majority of fits most of OL is lost at the surface, there is a large variability within sufficiently well-fitting parameter sets, ranging from less than 0.5 to more than 0.8 between the 10th and 90th percentile of model fits, respectively. The share of surface reaction increases with decreasing particle radius (EC and FT experiments). In contrast to this primary ozone chemistry, secondary chemistry takes place mostly in the bulk of particles (Figure S4) due to

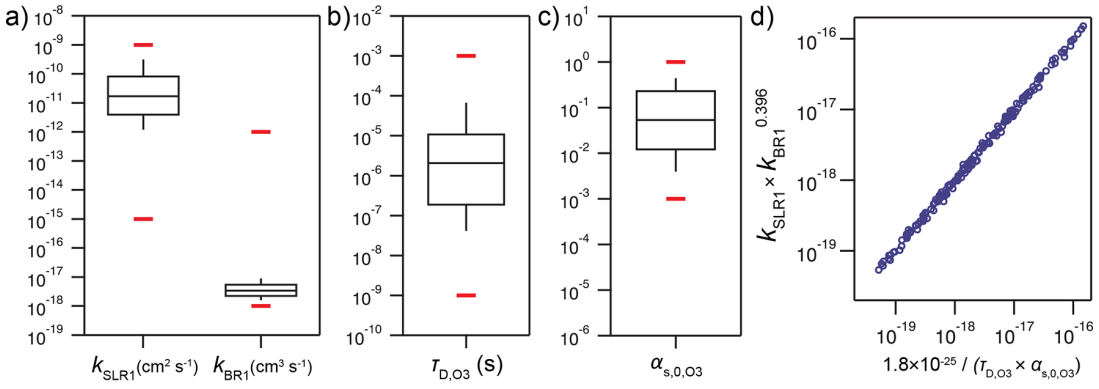

Figure 5. Parameters determined from fitting to experimental data under modeling scenario B (N = 167 fits). (a) Surface and bulk reaction rate coefficients of R1 (OL + O_3 → product), (b) surface desorption lifetime of O_3, (c) surface accommodation coefficient of O_3. The box-whisker plots display the 10, 25, 50, 75, 90 percentiles for each parameter. (d) Interdependence between k_{SLR1}, k_{BR1}, $\tau_{D,O3}$, and $\alpha_{s,0,O3}$. The red lines show the upper and lower fitting boundaries.

https://doi.org/10.1021/acsearthspacechem.1c00232
ACS Earth Space Chem. 2021, 5, 3313−3323

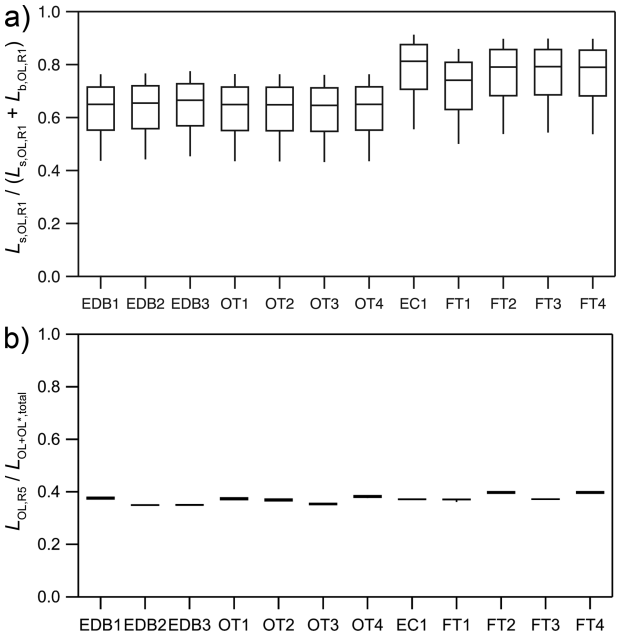

Figure 6. Aggregate KM-SUB model outputs for an ensemble of N = 167 fits to 12 experimental data sets using modeling scenario B. (a) The share of primary surface chemistry, R1 (O_3 + OL), in total primary OL loss and (b) the share of secondary Criegee chemistry, R5 (CI + OL), in total OL and OL* loss. The box-whisker plots display the 10, 25, 50, 75, and 90 percentiles for each model output value.

the longer lifetime and bulk solubility of CI compared to ozone.

Figure 6b shows the fraction of secondary chemistry (CI + OL, R5) in total turnover of OL and OL* ($L_{OL,R5}$/($L_{OL+OL^*,\,total}$). Our model results are comparable to the values estimated by Hearn et al.,[28] who propose that 36 ± 4% of OL loss is due to this secondary chemistry. We find a range of 35−40% with minimal variance between data sets. A more detailed breakdown of CI fate is given in Supporting Information (Figure S5).

Scenario C: Radical-chain chemistry. The decomposition of Criegee intermediates is known to produce hydroxyl radicals (OH) in the gas phase,[55] and this process has been found to be of importance for condensed phase ozonolysis.[42,43] This secondarily produced OH may add to the double bond, or abstract hydrogens from the aliphatic carbon chain. These reactions result in alkyl radicals (R), which quickly react with O_2, forming organic peroxy radicals (RO_2). These more stable radicals can in turn form CI, hereby closing the loop of a radical chain autoxidation mechanism[42,43] in which a single ozone molecule in theory is able to oxidize multiple equivalents of OL. We implement a simplified version of the chemical mechanism presented in Zeng and Wilson[42] into our kinetic model. In our model, the reaction of alkyl radicals with oxygen is not explicitly resolved but rather assumed to occur instantaneously for simplicity. The full chemical mechanism for modeling scenario C is shown in Supporting Information, Table S1. Because of the increased number of chemical reactions, it is even less likely to find a unique kinetic parameter than in modeling scenario B. Additionally, the increased computational cost associated with introduction of further chemical species makes global optimization increasingly difficult. Here, we explore the effect of including secondary OH production and a radical-chain mechanism on model-experiment correlation. A more comprehensive inverse modeling analysis will be subject to follow up studies.

Using this more complex chemical mechanism, very similar model-experiment correlations to the 12 experimental data sets are obtained (residual ∼0.105), that is, the fit is neither significantly improved nor worsened compared to modeling scenario B. Note, however, that the experimental data set used in this study only comprises OL decay data. While the behavior of the OL loss rate across experimental conditions may be invariant between these two reaction mechanisms, the O_3 consumption associated with each modeling scenario is not. Figure 7 shows that while modeling scenario A always returns a

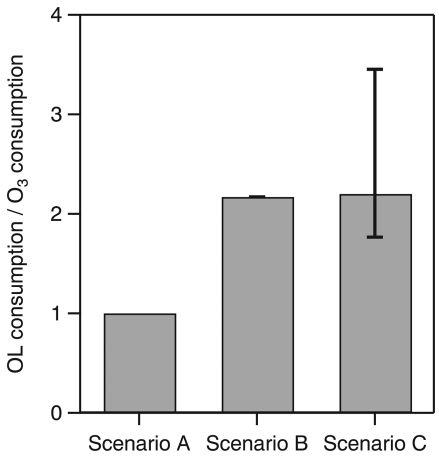

Figure 7. Ratio of OL and O_3 consumption for all three modeling scenarios presented in this study: simple mechanism (scenario A), secondary Criegee chemistry (scenario B); and radical chain chemistry involving secondarily produced OH (scenario C). Values are for conditions of experiment EDB1. Error bars are the 5th and 95th percentile of fits obtained from global optimization of 12 experimental data sets.

1:1 ratio of OL and O_3 consumption, and modeling scenario B fairly consistently leads to ratios of ∼2:1, in modeling scenario C up to 3.5 OL molecules are consumed. In these cases, as little as 28% of OL are consumed by direct reaction with O_3. The other 72% are then consumed by reaction with CI (8%), OH (36%), and alkoxy radicals RO (28%). These numbers remain fairly consistent over the range of experimental conditions. This is in line with the observations of Sage et al.[41] and Mendez et al.[56] who saw up to 3.75 and up to 4 molecules of OL lost per O_3, respectively. In our model, this value depends on the relative rates of the radical recombination reaction RO_2 + RO_2 versus the decomposition of RO_2 to CI, which were allowed to differ from the template mechanism during global optimization. Without experimental data on O_3 consumption, however, these parameters and the resulting OL/O_3 consumption ratios remain unconstrained in the inverse modeling.

■ CONCLUSIONS

This study shows an application of inverse modeling on a large set of experimental data of the oleic acid−ozone heterogeneous reaction system in three different modeling scenarios. For the first time, a model with a single kinetic parameter set leads to good agreement with such a large set of experimental data.

https://doi.org/10.1021/acsearthspacechem.1c00232
ACS Earth Space Chem. 2021, 5, 3313−3323

Previously, fits had only been obtained for single data sets[18,20,38] or a single parameter needed to remain flexible between data sets.[22] This is achieved through incorporation of explicit secondary chemistry involving Criegee intermediates, advances in global optimization methods that work with complex and underdetermined models and crucially a separate treatment of Raman-based and MS-based experimental data. Nonetheless, some experimental data (OT4) still could not be reconciled with the other data in the kinetic model. This may be due to measurement uncertainty, uncertainty in environmental parameters (O_3 concentration, particle radius), measurement artifacts, or a general shortcoming of the model.

Reaction rate coefficients of the three different reaction mechanisms constitute the optimization parameters in the inverse modeling approach: a simple mechanism with a single chemical reaction, a mechanism with seven chemical reactions including secondary chemistry, and a radical-chain mechanism with a total of 29 chemical reactions (11 unique rate coefficients). With increasing complexity of the chemical mechanism, the uniqueness of the obtained kinetic parameter set is reduced. Results from the inverse fitting process are treated as aggregate solution from an ensemble of fitting parameter sets. Despite the indeterminacy of the kinetic parameter sets, the aggregate solution predicts system parameters such as the share of secondary Criegee chemistry in total OL loss (Figure 6b) and the OL to O_3 consumption ratio (Figure 7), which are not inherently constrained by the input experimental data. The method has the additional advantage that experimental uncertainty and uncertainty related to parameter optimization are directly reflected in the model result and propagate to conditions outside the probed range. The uncertainty of these predictions, however, grows with the complexity of reaction mechanisms and hence the number of fitting parameters.

The inverse modeling shows that the bulk reaction rate coefficient of the OL + O_3 reaction k_{BR1} cannot exceed 4×10^{-17} cm^3 s^{-1} within the model constraints, which stands in contrast to much higher rate coefficients reported for oleic acid ozonolysis. Note here that most mass transport properties of the reaction system remained fixed in this inverse modeling study and a higher k_{BR1} could theoretically be realized if mass transport effects were limiting O_3 uptake into the particle or OL replenishment to the particle surface. Diffusion coefficients remained at the best guesses for unreacted oleic acid and it is possible that formation of oxidized and oligomeric products reduces the viscosity of the organic aerosol droplet, which may lead to mass transfer limitations.[57,58] We will further test this hypothesis in follow-up studies, however, a majority of the experiments show a fairly linear OL concentration−time profile, which does not suggest the onset of mass transport limitation over the course of the reaction.

The remaining uncertainties in kinetic parameters are challenging to resolve without targeted laboratory experiments or quantum-chemical calculations. For example, simultaneous measurement of the concentrations of both reactants, O_3 and OL, would likely lead to a much more constrained model fit. Similarly, including different types of experimental data already available in the literature, such as product formation, should further constrain the model fit. Model calculations as presented in this work can help finding suitable conditions for experiments that have the highest chances of reducing the remaining uncertainty associated with kinetic parameters of the reaction system. The ensemble of suitable model fits can be applied to experimental conditions (e.g., ozone concentration, particle radius), which have not been investigated previously. The degeneracy in model solutions then is an empirical measure for the usefulness of the corresponding experiment: if the spread in model solutions becomes large, an experiment at the probed experimental conditions would narrow down kinetic parameter uncertainty. Figure S6 provides an example of this process. It shows that an experiment with 10 nm particles and an O_3 concentration of 3 ppm (10^{15} cm^{-3}, panel a) would be much more beneficial than an experiment with 100 μm particles at 30 ppt O_3 (10^{10} cm^{-3}, panel b).

The ozonolysis of alkenes is not only important for atmospheric chemistry but also for human health.[59] Cell membranes and the lipid layer on top of the epithelial lining fluid contain unsaturated compounds and are exposed to ozone.[60−62] This study and other recent studies[42,43] point toward a large amount of reactive intermediates and radicals generated in alkene ozonolysis which might give rise to lipid peroxidation and *in vivo* production of hazardous reactive (oxygen) species. Thus, due to the wealth of data that are already available for oleic acid ozonolysis, it is a particularly useful reaction system to use in conjunction with kinetic modeling and draw conclusions regarding health effects of air pollution. Because of open questions regarding reaction rate coefficients and radical yield, it remains a relevant and interesting modeling system with many implications for atmospheric chemistry and health. We suggest that further studies should be conducted by, for example, monitoring O_3 loss, product formation, and by quantitative detection of reactive intermediates (e.g., with spin trapping techniques) to further constrain modeling studies and consolidate our knowledge about this important chemical reaction system.

■ ASSOCIATED CONTENT

Supporting Information

The Supporting Information is available free of charge at https://pubs.acs.org/doi/10.1021/acsearthspacechem.1c00232.

Figure S1 shows two experimental data that were omitted from global optimization; Figure S2 shows the effect of effective particle radius on model output for experiment EC1; Figure S3 shows the kinetic parameter sets derived from optimization according to modeling scenario B; Figure S4 shows the contribution of surface reactions to secondary chemistry in modeling scenario B; Figure S5 shows details on the fate of Criegee intermediates in modeling scenario B; Figure S6 shows the model output for two additional experimental conditions that have not been investigated previously. Table S1 shows the chemical mechanism used for modeling scenario C (PDF)

■ AUTHOR INFORMATION

Corresponding Authors

Thomas Berkemeier − *Multiphase Chemistry Department, Max Planck Institute for Chemistry, 55128 Mainz, Germany;* orcid.org/0000-0001-6390-6465; Email: t.berkemeier@mpic.de

Ulrich Pöschl − *Multiphase Chemistry Department, Max Planck Institute for Chemistry, 55128 Mainz, Germany;* orcid.org/0000-0003-1412-3557; Email: u.poschl@mpic.de

https://doi.org/10.1021/acsearthspacechem.1c00232
ACS Earth Space Chem. 2021, 5, 3313−3323

Authors

Ashmi Mishra − *Multiphase Chemistry Department, Max Planck Institute for Chemistry, 55128 Mainz, Germany*

Coraline Mattei − *Multiphase Chemistry Department, Max Planck Institute for Chemistry, 55128 Mainz, Germany*

Andrew J. Huisman − *Institute for Atmospheric and Climate Science, ETH Zurich, 8092 Zürich, Switzerland;* Present Address: Gentex Corporation, Applied Engineering Department, 600 N Centennial St., Zeeland, MI 49464, U.S.A

Ulrich K. Krieger − *Institute for Atmospheric and Climate Science, ETH Zurich, 8092 Zürich, Switzerland;* orcid.org/0000-0003-4958-2657

Complete contact information is available at: https://pubs.acs.org/10.1021/acsearthspacechem.1c00232

Funding

Open access funded by Max Planck Society.

Notes

The authors declare no competing financial interest.

■ ACKNOWLEDGMENTS

This article is dedicated to Nobel laureate Mario J. Molina and his outstanding engagement and achievements for the benefits of science and humanity. We gratefully acknowledge C. Chan, J. P. Reid, G. D. Smith, and P. J. Ziemann for providing published data in tabulated form. We would like to thank T. Peter, G. D. Smith, P. J. Ziemann, J. A. H. Wilson, and H. G. Kang for fruitful discussions.

■ REFERENCES

(1) Carslaw, K. S.; Boucher, O.; Spracklen, D. V.; Mann, G. W.; Rae, J. G. L.; Woodward, S.; Kulmala, M. A review of natural aerosol interactions and feedbacks within the Earth system. *Atmos. Chem. Phys.* **2010**, *10*, 1701−1737.

(2) *IPCC, Climate Change 2013, The Physical Science Basis*; Cambridge University Press: Cambridge, United Kingdom, 2013.

(3) Lohmann, U.; Feichter, J. Global indirect aerosol effects: a review. *Atmos. Chem. Phys.* **2005**, *5*, 715−737.

(4) Steiner, A. L.; Mermelstein, D.; Cheng, S. J.; Twine, T. E.; Oliphant, A. Observed Impact of Atmospheric Aerosols on the Surface Energy Budget. *Earth Interact.* **2013**, *17*, 1−22.

(5) Shiraiwa, M.; Selzle, K.; Pöschl, U. Hazardous components and health effects of atmospheric aerosol particles: reactive oxygen species, soot, polycyclic aromatic compounds and allergenic proteins. *Free Radical Res.* **2012**, *46*, 927−939.

(6) Pöschl, U.; Shiraiwa, M. Multiphase Chemistry at the Atmosphere−Biosphere Interface Influencing Climate and Public Health in the Anthropocene. *Chem. Rev.* **2015**, *115*, 4440−4475.

(7) Kanakidou, M.; et al. Organic aerosol and global climate modelling: a review. *Atmos. Chem. Phys.* **2005**, *5*, 1053−1123.

(8) Jimenez, J. L.; et al. Evolution of Organic Aerosols in the Atmosphere. *Science* **2009**, *326*, 1525−1529.

(9) Zahardis, J.; Petrucci, G. A. The oleic acid-ozone heterogeneous reaction system: products, kinetics, secondary chemistry, and atmospheric implications of a model system - a review. *Atmos. Chem. Phys.* **2007**, *7*, 1237−1274.

(10) Fu, P. Q.; Kawamura, K.; Chen, J.; Charrière, B.; Sempéré, R. Organic molecular composition of marine aerosols over the Arctic Ocean in summer: contributions of primary emission and secondary aerosol formation. *Biogeosciences* **2013**, *10*, 653−667.

(11) Tervahattu, J. J. K. K. H. Identification of an organic coating on marine aerosol particles by TOF-SIMS. *J. Geophys. Res.* **2002**, *107*, ACH 18-1−ACH18-7.

(12) Thornberry, T.; Abbatt, J. P. D. Heterogeneous reaction of ozone with liquid unsaturated fatty acids: detailed kinetics and gas-phase product studies. *Phys. Chem. Chem. Phys.* **2004**, *6*, 84−93.

(13) Morris, J. W.; Davidovits, P.; Jayne, J. T.; Jimenez, J. L.; Shi, Q.; Kolb, C. E.; Worsnop, D. R.; Barney, W. S.; Cass, G. Kinetics of submicron oleic acid aerosols with ozone: A novel aerosol mass spectrometric technique. *Geophys. Res. Lett.* **2002**, *29*, 71-1−71-4.

(14) King, M. D.; Thompson, K. C.; Ward, A. D. Laser Tweezers Raman Study of Optically Trapped Aerosol Droplets of Seawater and Oleic Acid Reacting with Ozone: Implications for Cloud-Droplet Properties. *J. Am. Chem. Soc.* **2004**, *126*, 16710−16711.

(15) Ziemann, P. J. Aerosol products, mechanisms, and kinetics of heterogeneous reactions of ozone with oleic acid in pure and mixed particles. *Faraday Discuss.* **2005**, *130*, 469−90.

(16) Hung, H.-M.; Ariya, P. Oxidation of Oleic Acid and Oleic Acid/Sodium Chloride(aq) Mixture Droplets with Ozone: Changes of Hygroscopicity and Role of Secondary Reactions. *J. Phys. Chem. A* **2007**, *111*, 620−632.

(17) Vesna, O.; Sax, M.; Kalberer, M.; Gaschen, A.; Ammann, M. Product study of oleic acid ozonolysis as function of humidity. *Atmos. Environ.* **2009**, *43*, 3662−3669.

(18) Shiraiwa, M.; Pfrang, C.; Pöschl, U. Kinetic multi-layer model of aerosol surface and bulk chemistry (KM-SUB): the influence of interfacial transport and bulk diffusion on the oxidation of oleic acid by ozone. *Atmos. Chem. Phys.* **2010**, *10*, 3673−3691.

(19) Shiraiwa, M.; Pfrang, C.; Koop, T.; Pöschl, U. Kinetic multi-layer model of gas-particle interactions in aerosols and clouds (KM-GAP): linking condensation, evaporation and chemical reactions of organics, oxidants and water. *Atmos. Chem. Phys.* **2012**, *12*, 2777−2794.

(20) Berkemeier, T.; Huisman, A. J.; Ammann, M.; Shiraiwa, M.; Koop, T.; Pöschl, U. Kinetic regimes and limiting cases of gas uptake and heterogeneous reactions in atmospheric aerosols and clouds: a general classification scheme. *Atmos. Chem. Phys.* **2013**, *13*, 6663−6686.

(21) Al-Kindi, S. S.; Pope, F. D.; Beddows, D. C.; Bloss, W. J.; Harrison, R. M. Size-dependent chemical ageing of oleic acid aerosol under dry and humidified conditions. *Atmos. Chem. Phys.* **2016**, *16*, 15561−15579.

(22) Gallimore, P. J.; Griffiths, P. T.; Pope, F. D.; Reid, J. P.; Kalberer, M. Comprehensive modeling study of ozonolysis of oleic acid aerosol based on real-time, online measurements of aerosol composition. *J. Geophys. Res. Atmos.* **2017**, *122*, 4364−4377.

(23) Moise, T.; Rudich, Y. Reactive Uptake of Ozone by Aerosol-Associated Unsaturated Fatty Acids: Kinetics, Mechanism, and Products. *J. Phys. Chem. A* **2002**, *106*, 6469−6476.

(24) Knopf, D. A.; Anthony, L. M.; Bertram, A. K. Reactive Uptake of O3 by Multicomponent and Multiphase Mixtures Containing Oleic Acid. *J. Phys. Chem. A* **2005**, *109*, 5579−5589.

(25) King, M. D.; Rennie, A. R.; Thompson, K. C.; Fisher, F. N.; Dong, C. C.; Thomas, R. K.; Pfrang, C.; Hughes, A. V. Oxidation of oleic acid at the air−water interface and its potential effects on cloud critical supersaturations. *Phys. Chem. Chem. Phys.* **2009**, *11*, 7699−7707.

(26) Lee, A. K. Y.; Chan, C. K. Single particle Raman spectroscopy for investigating atmospheric heterogeneous reactions of organic aerosols. *Atmos. Environ.* **2007**, *41*, 4611−4621.

(27) Hearn, J. D.; Smith, G. D. Kinetics and Product Studies for Ozonolysis Reactions of Organic Particles Using Aerosol CIMS. *J. Phys. Chem. A* **2004**, *108*, 10019−10029.

(28) Hearn, J. D.; Lovett, A. J.; Smith, G. D. Ozonolysis of oleic acid particles: evidence for a surface reaction and secondary reactions involving Criegee intermediates. *Phys. Chem. Chem. Phys.* **2005**, *7*, 501−11.

(29) Morris, J. W.; Davidovits, P.; Jayne, J. T.; Jimenez, J. L.; Shi, Q.; Kolb, C. E.; Worsnop, D. R.; Barney, W. S.; Cass, G. Kinetics of submicron oleic acid aerosols with ozone: A novel aerosol mass spectrometric technique. *Geophys. Res. Lett.* **2002**, *29*, 71-1−71-4.

(30) Worsnop, D. R.; Morris, J. W.; Shi, Q.; Davidovits, P.; Kolb, C. E. A chemical kinetic model for reactive transformations of aerosol particles. *Geophys. Res. Lett.* **2002**, *29*, 57.
(31) Smith, G. D.; Woods, E.; Baer, T.; Miller, R. E. Aerosol uptake described by numerical solution of the diffusion - Reaction equations in the particle. *J. Phys. Chem. A* **2003**, *107*, 9582−9587.
(32) Wilson, K. R.; Smith, J. D.; Kessler, S. H.; Kroll, J. H. The statistical evolution of multiple generations of oxidation products in the photochemical aging of chemically reduced organic aerosol. *Phys. Chem. Chem. Phys.* **2012**, *14*, 1468−1479.
(33) Roldin, P.; Eriksson, A. C.; Nordin, E. Z.; Hermansson, E.; Mogensen, D.; Rusanen, A.; Boy, M.; Swietlicki, E.; Svenningsson, B.; Zelenyuk, A.; Pagels, J. Modelling non-equilibrium secondary organic aerosol formation and evaporation with the aerosol dynamics, gas- and particle-phase chemistry kinetic multilayer model ADCHAM. *Atmos. Chem. Phys.* **2014**, *14*, 7953−7993.
(34) Houle, F. A.; Hinsberg, W. D.; Wilson, K. R. Oxidation of a model alkane aerosol by OH radical: the emergent nature of reactive uptake. *Phys. Chem. Chem. Phys.* **2015**, *17*, 4412−4423.
(35) Partridge, D. G.; Vrugt, J. A.; Tunved, P.; Ekman, A. M. L.; Gorea, D.; Sorooshian, A. Inverse modeling of cloud-aerosol interactions − Part 1: Detailed response surface analysis. *Atmos. Chem. Phys.* **2011**, *11*, 7269−7287.
(36) Partridge, D. G.; Vrugt, J. A.; Tunved, P.; Ekman, A. M. L.; Struthers, H.; Sorooshian, A. Inverse modelling of cloud-aerosol interactions − Part 2: Sensitivity tests on liquid phase clouds using a Markov chain Monte Carlo based simulation approach. *Atmos. Chem. Phys.* **2012**, *12*, 2823−2847.
(37) Lowe, S.; Partridge, D. G.; Topping, D.; Stier, P. Inverse modelling of Köhler theory − Part 1: A response surface analysis of CCN spectra with respect to surface-active organic species. *Atmos. Chem. Phys.* **2016**, *16*, 10941−10963.
(38) Berkemeier, T.; Ammann, M.; Krieger, U. K.; Peter, T.; Spichtinger, P.; Pöschl, U.; Shiraiwa, M.; Huisman, A. J. Technical note: Monte Carlo genetic algorithm (MCGA) for model analysis of multiphase chemical kinetics to determine transport and reaction rate coefficients using multiple experimental data sets. *Atmos. Chem. Phys.* **2017**, *17*, 8021−8029.
(39) Tikkanen, O.-P.; Hämäläinen, V.; Rovelli, G.; Lipponen, A.; Shiraiwa, M.; Reid, J. P.; Lehtinen, K. E. J.; Yli-Juuti, T. Optimization of process models for determining volatility distribution and viscosity of organic aerosols from isothermal particle evaporation data. *Atmos. Chem. Phys.* **2019**, *19*, 9333−9350.
(40) Reynolds, J. C.; Last, D. J.; McGillen, M.; Nijs, A.; Horn, A. B.; Percival, C.; Carpenter, L. J.; Lewis, A. C. Structural Analysis of Oligomeric Molecules Formed from the Reaction Products of Oleic Acid Ozonolysis. *Environ. Sci. Technol.* **2006**, *40*, 6674−6681.
(41) Sage, A. M.; Weitkamp, E. A.; Robinson, A. L.; Donahue, N. M. Reactivity of oleic acid in organic particles: changes in oxidant uptake and reaction stoichiometry with particle oxidation. *Phys. Chem. Chem. Phys.* **2009**, *11*, 7951−7962.
(42) Zeng, M.; Wilson, K. R. Efficient Coupling of Reaction Pathways of Criegee Intermediates and Free Radicals in the Heterogeneous Ozonolysis of Alkenes. *J. Phys. Chem. Lett.* **2020**, *11*, 6580−6585.
(43) Zeng, M.; Heine, N.; Wilson, K. R. Evidence that Criegee intermediates drive autoxidation in unsaturated lipids. *Proc. Natl. Acad. Sci. U. S. A.* **2020**, *117*, 4486−4490.
(44) Pfrang, C.; Shiraiwa, M.; Pöschl, U. Coupling aerosol surface and bulk chemistry with a kinetic double layer model (K2-SUB): oxidation of oleic acid by ozone. *Atmos. Chem. Phys.* **2010**, *10*, 4537−4557.
(45) Krieger, U. K.; Colberg, C. A.; Weers, U.; Koop, T.; Peter, T. Supercooling of single H2SO4/H2O aerosols to 158 K: No evidence for the occurrence of the octrahydrate. *Geophys. Res. Lett.* **2000**, *27*, 2097−2100.
(46) Steimer, S. S.; Krieger, U. K.; Te, Y.-F.; Lienhard, D. M.; Huisman, A. J.; Luo, B. P.; Ammann, M.; Peter, T. Electrodynamic balance measurements of thermodynamic, kinetic, and optical aerosol properties inaccessible to bulk methods. *Atmos. Meas. Tech.* **2015**, *8*, 2397−2408.
(47) Zardini, A. A.; Krieger, U. K.; Marcolli, C. White light Mie resonance spectroscopy used to measure very low vapor pressures of substances in aqueous solution aerosol particles. *Opt. Express* **2006**, *14*, 6951−6962.
(48) Berkemeier, T.; Steimer, S. S.; Krieger, U. K.; Peter, T.; Pöschl, U.; Ammann, M.; Shiraiwa, M. Ozone uptake on glassy, semi-solid and liquid organic matter and the role of reactive oxygen intermediates in atmospheric aerosol chemistry. *Phys. Chem. Chem. Phys.* **2016**, *18*, 12662−12674.
(49) Metropolis, N.; Rosenbluth, A. W.; Rosenbluth, M. N.; Teller, A. H.; Teller, E. Equation of State Calculations by Fast Computing Machines. *J. Chem. Phys.* **1953**, *21*, 1087−1092.
(50) Hastings, W. K. Monte Carlo sampling methods using Markov chains and their applications. *Biometrika* **1970**, *57*, 97−109.
(51) Dennis-Smither, B. J.; Hanford, K. L.; Kwamena, N. O.; Miles, R. E.; Reid, J. P. Phase, morphology, and hygroscopicity of mixed oleic acid/sodium chloride/water aerosol particles before and after ozonolysis. *J. Phys. Chem. A* **2012**, *116*, 6159−68.
(52) Lisitsyn, D. M.; Razumovskii, S. D.; Tishenin, M.; Titov, V. N. Kinetic parameters of oxidation of individual fatty acids with ozone. *Bull. Exp. Biol. Med.* **2004**, *138*, 457−459.
(53) Vereecken, L. The reaction of Criegee intermediates with acids and enols. *Phys. Chem. Chem. Phys.* **2017**, *19*, 28630−28640.
(54) Saltelli, A.; Ratto, M.; Andres, T.; Campolongo, F.; Cariboni, J.; Gatelli, D.; Saisana, M.; Tarantola, S. *Global Sensitivity Analysis. The Primer*; John Wiley & Sons, Ltd, 2007.
(55) Atkinson, R.; Aschmann, S. M. Hydroxyl radical production from the gas-phase reactions of ozone with a series of alkenes under atmospheric conditions. *Environ. Sci. Technol.* **1993**, *27*, 1357−1363.
(56) Mendez, M.; Visez, N.; Gosselin, S.; Crenn, V.; Riffault, V.; Petitprez, D. Reactive and Nonreactive Ozone Uptake during Aging of Oleic Acid Particles. *J. Phys. Chem. A* **2014**, *118*, 9471−9481.
(57) Pfrang, C.; Shiraiwa, M.; Pöschl, U. Chemical ageing and transformation of diffusivity in semi-solid multi-component organic aerosol particles. *Atmos. Chem. Phys.* **2011**, *11*, 7343−7354.
(58) King, M. D.; Jones, S. H.; Lucas, C. O. M.; Thompson, K. C.; Rennie, A. R.; Ward, A. D.; Marks, A. A.; Fisher, F. N.; Pfrang, C.; Hughes, A. V.; Campbell, R. A. The reaction of oleic acid monolayers with gas-phase ozone at the air water interface: the effect of sub-phase viscosity, and inert secondary components. *Phys. Chem. Chem. Phys.* **2020**, *22*, 28032−28044.
(59) Pryor, W. A.; Squadrito, G. L.; Friedman, M. The cascade mechanism to explain ozone toxicity: The role of lipid ozonation products. *Free Radical Biol. Med.* **1995**, *19*, 935.
(60) Mudway, I.; Kelly, F. Ozone and the lung: a sensitive issue. *Mol. Aspects Med.* **2000**, *21*, 1−48.
(61) Lakey, P. S. J.; Berkemeier, T.; Tong, H.; Arangio, A. M.; Lucas, K.; Pöschl, U.; Shiraiwa, M. Chemical exposure-response relationship between air pollutants and reactive oxygen species in the human respiratory tract. *Sci. Rep.* **2016**, *6*, 32916.
(62) Lelieveld, S.; Wilson, J.; Dovrou, E.; Mishra, A.; Lakey, P. S. J.; Shiraiwa, M.; Poschl, U.; Berkemeier, T. Hydroxyl Radical Production by Air Pollutants in Epithelial Lining Fluid Governed by Interconversion and Scavenging of Reactive Oxygen Species. *Environ. Sci. Technol.* **2021**, *55*, 14069−14079.

https://doi.org/10.1021/acsearthspacechem.1c00232
ACS Earth Space Chem. 2021, 5, 3313−3323

2.3. Kinetic modeling of product formation in the ozonolysis of oleic acid

The paper in this chapter has been published as a research article in the journal Physical Chemistry Chemical Physics. I am the second author of this paper. I optimized the kinetic model and performed the kinetic model simulations. I analyzed the model results together with the co-authors. I also contributed to the production of the figures and to the writing of the paper.

Müller, M., Mishra, A., Berkemeier, T., Hausammann, E., Peter, T., Krieger, U. K.: Electrodynamic balance–mass spectrometry reveals impact of oxidant concentration on product composition in the ozonolysis of oleic acid ***Phys. Chem. Chem. Phys.*** **24, 27086-27104 (2022).**

In this study, a new dataset was presented which not only considered the decay of oleic acid, but also the evolution of reaction products at two different oxidant concentrations using electrodynamic balance mass spectrometry. The decay rate of oleic acid as a function of ozone exposure (oxidant concentration multiplied by reaction time) was indifferent to ozone concentration, however the product formation was not. The kinetic model showed a competition between the evaporation of first-generation products and the formation of secondary products. At a higher ozone mixing ratio, a higher momentary Criegee intermediate concentration favored the formation of secondary ozonides over evaporation, leading to a higher signal of the reaction product in the mass spectrometer.

PCCP

ROYAL SOCIETY OF CHEMISTRY

PAPER

View Article Online
View Journal | View Issue

Cite this: *Phys. Chem. Chem. Phys.*, 2022, **24**, 27086

Electrodynamic balance–mass spectrometry reveals impact of oxidant concentration on product composition in the ozonolysis of oleic acid

Marcel Müller, *[a] Ashmi Mishra, [b] Thomas Berkemeier, [b] Edwin Hausammann, [a] Thomas Peter [a] and Ulrich K. Krieger *[a]

The chemical and physical properties of atmospheric aerosol particles change upon oxidative ageing, influencing their interaction with radiation, their propensity to serve as nuclei for cloud condensation and ice formation, and their adverse effects on human health. The investigation of atmospheric aerosol oxidation processes is complicated by low oxidant concentrations and long timescales, which are difficult to represent in laboratory studies. Experimental work often attempts to compensate for short timescales with elevated concentrations of oxidative agents, assuming that the ageing progress depends only on the oxidant exposure, *i.e.* on the product of oxidant concentration and time, [Ox] × *t*, and not on [Ox] or *t* independently. The application of electrodynamic balance–mass spectrometry of single particles allows the validity of this assumption to be investigated, since it provides information on the molecular composition of aerosol particles for a wide range of reaction durations under well-defined oxidation conditions. Here, we demonstrate the capabilities of a new setup on levitated oleic acid droplets reacting with ozone at mixing ratios of 0.2 and 15 ppm, *i.e.* spanning almost two orders of magnitude in [Ox]. We show that the reactive removal of oleic acid can be accurately expressed as a function of ozone exposure [Ox] × *t*, whereas the product concentrations depend on [Ox] and *t* independently. As the underlying reason for the breakdown of the exposure metric, we suggest a competition between evaporation of volatile first-generation products and their accretion reactions with reactive Criegee intermediates, converting them into low-volatility dimers and oligomers. This hypothesis is supported by kinetic model simulations using the aerosol process model KM-SUB, which explicitly resolves the competition between evaporation and secondary chemistry as a function of the experimental timescale and ozone mixing ratio. The model successfully reproduces final product distributions. The findings are further supported by the recorded changes of droplet sizes during oxidation. As a heuristic, the breakdown of the exposure metric in a chemical reaction system is possible, when competition between first- and second-order processes of reactive intermediates determines important system properties.

Received 18th July 2022,
Accepted 26th October 2022

DOI: 10.1039/d2cp03289a

rsc.li/pccp

1 Introduction

Oxidative ageing of atmospheric aerosol particles affects the constituents in terms of molecular weight and functional groups, which is reflected in different physicochemical properties such as the oxidation state, refractive index, vapour pressure or solubility. The reaction products may differ substantially from their parent compounds, which affects the relevant properties of these particles in terms of their radiative effects and their impact on human health. Most laboratory studies on aerosol ageing use significantly elevated oxidant concentrations and relatively short exposure times to study chemical reactions within aerosol particles. The assumption in these studies is that oxidant exposure (the product of oxidant concentration and reaction time) can be used as a metric for the particle ageing progress, regardless of the applied oxidant concentration.

There are only a handful of examples in the literature where the application of the exposure metric is thoroughly assessed.[1–5] In some of these studies, the exposure metric fails to represent different oxidant concentrations. For example, in modelling palmitic acid oxidation, the results differed when a short reaction time with high OH radical mixing ratio was

[a] *Institute for Atmospheric and Climate Science, ETH Zurich, Universitätstrasse 16, 8092 Zurich, Switzerland. E-mail: marcel.mueller@env.ethz.ch, ulrich.krieger@env.ethz.ch*
[b] *Multiphase Chemistry Department, Max Planck Institute for Chemistry, 55128 Mainz, Germany*

assumed instead of a long reaction with low OH mixing ratio, due to surface renewal and secondary chemistry processes.[2] In a laboratory study on the oxidation of squalane with chlorine, the exposure metric failed due to the occurrence of radical chain reactions.[4] In another experimental study, the dominating degradation pathway of linoleic acid depended on the ozone concentration, which led to different product distributions for the same exposure.[5] These examples show that high oxidant concentrations in short experiments may lead to significantly different ratios of reaction product concentrations or even different species compared to natural atmospheric oxidant concentrations, hence biasing data interpretation.

Oleic acid has been intensively studied in the context of atmospheric aerosol ageing. As a mono-unsaturated fatty acid, it has served in numerous studies as a proxy compound for organic aerosol matter susceptible to reacting with atmospheric ozone.[6–12] A chemical mechanism of oleic acid ozonolysis, including the principal secondary reactions, is given in Fig. 1 (from top up to and including the white box). Oleic acid reacts with ozone to form a short-lived primary ozonide (reaction R1), which decays into Criegee intermediates (CI) and aldehydes (R2a and R2b).[17] Because of the asymmetry of the primary ozonide, two different aldehydes (nonanal and 9-oxononanoic acid) and two CI (denoted with the m/z of the deprotonated species, CI-157 and CI-187) are formed. CI can undergo rearrangements to form the corresponding acids (nonanoic acid and azelaic acid, *via* R3a and R3b).[18] Both the acids and the aldehydes together are referred to here as first-generation products. Instead of undergoing rearrangements, the CI may also react with other functional groups, forming dimers and higher oligomers.[7,9,10,18,19] Reactions with acids (to form α-acyloxyalkyl hydroperoxides, AAHPs, R4) and reactions with aldehydes (to form secondary ozonides, SOZs, R5) are suggested in the literature to form secondary products.

A wide variety of experiments on oleic acid ozonolysis using different experimental setups and reaction conditions were recently compiled by Berkemeier *et al.*[20] Using a numerical model explicitly treating molecular transport and chemical reactions on the surface and in the bulk of the particle, the authors were able to describe the reactive loss of oleic acid over reaction times varying from a few seconds to 20 h with associated ozone concentrations varying between 240 ppb and 100 ppm ozone. However, Berkemeier *et al.*[20] had to rely on data from very different experimental techniques with their own subtleties, most of which are able to explore only a narrow range of oxidant concentration. Moreover, most of these studies focused on the loss of oleic acid itself rather than on products. Some studies grouped secondary products into categories such as peroxides, higher molecular weight compounds or unidentified products.[7,18,21,22] Very few studies aimed to (semi-)quantitatively follow the evolution of secondary chemistry products.[9,10,12]

In this study, we use single oleic acid droplets levitated in an electrodynamic balance (EDB) in combination with mass spectrometry (MS) to showcase compositional monitoring of droplets aged under strongly differing oxidant concentrations, and we investigate the validity of the exposure metric for this reaction system.

2 Instrumentation and method

An emerging tool for the detailed study of aerosol processes is the combination of an EDB with MS.[23–31] Trapping droplets in an EDB allows the contactless storage and examination of particles over hours and days under well-defined experimental conditions.[32] Transfer of the stored droplets to an MS unit allows to infer the particle composition at the time of ejection. Such a system is therefore well-suited to compare oxidation reactions with very different oxidant mixing ratios.

A schematic overview of our newly built setup is given in Fig. 2. The interested reader is referred to Appendix A, which contains a detailed description of the instrumentation and describes the typical experimental procedure. Very briefly, oleic acid particles are produced from solutions using an inkjet cartridge and charged inductively by a DC ring electrode at the time of injection. In the linear quadrupole type EDB, droplets are contained in an electrodynamic field and exposed to a controlled gas phase (T, p, RH) with known ozone mixing ratio. Size information is obtained by measuring the 2-D angular scattering pattern of laser-illuminated droplets before the experiment and during ageing of the droplets. Because the droplets can be stored in the EDB over extended reaction times of several days, complete oxidation of oleic acid has been achieved with ozone mixing ratios as low as 0.2 ppm. Complementary experiments have been carried out at an ozone mixing ratio of 15 ppm. All experiments were carried out under dry conditions (RH $<$ 15%). For the droplet composition analysis, single droplets are transferred to a heated evaporation unit, and the resulting gas-phase compounds are ionised in a very soft dielectric barrier discharge ion source prior to MS measurements using a triple quadrupole QTRAP instrument. The temperature of the evaporation unit was set at 190 °C because it allows the evaporation of most substances within a reasonable time frame and, hence, produces a signal that is well distinguishable from the background. However, elevated temperatures may lead to thermal decomposition depending on the thermal stability of the analyte.

In contrast to the previous EDB–MS setup described by Birdsall *et al.*,[23] the efficiency of droplet transfer from the EDB to the evaporation unit was significantly increased by introducing a gas flow through the EDB at the time of droplet transfer. Thus, in the present study MS data have been successfully obtained from every exposed droplet. Additionally, changing from a Corona discharge to dielectric barrier discharge ionisation reduced analyte fragmentation in the ion source substantially.

3 Results and discussion

3.1 Unreacted oleic acid droplets

The spectrum of an unreacted oleic acid droplet is shown in Fig. 3a and a more detailed version including information about the background subtraction is given in Fig. 8d in Appendix A.

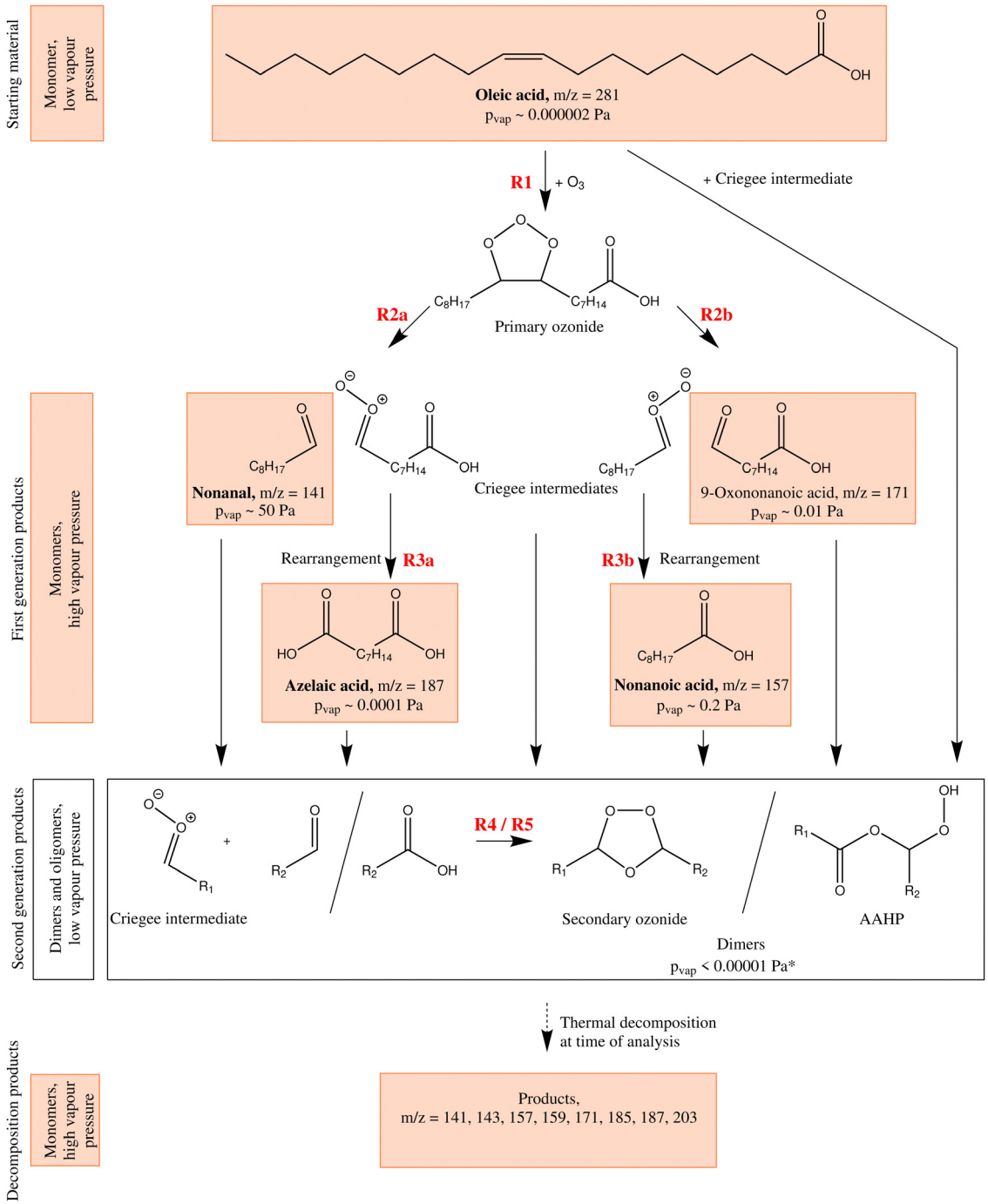

Fig. 1 Simplified reaction scheme of the ozonolysis of oleic acid. The general temporal development goes from top (oleic acid) to bottom (secondary products being thermally decomposed at time of analysis). Note that the aerosol ageing results in primary chemistry (leading to first-generation products) and secondary chemistry (leading to dimers, exemplarily summarised in the white box) whereas the final thermal decomposition is an effect of particle composition analysis. Not shown is the reaction of ozone with the dimer from the reaction of oleic acid with a Criegee intermediate. Stable monomer structures tentatively detected with MS in this study are shown in orange boxes with the *m*/*z* corresponding to deprotonated molecules. Commercially available substances are depicted with bold names. Vapour pressure for azelaic acid, nonanal, nonanoic acid and oleic acid are literature values,[13–15] all other vapour pressures are estimated using EVAPORATION.[16] *Only the secondary ozonide with two unfunctionalised alkyl rests is predicted to have a significant vapour pressure (~0.001 Pa) but is not expected to be a major aerosol constituent since its formation results from the reaction with the very volatile nonanal.

The most prominent peak is found at *m*/*z* 281, corresponding to the deprotonated oleic acid. It is accompanied by the isotope signal from oleic acid with one ^{13}C at *m*/*z* 282. Further peaks are detected at *m*/*z* 85, 87, and 101 but their signal intensities are more than three times lower than the corresponding background signal intensities (see Appendix A). These peaks indicate

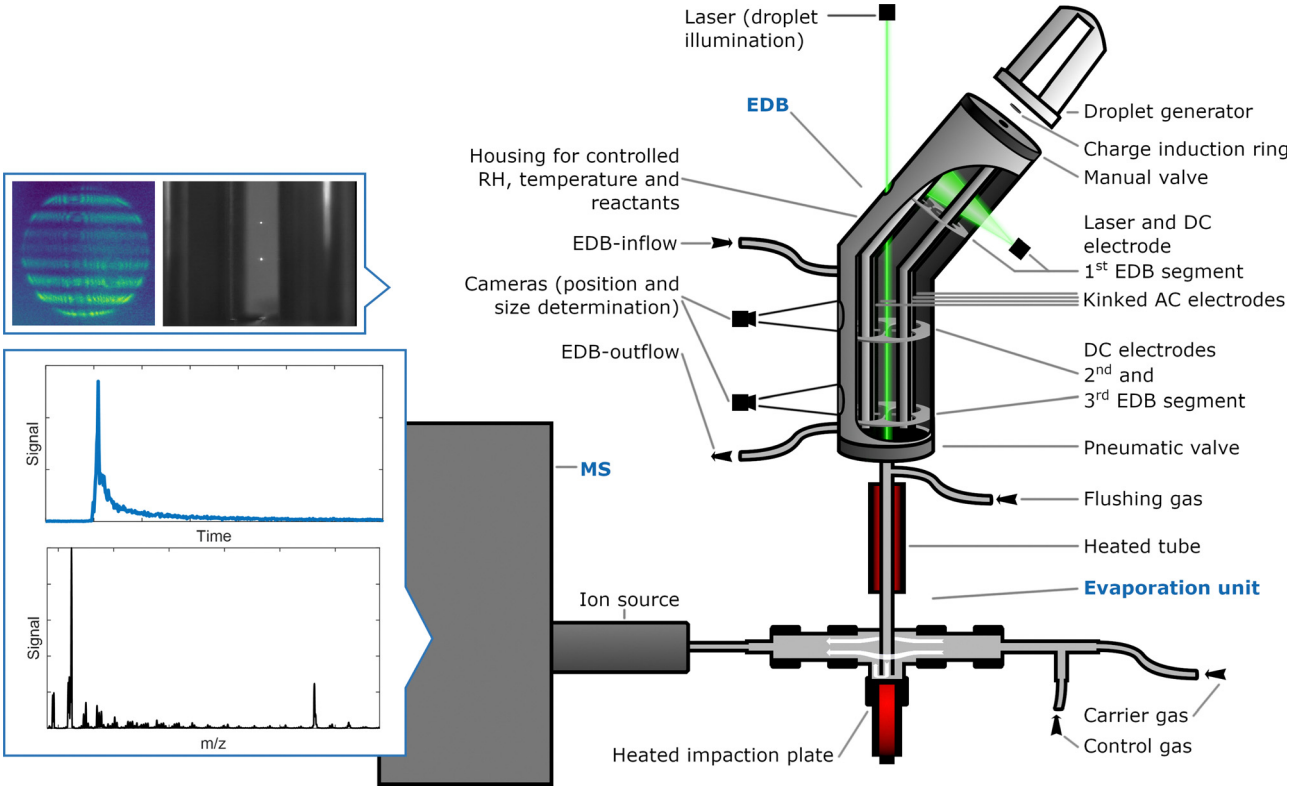

Fig. 2 Schematic representation of the instrumentation. In the electrodynamic balance (EDB), charged particles are stored and aged under specific reaction conditions (ozone mixing ratio and reaction time). Subsequently, single particles are transferred to the evaporation unit and the resulting gas-phase compounds are transported to the ionisation region and analysed by mass spectrometry (MS). Parts are not drawn to scale.

impurities or fragments formed either during ionisation or evaporation. Apart from these peaks, there is no sign of fragmentation in the ion source, which is consistent with our experience and literature knowledge about the ionisation method.[33–36] In preliminary experiments with other mono- and dicarboxylic acids, the detected fragments could all be assigned to products from thermal decomposition in the evaporation unit (inferred from the temperature dependence of the relative signal intensities).

In the following, we restrict the discussion to the unperturbed spectral range above m/z 110. Additional peaks at m/z 295, 297 and 312 most likely stem from impurities in the injected solution. However, we cannot rule out that they are caused by processes in the ion source. Because the intensity of these peaks decreases with increasing exposure (see Section 3.2), it is rather unlikely that they result from oxidation products of oleic acid. A similar pattern of additional peaks has also been reported in measurements using EESI-MS on the oleic acid ozonolysis system.[10]

To evaluate the quantitative capabilities of our setup and the experimental reproducibility, a calibration was carried out using a series of unreacted oleic acid droplets of different sizes. Fig. 10 in Appendix A shows the MS signals along with the estimated amount of substance, revealing a clear linear relationship between droplet volume and signal intensity. In addition, the sensitivity (signal per amount of substance) was estimated for commercially available products from the ozonolysis of oleic acid, nonanoic acid and azelaic acid, by means of mixed droplets of different compositions using the same approach (shown in Fig. 11 in Appendix A).

3.2 Heterogeneous oxidation of oleic acid by ozone

We studied the ozonolysis of oleic acid using droplet measurements at constant ozone mixing ratio and as a function of exposure. For the comparison of differently aged drops (82% with a radius in the range from 24 to 28.3 μm and 18% smaller droplets between 19.0 and 24 μm for comparison), the droplet signal was normalised by volume to a reference radius of 27 μm. Fig. 3 shows the evolution of the mass spectra at characteristic reaction times for experiments with 10 ppm of ozone.

All peaks detected in the spectra of unreacted oleic acid droplets (at m/z 281, 282, 295, 297 and 312), shown in Fig. 3(a) decrease in intensity upon exposure to ozone (b) and disappear at higher exposures (c). Product formation leads to the appearance of new peaks in the mass spectrum at m/z 141, 143, 157, 159, 171, 185, 187 and 203. Although peak intensities cannot be converted directly to amounts of substances, we note that the most intensive peaks of the product spectrum (at m/z 157, 171 and 187) are detected at the expected mass-to-charge ratios of deprotonated first-generation products nonanoic acid, 9-oxononanoic acid and azelaic acid (see Fig. 1). The additional first-generation product nonanal would be expected at m/z 141, where only a minor peak is observed (which is related to the high vapour pressure and evaporative loss of this species, see Section 3.4). The peak at m/z

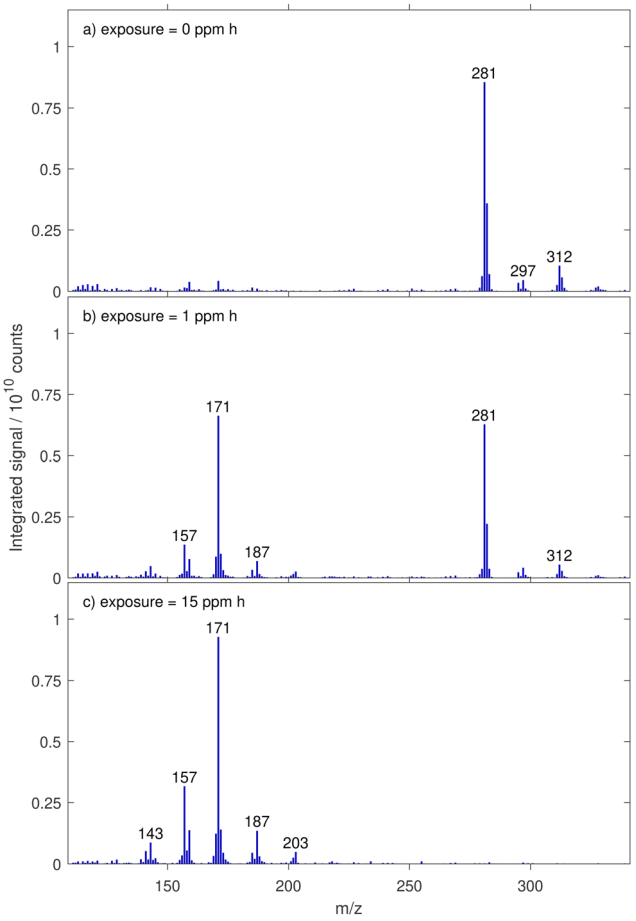

Fig. 3 Mass spectra from droplets of oleic acid and ozonolysis products before (a) and after different ozone exposures (b and c) aged with 10 ppm ozone.

143 has previously been reported as octanoic acid, a product potentially formed from CI-187 after splitting off CO_2.[21,22] The peak at *m*/*z* 203 has been associated with a fragment of a larger molecule, most likely a fragmentation product from an AAHP.[10,37]

In our experiments, we did not observe any peaks at the expected *m*/*z* of molecular ions of dimers or higher oligomers, which have been reported in the literature.[6,9,10] This absence is presumably caused by the droplet evaporation scheme in our setup, leading to thermal decomposition of dimers and higher oligomers. Such decompositions have been observed at temperatures well below the temperature used in our evaporation unit.[9,18] The absence of any further decomposition product suggests that dimers and higher oligomers decay predominantly into the corresponding monomer fragments and are therefore indirectly detected with the signal at the mass-to-charge ratio of the monomers (see also Fig. 1 and discussion in Section 3.4.1).

3.3 Verification of the exposure metric for oleic acid oxidation

To test the validity of the exposure metric, ozonolysis experiments of oleic acid were performed for several reaction times at two very different ozone mixing ratios. A total of 20 drops were investigated under low ozone conditions with an average ozone mixing ratio of 0.184 ± 0.008 ppm (denoted 0.2 ppm) and 14 drops were investigated under high ozone conditions with an average ozone mixing ratio of 14.66 ± 0.20 ppm (denoted 15 ppm). For comparison, 0.2 ppm ozone is a value frequently exceeded in cities in eastern China,[38] and about four times higher than the annual mean tropospheric background value in the northern hemisphere;[39] whereas 15 ppm is a value often used or exceeded in laboratory studies but out of range of typical environmental conditions (around 300 times higher than the annual mean tropospheric background concentration in the northern hemisphere).

By combining single droplet data from multiple droplets aged for different reaction times, the temporal evolution of the droplet composition can be constructed. We first discuss the decay of oleic acid and thereafter (Section 3.4) how the various product signals evolve with time. Fig. 4a shows the evolution of the integrated signal at *m*/*z* 281 for the two mixing ratios. It is clear that the difference in ozone mixing ratio directly translates into drastically different characteristic reaction times for oleic acid depletion in the droplets. However, when these data are plotted against exposure ($n_{O_3(g)} \times t$) instead of reaction time, they collapse on a single decay curve with a single characteristic exposure, see Fig. 4b. This demonstrates the capability of our EDB–MS setup and proves that the exposure metric holds true for the degradation of oleic acid within a range of ozone mixing ratios of almost two orders of magnitude.

As mentioned above, there is a broad collection of laboratory data for the specific case of oleic acid ozonolysis. Recently, Berkemeier *et al.*[20] applied the kinetic multilayer model of aerosol surface and bulk chemistry KM-SUB[41] to derive model parameters that represent a best fit to a collection of 12 literature data sets. In contrast to resistor model frameworks (*e.g.* Worsnop *et al.*[40]), the explicit treatment of coupled mass transport and chemistry with KM-SUB does not depend on the assumption of limiting cases[42] and enables to also treat the product chemistry (see below). A direct comparison of our oleic acid measurements with the model output (using the obtained parameter sets from model scenario B for MS experiments in Berkemeier *et al.*[20] and applying our experimental conditions without further fitting) is shown in Fig. 4c. The experimental data agree well with the model (the model predicts a slightly slower decay than suggested by the experiments but the deviation is comparable to the differences between the model and experimental data in the original study[20]) and, hence, fall in line with the available literature. The overlap of the model output for both mixing ratios shows that the model—without any unproven assumption—describes the decay of oleic acid to depend only on the exposure metric ($n_{O_3(g)} \times t$), not on $n_{O_3(g)}$ and t individually.

3.4 Product formation

Fig. 5 shows the evolution of the decay of oleic acid *vis-a-vis* the increase of the product signals at *m*/*z* corresponding to the first-generation products. The MS data for other product signals (cp. Fig. 3) can be found in Fig. 12 in Appendix C.

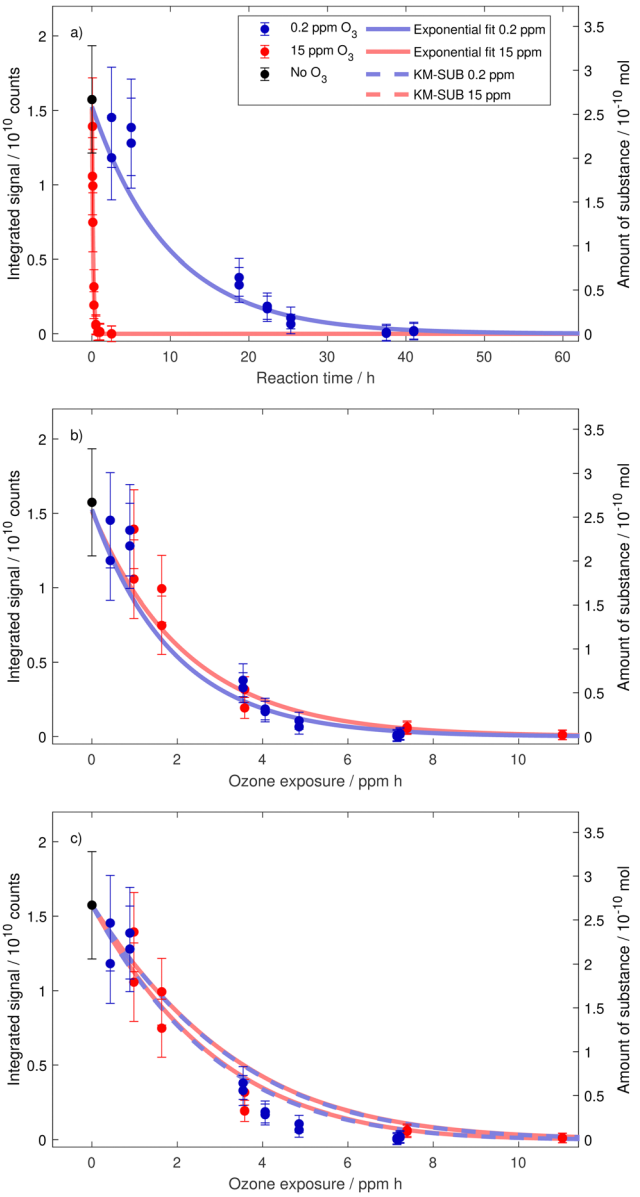

Fig. 4 Decay of oleic acid as a function of reaction time (a), ozone exposure (b) and in comparison to model scenario B for MS experiments in Berkemeier *et al.*[20] (c). If the decay is caused by a rate limiting surface reaction, we expect it to depend on the exposure metric ($[O_3](g) \times t$) in a simple exponential manner.[40] The error bars depict estimated uncertainties due to variability of the MS signal. Exponential fits take into account the uncertainties of individual data points (see Appendix B). In (c), we show the oleic acid decay predicted by KM-SUB model runs (167, each with individual parameter sets). Shown are fastest and slowest model runs.

In the following discussion we focus on two aspects: (i) the trend of product signal intensities with increasing exposure (Section 3.4.1) and (ii) the extension of the existing kinetic model to test the hypothesised processes (secondary chemistry *vs.* evaporation, Section 3.4.2) for *m*/*z* of first-generation products and the corresponding monomeric building blocks of dimers and oligomers.

3.4.1 Signals from second generation products. For all product peaks, we find that the signal intensity first increases and then remains relatively constant. Since the partitioning of semi-volatile species from the condensed phase to the gas phase affects the droplet composition, it is important to consider the evaporation of first generation products when analysing the increase of product signals. An estimate of the evaporation timescale of a given compound can be derived from Maxwell's equation for the evaporation of a droplet.[23] To estimate the relevant timescales, we simulated droplets (r = 27 μm) of binary mixtures of oleic acid and first-generation products at a 9 : 1 molar ratio and derived the time when 50% of the first-generation product had evaporated using the 'pyvap' tool presented by Birdsall *et al.*[23] The obtained evaporation times are summarised in Table 1.

Even though these calculations do not take into consideration the complex mixing state of the droplets, they reveal the relevant orders of magnitude to consider for the evaporation of the substances with the corresponding vapour pressures. It is therefore unlikely that products with the highest vapour pressure (*i.e.* nonanal and nonanoic acid) persist during an experiment with a duration of several days, which is in contrast to the observed constant product signal intensities at higher exposures ($\gtrapprox$7 ppm h, see Fig. 5). Similar considerations concern the additional product peaks, which are not corresponding to the first-generation products discussed above (shown in Fig. 12 in Appendix C).

The persistent signal at *m*/*z* of nonanoic acid, nonanal and 9-oxononanoic acid can only be explained with contributions of dimers and oligomers that thermally decompose in the evaporation unit prior to MS detection and are measured at the *m*/*z* of the corresponding monomers. This is in agreement with findings from thermal desorption particle beam MS and thermal desorption of filter-collected oleic acid ozonolysis products.[9,18] The vapour pressures of dimers are predicted to be lower than 10^{-5} Pa.† Therefore, dimers are assumed to be non-volatile for our experiment duration.

While at short exposure timescales nonanal, nonanoic acid and 9-oxononanoic acid can still contribute to the measured signal, we conclude from our data that dimers and oligomers must dominate the measured signal of the respective *m*/*z* at later reaction times. The experiment times, at which thermal decomposition products start impacting the measured signal depend on the vapour pressures of the first-generation products and on the reaction rates.

A closer look at Fig. 5 reveals some remarkable discrepancies between the final product concentrations under the two ozone mixing ratios. For the product peaks at *m*/*z* 141 and *m*/*z* 157, the final signal is substantially lower at low ozone conditions than at high ozone conditions. These peaks correspond to the first-generation products nonanal (*m*/*z* 141), nonanoic acid (*m*/*z* 157) and the respective monomeric building blocks of thermally decaying dimers and oligomers. For the other two peaks at *m*/*z* 171 and *m*/*z* 187, the final signal are similar at both ozone mixing ratios. These peaks correspond to the first-generation

† Only the secondary ozonide from the reaction of nonanal with CI-157 intermediate has a vapour pressure of around 10^{-3} Pa, but it is expected to be formed only in small amounts due to the rapid partitioning of nonanal to the gas phase.[16]

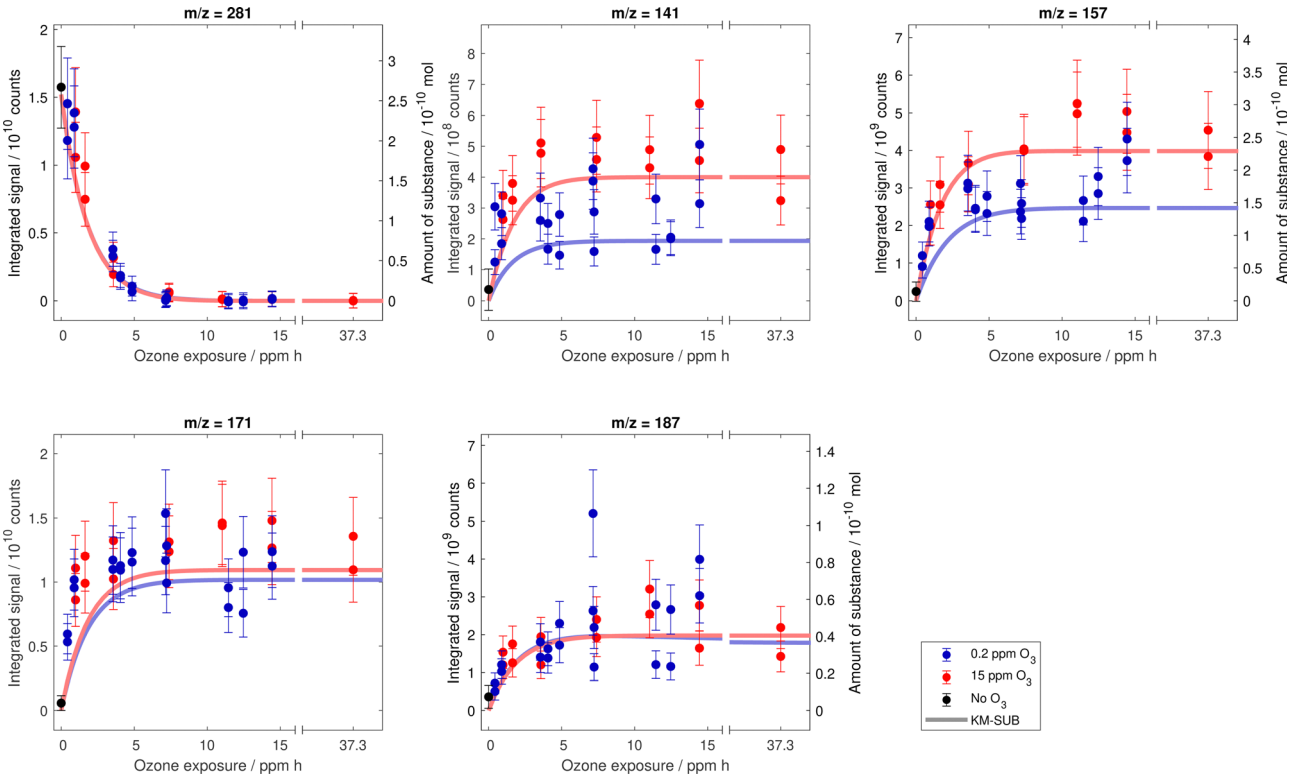

Fig. 5 Compilation of measured signal for MS peaks corresponding to first-generation products in dependence on exposure to ozone. For the *m*/*z* with commercially available substances, the integrated signal axis is supplemented with an additional axis showing the corresponding amount of substance. Error bars depict estimated uncertainties from MS sensitivity variability and the trend lines are the model results from the modified KM-SUB version.

Table 1 Evaporation timescales for first-generation products in binary droplets with oleic acid (r = 27 μm, 10% first-generation product by moles).[23] Gas-phase diffusivities D_v were calculated according to Bird *et al.*[43] using critical volumes and critical temperatures from UManSysProp.[44] Note the influence of vapour pressures on the evaporation timescales

Substance	D_v (m^2 s^{-1})	p (Pa)	t_{evap} (s)
Nonanal	5.6×10^{-6}	$4.9 \times 10^{+1\,14}$	2.4×10^{0}
Nonanoic acid	5.3×10^{-6}	$2.2 \times 10^{-1\,14}$	1.2×10^{3}
9-Oxononanoic acid	5.1×10^{-6}	$1.2 \times 10^{-2\,16}$	2.3×10^{4}
Azelaic acid	4.8×10^{-6}	$1.0 \times 10^{-4\,13}$	2.9×10^{6}

products 9-oxononanoic acid (*m*/*z* 171) and azelaic acid (*m*/*z* 187) and the respective monomeric building blocks.

Based on the volatility of the first-generation products and taking into account the expected contribution of dimers to the measured signal, we propose an influence of first-generation product evaporation on the final droplet composition. The faster evaporation of first-generation products with higher vapour pressure (*e.g.* nonanal and nonanoic acid) may lead to a stronger loss in the longer experiments with lower ozone mixing ratio. Therefore, these products are likely to be less available as reaction partners for dimerisation reactions with CI (R4 and R5 in Fig. 1) and contribute less to the non-volatile dimer and oligomer mass. A similar competition was described by Zeng and Wilson,[45] who investigated the ozonolysis of *cis*-9-tricosene and showed that the contributions of CI reactions (bimolecular accretion and unimolecular decomposition) could be separated using CI scavengers. In our setup, the non-volatile droplet components likely decompose thermally at the time of analysis and are then detected as monomeric building blocks.

3.4.2 Kinetic modelling of product signal curves. To test our hypothesis of competing evaporation and secondary reaction with an aerosol process model, we used the existing KM-SUB model of Berkemeier *et al.*[20] and complemented it with additional reactions following the recent study of Gallimore *et al.*[10] and with evaporation of semi-volatile first-generation products. The rearrangement of CI and their reactions with acids and aldehydes were added as presented in Fig. 1 and ozone was implemented to react with all C=C double bonds, including double bonds of AAHPs formed in the reaction of CI with oleic acid (not shown in Fig. 1). The evaporation of semi-volatile compounds (nonanal, nonanoic acid, 9-oxononanoic acid, azelaic acid and CI) was treated based on vapour pressures as presented previously.[46] To simulate the detection of thermal decay fragments at the time of analysis, the dimers are formed in the model and thermal decay is treated by assigning dimers to the signal of the corresponding monomeric building blocks, assuming quantitative turnover. For the decay of secondary ozonides, cleavage was assumed to occur at both C–O bonds with a probability of 50%, leading to different product pairs. Details of the model setup are provided in Appendix D.

A number of unknown kinetic model parameters of product formation and detection were optimised to make the model

match the experimental data. Surface and bulk reaction rates of oleic acid with ozone were used as fixed parameters as suggested by Berkemeier *et al.*[20] (R1 in Fig. 1). The bulk reaction rates for CI rearrangement (to the acid, R3) and for the reaction between CI with acids (to form AAHPs, R5) were adopted from Gallimore *et al.*[10] Further physico-chemical properties of involved species (such as vapour pressures and diffusion coefficients) were used as fixed parameters based on best estimates from the literature. All model parameters used in this study are summarised in Table 2 in Appendix D. Fitted parameters are the surface desorption lifetime of ozone, the branching ratio of primary ozonide decay (R2a *vs.* R2b), the bulk reaction rate for the formation of SOZs (R4), as well as factors for the conversion between model concentration and experimentally measured signal.

The model output for signal intensities of oleic acid and the first-generation products is included in Fig. 5. The model consolidates the experimental finding that product concentrations reach a constant final state, which for m/z 141 and m/z 157 depends strongly on the ozone mixing ratio. For m/z 187, the model suggests a slight signal decrease after 5 ppm h in the 0.2 ppm experiment, owing to evaporation of azelaic acid present in monomeric form.

Similar to the recent study of Gallimore *et al.*,[10] the dimer yield in our model is dominated by secondary ozonides. In their study, Gallimore *et al.*[10] also found a faster reaction of CI with aldehydes than with acids. However, in comparison to their study, we require even higher rates of secondary reactions in order to obtain the observed final ratio of product signals. Note that in our model configuration, the competition between secondary chemistry and evaporation is reflected mainly in the reaction rates of SOZ formation. This is due to the fact that in our scheme the AAHP formation rate is fixed and (besides the quickly evaporating nonanal) only SOZs are contributing to the signal at m/z 141. The higher rates of secondary reactions in our study may be a consequence from the much higher surface accommodation coefficient applied in our model. We used a fixed surface accommodation coefficient of 0.1 based on the recent evaluation by Berkemeier *et al.*[20] to ensure that the uptake is not limited by surface accommodation. Gallimore *et al.*[10] fitted the accommodation coefficient and obtained very low value of 0.001.

Using the kinetic model, we performed a kinetic flux analysis assessing the competition of first-order (*i.e.* evaporation and rearrangement) and second-order loss processes (*i.e.* secondary reaction) of reaction intermediates, *i.e.* first-generation products and CI (Fig. 13 and Table 3 in Appendix D). The analysis reveals that the applied ozone mixing ratio has an influence on the relative importance of evaporation, dimerisation, and rearrangement. The reaction rates and the vapour pressures determine the prevailing mode of action under specific reaction conditions. As the production and, hence, the concentration of CI is highest in the beginning, the relative importance of dimerisation generally decreases over time and for first-order processes it increases.

3.4.2.1 Final product concentrations for different ozone mixing ratios. For a quantitative comparison of the kinetic model with the experimental data, we fitted the experimental data for each of the MS peaks with an exponential curve

$$I(x) = I_\infty \cdot (1 - e^{-x/\tau}), \quad (1)$$

where $I(x)$ is the m/z signal intensity from a droplet after exposure x, I_∞ is the signal for $x \to \infty$ and τ is the characteristic e-folding exposure, which is inversely proportional to the initial slope of $I(x)$ for $x \to 0$. Eqn (1) is motivated by the fact that an exponential behaviour is a good approximation for simple reactive systems. For example, when considering the simple bulk reaction system of oleic acid + O_3 → CI + M → dimer, it can be shown that even with evaporating monomers M, the dimer concentration after reaction of the monomer M and the Criegee intermediate CI follows an exponential growth curve in cases of both, dominating or negligible evaporation (see Appendix E). Therefore, an exponential growth curve according to eqn (1) is expected to capture the obtained signal well if the products are formed from an exponentially decreasing starting material and if no other reactions or product partitioning is taking place.

Using the Bayesian inference module from the uncertainty quantification tool UQLab,[47,48] we extracted the two unknown quantities I_∞ and τ from the experimental data including their corresponding uncertainties for each MS peak individually (for more details see Appendix B). The exponential parameters were also extracted from the kinetic model curves, which (with the exception of the curve for m/z 187 at 0.2 ppm ozone) can be reasonably well described by exponential functions.

The pre-exponential factors I_∞ from the Bayesian inference analysis are compared to the corresponding pre-exponential factors from the kinetic model in Fig. 6a. For the low m/z product signals (m/z 141, 143, 157, 159), the pre-exponential factors are lower in the 0.2 ppm experiments than in their 15 ppm counterparts. For higher m/z product signals (m/z 171, 185, 187, 203), this difference becomes smaller. The kinetic model is able to reproduce this trend very well and attributes it to a lower degree of secondary chemistry for compounds with higher vapour pressure. Note that, secondary chemistry occurs through bimolecular reactions of intermediates (*i.e.*, Criegee intermediates, volatile primary products). These intermediates decay (in the case of Criegee intermediates) and evaporate in a first-order process. At the lower ozone mixing ratio (0.2 ppm), the low steady-state concentration of reactive intermediates leads to rather slow rates of secondary chemistry and evaporation of first-generation products is favoured. In turn, at the high ozone mixing ratio (15 ppm), secondary chemistry occurs much faster due to the higher steady-state concentration of reactive intermediates and is favoured over evaporation.

The diverging final concentrations at high exposures imply that the exposure metric, which holds for the degradation of oleic acid, is not valid for the product formation as the composition of the aerosol droplet depends ultimately on the ozone mixing ratio. For chemical schemes similar to the ozonolysis of oleic acid, where primary products may participate in further, bimolecular reactions, it is therefore possible that the concentrations of secondary products are overestimated in

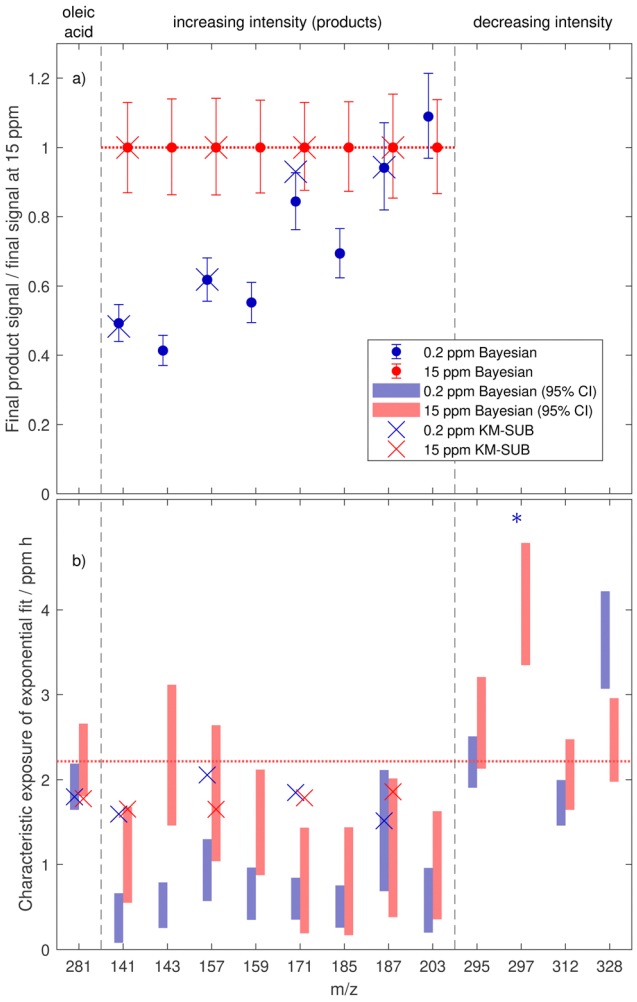

Fig. 6 Final product signal I_∞ (a) and characteristic e-folding exposures τ (b) of Bayesian inference exponential fits to experimental data in comparison to KM-SUB outputs. The error bars and shaded rectangles represent the 95% confidence intervals obtained from Bayesian inference. The signals from oleic acid, from products, and from m/z with decreasing intensity are separated with vertical dashed lines. In (a), the final signals of all species are normalised to the 15 ppm signals, for comparison. Horizontal dotted lines at the 15 ppm final signal (a) and at the estimated characteristic e-folding exposure of oleic acid for 15 ppm (b) help guiding the eye. For the peak at m/z 297, the characteristic exposure of the exponential fit for 0.2 ppm ozone (*) is not shown (estimated to be >100 ppm h).

experiments conducted at elevated oxidant concentrations. In this matter, our findings come to different conclusions than a study in which almost identical Raman signatures were detected on droplets aged at 260 ppb ozone for 20 h and in droplets exposed to over 10 ppm ozone for 1.5 h.[1] This result may arise because Raman spectroscopy detects contributions from functional groups and single bonds within a molecule rather than individual molecules.

3.4.2.2 Characteristic exposures for achieving final state for different ozone mixing ratios. In Fig. 6b, we show the characteristic exposures τ from the Bayesian inference analysis and the kinetic model. As the sample number at low ozone exposures is lower than at the final state, the characteristic exposure data is less constrained and is therefore discussed here in terms of the 95% confidence intervals. For all products (with the exception of the signal at m/z 143), the confidence intervals from both ozone mixing ratios overlap, suggesting insignificant differences between the apparent product formation rates. Nevertheless, it is remarkable that, especially at 0.2 ppm ozone, the characteristic exposures of product formation are smaller than the oleic acid decay for many products. In a simplified chemical scheme without evaporation where products may react further but decay quantitatively back into the monomers upon thermal decomposition, the characteristic exposure of product formation is expected to be identical with the characteristic exposure of starting material decay.

The shorter characteristic exposure for experiments under low ozone conditions could be caused by evaporation of first-generation products. However, in the simple bulk reaction system (oleic acid + O_3 → M + M → dimer), evaporation can only lead to a decrease in the characteristic exponential exposure up to a factor of two in the limiting case of very strong evaporation (as shown in Appendix E). The observation that the characteristic exposure depends on the ozone mixing ratio is also not captured in the numerical model, where the products show only slight deviations from the characteristic exposure of oleic acid. Although the model is able to produce a more pronounced dependency of the characteristic product formation exposure on the ozone mixing ratio when using increased CI rearrangement rates or decreased dimerisation reaction rates, such model parameters result in an inferior agreement with the experimental data of final product composition.

Further effects, which are not included in the model, such as the influence of the degree of polymerisation on thermal decomposition and the formation of other products, may also be responsible for the differences. If, for example, the process efficiency of thermal decomposition and evaporation at the time of particle analysis was decreasing with an increasing order of oligomerisation, the initial growth of product signal (dominated by monomers and dimers) would be disproportionately higher than the incline at later stages (formation of higher oligomers). Consequently, the curve-fitting would result in shorter characteristic exposures.

Note that, in the previously published model,[20] the decay of oleic acid (shown in Fig. 4) was based on the assumption that for MS data, AAHPs do not contribute to the oleic acid signal, while in Raman data, AAHPs containing a double bond are detected as oleic acid. In the previous work, these unsaturated AAHPs were important reactive intermediates and the distinction between MS and Raman data significantly improved the quality of the global fit. Similarly, Zhou *et al.*[12] reported a higher yield of AAHPs in comparison to the SOZ yield when studying oleic acid coating ozonolysis. In the extended KM-SUB model of this present study, the formation of AAHP adducts of oleic acid, however, is only a minor channel of secondary chemistry. The good agreement in Fig. 4 may thus indicate that the monomer signal is potentially more influential than AAHP contributions. Further product studies would be needed to distinguish the

contributions of secondary ozonides and AAHPs to the product spectrum.

3.4.3 Other products from the ozonolysis of oleic acid. The peaks at *m*/*z* 143, 159 and 185 (see Fig. 12 in Appendix C) show a similar behaviour as the peaks at *m*/*z* 141 or 157. Even though it remains impossible to confidently assign possible products with our MS resolution (*e.g.* to distinguish possible contributors to the peak at *m*/*z* 143, such as the proposed octanoic acid from nonanol, which could be formed at the time of analysis through thermal decomposition), the prevailing species in the droplet would most likely be a dimer or an oligomer. Otherwise the intensity would not remain constant after experiment durations of over two days, given the vapour pressures of these monomeric C9 acids or alcohols.

Although outside the focus of this work, it should be noticed that the signal from *m*/*z* 297 shows a significantly different behaviour between the two ozone mixing ratios. In the experiment with a high ozone mixing ratio, the decay is rather similar to that of oleic acid or other peaks at *m*/*z* 295, 312 or 328, yet a bit slower. At low ozone mixing ratios, however, there is hardly any decay detectable and the characteristic time is on the order of 100 ppm h. We can only speculate about the reason: the difference could be due to the formation of an oxidation product of oleic acid with molecular oxygen, which is favoured in the longer experiment over a reaction with either ozone or with CI. The addition of one oxygen atom would also explain the mass difference of 16 mass units between oleic acid and this additional peak. Further investigations with high resolution MS would be required to gain insight into the molecular structures and to propose a chemical mechanism.

3.5 Droplet size changes

Droplet size data from the reactions with different ozone mixing ratios allow testing the proposed evaporation effect. To do so, we tracked the change in particle radius for two particles at both ozone mixing ratios by comparing the evolution of the angular scattering pattern with simulated patterns.

The droplet size changes are shown in Fig. 7. As expected, experiments with longer reaction times lead to smaller droplets at a given exposure. The shown radius changes at 5 ppm h translate into volume decreases of about 18–22% for the droplets in 0.2 ppm ozone and about 13–14% for the droplets in 15 ppm ozone. Given the continued shrinking after 5 ppm h, the final droplet sizes agree with the measured non-volatile fraction of 50–85% reported by Dennis-Smither *et al.*[8] Yet, in our experiments we observed an increased evaporation in experiments at lower ozone mixing ratios whereas they see indications that the non-volatile fraction of substances was higher at lower ozone mixing ratios. If this discrepancy is due to the presence of NaCl cores in their droplets would need further investigations.

There is an apparent deceleration of size change after an exposure of around 5 ppm h, which is most likely because the oleic acid has reacted away in large part by then. While the shrinkage under high ozone concentrations seems to stagnate at exposures above 10 ppm h, there is still a steady radius

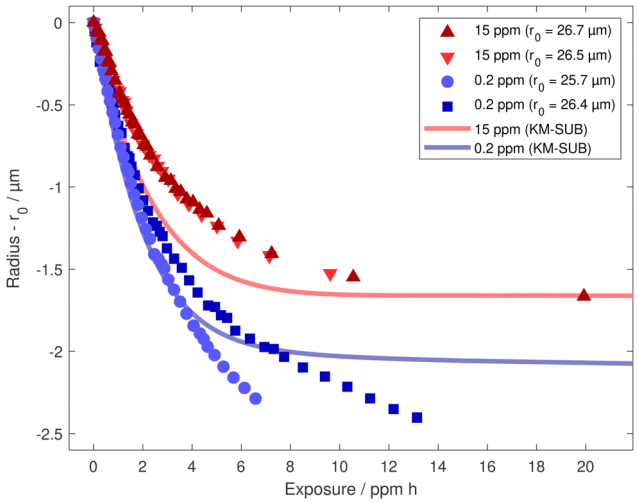

Fig. 7 Droplet size changes during the reaction under different ozone mixing ratios. The initial radius and radius changes were obtained by comparison of the angular scattering pattern to calculated scattering patterns assuming constant refractive indices. The assumption of an unchanged refractive index is expected to have an effect of less than 3% on the obtained volume.[8]

decrease detectable in the longer, low ozone experiments. Further oxidation reactions with ozone, which produce highly volatile species and therefore contribute to this size change cannot be ruled out but seem not to be the dominant reason because they would apply under both ozone mixing ratios equally.

While the change in droplet radius over the course of the experiment is not treated explicitly in the model, droplet sizes can be inferred from model output by converting particle mass to volume. For Fig. 7, we used a density of 0.89 g cm^{-3} for oleic acid and 1.12 g cm^{-3} for product species, based on findings by Katrib *et al.*[49] The model reproduces the general features in the droplet radius data even though this data was not used in the model fitting. The strongest diversion from the experimental data is observed at a low ozone mixing ratio and high exposure. This indicates that there is ongoing evaporation of semi-volatile species under low ozone conditions, which is not captured by the model, possibly due to a slow decomposition of dimers and oligomers, which is not treated in the model.

From measurements of the angular phase function, no major distortion in the regular patter could be observed, indicating that there is no extensive phase separation. Such a behaviour had been described for deposited droplets and films.[11,50]

4 Outlook

Using a new setup for EDB–MS measurements, we demonstrate the influence of first-generation product evaporation on secondary chemistry in the heterogeneous oxidation of oleic acid with ozone. While the starting material decay can be described with the exposure metric (*i.e.*, it is only dependent on oxidant concentration × time, for all oxidant concentrations), the metric is not fully applicable to concentrations of first-generation products, dimers and oligomers. Deviation from

typical atmospheric conditions in laboratory experiments may suppress the influence of first-order processes such as evaporation, happening on longer timescales, in favour of second-order processes such as bimolecular reactions of reactive intermediates, which are less relevant under atmospheric conditions. This is not limited to evaporation, but also includes other transport processes and unimolecular chemical reactions. In other chemical systems, semi-volatile reaction products could also compete with the starting material for oxidative agents and therefore influence the primary chemistry in dependence on the applied reaction conditions, which would make the exposure metric not applicable to the starting material decay. This highlights the necessity to fully understand the chemical system under consideration to safely gain knowledge from experiments with elevated oxidant concentration.

Author contributions

M. M. and U. K. K. designed the experimental setup with E. H. M. M. carried out the experiments and analysed the data. A. M. and T. B. set up the model and A. M. ran and optimised the model. T. P. derived the mathematical treatment of the simplified chemistry using differential equations. M. M., A. M., T. B., T. P., and U. K. K. discussed the results. M. M. produced the figures and wrote the original draft with help from A. M. The draft was revised by A. M., T. B., T. P., and U. K. K.

Conflicts of interest

There are no conflicts to declare.

Appendix A instrumentation and chemicals

For the injection of new particles, a droplet on demand generator (TIJ 1.0 print cartridge, Hewlett Packard; average drop volume 220 pl) is mounted on a translatable and tilting stage, orientated towards the EDB. Droplets are charged inductively upon ejection utilising a copper ring directly below the cartridge. Voltages of 20 to 300 V were applied to the ring to imply a sufficient charge on the droplet.

The linear quadrupole EDB consists of combined rod AC electrodes and perforated disk DC electrodes.[51–53] While the quadrupolar arrangement of the AC electrodes confines the path of charged particles to the central axis, three pairs of inserted DC electrodes are used to counteract the gravitational force of injected particles. The AC electrodes are kinked, which allows laser illumination along the central axis without removing the injector. Furthermore, tilting the first part of the trap prevents uncharged (satellite) droplets accidentally ejected from colliding with already stored particles. The DC electrode pairs define storage segments in the trap: a first segment before the kink is used to verify a successful injection, a second segment below the kink is used for droplet sizing and a third segment underneath is used for droplet storage (see Fig. 2). Typically, 3 kV were applied at 150–300 Hz at the AC rod electrodes and the DC voltage at the inserted disk electrodes was varied from ground potential to 1 kV for transfer and vertical droplet positioning. All electrodes are mounted inside a polyether ether ketone (PEEK) housing which holds a manual polytetrafluorethylene (PTFE) valve on the top end and a pneumatic valve (VAT Vakuumventile AG, Switzerland) at the bottom end of the trap. The AC rods of both EDB parts are approximately 13 cm long.

In the first segment, a DPSS laser module (532 nm, 4 mW, uniform 30° fan angle, Frankfurt Laser Company, Germany) is used for particle illumination from the side. For the lower arm of the EDB, a second DPSS laser module (532 nm, 3 mW TEM_{00}, Lasermate Group Inc., USA) is used along the central axis. At each segment, a Raspberry Pi with a camera (ArduCam UC-599) is mounted to observe the droplet position. For the second segment a feedback loop is utilised to adjust the DC voltage in order to maintain the vertical droplet position while sizing. An additional camera (Raspberry Pi HQ Camera V1.0) is installed at the second segment to capture the 2-D angular scattering pattern from 94.87° to 99.13° and particle sizes are determined based on the mean peak-to-peak distance in the angular scattering pattern which is compared to simulated scattering patterns using MiePlot (v4.6.20).[54,55]

To control the gas phase in the EDB and the gas flows in the evaporation unit, a set of valves and mass flow controllers (MKS Instruments, USA) are used for both nitrogen and compressed air. For ozone mixing ratios below or equal to 1.5 ppm a calibration ozone generator (Photometric O_3 Calibrator – Model 401, Advanced Pollution Instrumentation, USA) is used. For higher mixing ratios, an ambient ozone simulator (AOS 2 with bypassed pump, BMT Messtechnik, Germany) is used. An electrochemical ozone sensor (OX-B431 on Alphasense ISB, Alphasense, UK), calibrated with the ozone calibrator, is mounted at the outflow of the EDB to measure ozone concentrations. For the calibration of the ozone detector and to provide a reference signal there is a bypass between the ozone generator and the ozone detector (bypassing the EDB). The relative humidity and temperature in the outflow is measured using a digital humidity and temperature sensor (Sensirion SHT85, Switzerland).

The pneumatic valve at the bottom end of the EDB connects the EDB housing to a PEEK socket holding the evaporation unit. To allow a complete flushing of the evaporation unit, this socket also has a gas connection (labelled 'Flushing gas' in Fig. 2). The evaporation unit consists of a home-built combination of a jet heating cartridge (50 V, 50 W) welded together with a bored-up Swagelock Tee and connected to another heating cartridge (230 V, 100 W, both from Probag Wärmetechnik AG, Switzerland). Both heating cartridges are equipped with a Pt 100 temperature sensor and powered by temperature controllers (LTC-11, Neocera, USA and LTC-10, Conductus, USA), which allow to stabilise the temperature between 30 °C and 200 °C to better than 0.1 °C. The two remaining openings of the Swagelock Tee are connected *via* PEEK tubing to the ion source (towards the MS) on one side and to the gas inlet on the

other side. To allow a constant gas flow through the ion source (driven by a Venturi nozzle in the interface) a nitrogen overflow tube is connected as main gas inlet accompanied by a connection for a control gas flow (nitrogen flow through a gas washing bottle filled with a mixture of 1% toluene in ethanol).

Gas-phase compounds are ionised in a cold plasma dielectric barrier discharge ion source[56,57] (SICRIT SC-30X Ionisation Set, Plasmion GmbH, Germany) operated at ambient pressure. MS analysis is carried out with a triple quadrupole mass spectrometer (QTRAP 4500, AB Sciex LLC, USA) operated in negative Q3 mode at 2000 Da s^{-1} with unit resolution. It is operated with the provided instrument control and data processing software Analyst (Version 1.7, AB Sciex LLC, USA). For further analysis, MS data were processed in MATLAB (Version R2019a, MathWorks, USA).

Chemicals

Azelaic acid ($\geq$99% (GC), Fluka Chemika), ethanol–toluene mix (1% toluene, 94%, Thommen-Furler AG), methanol (UHPLC for MS, Sigma-Aldrich), nonanal (95%, Aldrich chemistry), nonanoic acid ($\geq$97%, Sigma life science) and oleic acid (selectophore, $\geq$99%, Sigma-Aldrich) were all used without further purification. For the carrier gas, nitrogen gas stemmed from a nitrogen generator (NGM-11, cmc Instruments GmbH, Germany) and for all other nitrogen applications, nitrogen gas was delivered from a liquid nitrogen reservoir Dewar. Zero Air was supplied by the zero air generator of the ozone calibrator or used from the in-house compressed air supply in combination with the ambient ozone simulator.

Typical experimental procedure

All measurements were carried out at ambient pressure and laboratory temperature (20–23 °C). Prior to any measurement, the EDB was flushed with 50 sccm N_2 for at least 30 minutes. Particles were produced from solutions of 2–10 wt% solute in methanol. Oleic acid solutions were stored at <6 °C and freshly prepared roughly every two weeks.

After the successful injection of two droplets the manual top valve was closed and a N_2 flow of 25 sccm was applied and maintained until the start of the experiment. The first drop was transferred to the second EDB segment and sized by recording its angular scattering pattern. It was subsequently transferred to the lowermost EDB segment and stored there. Afterwards, the second drop was transferred to the second EDB segment and its angular scattering pattern was continuously recorded for sizing throughout the whole experiment. The storage of a larger number of droplets is possible but here only one droplet in each lower segment was used. This two droplet configuration allows for an additional gas flow through the trap during droplet ejection which results in an efficient droplet transfer into the evaporation unit.

Before starting the heterogeneous oxidation reaction, the gas flow from the ozone generator (up to 400 sccm total flow, containing 0.2, 10 or 15 ppm O_3) was passed over the ozone sensor to check the sensor response in terms of magnitude and stability. To start the ozonolysis, this gas flow was redirected through the EDB and the ozone mixing ratio was monitored at the EDB outflow. These data are a lower bound of the mixing ratio of ozone in the two segments with the levitated droplets. In all experiments, the difference between ozone concentration before and after the EDB were less than 15% of the inflow mixing ratio. After the desired reaction time, the ozone generator was switched off and the EDB was purged with a nitrogen gas flow for one minute. Subsequently, the drops were ejected and analysed consecutively by an automated cascade of valve and electrode voltage switching. In a first step, the pneumatic valve between the EDB and the evaporation unit was opened and the third segment DC electrode voltage was set to zero. Afterwards, a pure nitrogen gas flow was forced through the EDB for one second (300 sccm). This led to a very reliable droplet transport from the lowest segment of the EDB to the evaporation unit with a transfer success rate of close to 100%. In a last step, the valve between the EDB and the evaporation unit was closed, the gas flow through the EDB was stopped and the evaporation unit was flushed with a flow of 300 sccm nitrogen gas. This flow was maintained for the entire MS measurement duration of 240 s. Afterwards, the remaining droplet was transferred to the third segment of the EDB and the analysis procedure was repeated.

For MS analysis, both heating cartridges in the evaporation unit were set to 190 °C and a control gas flow of 5 sccm N2 containing ethanol and toluene vapour was mixed with the carrier flow for both the background and for the droplet measurements.‡ Background measurements were used to check for inter-day variability with a focus on the stability of the ion source. These covered a range of m/z 40–340 in both positive and negative mode. Averaged peaks from ethanol and toluene (positive mode) as well as ethanol and NO_3^- in negative mode were extracted for comparison. Droplet measurements were carried out in negative mode either in the range of m/z 40–340 with a scan time of 0.155 s (6.45 full scans per second) or for a selection of ranges (m/z 140–145, 155–160, 168–175, 184–189, 200–204, 233–235, 278–284, 294–299, 320–315, 326–330) with a scan time of 0.075 s (13.4 full scans per second).

Because the MS signal during a droplet evaporation event is dominated by the gas-phase background signals from carrier-, flushing- and control gas (see Fig. 8b), the signal from the last 30 s of the flushing period was used for a background correction (subtraction of the average background, see Fig. 8). The main background peaks at m/z 45, 46, and 62 are produced by EtO^-, NO_2^- and NO_3^-, respectively.[36] In addition, also data from ejection sequences without any drop present was collected and subtracted from the droplet signal as also flushing the empty trap lead to a slight increase in signal. Individual peaks were extracted by binning the spectral data in segments of one mass unit width (containing m/z $i \pm 0.5$ for integer i). When focusing on the most prominent MS peak from the unreacted

‡ The chosen temperature lies still sufficiently below the processing temperature of PEEK and below typical autoclaving temperatures under which the bulk behaviour of reinforced PEEK is not yet affected.[58]

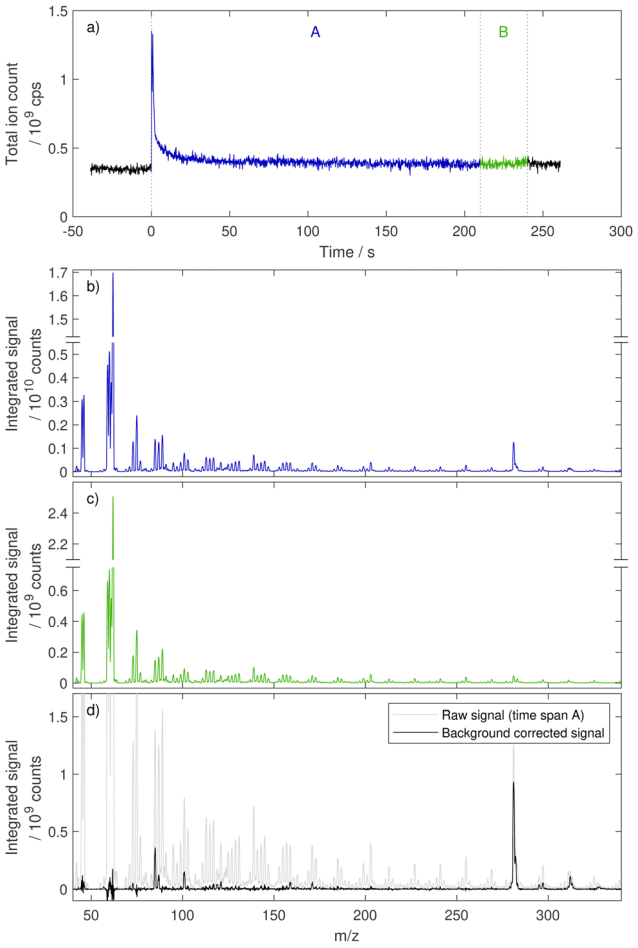

Fig. 8 Temporal evolution of the total ion count during a single, unreacted oleic acid droplet evaporation experiment (a), expansion to integrated mass spectra for selected time spans (b) and (c) and background corrected signal (d). Time span A denotes the interval with signal from the droplet whereas time span B is treated as background signal for background subtraction. Subtracting the average background signal from the droplet interval signal yields the background corrected spectrum. The main contribution to the total ion count peak is from the deprotonated oleic acid ion $[M-H]^-$ at m/z 281 and the background signal is dominated by NO_3^- at m/z 62.[36]

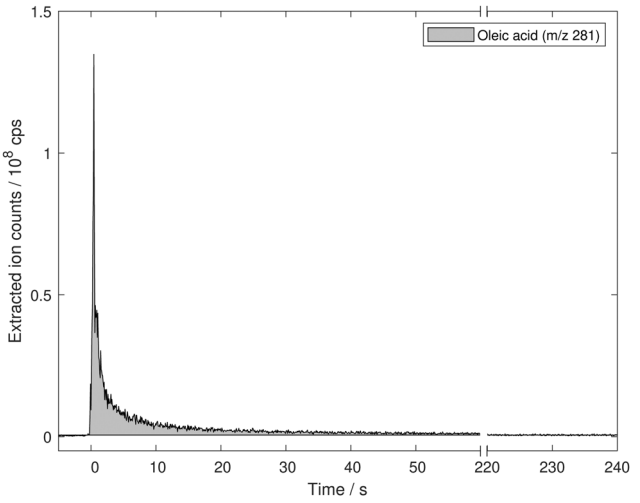

Fig. 9 Extracted ion count for m/z 281 from the evaporation of a single oleic acid droplet at 190 °C. After a sharp increase with the introduction of the droplet in the evaporation unit the signal intensity decays as the droplet shrinks and reaches background values before the end of the experiment at 240 s. The area below the curve corresponds to the amount of oleic acid in the drop.

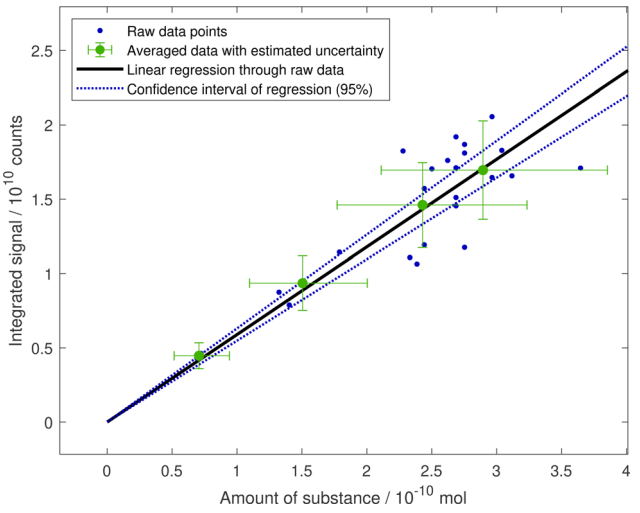

Fig. 10 Calibration of oleic acid MS signal with data from the evaporation of droplets of different sizes. The amount of substance was derived from the mean peak-to-peak distance in the droplet angular scattering pattern and using molar mass and density of oleic acid at standard temperature and pressure.[54,59] Data points with similar calculated amount of substance were averaged (n = 2, 3, 7, 12) and provided with error bars depicting an estimated uncertainty in the radius measurement of 10% and the standard deviation of the day-to-day variability in sensitivity extracted from the gas-phase methanol analysis. A linear fit through zero is applied to the raw data points and it is shown with the 95% confidence interval.

oleic acid droplet at m/z 281, a typical droplet 'evapogram' is obtained (see Fig. 9).

Calibration

The conversion from the MS signal into amount of substance was based on calibration experiments, assuming that the droplet composition (apart from the substance of interest) has no influence on the MS signal. Furthermore, it is assumed that the signal can be corrected for droplet size deviation (with the relative volume) and that the dimers and oligomers form again the same monomers when thermally decomposing.

For the calibration of oleic acid peaks, the signal at m/z 281 of 24 different droplet measurements was recorded on nine different days spread over seven weeks (see Fig. 10). A conservative uncertainty in the radius determination of 10% is assumed resulting in a corresponding uncertainty for the amount of substance of 30%.[60] The day-to-day variability of the MS-signal was estimated from gas-phase background measurements by analysing the response from ethanol, toluene and NO_3^-. While the alcohol signals in positive mode were constant over measurements on 14 different days in seven weeks (all values less than 3% off the mean), there was a considerable

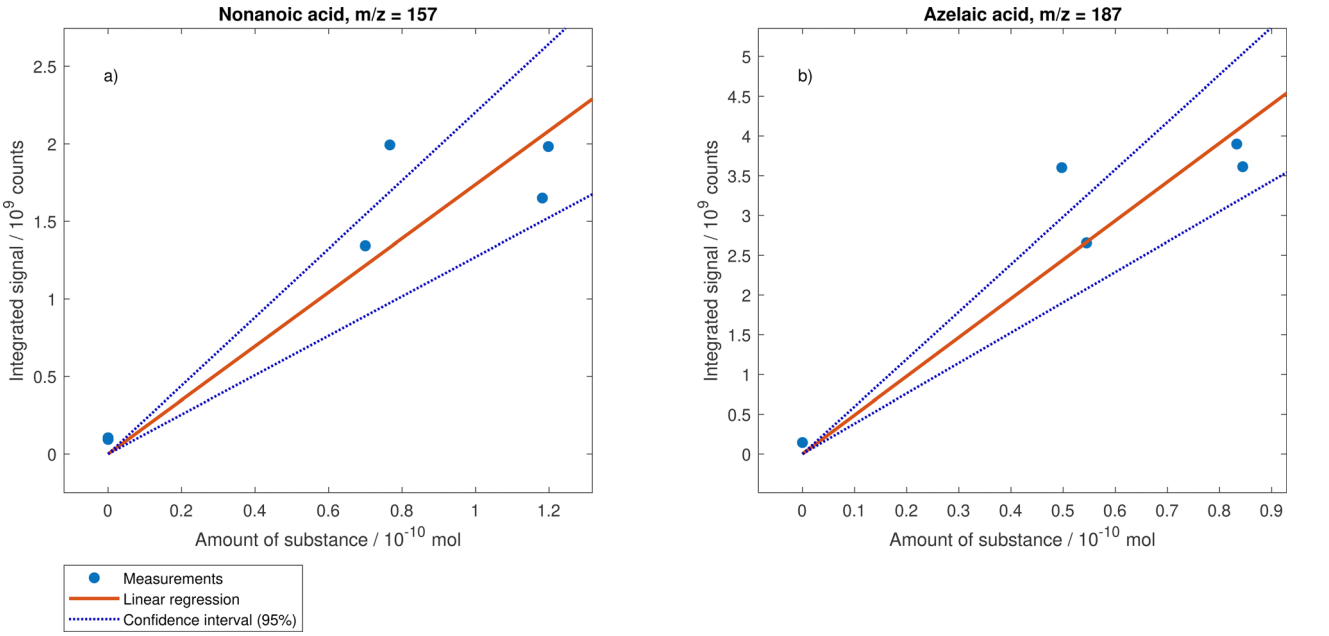

Fig. 11 Calibration curves for nonanoic acid (a) and azelaic acid (b). Mixed droplets with different droplet compositions were used. For the calculation of the amount of substance, the molar volume was used and a refractive index of 1.46 was assumed for all droplets. The linear regression was forced through zero.

spread but no clear trend in negative mode peaks of ethanol and NO_3^- (up to 45% above and 36% below the mean value). The relative standard deviation of the negative ethanol signal was applied to the averaged data points in Fig. 10 to illustrate the estimated uncertainty from inter-day variability. A linear regression through the unweighted data points and forced through zero results in a slope of $(5.9 \pm 0.20) \times 10^{19}$ counts per mol. Analogously, the calibration figures for nonanoic acid (slope of $(1.74 \pm 0.18) \times 10^{19}$ counts per mol) and azelaic acid (slope of $(4.9 \pm 0.4) \times 10^{19}$ counts per mol) is shown in Fig. 11.

Appendix B uncertainty quantification of exponential fits

This section describes the procedure for the uncertainty quantification of exponential fit parameters using the Bayesian inference module from the uncertainty quantification tool UQLab.[47,48]

The droplet signal from a drop after exposure x is denoted $I(x)$. For peaks with increasing intensity as exposure increases, an exponential curve according to $I(x) = I_\infty \cdot \left(1 - e^{-x/\tau}\right)$ was fitted. Similarly, a decrease according to $I(x) = I_0 \cdot e^{-x/\tau}$ was assumed for all other peaks. Here, I is the maximum signal (signal at infinite exposure I_∞ for increasing intensities and signal at zero exposure I_0 for others) and τ the characteristic exponential lifetime.

The sampling range for the τ parameters was set to a uniform distribution between 0 and 5 ppm h for all peaks except m/z 297 at 0.2 ppm where a distribution between 0 and 150 ppm h was used. For the pre-exponential parameter I, the sampling range was defined from 0 to 1.25 times the maximum measured signal intensity. A discrepancy model was used to account for the uncertainty of experimental measurements using Gaussian discrepancies with standard errors composed of a percent error (estimated from the signal variability extracted from the gas-phase methanol analyses) and a minimal uncertainty of 2.5% of the maximum signal. For each peak, the Markov chain Monte Carlo sampling of the Bayesian inversion tool was run with the adaptive metropolis algorithm until 100 000 parameter combinations were accepted of which the first 50 000 were discarded to prevent burn-in artefacts. The point estimates and the distributions of parameters were extracted and used for comparisons.

Appendix C: measured signal for further MS peaks

In Fig. 12, the course of measured signal intensities is shown for further m/z, not corresponding to deprotonated primary products or oleic acid.

Appendix D: kinetic multilayer model

The kinetic process model is based on the multilayer model of aerosol surface and bulk chemistry KM-SUB.[41] The implemented scheme and model parameters are based on a recent study focusing on the degradation of oleic acid in 12 different experimental data sets that span a wide range of oxidant concentration and particle size.[20] The spherically-symmetric KM-SUB model compartments are, from outside to inside, gas

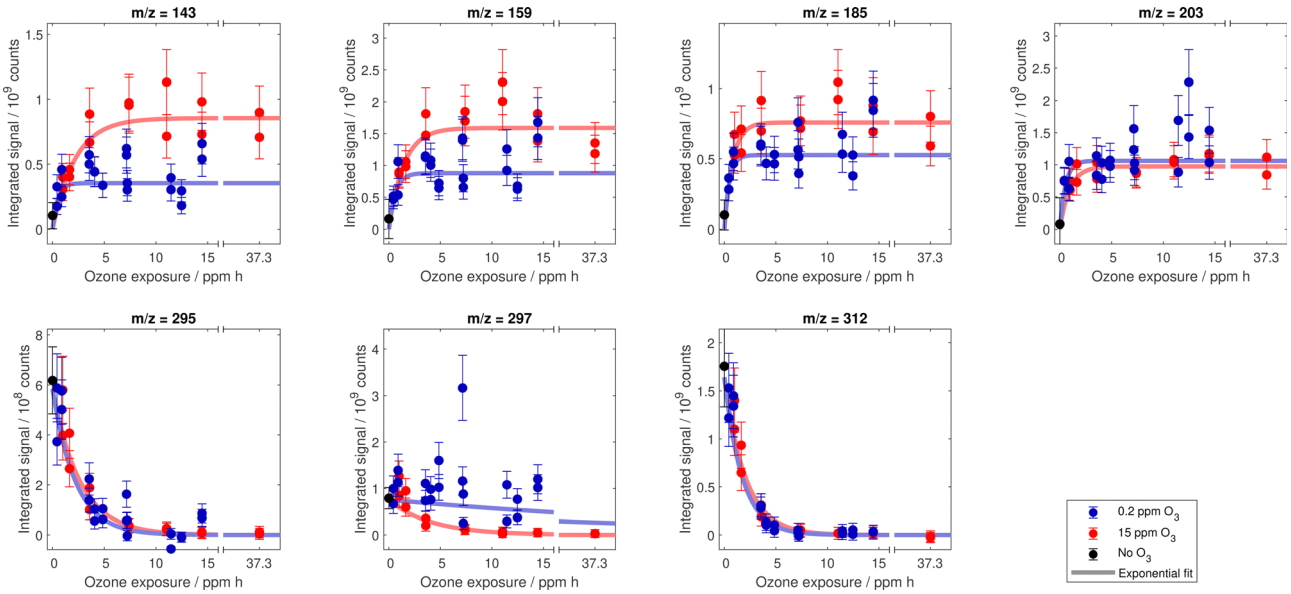

Fig. 12 Compilation of measured signal for prominent MS peaks in dependence on exposure to ozone. Error bars depict estimated uncertainties from size sensitivity variability. The trend lines are based on point estimates for the exponential parameters I and τ in $I_0 e^{-x/\tau}$ and $I_\infty(1 - e^{-x/\tau})$. More details on the uncertainty of these model parameters are given in Fig. 6.

phase, near-surface gas phase, sorption surface layer, quasi-static surface layer, and a number of bulk layers. Processes described in the KM-SUB model include gas-phase diffusion, adsorption and desorption, surface-bulk exchange, bulk diffusion of gaseous and bulk material as well as chemical reactions at the surface and in the particle bulk. The model code generates and solves a system of ordinary differential equations that describe the mass balance of each chemical species in each model layer. The corresponding Jacobian matrix is generated and evaluated explicitly to increase the numerical stability of the differential equation solver (ode23tb in Matlab).

Reaction rate coefficients and other input parameter values are presented in Table 2. The primary reaction of oleic acid with ozone was treated with a separate bulk (k_{BR1}) and surface reaction (k_{SLR1}). It was shown by Berkemeier *et al.*,[20] that the differentiation of surface and bulk reaction rates is important to reconcile the decay of oleic acid across multiple literature data sets. The secondary reactions of reactive intermediates considered in the model are the rearrangements of Criegee intermediates (CI) (k_{BR3}) as well as their reactions with aldehydes forming secondary ozonides (k_{BR4}) and with acids forming α-acyloxyalkyl hydroperoxides (AAHP) (k_{BR5}). We assume here

Table 2 Input parameters for KM-SUB and their values to fit the experimental data set

Parameter	Parameter value (best fit)	Parameter fit range	Description[Literature]
k_{SLR1} ($cm^2\ s^{-1}$)	1.0×10^{-9}		Surface reaction rate coefficient (olefin + O_3)[20]
k_{BR1} ($cm^3\ s^{-1}$)	1.0×10^{-18}		Bulk reaction rate coefficient (olefin + O_3)[20]
k_{BR3} (s^{-1})	500		Bulk reaction rate coefficient (rearrangement of CI)[10,61]
k_{BR4} ($cm^3\ s^{-1}$)	1.66×10^{-15}	1.7×10^{-21}–1.7×10^{-15}	Bulk reaction rate coefficient (SOZ formation)
k_{BR5} ($cm^3\ s^{-1}$)	2.5×10^{-19}		Bulk reaction rate coefficient (AAHP formation)[10]
$\alpha_{R2b/R2a}$ (—)	0.6	1.0×10^{-4}–1.0×10^{0}	Branching ratio of primary ozonide decay (share of 9-oxononanoic acid and CI(m/z 157) branch)
$\alpha_{s,0}$ (—)	0.1		Surface accommodation coefficient of O_3[20]
$D_{b,O3}$ ($cm^2\ s^{-1}$)	1.0×10^{-6}		Bulk diffusion coefficient of O_3 in OL[20]
$D_{b,OL}$ ($cm^2\ s^{-1}$)	1.9×10^{-7}		Diffusion coefficient of organic species
$D_{g,O3}$ ($cm^2\ s^{-1}$)	0.14		Gas-phase diffusion coefficient of O_3[20]
$D_{g,C9}$ ($cm^2\ s^{-1}$)	0.03		Gas-phase diffusion coefficient of C_9 species
$p_{vap,NN}$ (atm)	4.8×10^{-4}		Vapour pressure of nonanal[14]
$p_{vap,NA}$ (atm)	1.8×10^{-6}		Vapour pressure of nonanoic acid[14]
$p_{vap,ON}$ (atm)	1.2×10^{-7}		Vapour pressure of 9-oxononanoic acid[16]
$p_{vap,AA}$ (atm)	9.9×10^{-10}		Vapour pressure of azelaic acid[13]
$H_{cp,O3}$ ($mol\ cm^{-3}\ atm^{-1}$)	4.8×10^{-4}		Henry's law solubility coefficient of O_3 in OL[20]
$\tau_{D,O3}$ (s^{-1})	1.0×10^{-7}	1.0×10^{-9}–1.0×10^{-3}	Desorption lifetime of O_3
T (K)	293		Temperature
F_{141} (—)	0.075	1.0×10^{-4}–2.0×10^{0}	Scaling factor for signal at m/z 141
F_{157} (—)	0.7	1.0×10^{-4}–2.0×10^{0}	Scaling factor for signal at m/z 157
F_{171} (—)	1.5	1.0×10^{-4}–2.0×10^{0}	Scaling factor for signal at m/z 171
F_{187} (—)	0.25	1.0×10^{-4}–2.0×10^{0}	Scaling factor for signal at m/z 187

Table 3 Relative fractions of processes for first-generation products and CI depending on the applied ozone mixing ratio. The numbers represent the overall fate when integrating over the entire reaction time

Compound	O_3 mixing ratio (ppm)	Dimerisation (%)	Evaporation (%)	Isomerisation (%)
Nonanal	0.2	6.5	93.5	
	15	60.8	39.2	
Nonanoic acid	0.2	0.5	99.5	
	15	9.6	90.4	
9-Oxononanoic acid	0.2	99.3	0.7	
	15	99.97	0.03	
Azelaic acid	0.2	73.4	26.6	
	15	96.3	3.7	
CI-157	0.2	65.6	10.7	23.6
	15	83.6	7.3	9.1
CI-187	0.2	73.5	0.0	26.5
	15	90.2	0.0	9.8

that all aldehydes and acids, respectively, react with the same rate coefficients. Note that the AAHP formed in the reaction of CI with oleic acid is still able to undergo ozonolysis with a rate coefficient k_{BR1}/k_{SLR1}.

We assume that all first-generation products (nonanal, nonanoic acid, 9-oxononanoic acid and azelaic acid and the two CI) are semi-volatile and evaporate according to their vapour pressure (literature references in Table 2). The desorption flux from the particle surface to the gas phase is parameterised as a function of vapour pressure.[46] For CI, we assume the vapour pressures of the corresponding aldehydes. Oleic acid and secondary products are treated as non-volatile.

To compare primary model output to the mass spectra, mole fractions of chemical species are multiplied with scaling factors (F) to simulate the compound-specific detection efficiency in the experimental setup. Dimers are assumed to thermally decompose into their constituting monomers (nonanal, nonanoic acid, 9-oxononanoic acid and azelaic acid). For the secondary ozonides, the thermal decomposition is assumed to produce pairs of aldehydes and acids. The two possible sets of products of this decomposition are assumed to occur with equal likelihood.

The relative fractions of first order (evaporation and rearrangement) and second order processes (bimolecular reaction) are shown in Fig. 13 as a function of the remaining oleic acid concentration. Time-integrated relative fractions of the different processes are provided in Table 3. Overall, the secondary reaction dominates over evaporation for first-generation products with low volatility (azelaic acid and 9-oxononanoic acid), and for CI due to their high reaction rate coefficients. For nonanal, the vapour pressure is just high enough that evaporation dominates under low ozone conditions but dimerisation reactions dominate at the high ozone concentration. This is due to the high steady-state concentration of first-generation products and CI at high ozone mixing ratios, favouring the second-order reaction. In the case of nonanoic acid, the high volatility dictates the fate because of the low reactivity with CI (due to the absence of an aldehyde functional group, R4 *vs.* R5). For CI, the rearrangement provides another first-order process, which dominates over evaporation for CI-187 but is on the same order of magnitude as the evaporation for CI-157.

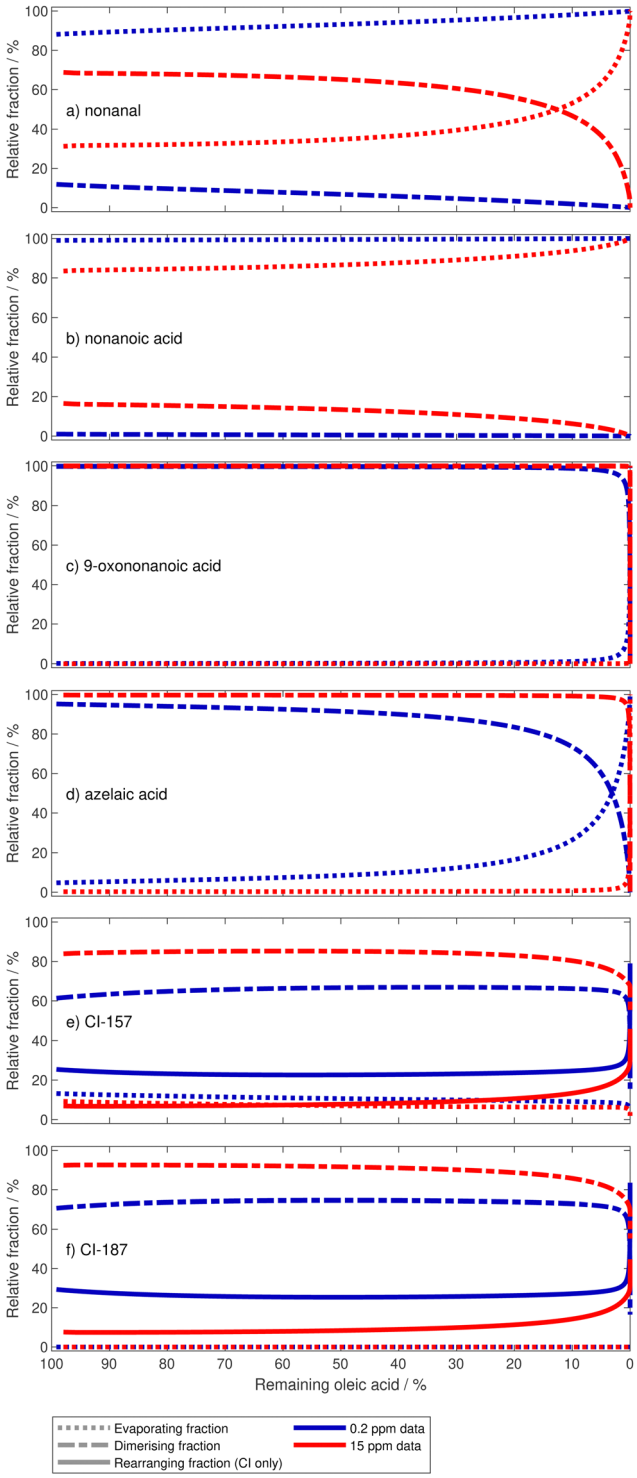

Fig. 13 Representation of the relative importance of evaporation, secondary reaction, and first-order rearrangement of first-generation products (a–d) and CI (e and f). The remaining fraction of oleic acid in the drop is used as abscissa.

Kinetic flux analysis reveals that, in our model, approximately 92% of the primary oleic acid loss is due to surface reaction.

Appendix E: simplified chemistry representation with differential equations

For the treatment of a simplified chemical scheme, we write oleic acid as 'OL', monomers as 'M' and dimers as 'D'. The following derivation may help to understand the characteristics of the product formation curve under specific conditions. We consider a reaction (E.1) with reaction rate coefficient k_1,

$$\mathrm{OL} + \mathrm{O_3} \rightarrow \mathrm{M} + \mathrm{M}, \tag{E.1}$$

and a reaction (E.2) with reaction rate coefficient k_2,

$$\mathrm{M} + \mathrm{M} \rightarrow \mathrm{D}. \tag{E.2}$$

Furthermore, we consider the evaporation of M as depending linearly on an evaporation rate E and the concentration [M]. Time-dependent concentrations are given in squared brackets (*e.g.* [M]) and initial concentrations are denoted explicitly (*e.g.* $[\mathrm{M}]_0$).

The change of the oleic acid concentration over time is then

$$\frac{\mathrm{d}}{\mathrm{d}t}[\mathrm{OL}] = -k_1[\mathrm{O_3}][\mathrm{OL}],$$

the monomer concentration changes as

$$\frac{\mathrm{d}}{\mathrm{d}t}[\mathrm{M}] = k_1[\mathrm{O_3}][\mathrm{OL}] - k_2[\mathrm{M}]^2 - E[\mathrm{M}]$$

and the dimer concentration change is given as

$$\frac{\mathrm{d}}{\mathrm{d}t}[\mathrm{D}] = k_2[\mathrm{M}]^2.$$

If $k_1[\mathrm{O_3}]$ is assumed to be constant, then the time-dependent concentration of oleic acid is simply

$$[\mathrm{OL}] = [\mathrm{OL}]_0 \mathrm{e}^{-\mathrm{k_1[O_3]}t} = [\mathrm{OL}]_0 \mathrm{e}^{-t/\tau},$$

with the characteristic e-folding exposure $\tau = \dfrac{1}{k_1[\mathrm{O_3}]}$. Assuming steady state conditions for [M] gives

$$\frac{\mathrm{d}}{\mathrm{d}t}[\mathrm{M}] = 0 = k_1[\mathrm{O_3}][\mathrm{OL}] - k_2[\mathrm{M}]^2 - E[\mathrm{M}],$$

which yields

$$[\mathrm{M}] = \left(\frac{E^2}{4k_2{}^2} + \frac{k_1[\mathrm{O_3}][\mathrm{OL}]_0 \mathrm{e}^{-t/\tau}}{k_2}\right)^{1/2} - \frac{E}{2k_2}$$

and therefore

$$\frac{\mathrm{d}}{\mathrm{d}t}[\mathrm{D}] = k_2\left[\left(\frac{E^2}{4k_2{}^2} + \frac{k_1[\mathrm{O_3}][\mathrm{OL}]_0 \mathrm{e}^{-t/\tau}}{k_2}\right)^{1/2} - \frac{E}{2k_2}\right]^2 = k_2[\mathrm{M}]^2.$$

By introducing a dimensionless relative dimer concentration $\Delta = [\mathrm{D}]/[\mathrm{OL}]_0$, a dimensionless relative evaporation $\varepsilon = E/\sqrt{4k_1[\mathrm{O_3}]k_2[\mathrm{OL}]_0}$ and a dimensionless time surrogate $\theta = t/\tau$, we may write

$$\frac{\mathrm{d}}{\mathrm{d}\theta}\Delta = \left[\left(\varepsilon^2 + \mathrm{e}^{-\theta}\right)^{1/2} - \varepsilon\right]^2. \tag{E.3}$$

In an extreme case without evaporation (*i.e.* $\varepsilon = 0$), eqn (E.3) simplifies to

$$\frac{\mathrm{d}}{\mathrm{d}\theta}\Delta = \mathrm{e}^{-\theta}$$

for which we obtain $\Delta = 1 - \mathrm{e}^{-\theta}$ and therefore

$$[\mathrm{D}] = [\mathrm{OL}]_0(1 - \mathrm{e}^{-t/\tau}).$$

In the other extreme case, where the evaporation is infinitely fast, eqn (E.3) can be reduce to

$$\frac{\mathrm{d}}{\mathrm{d}\theta}\Delta = \frac{\mathrm{e}^{-2\theta}}{4\varepsilon^2}.$$

using a Taylor expansion of $\left(1 + \dfrac{\mathrm{e}^{-\theta}}{\varepsilon^2}\right)^{1/2}$ for $\dfrac{\mathrm{e}^{-\theta}}{\varepsilon^2} \ll 1$ to the second term. Therefore, we obtain

$$\Delta = c - \frac{e^{-2\theta}}{8\varepsilon^2}$$

with constant c, which means [D] can be expressed as

$$[\mathrm{D}] = \frac{k_1k_2[\mathrm{OL}]_0{}^2[\mathrm{O_3}]}{2E^2}\left(1 - \mathrm{e}^{-2t/\tau}\right).$$

Note the deviation by a factor of two for the e-folding exposure compared to the limiting case without evaporation (the exponent changes from τ to $\tau/2$).

Acknowledgements

This work was supported by ETH Research Grant ETH-03 17-2. The authors would like to thank Nico Germann, Marco Vecellio and Uwe Weers for their contributions to design and construction of the instrumentation. Furthermore, scientific discussions with Nir Bluvshtein and support from Plasmion GmbH, Augsburg, Germany were much appreciated. A. M. was supported by the Max Planck Graduate Center with the Johannes Gutenberg University Mainz (MPGC).

Notes and references

1 A. K. Lee and C. K. Chan, *Atmos. Environ.*, 2007, **41**, 4611–4621.
2 V. F. McNeill, R. L. Yatavelli, J. A. Thornton, C. B. Stipe and O. Landgrebe, *Atmos. Chem. Phys.*, 2008, **8**, 5465–5476.
3 L. H. Renbaum and G. D. Smith, *Atmos. Chem. Phys.*, 2011, **11**, 6881–6893.
4 C. L. Liu, J. D. Smith, D. L. Che, M. Ahmed, S. R. Leone and K. R. Wilson, *Phys. Chem. Chem. Phys.*, 2011, **13**, 8993–9007.
5 Y. Chu, T. F. Cheng, M. Gen, C. K. Chan, A. K. Lee and M. N. Chan, *ACS Earth Space Chem.*, 2019, **3**, 779–788.
6 J. Zahardis and G. A. Petrucci, *Atmos. Chem. Phys.*, 2007, **7**, 1237–1274.

7 O. Vesna, M. Sax, M. Kalberer, A. Gaschen and M. Ammann, *Atmos. Environ.*, 2009, **43**, 3662–3669.
8 B. J. Dennis-Smither, R. E. Miles and J. P. Reid, *J. Geophys. Res. Atmos.*, 2012, **117**, 1–13.
9 M. Wang, L. Yao, J. Zheng, X. Wang, J. Chen, X. Yang, D. R. Worsnop, N. M. Donahue and L. Wang, *Environ. Sci. Technol.*, 2016, **50**, 5702–5710.
10 P. J. Gallimore, P. T. Griffiths, F. D. Pope, J. P. Reid and M. Kalberer, *J. Geophys. Res.*, 2017, **122**, 4364–4377.
11 A. Milsom, A. M. Squires, A. D. Ward and C. Pfrang, *Atmos. Chem. Phys.*, 2022, **22**, 4895–4907.
12 Z. Zhou, P. S. J. Lakey, M. von Domaros, N. Wise, D. J. Tobias, M. Shiraiwa and J. P. D. Abbatt, *Environ. Sci. Technol.*, 2022, **56**, 7716–7728.
13 M. Bilde, K. Barsanti, M. Booth, C. D. Cappa, N. M. Donahue, E. U. Emanuelsson, G. McFiggans, U. K. Krieger, C. Marcolli, D. Topping, P. Ziemann, M. Barley, S. Clegg, B. Dennis-Smither, M. Hallquist, Å. M. Hallquist, A. Khlystov, M. Kulmala, D. Mogensen, C. J. Percival, F. Pope, J. P. Reid, M. A. Ribeiro Da Silva, T. Rosenoern, K. Salo, V. P. Soonsin, T. Yli-Juuti, N. L. Prisle, J. Pagels, J. Rarey, A. A. Zardini and I. Riipinen, *Chem. Rev.*, 2015, **115**, 4115–4156.
14 T. E. Daubert and R. Danner, *Physical and thermodynamic properties of pure chemicals: data compilation*, Taylor and Francis, 1989.
15 C. D. Cappa, E. R. Lovejoy and A. R. Ravishankara, *J. Phys. Chem. A*, 2008, **112**, 3959–3964.
16 S. Compernolle, K. Ceulemans and J. F. Müller, *Atmos. Chem. Phys.*, 2011, **11**, 9431–9450.
17 R. Criegee, *Angew. Chem., Int. Ed. Engl.*, 1975, **14**, 745–752.
18 P. J. Ziemann, *Faraday Discuss.*, 2005, **130**, 469–490.
19 J. Zahardis, B. W. LaFranchi and G. A. Petrucci, *J. Geophys. Res., D: Atmos.*, 2005, **110**, 1–10.
20 T. Berkemeier, A. Mishra, C. Mattei, A. J. Huisman, U. K. Krieger and U. Pöschl, *ACS Earth Space Chem.*, 2021, **5**, 3313–3323.
21 H. M. Hung, Y. Katrib and S. T. Martin, *J. Phys. Chem. A*, 2005, **109**, 4517–4530.
22 S. S. Al-Kindi, F. D. Pope, D. C. Beddows, W. J. Bloss and R. M. Harrison, *Atmos. Chem. Phys.*, 2016, **16**, 15561–15579.
23 A. W. Birdsall, U. K. Krieger and F. N. Keutsch, *Atmos. Meas. Tech.*, 2018, **11**, 33–47.
24 M. I. Jacobs, J. F. Davies, L. Lee, R. D. Davis, F. Houle and K. R. Wilson, *Anal. Chem.*, 2017, **89**, 12511–12519.
25 M. I. Jacobs, R. D. Davis, R. J. Rapf and K. R. Wilson, *J. Am. Soc. Mass Spectrom.*, 2019, **30**, 339–343.
26 A. W. Birdsall, J. C. Hensley, P. S. Kotowitz, A. J. Huisman and F. N. Keutsch, *Atmos. Chem. Phys.*, 2019, **19**, 14195–14209.
27 M. D. Willis, G. Rovelli and K. R. Wilson, *Anal. Chem.*, 2020, **92**, 11943–11952.
28 R. Kaur Kohli and J. F. Davies, *Analyst*, 2020, **145**, 2639–2648.
29 J. C. Hensley, A. W. Birdsall and F. N. Keutsch, *Environ. Sci. Technol.*, 2021, **55**, 11549–11556.
30 J. C. Hensley, A. W. Birdsall, G. Valtierra, J. L. Cox and F. N. Keutsch, *Atmos. Chem. Phys.*, 2021, **21**, 8809–8821.
31 R. K. Kohli and J. F. Davies, *Anal. Chem.*, 2021, **93**, 12472–12479.
32 U. K. Krieger, C. Marcolli and J. P. Reid, *Chem. Soc. Rev.*, 2012, **41**, 6631–6662.
33 L. Bregy, P. M. L. Sinues, M. M. Nudnova and R. Zenobi, *J. Breath Res.*, 2014, **8**, 027102.
34 J. C. Wolf, M. Schaer, P. Siegenthaler and R. Zenobi, *Anal. Chem.*, 2015, **87**, 723–729.
35 M. F. Mirabelli, J. C. Wolf and R. Zenobi, *Analyst*, 2017, **142**, 1909–1915.
36 L. Gyr, J. C. Wolf, J. Franzke and R. Zenobi, *Anal. Chem.*, 2018, **90**, 2725–2731.
37 J. C. Reynolds, D. J. Last, M. McGillen, A. Nijs, A. B. Horn, C. Percival, L. J. Carpenter and A. C. Lewis, *Environ. Sci. Technol.*, 2006, **40**, 6674–6681.
38 G. Li, N. Bei, J. Cao, J. Wu, X. Long, T. Feng, W. Dai, S. Liu, Q. Zhang and X. Tie, *Atmos. Chem. Phys.*, 2017, **17**, 2759–2774.
39 J. Staehelin, F. Tummon, L. Revell, A. Stenke and T. Peter, *Atmosphere*, 2017, **8**, 1–20.
40 D. R. Worsnop, J. W. Morris, Q. Shi, P. Davidovits and C. E. Kolb, *Geophys. Res. Lett.*, 2002, **29**, 19–22.
41 M. Shiraiwa, C. Pfrang and U. Pöschl, *Atmos. Chem. Phys.*, 2010, **10**, 3673–3691.
42 T. Berkemeier, A. J. Huisman, M. Ammann, M. Shiraiwa, T. Koop and U. Pöschl, *Atmos. Chem. Phys.*, 2013, **13**, 6663–6686.
43 R. B. Bird, W. E. Stewart and E. N. Lightfoot, *Transport phenomena*, Wiley, New York, Rev. 2nd edn, 2007.
44 D. Topping, M. Barley, M. K. Bane, N. Higham, B. Aumont, N. Dingle and G. McFiggans, *Geosci. Model Dev.*, 2016, **9**, 899–914.
45 M. Zeng and K. R. Wilson, *J. Phys. Chem. Lett.*, 2020, **11**, 6580–6585.
46 T. Berkemeier, M. Takeuchi, G. Eris and N. L. Ng, *Atmos. Chem. Phys.*, 2020, **20**, 15513–15535.
47 S. Marelli and B. Sudret, *Vulnerability, Uncertainty, and Risk*, Reston, VA, 2014, pp. 2554–2563.
48 P.-R. Wagner, J. Nagel, S. Marelli and B. Sudret, *UQLab user manual – Bayesian inversion for model calibration and validation, Chair of risk, safety and uncertainty quantification*, ETH Zurich, Switzerland, Technical report, 2021.
49 Y. Katrib, S. T. Martin, Y. Rudich, P. Davidovits, J. T. Jayne and D. R. Worsnop, *Atmos. Chem. Phys.*, 2005, **5**, 275–291.
50 S. Xu, F. Mahrt, F. K. A. Gregson and A. K. Bertram, *ACS Earth Space Chem.*, 2022, **6**, 1836–1845.
51 P. H. Dawson, *Quadrupole mass spectrometry and its applications*, Elsevier Scientific Publishing Company, Amsterdam, Netherlands, 1976.
52 M. B. Hart, V. Sivaprakasam, J. D. Eversole, L. J. Johnson and J. Czege, *Appl. Opt.*, 2015, **54**, F174.
53 M. Woźniak, G. Derkachov, K. Kolwas, J. Archer, T. Wojciechowski, D. Jakubczyk and M. Kolwas, *Langmuir*, 2015, **31**, 7860–7868.
54 E. J. Davis and R. Periasamy, *Langmuir*, 1985, **1**, 373–379.
55 P. Laven, *Appl. Opt.*, 2003, **42**, 436.

56 M. M. Nudnova, L. Zhu and R. Zenobi, *Rapid Commun. Mass Spectrom.*, 2012, **26**, 1447–1452.
57 L. Gyr, F. D. Klute, J. Franzke and R. Zenobi, *Anal. Chem.*, 2019, **91**, 6865–6871.
58 S. M. Kurtz, *Chemical and Radiation Stability of PEEK*, Elsevier Inc., 2012, pp. 75–79.
59 W. J. Glantschnig and S.-H. Chen, *Appl. Opt.*, 1981, **20**, 2499.
60 A. K. Ray, A. Souyri, E. J. Davis and T. M. Allen, *Appl. Opt.*, 1991, **30**, 3974.
61 O. Welz, J. D. Savee, D. L. Osborn, S. S. Vasu, C. J. Percival, D. E. Shallcross and C. A. Taatjes, *Science*, 2012, **335**, 204–207.

2.4. Kinetic modeling of photochemical degradation of iron carboxylates

The paper in this chapter has been published as a research article in the journal ACS Earth and Space Chemistry. I am the first author and the main contributor of this paper. I developed the kinetic model together with Thomas Berkemeier. I optimized the model and I performed the kinetic model simulations. I analyzed the model results. I produced the figures and wrote the paper, with input from the co-authors. The supplement to this work can be found in Appendix B.2.

Mishra, A., Kilchhofer, K., Iezzi, L., Pöschl, U., Alpert, P. A., Ammann, M., Berkemeier, T.: Photochemical degradation of iron citrate in anoxic viscous films enhanced by redox cascades, *ACS Earth Space Chem.* 9, 689-698, (2025).

In this study, the effect of relative humidity on the photochemical aging of iron citrate (Fe(III)Cit), a proxy for iron carboxylates was explored. Following a rapid initial reaction, the photooxidation of Fe(III)Cit was limited by the reoxidation of Fe(II). The model analysis revealed two distinct regimes: at low humidity (RH < 65%), the bulk diffusion of O_2 limited the reoxidation of Fe(II), while at high humidity (RH > 85%), O_2 was fully saturated in the bulk, and the chemical reactions with Fe(II) limited the uptake of O_2. ROS, in particular HO_2 and H_2O_2, were crucial in Fe(II) reoxidation, thereby sustaining photooxidation chemistry. While previous studies found large discrepancies between the diffusion coefficient of CO_2 and O_2, the obtained result showed that the diffusion of CO_2 and O_2 were similar, as expected of two molecules with similar molecular diameters.

ACS EARTH AND SPACE CHEMISTRY

http://pubs.acs.org/journal/aesccq
Article

Photochemical Degradation of Iron Citrate in Anoxic Viscous Films Enhanced by Redox Cascades

Published as part of ACS Earth and Space Chemistry special issue "Hartmut Herrmann Festschrift".

Ashmi Mishra, Kevin Kilchhofer, Lucia Iezzi, Ulrich Pöschl, Peter A. Alpert, Markus Ammann, and Thomas Berkemeier*

Cite This: ACS Earth Space Chem. 2025, 9, 689−698

ABSTRACT: Iron contained in atmospheric aerosol particles can form complexes with organic ligands and initiate photochemical reactions that alter the composition and physicochemical properties of the particles. Depending on the temperature and humidity, organic particles exist in different phase states, which affects reactant diffusivity and chemical reaction rates. We performed coated-wall flow-tube experiments using citric acid films doped with iron as proxies for secondary organic aerosols. We quantified the CO_2 production under UV irradiation as a function of time and relative humidity (RH) and observed a pronounced decrease of CO_2 production with decreasing RH. The kinetic multilayer model of aerosol surface and bulk chemistry (KM-SUB) and a Monte Carlo-based global optimization method were applied to all measured data to determine the underlying effects of mass transport and chemical reactions. The model analysis revealed that after an initial rapid reaction, photooxidation becomes limited by the reoxidation of Fe^{II}. Under dry conditions (RH < 65%), the reoxidation of Fe^{II} is kinetically limited by the supply of O_2, as slow diffusion in the viscous organic matrix leads to anoxia in the interior of the film. At high humidity (RH > 85%), mass transport limitations cease, resulting in full O_2 saturation, and photooxidation becomes limited by the chemical reaction of Fe^{II} with oxidants. Reactive oxygen species play a key role in Fe^{II} reoxidation and thus in perpetuating photooxidation chemistry. A single O_2 molecule triggers a redox cascade from O_2 to HO_2, H_2O_2, and OH, leading to ≈3 cycles of the Fe^{II}/Fe^{III} redox pair. Our model and kinetic parameters provide new insights and constraints in the interplay of microphysical properties and photochemical aging of mixed organic−inorganic aerosol particles, which may influence their effects on air quality, climate, and public health.

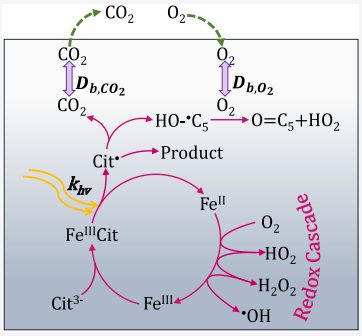

KEYWORDS: *Heterogeneous chemistry, Photochemistry, Reaction kinetics, Fenton reaction, Inverse modeling*

INTRODUCTION

Atmospheric aerosol is a suspension of solid and liquid particles in air that plays an important role in global climate, air quality, and public health.[1,2] Organic aerosol particles contribute to a large fraction (20 to 90%) of the total particulate mass.[3,4] Human activities including industrial operations, brake and tire wear, as well as combustion processes can release iron into the atmosphere.[5−8] Iron is also emitted naturally into the atmosphere in the form of mineral dust.[9] Organic materials can act as ligands for the complexation of iron.[10] Field studies have shown that soluble iron strongly correlates with concentrations of carboxylic acid.[11,12] Iron carboxylates undergo photochemistry, resulting in decarboxylation and the formation of organic radicals,[13−16] leading to the breakdown and processing of organic matter in the atmospheric aqueous phase. For such systems, the photochemical degradation of iron citrate (Fe^{III}Cit) has been established as a proxy system for laboratory and modeling studies.[15,17−19] Fe^{III} is photochemically reduced to Fe^{II} and can be reoxidized by O_2 and reactive oxygen species (ROS), closing the photochemical cycle. Alpert et al.[18] found that an excessive formation of ROS and organic radicals may lead to anoxic conditions as a result of the fast reaction between the radicals and oxygen and the slow diffusion of oxygen into particles exhibiting viscous phase states. Furthermore, the presence of iron will lead to the production of OH radicals through the Fenton reaction,[20] even in the absence of light.[21]

The rate at which chemical reactions occur in organic aerosol particles is strongly dependent on their phase state,[22,23] which varies from liquid to solid depending on composition and ambient conditions such as temperature and relative humidity (RH).[24−29] Photochemical aging can also trigger changes in the viscosity of secondary organic aerosol (SOA)

Received: December 3, 2024
Revised: February 4, 2025
Accepted: February 11, 2025
Published: February 25, 2025

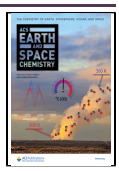

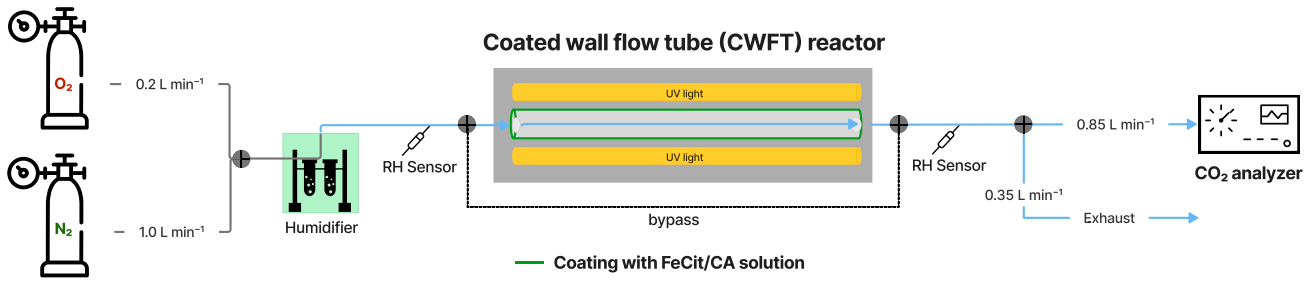

Figure 1. Schematic of the coated-wall flow-tube (CWFT) setup. The flow-tube was stored in a reactor casing surrounded by seven UVA lamps. The reactor casing contained silica oil to maintain T and RH. The geometry of the tubes was radius, r = 0.55 cm; length, l = 36 cm. The volume of the solution used for the coating was V = 500 μL.

Table 1. Environmental Input Parameters for KM-SUB Used with the Six Experimental Data Sets: Relative Humidity (RH), Film Thickness δ_{film}, Gas Phase Concentration of Oxygen $[O_2]_g$, and Bulk Phase Concentrations of Iron Citrate $[Fe^{III}Cit]_b$, Citric Acid $[CitH_3]_b$, and Water $[H_2O]_b$ in the Film

RH (%)	δ_{film} (cm)	$[O_2]_g$ (cm^{-3})	$[Fe^{III}Cit]_b$ (cm^{-3})	$[CitH_3]_b$ (cm^{-3})	$[H_2O]_b$ (cm^{-3})
30	6.12×10^{-5}	4.74×10^{18}	3.87×10^{20}	3.92×10^{21}	4.31×10^{21}
35	6.36×10^{-5}	4.74×10^{18}	3.76×10^{20}	3.81×10^{21}	5.19×10^{21}
45	6.80×10^{-5}	4.74×10^{18}	3.55×10^{20}	3.56×10^{21}	7.12×10^{21}
65	8.25×10^{-5}	4.74×10^{18}	2.90×10^{20}	2.94×10^{21}	1.20×10^{22}
85	1.24×10^{-4}	4.74×10^{18}	1.94×10^{20}	1.95×10^{21}	1.95×10^{22}
65	6.15×10^{-5}	0	2.90×10^{20}	2.94×10^{21}	1.20×10^{22}

particles.[30] Citric acid is used as a proxy for atmospheric SOA, mimicking particle hygroscopicity and viscosity.[31] In atmospheric multiphase chemistry, kinetic multilayer models have been established as helpful tools to achieve a detailed understanding of chemical reactions and mass transport processes of particles and films.[19,32−40]

In this study, we perform coated-wall flow-tube (CWFT) experiments to quantify CO_2 from the photolysis of $Fe^{III}Cit$ films at varying RH. To assess a possible viscosity dependence, we have carried out experiments from 30 to 85% RH. In this range, citric acid exhibits viscosities from approximately 10^2 Pa s (30% RH) to 10^{-2} Pa s (85% RH).[18,41] We analyze the time-resolved results of the experiments using the kinetic model KM-SUB[33] and a Monte Carlo genetic algorithm (MCGA)[42] for unbiased multiparameter fitting to gain mechanistic insights into the influence of microphysics on photochemical aging of mixed organic−inorganic aerosol particles.

METHODS

Flow-Tube Coating and Experimental Setup. Coatings on the inner wall of glass flow tubes were prepared from a solution of citric acid ($CitH_3$, ≥99.5%; CAS: 5949-29-1) and $Fe^{III}Cit$ tribasic monohydrate (18−20% Fe basis; CAS: 2338-05-8) purchased from Sigma-Aldrich. The dilute aqueous solutions were prepared in ultrapure water (18 M Ω cm^{-1}, Milli-Q) and in a 1:10 molar ratio ($CitH_3$ = 0.1 M, $Fe^{III}Cit$ = 0.01 M). The light-sensitive $Fe^{III}Cit$ solution was ensured to always be stored in the dark and was freshly prepared shortly before each experiment.

The coating solution (500 μL) was pipetted into the glass tube (length: 36 cm, radius: 0.55 cm) and evenly distributed on the interior surface. We used red light while coating to not initiate excitation of $Fe^{III}Cit$ before the experiment. A moist airflow of 1.0 L min^{-1} was used to allow the film coating to settle for 40−50 min by gently tilting and turning the tube until no visible liquid remained. The RH of this airflow was set to the same RH used later in the experiment in order to pre-equilibrate the coating and to achieve a homogeneous film thickness. The glass tube was then inserted into the reactor casing containing silica oil to maintain the temperature and RH, as depicted in Figure 1, between seven UVA lamps (Phillips, 20W). There, a constant flow of 0.2 L min^{-1} O_2 and 1.0 L min^{-1} N_2 carrier gas with a set temperature of 21 °C under certain RH conditions was used to equilibrate the coating before each experiment. The RH was adjusted by bubbling the gas flows through a temperature-controlled water bath upstream of the CWFT reactor, which was monitored up and downstream of the CWFT. A CO_2 analyzer (Teledyne, T200) sampled with a flow rate of 0.85 L min^{-1}, and the excess flow went to exhaust.

Experimental Procedure. Before each measurement, the background CO_2 concentration was observed for approximately 20 min by bypassing the CWFT reactor. Upon inserting the glass tube into the reactor, the flow was directed to the CWFT, and the background concentration of CO_2 was recorded until a steady state was reached. The film was exposed to light at two specific intervals. The irradiation periods lasted between 10 and 15 min in the first interval and between 5 and 10 min in the second interval.

Six different experiments were performed in this study, five of which were done in the presence of oxygen at 30, 35, 45, 65, and 85% RH, respectively. One experiment was performed in an oxygen-free environment at 65% RH. Table 1 provides a list of experimental parameters.

Kinetic Modeling. Kinetic modeling was performed using a variant of the kinetic multilayer model of aerosol surface and bulk chemistry (KM-SUB) for planar films.[33] The model consists of multiple compartments, including the gas phase, a sorption surface layer, and 15 bulk layers. The following processes were explicitly resolved for O_2, CO_2, the hydroperoxyl radical (HO_2), and hydrogen peroxide (H_2O_2): gas phase diffusion, adsorption, and desorption to and from the sorption layer, bulk diffusion, as well as chemical reactions in

https://doi.org/10.1021/acsearthspacechem.4c00364
ACS Earth Space Chem. 2025, 9, 689−698

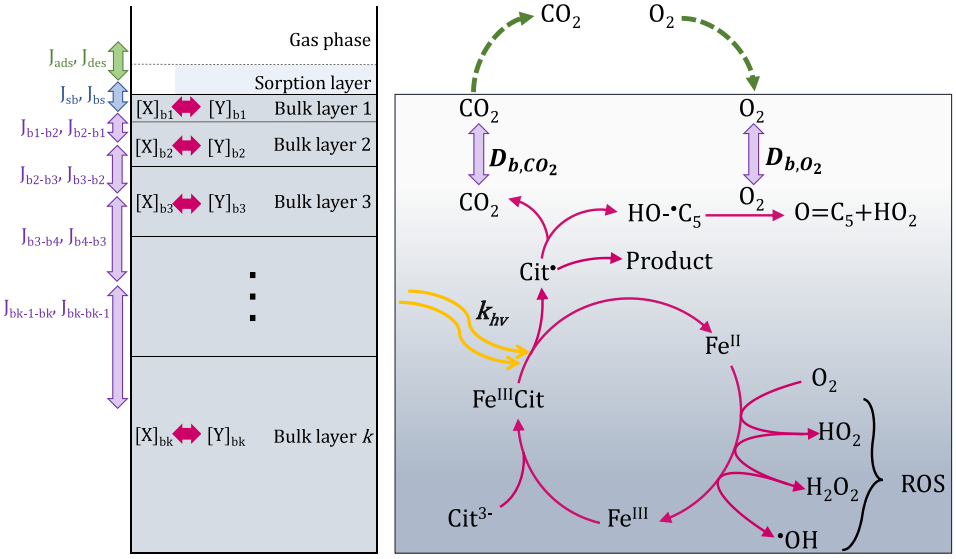

Figure 2. Model compartments (left) and simplified chemical mechanism (right) used in the kinetic multilayer model KM-SUB in this study. The model explicitly treats the flow reactor gas phase, a sorption surface layer, and multiple bulk layers. Transport fluxes are indicated as arrows in green (adsorption and desorption fluxes: J_{ads}, J_{des}), blue (mass transport between surface and bulk: J_{sb}, J_{bs}) and purple (mass transport within the bulk: $J_{bk,bk-1}$, $J_{bk-1,bk}$). The pink arrows represent the chemical reactions taking place in each bulk layer. The photochemical cycle produces reactive oxygen species (ROS) in the form of HO_2, OH, and H_2O_2.

Table 2. KM-SUB Kinetic Input Parameters[a]

parameter	range	description	reference
$D_{b,O2}$	1.0×10^{-13}–1.0×10^{-7} ($cm^2\ s^{-1}$)	bulk diffusion coefficient of O_2	this study
$D_{b,CO2}$	1.0×10^{-13}–1.0×10^{-7} ($cm^2\ s^{-1}$)	bulk diffusion coefficient of CO_2	this study
$D_{b,Fe^{III}Cit}$ 30% RH	[1.0×10^{-15}] ($cm^2\ s^{-1}$)	bulk diffusion coefficient of $Fe^{III}Cit$	Dou et al.[19]
$D_{b,Fe^{III}Cit}$ 35% RH	[3.0×10^{-15}] ($cm^2\ s^{-1}$)	bulk diffusion coefficient of $Fe^{III}Cit$	Dou et al.[19]
$D_{b,Fe^{III}Cit}$ 45% RH	[1.0×10^{-13}] ($cm^2\ s^{-1}$)	bulk diffusion coefficient of $Fe^{III}Cit$	Dou et al.[19]
$D_{b,Fe^{III}Cit}$ 65% RH	[2.0×10^{-12}] ($cm^2\ s^{-1}$)	bulk diffusion coefficient of $Fe^{III}Cit$	Dou et al.[19]
$D_{b,Fe^{III}Cit}$ 85% RH	[5.0×10^{-12}] ($cm^2\ s^{-1}$)	bulk diffusion coefficient of $Fe^{III}Cit$	Dou et al.[19]
$D_{b,H2O}$ 30% RH	[3.0×10^{-9}] ($cm^2\ s^{-1}$)	bulk diffusion coefficient of H_2O	Dou et al.[19]
$D_{b,H2O}$ 35% RH	[5.0×10^{-9}] ($cm^2\ s^{-1}$)	bulk diffusion coefficient of H_2O	Dou et al.[19]
$D_{b,H2O}$ 45% RH	[1.0×10^{-7}] ($cm^2\ s^{-1}$)	bulk diffusion coefficient of H_2O	Dou et al.[19]
$D_{b,H2O}$ 65% RH	[2.0×10^{-6}] ($cm^2\ s^{-1}$)	bulk diffusion coefficient of H_2O	Dou et al.[19]
$D_{b,H2O}$ 85% RH	[4.0×10^{-6}] ($cm^2\ s^{-1}$)	bulk diffusion coefficient of H_2O	Dou et al.[19]
$H_{cp,O2}$	[1.32×10^{-6}] ($mol\ cm^{-3}\ atm^{-1}$)	Henry's law solubility coefficient of O_2	Sander[45]
$H_{cp,CO2}$	[3.34×10^{-5}] ($mol\ cm^{-3}\ atm^{-1}$)	Henry's law solubility coefficient of CO_2	Sander[45]
$\alpha_{s,0,CO2}$, $\alpha_{s,0,O2}$	[1]	surface accommodation coefficient of CO_2 and O_2	-
$\tau_{D,O2}$	[1.4×10^{-11}] (s^{-1})	desorption lifetime of O_2	Knopf et al.[46]
$\tau_{D,CO2}$	[4.5×10^{-9}] (s^{-1})	desorption lifetime of CO_2	Knopf et al.[46]
$a_{\Gamma,CO2}$	1–10	CO_2 analyzer response curve, shape parameter	this study
$b_{\Gamma,CO2}$	1–10	CO_2 analyzer response curve, scale parameter	this study

[a]The respective lower and upper boundaries indicate the initial constraints of the fit ensemble. Values that were fixed during the fitting procedure are indicated using square brackets.

the bulk of the film. All other reactants remain exclusively in the film bulk.

The numerical model describes the flux-based mass balance for each layer in systems of differential equations that were autogenerated using the kinetic multilayer meta model generator (KM-MEMO, Berkemeier et al., in preparation) based on the chemical mechanism and system geometry. An autogenerated Jacobian matrix is used to accelerate and increase the numerical stability of the model calculations. The KM-SUB model was modified such that the thickness of the layers increased exponentially, with the thickness of the closest layer to the surface being 0.3 nm (see the Supporting Information (SI) for details). Near the surface of the film, narrowly spaced layers ensured a smooth concentration gradient of O_2, which allowed numerical convergence to be achieved at much lower bulk layer counts. Previous studies on similar reaction systems have introduced the Photochemical Reaction and Diffusion (PRAD) model,[19] which solved the coupled equilibria of acid–base and complexation chemistry using instantaneous equilibration at dedicated time steps. The KM-SUB model employed here solves the coupled equilibria dynamically using explicit protonation and deprotonation reactions. We initially run the model without UV irradiation to determine the equilibrium pH. This pH remains fixed in the

https://doi.org/10.1021/acsearthspacechem.4c00364
ACS Earth Space Chem. 2025, 9, 685−698

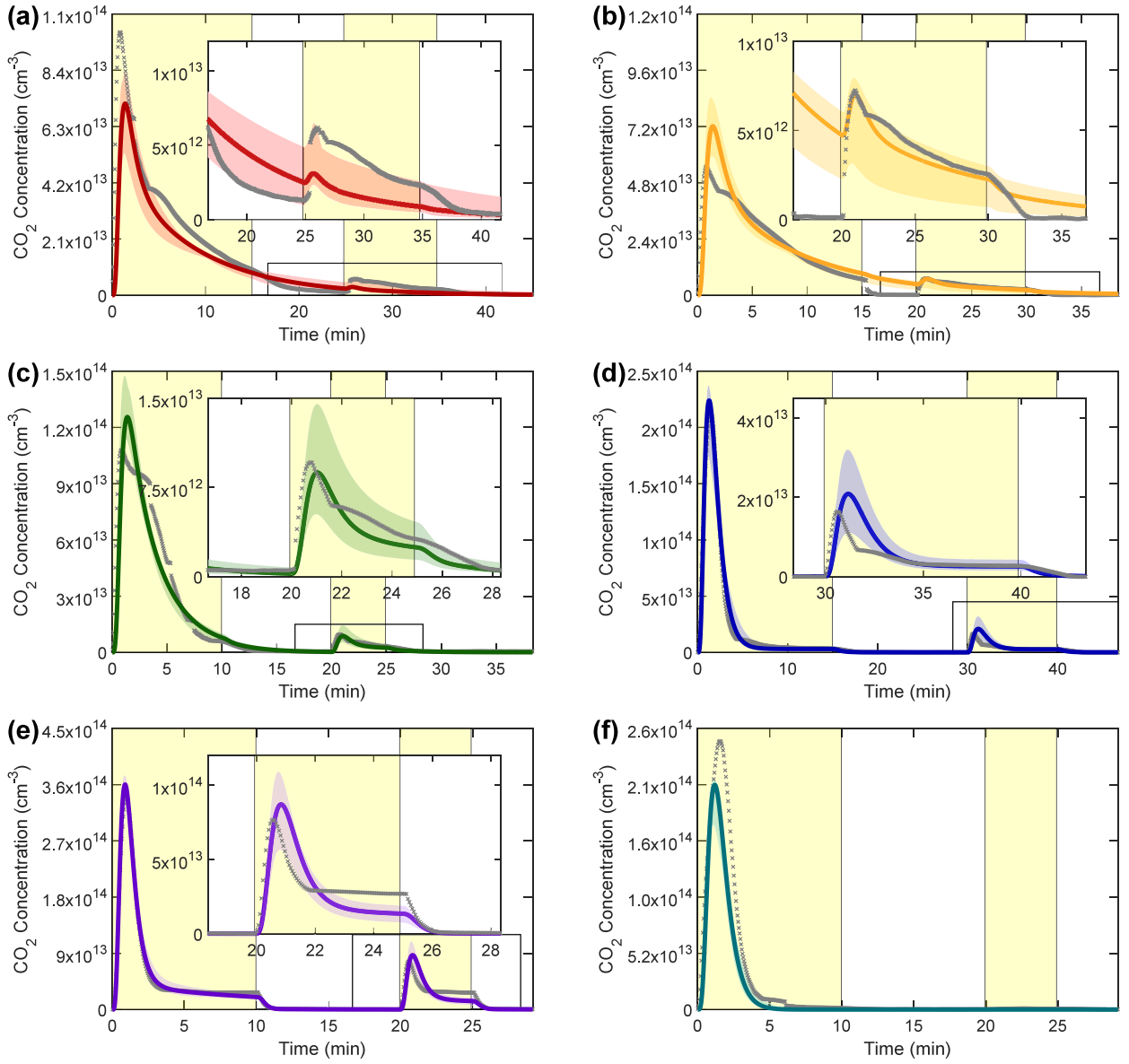

Figure 3. CO_2 production from the photolysis of iron citrate films in the coated-wall flow-tube experiments (gray markers) and the corresponding KM-SUB modeling results (dark colored lines) at different RH (30% (a), 35% (b), 45% (c), 65% (d), 85% (e), and 65% in the absence of O_2 (f)). The colored solid lines represent the globally best-fitting kinetic parameter set, and the colored shadings indicate the variability within the fit ensemble of N = 55 fits. The light yellow shaded regions represent irradiation periods.

later calculations involving photochemistry, as the pK_a values of the products are not established in the literature. Since the Fe^{III}Cit:citric acid molar ratio M_r was always 1:10 in the experiments, citric acid dominates the pH, which we find to be in the range of 1−2.

Figure 2 shows the key reactions involved in the Fe^{III}Cit photochemical system to produce radicals in the presence of O_2. Fe^{III}Cit is photoactive, which after excitation forms a radical complex that quickly dissociates into Fe^{II} and an organic radical with a $-C(=O)O^{\bullet}$ group at the central carbon,[43,44] $Cit^{\bullet 2-}$, herein further referred to as $Cit^{\bullet}$. $Cit^{\bullet}$ either decarboxylates, leading to the loss of CO_2 and production of a ketyl radical,[13,19] or stabilizes. The branching between these determines the CO_2 yield. Note that as the reactions of $Cit^{\bullet}$ are not well established in the literature, we fit a first-order loss rate to minimize the number of fitting parameters. The ketyl radical can react with another Fe^{III}Cit complex to yield Fe^{II} citrate (Fe^{II}CitH) and ketone.[13] Reactive oxygen species (ROS: H_2O_2, HO_2, O_2^-, OH) are generated when O_2 taken up by the film is reduced, e.g., through the ketyl radical, or through Fe^{II} being reoxidized to Fe^{III}, closing the photochemical cycle. $Cit^{\bullet}$ is also formed through the reaction of the hydroxyl radical (OH) with citrate. Table 2 and Tables S1 and S2 provide a list of all model input parameters used in this study. In the fitting of diffusion coefficients, we prescribed a monotonous increase with relative humidity.

Global Optimization. The kinetic model KM-SUB was fitted to experimental observations using a global optimization algorithm (Monte Carlo genetic algorithm, MCGA).[42] Model input parameters are inferred by simultaneously fitting the kinetic model to all of the available experimental data. MCGA is comprised of two steps. The first step consists of performing

https://doi.org/10.1021/acsearthspacechem.4c00364
ACS Earth Space Chem. 2025, 9, 689−698

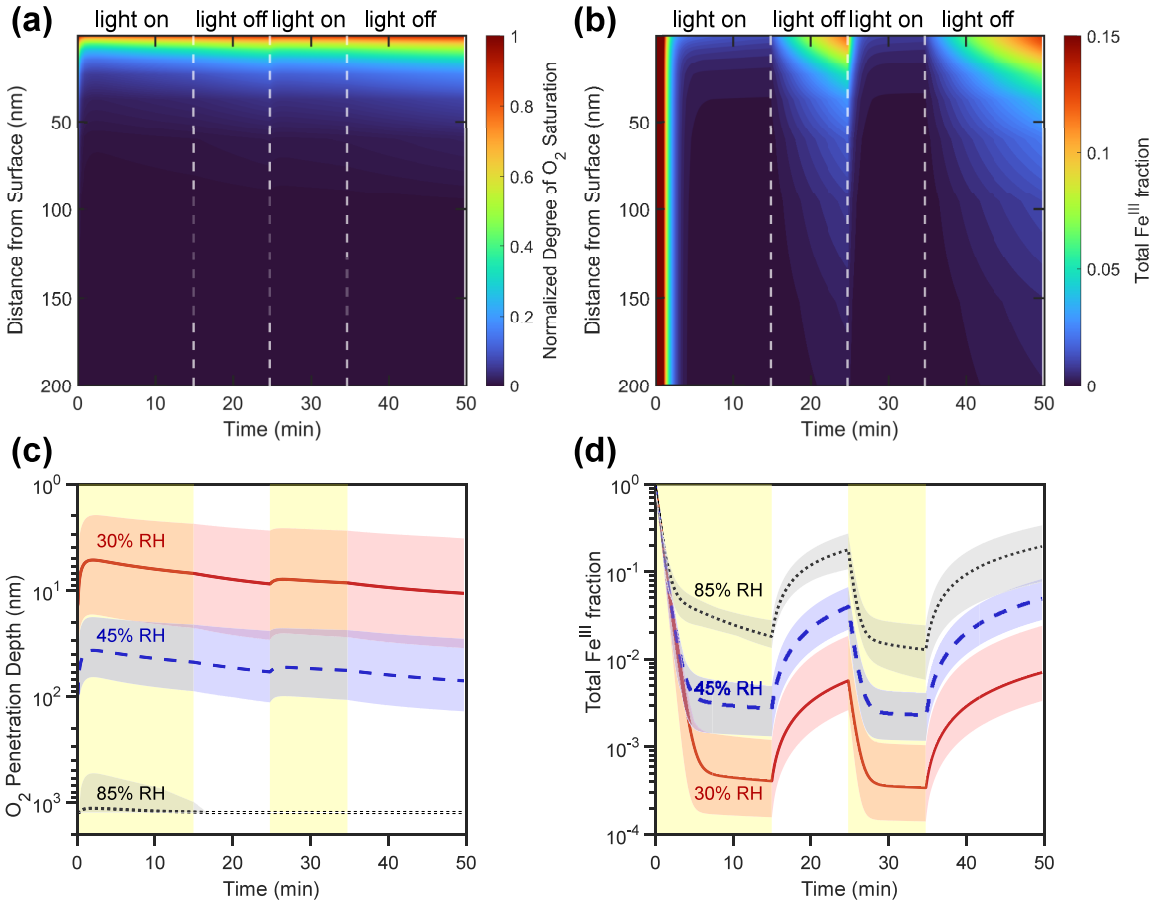

Figure 4. Depth profiles of the O_2 concentration (a) and Fe^{III} fraction (b) in a film as a function of time at 30% RH. The *y*-axis indicates the distance from the film surface. (c) Penetration depth of O_2, i.e., the position in the film at which the O_2 saturation reaches 0.5. (d) Model results for the total Fe^{III} fraction as a function of time. In panels (c) and (d), the solid lines represents the mean model result obtained from the ensemble solution, while the shaded areas indicate the ensemble variability. The light yellow shadings represent irradiation periods. For ease of comparison, the irradiation periods were simulated for all humidities as they occurred in the 30% RH experiment. Note that panels (a) and (b) only depict the top 200 nm of the film.

a Monte Carlo search by randomly sampling parameters from a range of predefined boundaries. The globally best-fitting parameter sets are then fed into the starting population of GA, in which they are optimized by processes mimicking survival, recombination, and mutation in evolutionary biology. The optimization was stopped when the population was homogeneous, and therefore, the increase in correlation with the experimental data ceased. Ideally, global optimization leads to a unique fit, i.e., a parameter set that is invariant when repeating the fitting process. In practice, however, multiphase chemical systems are often underdetermined, as they contain too many or nonorthogonal parameters or there are not enough data to achieve a unique fit.[37,42] In such instances, finding kinetic parameter sets that best fit the data is less beneficial. Thus, in this study, we identified an ensemble of adequately fitting parameter sets and collectively analyzed the kinetic model solutions that corresponded to those parameter sets.

RESULTS AND DISCUSSION

CO_2 Production. Figure 3 shows the gas phase number concentration of CO_2 produced in the coated-wall flow-tube (CWFT) experiments and compares the measurement with the KM-SUB model results. The experimental data are shown using gray markers, while the model results are depicted with solid lines and colored shadings. Using the MCGA, we generated an ensemble (N = 55) of model parameter sets that exhibit a satisfactory correlation to the experimental data. The lines depict the best-fitting model result, while the shadings denote the range of model results in the fit ensemble. The light yellow shaded regions show periods in which irradiation with UV light occurred. There is a stark difference in the intensity of the CO_2 signal between irradiation and dark periods. During the irradiation periods, the CO_2 concentrations increase sharply, peaking within seconds of the light being turned on. We see an increase in the peak concentrations with increasing RH, with the experiment at 85% RH (panel e) showing ~4 times higher CO_2 compared to the lowest RH experiment (30%, panel a). At lower RH (30−45%, panels a−c), the CO_2 signal decreases continuously after the initial peak, while at higher RH (65−85%, panels d and e), the signal eventually reaches a plateau after minutes of irradiation, which points toward a steady state of CO_2 production and evaporation. The model ascribes the sharp peak in the CO_2 concentration to rapid photolysis and depletion of Fe^{III}Cit. Continued CO_2 production is limited by the availability of Fe^{III}Cit for photolytic degradation and, to a lesser extent, limited by the formation of hydroxyl radicals (OH) that can react with citrate.

https://doi.org/10.1021/acsearthspacechem.4c00364
ACS Earth Space Chem. 2025, 9, 687−698

We note that while all $Fe^{III}Cit$ photolyzes within minutes, the area under the initial CO_2 peak is smaller than the total amount of $Fe^{III}Cit$ in the system. Hence, we assume that not all photolyzed $Fe^{III}Cit$ leads to the production of CO_2. We find a CO_2 yield, defined as the ratio of the production of CO_2 and the photolysis loss of $Fe^{III}Cit$, of around 15%, irrespective of the experimental conditions (Figure S1). We find that a higher CO_2 yield cannot be compensated by lowering the $Fe^{III}Cit$ photolysis rate in the model, as this leads to a broadening of the initial CO_2 peak (Figure S2). We also note that the CO_2 peaks in the experimental data show a shoulder feature that is not captured by the model. This is seen in all but the highest humidity experiments and may be related to the presence of other photoactive species such as carboxylate complexes of reaction products with iron or a dinuclear iron citrate complex.[43]

During dark periods, the CO_2 signals tend toward zero. The decay of the CO_2 signal during dark periods is governed by the diffusivity of the CO_2 in the model. The CO_2 peak from the second irradiation period is generally much smaller than the initial CO_2 peak, which indicates that the film has not returned to its original state after 5−10 min of darkness. In the model, this is due to the incomplete reoxidation of Fe^{II} to Fe^{III}. The height of the second peak delivers important information about the O_2 diffusivity and Fe^{II} reoxidation rate. Generally, at higher RH, O_2 diffuses more quickly into the film, leading to faster Fe^{II} reoxidation. This is corroborated by experiments in the absence of O_2 (panel f), in which the film's ability to produce CO_2 is not recovered in the dark. Furthermore, OH cannot be formed via ROS cycling in the absence of O_2, meaning there is no formation of $Cit^{\bullet}$ through this reaction channel. In the following, we discuss the RH-dependent mass transport limitations of CO_2 and O_2 in greater detail.

Regeneration of $Fe^{III}Cit$ by Oxidation Reactions. Panels a and b of Figure 4 show the simulated depth profiles of the normalized degree of oxygen saturation ($S_{O_2} = [O_2]_{bulk}/[O_2]_{bulk,sat}$) and the fraction of Fe^{III} to total iron ($[Fe^{III}]/([Fe^{II}]+[Fe^{III}])$) in the topmost 200 nm of the CWFT film, respectively, for the lowest humidity experiment (30% RH). We find that high saturation of O_2 only occurs very close to the surface. The iron concentration in the film (~500 mM) is much larger than the saturation concentration of O_2 (~0.25 mM), causing anoxia upon irradiation with light. This indicates that O_2 diffusion is slow compared to reactive consumption, leading to a reacto-diffusive kinetic regime.[47] The reacto-diffusive length[48] and penetration depth of O_2 (Figure 4c) are near-constant over the course of the experiment. We define the penetration depth as the point at which S_{O_2} reaches 0.5, which occurs at ~5−10 nm for the experiment at 30% RH. Accordingly, the reoxidation of Fe^{II} back to Fe^{III} also occurs close to the surface. Notably, the shapes of the depth profiles of oxygen saturation and Fe^{III} fraction differ visually due to the different time evolutions of their sink terms. While the O_2 is removed at a near-constant rate, Fe^{III} only recovers during dark periods of the experiment in the absence of its strong photochemical sink. Note that recomplexation of Fe^{3+} with citrate is not a limiting step in the chemical mechanism, and the steady-state concentration of Fe^{III} is much higher than that of the free Fe^{3+} ion in the model. Full depth profiles of oxygen saturation and Fe^{III} fraction for all experiments are provided in the Supporting Information (Figures S3 and S4).

Note that O_2 is not the only oxidant of Fe^{II} in this system. In the model, the dominant Fe^{II} species is $Fe^{II}CitH$. In fact, H_2O_2 and HO_2 are the species that contribute most to the oxidation of Fe^{II} in the model simulations (Figure S5). However, O_2 starts the chain of ROS production, and its reactive uptake to the film perpetuates photooxidation of citric acid. In the model, O_2 reacts with a ketyl radical and Fe^{II} to produce HO_2. We find Fe^{II} to be the main sink for HO_2 and H_2O_2, and hence, every O_2 molecule that diffuses into the film triggers a redox cascade from O_2 to HO_2, H_2O_2, and OH. We find that HO_2 and H_2O_2 react predominantly with Fe^{II}, yielding at least three equivalents of Fe^{II} oxidation per O_2 taken up into the film. Evaporation of HO_2 and H_2O_2 from the film constituted a minor loss channel in all model calculations. In the case of the very reactive OH radical, the largest sink is citrate rather than Fe^{II}, and therefore, it does not contribute significantly to Fe^{II} oxidation. We note, however, that the oxidation products of the reaction between citrate with OH (i.e., alkyl and peroxy radicals) may decarboxylate themselves, undergo radical−radical recombination, or oxidize Fe^{II}.[49] The model currently does not consider the downstream organic radical chemistry toward further degradation of citric acid.

Humidity Dependence of Reactant Concentration Profiles. Figure 4c,d compares the O_2 penetration depth and Fe^{III} fraction for different humidities (35, 45, and 85% RH). Upon increasing the RH, increased bulk diffusion coefficients (Figure 5) lead to a larger reaction zone of O_2 with Fe^{II}. At

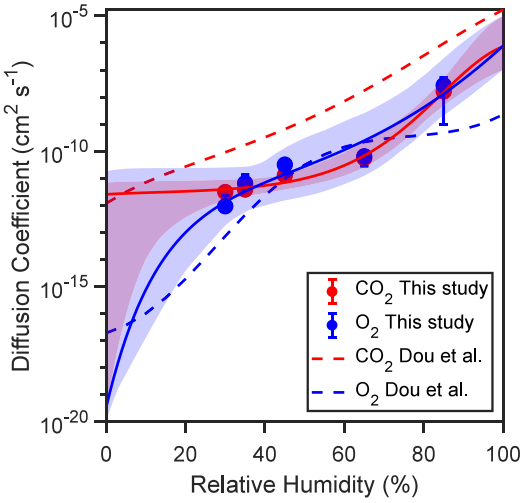

Figure 5. Bulk diffusion coefficients of O_2 (blue markers) and CO_2 (red markers) as functions of humidity. The shaded blue and red areas represent ensembles of fits to a Vignes-type equation (eq 2), with the blue and red lines showing the best fits for O_2 and CO_2, respectively.

85% RH, O_2 and ROS reach deep into the bulk of the film, and we observe the largest recovery of Fe^{III} in the simulation of this experiment, accordingly. However, despite full saturation of O_2, the Fe^{III} fraction recovers to at most ~0.25 after initial irradiation, which means that the reaction with Fe^{II} must limit O_2 uptake, indicating a kinetic regime limited by chemical reaction. This is in line with Alpert et al.[18] and Dou et al.,[19] who showed that even after almost 2 h in the dark, $Fe^{III}Cit$ particles do not reach a Fe^{III} fraction of 1. This incomplete reoxidation affects the extent of CO_2 production during the second irradiation period, resulting in the peak concentration

https://doi.org/10.1021/acsearthspacechem.4c00364
ACS Earth Space Chem. 2025, 9, 689−698

of the second irradiation being smaller than the peak concentration of CO_2 during the initial irradiation period at all humidities (Figure 3). Nonetheless, faster diffusion of O_2 at high humidity leads to higher CO_2 production in the second irradiation period, as observed in the experiments.

Due to the relatively short chemical lifetime of HO_2, we find its concentration profile to track the penetration depth of O_2 closely (Figure S6). As H_2O_2 is less reactive than HO_2, it is more evenly distributed in the film and found to be well-mixed at 65% RH and above (Figure S7).

Humidity Dependence of Diffusion Coefficients. Figure 5 shows the humidity dependence of the bulk diffusion coefficients of CO_2 and O_2 as determined by MCGA. The closed markers represent the mean diffusion coefficients from the ensemble of fitting parameter sets. We find that both diffusion coefficients increase with RH. The diffusion coefficients of both O_2 and CO_2 are overall similar, as one would expect from their molecular size. The diffusion coefficients are fitted using a Vignes-type equation as a function of the molar fraction of organics (x_{org}), as introduced in Lienhard et al.:[31]

$$\ln \alpha = x_{org}^{2}(C + 3D - 4Dx_{org}) \quad (1)$$

$$D_b = D_{b,w}^{\alpha(1-x_{org})} D_{b,org}^{1-\alpha(1-x_{org})} \quad (2)$$

The best-fitting Vignes-type parametrizations are shown as solid lines. For uncertainty estimation, we sampled the parameters C, D, $D_{b,org}$, and $D_{b,w}$ 100 000 times within predetermined fitting boundaries (Table S3) following a Monte Carlo Markov Chain (Metropolis−Hastings algorithm) and selected an ensemble of fits based on two acceptance criteria: a monotonous increase of the diffusion coefficients with RH and a residual less than twice that of the best fit. The ensemble of Vignes-type fits shows a range of behaviors encompassing a double S-shaped curve as seen in Berkemeier et al.,[35] as well as a single S-shaped curve as seen for citric acid in Lienhard et al.[31] Without experimental data at humidities <30% RH, we find a larger uncertainty in this humidity range and therefore cannot distinguish between both behaviors; however, we find that the best fit for CO_2 exhibits a single S-shape, while the best fit for O_2 shows a double S-shape. The diffusion coefficients of O_2 and CO_2 inferred in this study follow a similar trend as in the study by Dou et al.[14] on the same reaction system. Dou et al.[19] found a higher diffusivity of CO_2 compared to the CO_2 in this study. Note that, in Dou et al.,[14] CO_2 diffusivity was inferred based on particle mass loss, which is also affected by water uptake into the particle, while this study uses time profiles of CO_2 gas phase concentration. As CO_2 is formed only during irradiation, switching between light and dark periods allows the disentangling of chemical and mass transport kinetics of CO_2 production in the film. Diffusion coefficients are kept fixed during the simulations for simplicity. However, product formation could affect the diffusion coefficients. The diffusion may increase as smaller organic molecules are formed[19] or may decrease as dimers are produced.[15]

■ ATMOSPHERIC RELEVANCE

To assess the impact of iron carboxylate photochemistry on SOA particles in the atmosphere, we extrapolate the kinetic model from laboratory to atmospheric conditions by changing the geometry from thin films to spherical particles, reducing the Fe^{III} concentrations to 0.41 M,[50] which is a concentration representative of iron-containing aerosol particles, and using a photon flux according to solar irradiation at the Earth's surface at a zenith angle of 0°. Figure 6 shows the normalized degree of oxygen saturation (S_{O_2}) in the particles after 12 h of solar irradiation as a function of particle size and RH. Particle size and humidity were kept constant during the simulations. Figure 6 uses the best-fitting Vignes-type parametrization (Figure 5) for the diffusion coefficients. We find that at low humidities, particles become fully anoxic, irrespective of the particle size, while at medium RH, S_{O_2} depends strongly on the particle size. At high humidities (>70%), oxygen remains fully saturated in the simulations, irrespective of particle size. Thus, for dilute aerosols and cloud water, we expect a well-mixed reaction system in which oxidative processing is limited by the chemical reaction of Fe^{II} with O_2 and ROS. We note that the oxygen concentration shown here is the volume-weighted, average bulk concentration, and anoxia will be more pronounced in the interior of particles. Panels a and b of Figure S8 are generated using the upper and lower limits of the diffusion coefficients in Figure 5, respectively. Using the upper estimate of the diffusion coefficients (Figure S8a), we see a particle size dependence in S_{O_2} at both low and medium humidities: S_{O_2} becomes as low as ~0.05 for large particles. Using the lower estimate of diffusion coefficients (Figure S8b), we find a similar behavior to that of the best fit: at low humidities particles become fully anoxic, irrespective of the particle size, while at medium RH, S_{O_2} depends strongly on particle size. In both diffusivity limits, at high humidities, oxygen is fully saturated in the simulations for all particle sizes.

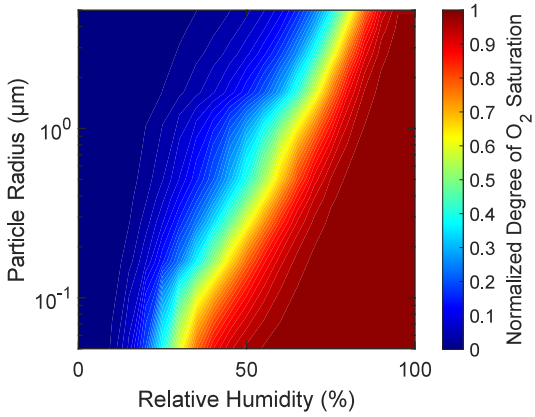

Figure 6. Degree of oxygen saturation (S_{O_2}) as a function of particle size and relative humidity. The photon flux was set to solar irradiation at the Earth's surface at a zenith angle of 0°. The Fe^{III}Cit concentration was 0.41 M following Khaled et al.,[50] and citric acid was added to maintain a Fe^{III}Cit to organics mole ratio of 1:10.

■ CONCLUSIONS

In this study, we performed detailed kinetic laboratory experiments and kinetic modeling on the iron citrate heterogeneous photooxidation system, which serves as an important proxy for the aging of transition-metal-containing organic aerosol particles, and thus the breakdown of organic matter, in the atmosphere.[51] Iron carboxylate photochemistry is considered a dominant sink for carboxylic acids compared to

https://doi.org/10.1021/acsearthspacechem.4c00364
ACS Earth Space Chem. 2025, 9, 689−698

oxidation with radicals such as OH.[51] Our model simulations corroborate these findings and show that CO_2 production through iron citrate photolysis dominates over CO_2 production through oxidation with the OH radical under the conditions studied here. The time-resolved and humidity-dependent data from the coated-wall flow-tube system, using an experimental protocol that includes light-on and light-off periods, allowed the kinetic model to disentangle the effects of phase state and chemical reaction. The combined experiments and model calculations demonstrate that relative humidity and therefore the phase state can strongly affect the rate of chemical aging of organic aerosol particles. We show the effects of relative humidity on the diffusion of O_2 and CO_2 and find that compared to previous studies, the diffusion coefficients of these two molecules are very similar.

Using the kinetic model, we can distinguish two distinct kinetic regimes of photooxidation. At low humidities, O_2 only penetrates the film close to the surface due to the fast chemical consumption and kinetic transport limitation in the viscous film. At high humidities, we find that O_2 can fully penetrate the bulk of the film and that the reactions with Fe^{II} are limiting O_2 uptake. We find that the absence of oxygen stops further decarboxylation from occurring, while the presence of O_2 results in a cascade of reactive oxygen species (ROS) formation that perpetuates redox cycling and thus the photooxidation reaction, which is limited by the availability of reduced Fe. We note that other photosensitizers are also known to initiate free radical chemistry by reacting with O_2 to produce HO_2, even in the absence of transition metals.[52,53] Using the physical and chemical parameters derived from the kinetic model, we extrapolate the model from the laboratory to atmospheric conditions. We find that at low and intermediate RH, the presence of anoxic conditions will strongly depend on particle size.

Uncertainties remain in the chemical mechanism with respect to minor and later generation reaction products. We find that only ≈15% of Fe^{III}Cit photolysis leads to the formation of CO_2, which is determined by the chemical fate of $Cit^{\bullet}$. The downstream chemistry of $Cit^{\bullet}$ has not been well studied and is simplified in the model to a first-order loss rate. Detailed analysis of the fate of $Cit^{\bullet}$ could help in the understanding of the lowered CO_2 yield. Furthermore, the reaction of $CitH_3$ with OH yields an alkyl radical, which may decarboxylate, or in the presence of O_2 forms peroxy radicals. The downstream chemistry of organic radicals is currently not considered in the model. This could mean that under high humidity conditions, our model may underestimate sinks of O_2.

Future experimental studies are needed to reduce the model uncertainty. We suggest that future studies include simultaneous experimental data of other observables from the system, such as measurements of reactive oxygen species (e.g., gas phase HO_2), or a more detailed chemical analysis of oxidation products, such as volatile organic decomposition products in the gas phase (e.g., acetic acid) or nonvolatile radical−radical recombination products in the condensed phase, to help constrain the model and chemical mechanism of the reaction system further. Future studies should also investigate the effects of temperature since it affects both the phase state and chemical reaction rates.

■ ASSOCIATED CONTENT

Supporting Information

The Supporting Information is available free of charge at https://pubs.acs.org/doi/10.1021/acsearthspacechem.4c00364.

CO_2 yield as a function of humidity, comparison of model results with 100% CO_2 yield, depth profiles of O_2 and total Fe^{III} at different humidities, relative sinks of Fe^{II} as a function of time and humidity, depth profiles of HO_2 and H_2O_2 at different humidities, S_{O_2} as a function of particle size and relative humidity at two different diffusion coefficient extremes, acid−base equilibria, chemical reactions, input parameters for the Vignes-type equation, and additional method details (PDF)

■ AUTHOR INFORMATION

Corresponding Author

Thomas Berkemeier − *Multiphase Chemistry Department, Max Planck Institute for Chemistry, 55128 Mainz, Germany;* orcid.org/0000-0001-6390-6465; Email: t.berkemeier@mpic.de

Authors

Ashmi Mishra − *Multiphase Chemistry Department, Max Planck Institute for Chemistry, 55128 Mainz, Germany;* orcid.org/0000-0003-1751-1643

Kevin Kilchhofer − *PSI Center for Energy and Environmental Sciences, 5232 Villigen, Switzerland; Department of Environmental System Science, Institute for Atmospheric and Climate Science, ETH Zurich, 8092 Zurich, Switzerland*

Lucia Iezzi − *PSI Center for Energy and Environmental Sciences, 5232 Villigen, Switzerland; Department of Environmental System Science, Institute for Atmospheric and Climate Science, ETH Zurich, 8092 Zurich, Switzerland*

Ulrich Pöschl − *Multiphase Chemistry Department, Max Planck Institute for Chemistry, 55128 Mainz, Germany;* orcid.org/0000-0003-1412-3557

Peter A. Alpert − *PSI Center for Energy and Environmental Sciences, 5232 Villigen, Switzerland;* orcid.org/0000-0002-7582-9206

Markus Ammann − *PSI Center for Energy and Environmental Sciences, 5232 Villigen, Switzerland;* orcid.org/0000-0001-5922-9000

Complete contact information is available at: https://pubs.acs.org/10.1021/acsearthspacechem.4c00364

Funding

Open access funded by Max Planck Society. A. M. was supported by the Max Planck Graduate Center with the Johannes Gutenberg-Universität Mainz (MPGC). K. K., L. I., and M. A. thank the Swiss National Science Foundation for financial support with Grant no. 188662.

Notes

The authors declare no competing financial interest.

■ ACKNOWLEDGMENTS

This article is dedicated to Hartmut Herrmann and his outstanding engagement and achievements in physical and atmospheric chemistry. We thank H. G. Kang, U. K. Krieger, and B. Luo for helpful discussions.

REFERENCES

(1) Pöschl, U. Atmospheric Aerosols: Composition, Transformation, Climate and Health Effects. *Angew. Chem.* **2005**, *44*, 7520−7540.

(2) Pye, H. O. T.; Ward-Caviness, C. K.; Murphy, B. N.; Appel, K. W.; Seltzer, K. M. Secondary organic aerosol association with cardiorespiratory disease mortality in the United States. *Nat. Commun.* **2021**, *12*, 7215.

(3) Kanakidou, M.; et al. Organic aerosol and global climate modelling: a review. *Atmos. Chem. Phys.* **2005**, *5*, 1053−1123.

(4) Jimenez, J. L.; et al. Evolution of Organic Aerosols in the Atmosphere. *Science* **2009**, *326*, 1525−1529.

(5) Deguillaume, L.; Leriche, M.; Desboeufs, K.; Mailhot, G.; George, C.; Chaumerliac, N. Transition Metals in Atmospheric Liquid Phases: Sources, Reactivity, and Sensitive Parameters. *Chem. Rev.* **2005**, *105*, 3388−3431.

(6) Harrison, R. M.; Jones, A. M.; Gietl, J.; Yin, J.; Green, D. C. Estimation of the Contributions of Brake Dust, Tire Wear, and Resuspension to Nonexhaust Traffic Particles Derived from Atmospheric Measurements. *Environ. Sci. Technol.* **2012**, *46*, 6523−6529.

(7) Ito, A. Atmospheric Processing of Combustion Aerosols as a Source of Bioavailable Iron. *Environ. Sci. Technol. Lett.* **2015**, *2*, 70−75.

(8) Lopez, B.; Wang, X.; Chen, L.-W. A.; Ma, T.; Mendez-Jimenez, D.; Cobb, L. C.; Frederickson, C.; Fang, T.; Hwang, B.; Shiraiwa, M.; Park, M.; Park, K.; Yao, Q.; Yoon, S.; Jung, H. Metal contents and size distributions of brake and tire wear particles dispersed in the near-road environment. *Sci. Total Environ.* **2023**, *883*, 163561.

(9) Shi, Z.; Krom, M. D.; Jickells, T. D.; Bonneville, S.; Carslaw, K. S.; Mihalopoulos, N.; Baker, A. R.; Benning, L. G. Impacts on iron solubility in the mineral dust by processes in the source region and the atmosphere: A review. *Aeolian Res.* **2012**, *5*, 21−42.

(10) Al-Abadleh, H. A. Iron content in aerosol particles and its impact on atmospheric chemistry. *Chem. Commun.* **2024**, *60*, 1840−1855.

(11) Tao, Y.; Murphy, J. G. The Mechanisms Responsible for the Interactions among Oxalate, pH, and Fe Dissolution in PM2.5. *ACS Earth Space Chem.* **2019**, *3*, 2259−2265.

(12) Tapparo, A.; Di Marco, V.; Badocco, D.; D'Aronco, S.; Soldà, L.; Pastore, P.; Mahon, B. M.; Kalberer, M.; Giorio, C. Formation of metal-organic ligand complexes affects solubility of metals in airborne particles at an urban site in the Po valley. *Chemosphere* **2020**, *241*, 125025.

(13) Weller, C.; Horn, S.; Herrmann, H. Photolysis of Fe(III) carboxylato complexes: Fe(II) quantum yields and reaction mechanisms. *J. Photochem. Photobiol., A* **2013**, *268*, 24−36.

(14) Dou, J.; Luo, B.; Peter, T.; Alpert, P. A.; Corral Arroyo, P.; Ammann, M.; Krieger, U. K. Carbon Dioxide Diffusivity in Single, Levitated Organic Aerosol Particles. *J. Phys. Chem. Lett.* **2019**, *10*, 4484−4489.

(15) West, C. P.; Morales, A. C.; Ryan, J.; Misovich, M. V.; Hettiyadura, A. P. S.; Rivera-Adorno, F.; Tomlin, J. M.; Darmody, A.; Linn, B. N.; Lin, P.; Laskin, A. Molecular investigation of the multi-phase photochemistry of Fe(iii)-citrate in aqueous solution. Environ. *Environ. Sci.: Process. Impacts* **2023**, *25*, 190−213.

(16) Wang, J.; Huang, D.; Chen, F.; Chen, J.; Jiang, H.; Zhu, Y.; Chen, C.; Zhao, J. Rapid Redox Cycling of Fe(II)/Fe(III) in Microdroplets during Iron−Citric Acid Photochemistry. *Environ. Sci. Technol.* **2023**, *57*, 4434−4442.

(17) Wang, Z.; Chen, C.; Ma, W.; Zhao, J. Photochemical Coupling of Iron Redox Reactions and Transformation of Low-Molecular-Weight Organic Matter. *J. Phys. Chem. Lett.* **2012**, *3*, 2044−2051.

(18) Alpert, P. A.; Dou, J.; Corral Arroyo, P.; Schneider, F.; Xto, J.; Luo, B.; Peter, T.; Huthwelker, T.; Borca, C. N.; Henzler, K. D.; Schaefer, T.; Herrmann, H.; Raabe, J.; Watts, B.; Krieger, U. K.; Ammann, M. Photolytic radical persistence due to anoxia in viscous aerosol particles. *Nat. Commun.* **2021**, *12*, 1769.

(19) Dou, J.; Alpert, P. A.; Corral Arroyo, P.; Luo, B.; Schneider, F.; Xto, J.; Huthwelker, T.; Borca, C. N.; Henzler, K. D.; Raabe, J.; Watts, B.; Herrmann, H.; Peter, T.; Ammann, M.; Krieger, U. K. Photochemical degradation of iron(III) citrate/citric acid aerosol quantified with the combination of three complementary experimental techniques and a kinetic process model. *Atmos. Chem. Phys.* **2021**, *21*, 315−338.

(20) Zhang, C.; Wang, L.; Wu, F.; Deng, N. Quantitation of Hydroxyl Radicals from Photolysis of Fe(III)-Citrate Complexes in Aerobic Water (5 pp). *Environ. Sci. Pollut. Res.* **2006**, *13*, 156−160.

(21) Garner, N. M.; Top, J.; Mahrt, F.; El Haddad, I.; Ammann, M.; Bell, D. M. Iron-Containing Seed Particles Enhance a-Pinene Secondary Organic Aerosol Mass Concentration and Dimer Formation. *Environ. Sci. Technol.* **2024**, *58* (38), 16984.

(22) Shiraiwa, M.; Ammann, M.; Koop, T.; Pöschl, U. Gas uptake and chemical aging of semisolid organic aerosol particles. *Proc. Natl. Acad. Sci. U.S.A.* **2011**, *108*, 11003−11008.

(23) Slade, J. H.; Knopf, D. A. Multiphase OH oxidation kinetics of organic aerosol: The role of particle phase state and relative humidity. *Geophys. Res. Lett.* **2014**, *41*, 5297−5306.

(24) Zobrist, B.; Marcolli, C.; Pedernera, D. A.; Koop, T. Do atmospheric aerosols form glasses? *Atmos. Chem. Phys.* **2008**, *8*, 5221−5244.

(25) Pfrang, C.; Shiraiwa, M.; Pöschl, U. Chemical ageing and transformation of diffusivity in semi-solid multi-component organic aerosol particles. *Atmos. Chem. Phys.* **2011**, *11*, 7343−7354.

(26) Koop, T.; Bookhold, J.; Shiraiwa, M.; Pöschl, U. Glass transition and phase state of organic compounds: dependency on molecular properties and implications for secondary organic aerosols in the atmosphere. *Phys. Chem. Chem. Phys.* **2011**, *13*, 19238−19255.

(27) Renbaum-Wolff, L.; Grayson, J. W.; Bateman, A. P.; Kuwata, M.; Sellier, M.; Murray, B. J.; Shilling, J. E.; Martin, S. T.; Bertram, A. K. Viscosity of a-pinene secondary organic material and implications for particle growth and reactivity. *Proc. Natl. Acad. Sci. U.S.A.* **2013**, *110*, 8014−8019.

(28) Price, H. C.; Murray, B. J.; Mattsson, J.; O'Sullivan, D.; Wilson, T. W.; Baustian, K. J.; Benning, L. G. Quantifying water diffusion in high-viscosity and glassy aqueous solutions using a Raman isotope tracer method. *Atmos. Chem. Phys.* **2014**, *14*, 3817−3830.

(29) Davies, J. F.; Wilson, K. R. Nanoscale interfacial gradients formed by the reactive uptake of OH radicals onto viscous aerosol surfaces. *Chem. Sci.* **2015**, *6*, 7020−7027.

(30) Baboomian, V. J.; Crescenzo, G. V.; Huang, Y.; Mahrt, F.; Shiraiwa, M.; Bertram, A. K.; Nizkorodov, S. A. Sunlight can convert atmospheric aerosols into a glassy solid state and modify their environmental impacts. *Proc. Natl. Acad. Sci. U.S.A.* **2022**, *119*, e2208121119.

(31) Lienhard, D. M.; Huisman, A. J.; Bones, D. L.; Te, Y.-F.; Luo, B. P.; Krieger, U. K.; Reid, J. P. Retrieving the translational diffusion coefficient of water from experiments on single levitated aerosol droplets. *Phys. Chem. Chem. Phys.* **2014**, *16*, 16677−16683.

(32) Zaveri, R. A.; Easter, R. C.; Fast, J. D.; Peters, L. K. Model for Simulating Aerosol Interactions and Chemistry (MOSAIC). *J. Geophys. Res. D: Atmos.* **2008**, *113*, 1.

(33) Shiraiwa, M.; Pfrang, C.; Pöschl, U. Kinetic multi-layer model of aerosol surface and bulk chemistry (KM-SUB): the influence of interfacial transport and bulk diffusion on the oxidation of oleic acid by ozone. *Atmos. Chem. Phys.* **2010**, *10*, 3673−3691.

(34) Shiraiwa, M.; Pfrang, C.; Koop, T.; Pöschl, U. Kinetic multi-layer model of gas-particle interactions in aerosols and clouds (KM-GAP): linking condensation, evaporation and chemical reactions of organics, oxidants and water. *Atmos. Chem. Phys.* **2012**, *12*, 2777−2794.

(35) Berkemeier, T.; Steimer, S. S.; Krieger, U. K.; Peter, T.; Pöschl, U.; Ammann, M.; Shiraiwa, M. Ozone uptake on glassy, semi-solid and liquid organic matter and the role of reactive oxygen intermediates in atmospheric aerosol chemistry. *Phys. Chem. Chem. Phys.* **2016**, *18*, 12662−12674.

(36) O'Meara, S.; Topping, D. O.; McFiggans, G. The rate of equilibration of viscous aerosol particles. *Atmos. Chem. Phys.* **2016**, *16*, 5299−5313.

https://doi.org/10.1021/acsearthspacechem.4c00364
ACS Earth Space Chem. 2025, 9, 689−698

(37) Berkemeier, T.; Mishra, A.; Mattei, C.; Huisman, A. J.; Krieger, U. K.; Pöschl, U. Ozonolysis of Oleic Acid Aerosol Revisited: Multiphase Chemical Kinetics and Reaction Mechanisms. *ACS Earth Space Chem.* **2021**, *5*, 3313−3323.
(38) Milsom, A.; Lees, A.; Squires, A. M.; Pfrang, C. MultilayerPy (v1.0): a Python-based framework for building, running and optimizing kinetic multi-layer models of aerosols and films. *Geosci. Model Dev.* **2022**, *15*, 7139−7151.
(39) Wilson, K. R.; Prophet, A. M.; Willis, M. D. A Kinetic Model for Predicting Trace Gas Uptake and Reaction. *J. Phys. Chem. A* **2022**, *126*, 7291−7308.
(40) Luo, Z.; Zang, H.; Li, Z.; Li, C.; Zhao, Y. Species-specific effect of particle viscosity and particle-phase reactions on the formation of secondary organic aerosol. *Sci. Total Environ.* **2024**, *950*, 175207.
(41) Song, Y. C.; Haddrell, A. E.; Bzdek, B. R.; Reid, J. P.; Bannan, T.; Topping, D. O.; Percival, C.; Cai, C. Measurements and Predictions of Binary Component Aerosol Particle Viscosity. *J. Phys. Chem. A* **2016**, *120*, 8123−8137.
(42) Berkemeier, T.; Ammann, M.; Krieger, U. K.; Peter, T.; Spichtinger, P.; Pöschl, U.; Shiraiwa, M.; Huisman, A. J. Technical note: Monte Carlo genetic algorithm (MCGA) for model analysis of multiphase chemical kinetics to determine transport and reaction rate coefficients using multiple experimental data sets. *Atmos. Chem. Phys.* **2017**, *17*, 8021−8029.
(43) Abrahamson, H. B.; Rezvani, A. B.; Brushmiller, J. Photochemical and spectroscopic studies of complexes, of iron(III) with citric acid and other carboxylic acids. *Inorg. Chim. Acta* **1994**, *226*, 117−127.
(44) Pozdnyakov, I. P.; Melnikov, A. A.; Tkachenko, N.; Chekalin, S. V.; Lemmetyinen, H.; Plyusnin, V. F. Ultrafast photophysical processes for Fe(iii)-carboxylates. *Dalton Trans.* **2014**, *43*, 17590−17595.
(45) Sander, R. Compilation of Henry's law constants (version 4.0) for water as solvent. *Atmos. Chem. Phys.* **2015**, *15*, 4399−4981.
(46) Knopf, D. A.; Ammann, M.; Berkemeier, T.; Pöschl, U.; Shiraiwa, M. Desorption lifetimes and activation energies influencing gas-surface interactions and multiphase chemical kinetics. *Atmos. Chem. Phys.* **2024**, *24*, 3445−3528.
(47) Berkemeier, T.; Huisman, A. J.; Ammann, M.; Shiraiwa, M.; Koop, T.; Pöschl, U. Kinetic regimes and limiting cases of gas uptake and heterogeneous reactions in atmospheric aerosols and clouds: a general classification scheme. *Atmos. Chem. Phys.* **2013**, *13*, 6663−6686.
(48) Hanson, D. R.; Ravishankara, A. R.; Solomon, S. Heterogeneous reactions in sulfuric acid aerosols: A framework for model calculations. *J. Geophys. Res. D: Atmos.* **1994**, *99*, 3615−3629.
(49) Pignatello, J. J.; Oliveros, E.; MacKay, A. Advanced Oxidation Processes for Organic Contaminant Destruction Based on the Fenton Reaction and Related Chemistry. *Crit. Rev. Environ. Sci. Technol.* **2006**, *36*, 1−84.
(50) Khaled, A.; Zhang, M.; Ervens, B. The number fraction of iron-containing particles affects OH, HO_2 and H_2O_2 budgets in the atmospheric aqueous phase. *Atmos. Chem. Phys.* **2022**, *22*, 1989−2009.
(51) Weller, C.; Tilgner, A.; Bräuer, P.; Herrmann, H. Modeling the Impact of Iron-Carboxylate Photochemistry on Radical Budget and Carboxylate Degradation in Cloud Droplets and Particles. *Environ. Sci. Technol.* **2014**, *48*, 5652−5659.
(52) González Palacios, L.; Corral Arroyo, P.; Aregahegn, K. Z.; Steimer, S. S.; Bartels-Rausch, T.; Nozière, B.; George, C.; Ammann, M.; Volkamer, R. Heterogeneous photochemistry of imidazole-2-carboxaldehyde: HO_2 radical formation and aerosol growth. *Atmos. Chem. Phys.* **2016**, *16*, 11823−11836.
(53) Corral Arroyo, P.; Bartels-Rausch, T.; Alpert, P. A.; Dumas, S.; Perrier, S.; George, C.; Ammann, M. Particle-Phase Photosensitized Radical Production and Aerosol Aging. *Environ. Sci. Technol.* **2018**, *52*, 7680−7688.

2.5. Kinetic modeling of aerosol oxidative potential (KM-OP)

This chapter contains a first complete manuscript draft. I am the first author and the main contributor of this work. I designed the research and developed the model together with Thomas Berkmeier. I optimized the kinetic model and I performed the kinetic model simulations. I analyzed the model results. I produced the figures and wrote the paper, with input from the co-authors. After further exchange with co-authors and optimization, it will be submitted to a peer-reviewed journal. The supplement to this work can be found in Appendix B.3.

Mishra, A., Lelieveld S., Krüger M., Campbell C. J., Srivastava, D., Lanzafame, G. M., Tomaz, S., Favez, O., Bonnaire, N., Lucarelli, F., Alleman, L., Uzu, G., Jaffrezo, J-L., Green D. C., Priestman, M., Tremper, A. H., Barth, A., Kalberer, M., Bandowe, B. A. M., Lammel, G., Pöschl, U., Shahpoury, P., Albinet, A., Berkemeier, T.: Chemical kinetics and reaction mechanisms of reactive species production and antioxidant depletion in different assays measuring aerosol oxidative potential, ***in preparation*****.**

In this study, a kinetic model of oxidative potential (KM-OP) was developed to elucidate and quantify the effects of particulate pollutants on the production of ROS and consumption of antioxidants. The chemical reaction mechanism of the model was based on literature rate coefficients and a large compilation of laboratory OP data of transition metals, quinones, and secondary organic aerosol (SOA). The model was applied to field measurement data of PM composition and OP, obtaining good agreement for three different urban locations (Paris, Grenoble, and London). SOA was identified to be the strongest contributor to oxidative potential in Paris and Grenoble, while in London, the transition metals Cu and Fe also influenced OP.

Abstract

Exposure to ambient air pollution is a major risk factor for human health, contributing to morbidity and mortality. However, the chemical interactions and physiological effects of inhaled aerosols remain poorly understood at the molecular level. Oxidative stress due to excess formation of reactive oxygen species (ROS) in the respiratory tract is one of the leading hypothesis for the molecular mechanism causing adverse health effects of atmospheric particulate matter (PM). Thus, measurements of ROS production and antioxidant depletion are widely used to asses the oxidative potential (OP) and potential toxicity of atmospheric particles.

Here we introduce a chemical kinetic model of oxidative potential (KM-OP) to elucidate and quantify the effects of particulate pollutants on the production of ROS and consumption of antioxidants, such as ascorbic acid (AA) and dithiothreitol (DTT; a surrogate for the lung thiol antioxidants). The chemical reaction mechanism of the model is based on literature rate coefficients and a large compilation of laboratory data on the effects of transition metal ions, quinones, and secondary organic aerosol (SOA). We apply the KM-OP model to field measurement data of PM composition and OP, obtaining good agreement for three different urban and suburban locations (Paris area, Grenoble, and London).

Previous studies have found that PM may inflict direct damage to biomolecules in the lungs mainly via the production of hydroxyl (OH) radicals. For the individual locations, the antioxidant-based OP assays investigated in this study, especially the AA assay, show a good correlation with modeled OH radical production. Across the different locations, the correlations are less pronounced. We identify SOA as the strongest contributor to OP in Paris and Grenoble, while in London, we find that Cu and Fe ions also drive OP. Cu dominates the production of H_2O_2, but does not substantially affect OH production. Our model and results provide a basis for further investigation and comparison of different metrics of the potential toxicity of different air pollutants.

1 Introduction

Epidemiological studies have shown that inhalation of particulate matter (PM) leads to increased morbidity and mortality (Dockery et al., 1993; Cohen et al., 2017; Brauer et al., 2024), however, the molecular level understanding behind PM-related health effects remains poor (Wang et al., 2025). The ability of the inhaled PM to induce oxidative stress is the leading hypothesis to explain adverse health outcomes of PM (Donaldson et al., 2001; Kelly, 2003; Hayes et al., 2020; Miller, 2020). The oxidative potential (OP) of PM refers to its ability to oxidize specific target molecules over a period of time (Bates et al., 2019; Gao et al., 2020). OP has received increasing attention as a more comprehensive health-relevant measure of ambient PM toxicity than PM mass concentration (Borm et al., 2007; Ayres et al., 2008; Bates et al., 2015; Abrams et al., 2017; Weichenthal et al., 2016;

Gao et al., 2020). Consequently, measurements of PM in OP assays are an increasingly popular means to assess its toxicity (Cheung et al., 2009; Lin and Yu, 2019; Daellenbach et al., 2020; Hwang et al., 2021).

Many acellular assays, both offline and online, have been developed to evaluate OP (Cho et al., 2005; Ayres et al., 2008; Page et al., 2010; Fang et al., 2015; Laulagnet et al., 2015; Calas et al., 2018; Bates et al., 2019; Campbell et al., 2019; Lin and Yu, 2019; Gao et al., 2020; Utinger et al., 2023; Carlino et al., 2023). OP assays can be categorized into those that quantify the production of oxidants and those that evaluate the depletion of lung antioxidants or surrogates for these. Common acellular OP assays include electron paramagnetic resonance (OP^{EPR}, Tong et al., 2016), the hydroxyl radical assay (OP^{OH}, Charrier and Anastasio, 2015; Son et al., 2015; Gonzalez et al., 2017, 2021; Shen et al., 2022), the hydrogen peroxide assay (OP^{H2O2}, Charrier et al., 2014; Fuller et al., 2014; Wragg et al., 2016), the dithiothreitol assay (OP^{DTT}, Cho et al., 2005; Charrier and Anastasio, 2012), the ascorbic acid assay (OP^{AA}, Pietrogrande et al., 2019; Shen et al., 2021; Campbell et al., 2023; Utinger et al., 2023), and the glutathione assay (OP^{GSH}, Zielinski et al., 1999; Shahpoury et al., 2019). OP^{OH} and $OP^{H_2O_2}$ measure the generation of hydroxyl radicals and hydrogen peroxide respectively, while OP^{EPR} the measures production of free radicals using electron paramagnetic resonance spectroscopy. OP^{DTT}, OP^{AA}, and OP^{GSH} measure the depletion rate of antioxidants (AA, GSH) or surrogates for these (DTT). Although OP assays are widely used, the exact methodologies often differ between studies (Calas et al., 2017; Frezzini et al., 2022; Shahpoury et al., 2022; Dominutti et al., 2025; Campbell et al., 2025).

Considerable efforts have been made to determine the specific particle properties, such as chemical composition and size, that most influence OP values (Charrier and Anastasio, 2012; Verma et al., 2014; Xiong et al., 2017; Calas et al., 2017; Fang et al., 2017; Yu et al., 2018; Lin and Yu, 2019; Pietrogrande et al., 2019; Fang et al., 2019; Gao et al., 2020; Daellenbach et al., 2020; Puthussery et al., 2020; Farahani et al., 2022; Expósito et al., 2024; Bhattu et al., 2024; Shahpoury et al., 2024a,b). Studies have shown that the AA assay effectively captures the redox activities of transition-metal ions such as iron and copper (Pietrogrande et al., 2019; Shen et al., 2021; Utinger et al., 2023) and organic compounds (Calas et al., 2018; Campbell et al., 2023). The DTT assay is sensitive to transition-metal ions such as iron, copper, and manganese (Netto and Stadtman, 1996; Kachur et al., 1997; Charrier and Anastasio, 2012; Charrier et al., 2015, 2016; Lin and Yu, 2019) as well as organic substances (Calas et al., 2017; Janssen et al., 2014), including quinones (Kumagai et al., 2002), humic-like substances (Lin and Yu, 2011), and secondary organic aerosol (SOA) (McWhinney et al., 2013b; Tuet et al., 2017; Daellenbach et al., 2020; Bhattu et al., 2024). The OH assay is sensitive to iron and copper due to Fenton chemistry (Charrier et al., 2015; Gonzalez et al., 2018; Wei et al., 2019; Campbell et al., 2024b). Some studies have also indicated an association between OH assays and organic compounds (Tong et al., 2016; Wei et al., 2021; Campbell et al., 2023). Correlations and positive matrix factorization (PMF) analyses (Paatero and Tapper, 1994) have been employed to investigate the relationship between OP assays and the PM sources, as well as to identify the specific PM components that are driving

OP activities (Borlaza et al., 2021; Weber et al., 2021; Ngoc Thuy et al., 2024; Camman et al., 2024; Shahpoury et al., 2024a,b; Liu et al., 2025). However, the chemical reactions responsible for the observed effects of PM on OP assays remain unclear. Furthermore, the chemical mechanisms and rate coefficients are not fully elucidated for all assays, making it challenging to extrapolate the OP of PM to its effects in the human body. Thus, a kinetic model that estimates the OP based on the composition of PM would be highly beneficial to improve our mechanistic, process-level understanding of the health effects of air pollution. In this study, we develop and apply a detailed chemical kinetics model of aerosol oxidative potential, KM-OP. The predictive model uses PM composition data to estimate the production of ROS (OP^{OH} and $OP^{H_2O_2}$) and the depletion of antioxidant probes in common OP assays (ascorbic acid, OP^{AA}; dithiothreitol, OP^{DTT}). We apply the model to combined measurement data of PM composition and OP at three sites in Europe.

2 Methods

2.1 Kinetic model of oxidative potential (KM-OP)

A kinetic box model is applied to a compilation of multiple experimental data of ROS production (Charrier et al., 2014; Charrier and Anastasio, 2015; Tong et al., 2018), as well as DTT consumption (Charrier and Anastasio, 2012; Xiong et al., 2017; Expósito et al., 2024; Tuet et al., 2017; Fang et al., 2015) and AA oxidation (Shen et al., 2021; Expósito et al., 2024) in the presence of transition metals (TMs: iron Fe(II), copper Cu(II), and manganese Mn(II)), quinones (9,10-phenanthrenequinone (PQN), 1,4-naphthoquinone (1,4-NQN), and 1,2-naphthoquinone (1,2-NQN)) as well as secondary organic aerosol (SOA). These species were selected due to their high ambient concentration, their ability to form ROS, and their high reactivity in OP assays. Note, the model is calibrated on simple systems, however, there may be both synergistic and antagonistic interactions between the PM components which are currently not considered in the model. Fig. 1 illustrates the chemical reaction mechanism used in this study to analyze and reproduce the production of ROS (OP^{OH} and $OP^{H_2O_2}$), the depletion of ascorbic acid (OP^{AA}), and dithiothreitol (OP^{DTT}) as obtained in laboratory experiments. This mechanism integrates and builds on earlier studies investigating the oxidation of AA and DTT (Netto and Stadtman, 1996; Kachur et al., 1997; Kumagai et al., 2002; Shen et al., 2021). The mechanism includes the production of ROS by TM ions, which can in turn oxidize both AA and DTT. Furthermore, TMs themselves are also able to oxidize AA and DTT. Fig. 1 (A) shows the main reaction pathways for ROS formation and interconversion: reduced TMs and quinones catalyze a redox cascade from O_2 to superoxide (O_2^-) and hydrogen peroxide (H_2O_2). Reduced TMs react with H_2O_2, leading to the formation of hydroxyl radical (OH) through Fenton and Fenton-like reactions. Fig. 1 (B) shows that AA can cycle the oxidized forms of the metals and quinones back to its reduced form. ROS species also react with AA forming the ascorbyl radical ($AA^{\bullet}$). $AA^{\bullet}$ forms

dehydroascorbic acid (DHA) through disproportionation. DHA can undergo hydrolysis reaction to produce 2,3-diketogulonic acid (DKG). Fig. 1 (C) shows the oxidation of DTT in the presence of ROS, TMs, and quinones. We incorporate the mechanism proposed by Kachur et al. (1997) in which oxidation of DTT in the presence of Cu involves the formation of a Cu-DTT complex. Fig. 1 (D) shows the main pathway for ROS formation from SOA. The labile organic peroxides contained within SOA can decompose to form OH and RO radicals. These radicals can react with organic hydroperoxides, yielding an alcohol and either a hydroperoxyl radical (HO_2) or a RO_2 radical, respectively. In the presence of Fe, the hydroperoxide groups can undergo Fenton-like reactions, leading to the heterolytic cleavage of the O–O bond in two ways: One leads to the formation of the OH radical, while the other forms the RO radical. The OH, RO, and RO_2 radicals can react with both AA and DTT. KM-OP is an autogenerated model script based on a user-supplied chemical mechanism and consists of a system of differential equations, which are solved iteratively using the stiff differential equation solver ode23tb in Matlab.

2.2 Comparison with laboratory data

Since some of the kinetic rate coefficients of the chemical reaction mechanism are unknown or are uncertain in the literature, we infer those by fitting the kinetic model to experimental observations (inverse modeling). To this end, we set up the kinetic model to mimic the detailed experimental protocols from each experiment. A description of details of each model simulation can be found in the Supplementary Information (SI, Section 3). In brief, the chemical mechanism was optimized using experimental data from Charrier and Anastasio (2012); Charrier et al. (2014); Charrier and Anastasio (2015); Xiong et al. (2017); Shen et al. (2021); Expósito et al. (2024). The SOA chemical mechanism is ported from the literature (Walling, 1967; Chevallier et al., 2004; Mouchel-Vallon et al., 2017; Tong et al., 2018; Wei et al., 2022; Campbell et al., 2023) and was compared to DTT activity and radical production rate measured and compiled by Tuet et al. (2017) and Tong et al. (2018), respectively. Tuet et al. (2017) showed that the majority of anthropogenic and biogenic SOA exhibit similar DTT activity, with the exception of naphthalene SOA. Thus, in the model, we do not differentiate biogenic SOA from anthropogenic SOA.

2.3 Monte Carlo Genetic Algorithm

Inverse modeling was performed using the Monte Carlo Genetic Algorithm (MCGA, Berkemeier et al., 2017). MCGA consists of two steps. The first step consists of Monte Carlo search, in which model parameters are randomly sampled within predefined boundaries. The globally best-fitting parameter sets are then fed into the starting population of a GA, in which they are optimized through processes mimicking survival, recombination, and mutation in evolutionary biology. The optimization ceased when a set number of generations was reached. Ideally, a unique fit would result from global optimization; however, this system is under-determined, since it contains too

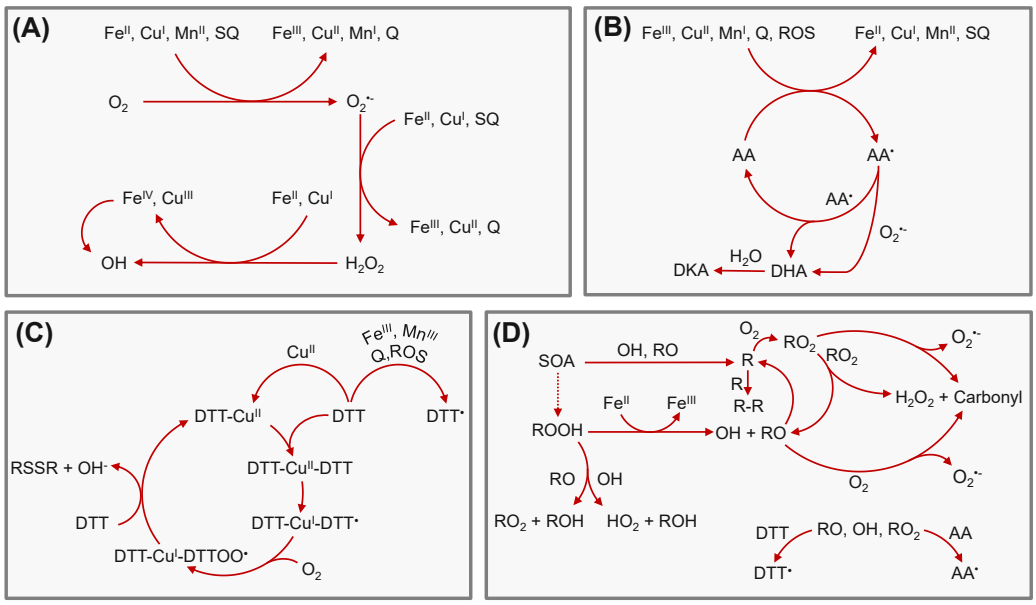

Figure 1: *Chemical reaction mechanisms used in KM-OP. Transition metal ions, quinones, and SOA can produce and convert ROS. Panel A shows the main reaction pathways for ROS formation and interconversion in the presence of transition metal ions and quinones. Panels B and C show the main reaction pathways for ascorbic acid and dithiothreitol oxidation through the reaction with ROS, transition metal ions and quinones. Panel D shows the main reaction pathways for ROS formation and interconversion in the presence of SOA.*

many and non-orthogonal parameters (Berkemeier et al., 2021). Therefore, it is more beneficial to identify an ensemble of adequately well-fitting parameter sets and analyze the corresponding kinetic model solutions. In this study, we apply MCGA, generate an ensemble of parameter sets, and analyze the corresponding kinetic model solutions collectively. Tab. S1 provides a list of all the chemical reactions used in this study and their corresponding rate coefficients.

2.4 Application to field data

We extrapolate the findings from the laboratory experiments to field data with detailed PM chemical characterization and source apportionment outputs at three different sites across Europe: a suburban background station near Paris, France (SIRTA, Srivastava et al. (2018a)); an urban background site in Grenoble, France (Les Frênes, Srivastava et al. (2018b)); and a roadside (summer, Campbell et al. (2024a)) and urban background site (winter, Campbell *et al., in preparation*) in London, United Kingdom. No fitting of model parameters was performed on the field data (forward modeling). The model uses chemical composition data of organics, soluble fractions of transition metals, and if available, quinone data from the field as input parameters. We assume an organic peroxide content in SOA of 50% (Docherty et al., 2005; Chowdhury et al., 2018). Offline OP^{DTT} and OP^{AA} were measured at the Paris and Grenoble sites, while online OP^{AA}

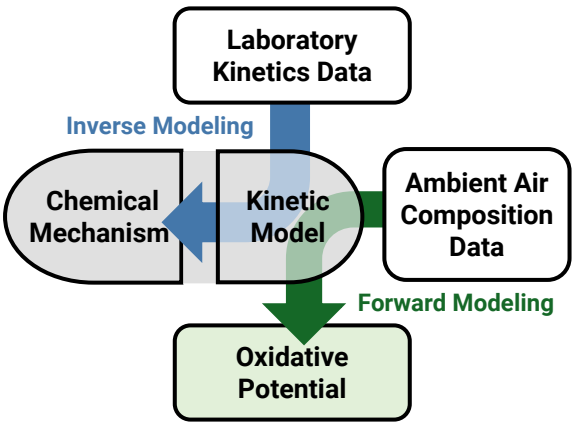

Figure 2: *Modeling approach applied in this study. Experimental data sets are used in conjunction with the kinetic model and a global optimization algorithm (Monte Carlo Genetic Algorithm, MCGA, Berkemeier et al., 2017). Unknown rate coefficients are sampled and improved within boundaries until a good correlation between the model output and experimental data points is achieved (inverse modeling). To the fitted model, we use ambient chemical composition data (with no additional fitting) to predict OP in a given location (forward modeling).*

was measured in London. At the London site, OP^{AA} was determined by the formation of dehydroascorbic acid (DHA), while at the two sites in France, OP^{AA} was determined as consumption of ascorbic acid. For clarity, the London data will be referred to as OP^{DHA}, while the data from France will be referred to as OP^{AA}.

Note that in the filter-based assays, there is generally an extraction step during which the filter samples are exposed to solvent in the absence of a probe reactant species. While this extraction increases solubility and thus, e.g., DTT activity (Calas et al., 2017), it may also lead to loss of ROS as a result of aqueous chemistry (Campbell et al., 2025). As the extraction kinetics and aqueous-phase chemistry during extraction are less well studied, the extraction period is not explicitly considered in KM-OP and simulations start with addition of the probe species.

Fig. 2 outlines the methodology used in this study. To summarize, we fit a model to laboratory data in a process termed inverse modeling in order to infer the rate coefficients of the chemical reaction mechanism. After optimizing the model to the laboratory data, inferring the unknown or uncertain reaction rate coefficients, we apply the model using ambient chemical composition data as input, with no further fitting to predict and estimate the OP.

3 Results and discussion

3.1 H_2O_2 and OH formation from transition metals and quinones

Figure 3A shows H_2O_2 production curves of Cu(II), 1,2-NQN, 1,4-NQN and PQN in a buffered surrogate lung lining fluid containing ascorbic acid, glutathione, uric acid,

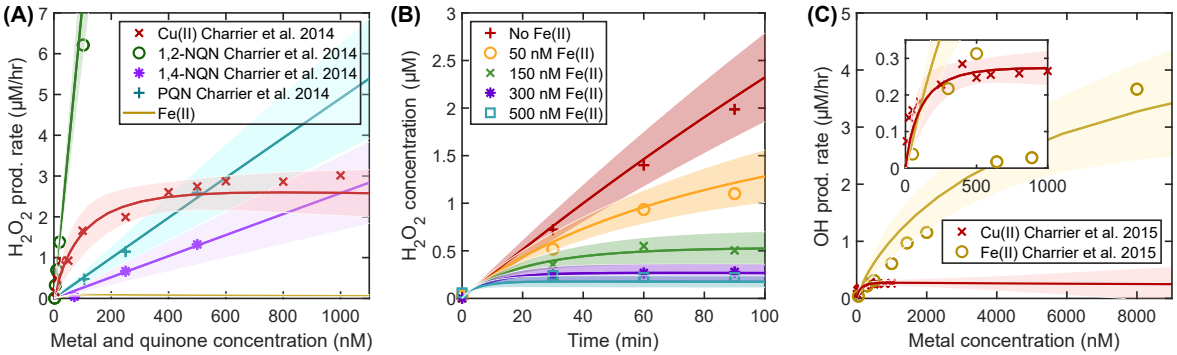

Figure 3: *Production of reactive oxygen species in surrogate lung lining fluid. Production rate of H_2O_2 as a function of Cu(II), 1,2-NQN, 1,4-NQN, PQN (A), H_2O_2 concentration over time at different Fe concentrations (B), and OH production rate as a function of Cu(II) and Fe(II) (C). The markers are experimental data (for H_2O_2 (Charrier et al., 2014) and OH (Charrier and Anastasio, 2015)), and the lines depict the mean of the fit ensemble, while the shadings denote two standard deviations around the mean.*

and citric acid. The experimental data from Charrier et al. (2014) (markers) is compared with KM-OP model results. The lines depict the mean of an ensemble of fits (N = 15) to all the laboratory data presented in this study, while the shadings denote two standard deviations around the mean. Generally, production of H_2O_2 increases as the metal and quinone concentrations increase. For the quinones, the increase of H_2O_2 production is linear, with 1,2-NQN showing the highest reactivity.

The mechanism of H_2O_2 formation by quinones (Q) in KM-OP is outlined in Fig. 1A and B and listed below. Briefly, AA reduces quinones to semiquinones (SQ), and in turn is converted into the ascorbyl radical ($AA^\bullet$, R1). The semiquinones then reduce O_2 to superoxide (O_2^-, R2). A second equivalent of AA then reacts with HO_2 to H_2O_2 (R3), also producing another $AA^\bullet$. SQ and $AA^\bullet$ also react with O_2^- to form H_2O_2 (R4 and R5). Fig. S1 details the main sources of H_2O_2 in the simulations. As we do not assume further reaction of H_2O_2 with quinones or semiquinones, H_2O_2 formation increases linearly with quinone concentrations.

Conversely, the production of H_2O_2 increases non-linearly with the concentration of Cu(II), with the production rate ofH_2O_2 plateauing at higher Cu concentrations. The H_2O_2 formation mechanism of Cu in KM-OP is outlined in Fig. 1A and above. Cu(II) is reduced to Cu(I) by AA (R6). Cu(I) then reacts with O_2, forming O_2^- (R7). At low Cu concentrations, H_2O_2 production occurs mostly through the reaction of AA with HO_2 (R3), while at higher concentrations of Cu, the reaction of Cu(I) with O_2^- is most important (Fig. S2, R8). The non-linearity in H_2O_2 production in the presence of Cu stems from the destruction of H_2O_2 through the Fenton-like reaction of H_2O_2 with Cu(I), leading to a steady state of H_2O_2 production and destruction.

$$AA + Q \rightarrow AA^{\bullet} + SQ \quad \text{(R1)}$$
$$SQ + O_2 \rightarrow Q + O_2^- \quad \text{(R2)}$$
$$AA + HO_2\ (+\ H^+) \rightarrow AA^{\bullet} + H_2O_2 \quad \text{(R3)}$$
$$SQ + O_2^-\ (+\ 2\ H^+) \rightarrow Q + H_2O_2 \quad \text{(R4)}$$
$$AA^{\bullet} + O_2^-\ (+\ 2\ H^+) \rightarrow DHA + H_2O_2 \quad \text{(R5)}$$
$$AA + Cu(II) \rightarrow AA^{\bullet} + Cu(I) \quad \text{(R6)}$$
$$O_2 + Cu(I) \rightarrow O_2^- + Cu(II) \quad \text{(R7)}$$
$$O_2^- + Cu(I)\ (+\ 2\ H^+) \rightarrow H_2O_2 + Cu(II) \quad \text{(R8)}$$
$$H_2O_2 + Cu(I) \rightarrow OH + OH^- + Cu(II) \quad \text{(R9)}$$
$$AA + Fe(III) \rightarrow AA^{\bullet} + Fe(II) \quad \text{(R10)}$$
$$O_2 + Fe(II) \rightarrow O_2^- + Fe(III) \quad \text{(R11)}$$
$$O_2^- + Fe(II)\ (+\ 2\ H^+) \rightarrow H_2O_2 + Fe(III) \quad \text{(R12)}$$
$$H_2O_2 + Fe(II) \rightarrow OH + OH^- + Fe(III) \quad \text{(R13)}$$
$$H_2O_2 + AA \rightarrow OH + OH^- + AA^{\bullet} \quad \text{(R14)}$$

As experimental data for H_2O_2 production with Fe(II) ions alone is not available, we fitted published time series data (Charrier et al., 2014) that contain 20 nM 1,2-NQN at varying Fe(II) concentrations (Fig. 3B). Fig. 3B illustrates that H_2O_2 concentration decreases as Fe(II) concentration increases. As shown in Fig. 3A, H_2O_2 destruction can be larger than H_2O_2 production in aqueous Fe solutions, because Fe(II) reacts rapidly with H_2O_2 via the Fenton reaction, leading to a very low steady state concentrations of H_2O_2 (dark yellow solid line) and OH radical production (Fig. 3C).

Fig. 3C shows the OH concentration-response curve for Cu(II) and Fe(II) in buffered surrogate lung lining fluid containing ascorbic acid, glutathione, uric acid, citric acid, and sodium benzoate, which is used as an OH probe. The production of OH increases non-linearly with the concentration of Cu(II), with OH production rate plateauing at higher Cu concentrations. At low Cu concentrations, OH production occurs mostly through the reaction of AA with H_2O_2 (R14), while at higher concentrations of Cu, the pseudo-Fenton reaction of Cu(I) with H_2O_2 is most important (Fig. S3, R9).

3.2 Ascorbic acid assay (OP^{AA} and OP^{DHA})

Figure 4A shows the modeled concentration-time profiles of ascorbic acid with Cu(II), Fe(II), and 1,4-NQN. The model output shows a good agreement with the published experimental data (Expósito et al., 2024). The concentrations of Cu(II), 1,4-NQN, and Fe(II) are 0.5, 1, and 5 µM, respectively. Despite a lower concentration of Cu(II) compared to Fe(II) and 1,4-NQN, AA decays much more quickly in the presence of Cu. In the model, this is due to the faster reaction rate coefficient of the redox reaction between

AA and Cu(II) compared to the reaction between AA and Fe(III) (Tab. S1, R16 and R33). Note, the direct reactions of the TM ions with AA dominate compared to the reaction of AA with ROS. In the presence of Cu, while H_2O_2 concentration is higher than the concentration of Cu(II) (Fig. S4A), the best-fit rate coefficient of AA with Cu(II) is three orders of magnitude higher than the best-fit rate coefficient of AA with H_2O_2 (Tab. S1, R33 and R48), leading to over 700 times larger turnover of AA with Cu. In the presence of Fe, the concentration of Fe(III) is higher than the concentration of ROS (Fig. S4B), and the rate coefficient of AA with Fe(III) is also higher than the rate coefficient of AA with H_2O_2 (Tab. S1, R16 and R48), leading to over 4000 times larger turnover of AA with Fe. As shown in Fig. 1A and mentioned above, AA reduces metals and quinones by redox cycling from their oxidized to reduced forms. The reduced metals and semiquinone can react with oxygen, leading to the formation of O_2^-, which in turn is another reaction partner for AA. As shown in Fig. 1B and outlined below, in the KM-OP mechanism, the oxidation of AA leads to the formation of dehydroascorbic acid (DHA; Shen et al., 2021). Note, while the KM-OP mechanism includes a redox reaction for the reaction of AA and metals, a catalytic reaction mechanism has also been proposed in the literature (Shen et al., 2021). Fig. 4B shows DHA concentrations as a function of Cu(II) and Fe(II) concentrations, and compares the model output to experimental data from Shen et al. (2021). We find a linear increase in DHA concentration with increasing Fe(II) concentration. The largest source of DHA is the disproportionation reaction of the ascorbyl radical ($AA^\bullet$), which in turn is formed from the redox reaction between AA and the transition metals (Fig. S5). On the contrary, with Cu, the DHA concentration increases non-linearly and saturates at higher Cu(II) concentrations because DHA formation is second order with respect to $AA^\bullet$, however, DHA loss is a first-order reaction:

$$AA^\bullet + AA^\bullet \rightarrow DHA + AA \quad \text{(R15)}$$

$$DHA\ (+\ H_2O) \rightarrow DKG \quad \text{(R16)}$$

3.3 DTT assay (OP^{DTT})

Figure 5A, B, and D show the rates of DTT loss at various concentrations of metal ions and quinones as measured by Charrier and Anastasio (2012) and Expósito et al. (2024). DTT consumption generally increases with increasing metal and quinone concentrations, and overall, the experimental data is well captured by the model. Fig. 5A shows that DTT oxidation in the presence of Cu(II) and Mn(II) is faster than in the presence of Fe. There is a linear increase in the rate of DTT loss with increasing Fe concentration. As shown in Fig. 1 and outlined below, in the KM-OP mechanism, DTT reduces Fe(III) to Fe(II) and in turn forms a thiyl radical (Netto and Stadtman, 1996). The experimental data shows a slightly higher rate of DTT loss for Fe(II) compared to Fe(III), which is not captured by the model. This may be related to Fe(III) forming precipitate in the

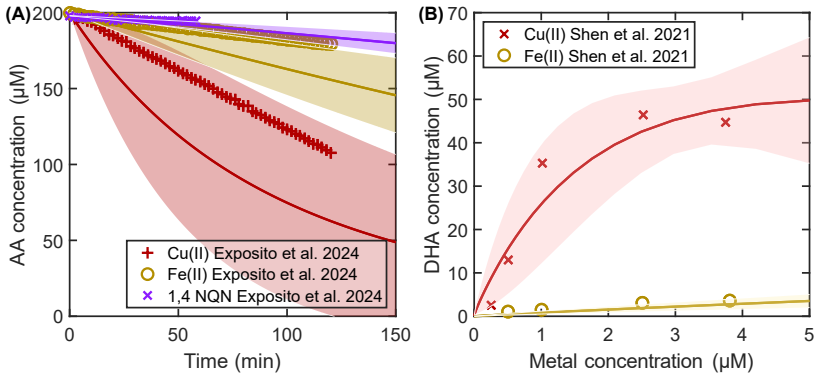

Figure 4: *Ascorbic acid concentration as a function of time at different concentrations of 1,4-NQN, Fe(II) and Cu(II) ions (A). DHA concentration as a function of Fe(II) and Cu(II) concentration (B). The markers are measurement data points (Shen et al., 2021; Expósito et al., 2024), and the dark-colored lines depict the mean of the fit ensemble, while the shadings denote two standard deviations around the mean.*

presence of phosphate buffer (Yalamanchili et al., 2022; Campbell et al., 2023), which is not currently considered in the model.

Fig. 5B shows oxidation rates of DTT in the presence of Mn(II) as measured by Expósito et al. (2024). The data show thatthe rate of DTT loss increases non-linearly and eventually plateaus at higher Mn(II) concentrations. The largest sink for DTT at low Mn(II) concentrations is HO_2 (R18), while at higher concentrations, it is the metal ions Mn(II) and Mn(III) (R21, Fig. S6A). This occurs because the rate coefficient of HO_2 with DTT is larger than the rate coefficients of Mn(II) and Mn(III) with DTT. The non-linearity stems from the fact that at high Mn(II) concentrations (> 20 μM), DTT is depleted by more than 50% (Fig. S6B), leading to an apparent slow down of the kinetics. Moreover, at higher Mn(II) concentrations, HO_2 undergoes a self-reaction to form H_2O_2, and also reacts with Mn(II) to form MnO_2^+ (Fig. S6C), where the latter then accumulates in the kinetic model (Fig. S6D).

Fig. 5C shows the temporal evolution of the DTT concentration at two different concentrations of Cu(II) from the study of Xiong et al. (2017). The data shows that the concentration of DTT decreases faster at higher Cu(II) concentrations. The loss of DTT due to Cu(II) is non-linear over time (Fig. 5A). As shown in Fig. 1, in KM-OP, the oxidation of DTT in the presence of Cu(II) involves the formation of a $[Cu^{2+}(DTT^{2-})_2]^{2-}$ complex, which has been identified as a catalyst for DTT oxidation (Kachur et al., 1997). The DTT loss rate increases non-linearly with increasing Cu(II) concentrations because the largest sink of DTT is the formation of $[Cu^{2+}(DTT^{2-})_2]^{2-}$ (R23, Fig. S7), which is second order with respect to DTT, while the loss of $[Cu^{2+}(DTT^{2-})_2]^{2-}$ is first order (Tab. S1, R63).

Fig. 5D illustrates the oxidation rates of DTT in the presence of quinones, as measured by Charrier and Anastasio (2012). Fig. 5E shows that PQN is the most reactive quinone examined in this study, followed by 1,2-NQN and 1,4-NQN, respectively. The kinetic model simulations show that quinones are reduced by DTT, resulting in the formation

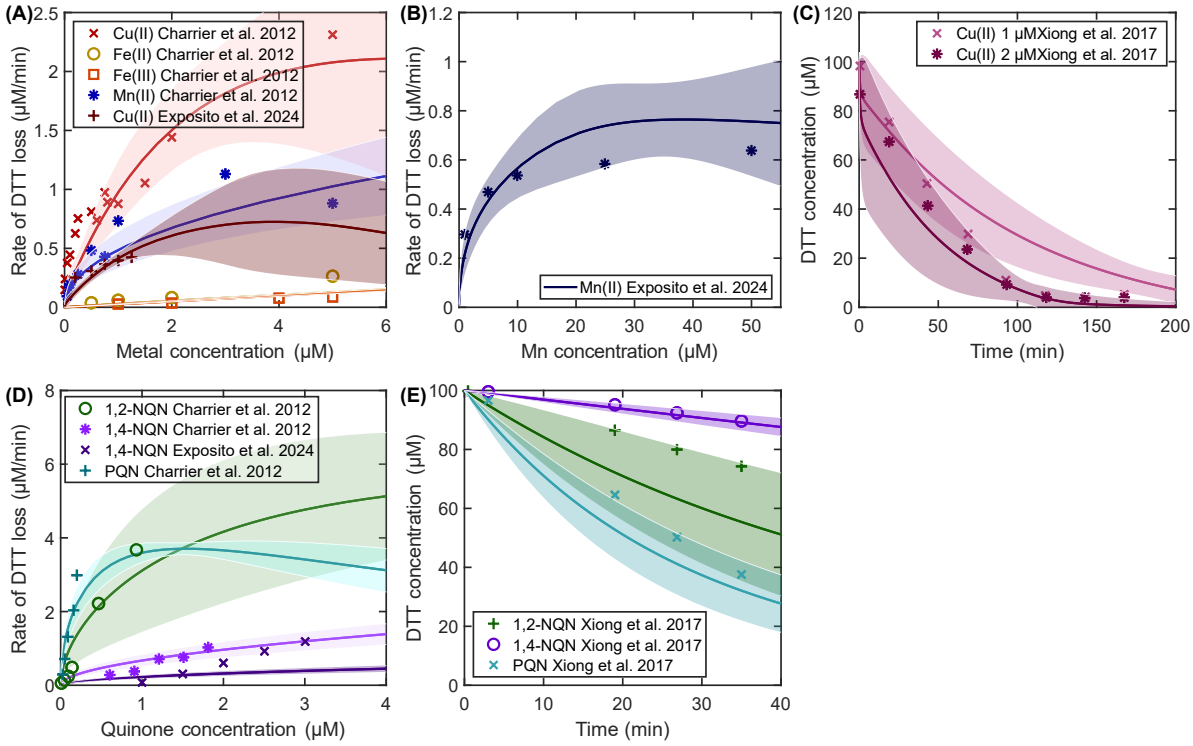

Figure 5: *Rate of DTT loss as a function different concentrations of transition metal ions (A and B) and quinones (D). DTT concentration as a function of time at different Cu(II) (C) and quinone (D) concentrations. The symbols are measurement data (Charrier and Anastasio, 2012; Xiong et al., 2017; Expósito et al., 2024), and the dark-colored lines depict the mean of fit ensembles from the model; shadings denote two standard deviations around the mean. The DTT concentration in Charrier and Anastasio (2012) and Xiong et al. (2017) data is 100 μM, while Expósito et al. (2024) use 50 μM of DTT.*

of the semiquinone radical and a thiyl radical (R24), both of which react with molecular oxygen to form HO_2 (Kumagai et al., 2002). We find that at higher 1,2-NQN and PQN concentrations, the main sink of DTT is the quinone itself (R24), while at lower concentrations of quinones, the main sink is HO_2 (R18, Fig. S8A, C). For 1,4-NQN, we find a rate coefficient with DTT that is slower compared to the rate coefficient of PQN and 1,2-NQN. Thus, in the presence of 1,4-NQN, the main sink for DTT is always HO_2 (Fig. S8B). While the inferred reaction rate coefficient of HO_2 with DTT (R18) is larger than the rate coefficient of PQN and 1,2-NQN with DTT (R24), the HO_2 concentration does not increase linearly with the concentration of quinones, and therefore the rate of reaction of PQN and 1,2-NQN with DTT becomes dominant at high PQN and 1,2-NQN concentrations. The DTT loss rate increases non-linearly with increasing quinone concentration because at higher concentrations of 1,2-NQN and PQN, the DTT concentration decreases by more than 50% at the end of the model simulation (Fig. S9), leading to an apparent slow down of the kinetics.

$$\mathrm{OH} + \mathrm{DTT} \rightarrow \mathrm{DTT}^{\bullet} + \mathrm{H_2O} \tag{R17}$$
$$\mathrm{HO_2} + \mathrm{DTT} \rightarrow \mathrm{DTT}^{\bullet} + 2\mathrm{OH}^{-} \tag{R18}$$
$$\mathrm{H_2O_2} + \mathrm{DTT} \rightarrow \mathrm{DTT}^{\bullet} + \mathrm{H_2O} + \mathrm{OH}^{-} \tag{R19}$$
$$\mathrm{Fe(III)} + \mathrm{DTT} \rightarrow \mathrm{Fe(II)} + \mathrm{DTT}^{\bullet} \tag{R20}$$
$$\mathrm{Mn(III)} + \mathrm{DTT} \rightarrow \mathrm{Mn(II)} + \mathrm{DTT}^{\bullet} \tag{R21}$$
$$\mathrm{Cu(II)} + \mathrm{DTT} \rightarrow [\mathrm{Cu}^{2+}(\mathrm{DTT}^{2-})] + 2\mathrm{H}^{+} \tag{R22}$$
$$[\mathrm{Cu}^{2+}(\mathrm{DTT}^{2-})] + \mathrm{DTT} \rightarrow [\mathrm{Cu}^{2+}(\mathrm{DTT}^{2-})_2]^{2-} + 2\mathrm{H}^{+} \tag{R23}$$
$$\mathrm{Q} + \mathrm{DTT} \rightarrow \mathrm{SQ} + \mathrm{DTT}^{\bullet} \tag{R24}$$

To test the chemical mechanism involving SOA (Fig. 1D), KM-OP results are compared to DTT data presented in Tuet et al. (2017) and radical production rate presented in Tong et al. (2018). Tong et al. (2018) measured the formation of OH, RO, HO_2, and R radicals from SOA using the EPR. Fig. 6A shows the radical production rate of SOA in water. We find a good agreement with the experimental data for isoprene and β-pinene SOA when using an organic hydroperoxide content within SOA to be 10%. For naphthalene SOA, we are able to capture the experimental data by lowering the organic hydroperoxide content to 3% (Wang et al., 2018). We assume that 5% of naphthalene SOA is 1,2-naphthoquinone (Tong et al., 2018; Daellenbach et al., 2020), although this does not affect radical production in this assay due to the lack of reductant to induce redox cycling of the quinones. Fig. 6B shows DTT activity using the same model parameters. The model result aligns well with the DTT activity from a majority of chamber-generated SOA (isoprene, α-pinene. β-caryophyllene, pentadecane, *m*-xylene). Including 1,2-naphthoquinone as part of the naphthalene SOA increases the DTT activity predicted by the model, since naphthoquinone are DTT-active. Note, this is only included in the comparison with experimental data, but is not considered for the ambient data. To

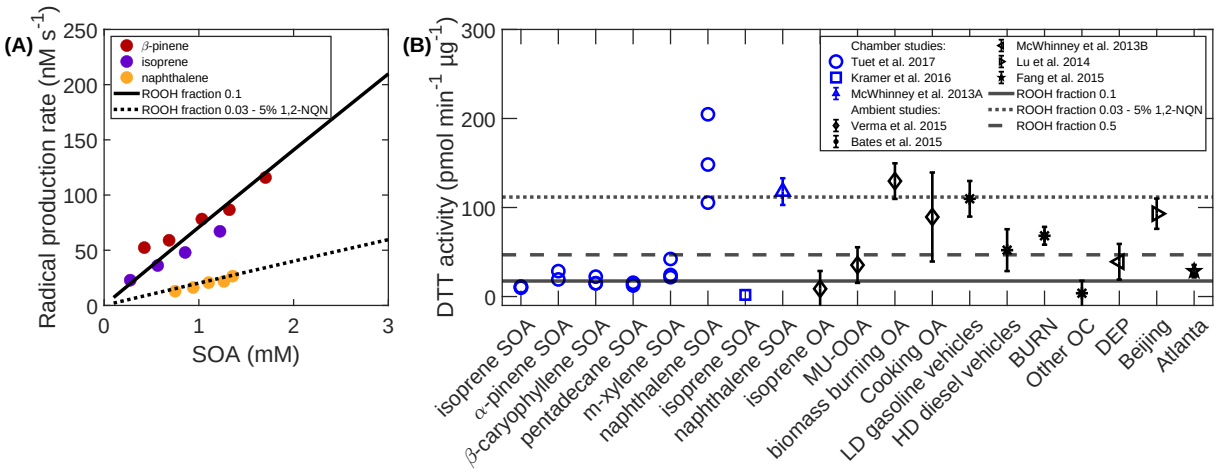

Figure 6: *Comparison of KM-OP model results with published data of radical production and DTT activity of secondary organic aerosol (SOA). Radical production rates as a function of SOA concentration published in Tong et al. (2018) for three different SOA precursors (markers) (A). Model results are depicted as solid lines. DTT activity for different types of chamber-generated (blue markers) and ambient SOA (black markers) adapted and including data from Tuet et al. (2017) and studies cited therein (McWhinney et al., 2013a,b; Lu et al., 2014; Bates et al., 2015; Fang et al., 2015; Verma et al., 2015; Kramer et al., 2016; Tuet et al., 2017) (B). Labels are reproduced from Tuet et al. (2017): Isoprene-OA: isoprene-derived OA, MO-OOA: more-oxidized oxygenated OA, LD: light-duty, HD: heavy-duty, BURN: biomass burning, DEP: diesel exhaust particles.*

compare the model results with the DTT activity of ambient measurements, we increase the organic hydroperoxide content within the SOA to 50% as these SOA are likely more aged (Docherty et al., 2005; Chowdhury et al., 2018) and find that the data are generally well-captured by the model. Note that the DTT assay reported in Tuet et al. (2017) (protocol from Fang et al. (2015)), uses EDTA to chelate transition metals. Charrier and Anastasio (2012) have shown that including EDTA in the experimental protocol reduces the DTT activity from both transition metals and quinones. In the model, we account for the effects of EDTA by assuming that its addition reduces the original DTT activity to one-tenth of the initial value (Charrier and Anastasio, 2012).

$$\mathrm{ROOH} \rightarrow \mathrm{OH} + \mathrm{RO} \tag{R25}$$
$$\mathrm{OH} + \mathrm{ROOH} \rightarrow \mathrm{HO_2} + \mathrm{ROH} \tag{R26}$$
$$\mathrm{RO} + \mathrm{ROOH} \rightarrow \mathrm{RO_2} + \mathrm{ROH} \tag{R27}$$
$$\mathrm{OH} + \mathrm{SOA} \rightarrow \mathrm{R} + \mathrm{H_2O} \tag{R28}$$
$$\mathrm{RO} + \mathrm{SOA} \rightarrow \mathrm{R} + \mathrm{ROH} \tag{R29}$$
$$\mathrm{AA} + \mathrm{RO} \rightarrow \mathrm{AA^{\bullet}} + \mathrm{ROH} \tag{R30}$$
$$\mathrm{AA} + \mathrm{RO_2} \rightarrow \mathrm{AA^{\bullet}} + \mathrm{ROOH} \tag{R31}$$
$$\mathrm{DTT} + \mathrm{RO} \rightarrow \mathrm{DTT^{\bullet}} + \mathrm{ROH} \tag{R32}$$
$$\mathrm{DTT} + \mathrm{RO_2} \rightarrow \mathrm{DTT^{\bullet}} + \mathrm{ROOH} \tag{R33}$$

Table 1: *Mean PM, Fe, Cu, SOA, and quinone mass concentrations at each of the different locations explored in this study.*

Location	PM ($\mu g\ m^{-3}$)	Fe ($ng\ m^{-3}$)	Cu ($ng\ m^{-3}$)	Mn ($ng\ m^{-3}$)	SOA ($\mu g\ m^{-3}$)	1,2-NQN ($ng\ m^{-3}$)	1,4-NQN ($ng\ m^{-3}$)	PQN ($ng\ m^{-3}$)
Grenoble	21.9	6.10	11.1	4.80	10.6	0.00700	0.00580	0.0202
Paris	49.3	31.8	10.9	13.2	9.40	0.0685	0.115	0.430
London Winter	13.0	128	6.70	0.562	4.16			
London Summer	10.2	254	6.40	1.20	4.28			

3.4 Comparison to field data

Figure 7 shows the correlation scatter plot of experimentally-determined and simulated OP for particulate matter samples collected at three different sites across Europe (Grenoble, Paris, and London). Overall, we find good agreement between model simulations and field data as evaluated by correlation coefficients and the mean squared logarithmic errors (MSLE). For the Grenoble site (Figs. 7A and D), the model shows slightly better correlation (R^2 = 0.75-0.83, MSLE = 0.04-0.05) with the data compared to the Paris site (Figs. 7B and E, R^2 = 0.69-0.74, MSLE = 0.05-0.08) for both assays. Nonetheless, the model overall slightly underestimates OP in both locations in France. This underestimation of OP likely stems from the limited number of chemical species in the model, which considers only three transition metals, three quinones, as well as SOA, and at present does not consider other chemical species or possible synergetic and antagonistic effects in mixtures that may also contribute to OP due to lack of experimental data availability (Charrier and Anastasio, 2012; Antiñolo et al., 2015). Furthermore, the model does not currently differentiate between biogenic and anthropogenic SOA, the latter of which has shown to be particularly OP-active in the case of naphthalene SOA (Fig. 6B). Nevertheless, as the model shows a good agreement with field data, ROS production and OP activity of anthropogenic and biogenic SOA may be quite similar. For the London sites (roadside location in the Summer, Fig. 7C and urban background location in Winter, Fig. 7F), the OP values between the model and field are within the same order of magnitude. However, the correlation between the model and field data is rather poor at the roadside location in the summer (R^2 = -0.06, MSLE = 0.15). In the winter, the correlation is high but the model still generally underestimates OP^{DHA} (R^2 = 0.76, MSLE = 0.11). Overall, the model captures the field data at the French sites better than at the London site. This could be because some OP-active components of PM are short-lived and while they can be detected using the online OP assay employed at the London site, likely contributing to more than 50% of the online OP^{DHA} (Campbell et al., 2019; Utinger et al., 2023; Campbell et al., 2025), such compounds may not be detected in the offline compositional analyses, and may not be considered in the data that was used for training of the model. Moreover, the compositional analysis for the London dataset presented in Campbell et al. (2024a) does not contain quantitative data for quinones, which may be another reason for the overall lower model-data correlation in the summer, and the underestimation of OP in the winter.

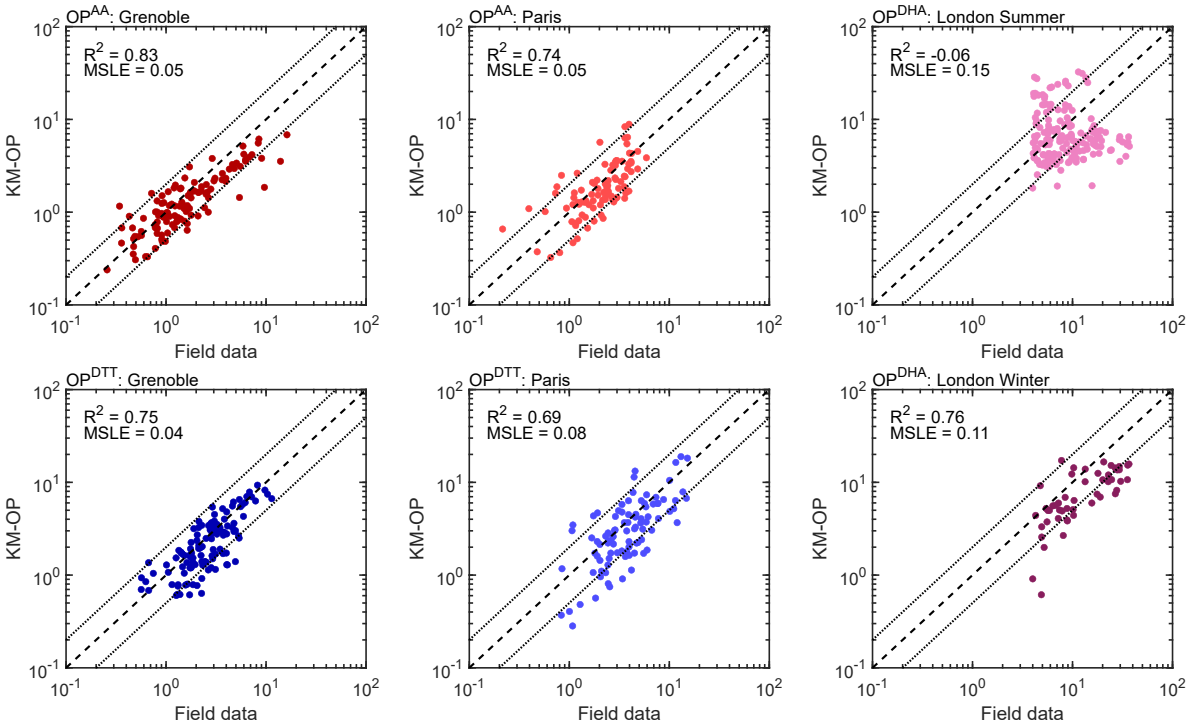

Figure 7: *Correlation scatter plots of model-predicted and measured OP for particulate matter samples collected in three different sites across Europe: Grenoble (OP^{AA}: panel A, and OP^{DTT}: panel D), Paris (OP^{AA}: panel B, and OP^{DTT}: panel E), and OP^{DHA} in London during the summer (C) and during the winter (F). Data shown in blue indicate OP^{DTT} (in units of nmol min^{-1} m^{-3}), while the red and pink data show OP^{AA} (in units of nmol min^{-1} m^{-3}) and OP^{DHA} (in units of nmol m^{-3}). The dashed lines indicate the 1:1 line.*

To gain insight into the chemical species which are key drivers of OP, we perform model sensitivity studies for each assay and each PM constituent. Fig. 8A shows the contribution of the model species towards OP^{AA}, OP^{DTT}, OP^{OH}, and OP^{H2O2} for Grenoble, using the average chemical composition (Tab. 1). The results for the other sites are shown in Fig. S10, S11, and S12. The white bar labelled "mixture" shows the default model result with all pollutants included. The "single pollutants" bar shows the sum of OP values calculated in model runs that only contain a single PM component. The contribution of each PM component is then highlighted in the colored bar segments. The "Shapley values" bar is calculated using the Shapley method. The normalized contributions to the mixture (default model result) for all data points at each site are shown in Fig. S13, S14, S15, and S16.

Model sensitivity calculations for OP^{AA} (Fig. 8A) show that the dominant contributions come from Cu and SOA. In the model, Cu contributes to AA oxidation through direct redox reaction with AA, but also through the production of O_2^- that further oxidizes AA. SOA contributes towards OP^{AA} through the decomposition of organic peroxides to RO and OH (Tong et al., 2016, 2018; Wei et al., 2021; Campbell et al., 2023), which in turn oxidize ascorbic acid (Fig. S17). Moreover, RO_2 also oxidizes AA. OP^{DHA}, predicted for the London sites (panels Fig. S15A and S16A), shows high contribution

from Cu, Fe, and SOA, all of which contribute to the formation of $AA^{\bullet}$, which then undergoes a disproportionation reaction to form DHA (Fig. S18).

Fig. 8B shows the contribution of PM constituents towards OP^{DTT}. We find that SOA contributes most to OP, consistent with previous studies that identified organic compounds as strongly correlated with DTT loss (Tuet et al., 2017; Fang et al., 2015). Notably, the "Shapley values" bar for SOA is smaller than its "single pollutants" bar. Cu alone contributes to OP, in line with previous studies that show that the DTT signal is correlated with Cu (Charrier and Anastasio, 2012; Pietrogrande et al., 2019; Lin and Yu, 2019). However, as indicated by negative values in the "Shapley values" bar, the presence of both Fe and Cu lowers OP in the mixture. This is due to the reactions of Cu(II) and Fe(III) with HO_2 producing O_2 (Tab. S1. R21, R40), effectively leading to a loss of an oxidant (Fig. S19). This is in line with Yu et al. (2018), who show antagonistic effects of Cu and Fe towards OP^{DTT} in mixtures with humic-like substances and Samake et al. (2017), who show antagonistic effects of Cu in mixture with bioaerosols.

Figure 8C shows the normalized contribution of PM constituents towards OP^{OH} in Grenoble. We find that SOA is a major contributor to OP^{OH}, through peroxide decomposition pathway (Tong et al., 2016), while Cu shows only a minor contribution (Fig. 8C). Fe can show a negative contribution to OP^{OH}, which is especially pronounced using the PM composition typical for Paris (Figs. S10C and S14C). Individually, both Fe and SOA contribute to OP^{OH} through Fenton chemistry (R13) and peroxide decomposition (R25), respectively. Their antagonistic interaction can be understood by considering the Fenton-like reaction of ROOH and Fe(II) to RO (R34). This reaction is a large sink of both SOA and Fe(II) that does not lead to the formation OH, since the reaction of ROOH with Fe(II) preferentially generates RO (R34) over OH (R35) as radical species (Campbell et al., 2023). Hence, the presence of SOA lowers the OH yield from R13 and Fe lowers the OH yield from R25. We find that SOA strongly contributes to OP^{OH} at the French sites. At the London site, the mass fractions of Fe are so high that ROOH predominantly reacts through reaction R34 (Fig. S22). Accordingly, as the OH assay does not capture RO, SOA contributions to OP^{OH} are negligible in London. These results highlight the importance of capturing reactant interactions, as they can have either synergistic or antagonistic effects in different OP assays. SOA and Fe contributes similarly to OP^{OH} as single pollutants in London, while their contribution to the mixture is much smaller. Note that the effect of Fe on OP^{OH} in London is highly variable, with some samples showing a positive effect, while others show a negative effect (S15C, S16C). Note, a rather uncertain reaction in these calculations is the Fenton-like reaction of ROOH with Fe(II), as these are not subject to experiments used in this study when building the kinetic model.

$$\mathrm{Fe(II)} + \mathrm{ROOH} \rightarrow \mathrm{Fe(III)} + \mathrm{RO} + \mathrm{OH^-} \quad \text{(R34)}$$

$$\mathrm{Fe(II)} + \mathrm{ROOH} \rightarrow \mathrm{Fe(III)} + \mathrm{RO^-} + \mathrm{OH} \quad \text{(R35)}$$

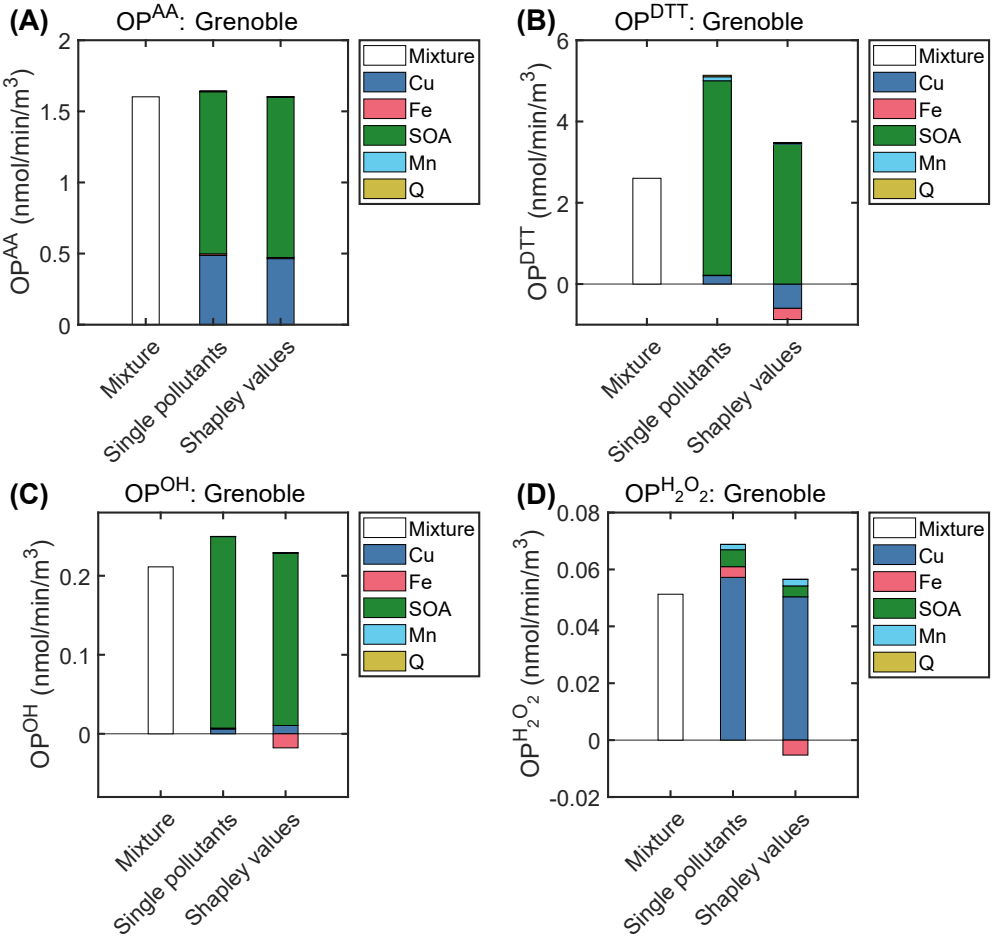

Figure 8: *Contributions of different PM constituents to OP^{AA} (A), OP^{DTT} (B), OP^{OH} (C), and $OP^{H_2O_2}$ (D) in Grenoble. The "mixture" bar shows the model result when all species are included in the model. The "single pollutants" bar sums the result of model simulations where only one specific species was included. The "Shapley values" bar is calculated using the Shapley analysis*

We note that there may also be synergistic interactions between organics and Fe as a result of Fe-organic complex formation (Yu et al., 2018), which may have a higher rate coefficient for the Fenton reaction than that used in this study (Gonzalez et al., 2017). Nonetheless, the rate coefficient derived in this study is based on experiments containing Fe and citric acid, which form Fe-citrate complexes that likely react faster than free Fe (Rush and Koppenol, 1990; Gonzalez et al., 2017).

Figure 8D shows the normalized contribution of PM constituents towards $OP^{H_2O_2}$ of PM typical for Grenoble. We find that Cu is a major contributor to $OP^{H_2O_2}$ in the model, while Mn plays a minor role. Fe contributes negatively to $OP^{H_2O_2}$ in mixtures across all locations considered in this study (Fig. S13D, S14D, S15D, S16D). As shown in Fig. 3B earlier, Fe can react with H_2O_2 through the Fenton reaction leading to a low steadystate concentration of H_2O_2, and hence a lowering the OP.

Fig. 9A uses the average chemical composition at the Grenoble, Paris, and London sites to compare the model results for the various OP assays. In general, OP values are higher in France compared to London, both during winter and summer. In France, on average, the concentrations of SOA and Cu are higher compared to London (Tab. 1), which are large drivers of OP in the model, as seen in Figs. 8, S10, S11, and S12. Likewise, the model predicts similar OP values in Paris and Grenoble due to very similar SOA and Cu concentrations. In contrast, Fe concentrations are higher in London during summer, which leads to a slightly higher OP^{AA} compared to OP^{DTT} since Fe has a strong negative contribution to OP^{DTT}.

Fig. 9B shows the correlations between the different intrinsic OP assays simulated in the study. To obtain the correlation coefficients, intrinsic OP is calculated for the composition data from all locations. We find that OP^{AA}, OP^{DHA}, and OP^{DTT} correlate well with OP^{OH}. Correlations at individual locations are shown in Figs S23-26. At these single locations, the correlation between OP^{OH} and OP^{AA}, OP^{DHA}, and OP^{DTT} is higher than the correlation in the full data set (Fig. 9B). This is because PM composition can be fairly similar at one site, but may differ strongly across sites (Tab. 1). In France, OP^{OH}, OP^{DTT}, OP^{AA} and OP^{DHA} simulated in the model are primarily driven by SOA. In contrast, in London, OP^{OH}, OP^{AA} and OP^{DHA} are also driven by the transition metals. The simulation results indicate that the differences in OP assays are exacerbated by larger differences in aerosol composition.

$OP^{H_2O_2}$ shows a lower correlation with OP^{OH}, both in individual locations, as well as when combining all the data points. This can be understood by considering the sensitivities to aerosol components investigated above (Fig. 8, S10, S11, and S12): while the majority of the OP assays are driven by SOA, $OP^{H_2O_2}$ is mostly influenced by the presence of Cu. We find negative contribution of Fe to $OP^{H_2O_2}$.

4 conclusions

In this study, we develop a chemical kinetics model of aerosol oxidative potential, KM-OP, to quantify the effects of particulate pollutants on the production of ROS

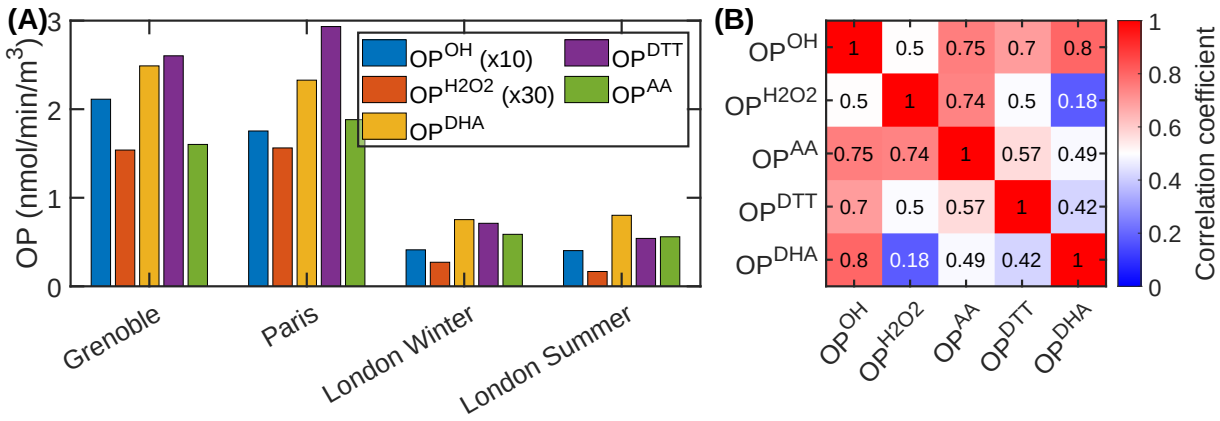

Figure 9: *Comparison and correlation of different simulated OP assays. (A) Simulations of different OP assays explored in this study using the average chemical composition data from Grenoble, Paris and London (Tab. 1). OP^{OH} and $OP^{H_2O_2}$ results are multiplied by 10 and 30, respectively. (B) Correlation matrix between intrinsic OP assays explored in this study using data from all study sites.*

(OH, H_2O_2) and the depletion of ascorbic acid (OP^{AA}, OP^{DHA}), and dithiothreitol (OP^{DTT}). We performed detailed kinetic modeling on a large set of laboratory data from various OP assays to infer the optimal kinetic model parameters. For the first time, a model with a single kinetic parameter set leads to good agreement with such a large set of experimental data. Previously, fits had only been obtained for single datasets (Campbell et al., 2023; Expósito et al., 2024). We extrapolate the findings from the laboratory experiments to field data from urban sites including detailed PM chemical characterization and source apportionment outputs. We find a good agreement between the model and field data at three urban sites across Europe.

Dominutti et al. (2025) highlights the lack of harmonization and robustness of OP assays. This is in contrast to the analytical protocols that are widely available for the key species influencing OP. The implications of the newly developed KM-OP are illustrated in Fig. 10. KM-OP is a predictive model, meaning that it is able to predict OP and thus possible health effects of particulate matter solely when chemical composition data are available. The importance of focusing on integrating PM chemical composition into epidemiological health assessments when developing new regulatory metrics has been recently emphasized, and KM-OP may help provide a bridge between chemical composition of PM and epidemiological health assessments.

Antioxidant-depleting assays are generally not specific to certain ROS (Bates et al., 2019) and ROS such as O_2^- and H_2O_2 are ubiquitous in the lung lining fluid (Fang et al., 2022; Dovrou et al., 2023; Mishra et al., 2023). The presence of ROS alone does not indicate the presence of oxidative distress because the human body possesses many systems that establish and maintain redox homeostasis (Sies, 2017, 2021). Likewise, previous studies have suggested that PM health effects may not be driven by the production of H_2O_2, but rather by its conversion into the OH radical, which reacts much more quickly and often irreversibly with biomolecules (Lelieveld et al., 2021; Dovrou et al., 2023; Mishra et al., 2023). Thus, correlation with H_2O_2 formation may not be a

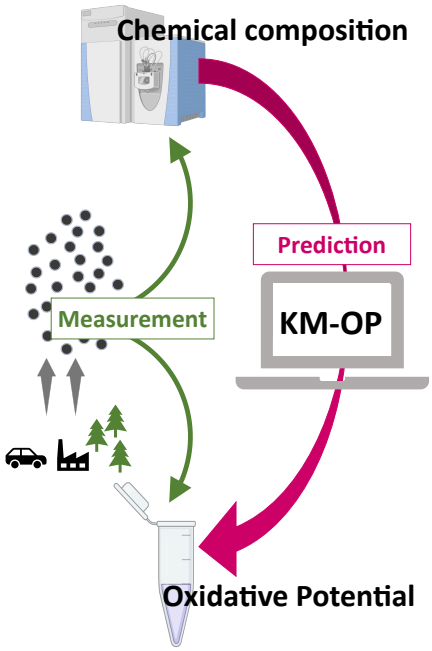

Figure 10: *Implications of the KM-OP model. Measurements of chemical composition and OP of ambient PM are common. OP cannot be predicted from measurements of chemical composition alone, however the newly developed KM-OP is able to predict OP when chemical composition data are available.*

sufficient property of OP assays to capture the health effects of PM, while assays that correlate well with OH formation may be more suitable. Furthermore, while some PM components efficiently generate ROS, others are more effective at depleting antioxidants or their surrogates (Xiong et al., 2017). Our model results indicate that most OP assays are well correlated with OP^{OH}. Using the kinetic model, we find that OP^{DTT} is primarily driven by SOA, while OP^{OH}, OP^{AA} and OP^{DHA} are also influenced by Fe and Cu. SOA has only a marginal effect on $OP^{H_2O_2}$, which we find to be strongly associated with Cu and also affected by Mn and quinones. Interestingly, while both OP^{OH} and OP^{DTT} are affected by SOA, the correlation between the two assays is lower (R^2 = 0.7) than the correlation between OP^{OH} and OP^{AA} or between OP^{OH} and OP^{DHA} (R^2 = 0.75 - 0.8). This is because some reactive species that originate from the dissolution of SOA, such as RO, react with antioxidants, but are not captured by the OH assay in the model. Consequently, experimental techniques that capture other radicals in addition to the OH, such as the EPR, may be particularly useful.

Further experimental studies under controlled laboratory conditions are needed to reduce model uncertainty regarding the interaction of pollutants within the assay, such as mixtures of transition metals, and substances not yet introduced in KM-OP (e.g., Zn, elemental carbon, nitro-PAHs, nitrophenols, other quinones including PPD-quinones and other oxygenated aromatics, chelating organics) as well as interactions of transition metals with organic compounds. Laboratory studies integrating the measurement of ROS production while simultaneously monitoring the decay of DTT or AA could be particularly helpful (Xiong et al., 2017; Shahpoury et al., 2024a). Extensive kinetic exper-

iments with SOA for different OP assays could help improve the model, in particular, OP response may be affected by both precursor identity or the degree of SOA aging (Tuet et al., 2017; Antiñolo et al., 2015; Chowdhury et al., 2018), which is currently not represented in the model. Future studies should investigate how to integrate such properties of SOA from filter analysis. Ambient PM chemical characterization could include additional water soluble metals and chelating species, such as alcohols and amines. Moreover, online OP assays may capture short-lived compounds that are not captured by filter-based assays. To obtain a kinetic model that can represent such short-lived compounds, it is pertinent to perform well-controlled laboratory experiments for model training under immediate dissolution and exposure of the sampled PM to probe species.

Future work will also include the extrapolation of the chemistry from OP assays into the chemical environment of the lung lining fluid, to translate assay-based OP into markers for physiological health endpoints, and to identify the assays that most closely correlate with markers of oxidative stress. Additionally, we plan to use chemical composition data from global models as inputs for KM-OP in order to predict and compare modeled OP with measurements of OP across the world.

5 References

Abrams, J. Y., Weber, R. J., Klein, M., Samat, S. E., Chang, H. H., Strickland, M. J., Verma, V., Fang, T., Bates, J. T., Mulholland, J. A., Russell, A. G., and Tolbert, P. E.: Associations between Ambient Fine Particulate Oxidative Potential and Cardiorespiratory Emergency Department Visits, Environ. Health Perspect., 125, 107 008, 2017.

Antiñolo, M., Willis, M. D., Zhou, S., and Abbatt, J. P.: Connecting the oxidation of soot to its redox cycling abilities, Nat. Commun., 6, 6812, 2015.

Ayres, J. G., , Paul, B., , Flemming R., C., , Vincent, C., , Ken, D., , Andy, G., , Roy M., H., , Robert, H., , Frank, K., , Ingeborg M., K., , Francelyne, M., , Robert L., M., , Ian, M., , Andre, N., , Constantinos, S., , Steve, S., , Armelle, B.-S., , Art, C., , Sean, D., , and Froines, J.: Evaluating the Toxicity of Airborne Particulate Matter and Nanoparticles by Measuring Oxidative Stress Potential—A Workshop Report and Consensus Statement, Inhal. Toxicol., 20, 75–99, 2008.

Bates, J. T., Weber, R. J., Abrams, J., Verma, V., Fang, T., Klein, M., Strickland, M. J., Sarnat, S. E., Chang, H. H., Mulholland, J. A., Tolbert, P. E., and Russell, A. G.: Reactive Oxygen Species Generation Linked to Sources of Atmospheric Particulate Matter and Cardiorespiratory Effects, Environ. Sci. Technol., 49, 13 605–13 612, 2015.

Bates, J. T., Fang, T., Verma, V., Zeng, L., Weber, R. J., Tolbert, P. E., Abrams, J. Y., Sarnat, S. E., Klein, M., Mulholland, J. A., and Russell, A. G.: Review of Acellular Assays of Ambient Particulate Matter Oxidative Potential: Methods and Relationships with Composition, Sources, and Health Effects, Environ. Sci. Technol., 53, 4003–4019, 2019.

Berkemeier, T., Ammann, M., Krieger, U. K., Peter, T., Spichtinger, P., Pöschl, U., Shiraiwa, M., and Huisman, A. J.: Technical note: Monte Carlo genetic algorithm (MCGA) for model analysis of multiphase chemical kinetics to determine transport and reaction rate coefficients using multiple experimental data sets, Atmos. Chem. Phys., 17, 8021–8029, 2017.

Berkemeier, T., Mishra, A., Mattei, C., Huisman, A. J., Krieger, U. K., and Pöschl, U.: Ozonolysis of Oleic Acid Aerosol Revisited: Multiphase Chemical Kinetics and Reaction Mechanisms, ACS Earth Space Chem., 5, 3313–3323, 2021.

Bhattu, D., Tripathi, S. N., Bhowmik, H. S., Moschos, V., Lee, C. P., Rauber, M., Salazar, G., Abbaszade, G., Cui, T., Slowik, J. G., Vats, P., Mishra, S., Lalchandani, V., Satish, R., Rai, P., Casotto, R., Tobler, A., Kumar, V., Hao, Y., Qi, L., Khare, P., Manousakas, M. I., Wang, Q., Han, Y., Tian, J., Darfeuil, S., Minguillon, M. C., Hueglin, C., Conil, S., Rastogi, N., Srivastava, A. K., Ganguly, D., Bjelic, S., Canonaco, F., Schnelle-Kreis, J., Dominutti, P. A., Jaffrezo, J.-L., Szidat, S., Chen, Y., Cao, J., Baltensperger, U., Uzu, G., Daellenbach, K. R., El Haddad, I., and Prévôt, A. S. H.: Local incomplete combustion emissions define the PM2.5 oxidative potential in Northern India, Nat. Commun., 15, 3517, 2024.

Borlaza, L. J. S., Weber, S., Jaffrezo, J.-L., Houdier, S., Slama, R., Rieux, C., Albinet, A., Micallef, S., Trébluchon, C., and Uzu, G.: Disparities in particulate matter (PM10) origins and oxidative potential at a city scale (Grenoble, France) – Part 2: Sources of PM10 oxidative potential using multiple linear regression analysis and the predictive applicability of multilayer perceptron neural network analysis, Atmos. Chem. Phys., 21, 9719–9739, 2021.

Borm, P. J. A., Kelly, F., Künzli, N., Schins, R. P. F., and Donaldson, K.: Oxidant generation by particulate matter: from biologically effective dose to a promising, novel metric, Occup. Environ. Med., 64, 73, 2007.

Brauer, M. et al.: Global burden and strength of evidence for 88 risk factors in 204 countries and 811 subnational locations, 1990–2021: a systematic analysis for the Global Burden of Disease Study 2021, Lancet, 403, 2162–2203, 2024.

Calas, A., Uzu, G., Martins, J. M. F., Voisin, D., Spadini, L., Lacroix, T., and Jaffrezo, J.-L.: The importance of simulated lung fluid (SLF) extractions for a more relevant evaluation of the oxidative potential of particulate matter, Sci. Rep., 7, 11 617, 2017.

Calas, A., Uzu, G., Kelly, F. J., Houdier, S., Martins, J. M. F., Thomas, F., Molton, F., Charron, A., Dunster, C., Oliete, A., Jacob, V., Besombes, J.-L., Chevrier, F., and Jaffrezo, J.-L.: Comparison between five acellular oxidative potential measurement assays performed with detailed chemistry on PM10 samples from the city of Chamonix (France), Atmos. Chem. Phys., 18, 7863–7875, 2018.

Camman, J., Chazeau, B., Marchand, N., Durand, A., Gille, G., Lanzi, L., Jaffrezo, J.-L., Wortham, H., and Uzu, G.: Oxidative potential apportionment of atmospheric PM1: a new approach combining high-sensitive online analysers for chemical composition and offline OP measurement technique, Atmos. Chem. Phys., 24, 3257–3278, 2024.

Campbell, S. J., Utinger, B., Lienhard, D. M., Paulson, S. E., Shen, J., Griffiths, P. T., Stell, A. C., and Kalberer, M.: Development of a Physiologically Relevant Online Chemical Assay To Quantify Aerosol Oxidative Potential, Anal. Chem., 91, 13 088–13 095, 2019.

Campbell, S. J., Utinger, B., Barth, A., Paulson, S. E., and Kalberer, M.: Iron and Copper Alter the Oxidative Potential of Secondary Organic Aerosol: Insights from Online Measurements and Model Development, Environ. Sci. Technol., 57, 13 546–13 558, 2023.

Campbell, S. J., Barth, A., Chen, G. I., Tremper, A. H., Priestman, M., Ek, D., Gu, S., Kelly, F. J., Kalberer, M., and Green, D. C.: High time resolution quantification of PM2.5 oxidative potential at a Central London roadside supersite, Environ. Int., 193, 109 102, 2024a.

Campbell, S. J., La, C., Zhou, Q., Le, J., Galvez-Reyes, J., Banach, C., Houk, K. N., Chen, J. R., and Paulson, S. E.: Characterizing Hydroxyl Radical Formation from

the Light-Driven Fe(II)–Peracetic Acid Reaction, a Key Process for Aerosol-Cloud Chemistry, Environ. Sci. Technol., 58, 7505–7515, 2024b.

Campbell, S. J., Utinger, B., Barth, A., Leni, Z., Zhang, Z.-H., Resch, J., Li, K., Steimer, S. S., Banach, C., Gfeller, B., Wragg, F. P. H., Westwood, J., Wolfer, K., Bukowiecki, N., Ihalainen, M., Yli-Pirilä, P., Somero, M., Kortelainen, M., Louhisalmi, J., Sklorz, M., Czech, H., di Bucchianico, S., Streibel, T., Delaval, M. N., Ruger, C., Baumlin, N., Salathe, M., Fang, Z., Pardo, M., D'Aronco, S., Giorio, C., Shi, Z., Harrison, R. M., Green, D. C., Kelly, F. J., Rudich, Y., Paulson, S. E., Sippula, O., Zimmermann, R., Geiser, M., and Kalberer, M.: Short-lived reactive components substantially contribute to particulate matter oxidative potential, Sci. Adv., 11, eadp8100, 2025.

Carlino, A., Romano, M. P., Lionetto, M. G., Contini, D., and Guascito, M. R.: An Overview of the Automated and On-Line Systems to Assess the Oxidative Potential of Particulate Matter, Atmosphere, 14, 2023.

Charrier, J. G. and Anastasio, C.: On dithiothreitol (DTT) as a measure of oxidative potential for ambient particles: evidence for the importance of soluble transition metals, Atmos. Chem. Phys., 12, 9321–9333, 2012.

Charrier, J. G. and Anastasio, C.: Rates of Hydroxyl Radical Production from Transition Metals and Quinones in a Surrogate Lung Fluid, Environ. Sci. Technol., 49, 9317–9325, 2015.

Charrier, J. G., McFall, A. S., Richards-Henderson, N. K., and Anastasio, C.: Hydrogen Peroxide Formation in a Surrogate Lung Fluid by Transition Metals and Quinones Present in Particulate Matter, Environ. Sci. Technol., 48, 7010–7017, 2014.

Charrier, J. G., Richards-Henderson, N. K., Bein, K. J., McFall, A. S., Wexler, A. S., and Anastasio, C.: Oxidant production from source-oriented particulate matter – Part 1: Oxidative potential using the dithiothreitol (DTT) assay, Atmos. Chem. Phys., 15, 2327–2340, 2015.

Charrier, J. G., McFall, A. S., Vu, K. K.-T., Baroi, J., Olea, C., Hasson, A., and Anastasio, C.: A bias in the "mass-normalized" DTT response – An effect of non-linear concentration-response curves for copper and manganese, Atmos. Environ., 144, 325–334, 2016.

Cheung, K. L., Polidori, A., Ntziachristos, L., Tzamkiozis, T., Samaras, Z., Cassee, F. R., Gerlofs, M., and Sioutas, C.: Chemical Characteristics and Oxidative Potential of Particulate Matter Emissions from Gasoline, Diesel, and Biodiesel Cars, Environ. Sci. Technol., 43, 6334–6340, 2009.

Chevallier, E., Jolibois, R., Meunier, N., Carlier, P., and Monod, A.: "Fenton-like" reactions of methylhydroperoxide and ethylhydroperoxide with Fe2+ in liquid aerosols under tropospheric conditions, Atmos. Environ., 38, 921–933, 2004.

Cho, A. K., Sioutas, C., Miguel, A. H., Kumagai, Y., Schmitz, D. A., Singh, M., Eiguren-Fernandez, A., and Froines, J. R.: Redox activity of airborne particulate matter at different sites in the Los Angeles Basin, Environ. Res., 99, 40–47, 2005.

Chowdhury, P. H., He, Q., Lasitza Male, T., Brune, W. H., Rudich, Y., and Pardo, M.: Exposure of Lung Epithelial Cells to Photochemically Aged Secondary Organic Aerosol Shows Increased Toxic Effects, Environ. Sci. Technol. Lett., 5, 424–430, 2018.

Cohen, A. J., Brauer, M., Burnett, R., Anderson, H. R., Frostad, J., Estep, K., Balakrishnan, K., Brunekreef, B., Dandona, L., Dandona, R., Feigin, V., Freedman, G., Hubbell, B., Jobling, A., Kan, H., Knibbs, L., Liu, Y., Martin, R., Morawska, L., Pope, III, C. A., Shin, H., Straif, K., Shaddick, G., Thomas, M., van Dingenen, R., van Donkelaar, A., Vos, T., Murray, C. J. L., and Forouzanfar, M. H.: Estimates and 25-year trends of the global burden of disease attributable to ambient air pollution: an analysis of data from the Global Burden of Diseases Study 2015, Lancet, 389, 1907–1918, 2017.

Daellenbach, K. R., Uzu, G., Jiang, J., Cassagnes, L.-E., Leni, Z., Vlachou, A., Stefenelli, G., Canonaco, F., Weber, S., Segers, A., Kuenen, J. J. P., Schaap, M., Favez, O., Albinet, A., Aksoyoglu, S., Dommen, J., Baltensperger, U., Geiser, M., El Haddad, I., Jaffrezo, J.-L., and Prévôt, A. S. H.: Sources of particulate-matter air pollution and its oxidative potential in Europe, Nature, 587, 414–419, 2020.

Docherty, K. S., Wu, W., Lim, Y. B., and Ziemann, P. J.: Contributions of Organic Peroxides to Secondary Aerosol Formed from Reactions of Monoterpenes with O3, Environ. Sci. Technol., 39, 4049–4059, 2005.

Dockery, D. W., Pope, C. A., Xu, X., Spengler, J. D., Ware, J. H., Fay, M. E., Ferris, B. G., and Speizer, F. E.: An Association between Air Pollution and Mortality in Six U.S. Cities, N. Engl. J. Med., 329, 1753–1759, 1993.

Dominutti, P. A., Jaffrezo, J.-L., Marsal, A., Mhadhbi, T., Elazzouzi, R., Rak, C., Cavalli, F., Putaud, J.-P., Bougiatioti, A., Mihalopoulos, N., Paraskevopoulou, D., Mudway, I., Nenes, A., Daellenbach, K. R., Banach, C., Campbell, S. J., Cigánková, H., Contini, D., Evans, G., Georgopoulou, M., Ghanem, M., Glencross, D. A., Guascito, M. R., Herrmann, H., Iram, S., Jovanović, M., Jovašević-Stojanović, M., Kalberer, M., Kooter, I. M., Paulson, S. E., Patel, A., Perdrix, E., Pietrogrande, M. C., Mikuška, P., Sauvain, J.-J., Seitanidi, K., Shahpoury, P., Souza, E. J. d. S., Steimer, S., Stevanovic, S., Suarez, G., Subramanian, P. S. G., Utinger, B., van Os, M. F., Verma, V., Wang, X., Weber, R. J., Yang, Y., Querol, X., Hoek, G., Harrison, R. M., and Uzu, G.: An interlaboratory comparison to quantify oxidative potential measurement in aerosol particles: challenges and recommendations for harmonisation, Atmos. Meas. Tech., 18, 177–195, 2025.

Donaldson, K., Stone, V., Seaton, A., and MacNee, W.: Ambient particle inhalation and the cardiovascular system: potential mechanisms., Environ. Health Perspect., 109, 523–527, 2001.

Dovrou, E., Lelieveld, S., Mishra, A., Pöschl, U., and Berkemeier, T.: Influence of ambient and endogenous H2O2 on reactive oxygen species concentrations and OH radical production in the respiratory tract, Environ. Sci.: Atmos., 2023.

Expósito, A., Maillo, J., Uriarte, I., Santibáñez, M., and Fernández-Olmo, I.: Kinetics of ascorbate and dithiothreitol oxidation by soluble copper, iron, and manganese, and 1,4-naphthoquinone: Influence of the species concentration and the type of fluid, Chemosphere, 361, 142 435, 2024.

Fang, T., Verma, V., Guo, H., King, L. E., Edgerton, E. S., and Weber, R. J.: A semi-automated system for quantifying the oxidative potential of ambient particles in aqueous extracts using the dithiothreitol (DTT) assay: results from the Southeastern Center for Air Pollution and Epidemiology (SCAPE), Atmos. Meas. Tech., 8, 471–482, 2015.

Fang, T., Zeng, L., Gao, D., Verma, V., Stefaniak, A. B., and Weber, R. J.: Ambient Size Distributions and Lung Deposition of Aerosol Dithiothreitol-Measured Oxidative Potential: Contrast between Soluble and Insoluble Particles, Environ. Sci. Technol., 51, 6802–6811, 2017.

Fang, T., Lakey, P. S. J., Weber, R. J., and Shiraiwa, M.: Oxidative Potential of Particulate Matter and Generation of Reactive Oxygen Species in Epithelial Lining Fluid, Environ. Sci. Technol., 53, 12 784–12 792, 2019.

Fang, T., Huang, Y.-K., Wei, J., Monterrosa Mena, J. E., Lakey, P. S. J., Kleinman, M. T., Digman, M. A., and Shiraiwa, M.: Superoxide Release by Macrophages through NADPH Oxidase Activation Dominating Chemistry by Isoprene Secondary Organic Aerosols and Quinones to Cause Oxidative Damage on Membranes, Environ. Sci. Technol., 56, 17 029–17 038, 2022.

Farahani, V. J., Altuwayjiri, A., Pirhadi, M., Verma, V., Ruprecht, A. A., Diapouli, E., Eleftheriadis, K., and Sioutas, C.: The oxidative potential of particulate matter (PM) in different regions around the world and its relation to air pollution sources, Environ. Sci.: Atmos., 2, 1076–1086, 2022.

Frezzini, M. A., De Francesco, N., Massimi, L., and Canepari, S.: Effects of operating conditions on PM oxidative potential assays, Atmos. Environ., 268, 118 802, 2022.

Fuller, S., Wragg, F., Nutter, J., and Kalberer, M.: Comparison of on-line and off-line methods to quantify reactive oxygen species (ROS) in atmospheric aerosols, Atmos. Environ., 92, 97–103, 2014.

Gao, D., Ripley, S., Weichenthal, S., and Godri Pollitt, K. J.: Ambient particulate matter oxidative potential: Chemical determinants, associated health effects, and strategies for risk management, Free Radic. Biol. Med., 151, 7–25, 2020.

Gonzalez, D. H., Cala, C. K., Peng, Q., and Paulson, S. E.: HULIS Enhancement of Hydroxyl Radical Formation from Fe(II): Kinetics of Fulvic Acid–Fe(II) Complexes in the Presence of Lung Antioxidants, Environ. Sci. Technol., 51, 7676–7685, 2017.

Gonzalez, D. H., , Xiaobi M., K., , John A., S., , Gisele Olimpio, R., , and Paulson, S. E.: Terephthalate Probe for Hydroxyl Radicals: Yield of 2-Hydroxyterephthalic Acid and Transition Metal Interference, Anal. Lett., 51, 2488–2497, 2018.

Gonzalez, D. H., Diaz, D. A., Baumann, J. P., Ghio, A. J., and Paulson, S. E.: Effects of albumin, transferrin and humic-like substances on iron-mediated OH radical formation in human lung fluids, Free Radic. Biol. Med., 165, 79–87, 2021.

Hayes, J. D., Dinkova-Kostova, A. T., and Tew, K. D.: Oxidative Stress in Cancer, Cancer Cell, 38, 167–197, 2020.

Hwang, B., Fang, T., Pham, R., Wei, J., Gronstal, S., Lopez, B., Frederickson, C., Galeazzo, T., Wang, X., Jung, H., and Shiraiwa, M.: Environmentally Persistent Free Radicals, Reactive Oxygen Species Generation, and Oxidative Potential of Highway PM2.5, ACS Earth Space Chem., 5, 1865–1875, 2021.

Janssen, N. A., Yang, A., Strak, M., Steenhof, M., Hellack, B., Gerlofs-Nijland, M. E., Kuhlbusch, T., Kelly, F., Harrison, R., Brunekreef, B., Hoek, G., and Cassee, F.: Oxidative potential of particulate matter collected at sites with different source characteristics, Sci. Total Environ., 472, 572–581, 2014.

Kachur, A. V., Held, K. D., Koch, C. J., and Biaglow, J. E.: Mechanism of Production of Hydroxyl Radicals in the Copper-Catalyzed Oxidation of Dithiothreitol, Radiat. Res., 147, 409–415, 1997.

Kelly, F. J.: Oxidative stress: its role in air pollution and adverse health effects, Occup. Environ. Med., 60, 612, 2003.

Kramer, A. J., Rattanavaraha, W., Zhang, Z., Gold, A., Surratt, J. D., and Lin, Y.-H.: Assessing the oxidative potential of isoprene-derived epoxides and secondary organic aerosol, Atmos. Environ., 130, 211–218, 2016.

Kumagai, Y., Koide, S., Taguchi, K., Endo, A., Nakai, Y., Yoshikawa, T., and Shimojo, N.: Oxidation of Proximal Protein Sulfhydryls by Phenanthraquinone, a Component of Diesel Exhaust Particles, Chem. Res. Toxicol., 15, 483–489, 2002.

Laulagnet, A., Sauvain, J., Concha-Lozano, N., Riediker, M., and Suárez, G.: Sensitive Photonic System to Measure Oxidative Potential of Airborne Nanoparticles and ROS Levels in Exhaled Air, Procedia Eng., 120, 632–636, 2015.

Lelieveld, S., Wilson, J., Dovrou, E., Mishra, A., Lakey, P. S. J., Shiraiwa, M., Pöschl, U., and Berkemeier, T.: Hydroxyl Radical Production by Air Pollutants in Epithelial Lining Fluid Governed by Interconversion and Scavenging of Reactive Oxygen Species, Environ. Sci. Technol., 55, 14 069–14 079, 2021.

Lin, M. and Yu, J. Z.: Dithiothreitol (DTT) concentration effect and its implications on the applicability of DTT assay to evaluate the oxidative potential of atmospheric aerosol samples, Environ. Pollut., 251, 938–944, 2019.

Lin, P. and Yu, J. Z.: Generation of Reactive Oxygen Species Mediated by Humic-like Substances in Atmospheric Aerosols, Environ. Sci. Technol., 45, 10 362–10 368, 2011.

Liu, X., Zhang, X., Jin, B., Wang, T., Qian, S., Zou, J., Dinh, V. N. T., Jaffrezo, J.-L., Uzu, G., Dominutti, P., Darfeuil, S., Favez, O., Conil, S., Marchand, N., Castillo, S., de la Rosa, J. D., Grange, S., Hueglin, C., Eleftheriadis, K., Diapouli, E., Manousakas, M.-I., Gini, M., Nava, S., Calzolai, G., Alves, C., Monge, M., Reche, C., Harrison, R. M., Hopke, P. K., Alastuey, A., and Querol, X.: Source apportionment of PM10 based on offline chemical speciation data at 24 European sites, npj Clim. Atmos. Sci., 8, 255, 2025.

Lu, Y., Su, S., Jin, W., Wang, B., Li, N., Shen, H., Li, W., Huang, Y., Chen, H., Zhang, Y., Chen, Y., Lin, N., Wang, X., and Tao, S.: Characteristics and cellular effects of ambient particulate matter from Beijing, Environ. Pollut., 191, 63–69, 2014.

McWhinney, R. D., Badali, K., Liggio, J., Li, S.-M., and Abbatt, J. P. D.: Filterable Redox Cycling Activity: A Comparison between Diesel Exhaust Particles and Secondary Organic Aerosol Constituents, Environ. Sci. Technol., 47, 3362–3369, 2013a.

McWhinney, R. D., Zhou, S., and Abbatt, J. P. D.: Naphthalene SOA: redox activity and naphthoquinone gas–particle partitioning, Atmos. Chem. Phys., 13, 9731–9744, 2013b.

Miller, M. R.: Oxidative stress and the cardiovascular effects of air pollution, Free Radic. Biol. Med., 151, 69–87, 2020.

Mishra, A., Lelieveld, S., Pöschl, U., and Berkemeier, T.: Multiphase Kinetic Modeling of Air Pollutant Effects on Protein Modification and Nitrotyrosine Formation in Epithelial Lining Fluid, Environ. Sci. Technol., 57, 12 642–12 653, 2023.

Mouchel-Vallon, C., Deguillaume, L., Monod, A., Perroux, H., Rose, C., Ghigo, G., Long, Y., Leriche, M., Aumont, B., Patryl, L., Armand, P., and Chaumerliac, N.: CLEPS 1.0: A new protocol for cloud aqueous phase oxidation of VOC mechanisms, Geosci. Model Dev., 10, 1339–1362, 2017.

Netto, L. E. and Stadtman, E. R.: The Iron-Catalyzed Oxidation of Dithiothreitol Is a Biphasic Process: Hydrogen Peroxide Is Involved in the Initiation of a Free Radical Chain of Reactions, Arch. Biochem. Biophys., 333, 233–242, 1996.

Ngoc Thuy, V. D., Jaffrezo, J.-L., Hough, I., Dominutti, P. A., Salque Moreton, G., Gille, G., Francony, F., Patron-Anquez, A., Favez, O., and Uzu, G.: Unveiling the optimal regression model for source apportionment of the oxidative potential of PM10, Atmos. Chem. Phys., 24, 7261–7282, 2024.

Paatero, P. and Tapper, U.: Positive matrix factorization: A non-negative factor model with optimal utilization of error estimates of data values, Environmetrics, 5, 111–126, 1994.

Page, S. E., Arnold, W. A., and McNeill, K.: Terephthalate as a probe for photochemically generated hydroxyl radical, J. Environ. Monit., 12, 1658–1665, 2010.

Pietrogrande, M. C., Bertoli, I., Manarini, F., and Russo, M.: Ascorbate assay as a measure of oxidative potential for ambient particles: Evidence for the importance of cell-free surrogate lung fluid composition, Atmos. Environ., 211, 103–112, 2019.

Puthussery, J. V., Singh, A., Rai, P., Bhattu, D., Kumar, V., Vats, P., Furger, M., Rastogi, N., Slowik, J. G., Ganguly, D., Prevot, A. S. H., Tripathi, S. N., and Verma, V.: Real-Time Measurements of PM2.5 Oxidative Potential Using a Dithiothreitol Assay in Delhi, India, Environ. Sci. Technol. Lett., 7, 504–510, 2020.

Rush, J. and Koppenol, W.: Reactions of Fe(II)-ATP and Fe(II)-citrate complexes with t-butyl hydroperoxide and cumyl hydroperoxide, FEBS Lett., 275, 114–116, 1990.

Samake, A., Uzu, G., Martins, J. M. F., Calas, A., Vince, E., Parat, S., and Jaffrezo, J. L.: The unexpected role of bioaerosols in the Oxidative Potential of PM, Sci. Rep., 7, 10 978, 2017.

Shahpoury, P., Harner, T., Lammel, G., Lelieveld, S., Tong, H., and Wilson, J.: Development of an antioxidant assay to study oxidative potential of airborne particulate matter, Atmos. Meas. Tech., 12, 6529–6539, publisher: Copernicus Publications, 2019.

Shahpoury, P., Zhang, Z. W., Filippi, A., Hildmann, S., Lelieveld, S., Mashtakov, B., Patel, B. R., Traub, A., Umbrio, D., Wietzoreck, M., Wilson, J., Berkemeier, T., Celo, V., Dabek-Zlotorzynska, E., Evans, G., Harner, T., Kerman, K., Lammel, G., Noroozifar, M., Pöschl, U., and Tong, H.: Inter-comparison of oxidative potential metrics for airborne particles identifies differences between acellular chemical assays, Atmos. Pollut. Res., 13, 101 596, 2022.

Shahpoury, P., Lelieveld, S., Johannessen, C., Berkemeier, T., Celo, V., Dabek-Zlotorzynska, E., Harner, T., Lammel, G., and Nenes, A.: Influence of aerosol acidity and organic ligands on transition metal solubility and oxidative potential of fine particulate matter in urban environments, Sci. Total Environ., 906, 167 405, 2024a.

Shahpoury, P., Lelieveld, S., Srivastava, D., Baccarini, A., Mastin, J., Berkemeier, T., Celo, V., Dabek-Zlotorzynska, E., Harner, T., Lammel, G., and Nenes, A.: Seasonal Changes in the Oxidative Potential of Urban Air Pollutants: The Influence of Emission Sources and Proton- and Ligand-Mediated Dissolution of Transition Metals, Environ. Sci. Technol. Air, 1, 1262–1275, publisher: American Chemical Society, 2024b.

Shen, J., Griffiths, P. T., Campbell, S. J., Utinger, B., Kalberer, M., and Paulson, S. E.: Ascorbate oxidation by iron, copper and reactive oxygen species: review, model development, and derivation of key rate constants, Sci. Rep., 11, 7417, 2021.

Shen, J., Taghvaee, S., La, C., Oroumiyeh, F., Liu, J., Jerrett, M., Weichenthal, S., Del Rosario, I., Shafer, M. M., Ritz, B., Zhu, Y., and Paulson, S. E.: Aerosol Oxidative Potential in the Greater Los Angeles Area: Source Apportionment and Associations with Socioeconomic Position, Environ. Sci. Technol., 56, 17 795–17 804, 2022.

Sies, H.: Hydrogen peroxide as a central redox signaling molecule in physiological oxidative stress: Oxidative eustress, Redox Biol., 11, 613–619, 2017.

Sies, H.: Oxidative eustress: On constant alert for redox homeostasis, Redox Biol., 41, 101 867, 2021.

Son, Y., Mishin, V., Welsh, W., Lu, S.-E., Laskin, J. D., Kipen, H., and Meng, Q.: A Novel High-Throughput Approach to Measure Hydroxyl Radicals Induced by Airborne Particulate Matter, Int. J. Environ. Res. Public Health, 12, 13 678–13 695, 2015.

Srivastava, D., Favez, O., Bonnaire, N., Lucarelli, F., Haeffelin, M., Perraudin, E., Gros, V., Villenave, E., and Albinet, A.: Speciation of organic fractions does matter for aerosol source apportionment. Part 2: Intensive short-term campaign in the Paris area (France), Sci. Total Environ., 634, 267–278, 2018a.

Srivastava, D., Tomaz, S., Favez, O., Lanzafame, G. M., Golly, B., Besombes, J.-L., Alleman, L. Y., Jaffrezo, J.-L., Jacob, V., Perraudin, E., Villenave, E., and Albinet, A.: Speciation of organic fraction does matter for source apportionment. Part 1: A one-year campaign in Grenoble (France), Sci. Total Environ., 624, 1598–1611, 2018b.

Tong, H., Arangio, A. M., Lakey, P. S. J., Berkemeier, T., Liu, F., Kampf, C. J., Brune, W. H., Pöschl, U., and Shiraiwa, M.: Hydroxyl radicals from secondary organic aerosol decomposition in water, Atmos. Chem. Phys., 16, 1761–1771, 2016.

Tong, H., Lakey, P. S. J., Arangio, A. M., Socorro, J., Shen, F., Lucas, K., Brune, W. H., Pöschl, U., and Shiraiwa, M.: Reactive Oxygen Species Formed by Secondary Organic Aerosols in Water and Surrogate Lung Fluid, Environ. Sci. Technol., 52, 11 642–11 651, 2018.

Tuet, W. Y., Chen, Y., Xu, L., Fok, S., Gao, D., Weber, R. J., and Ng, N. L.: Chemical oxidative potential of secondary organic aerosol (SOA) generated from the photooxidation of biogenic and anthropogenic volatile organic compounds, Atmos. Chem. Phys., 17, 839–853, 2017.

Utinger, B., Campbell, S. J., Bukowiecki, N., Barth, A., Gfeller, B., Freshwater, R., Rüegg, H.-R., and Kalberer, M.: An automated online field instrument to quantify the oxidative potential of aerosol particles via ascorbic acid oxidation, Atmos. Meas. Tech., 16, 2641–2654, 2023.

Verma, V., Fang, T., Guo, H., King, L., Bates, J. T., Peltier, R. E., Edgerton, E., Russell, A. G., and Weber, R. J.: Reactive oxygen species associated with water-soluble PM2.5 in the southeastern United States: spatiotemporal trends and source apportionment, Atmos. Chem. Phys., 14, 12 915–12 930, 2014.

Verma, V., Fang, T., Xu, L., Peltier, R. E., Russell, A. G., Ng, N. L., and Weber, R. J.: Organic Aerosols Associated with the Generation of Reactive Oxygen Species (ROS) by Water-Soluble PM2.5, Environ. Sci. Technol., 49, 4646–4656, 2015.

Walling, C.: Some aspects of the chemistry of alkoxy radicals, 15, 69–80, 1967.

Wang, Q., Song, H., Dong, H., Guo, S., Yao, M., Wan, Y., and Lu, K.: Multiphase Radical Chemical Processes Induced by Air Pollutants and the Associated Health Effects, Environ. Health, 3, 1–13, 2025.

Wang, S., Ye, J., Soong, R., Wu, B., Yu, L., Simpson, A. J., and Chan, A. W. H.: Relationship between chemical composition and oxidative potential of secondary organic aerosol from polycyclic aromatic hydrocarbons, Atmos. Chem. Phys., 18, 3987–4003, 2018.

Weber, S., Uzu, G., Favez, O., Borlaza, L. J. S., Calas, A., Salameh, D., Chevrier, F., Allard, J., Besombes, J.-L., Albinet, A., Pontet, S., Mesbah, B., Gille, G., Zhang, S., Pallares, C., Leoz-Garziandia, E., and Jaffrezo, J.-L.: Source apportionment of atmospheric PM10 oxidative potential: synthesis of 15 year-round urban datasets in France, Atmos. Chem. Phys., 21, 11 353–11 378, 2021.

Wei, J., Yu, H., Wang, Y., and Verma, V.: Complexation of Iron and Copper in Ambient Particulate Matter and Its Effect on the Oxidative Potential Measured in a Surrogate Lung Fluid, Environ. Sci. Technol., 53, 1661–1671, 2019.

Wei, J., Fang, T., Wong, C., Lakey, P. S. J., Nizkorodov, S. A., and Shiraiwa, M.: Superoxide Formation from Aqueous Reactions of Biogenic Secondary Organic Aerosols, Environ. Sci. Technol., 55, 260–270, 2021.

Wei, J., Fang, T., Lakey, P. S. J., and Shiraiwa, M.: Iron-Facilitated Organic Radical Formation from Secondary Organic Aerosols in Surrogate Lung Fluid, Environ. Sci. Technol., 56, 7234–7243, 2022.

Weichenthal, S., Crouse, D. L., Pinault, L., Godri-Pollitt, K., Lavigne, E., Evans, G., van Donkelaar, A., Martin, R. V., and Burnett, R. T.: Oxidative burden of fine particulate air pollution and risk of cause-specific mortality in the Canadian Census Health and Environment Cohort (CanCHEC), Environ. Res., 146, 92–99, 2016.

Wragg, F. P. H., Fuller, S. J., Freshwater, R., Green, D. C., Kelly, F. J., and Kalberer, M.: An automated online instrument to quantify aerosol-bound reactive oxygen species (ROS) for ambient measurement and health-relevant aerosol studies, Atmos. Meas. Tech., 9, 4891–4900, 2016.

Xiong, Q., Yu, H., Wang, R., Wei, J., and Verma, V.: Rethinking Dithiothreitol-Based Particulate Matter Oxidative Potential: Measuring Dithiothreitol Consumption versus Reactive Oxygen Species Generation, Environ. Sci. Technol., 51, 6507–6514, 2017.

Yalamanchili, J., Hennigan, C. J., and Reed, B. E.: Precipitation of aqueous transition metals in particulate matter during the dithiothreitol (DTT) oxidative potential assay, Environ. Sci.: Process. Impacts, 24, 762–772, 2022.

Yu, H., Wei, J., Cheng, Y., Subedi, K., and Verma, V.: Synergistic and Antagonistic Interactions among the Particulate Matter Components in Generating Reactive Oxygen Species Based on the Dithiothreitol Assay, Environ. Sci. Technol., 52, 2261–2270, 2018.

Zielinski, H., Mudway, I. S., Bérubé, K. A., Murphy, S., Richards, R., and Kelly, F. J.: Modeling the interactions of particulates with epithelial lining fluid antioxidants, Am. J. Physiol., 277, L719–L726, 1999.

2.6. Kinetic modeling of protein modification due to oxidative stress by air pollution in the epithelial lining fluid

The paper in this chapter has been published as a research article in the journal Environmental Science and Technology. I am the first author and the main contributor of this paper. I designed the research together with Thomas Berkemeier. I developed the kinetic model together with my co-authors and I performed the kinetic model simulations. I analyzed the model results. I produced the figures and wrote the paper, with input from the co-authors. The supplement to this work can be found in Appendix B.4.

Mishra, A., Lelieveld, S., Pöschl, U., Berkemeier, T.: Multiphase Kinetic Modeling of Air Pollutant Effects on Protein Modification and Nitrotyrosine Formation in Epithelial Lining Fluid, *Environ. Sci. Technol.* 57, 12642-12653, (2023).

In this study, chemical reaction mechanism was developed that evaluates the damage to proteins by biological and atmospheric oxidants. A multiphase chemical kinetics model of the human epithelial lining fluid, KM-SUB-ELF was developed and extended for this purpose. NO_2 and PM2.5 acted synergistically to form nitrotyrosine (Ntyr). In the model, the presence of PM2.5 led to the production of hydroxyl radicals (OH) in the ELF via Fenton(-like) chemistry of transition metals and peroxides. The highly reactive OH radical reacted with a tyrosine residue of a protein, forming a tyrosyl radical, which further reacted with NO_2 to form Ntyr. While O_3 was mostly a burden on the antioxidants, it did not significantly increase the concentration of Ntyr in the model simulations.

Environmental Science & Technology

pubs.acs.org/est

Article

Multiphase Kinetic Modeling of Air Pollutant Effects on Protein Modification and Nitrotyrosine Formation in Epithelial Lining Fluid

Ashmi Mishra, Steven Lelieveld, Ulrich Pöschl, and Thomas Berkemeier*

Cite This: *Environ. Sci. Technol.* 2023, 57, 12642−12653

Read Online

ACCESS | Metrics & More | Article Recommendations | Supporting Information

ABSTRACT: Exposure to ambient air pollution is a major risk factor for human health. Inhalation of air pollutants can enhance the formation of reactive species in the epithelial lining fluid (ELF) of the respiratory tract and can lead to oxidative stress and oxidative damage. Here, we investigate the chemical modification of proteins by reactive species from air pollution and endogenous biological sources using an extended version of the multiphase chemical kinetic model KM-SUB-ELF 2.0 with a detailed mechanism of protein modification. Fine particulate matter ($PM_{2.5}$) and nitrogen dioxide ($^{\bullet}NO_2$) act synergistically and increase the formation of nitrotyrosine (Ntyr), a common biomarker of oxidative stress. Ozone (O_3) is found to be a burden on the antioxidant defense system but without substantial influence on the Ntyr concentration. In simulations with low levels of air pollution, the Ntyr concentration in the ELF is consistent with the range of literature values for bronchoalveolar lavage fluid from healthy individuals. With high levels of air pollution, however, we obtain strongly elevated Ntyr concentrations. Our model analysis shows how chemical reactions of air pollutants can modify proteins and thus their functionality in the human body, elucidating a molecular pathway that may explain air pollutant effects on human health.

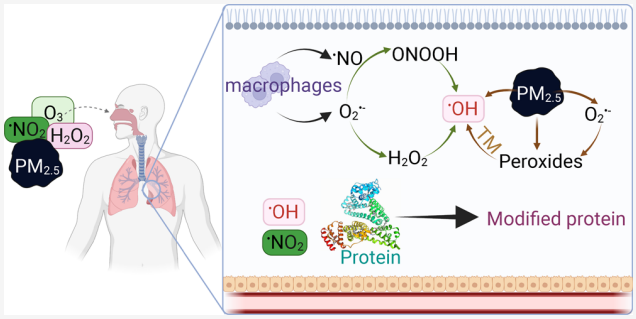

KEYWORDS: *Tyrosine, Epithelial lining fluid, Oxidants, Air pollution, Antioxidants, Oxidative stress*

INTRODUCTION

Biological systems are subject to oxidants, including reactive oxygen species (ROS) and reactive nitrogen species (RNS). Oxidant production is essential to maintain cellular redox homeostasis,[1] but an imbalance of oxidant production and antioxidant (AO) defense can lead to oxidative stress (distress).[2,3] Oxidative damage to biological molecules is associated with development of diseases and aging processes.[4] Both biological endogenous sources, such as mitochondria and phagocytic cells,[5,6] as well as exogenous sources, such as air pollution and tobacco smoke, contribute to production of oxidants.[7−9] Studies have shown elevated levels of oxidative damage in humans as a result of exposure to air pollution, which may cause increased oxidant production, decreased AO defense activity, or a combination of both.[10−12]

Exposure to ambient air pollution can cause adverse health outcomes and mortality.[13−15] Fine particulate matter with a diameter less than 2.5 μm ($PM_{2.5}$) and gaseous oxidants such as ozone (O_3) and nitrogen dioxide ($^{\bullet}NO_2$) are the most noxious components of air pollution, contributing to millions of excess deaths[16−18] and emergency room visits annually.[19]

$PM_{2.5}$ is made up of a variety of substances, including mineral dust, soot, and organic matter, and can come from a variety of natural and anthropogenic sources, such as residential energy use, power generation, break and tire wear, wildfires, and wind-blown dust.[20−23] $PM_{2.5}$ encompasses organic and inorganic compounds, including redox-active components such as transition metals, secondary organic aerosol (SOA), and quinones.[9,24,25] Upon inhalation, $PM_{2.5}$ generates reactive species in the respiratory tract, either directly through chemical reactions of redox-active components in $PM_{2.5}$[9,26,27] or by triggering oxidant production by cells such as neutrophils or macrophages.[28,29]

O_3 exposure has been shown to contribute to risk of respiratory and circulatory mortality. The toxicity of O_3 is displayed upon its inhalation and absorption into the respiratory tract.[30−32] Through its strong oxidizing ability, O_3 can react with biomolecular targets in the respiratory tract, such as proteins, lipids, and AOs.[33,34] O_3 can react with proteins, which make up a large fraction of biomolecules present in the respiratory tract, leading to protein modification.[35,36]

Received: May 12, 2023
Revised: August 4, 2023
Accepted: August 7, 2023
Published: August 17, 2023

$^{\bullet}NO_2$ originates mostly from combustion sources and atmospheric photochemistry.[23,37−39] Exposure to high levels of $^{\bullet}NO_2$ can irritate the airways and cause respiratory problems, particularly in people with asthma and other pre-existing lung conditions.[40,41] Long-term exposure to $^{\bullet}NO_2$ may be associated with an increased risk of mortality from respiratory and cardiovascular diseases;[42,43] however, it is unclear if this is due to effects of $^{\bullet}NO_2$ itself or a confounder from co-emission alongside other harmful pollutants like $PM_{2.5}$.[44−46]

Peroxynitrite ($ONOO^-$) is a short-lived species that is formed in the fast reaction of $^{\bullet}NO$ and the superoxide radical ($O_2^{\bullet-}$).[47−49] $^{\bullet}NO$ is produced enzymatically in the body by nitric oxide synthase (NOS).[50] $O_2^{\bullet-}$ is ubiquitous in biological systems but is also formed in the respiratory tract upon inhalation of $PM_{2.5}$.[9,26,29] $ONOO^-$ undergoes rapid reaction with carbon dioxide in biological systems, forming carbonate radicals ($CO_3^{\bullet-}$) and $^{\bullet}NO_2$, both of which are one-electron oxidants.[51] Alternatively, the protonated form of $ONOO^-$, peroxynitrous acid ($ONOOH$), can decompose to the hydroxyl radical ($^{\bullet}OH$) and $^{\bullet}NO_2$.[47]

A mechanism by which air pollutants may cause adverse health outcomes is through the formation of oxidants, such as ROS and RNS, upon deposition in the epithelial lining fluid (ELF) of the respiratory tract.[9,52] Highly reactive oxidants, such as $^{\bullet}OH$ and $CO_3^{\bullet-}$, react rapidly with all biological molecules, such as DNA, cholesterol, lipids, carbohydrates, proteins, and AOs.[12,49,53] $^{\bullet}OH$ has been identified as a major inducer of oxidative stress.[25] In contrast, less-reactive oxidants, like hydrogen peroxide (H_2O_2), cause modifications at specific sites of biomolecules.[12,53]

Proteins are a major target of oxidants because of their high reactivity and their high abundance in cells and extracellular fluids such as the ELF.[12,25] Gaseous and particulate air pollutants can interact with proteins and promote oxidation and nitration.[54,55] For example, tyrosine residues can be oxidized by reactive species from air pollution (e.g., O_3 and $^{\bullet}NO_2$)[36,56] and endogenous biological sources (e.g., $ONOO^-$),[49] leading to the formation of tyrosyl radicals that can undergo nitration by $^{\bullet}NO_2$ and irreversibly form 3-nitrotyrosine (Ntyr).[48,57,58] Increased concentrations of Ntyr have been detected in the bronchoalveolar lavage fluid of mice after inhalation exposure to $PM_{2.5}$ but not after exposure to O_3 alone.[59] The post-translational modification of tyrosine can alter protein structure and function[48,49] and has been proposed as a molecular rationale for the enhancement of allergic diseases by traffic-related air pollution.[58,60]

However, the interactions of multiple gas-phase and particulate pollutants with proteins in the respiratory tract have not been studied in detail previously. While there have been many studies that determined the reaction rates of oxidants with proteins,[12,35,53] there is a lack of studies quantifying the influence of atmospheric air pollution on protein modification in the human respiratory tract. Further, the relative importance of exogenous atmospheric oxidants compared to endogenous biological oxidants on protein modification is unclear.

In this study, we extend the kinetic multilayer model of surface and bulk chemistry in the epithelial lining fluid of the respiratory tract (KM-SUB-ELF 2.0)[9,25,27] by an explicit chemical mechanism of protein oxidation, including tyrosine modification. We aim to translate experimental studies into a mechanistic understanding of how air pollutants lead to protein oxidation. We quantify the chemical modification of proteins by oxidants from biological and atmospheric sources and compare our model results to measurements of nitrotyrosine as a marker for oxidative stress.

MATERIALS AND METHODS

Kinetic Modeling. The kinetic model used in this study extends on the KM-SUB-ELF 2.0 model (Section S1).[9,25,27] The model compartments include the respiratory tract gas phase, the surfactant layer, the aqueous ELF, a cellular layer, and a blood layer (Figures 1 and S1). The following processes in the model are explicitly resolved: inhalation, adsorption, and desorption of gas-phase molecules to and from the surfactant layer, diffusion between the surfactant layer, ELF, cells, and blood vessels, as well as a number of chemical reactions across the respiratory tract gas phase, surfactant layer, aqueous ELF, and the cellular layer.

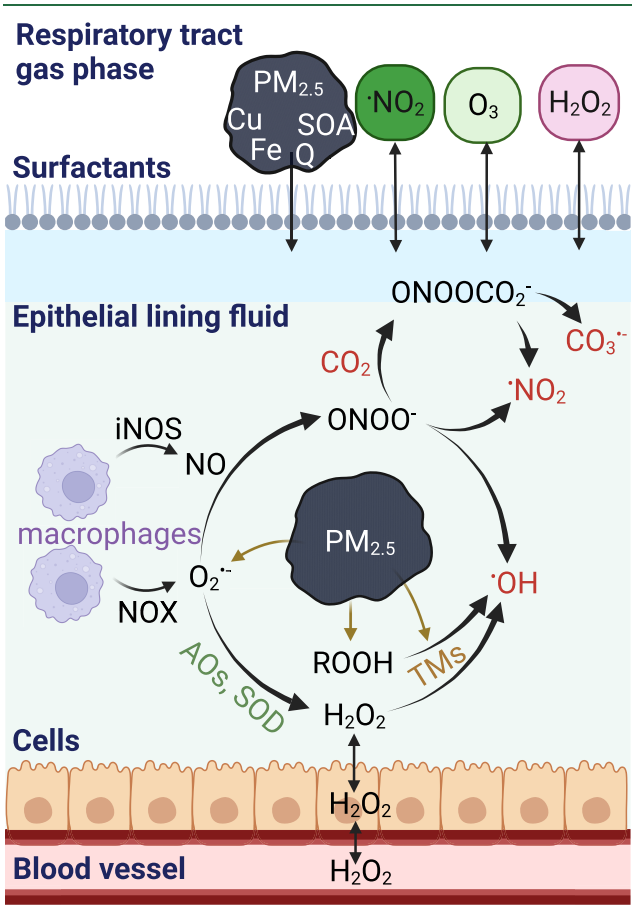

Figure 1. Pathways of endogenous and exogenous oxidant production that are included in the KM-SUB-ELF 2.0 model. The gaseous oxidants included in the model are $^{\bullet}NO_2$, H_2O_2, and O_3. Endogenous sources produce superoxide ($O_2^{\bullet-}$) which, in the presence of antioxidants (AOs) and enzymes, such as superoxide dismutase (SOD), can lead to the formation of hydrogen peroxide (H_2O_2). Transition metals (TMs) in $PM_{2.5}$ catalyze the formation of hydroxyl radicals ($^{\bullet}OH$) through Fenton(-like) reactions of iron (Fe) with H_2O_2 or organic peroxides (ROOHs) contained within secondary organic aerosol (SOA). $^{\bullet}OH$ radicals are also formed by the decomposition of peroxynitrite ($ONOO^-$), which is formed by the reaction of $O_2^{\bullet-}$ and nitric oxide ($^{\bullet}NO$). $ONOO^-$ reacts with CO_2, decomposing to carbonate radicals $CO_3^{\bullet-}$. Created with BioRender.com.

https://doi.org/10.1021/acs.est.3c03556
Environ. Sci. Technol. 2023, 57, 12642−12653

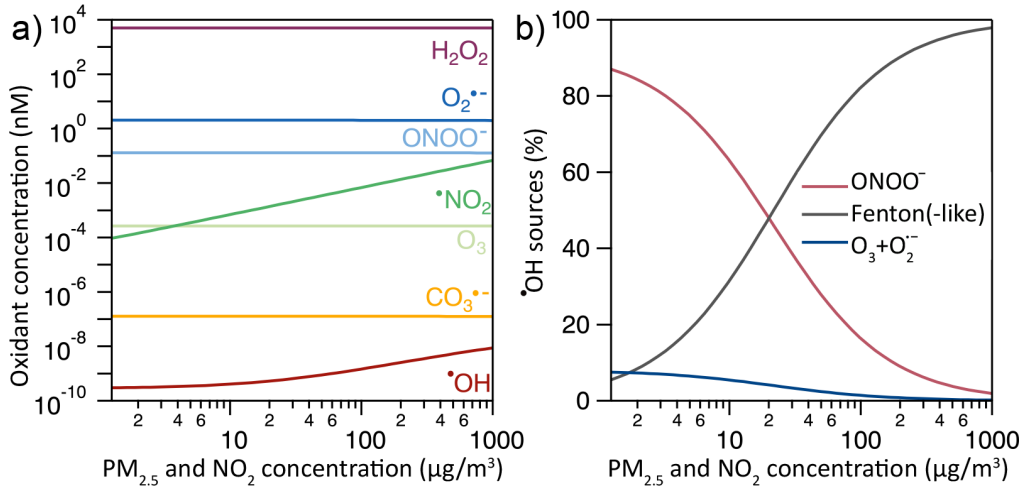

Figure 2. Oxidant concentration (a) and sources of •OH (b) in the ELF as functions of ambient $PM_{2.5}$ concentrations. Inhaled $•NO_2$ concentrations are varied alongside $PM_{2.5}$ with a 1:1 mass ratio.

The temporal evolution of reactants and reaction products is determined using a system of ordinary differential equations. In this study, the following air pollutants are considered: $PM_{2.5}$ as a particulate pollutant (Section S2) as well as $•NO_2$, O_3, and H_2O_2 as gaseous pollutants. The model simulates 2-h exposure scenarios during which the particulates are deposited in the ELF with a deposition fraction of 45%.[9,25,61,62] For simplicity, the model does not account for the concentration gradient of gases or particles between the upper and lower sections of the respiratory system. Hence, the concentrations calculated in the model are averages over the entire respiratory tract.

A previously reported, standardized composition of $PM_{2.5}$ is used in the model calculations. The composition was derived from median mass fractions of redox-active $PM_{2.5}$ constituents in a large set of atmospheric field measurements.[25] The mass fractions applied to all inhaled $PM_{2.5}$ masses in the model are 3.1×10^{-4}, 8.1×10^{-3}, and 0.33 for copper, iron, and secondary organic aerosol (SOA), respectively, as well as 1.6×10^{-5} across three quinones: phenanthrenequinone, 1,2-naphthoquinone, and 1,4-naphthoquinone. The solubilities of the $PM_{2.5}$ constituents copper and iron in the ELF were assumed to be 40% and 10%, respectively. Quinones and SOA are assumed to fully dissolve. Since $PM_{2.5}$ and $•NO_2$ are often co-emitted, the gas-phase concentration of $•NO_2$ is co-varied with $PM_{2.5}$ concentration with a factor of 1 $\mu g\ m^{-3}$ $•NO_2$ for each $\mu g\ m^{-3}$ $PM_{2.5}$ in the model simulations. O_3 is treated with a fixed concentration of 30 ppb.

The following low molecular mass antioxidants (AOs) are included in the model: ascorbate (AscH), glutathione (GSH), uric acid (UAH), and α-tocopherol (α-Toc). Studies using healthy volunteers suggest that the AOs in the ELF do not fully deplete, despite exposure to 1 ppm $•NO_2$ for several hours.[63] Therefore, the AO concentrations are fixed during the 2-h exposure simulation in this study to account for fast replenishment. The AscH, GSH, and UAH concentrations are 40 μM, 108 μM, and 200 μM, respectively.[64] α-Toc is assumed to be in the surfactant layer only, with a concentration of 200 μM, which corresponds to a total ELF concentration of 0.7 μM.[64] Other species included in the surfactant layer are surfactant lipid, 1-palmitoyl-2-oleoyl-*sn*-glycerol (POG), and surfactant protein ($SP\text{-}B_{1-25}$). The reaction of O_3 with POG in the surfactant layer produces H_2O_2 with a yield of 17% in the presence of water.[65,66] Reactions of superoxide dismutase (SOD) and catalase are included in the ELF as enzymatic reactions,[67] while in cells, a range of H_2O_2 scavenging enzymes (peroxiredoxins, catalase, GSH peroxidase) is considered (Section S3).

The model KM-SUB-ELF 2.0[9,25,27] is extended in this study by inclusion of explicit reactions of amino acids in the ELF with various oxidants. Table S1 shows the full chemical mechanism used in this study. The model autogenerates a script based on an input chemical mechanism and consists of a system of differential equations. An autogenerated Jacobian matrix is used to accelerate and increase numerical stability of the differential equation solver (ODE23tb in MATLAB).

Calculation of the Surface-Accessible Amino Acid Concentration. Some amino acids are buried within the protein and are not exposed on the surface, while others are on the surface and are, therefore, readily accessible for chemical reaction with dissolved molecules. Relative accessible surface area (RSA) is a measure of how exposed a particular amino acid is on the surface of a protein. We used Surface Racer[68] to calculate RSA for amino acids present in human albumin as model protein. Human albumin is the protein with the highest mass fraction in the ELF.[69] We calculate RSA by dividing the actual accessible surface area (ASA) of the amino acid by the maximum ASA that the amino acids could have if it were completely exposed on the surface of the protein (maxASA, eq 1). MaxASA values are available from previous studies that used Gly-X-Gly tripeptides, where X represents the amino acid residue of interest, as models.[70] An RSA of 0 indicates that the amino acid is completely buried within the protein structure, and an RSA of 1 indicates that it is fully exposed on the surface.

$$\mathrm{RSA} = \frac{\mathrm{ASA}}{\mathrm{maxASA}} \tag{1}$$

The mass of proteins within the ELF is approximately 10 mg/mL lung fluid. Based on the average molecular weight of an individual amino acid, which is about 125 g mol^{-1}, the total concentration of amino acids in the ELF (c_{AA}) is estimated to be around 80 mmol L^{-1}. We use the RSA of every amino acid (RSA_i), the total protein concentration c_{AA} divided by the total number of amino acids in the protein (N_{AA}), and the number

https://doi.org/10.1021/acs.est.3c03556
Environ. Sci. Technol. 2023, 57, 12644−12653

Table 1. Second-Order Reaction Rate Coefficients (M^{-1} s^{-1}) of Oxidants with Amino Acids

Amino acid	$^{\bullet}OH$	O_3	$CO_3^{\bullet-}$	$ONOO^-$	H_2O_2	$O_2^{\bullet-}$
Alanine	$7.7 \times 10^{7,a}$	$1.0 \times 10^{3,c}$				
Arginine	$3.5 \times 10^{9,a}$	$5.3 \times 10^{3,c}$				
Asparagine	$4.9 \times 10^{7,a}$	$8.0 \times 10^{3,c}$				
Aspartic acid	$7.5 \times 10^{7,a}$	$6.2 \times 10^{2,c}$				
Cysteine	$3.4 \times 10^{10,a}$	$2.0 \times 10^{4,c}$	$2.0 \times 10^{8,e}$	3.8×10^{3f}	2.3^{f}	
Glutamine	$5.4 \times 10^{8,a}$	$1.9 \times 10^{3,c}$				
Glutamic acid	$2.3 \times 10^{8,a}$	$8.8 \times 10^{2,c}$				
Glycine	$1.7 \times 10^{7,a}$	$3.5 \times 10^{3,c}$				
Histidine	$1.3 \times 10^{10,a}$	$1.7 \times 10^{4,c}$				
Isoleucine	$1.8 \times 10^{9,a}$	$9.8 \times 10^{2,c}$				
Leucine	$1.7 \times 10^{9,a}$	$9.6 \times 10^{2,c}$				
Lysine	$3.4 \times 10^{8,a}$	$3.5 \times 10^{3,c}$				
Methionine	$8.3 \times 10^{9,a}$	$3.8 \times 10^{6,c}$	$1.2 \times 10^{8,f}$	$3.6 \times 10^{2,f}$	$2.0 \times 10^{-2,f}$	$3.0 \times 10^{-1,f}$
Phenylalanine	$6.5 \times 10^{9,a}$	$1.9 \times 10^{4,c}$				
Proline	$4.8 \times 10^{8,a}$	$1.1 \times 10^{4,c}$				
Serine	$3.2 \times 10^{8,a}$	$8.0 \times 10^{3,c}$				
Threonine	$5.1 \times 10^{8,a}$	$3.6 \times 10^{3,c}$				
Tryptophan	$1.3 \times 10^{10,a}$	$7.0 \times 10^{6,c}$		$4.0 \times 10^{1,g}$		
Tyrosine	$1.2 \times 10^{10,b}$	$2.8 \times 10^{6,d}$	$4.5 \times 10^{7,g}$			
Valine	$7.6 \times 10^{8,a}$	$1.2 \times 10^{3,c}$				

[a]Davies.[53] [b]Solar et al.[71] [c]Sharma and Graham.[35] [d]Pryor et al.[72] [e]Huie et al.[73] [f]Davies.[12] [g]Radi.[57]

of the individual amino acids in the protein ($N_{AA,i}$), to calculate the concentration of individual amino acids in the ELF ($c_{AA,i}$).

$$c_{AA,i} = \frac{c_{AA}}{N_{AA}} \cdot N_{AA,i} \cdot RSA_i \quad (2)$$

Hence, the model assumes that the reactivity of proteins is a linear combination of the reactivities of surface-accessible amino acids. The calculated surface-accessible amino acid concentrations are used as input parameters for the kinetic model and listed in Table S2.

RESULTS AND DISCUSSION

Oxidants in Epithelial Lining Fluid. Inhalation of air pollution influences the endogenous baseline concentrations of oxidants in the epithelial lining fluid (ELF). The pathways of endogenous and exogenous oxidant production included in the kinetic model are presented in Figure 1. Superoxide ($O_2^{\bullet-}$) is a key intermediate in many of these pathways. It is produced in the human body by NADPH oxidase (NOX) enzymes, which are highly expressed on the cell membrane of macrophages in the ELF.[6] $O_2^{\bullet-}$ is also formed through chemical reactions of redox-active components of air pollution (e.g., transition metals and quinones) in the ELF. Antioxidants (AOs) and enzymes, such as superoxide dismutase (SOD), transform $O_2^{\bullet-}$ into hydrogen peroxide (H_2O_2). Due to its stability, H_2O_2 can diffuse through cell membranes and tissues. It is efficiently buffered by enzymes in the ELF but also converted into the highly reactive hydroxyl radical ($^{\bullet}OH$) through Fenton chemistry. The transition metals (TMs) necessary for Fenton reactions are inhaled through $PM_{2.5}$. Secondary organic aerosol (SOA) contributes to the formation of $^{\bullet}OH$ in the ELF through Fenton-like reactions of organic peroxides (Section S4). Macrophages also produce nitric oxide ($^{\bullet}NO$) through the enzyme inducible nitric oxide synthase (iNOS). $^{\bullet}NO$ competes with SOD and AOs for the consumption of $O_2^{\bullet-}$. The reaction of $^{\bullet}NO$ with $O_2^{\bullet-}$ produces peroxynitrite ($ONOO^-$), which in turn can react with CO_2 to form carbonate radicals ($CO_3^{\bullet-}$). The decomposition of $ONOO^-$ is another pathway for the production of $^{\bullet}OH$.

Figure 2 shows the concentration of oxidants in the ELF as a function of ambient $PM_{2.5}$ and $^{\bullet}NO_2$ concentration. The model calculations show that H_2O_2 dominates the total concentration of oxidants. The other oxidants in the model, in descending order of their concentration, are $O_2^{\bullet-}$, $ONOO^-$, $^{\bullet}NO_2$, O_3, $CO_3^{\bullet-}$, and finally $^{\bullet}OH$. The modeled H_2O_2 concentration in the ELF is higher than reported in previous studies,[9,25,27] as a result of the inclusion of $O_2^{\bullet-}$ production by alveolar macrophages (Section S5).[29] The concentrations of $^{\bullet}NO_2$ and $^{\bullet}OH$ show an increasing trend with ambient $PM_{2.5}$ and $^{\bullet}NO_2$, while the concentrations of O_3, $O_2^{\bullet-}$, H_2O_2, and $CO_3^{\bullet-}$ remain constant. The ambient-gas-phase concentration of O_3 is fixed in the model, which translates into the steady concentration of dissolved O_3. For $O_2^{\bullet-}$, H_2O_2, $CO_3^{\bullet-}$, and $ONOO^-$ the biological sources shown in Figure 1 dominate, as detailed in Figure S2. In the model, the biological production of $O_2^{\bullet-}$ is parametrized according to the baseline production observed in Fang et al.[29] using a rate of 2×10^{14} cm^{-3} s^{-1} (Section S5).

As shown in Figure 2b, $^{\bullet}OH$ production is mostly dependent on Fenton(-like) reactions involving $PM_{2.5}$, the decomposition of $ONOO^-$, and, to a lesser extent, the reaction of O_3 and $O_2^{\bullet-}$. At low $PM_{2.5}$ and $^{\bullet}NO_2$ concentrations, the $ONOO^-$ pathway of $^{\bullet}OH$ production dominates, while at high $PM_{2.5}$ and $^{\bullet}NO_2$ concentrations, the Fenton chemistry dominates. At ~25 μg m^{-3}, the relative shares are roughly equal. Note that, when macrophages are exposed to $PM_{2.5}$, higher rates of $O_2^{\bullet-}$ production have been observed.[29] Under such conditions, the $ONOO^-$ pathway to $^{\bullet}OH$ production becomes more important in the model (Figure S3), which constitutes another PM-dependent $^{\bullet}OH$ production pathway.

Reaction Pathways of Amino Acid Oxidation and Modification. Table 1 shows a compilation of reaction rate coefficients for the oxidation of amino acids with various oxidants. The $^{\bullet}OH$ radical reacts with all amino acid residues at a rate coefficient approaching the diffusion limit, while the

https://doi.org/10.1021/acs.est.3c03556
Environ. Sci. Technol. 2023, 57, 12642−12653

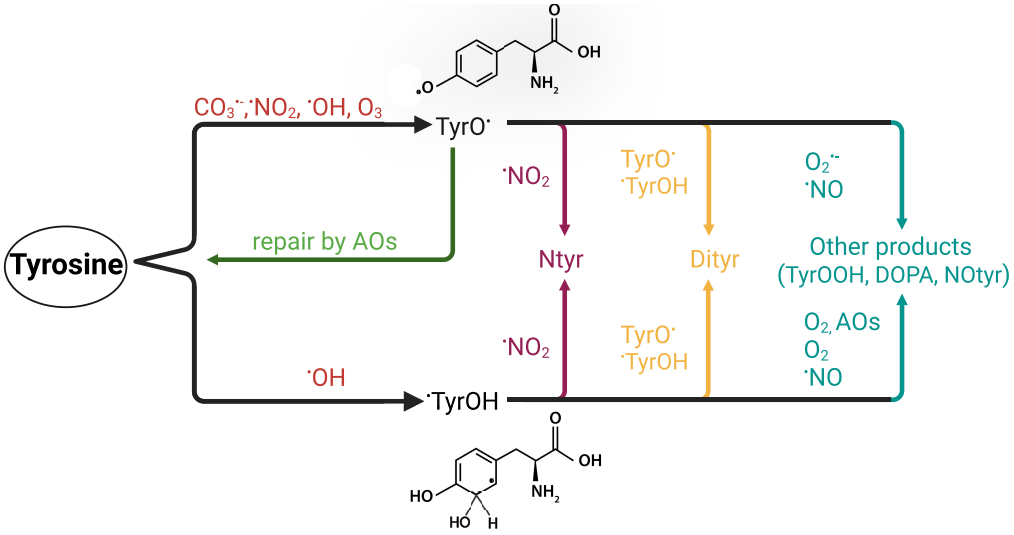

Figure 3. Pathways of tyrosine oxidation that are included in the KM-SUB-ELF 2.0 model. Oxidants ($^{\bullet}OH$, $^{\bullet}NO_2$, O_3, and $CO_3^{\bullet-}$) react with tyrosine, leading to the formation of tyrosyl radicals. TyrO$^{\bullet}$ radicals are repaired by antioxidants (AOs). Tyrosyl radicals react with $^{\bullet}NO_2$ to form nitrotyrosine (Ntyr). Two tyrosyl radicals react together to form dityrosine (Dityr). Reaction of tyrosyl radicals with O_2 leads to the formation of other products, such as tyrosine peroxide (TyrOOH) and DOPA, while reaction with $^{\bullet}NO$ leads to the formation of nitrosotyrosine (NOtyr). Created with BioRender.com.

less-reactive oxidants, such as H_2O_2 and $O_2^{\bullet-}$, react only with certain amino acids. O_3 reacts with all amino acids, albeit at a slower rate than $^{\bullet}OH$. We note that, while $CO_3^{\bullet-}$ likely reacts with more amino acids than indicated in Table 1, studies on this oxidant with other amino acids are lacking. However, since $CO_3^{\bullet-}$ is of minor importance for the oxidation of tyrosine, cysteine, and methionine, the effect from $CO_3^{\bullet-}$ on the oxidation of other amino acids may also be negligible.

Recent studies suggest that the catalytic production of $^{\bullet}OH$ radicals may be the main driver of the adverse health effects of $PM_{2.5}$, rather than the chemical production of other oxidants such as H_2O_2.[27,74] This explanation is plausible given the high reactivity of $^{\bullet}OH$ with the amino acids contained in proteins. Moreover, modified tyrosine residues in proteins, such as nitrotyrosine (Ntyr) and dityrosine (Dityr), are used as markers of oxidative stress.[10,11,75] Thus, in this study, we focus on the oxidation chemistry of tyrosine.

Figure 3 illustrates the main reaction pathways leading to modified tyrosine residues in the ELF. The reaction mechanism and rate coefficients of tyrosine modification in the model are presented in Table 2. The modification of tyrosine residues is a multistep process involving radical intermediates. There are several different biological, peroxynitrite-derived oxidants that oxidize tyrosine: ONOOH homolysis produces $^{\bullet}OH$ and $^{\bullet}NO_2$ radicals, while the reaction of $ONOO^-$ with carbon dioxide leads to $CO_3^{\bullet-}$. The ambient oxidants O_3 and $^{\bullet}NO_2$, as well as $^{\bullet}OH$ formed from $PM_{2.5}$, also oxidize tyrosine.[36,71,76]

Oxidation of tyrosine forms tyrosyl radicals in two ways: H abstraction on the hydroxyl group leads to a phenoxyl radical (TyrO$^{\bullet}$),[36,71,81] while the addition of $^{\bullet}OH$ to the ring produces a $^{\bullet}$TyrOH radical.[49,82,83] During tyrosine nitration, both radicals react with $^{\bullet}NO_2$ in a radical—radical recombination reaction to Ntyr.[76,84,85] Tyrosyl radicals also give rise to other modification products. Reaction of two tyrosyl radicals may form dityrosine (Dityr).[71,79,81] Other products include TyrOOH, which is produced in the reaction of $^{\bullet}$TyrOH with O_2 and AOs[12,77,86,87] or the reaction of TyrO$^{\bullet}$ with $O_2^{\bullet-}$.[81,88,89] The reaction of $^{\bullet}$TyrOH with O_2, followed by elimination of a hydroperoxyl group, can also lead to the formation of 3,4-dihydroxyphenylalanine (DOPA).[82] Note that we currently do not differentiate between these two reaction pathways in the model as the branching ratio is unknown; therefore, DOPA is implicitly considered in TyrOOH in this study. Another product considered in the model is nitrosotyrosine (NOtyr), which is formed from the reaction of both tyrosyl radicals with $^{\bullet}NO$ (Figure S4).

Figure 4 shows the contribution of the oxidants ($^{\bullet}NO_2$, O_3, $CO_3^{\bullet-}$ and $^{\bullet}OH$) to the initial step of tyrosine modification (formation of tyrosyl radicals) as a function of $PM_{2.5}$ and $^{\bullet}NO_2$. The model shows that at low $^{\bullet}NO_2$ concentrations, tyrosine reacts almost exclusively with O_3, while reactions with $^{\bullet}NO_2$, $^{\bullet}OH$, and $CO_3^{\bullet-}$ are minor. At higher ambient concentrations, $^{\bullet}NO_2$ increasingly contributes to the oxidation of tyrosine and is the dominant oxidant at very high levels. At roughly 25 $\mu g\ m^{-3}$ $PM_{2.5}$ and $^{\bullet}NO_2$, tyrosine reacts with O_3 and $^{\bullet}NO_2$ in equal quantities. Here, $^{\bullet}OH$ and $CO_3^{\bullet-}$ radicals only contribute about 2%. This is due to the much higher concentrations of O_3 and $^{\bullet}NO_2$ compared to those of $^{\bullet}OH$ and $CO_3^{\bullet-}$, as shown in Figure 2a.

Figure 5 shows the competing reactions of the two different tyrosyl radicals as a function of the $PM_{2.5}$ and $^{\bullet}NO_2$ concentrations. The model shows that almost all TyrO$^{\bullet}$ produced in the ELF are scavenged by antioxidants (AOs) under full repair (Figure 5a).[76,79] At very high concentrations of $PM_{2.5}$ and $^{\bullet}NO_2$, there is a slight increase in the formation of Ntyr and Dityr from TyrO$^{\bullet}$, but the repair pathway still dominates. For the $^{\bullet}$TyrOH radical, however, a repair pathway has not been reported in the literature to our knowledge. An in vitro study even found an increase in the formation of DOPA when adding AscH.[90] DOPA is associated with the $^{\bullet}OH$-derived radical $^{\bullet}$TyrOH.[82] Therefore, in the model, the $^{\bullet}OH$-induced formation of $^{\bullet}$TyrOH always leads to modification of tyrosine.

The simulation shows that peroxide formation is the dominant reaction pathway over nitration and dimerization

https://doi.org/10.1021/acs.est.3c03556
Environ. Sci. Technol. 2023, 57, 12642−12653

Table 2. Second-Order Reaction Rate Coefficients (M^{-1} s^{-1}) in the Chemical Mechanism of Tyrosine Modification Including Primary Reaction with Oxidants ($^{\bullet}OH$, O_3, $CO_3^{\bullet-}$, $^{\bullet}NO_2$), Secondary Reactions of Tyrosyl Radical Intermediates ($TyrO^{\bullet}$, $^{\bullet}TyrOH$), and Repair by Antioxidants[a]

	Reaction	Rate coefficient (M^{-1} s^{-1})	Reference
1	Tyrosine + $^{\bullet}OH$ → $^{\bullet}TyrOH$	1.2×10^{10}	Solar et al.[71]
2	Tyrosine + $^{\bullet}OH$ → $TyrO^{\bullet}$	6.0×10^{8}	Solar et al.[71]
3	Tyrosine + O_3 → $TyrO^{\bullet}$	2.8×10^{6}	Pryor et al.[72]
4	Tyrosine + $CO_3^{\bullet-}$ → $TyrO^{\bullet}$	4.5×10^{7}	Ferrer-Sueta et al.[49]
5	Tyrosine + $^{\bullet}NO_2$ → $TyrO^{\bullet}$	3.2×10^{5}	Ferrer-Sueta et al.[49]
6	$TyrO^{\bullet}$ + $^{\bullet}NO_2$ → Ntyr	3.0×10^{9}	Ferrer-Sueta et al.[49]
7	$TyrO^{\bullet}$ + $^{\bullet}NO$ → NOtyr	1.0×10^{9}	Ferrer-Sueta et al.[49]
8	$TyrO^{\bullet}$ + $TyrO^{\bullet}$ → Dityr	2.3×10^{8}	Ferrer-Sueta et al.[49]
9	$TyrO^{\bullet}$ + $O_2^{\bullet-}$ → TyrOOH	1.5×10^{9}	Ferrer-Sueta et al.[49]
10	$^{\bullet}TyrOH$ + $^{\bullet}NO_2$ → Ntyr	3.0×10^{9}	inferred from R6
11	$^{\bullet}TyrOH$ + $^{\bullet}NO$ → NOtyr	1.0×10^{9}	inferred from R7
12	$^{\bullet}TyrOH$ + $^{\bullet}TyrOH$ → Dityr	3.0×10^{8}	Solar et al.[71]
13	$^{\bullet}TyrOH$ + $TyrO^{\bullet}$ → Dityr	2.3×10^{8}	Ferrer-Sueta et al.[49]
14	$^{\bullet}TyrOH$ + O2 → $^{\bullet}OOTyrOH$	1.0×10^{3}	Candeias et al.[77]
15	$TyrO^{\bullet}$ + GSH → Tyrosine	2.0×10^{6}	Folkes et al.[78]
16	$TyrO^{\bullet}$ + AscH → Tyrosine	4.4×10^{8}	Hunter et al.[79]
17	$TyrO^{\bullet}$ + UAH → Tyrosine	2.4×10^{8}	Ferrer-Sueta et al.[49]
18	$^{\bullet}OOTyrOH$ + AscH → TyrOOH	7.0×10^{6}	Alfassi et al.[80]
19	$^{\bullet}OOTyrOH$ + UAH → TyrOOH	1.9×10^{6}	Alfassi et al.[80]

[a]Glutathione, GSH; ascorbic acid, AscH; uric acid, UAH.

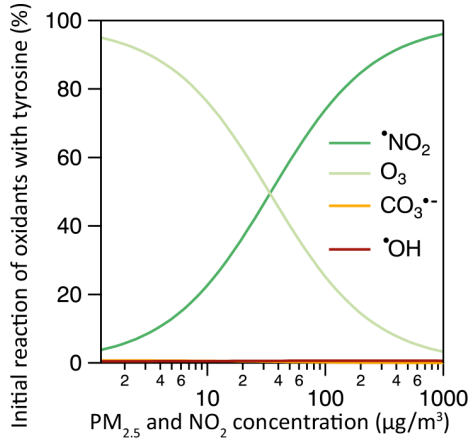

Figure 4. Contribution of oxidants to tyrosyl radical formation as a function of the ambient pollutant concentrations. Inhaled $^{\bullet}NO_2$ concentrations are varied alongside $PM_{2.5}$ with a 1:1 mass ratio. The calculations assume a fixed O_3 concentration of 30 ppb and a biological $O_2^{\bullet-}$ production rate of 2×10^{14} cm^{-3} s^{-1}.

(Figure 5b). This is due to the much higher steady-state concentration of O_2 in the ELF compared to that of $^{\bullet}NO_2$ and $Tyr^{\bullet}$. At low pollutant concentrations, the formation of Ntyr and Dityr does not show a dependence on $PM_{2.5}$ and $^{\bullet}NO_2$ concentrations. At high pollutant concentrations, however, increasing $PM_{2.5}$ and $^{\bullet}NO_2$ directly increases the fraction of $^{\bullet}TyrOH$ forming Ntyr and Dityr. This is because only above a $PM_{2.5}$ and $^{\bullet}NO_2$ concentration of 25 μg m^{-3}, the production of $^{\bullet}OH$ becomes dominated by $PM_{2.5}$ (Figure 2b). The production of Ntyr is higher than that of Dityr due to the low steady-state concentration of the $^{\bullet}TyrOH$ radical.

Figure 5c shows that, despite the low steady-state concentration of $^{\bullet}OH$, and thus a much lower fraction of tyrosine reacting with $^{\bullet}OH$, modification of tyrosine occurs predominantly via $^{\bullet}TyrOH$. Thus, although the initial attack to tyrosine by O_3 and $^{\bullet}NO_2$ is much higher than by $^{\bullet}OH$ (shown in Figure 4), $^{\bullet}OH$ is largely responsible for the formation of modified tyrosine (Figure S5). $^{\bullet}OH$ is formed in reactions involving transition metals contained in particulate matter (Figure 2b). Hence, this result is consistent with the findings of Kelly and Fussell, who compiled studies linking air pollution exposure to markers of oxidative stress and found increased Ntyr concentrations after exposure to particulate matter.[91] In contrast, the simulation results suggest that O_3 is less involved in the formation of Ntyr due to the efficient repair of the tyrosyl radicals derived from O_3.

Influence of Individual Air Pollutants on Tyrosine Modification. Figure 6 breaks down the individual contributions of air pollutants to the modification of tyrosine. The pollutant concentrations are derived from a standard pollution scenario (25 μg m^{-3} $PM_{2.5}$, 25 μg m^{-3} $^{\bullet}NO_2$, and 30 ppb O_3). The biological sources of $^{\bullet}NO$ and $O_2^{\bullet-}$ lead to an endogenous baseline concentration (red bar). Panel a shows the production of Ntyr from $PM_{2.5}$ (gray), O_3 (blue), and $^{\bullet}NO_2$ (green). Simulations were carried out using only the single pollutant. A scenario including all pollutants (dark gray) is shown for comparison. The single pollutant that is most correlated with the formation of Ntyr is $^{\bullet}NO_2$, followed by $PM_{2.5}$ and then O_3.

Note that endogenous $ONOO^-$ plays a key role in both $PM_{2.5}$- and $^{\bullet}NO_2$-only scenarios. In the $PM_{2.5}$-only scenario, the $^{\bullet}NO_2$ required for nitration is solely produced from the decomposition of $ONOO^-$ and thus becomes a limiting factor for the production of Ntyr. In the same regard, for the $^{\bullet}NO_2$-only scenario, $^{\bullet}OH$ is only produced from the decomposition of $ONOO^-$ and, in this case, becomes a limiting factor for the initial $^{\bullet}TyrOH$ formation. The "all pollutant" scenario shows a higher production of Ntyr compared to the sum of only $PM_{2.5}$ or only $^{\bullet}NO_2$ scenarios suggesting that $PM_{2.5}$ and $^{\bullet}NO_2$ show synergistic effects toward the formation of Ntyr, i.e., Ntyr production depends nonlinearly on the presence of both $PM_{2.5}$ and $^{\bullet}NO_2$. The synergistic effect contributing to the simulated Ntyr concentrations is quantified for a wide range of $PM_{2.5}$ and $^{\bullet}NO_2$ concentrations in the Supporting Information (Figure S6).

Traffic-related air pollution encompasses a wide range of gases and particles resulting from the use of motor vehicles, particularly $^{\bullet}NO_2$ and $PM_{2.5}$.[46,92,93] Meta analyses show that long-term exposure to $^{\bullet}NO_2$ and $PM_{2.5}$ has been associated with adverse health effects.[46,94] Thus, the synergistic formation of Ntyr by exposure to $^{\bullet}NO_2$ and $PM_{2.5}$ is consistent with the epidemiological evidence and may give indications why the co-emission of $^{\bullet}NO_2$ and $PM_{2.5}$ from traffic-related sources leads to particularly negative health outcomes.

https://doi.org/10.1021/acs.est.3c03556
Environ. Sci. Technol. 2023, 57, 12642−12653

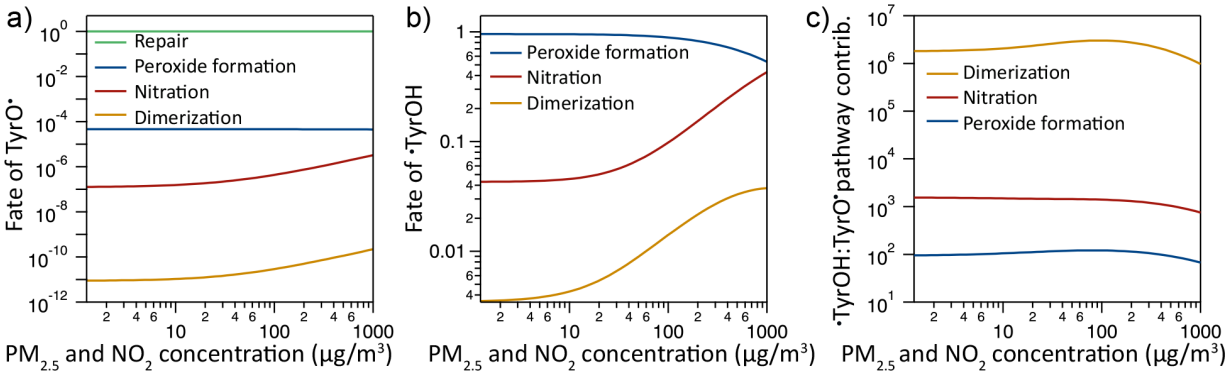

Figure 5. Reaction pathways of tyrosyl radicals in the chemical mechanism. Contribution of different reaction pathways to the fate of (a) TyrO• and (b) •TyrOH as a function of $PM_{2.5}$ and $^{\bullet}NO_2$ in the ELF. (c) The ratio of modified tyrosine products generated through the •TyrOH pathway to the amount generated through the TyrO• pathway.

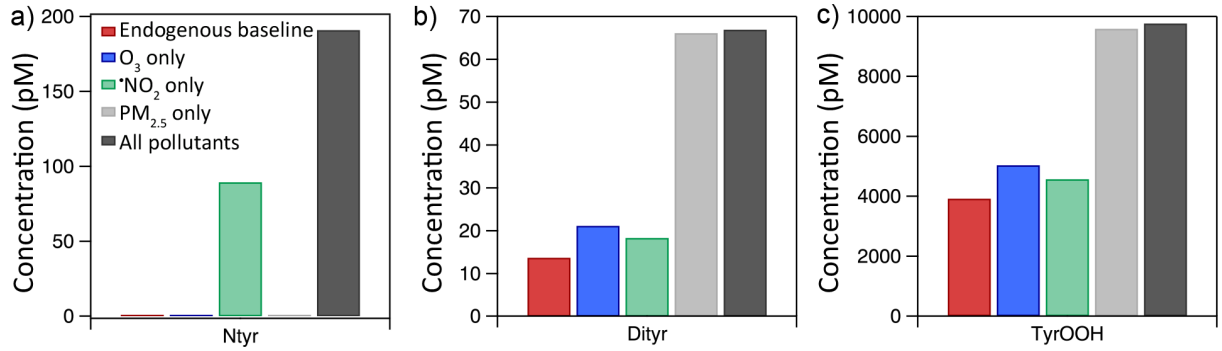

Figure 6. Concentration of modified tyrosine species in the ELF after the 2-h exposure in different pollution scenarios in KM-SUB-ELF 2.0. The contribution of individual pollutants (O_3, $PM_{2.5}$, and $^{\bullet}NO_2$) is evaluated by simulation of exposure to only the single pollutant, a scenario without pollutants (endogenous baseline, red), and a scenario with all pollutants (black). Panels a, b, and c show results for three tyrosine modifications, nitrotyrosine, dityrosine, and tyrosine peroxide, respectively. Note that in panel a, the *y*-axis is slightly offset for visualization purposes.

Panel b shows the same analysis for the formation of Dityr. The $PM_{2.5}$-only scenario shows much higher Dityr production than the baseline scenario and is comparable to that of the scenario involving all pollutants. This is due to the additional production of $^{\bullet}OH$ by $PM_{2.5}$, which increases the steady-state concentration of •TyrOH. The O_3-only scenario exhibits a slightly higher Dityr production compared with the baseline scenario. This is due to the reaction of O_3 with $O_2^{\bullet-}$, which contributes roughly 3.5% to the total $^{\bullet}OH$ production under these conditions (Figure 2b). $^{\bullet}NO_2$ does not lead to an increase in Dityr production.

Panel c shows the contribution of the individual air pollutants to the other products considered in the model. The total concentrations of other products (i.e., TyrOOH) are much higher than the concentrations of Ntyr and Dityr, reaching roughly 9 nM in the pollution scenario considered here. As seen for Dityr in panel b, the $PM_{2.5}$-only scenario has a much higher contribution to tyrosine modification compared to the other individual pollutants.

Note that compared to Ntyr, the baseline values for Dityr and other tyrosine modification products are significantly higher. This is because the $^{\bullet}NO_2$ required for Ntyr formation is much more efficiently scavenged by AOs than $^{\bullet}OH$ radicals. $^{\bullet}OH$ radicals are continuously produced from the decomposition of $ONOO^-$, leading to a baseline production of Dityr and other modification products. The low endogenous baseline and pronounced increase in concentration is a favorable property of Ntyr as a marker substance assessing oxidative stress from exposure to air pollution.

We also note that protein hydroperoxides such as TyrOOH may be labile and produce free radicals in secondary reactions. In reactions with enzymes (e.g., catalase), the hydroperoxides may react to the more stable alcohols, but in the presence of transition metals, Fenton-like chemistry may generate alkoxy radicals and $^{\bullet}OH$.[87] As the rate coefficients of these reactions are rather uncertain, a detailed chemical kinetic analysis of such products is beyond the scope of this article and will be addressed in future studies. Instead, we perform a sensitivity analysis for the reaction of protein peroxides with catalase (Figure S7) by assuming that TyrOOH reacts with the same rate coefficient as reported for hydrogen peroxide in the literature and found that model results are insensitive. Therefore, enzymes may not easily repair the peroxide. This is consistent with an experimental study in which about 40% of protein hydroperoxides decayed spontaneously in 24 h.[87,95] Thus, in the 2-h exposure window considered in the model, the decay might be minor.

Markers of Oxidative Stress in BAL Fluid. Figure 7 shows the Ntyr concentrations in different pollution scenarios (i.e., ambient concentrations of $PM_{2.5}$, $^{\bullet}NO_2$, and O_3) in the model (Table S3). We observe that less-polluted conditions typical for remote and rural areas, as well as indoor air, lead to low Ntyr concentrations of 1.8−5.2 nmol/mg. These numbers are consistent with experimental studies of Ntyr in bronchoalveolar lavage (BAL) fluid.[10,11] BAL is a procedure

https://doi.org/10.1021/acs.est.3c03556
Environ. Sci. Technol. 2023, 57, 12642−12653

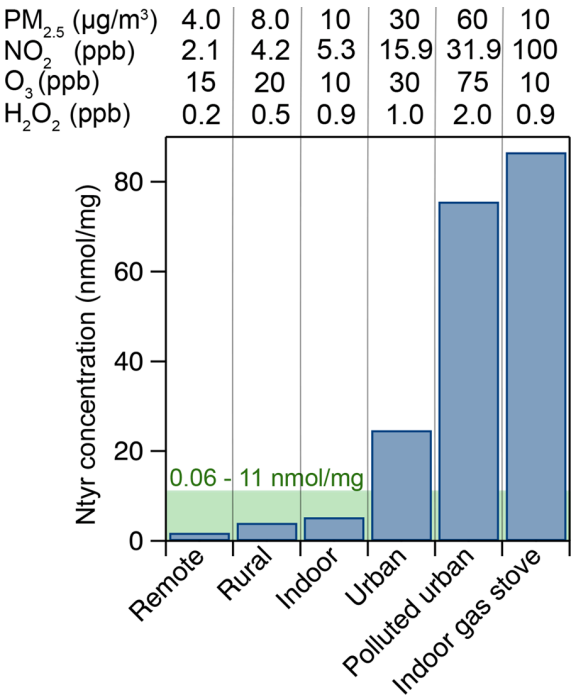

Figure 7. Concentration of nitrotyrosine (Ntyr) after the 2-h exposure to air pollution under different pollution scenarios in KM-SUB-ELF 2.0. The green shaded region shows Ntyr concentrations derived from the extraction of bronchoalveolar lavage (BAL) fluid.[10,11] The pollutant concentrations are chosen based on measurements reported in the literature (Table S3).[66,101−114]

used to determine the composition of the ELF. However, the ELF is diluted by the lavage procedure, and a dilution factor, often calculated from the concentration of urea, is used to infer concentrations in the ELF of the respiratory tract.[96] When correcting for the dilution process during the extraction of BAL fluid, the measurement values correspond to concentrations of Ntyr of 0.6−11 nmol/mg in the ELF. In more-polluted conditions typical for urban locations, however, the modeled Ntyr concentrations are strongly elevated at 24.7−75.6 nmol/mg and thus exceed the concentrations typically found in the ELF.

Gas stoves and ovens emit significant amounts of $^{\bullet}NO_2$.[97−99] In indoor environments where gas stoves are used, particularly in kitchens with inadequate ventilation, inhaled $^{\bullet}NO_2$ concentrations commonly reach 100 ppb.[98] Using such a high concentration of $^{\bullet}NO_2$ in the indoor air scenario, the model yields a Ntyr concentration that is comparable to that of the polluted urban scenario.

We note that the turnover time of the ELF and therefore the half-life of modified proteins in the ELF are uncertain and influence the computed and experimentally derived values. A practical consequence of a rapid turnover of the ELF would be that test subjects in polluted areas might quickly adopt Ntyr concentrations that are typical for indoor concentrations of air pollution before a BAL procedure. Other sources of uncertainty in the model include endogenous production rates of ROS and concentrations and activity of antioxidant enzymes, as well as reaction rate coefficients involving peroxides from secondary organic aerosol (SOA).[25,27] Furthermore, there is variability in the literature concerning the levels of antioxidants in the ELF. For instance, Rahman et al.[100] report concentrations that differ from the values presented by van der Vliet et al.[64] and used in KM-SUB-ELF. Antioxidants represent the largest sink of $^{\bullet}NO_2$ in the model. The uncertainty in Ntyr production from the choice of antioxidant concentrations is in the range of a factor of 2 (Figure S8). Moreover, the deposition fraction of $PM_{2.5}$ depends on the shape of the particle size distribution. The deposition fraction of 45% used here is a value typical for 1 μm particles.[61,62] A lower limit for the deposition fraction is 20%, which yields Ntyr concentrations that are ∼40% lower (Figure S9). Some uncertainty may arise from concentration gradients of particles and gases along the respiratory tract. Using an extension to KM-SUB-ELF that is currently under development, we estimate that losses of O_3 and $^{\bullet}NO_2$ in the upper respiratory tract could reduce their concentrations in the lower respiratory tract by ∼15%. Together with a (re)distribution of deposited particles, this could translate into a reduction of model-predicted Ntyr concentrations by ∼35% (Figure S10). Overall, the Ntyr concentrations determined in this study should be seen as order-of-magnitude estimate. Future studies will be needed to reduce the model uncertainty.

By linking reaction kinetics with observed markers of oxidative stress, this study provides a mechanistic understanding of the chemistry by which air pollution may affect human health. We find that the permanent modification of tyrosine residues is mostly caused by initial oxidation with the $^{\bullet}OH$ radical, which is generated in processes involving particulate pollutants ($PM_{2.5}$). The gas-phase pollutants O_3 and $^{\bullet}NO_2$ also oxidize tyrosine, but the resulting intermediates are efficiently repaired by antioxidants according to the model simulations. Thus, this pathway may only be a burden on the antioxidant defense rather than causing irreversible chemical modification of proteins. According to the model, the air pollutants most responsible for the formation of nitrotyrosine are $PM_{2.5}$ and $^{\bullet}NO_2$, which are also the two air pollutants most commonly associated with increased mortality from traffic-related air pollution. These insights into the specific interactions and differential toxicity of individual air pollutants provide a foundation and direction for further research on the adverse health effects of air pollution.

■ ASSOCIATED CONTENT

Supporting Information

The Supporting Information is available free of charge at https://pubs.acs.org/doi/10.1021/acs.est.3c03556.

Overview KM-SUB-ELF 2.0 (S1); Particulate pollutant concentrations in the ELF (S2); Enzyme concentrations and reactions (S3); Parameterization of ROS formation from secondary organic aerosol (S4); Endogenous superoxide production from macrophages (S5); Chemical reactions (Table S1); Input parameters of the KM-SUB-ELF 2.0 model (Table S2); Concentrations of pollutants used in the pollution scenarios (Table S3); Schematic overview of KM-SUB-ELF 2.0 (Figure S1); Biological vs atmospheric contribution of various oxidants explored in the study (Figure S2); Contribution of different sources to $^{\bullet}OH$ production in the model as a function of endogenous superoxide production (Figure S3); Modified tyrosine concentration in the ELF as a function of the concentration of three distinct pollutants (Figure S4); Fraction of modified tyrosine attributed to different tyrosyl radicals (Figure S5); Nitrotyrosine

concentration in the epithelial lining fluid as a function of $PM_{2.5}$ and $^{\bullet}NO_2$ levels (Figure S6); Sensitivity of tyrosine peroxide concentration to decomposition reaction with catalase (Figure S7); Concentration of nitrotyrosine and dityrosine as a function of antioxidant concentrations (Figure S8); Sensitivity of $PM_{2.5}$ deposition fractions to concentration of Ntyr after 2-h exposure to air pollution under different pollution scenarios (Figure S9); Concentration of nitrotyrosine in the gas phase of the upper and lower respiratory tract (Figure S10) (PDF)

AUTHOR INFORMATION

Corresponding Author

Thomas Berkemeier − *Multiphase Chemistry Department, Max Planck Institute for Chemistry, 55128 Mainz, Germany;* orcid.org/0000-0001-6390-6465; Email: t.berkemeier@mpic.de

Authors

Ashmi Mishra − *Multiphase Chemistry Department, Max Planck Institute for Chemistry, 55128 Mainz, Germany;* orcid.org/0000-0003-1751-1643

Steven Lelieveld − *Multiphase Chemistry Department, Max Planck Institute for Chemistry, 55128 Mainz, Germany;* orcid.org/0000-0002-6057-3404

Ulrich Pöschl − *Multiphase Chemistry Department, Max Planck Institute for Chemistry, 55128 Mainz, Germany;* orcid.org/0000-0003-1412-3557

Complete contact information is available at: https://pubs.acs.org/10.1021/acs.est.3c03556

Funding

Open access funded by Max Planck Society.

Notes

The authors declare no competing financial interest.

ACKNOWLEDGMENTS

A.M. was supported by the Max Planck Graduate Center with the Johannes Gutenberg University (MPGC). We would like to thank A. T. Backes, E. Dovrou, J. Fröhlich, K. Lucas, and M. Weller for helpful discussions.

ABBREVIATIONS USED

Dityr	Dityrosine
Ntyr	Nitrotyrosine
TyrOOH	Tyrosine peroxide
$PM_{2.5}$	Particulate matter
ROS	Reactive oxygen species
BAL	Bronchoalveolar lavage

REFERENCES

(1) Sies, H. Hydrogen peroxide as a central redox signaling molecule in physiological oxidative stress: Oxidative eustress. *Redox Biol.* **2017**, *11*, 613−619.

(2) Sies, H. Oxidative stress: oxidants and antioxidants. *Exp. Physiol.* **1997**, *82*, 291−295.

(3) Lin, J.-L.; Thomas, P. S. Current Perspectives of Oxidative Stress and its Measurement in Chronic Obstructive Pulmonary Disease. *Int. J. Chronic Obstr. Pulm. Dis.* **2010**, *7*, 291−306.

(4) Valko, M.; Leibfritz, D.; Moncol, J.; Cronin, M. T. D.; Mazur, M.; Telser, J. Free radicals and antioxidants in normal physiological functions and human disease. *Int. J. Biochem. Cell Biol.* **2007**, *39*, 44−84.

(5) Cadenas, E.; Davies, K. J. A. Mitochondrial free radical generation, oxidative stress, and aging. *Free Radic. Biol. Med.* **2000**, *29*, 222−230.

(6) Forman, H. J.; Torres, M. Reactive Oxygen Species and Cell Signaling. *Am. J. Respir. Crit. Care Med.* **2002**, *166*, S4−S8.

(7) Verma, V.; Rico-Martinez, R.; Kotra, N.; King, L.; Liu, J.; Snell, T. W.; Weber, R. J. Contribution of Water-Soluble and Insoluble Components and Their Hydrophobic/Hydrophilic Subfractions to the Reactive Oxygen Species-Generating Potential of Fine Ambient Aerosols. *Environ. Sci. Technol.* **2012**, *46*, 11384−11392.

(8) Bates, J. T.; Weber, R. J.; Abrams, J.; Verma, V.; Fang, T.; Klein, M.; Strickland, M. J.; Sarnat, S. E.; Chang, H. H.; Mulholland, J. A.; Tolbert, P. E.; Russell, A. G. Reactive Oxygen Species Generation Linked to Sources of Atmospheric Particulate Matter and Cardiorespiratory Effects. *Environ. Sci. Technol.* **2015**, *49*, 13605−13612.

(9) Lakey, P. S. J.; Berkemeier, T.; Tong, H.; Arangio, A. M.; Lucas, K.; Pöschl, U.; Shiraiwa, M. Chemical exposure-response relationship between air pollutants and reactive oxygen species in the human respiratory tract. *Sci. Rep.* **2016**, *6*, 32916.

(10) DeAndrade, J.; Crow, J.; Viera, L.; Bruce Alexander, C.; Randall Young, K.; McGiffin, D.; Zorn, G.; Zhu, S.; Matalon, S.; Jackson, R. Protein Nitration, Metabolites of Reactive Nitrogen Species, and Inflammation in Lung Allografts. *Am. J. Respir. Crit. Care Med.* **2000**, *161*, 2035−2042.

(11) Sittipunt, C.; Steinberg, K. P.; Ruzinski, J. T.; Myles, C.; Zhu, S.; Goodman, R. B.; Hudson, L. D.; Matalon, S.; Martin, T. R. Nitric Oxide and Nitrotyrosine in the Lungs of Patients with Acute Respiratory Distress Syndrome. *Am. J. Respir. Crit. Care Med.* **2001**, *163*, 503−510.

(12) Davies, M. J. Protein oxidation and peroxidation. *Biochem. J.* **2016**, *473*, 805−825.

(13) Pope, C. A.; Thun, M. J.; Namboodiri, M. M.; Dockery, D. W.; Evans, J. S.; Speizer, F. E.; Heath, C. W. Particulate Air Pollution as a Predictor of Mortality in a Prospective Study of U.S. Adults. *Am. J. Respir. Crit. Care Med.* **1995**, *151*, 669−674.

(14) Lelieveld, J.; Evans, J. S.; Fnais, M.; Giannadaki, D.; Pozzer, A. The contribution of outdoor air pollution sources to premature mortality on a global scale. *Nature* **2015**, *525*, 367−371.

(15) Pye, H. O. T.; Ward-Caviness, C. K.; Murphy, B. N.; Appel, K. W.; Seltzer, K. M. Secondary organic aerosol association with cardiorespiratory disease mortality in the United States. *Nat. Commun.* **2021**, *12*, 7215.

(16) Malley, C. S.; Henze, D. K.; Kuylenstierna, J. C.; Vallack, H. W.; Davila, Y.; Anenberg, S. C.; Turner, M. C.; Ashmore, M. R. Updated Global Estimates of Respiratory Mortality in Adults 30Years of Age Attributable to Long-Term Ozone Exposure. *Environ. Health Perspect.* **2017**, *125*, 087021.

(17) Murray, C. J. L.; et al. Global burden of 87 risk factors in 204 countries and territories, 1990−2019: a systematic analysis for the Global Burden of Disease Study 2019. *Lancet* **2020**, *396*, 1223−1249.

(18) McDuffie, E. E.; et al. Source sector and fuel contributions to ambient PM2.5 and attributable mortality across multiple spatial scales. *Nat. Commun.* **2021**, *12*, 3594.

(19) Anenberg, S. C.; et al. Estimates of the Global Burden of Ambient PM2.5, Ozone, and NO2 on Asthma Incidence and Emergency Room Visits. *Environ. Health Perspect.* **2018**, *126*, 107004.

(20) Balasubramanian, R.; Qian, W.-B.; Decesari, S.; Facchini, M. C.; Fuzzi, S. Comprehensive characterization of PM2.5 aerosols in Singapore. *J. Geophys. Res. Atmos.* **2003**, *108*, 4523.

(21) Pöschl, U. Atmospheric Aerosols: Composition, Transformation, Climate and Health Effects. *Angew. Chem., Int. Ed.* **2005**, *44*, 7520−7540.

(22) Jimenez, J. L.; et al. Evolution of Organic Aerosols in the Atmosphere. *Science* **2009**, *326*, 1525−1529.

(23) Seinfeld, J. H.; Pandis, S. N. *Atmospheric Chemistry and Physics: From Air Pollution to Climate Change*, 3rd ed.; Wiley: 2016.

(24) Cho, A. K.; Sioutas, C.; Miguel, A. H.; Kumagai, Y.; Schmitz, D. A.; Singh, M.; Eiguren-Fernandez, A.; Froines, J. R. Redox activity of airborne particulate matter at different sites in the Los Angeles Basin. *Environ. Res.* **2005**, *99*, 40−47.
(25) Lelieveld, S.; Wilson, J.; Dovrou, E.; Mishra, A.; Lakey, P. S. J.; Shiraiwa, M.; Pöschl, U.; Berkemeier, T. Hydroxyl Radical Production by Air Pollutants in Epithelial Lining Fluid Governed by Interconversion and Scavenging of Reactive Oxygen Species. *Environ. Sci. Technol.* **2021**, *55*, 14069−14079.
(26) Charrier, J. G.; Anastasio, C. Rates of Hydroxyl Radical Production from Transition Metals and Quinones in a Surrogate Lung Fluid. *Environ. Sci. Technol.* **2015**, *49*, 9317−9325.
(27) Dovrou, E.; Lelieveld, S.; Mishra, A.; Pöschl, U.; Berkemeier, T. Influence of ambient and endogenous H2O2 on reactive oxygen species concentrations and OH radical production in the respiratory tract. *Environ. Sci.: Atmos.* **2023**, *3*, 1066−1074.
(28) Valderrama, A.; Ortiz-Hernández, P.; Agraz-Cibrián, J. M.; Tabares-Guevara, J. H.; Gómez, D. M.; Zambrano-Zaragoza, J. F.; Taborda, N. A.; Hernandez, J. C. Particulate matter (PM10) induces in vitro activation of human neutrophils, and lung histopathological alterations in a mouse model. *Sci. Rep.* **2022**, *12*, 7581.
(29) Fang, T.; Huang, Y.-K.; Wei, J.; Monterrosa Mena, J. E.; Lakey, P. S. J.; Kleinman, M. T.; Digman, M. A.; Shiraiwa, M. Superoxide Release by Macrophages through NADPH Oxidase Activation Dominating Chemistry by Isoprene Secondary Organic Aerosols and Quinones to Cause Oxidative Damage on Membranes. *Environ. Sci. Technol.* **2022**, *56*, 17029−17038.
(30) Mehlman, M. A.; Borek, C. Toxicity and biochemical mechanisms of ozone. *Environ. Res.* **1987**, *42*, 36−53.
(31) Cueto, R.; Squadrito, G. L.; Bermudez, E.; Pryor, W. A. Identification of heptanal and nonanal in bronchoalveolar lavage from rats exposed to low levels of ozone. *Biochem. Biophys. Res. Commun.* **1992**, *188*, 129−134.
(32) Pryor, W.; Uppu, R. A kinetic model for the competitive reactions of ozone with amino acid residues in proteins in reverse micelles. *J. Biol. Chem.* **1993**, *268*, 3120−3126.
(33) Bassett, D. J. P.; Bowen-Kelly, E.; Brewster, E. L.; Elbon, C. L.; Reichenbaugh, S. S.; Bunton, T.; Kerr, J. S. A reversible model of acute lung injury based on ozone exposure. *Lung* **1988**, *166*, 355−369.
(34) Pryor, W. A. How far does ozone penetrate into the pulmonary air/tissue boundary before it reacts? *Free Radic. Biol. Med.* **1992**, *12*, 83−88.
(35) Sharma, V. K.; Graham, N. J. Oxidation of Amino Acids, Peptides and Proteins by Ozone: A Review. *Ozone: Sci. Eng.* **2010**, *32*, 81−90.
(36) Sandhiya, L.; Kolandaivel, P.; Senthilkumar, K. Oxidation and Nitration of Tyrosine by Ozone and Nitrogen Dioxide: Reaction Mechanisms and Biological and Atmospheric Implications. *J. Phys. Chem. B* **2014**, *118*, 3479−3490.
(37) Logan, J. A. Nitrogen oxides in the troposphere: Global and regional budgets. *J. Geophys. Res. Oceans* **1983**, *88*, 10785−10807.
(38) Bond, D. W.; Zhang, R.; Tie, X.; Brasseur, G.; Huffines, G.; Orville, R. E.; Boccippio, D. J. NOx production by lightning over the continental United States. *J. Geophys. Res. Atmos.* **2001**, *106*, 27701−27710.
(39) Lin, J.-T.; McElroy, M. B. Detection from space of a reduction in anthropogenic emissions of nitrogen oxides during the Chinese economic downturn. *Atmos. Chem. Phys.* **2011**, *11*, 8171−8188.
(40) Chowdhury, S.; Haines, A.; Klingmüller, K.; Kumar, V.; Pozzer, A.; Venkataraman, C.; Witt, C.; Lelieveld, J. Global and national assessment of the incidence of asthma in children and adolescents from major sources of ambient NO2. *Environ. Res. Lett.* **2021**, *16*, 035020.
(41) Anenberg, S. C.; Mohegh, A.; Goldberg, D. L.; Kerr, G. H.; Brauer, M.; Burkart, K.; Hystad, P.; Larkin, A.; Wozniak, S.; Lamsal, L. Long-term trends in urban NO2 concentrations and associated paediatric asthma incidence: estimates from global datasets. *Lancet Planet. Health.* **2022**, *6*, e49−e58.
(42) Faustini, A.; Rapp, R.; Forastiere, F. Nitrogen dioxide and mortality: review and meta-analysis of long-term studies. *Eur. Respir. J.* **2014**, *44*, 744.
(43) Zhang, Y.; Li, Z.; Wei, J.; Zhan, Y.; Liu, L.; Yang, Z.; Zhang, Y.; Liu, R.; Ma, Z. Long-term exposure to ambient NO2 and adult mortality: A nationwide cohort study in China. *J. Adv. Res.* **2022**, *41*, 13−22.
(44) Burnett, R. T.; Stieb, D.; Brook, J. R.; Cakmak, S.; Dales, R.; Raizenne, M.; Vincent, R.; Dann, T. Associations between Short-Term Changes in Nitrogen Dioxide and Mortality in Canadian Cities. *Arch. Environ. Health* **2004**, *59*, 228−236.
(45) Ji, J. S.; Liu, L.; Zhang, J. J.; Kan, H.; Zhao, B.; Burkart, K. G.; Zeng, Y. NO2 and PM2.5 air pollution co-exposure and temperature effect modification on pre-mature mortality in advanced age: a longitudinal cohort study in China. *Environ. Health* **2022**, *21*, 97.
(46) Boogaard, H.; et al. Long-term exposure to traffic-related air pollution and selected health outcomes: A systematic review and meta-analysis. *Environ. Int.* **2022**, *164*, 107262.
(47) Beckman, J. S.; Beckman, T. W.; Chen, J.; Marshall, P. A.; Freeman, B. A. Apparent hydroxyl radical production by peroxynitrite: implications for endothelial injury from nitric oxide and superoxide. *Proc. Natl. Acad. Sci. U. S. A.* **1990**, *87*, 1620−1624.
(48) Radi, R. Nitric oxide, oxidants, and protein tyrosine nitration. *Proc. Natl. Acad. Sci. U. S. A.* **2004**, *101*, 4003−4008.
(49) Ferrer-Sueta, G.; Campolo, N.; Trujillo, M.; Bartesaghi, S.; Carballal, S.; Romero, N.; Alvarez, B.; Radi, R. Biochemistry of Peroxynitrite and Protein Tyrosine Nitration. *Chem. Rev.* **2018**, *118*, 1338−1408.
(50) Förstermann, U.; Sessa, W. C. Nitric oxide synthases: regulation and function. *Eur. Heart J.* **2012**, *33*, 829−837.
(51) Denicola, A.; Freeman, B. A.; Trujillo, M.; Radi, R. Peroxynitrite Reaction with Carbon Dioxide/Bicarbonate: Kinetics and Influence on Peroxynitrite-Mediated Oxidations. *Arch. Biochem. Biophys.* **1996**, *333*, 49−58.
(52) Mudway, I.; Kelly, F.; Holgate, S. Oxidative stress in air pollution research. *Free Radic. Biol. Med.* **2020**, *151*, 2−6.
(53) Davies, M. J. The oxidative environment and protein damage. *Biochim. Biophys. Acta Proteins Proteom.* **2005**, *1703*, 93−109.
(54) Reinmuth-Selzle, K.; Ackaert, C.; Kampf, C. J.; Samonig, M.; Shiraiwa, M.; Kofler, S.; Yang, H.; Gadermaier, G.; Brandstetter, H.; Huber, C. G.; Duschl, A.; Oostingh, G. J.; Pöschl, U. Nitration of the Birch Pollen Allergen Bet v 1.0101: Efficiency and Site-Selectivity of Liquid and Gaseous Nitrating Agents. *J. Proteome Res.* **2014**, *13*, 1570−1577.
(55) Backes, A. T.; Reinmuth-Selzle, K.; Leifke, A. L.; Ziegler, K.; Krevert, C. S.; Tscheuschner, G.; Lucas, K.; Weller, M. G.; Berkemeier, T.; Pöschl, U.; Fröhlich-Nowoisky, J. Oligomerization and Nitration of the Grass Pollen Allergen Phl p 5 by Ozone, Nitrogen Dioxide, and Peroxynitrite: Reaction Products, Kinetics, and Health Effects. *Int. J. Mol. Sci.* **2021**, *22*, 7616.
(56) Shiraiwa, M.; Selzle, K.; Yang, H.; Sosedova, Y.; Ammann, M.; Pöschl, U. Multiphase Chemical Kinetics of the Nitration of Aerosolized Protein by Ozone and Nitrogen Dioxide. *Environ. Sci. Technol.* **2012**, *46*, 6672−6680.
(57) Radi, R. Peroxynitrite, a Stealthy Biological Oxidant*. *J. Biol. Chem.* **2013**, *288*, 26464−26472.
(58) Reinmuth-Selzle, K.; et al. Air Pollution and Climate Change Effects on Allergies in the Anthropocene: Abundance, Interaction, and Modification of Allergens and Adjuvants. *Environ. Sci. Technol.* **2017**, *51*, 4119−4141.
(59) Kumarathasan, P.; Blais, E.; Saravanamuthu, A.; Bielecki, A.; Mukherjee, B.; Bjarnason, S.; Guénette, J.; Goegan, P.; Vincent, R. Nitrative stress, oxidative stress and plasma endothelin levels after inhalation of particulate matter and ozone. *Part. Fibre Toxicol.* **2015**, *12*, 28.
(60) Franze, T.; Weller, M. G.; Niessner, R.; Pöschl, U. Protein Nitration by Polluted Air. *Environ. Sci. Technol.* **2005**, *39*, 1673−1678.
(61) Hofmann, W. Modelling inhaled particle deposition in the human lung—A review. *J. Aerosol Sci.* **2011**, *42*, 693−724.

(62) Klumpp, J.; Bertelli, L. KDEP: A Resource for Calculating Particle Deposition in the Respiratory Tract. *Health Phys.* **2017**, *113*, 110.
(63) Kelly, F. J.; Tetley, T. D. Nitrogen dioxide depletes uric acid and ascorbic acid but not glutathione from lung lining fluid. *Biochem. J.* **1997**, *325*, 95−99.
(64) van der Vliet, A.; O'Neill, C. A.; Cross, C. E.; Koostra, J. M.; Volz, W. G.; Halliwell, B.; Louie, S. Determination of low-molecular-mass antioxidant concentrations in human respiratory tract lining fluids. *Am. J. Physiol. Lung Cell Mol. Physiol.* **1999**, *276*, L289−L296.
(65) Hasson, A. S.; Ho, A. W.; Kuwata, K. T.; Paulson, S. E. Production of stabilized Criegee intermediates and peroxides in the gas phase ozonolysis of alkenes: 2. Asymmetric and biogenic alkenes. *J. Geophys. Res.* **2001**, *106*, 34143−34153.
(66) Zhou, Z.; Abbatt, J. P. D. Formation of Gas-Phase Hydrogen Peroxide via Multiphase Ozonolysis of Unsaturated Lipids. *Environ. Sci. Technol. Lett.* **2021**, *8*, 114−120.
(67) Cantin, A. M.; Fells, G. A.; Hubbard, R. C.; Crystal, R. G. Antioxidant macromolecules in the epithelial lining fluid of the normal human lower respiratory tract. *J. Clin. Invest.* **1990**, *86*, 962−971.
(68) Tsodikov, O. V.; Record, M. T., Jr.; Sergeev, Y. V. Novel computer program for fast exact calculation of accessible and molecular surface areas and average surface curvature. *J. Comput. Chem.* **2002**, *23*, 600−609.
(69) Cross, C. E.; van der Vliet, A.; O'Neill, C. A.; Louie, S.; Halliwell, B. Oxidants, Antioxidants, and Respiratory Tract Lining Fluids. *Environ. Health Perspect.* **1994**, *102*, 185−191.
(70) Tien, M. Z.; Meyer, A. G.; Sydykova, D. K.; Spielman, S. J.; Wilke, C. O. Maximum Allowed Solvent Accessibilites of Residues in Proteins. *PLoS One* **2013**, *8*, e80635.
(71) Solar, S.; Solar, W.; Getoff, N. Reactivity of hydroxyl with tyrosine in aqueous solution studied by pulse radiolysis. *J. Phys. Chem.* **1984**, *88*, 2091−2095.
(72) Pryor, W. A.; Giamalva, D. H.; Church, D. F. Kinetics of ozonation. 2. Amino acids and model compounds in water and comparisons to rates in nonpolar solvents. *J. Am. Chem. Soc.* **1984**, *106*, 7094−7100.
(73) Huie, R. E.; Shoute, L. C. T.; Neta, P. Temperature dependence of the rate constants for reactions of the carbonate radical with organic and inorganic reductants. *Int. J. Chem. Kinet.* **1991**, *23*, 541−552.
(74) Shen, J.; Taghvaee, S.; La, C.; Oroumiyeh, F.; Liu, J.; Jerrett, M.; Weichenthal, S.; Del Rosario, I.; Shafer, M. M.; Ritz, B.; Zhu, Y.; Paulson, S. E. Aerosol Oxidative Potential in the Greater Los Angeles Area: Source Apportionment and Associations with Socioeconomic Position. *Environ. Sci. Technol.* **2022**, *56*, 17795−17804.
(75) Davies, M. J.; Fu, S.; Wang, H.; Dean, R. T. Stable markers of oxidant damage to proteins and their application in the study of human disease. *Free Radic. Biol. Med.* **1999**, *27*, 1151−1163.
(76) Prütz, W. A.; Mönig, H.; Butler, J.; Land, E. J. Reactions of nitrogen dioxide in aqueous model systems: Oxidation of tyrosine units in peptides and proteins. *Arch. Biochem. Biophys.* **1985**, *243*, 125−134.
(77) Candeias, L. P.; Wardman, P.; Mason, R. P. The reaction of oxygen with radicals from oxidation of tryptophan and indole-3-acetic acid. *Biophys. Chem.* **1997**, *67*, 229−237.
(78) Folkes, L. K.; Trujillo, M.; Bartesaghi, S.; Radi, R.; Wardman, P. Kinetics of reduction of tyrosine phenoxyl radicals by glutathione. *Arch. Biochem. Biophys.* **2011**, *506*, 242−249.
(79) Hunter, E. P.; Desrosiers, M. F.; Simic, M. G. The effect of oxygen, antioxidants, and superoxide radical on tyrosine phenoxyl radical dimerization. *Free Radic. Biol. Med.* **1989**, *6*, 581−585.
(80) Alfassi, Z. B.; Huie, R. E.; Kumar, M.; Neta, P. Temperature dependence of the rate constants for oxidation of organic compounds by peroxyl radicals in aqueous alcohol solutions. *J. Phys. Chem.* **1992**, *96*, 767−770.
(81) Radi, R. Protein Tyrosine Nitration: Biochemical Mechanisms and Structural Basis of Functional Effects. *Acc. Chem. Res.* **2013**, *46*, 550−559.
(82) López-Alarcón, C.; Arenas, A.; Lissi, E.; Silva, E. The role of protein-derived free radicals as intermediaries of oxidative processes. *Biomol. Concepts* **2014**, *5*, 119−130.
(83) Enami, S.; Hoffmann, M. R.; Colussi, A. J. Extensive H-atom abstraction from benzoate by OH-radicals at the air−water interface. *Phys. Chem. Chem. Phys.* **2016**, *18*, 31505−31512.
(84) Goldstein, S.; Czapski, G.; Lind, J.; Merényi, G. Tyrosine Nitration by Simultaneous Generation of NO and O2 under Physiological Conditions: HOW THE RADICALS DO THE JOB. *J. Biol. Chem.* **2000**, *275*, 3031−3036.
(85) Barzaghi, P.; Herrmann, H. A mechanistic study of the oxidation of phenol by OH/NO2/NO3 in aqueous solution. *Phys. Chem. Chem. Phys.* **2002**, *4*, 3669−3675.
(86) Davies, M. J.; Fu, S.; Dean, R. T. Protein hydroperoxides can give rise to reactive free radicals. *Biochem. J.* **1995**, *305*, 643−649.
(87) Gebicki, J. M. Protein hydroperoxides as new reactive oxygen species. *Redox Rep.* **1997**, *3*, 99−110.
(88) d'Alessandro, N.; Bianchi, G.; Fang, X.; Jin, F.; Schuchmann, H.-P.; von Sonntag, C. Reaction of superoxide with phenoxyl-type radicals. *J. Chem. Soc., Perkin trans. II* **2000**, 1862−1867.
(89) Winterbourn, C.; Parsons-Mair, H.; Gebicki, S.; Gebicki, J.; Davies, M. Requirements for superoxide-dependent tyrosine hydroperoxide formation in peptides. *Biochem. J.* **2004**, *381*, 241−248.
(90) Seitz, G.; Gebhardt, S.; Beck, J. F.; Böhm, W.; Lode, H. N.; Niethammer, D.; Bruchelt, G. Ascorbic acid stimulates DOPA synthesis and tyrosine hydroxylase gene expression in the human neuroblastoma cell line SK-N-SH. *Neurosci. Lett.* **1998**, *244*, 33−36.
(91) Kelly, F. J.; Fussell, J. C. Role of oxidative stress in cardiovascular disease outcomes following exposure to ambient air pollution. *Free Radic. Biol. Med.* **2017**, *110*, 345−367.
(92) Kim, J. J.; Smorodinsky, S.; Lipsett, M.; Singer, B. C.; Hodgson, A. T.; Ostro, B. Traffic-related Air Pollution near Busy Roads. *Am. J. Respir. Crit. Care Med.* **2004**, *170*, 520−526.
(93) Health Effects Institute. *Traffic-Related Air Pollution: A Critical Review of the Literature on Emissions, Exposure, and Health Effects*; Health Effects Institute: Boston, MA, USA, 2010.
(94) Gan, W. Q.; Tamburic, L.; Davies, H. W.; Demers, P. A.; Koehoorn, M.; Brauer, M. Changes in Residential Proximity to Road Traffic and the Risk of Death From Coronary Heart Disease. *Epidemiology* **2010**, *21*, 642.
(95) Simpson, J. A.; Narita, S.; Gieseg, S.; Gebicki, S.; Gebicki, J. M.; Dean, R. T. Long-lived reactive species on free-radical-damaged proteins. *Biochem. J.* **1992**, *282*, 621−624.
(96) Rennard, S. I.; Basset, G.; Lecossier, D.; O'Donnell, K. M.; Pinkston, P.; Martin, P. G.; Crystal, R. G. Estimation of volume of epithelial lining fluid recovered by lavage using urea as marker of dilution. *J. Appl. Physiol.* **1986**, *60*, 532−538.
(97) Logue, J. M.; Klepeis Neil, E.; Lobscheid Agnes, B.; Singer Brett, C. Pollutant Exposures from Natural Gas Cooking Burners: A Simulation-Based Assessment for Southern California. *Environ. Health Perspect.* **2014**, *122*, 43−50.
(98) Farmer, D. K.; et al. Overview of HOMEChem: House Observations of Microbial and Environmental Chemistry. *Environ. Sci.: Processes Impacts* **2019**, *21*, 1280−1300.
(99) Lebel, E. D.; Finnegan, C. J.; Ouyang, Z.; Jackson, R. B. Methane and NOx Emissions from Natural Gas Stoves, Cooktops, and Ovens in Residential Homes. *Environ. Sci. Technol.* **2022**, *56*, 2529−2539.
(100) Rahman, I.; Biswas, S. K.; Kode, A. Oxidant and antioxidant balance in the airways and airway diseases. *Eur. J. Pharmacol.* **2006**, *533*, 222−239.
(101) Williams, J.; Keßel, S. U.; Nölscher, A. C.; Yang, Y.; Lee, Y.; Yáñez-Serrano, A. M.; Wolff, S.; Kesselmeier, J.; Klüpfel, T.; Lelieveld, J.; Shao, M. Opposite OH reactivity and ozone cycles in the Amazon rainforest and megacity Beijing: Subversion of biospheric oxidant

control by anthropogenic emissions. *Atmos. Environ.* **2016**, *125*, 112−118.
(102) Salonen, H.; Salthammer, T.; Morawska, L. Human exposure to ozone in school and office indoor environments. *Environ. Int.* **2018**, *119*, 503−514.
(103) Yang, G.; Liu, Y.; Li, X. Spatiotemporal distribution of ground-level ozone in China at a city level. *Sci. Rep.* **2020**, *10*, 7229.
(104) O'Sullivan, D. W.; Heikes, B. G.; Snow, J.; Burrow, P.; Avery, M.; Blake, D. R.; Sachse, G. W.; Talbot, R. W.; Thornton, D. C.; Bandy, A. R. Long-term and seasonal variations in the levels of hydrogen peroxide, methylhydroperoxide, and selected compounds over the Pacific Ocean. *J. Geophys. Res. Atmos* **2004**, *109*, D15S13.
(105) Das, M.; Aneja, V. P. Analysis of Gaseous Hydrogen Peroxide Concentrations in Raleigh, North Carolina. *J. Air Waste Manage. Assoc.* **1994**, *44*, 176−183.
(106) Li, T.-H.; Turpin, B. J.; Shields, H. C.; Weschler, C. J. Indoor Hydrogen Peroxide Derived from Ozone/d-Limonene Reactions. *Environ. Sci. Technol.* **2002**, *36*, 3295−3302.
(107) Kok, G. L.; Darnall, K. R.; Winer, A. M.; Pitts, J. N. J.; Gay, B. W. Ambient air measurements of hydrogen peroxide in the California South Coast Air Basin. *Environ. Sci. Technol.* **1978**, *12*, 1077−1080.
(108) He, S. Z.; Chen, Z. M.; Zhang, X.; Zhao, Y.; Huang, D. M.; Zhao, J. N.; Zhu, T.; Hu, M.; Zeng, L. M. Measurement of atmospheric hydrogen peroxide and organic peroxides in Beijing before and during the 2008 Olympic Games: Chemical and physical factors influencing their concentrations. *J. Geophys. Res. Atmos* **2010**, *115*, D17307.
(109) Artaxo, P.; Rizzo, L. V.; Brito, J. F.; Barbosa, H. M. J.; Arana, A.; Sena, E. T.; Cirino, G. G.; Bastos, W.; Martin, S. T.; Andreae, M. O. Atmospheric aerosols in Amazonia and land use change: from natural biogenic to biomass burning conditions. *Faraday Discuss.* **2013**, *165*, 203−235.
(110) Clements, N.; Hannigan, M. P.; Miller, S. L.; Peel, J. L.; Milford, J. B. Comparisons of urban and rural $PM_{10-2.5}$ and $PM_{2.5}$ mass concentrations and semi-volatile fractions in northeastern Colorado. *Atmos. Chem. Phys.* **2016**, *16*, 7469−7484.
(111) Kundu, S.; Stone, E. A. Composition and sources of fine particulate matter across urban and rural sites in the Midwestern United States. *Environ. Sci.: Process. Impacts* **2014**, *16*, 1360−1370.
(112) Patel, S.; Sankhyan, S.; Boedicker, E. K.; DeCarlo, P. F.; Farmer, D. K.; Goldstein, A. H.; Katz, E. F.; Nazaroff, W. W.; Tian, Y.; Vanhanen, J.; Vance, M. E. Indoor Particulate Matter during HOMEChem: Concentrations, Size Distributions, and Exposures. *Environ. Sci. Technol.* **2020**, *54*, 7107−7116.
(113) Karambelas, A.; Holloway, T.; Kinney, P. L.; Fiore, A. M.; DeFries, R.; Kiesewetter, G.; Heyes, C. Urban versus rural health impacts attributable to PM2.5 and O3 in northern India. *Environ. Res. Lett.* **2018**, *13*, 064010.
(114) Liu, T.; et al. Urban-rural disparity of the short-term association of PM2.5 with mortality and its attributable burden. *Innovation* **2021**, *2*, 100171.

NOTE ADDED AFTER ASAP PUBLICATION

This paper was published ASAP on August 17, 2023, with errors in Equation 2. The corrected version was reposted on August 17, 2023.

2.7. Kinetic modeling of ambient and endogenous hydrogen peroxide production in the epithelial lining fluid

The paper in this chapter has been published as a research article in the journal Environmental Science: Atmospheres. I am the third author of this paper. I helped in the development of the kinetic model. I performed the kinetic modeling, and analyzed the results together with the co-authors. I also contributed to the writing of the paper. The supplement to this work can be found in Appendix B.5.

Dovrou, E., Lelieveld, S., Mishra, A., Pöschl, U., Berkemeier, T.: Influence of ambient and endogenous H_2O_2 on reactive oxygen species concentrations and OH radical production in the respiratory tract, *Environ. Sci.: Atmos* 3, 1066-1074, (2023).

In this study, the effects of gas-phase and particulate pollutants on the production of ROS in the epithelial lining fluid of the lung was quantified and compared to endogenous sources using the multiphase chemical kinetics model of the human epithelial lining fluid, KM-SUB-ELF. H_2O_2 concentrations in the ELF were found to be dominated by endogenous H_2O_2 production and by inhaling ambient gas-phase H_2O_2, rather than the direct chemical production by PM2.5 constituents. The model analysis revealed that the health impacts of PM2.5 may not necessarily arise from the direct chemical production of ROS, but instead via Fenton(-like) chemistry, where the transition metals convert the peroxides into the highly reactive OH radical.

Environmental Science: Atmospheres

ROYAL SOCIETY OF CHEMISTRY

PAPER

View Article Online
View Journal | View Issue

Cite this: *Environ. Sci.: Atmos.*, 2023, **3**, 1066

Influence of ambient and endogenous H_2O_2 on reactive oxygen species concentrations and OH radical production in the respiratory tract†

Eleni Dovrou,‡* Steven Lelieveld, Ashmi Mishra, Ulrich Pöschl and Thomas Berkemeier *

Air pollution is a major health risk, but the underlying chemical mechanisms are not yet well understood. Fine particulate matter (PM2.5) and gaseous pollutants can generate reactive oxygen species (ROS) in the epithelial lining fluid (ELF), and hydrogen peroxide (H_2O_2) is the most abundant ROS in the human body. Here, we show that H_2O_2 concentrations in the ELF may be primarily determined by the release of endogenous H_2O_2 and the inhalation of ambient gas-phase H_2O_2, while the chemical production of H_2O_2 through inhaled PM2.5 is less important. The production of hydroxyl radicals ($^{\bullet}OH$), however, was strongly correlated with Fenton chemistry of PM2.5 in the model calculations. Hence, our findings suggest that the adverse health effects of PM2.5 may not be primarily related to direct chemical production of H_2O_2, but rather to the conversion of peroxides into more reactive species such as the $^{\bullet}OH$ radical, or the stimulation of biological ROS production. The analysis highlights remaining uncertainties in the relevant physical, chemical and biological parameters, suggesting a critical reassessment of current paradigms in elucidating and mitigating the health effects of different types of air pollutants.

Received 19th December 2022
Accepted 28th April 2023

DOI: 10.1039/d2ea00179a

rsc.li/esatmospheres

Environmental significance

Epidemiological studies show that fine particulate matter (PM2.5) is the main component responsible for the adverse health effects of air pollution. The oxidative potential of PM2.5 is defined as its ability to produce reactive oxygen species (ROS) and it is increasingly used as a marker for the toxicity of PM2.5 in air quality monitoring and field investigations. Here, we compare and contrast the ability of PM2.5 to produce ROS in the epithelial lining fluid of the lung with the influence of ambient and endogenous hydrogen peroxide. We find that, under physiological conditions, PM2.5 may only play a minor role compared to other ROS sources, which may have far-reaching implications for the assessment of air pollution toxicity.

1. Introduction

Ambient air pollution is associated with adverse health effects and excess mortality.[1,2] Fine particulate matter (PM2.5), ozone (O_3), and nitrogen oxides ($^{\bullet}NO_x \equiv {}^{\bullet}NO$, $^{\bullet}NO_2$) have been identified as the most hazardous components of air pollution.[3,4] The causes of the toxicity of individual components and mixtures, however, remain poorly understood.[5,6] PM2.5 is a complex mixture of organic and inorganic compounds, containing, also, redox-active components such as transition metals, quinones, and highly oxidized organic molecules.[7–9] In the epithelial lining fluid (ELF) of the respiratory tract, a thin aqueous film and direct interface between air and body,[10,11] air pollutants can dissolve and undergo chemical reactions that produce reactive oxygen species (ROS), including hydrogen peroxide (H_2O_2) and oxygen-centered free radicals like the superoxide anion ($O_2^{\bullet-}$) and the hydroxyl radical ($^{\bullet}OH$).[12,13] Excessive concentrations of ROS, especially in the form of $^{\bullet}OH$, cause damage to cells and tissue, leading to oxidative stress and inflammation.[13,14] The so-called oxidative potential or the ability to produce H_2O_2 and other ROS in aqueous solution is often used as a measure for the toxicity of particulate air pollutants.[15–17] The oxidative potential of PM2.5 samples can be determined in acellular assays, which either detect the formation of ROS such as H_2O_2 and $^{\bullet}OH$ directly, or indirectly through the decay of antioxidants such as glutathione or ascorbic acid.[18,19] However, H_2O_2 is also produced in cells and tissues and formed in the ozonolysis of surfactant lipids in the ELF.[9,20–22] Additionally, it is an ubiquitous atmospheric trace gas with high water solubility. Atmospheric H_2O_2 is mainly produced *via* self-reaction of the hydroperoxyl radical ($HO_2^{\bullet}$), which is an abundant atmospheric

Multiphase Chemistry Department, Max Planck Institute for Chemistry, Mainz 55128, Germany. E-mail: dovrouel@gmail.com; t.berkemeier@mpic.de

† Electronic supplementary information (ESI) available. See DOI: https://doi.org/10.1039/d2ea00179a

‡ Present address: Institute of Chemical Engineering Sciences, Foundation for Research and Technology Hellas, Patra 26504, Greece.

radical formed in many (photo-)chemical processes (ESI Section S1†).[23,24] In contrast to H_2O_2 formation by PM2.5, the contribution of endogenous aqueous and ambient gaseous H_2O_2 to ROS concentrations in the lung is often not considered in the assessment of air pollution toxicity.[7,9,16]

In this work, we develop and apply a detailed kinetic multi-layer model of surface and bulk chemistry in the epithelial lining fluid of the respiratory tract (KM-SUB-ELF 2.0) to quantify the interplay of chemical ROS production from PM2.5 with the diffusion and exchange of H_2O_2 between the air, ELF, cellular tissues and blood vessels in the respiratory tract. Fig. 1 outlines the principal interactions of air pollutants (PM2.5, O_3, $^{\bullet}NO_2$, and H_2O_2) with radical and redox reaction cycles in the ELF and underlying tissues. H_2O_2 assumes a central position in the reaction scheme as it is an intermediate in many redox cycles and partitions to and from both the blood stream and inhaled air. Redox-active components of PM2.5 such as transition metal ions (Cu^+, Fe^{2+}) contribute to formation of H_2O_2 through production and conversion of superoxide.[7,9] H_2O_2 is efficiently buffered by enzymes such as catalase in the ELF and peroxiredoxins in the cells, but can be converted into the highly reactive and noxious $^{\bullet}OH$ radical through Fenton chemistry.[7–9] Secondary organic aerosol (SOA) is a major component of ambient PM2.5 (ref. 25 and 26) and contributes to the formation of ROS in the ELF.[8]

2. Methods

2.1 Kinetic multi-layer model

The model KM-SUB-ELF 2.0 consists of six compartments: the ambient gas phase, the gas phase of the respiratory tract, the surfactant layer, the aqueous ELF, the cellular layer, and the blood layer (Fig. 1). The model is an extended version of the model KM-SUB-ELF,[7,9] which it expands through the inclusion of the cellular layer, the blood layer, and H_2O_2 as gas-phase pollutant. The model explicitly treats inhalation from the

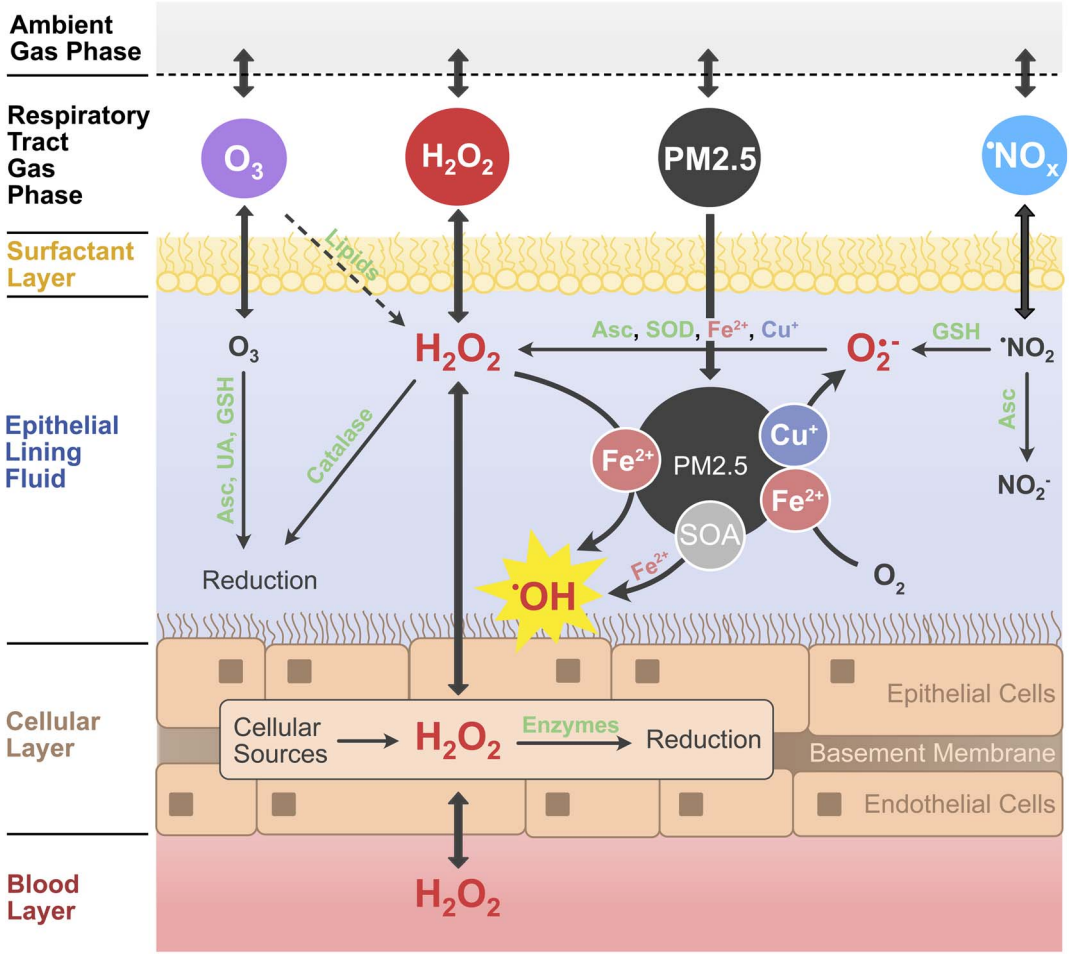

Fig. 1 Simplified schematic representation of the chemical reactions and diffusion of H_2O_2 and other air pollutants (PM2.5, $^{\bullet}NO_x$, O_3) considered in the KM-SUB-ELF 2.0 model. The model consists of five major compartments: the respiratory tract gas phase, surfactant layer, the epithelial lining fluid, a layer of cells, and blood vessels. The cell layer comprises epithelial and endothelial cells as well as an intermediary basement membrane into a single compartment. Transition metals copper (Cu) and iron (Fe) contained in PM2.5 catalyze the formation and conversion of reactive oxygen species (ROS; red font). Hydroxyl radicals ($^{\bullet}OH$) are produced from Fenton(-like) reactions of iron with H_2O_2 or organic peroxides contained within secondary organic aerosol (SOA). Antioxidants and enzymes (green font) including ascorbic acid (Asc), uric acid (UA), glutathione (GSH), superoxide dismutase (SOD), catalase, GSH peroxidase, and peroxiredoxins convert and scavenge ROS as well as oxidants such as O_3 and $^{\bullet}NO_2$.

ambient gas phase, adsorption and desorption of gas-phase molecules to and from the surfactant layer, diffusion between the surfactant layer, ELF, cells and blood vessels, as well as 131 chemical reactions across the respiratory tract gas phase, surfactant layer, aqueous ELF, and the cellular layer (Table S1†). The air pollutants considered in the model are fine particulates smaller than 2.5 μm (PM2.5) as well as $^{\bullet}NO_2$, O_3, and H_2O_2 from the gas phase. The model simulates a 2 h exposure window in which pollutants are inhaled into the gas phase of the respiratory tract with a breathing rate of 1.5 m^3 h^{-1}. A fraction of 45% of inhaled particulates is deposited into the ELF at the beginning of the exposure window. We use a standardized PM2.5 composition that was established previously using the median mass fractions of redox-active PM2.5 constituents from a large set of atmospheric field measurements.[9] The median mass fractions are 3.1×10^{-4} for copper, 8.1×10^{-3} for iron, 1.6×10^{-5} across three quinones, and 0.33 for secondary organic aerosol (SOA). For simplicity, the model does not resolve concentration gradients of gases or particulates between the upper and lower parts of the respiratory tract.

The model considers three individual quinone compounds, phenanthrenequinone, 1,2-naphthoquinone, and 1,4-naphthoquinone, which were found to be most important for ROS production in acellular assays.[7,16] Solubilities of the transition metals iron and copper are 10% and 40%, respectively, while quinones and SOA are assumed to fully dissolve. Low molecular mass antioxidants included in the model are ascorbate (Asc), glutathione (GSH), uric acid (UA), and α-tocopherol (α-Toc). The concentrations of antioxidants remained fixed during the 2 h exposure simulation. The surfactant layer consists of a surfactant lipid, 1-palmitoyl-2-oleoyl-*sn*-glycerol (POG), a surfactant protein ($SP\text{-}B_{1-25}$), and α-Toc, following Lelieveld *et al.*[9] The ozonolysis of POG in the surfactant layer yields Criegee intermediates, which are assumed to hydrolyze to H_2O_2 with a yield of 0.17.[27] Enzymatic reactions are considered within ELF and cellular compartments: superoxide dismutase (SOD) and catalase are included in ELF, while in cells a range of H_2O_2-scavenging enzymes (peroxiredoxins, catalase, GSH peroxidase) are considered. Aside from transport from the blood layer, endogenous H_2O_2 is produced at a constant rate of 1×10^{14} cm^{-3} s^{-1} inside the cellular layer.[28,29] The H_2O_2 concentration in the blood layer is held constant due to constant supply from the blood stream. A more detailed description of the model, including antioxidant concentrations, enzymatic reactions, biological ROS production rates, and the treatment of SOA can be found in the ESI (Sections S2–S5†).

The model code solves a system of ordinary differential equations using the stiff differential equation solver ode23tb in Matlab, and calculates the evolution of reactant concentrations over time. An explicit Jacobian matrix is provided to aid in computation. An overview of model input parameters is given in Tables S1–S4.†

2.2 Source apportionment of H_2O_2 and $^{\bullet}OH$ in ELF

In this study, the source apportionment of H_2O_2 in the ELF could not be achieved with traditional flux analyses, *i.e.* comparing chemical and diffusion fluxes, due to the inherent coupling of chemical reaction and diffusion in multiple compartments. Instead, we performed a sensitivity analysis and compared five scenarios in which only a single source of H_2O_2 was present in the model at a time (endogenous H_2O_2, ambient H_2O_2, $^{\bullet}NO_2$, O_3, and PM2.5) to the scenario with all sources as further detailed in the ESI (Section S6†). Note that this approach was only possible because non-linear effects were almost non-existent, *i.e.* the H_2O_2 production in scenario with all sources agrees to more than 99% with the sum of the H_2O_2 produced in the single-source scenarios. For source apportionment of $^{\bullet}OH$, a traditional flux analysis could be performed due to negligible diffusion of the reactive radical across compartment boundaries.

3. Results and discussion

The model calculations show that concentrations of H_2O_2 in ELF and cells are strongly affected by H_2O_2 mass transport through membranes and are sensitive to membrane permeability (Fig. 2A). Permeability of H_2O_2 through a single cell membrane has been reported over the large range of 10^{-6} to 10^{-3} cm s^{-1}.[30–32] H_2O_2 permeation in the respiratory tract may involve diffusion through several membranes, which requires introduction of an effective permeability, μ_{eff}, through tissue. Fig. 2A shows the computed H_2O_2 concentrations in cells and ELF as a function of μ_{eff}.

In line with previous estimations, the modelled H_2O_2 concentration in the cellular layer (~5 nM) is three orders of magnitude lower than H_2O_2 concentration in the blood (~5 μM) and four orders of magnitude lower than a liquid that is in equilibrium with the ambient gas concentration of H_2O_2 (~50 μM). The supply of H_2O_2 from inhalation, membrane transport, as well as biological and chemical production is counteracted by enzymatic H_2O_2 consumption in the cells, especially peroxiredoxins, maintaining a low cellular concentration of H_2O_2 (Fig. S1†). The cellular consumption causes the human respiratory tract to act as a net sink of ambient H_2O_2, *i.e.*, inhaled concentrations are generally larger than exhaled concentrations (Fig. S2†). This leads to very low gas-phase concentrations of H_2O_2 in the respiratory tract in the sub-ppt range (Fig. S3†).

The KM-SUB-ELF 2.0 results agree well with reported values for typical H_2O_2 concentrations in cells (1–10 nM) when μ_{eff} is smaller than 4×10^{-5} cm s^{-1} (Fig. 2A). In this range, the H_2O_2 concentration in ELF (black solid line) shows a distinct minimum at a μ_{eff} of 1×10^{-5} cm s^{-1}. This minimum marks a change in the regime of H_2O_2 supply to the ELF in the model: at $\mu_{eff} > 1 \times 10^{-5}$ cm s^{-1}, H_2O_2 is transported rapidly and predominantly from the blood, leading to high cellular and ELF concentrations (endogenous H_2O_2 regime). In contrast, at a low $\mu_{eff} < 1 \times 10^{-5}$ cm s^{-1}, the ELF is more insulated from cells and blood vessels and H_2O_2 concentration in the ELF is determined rather by inhaled H_2O_2 (ambient H_2O_2 regime). In the following, we will discuss results in terms of the central value of 1×10^{-5} cm s^{-1} for μ_{eff}.

Fig. 2B shows the attribution of the H_2O_2 concentration in ELF to its main sources in the model. The analysis is performed

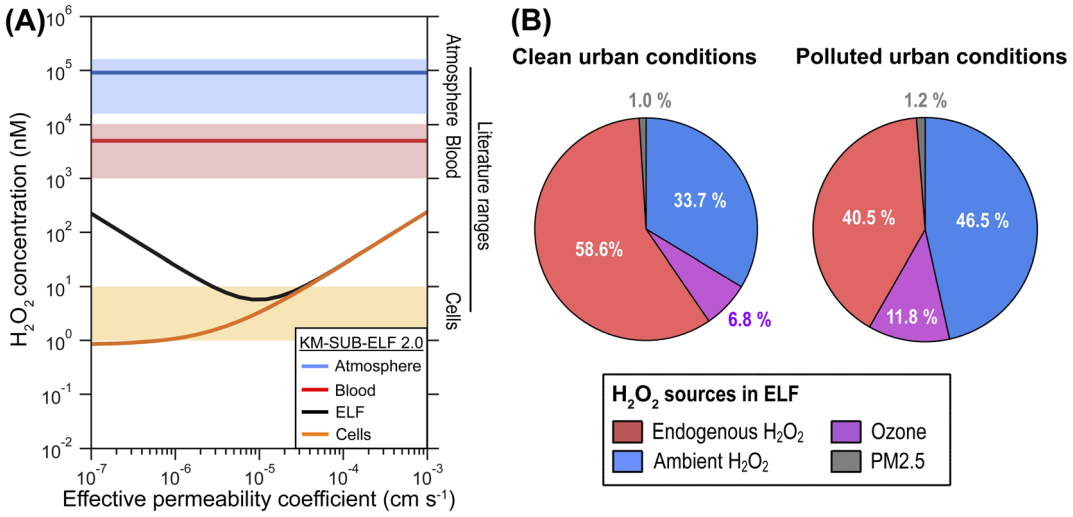

Fig. 2 Influence of membrane permeability and sources of H_2O_2 in ELF. (A) H_2O_2 concentration in blood (red line), epithelial lining fluid (ELF; black line), and cells (orange line) as a function of the effective permeability of membranes between ELF and blood layer for H_2O_2 (μ_{eff}) under ambient air pollution typical for a clean urban environment (PM2.5 = 30 μg m^{-3}, $^{\bullet}NO_2$ = 30 μg m^{-3}, O_3 = 30 ppb, H_2O_2 = 1 ppb). The blue line represents an aqueous-phase concentration of H_2O_2 in equilibrium with the ambient gas phase concentration. The blue, red and orange shaded areas represent characteristic ranges of atmospheric, blood and cellular H_2O_2 concentration reported in the literature, respectively, where physiological values represent healthy individuals (Table S1†). (B) Relative contributions of different sources to the H_2O_2 concentration in ELF at a μ_{eff} of 1×10^{-5} cm s^{-1} for two ambient pollution scenarios: clean urban conditions (PM2.5 = 30 μg m^{-3}, $^{\bullet}NO_2$ = 30 μg m^{-3}, O_3 = 30 ppb, H_2O_2 = 1 ppb) and polluted urban conditions (PM2.5 = 60 μg m^{-3}, $^{\bullet}NO_2$ = 60 μg m^{-3}, O_3 = 75 ppb, H_2O_2 = 2 ppb).

for two different air pollution scenarios. Under clean urban conditions, H_2O_2 originates mostly from gas-phase and endogenous sources with 33.7% and 58.6%, respectively (Fig. 2B). The endogenous sources include transport from the blood stream and production of H_2O_2 in the cellular layer. The reaction of O_3 with surfactant lipids accounts for 6.8% of H_2O_2 production. Only a minor portion, 1%, is due to production by constituents of PM2.5. In the scenario reflecting polluted urban conditions, elevated ambient gas-phase H_2O_2 levels contribute strongest to the H_2O_2 concentration in ELF at 46.5%. The contribution of O_3 increases to 11.8% while the contribution of PM2.5 constituents remains minor at 1.2%. $^{\bullet}NO_x$ (in the form of $^{\bullet}NO_2$) shows only negligible contributions (<0.1%) to H_2O_2 in both scenarios. Even higher pollution levels can be observed during haze events in megacities.[33] Under such conditions (PM2.5 = 300 μg m^{-3}),[34,35] the contribution of PM2.5 constituents can reach 10% in the model calculations (Fig. S4†). We note that these numbers must be interpreted as averages over the entire respiratory tract and concentrations of the water-soluble gases H_2O_2 and O_3 will be higher in the upper parts of the respiratory tract,[36] which likely decreases their importance for the deep lung as detailed in the ESI (Section S7†). A very sensitive and rather uncertain model parameter in these calculations is the cellular production rate of H_2O_2, for which we can give only an order of magnitude estimate as detailed in the ESI (Section S4†), and which may dominate H_2O_2 sources at higher values (Fig. S4d†).

Fig. 3A shows the influence of ambient gas-phase H_2O_2 and PM2.5 levels on H_2O_2 concentration in the ELF for a range of ambient conditions. The predominantly horizontal contour lines indicate that increasing ambient H_2O_2 has a direct effect on the aqueous peroxide concentration in the ELF, while the influence of PM2.5 becomes evident only at very high mass loadings. In contrast, $^{\bullet}OH$ production is primarily driven by PM2.5 levels in the model, as indicated by predominantly vertical contour lines in Fig. 3B. The secondary influence of ambient H_2O_2 becomes evident when levels exceed typical atmospheric values of 0–5 ppb. The concentration of H_2O_2 in the blood has a similar influence on model results as the ambient H_2O_2 concentration (Fig. S5†). These model results, however, are highly dependent on the choice of the effective membrane permeability coefficient μ_{eff} as discussed in Section S8† and shown in Fig. S5 and S6 of the ESI.†

Fig. 3 also presents H_2O_2 concentrations (Fig. 3C) and $^{\bullet}OH$ production (Fig. 3D) for six selected scenarios of typical atmospheric conditions (Table S2†). We find that remote, rural, and indoor air is associated with the lowest H_2O_2 concentrations and $^{\bullet}OH$ production. High ambient gas-phase H_2O_2 in polluted urban air may cause slightly elevated H_2O_2 concentrations in ELF, while the high PM2.5 levels may cause significantly increased $^{\bullet}OH$ production. In a heavily cleaned indoor space, very high ambient gas-phase H_2O_2 may not only control the H_2O_2 concentrations in ELF, but may also raise $^{\bullet}OH$ production due to Fenton chemistry of H_2O_2. This scenario is in the ambient H_2O_2 regime, while the other scenarios are in the transition range between the ambient H_2O_2 and endogenous H_2O_2 regime. Variation of PM2.5 concentration for all scenarios (solid grey lines in Fig. 3D) reveals a steeper slope and thus a stronger sensitivity to PM2.5 in the heavily cleaned indoor space compared to the other scenarios. This result shows that ambient gas-phase H_2O_2 can synergistically increase the $^{\bullet}OH$ production capability of PM2.5 and suggests a non-linear effect

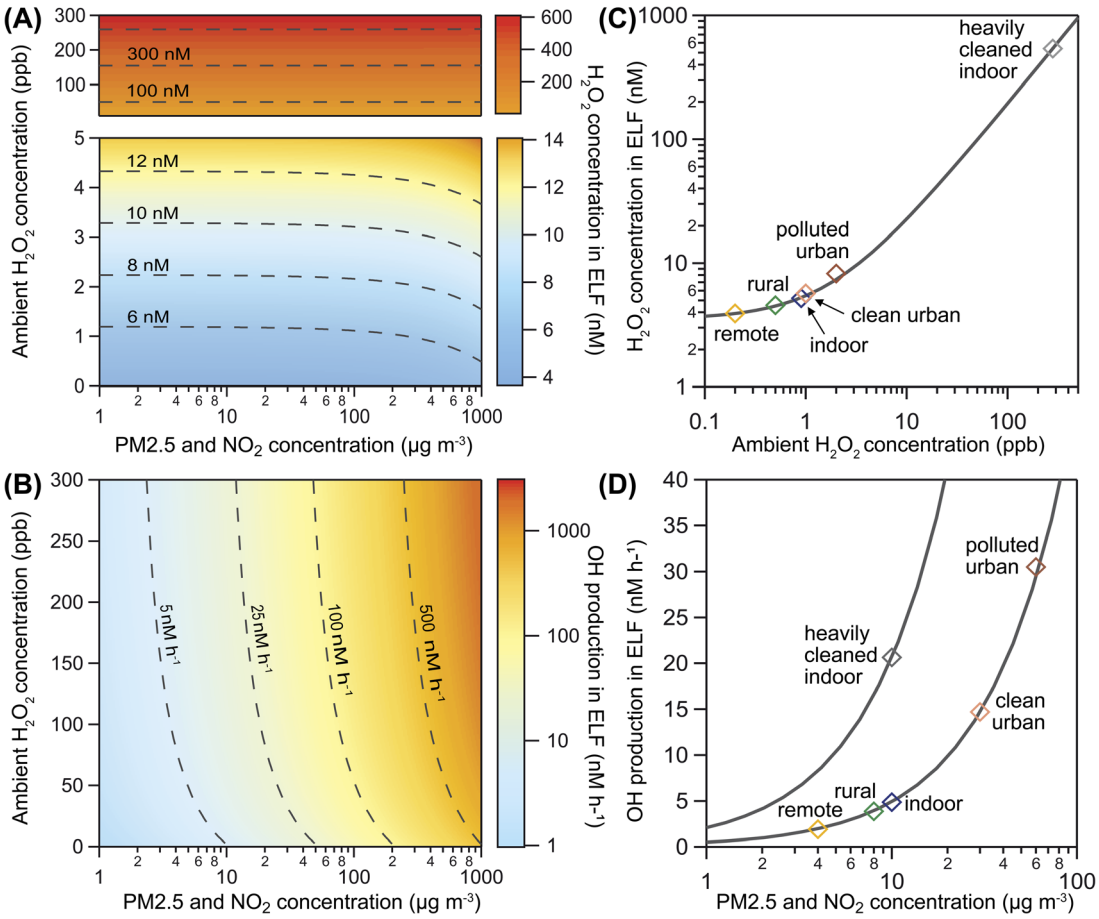

Fig. 3 H_2O_2 concentration and ˙OH production in ELF. (A) H_2O_2 concentration in ELF and (B) ˙OH production in ELF as a function of ambient gas-phase H_2O_2 and PM2.5 levels. Dashed contour lines indicate conditions that lead to the same model outcome. (C) H_2O_2 concentrations in ELF and (D) ˙OH production in ELF for six selected air pollution scenarios (markers). Solid lines indicate the sensitivity due to variation of only ambient gas-phase H_2O_2 (panel C, one scenario representative for all) and PM2.5 levels (panel D, two representative scenarios).

on oxidative stress upon exposure to both pollutants. Because of the high water solubility and efficient enzymatic removal of H_2O_2, we expect this effect to be most relevant in the upper respiratory tract.

The model KM-SUB-ELF 2.0 applied in this study yields H_2O_2 concentration levels (~5 nM) lower than reported in earlier studies that did not consider cellular H_2O_2 sinks (~100 nM)[7,9] and lower than measurements of exhaled breath condensate or bronchoalveolar lavage fluid (~100–1000 nM).[37–40] The deviation from measurements may be due to an underestimation of the H_2O_2 production rate of epithelial cells (ESI Section S4†) or a missing endogenous source of ROS, possibly superoxide production by alveolar macrophages,[41] which will be further investigated in a follow-up study. This follow-up study will also address the gradients of water-soluble trace gases between the upper and lower respiratory tract. Both aspects may reconcile the agreement with measurement data and would decrease the importance of ambient H_2O_2 for the deep lung. First preliminary estimations are outlined and discussed in ESI Section S7.† The main conclusion of this study that aqueous-phase chemistry of PM2.5 does not have a large contribution to the H_2O_2 concentration in ELF, remains unchanged (Fig. S4†).

The principal source of ˙OH among PM2.5 constituents, however, is directly affected by the H_2O_2 concentration in the ELF. At a low H_2O_2 concentration, ˙OH is produced predominantly through Fenton-like reactions of the organic peroxides contained in SOA (Fig. S7†), which may be labile and decay with a short half-life[42] or follow a similar chemistry to H_2O_2 by forming ˙OH radicals in reactions with transition metals and water.[8] In contrast, previous analyses of ELF redox chemistry identified the Fenton reaction of H_2O_2 as dominant ˙OH source, albeit at higher H_2O_2 concentrations in the ELF.[7,9,15] We note that the relative contribution of the individual pathways not only depends upon the H_2O_2 concentration in the ELF, but may also vary with the exact composition of PM2.5 and the aqueous-phase chemistry of SOA (Fig. S8†). SOA has a highly complex and variable composition and quantitative ˙OH yields from SOA samples in epithelial lining fluid have only been reported by a few studies.[8,12,43] Furthermore, organic peroxides inhaled through SOA may also be scavenged by enzymes such as peroxiredoxins and peroxidases before significant conversion to ˙OH occurs.[44,45] This gap between the potential high importance of SOA in air pollution health effects and the lack of quantitative kinetic data highlights the need for further studies under

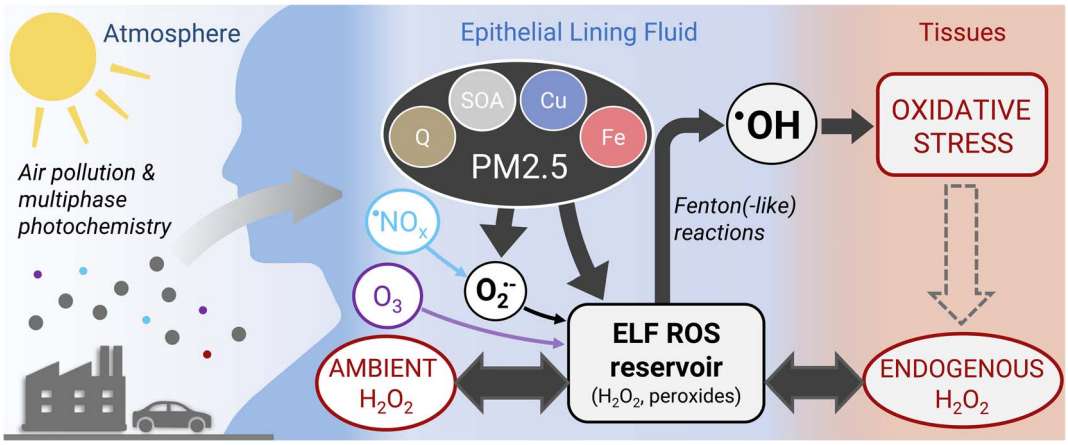

Fig. 4 Health effects of atmospheric air pollution. The epithelial lining fluid (ELF) is a thin aqueous film at the air–body interface in which inhaled air pollutants dissolve and deposit. H_2O_2 and other peroxides form a reservoir of reactive oxygen species (ROS) in the ELF. H_2O_2 levels in the ELF are controlled by endogenous processes (endogenous H_2O_2 regime) or inhalation of gas-phase H_2O_2 (ambient H_2O_2 regime). A small fraction of H_2O_2 originates from conversion of superoxide ($O_2^{\bullet-}$) generated from interaction of fine particulate matter (PM2.5) and nitrogen oxides ($^{\bullet}NO_x$) with ELF. Other peroxides are supplied through secondary organic aerosol (SOA) contained within PM2.5 or by chemical reactions of ozone (O_3). Transition metal-mediated, catalytic conversion of peroxides leads to formation of the highly reactive $^{\bullet}OH$ radical that can trigger oxidative stress and, ultimately, cell death.

controlled conditions to assess the relative importance of these two major $^{\bullet}OH$ production channels.

4. Conclusions

The model simulations in this study show that under typical atmospheric pollution scenarios, the concentration of H_2O_2 in the respiratory tract is dictated by endogenous sources and ambient gas phase sources (H_2O_2 and O_3) with similar contributions. However, a recent study suggests that macrophages contribute to ROS levels in the ELF through release of superoxide, which can be significantly enhanced through stimulation with PM2.5 constituents.[41] Such an additional source of ROS, which is outside the scope of this study, may tip the scales fully in favor of endogenous sources of H_2O_2. Air pollution-induced changes of H_2O_2 concentration in the ELF thus may only be achieved directly during severe haze events, heavy indoor cleaning, or indirectly through stimulation of macrophages causing enhanced endogenous release of superoxide. As superoxide and H_2O_2 in ELF are likely dominated by endogenous sources, direct chemical production of superoxide and H_2O_2 may only play a secondary role in the adverse effects of fine particulate matter (PM2.5).

Acellular oxidative potential assays, which are commonly used to assess potential PM2.5 toxicity, tend to be sensitive to superoxide and H_2O_2 producers such as copper ions and quinones.[46] However, the findings in this study challenge the view that adverse health effects of PM2.5 are closely related to their ability of increasing ROS concentrations in the lungs. ROS are already ubiquitous in the human body, primarily in the form of H_2O_2, which can diffuse readily through tissues and epithelial lining fluid.[47] In the ELF, H_2O_2 and other peroxides form a reservoir of ROS, which is tightly controlled by endogenous processes (Fig. 4). The model simulations in this study show that PM2.5 acts by conversion of peroxides into highly reactive $^{\bullet}OH$ radicals that cause oxidative stress and damage to cells and tissues. PM2.5 may further act by stimulating the production of superoxide from endogenous sources. We therefore propose that chemical production of superoxide and H_2O_2 in a cell-free assay may not be a suitable metric for assessing the differential toxicity of individual PM2.5 components and some acellular oxidative potential assays may not capture the actual deleterious effects of PM2.5. Alternatives may be cellular cytotoxicity assays using air–liquid interface cell culture[48] or acellular assays determining the production of $^{\bullet}OH$ radicals,[49] preferably in the presence of physiological concentrations of H_2O_2.

Oxidative stress and disease may alter the physiological properties and redox homeostasis in the respiratory tract through effects on membrane permeability, enzyme expression, and pH value.[50] This may further increase the susceptibility of diseased individuals to air pollution in the form of PM2.5 and trigger reinforcing feedback loops.[51] Further investigations will be required to resolve such biological feedbacks, the differential toxicity of individual air pollutants from different sources (traffic, combustion *etc.*), and the cumulative effects of long-term exposure.

Author contributions

Conceptualization: E. D., S. L., U. P. and T. B., methodology: all authors, numerical simulation and validation: E. D., S. L., A. M., and T. B., formal analysis: E. D. and T. B. with assistance from S. L. and A. M., visualization: E. D., S. L., U. P. and T. B., writing–original draft: E. D. and T. B., writing–review and editing: all authors.

Conflicts of interest

There are no conflicts to declare.

Acknowledgements

This work was funded by the Max Planck Society. A. M. and S. L. were supported by the Max Planck Graduate Center with the Johannes Gutenberg-Universität Mainz (MPGC). We gratefully acknowledge Helmut Sies and Roel P. F. Schins for helpful discussions. Open Access funding provided by the Max Planck Society.

Notes and references

1 J. Lelieveld, J. S. Evans, M. Fnais, D. Giannadaki and A. Pozzer, The contribution of outdoor air pollution sources to premature mortality on a global scale, *Nature*, 2015, **525**, 367–371.

2 R. Burnett, H. Chen, M. Szyszkowicz, N. Fann, B. Hubbell, C. A. Pope, J. S. Apte, M. Brauer, A. Cohen, S. Weichenthal, J. Coggins, Q. Di, B. Brunekreef, J. Frostad, S. S. Lim, H. Kan, K. D. Walker, G. D. Thurston, R. B. Hayes, C. C. Lim, M. C. Turner, M. Jerrett, D. Krewski, S. M. Gapstur, W. R. Diver, B. Ostro, D. Goldberg, D. L. Crouse, R. V. Martin, P. Peters, L. Pinault, M. Tjepkema, A. Van Donkelaar, P. J. Villeneuve, A. B. Miller, P. Yin, M. Zhou, L. Wang, N. A. H. Janssen, M. Marra, R. W. Atkinson, H. Tsang, T. Q. Thach, J. B. Cannon, R. T. Allen, J. E. Hart, F. Laden, G. Cesaroni, F. Forastiere, G. Weinmayr, A. Jaensch, G. Nagel, H. Concin and J. V. Spadaro, Global estimates of mortality associated with longterm exposure to outdoor fine particulate matter, *Proc. Natl. Acad. Sci. U. S. A.*, 2018, **115**, 9592–9597.

3 T. Chen, J. Gokhale, S. Shofer and W. G. Kuschner, Outdoor Air Pollution : Nitrogen Dioxide , Sulfur Dioxide , and Carbon Monoxide Health Effects, *Med. Sci.*, 1994, **333**, 249–256.

4 T. Fang, P. S. J. Lakey, J. C. Rivera-Rios, F. N. Keutsch and M. Shiraiwa, Aqueous-Phase Decomposition of Isoprene Hydroxy Hydroperoxide and Hydroxyl Radical Formation by Fenton-like Reactions with Iron Ions, *J. Phys. Chem. A*, 2020, **124**, 5230–5236.

5 J. Lelieveld and U. Pöschl, the Air-Pollution Health Crisis, *Nat. Commun.*, 2017, **551**, 291–293.

6 J. J. West, A. Cohen, F. Dentener, B. Brunekreef, T. Zhu, B. Armstrong, M. L. Bell, M. Brauer, G. Carmichael, D. L. Costa, D. W. Dockery, M. Kleeman, M. Krzyzanowski, N. Künzli, C. Liousse, S. C. C. Lung, R. V. Martin, U. Pöschl, C. A. Pope, J. M. Roberts, A. G. Russell and C. Wiedinmyer, What We Breathe Impacts Our Health: Improving Understanding of the Link between Air Pollution and Health, *Environ. Sci. Technol.*, 2016, **50**, 4895–4904.

7 P. S. J. Lakey, T. Berkemeier, H. Tong, A. M. Arangio, K. Lucas, U. Pöschl and M. Shiraiwa, Chemical exposure-response relationship between air pollutants and reactive oxygen species in the human respiratory tract, *Sci. Rep.*, 2016, **6**, 1–6.

8 H. Tong, A. M. Arangio, P. S. J. Lakey, T. Berkemeier, F. Liu, C. J. Kampf, W. H. Brune, U. Poschl and M. Shiraiwa, Hydroxyl radicals from secondary organic aerosol decomposition in water, *Atmos. Chem. Phys.*, 2016, **16**, 1761–1771.

9 S. Lelieveld, J. Wilson, E. Dovrou, A. Mishra, P. S. J. Lakey, M. Shiraiwa, U. Pöschl and T. Berkemeier, Hydroxyl Radical Production by Air Pollutants in Epithelial Lining Fluid Governed by Interconversion and Scavenging of Reactive Oxygen Species, *Environ. Sci. Technol.*, 2021, **55**, 14069–14079.

10 K. A. Jellinger, Neuroproteomics Methods and Protocols, *Eur. J. Neurol.*, 2010, **17**, e33.

11 K. A. Rodvold, M. H. Gotfried, J. G. Still, K. Clark and P. Fernandes, Comparison of plasma, epithelial lining fluid, and alveolar macrophage concentrations of solithromycin (CEM-101) in healthy adult subjects, *Antimicrob. Agents Chemother.*, 2012, **56**, 5076–5081.

12 J. Wei, T. Fang, P. S. J. Lakey and M. Shiraiwa, Iron-Facilitated Organic Radical Formation from Secondary Organic Aerosols in Surrogate Lung Fluid, *Environ. Sci. Technol.*, 2022, **56**(11), 7234–7243.

13 H. Sies, Hydrogen peroxide as a central redox signaling molecule in physiological oxidative stress: Oxidative eustress, *Redox Biol.*, 2017, **11**, 613–619.

14 A. Peters, T. S. Nawrot and A. A. Baccarelli, Hallmarks of environmental insults, *Cell*, 2021, **184**, 1455–1468.

15 T. Fang, P. S. J. Lakey, R. J. Weber and M. Shiraiwa, Oxidative Potential of Particulate Matter and Generation of Reactive Oxygen Species in Epithelial Lining Fluid, *Environ. Sci. Technol.*, 2019, **53**, 12784–12792.

16 J. G. Charrier, A. S. McFall, N. K. Richards-Henderson and C. Anastasio, Hydrogen peroxide formation in a surrogate lung fluid by transition metals and quinones present in particulate matter, *Environ. Sci. Technol.*, 2014, **48**, 7010–7017.

17 H. Sakugawa, I. R. Kaplan, W. Tsai and Y. Cohen, Atmospheric hydrogen peroxide, *Environ. Sci. Technol.*, 1990, **24**, 1452–1462.

18 P. Shahpoury, Z. Zhang, A. Filippi, S. Hildmann, S. Lelieveld, B. R. Patel, A. Traub, D. Umbrio, M. Wietzoreck, J. Wilson, T. Berkemeier, V. Celo, E. Dabek-Zlotorzynska, G. Evans, T. Harner, K. Kerman, G. Lammel, M. Noroozifar, U. Pöschl and H. Tong, Inter-comparison of oxidative potential metrics for airborne particles identifies differences between acellular chemical assays, *Atmos. Pollut. Res.*, 2022, **13**, 1–14.

19 J. T. Bates, T. Fang, V. Verma, L. Zeng, R. J. Weber, P. E. Tolbert, J. Y. Abrams, S. E. Sarnat, M. Klein, J. A. Mulholland and A. G. Russell, Review of Acellular Assays of Ambient Particulate Matter Oxidative Potential: Methods and Relationships with Composition, Sources, and Health Effects, *Environ. Sci. Technol.*, 2019, **53**, 4003–4019.

20 H. Sies, C. Berndt and D. P. Jones, Oxidative stress, *Annu. Rev. Biochem.*, 2017, **86**, 715–748.

21 P. Neeb, F. Sauer, O. Horie and G. K. Moortgat, Formation of hydroxymethyl hydroperoxide and formic acid in alkene

ozonolysis in the presence of water vapour, *Atmos. Environ.*, 1997, **31**, 1417–1423.

22 M. Zeng, N. Heine and K. R. Wilson, Evidence that criegee intermediates drive autoxidation in unsaturated lipids, *Proc. Natl. Acad. Sci. U. S. A.*, 2020, **117**, 4486–4490.

23 D. Vione, V. Maurino, C. Minero and E. Pelizzetti, The atmospheric chemistry of hydrogen peroxide: A review, *Ann. Chim.*, 2003, **93**, 477–488.

24 J. H. Seinfeld and S. N. Pandis, *Atmospheric Chemistry and Physics: from Air Pollution to Climate Change*, 3rd edn, 2016.

25 J. L. Jimenez, M. R. Canagaratna, N. M. Donahue, A. S. H. Prevot, Q. Zhang, J. H. Kroll, P. F. DeCarlo, J. D. Allan, H. Coe, N. L. Ng, A. C. Aiken, K. S. Docherty, I. M. Ulbrich, A. P. Grieshop, A. L. Robinson, J. Duplissy, J. D. Smith, K. R. Wilson, V. A. Lanz, C. Hueglin, Y. L. Sun, J. Tian, A. Laaksonen, T. Raatikainen, J. Rautiainen, P. Vaattovaara, M. Ehn, M. Kulmala, J. M. Tomlinson, D. R. Collins, M. J. Cubison, E. J. Dunlea, J. A. Huffman, T. B. Onasch, M. R. Alfarra, P. I. Williams, K. Bower, Y. Kondo, J. Schneider, F. Drewnick, S. Borrmann, S. Weimer, K. Demerjian, D. Salcedo, L. Cottrell, R. Griffin, A. Takami, T. Miyoshi, S. Hatakeyama, A. Shimono, J. Y. Sun, Y. M. Zhang, K. Dzepina, J. R. Kimmel, D. Sueper, J. T. Jayne, S. C. Herndon, A. M. Trimborn, L. R. Williams, E. C. Wood, A. M. Middlebrook, C. E. Kolb, U. Baltensperger and D. R. Worsnop, Evolution of organic aerosols in the atmosphere, *Science*, 2009, **326**, 1525–1529.

26 M. Hallquist, J. C. Wenger, U. Baltensperger, Y. Rudich, D. Simpson, M. Claeys, J. Dommen, N. M. Donahue, C. George, A. H. Goldstein, J. F. Hamilton, H. Herrmann, T. Hoffmann, Y. Iinuma, M. Jang, M. E. Jenkin, J. L. Jimenez, A. Kiendler-Scharr, W. Maenhaut, G. McFiggans, T. F. Mentel, A. Monod, A. S. H. Prévôt, J. H. Seinfeld, J. D. Surratt, R. Szmigielski and J. Wildt, The formation, properties and impact of secondary organic aerosol: Current and emerging issues, *Atmos. Chem. Phys.*, 2009, **9**, 5155–5236.

27 Z. Zhou and J. P. D. Abbatt, Formation of Gas-Phase Hydrogen Peroxide via Multiphase Ozonolysis of Unsaturated Lipids, *Environ. Sci. Technol. Lett.*, 2021, **8**, 114–120.

28 V. L. Kinnula, J. I. Everitt, A. R. Whorton and J. D. Crapo, Hydrogen peroxide production by alveolar type II cells, alveolar macrophages, and endothelial cells, *Am. J. Physiol.: Lung Cell. Mol. Physiol.*, 1991, **261**, L84–L91.

29 W. J. Piotrowski, J. Marczak, D. Dinsdale, Z. Kurmanowska, Y. Tarasow, J. Komos and D. Nowak, Release of hydrogen peroxide by rat type II pneumocytes in the prolonged culture, *Toxicol. In Vitro*, 2000, **14**, 85–93.

30 G. P. Bienert, J. K. Schjoerring and T. P. Jahn, Membrane transport of hydrogen peroxide, *Biochim. Biophys. Acta, Biomembr.*, 2006, **1758**, 994–1003.

31 D. Wragg, S. Leoni and A. Casini, Aquaporin-driven hydrogen peroxide transport: a case of molecular mimicry?, *RSC Chem. Biol.*, 2020, **1**, 390–394.

32 F. Orrico, A. C. Lopez, D. Saliwonczyk, C. Acosta, I. Rodriguez-Grecco, I. Mouro-Chanteloup, M. A. Ostuni, A. Denicola, L. Thomson and M. N. Möller, The permeability of human red blood cell membranes to hydrogen peroxide is independent of aquaporins, *J. Biol. Chem.*, 2022, **298**, 101503.

33 K. Li, D. J. Jacob, H. Liao, Y. Qiu, L. Shen, S. Zhai, K. H. Bates, M. P. Sulprizio, S. Song, X. Lu, Q. Zhang, B. Zheng, Y. Zhang, J. Zhang, H. C. Lee and S. K. Kuk, Ozone pollution in the North China Plain spreading into the late-winter haze season, *Proc. Natl. Acad. Sci. U. S. A.*, 2021, **118**, 1–7.

34 Z. Rao, Z. Chen, H. Liang, L. Huang and D. Huang, Carbonyl compounds over urban Beijing: Concentrations on haze and non-haze days and effects on radical chemistry, *Atmos. Environ.*, 2016, **124**, 207–216.

35 C. Ye, P. Liu, Z. Ma, C. Xue, C. Zhang, Y. Zhang, J. Liu, C. Liu, X. Sun and Y. Mu, High H2O2 Concentrations Observed during Haze Periods during the Winter in Beijing: Importance of H2O2 Oxidation in Sulfate Formation, *Environ. Sci. Technol. Lett.*, 2018, **5**, 757–763.

36 M. P. Hlastala, F. L. Powell and J. C. Anderson, Airway exchange of highly soluble gases, *J. Appl. Physiol.*, 2013, **114**, 675–680.

37 T. Kakeshpour, B. Metaferia, R. N. Zare and A. Bax, Quantitative detection of hydrogen peroxide in rain, air, exhaled breath, and biological fluids by NMR spectroscopy, *Proc. Natl. Acad. Sci. U. S. A.*, 2022, **119**, 1–3.

38 W. B. Gerritsen, P. Zanen, A. A. Bauwens, J. M. van den Bosch and F. J. Haas, Validation of a new method to measure hydrogen peroxide in exhaled breath condensate, *Respir. Med.*, 2005, **99**, 1132–1137.

39 M. Corradi, P. Pignatti, G. Brunetti, M. Goldoni, A. Caglieri, S. Nava, G. Moscato and B. Balbi, Comparison between exhaled and bronchoalveolar lavage levels of hydrogen peroxide in patients with diffuse interstitial lung diseases, *Acta Bio Med. Atenei Parmensis*, 2008, **79**, 73–78.

40 A. S. Jackson, A. Sandrini, C. Campbell, S. Chow, P. S. Thomas and D. H. Yates, Comparison of biomarkers in exhaled breath condensate and bronchoalveolar lavage, *Am. J. Respir. Crit. Care Med.*, 2007, **175**, 222–227.

41 T. Fang, Y. Huang, J. Wei, J. E. M. Mena, P. S. J. Lakey, M. T. Kleinman, M. A. Digman and M. Shiraiwa, Superoxide Release by Macrophages through NADPH Oxidase Activation Dominating Chemistry by Isoprene Secondary Organic Aerosols and Quinones to Cause Oxidative Damage on Membranes, *Environ. Sci. Technol.*, 2022, **56**(23), 17029–17038.

42 M. Krapf, I. El Haddad, E. A. Bruns, U. Molteni, K. R. Daellenbach, A. S. H. Prévôt, U. Baltensperger and J. Dommen, Labile Peroxides in Secondary Organic Aerosol, *Chem*, 2016, **1**, 603–616.

43 J. Wei, T. Fang, C. Wong, P. S. J. Lakey, S. A. Nizkorodov and M. Shiraiwa, Superoxide Formation from Aqueous Reactions of Biogenic Secondary Organic Aerosols, *Environ. Sci. Technol.*, 2021, **55**, 260–270.

44 L. B. Poole, A. Hall and K. J. Nelson, Overview of peroxiredoxins in oxidant defense and redox regulation, *Curr. Protoc. Toxicol.*, 2011, **7.9**, 1–20.

45 V. L. Kinnula, S. Lehtonen, R. Kaarteenaho-Wiik, E. Lakari, P. Pääkkö, S. W. Kang, S. G. Rhee and Y. Soini, Cell specific expression of peroxiredoxins in human lung and pulmonary sarcoidosis, *Thorax*, 2002, **57**, 157–164.

46 J. G. Charrier and C. Anastasio, On dithiothreitol (DTT) as a measure of oxidative potential for ambient particles: evidence for the importance of soluble transition metals, *Atmos. Chem. Phys.*, 2012, **12**(5), 11317–11350.

47 C. C. Winterbourn, Reconciling the chemistry and biology of reactive oxygen species, *Nat. Chem. Biol.*, 2008, **4**, 278–286.

48 G. Lacroix, W. Koch, D. Ritter, A. C. Gutleb, S. T. Larsen, T. Loret, F. Zanetti, S. Constant, S. Chortarea, B. Rothen-Rutishauser, P. S. Hiemstra, E. Frejafon, P. Hubert, L. Gribaldo, P. Kearns, J. M. Aublant, S. Diabaté, C. Weiss, A. De Groot and I. Kooter, Air-Liquid Interface in Vitro Models for Respiratory Toxicology Research: Consensus Workshop and Recommendations, *Appl. In Vitro Toxicol.*, 2018, **4**, 91–106.

49 D. H. Gonzalez, D. A. Diaz, J. P. Baumann, A. J. Ghio and S. E. Paulson, Effects of albumin, transferrin and humic-like substances on iron-mediated OH radical formation in human lung fluids, *Free Radical Biol. Med.*, 2021, **165**, 79–87.

50 L. K. Rogers, M. J. Cismowski, C. Ohio and C. Ohio, *HHS Public Access*, 2019, 37–43.

51 K. Ziegler, A. T. Kunert, K. Reinmuth-selzle, A. Lena, D. Widera, M. G. Weller, D. Schuppan, J. Fröhlich-nowoisky, K. Lucas and U. Pöschl, Redox Biology Chemical modi fi cation of pro-in fl ammatory proteins by peroxynitrite increases activation of TLR4 and NF- κ B : Implications for the health e ff ects of air pollution and oxidative stress, *Redox Biol.*, 2020, **37**, 1–9.

3. Conclusions and outlook

This PhD project focused on the application of kinetic flux models of multiphase chemistry to quantify the production of reactive oxygen species (ROS) in atmospheric aerosols and in the epithelial lining fluid. Computational tools were used to analyze model behavior, enabling the determination of kinetic parameters like chemical reaction rate coefficients as well as diffusion coefficients in multiphase systems. These tools were used to accurately simulate gas uptake by iron-carboxylates during photochemical aging at various phase states between liquid, semi-solid, and solid. The newly developed model serves as a basis to further explore the interplay between ROS, transition metal ions and secondary organic aerosol components during photochemical aging and to investigate how this interplay may affect the budget of important trace gas species, such as NO_2. Moreover, the model may also be used to explore the chemistry of Fe with other transition metals present in the particles, such as Cu.

A detailed chemical kinetics model of aerosol oxidative potential was developed, which enables the attribution of chemical reactions responsible for the observed effects of particulate matter (PM) on different OP assays. The model describes the interaction of ROS, SOA, transition metals, quinones, and antioxidant probes across a large set of laboratory data from various research groups. The model was further applied to field measurement data of PM composition and OP at three different sites in Europe and showed good agreement with measurement data. KM-OP may be able to bridge the gap between PM chemical composition and epidemiological health assessments when developing new regulatory metrics (El Haddad et al., 2024).

The kinetic models enabled the quantification of protein modification in the lung due to ambient air pollutants and biological oxidants. Model analysis indicated that fine particulate matter and nitrogen dioxide show synergistic effects in the production of nitrotyrosine (Ntyr). Furthermore, the model analysis showed that ozone was mostly a burden on the antioxidants but did not considerably impact the Ntyr concentration. These results from the kinetic model can be used as a basis for experimental design in systems that include air pollutants, proteins, and antioxidants to test and further improve the mechanistic understanding of health impacts of air pollution.

Finally, the computational tools enabled the accurate description of oleic acid decay during ozonolysis reaction across a large dataset. This dataset encompassed an extensive range of ozone concentrations and particle sizes and was collected using various experimental approaches and multiple detection methods. The majority of the experimental data were reconciled with ensembles of multiphase chemical kinetic parameter sets. Moreover, the mechanistic insights gained from the ozonolysis of oleic

acid can also be used in kinetic models of the epithelial lining fluid to assess the health effects of ozone in the lung surfactant layer, which contains unsaturated fatty acids.

Hence, kinetic models were used to describe highly complex systems, which enabled the determination of multiple sets of kinetic parameters. However, a remaining problem in such studies is the unique determination of these parameters. To this end, future work should include additional experiments where multiple observables are measured under distinct experimental scenarios to constrain the model further, and to determine unique kinetic parameters (Krüger et al., 2024).

4. Bibliography

Abbatt, J. P. D. and Ravishankara, A. R.: Opinion: Atmospheric multiphase chemistry – past, present, and future, Atmos. Chem. Phys., 23, 9765–9785, 2023.

Abbatt, J. P. D., Lee, A. K. Y., and Thornton, J. A.: Quantifying trace gas uptake to tropospheric aerosol: recent advances and remaining challenges, Chem. Soc. Rev., 41, 6555–6581, 2012.

Abrams, J. Y., Weber, R. J., Klein, M., Samat, S. E., Chang, H. H., Strickland, M. J., Verma, V., Fang, T., Bates, J. T., Mulholland, J. A., Russell, A. G., and Tolbert, P. E.: Associations between Ambient Fine Particulate Oxidative Potential and Cardiorespiratory Emergency Department Visits, Environ. Health Perspect., 125, 107 008, 2017.

Achakulwisut, P., Brauer, M., Hystad, P., and Anenberg, S. C.: Global, national, and urban burdens of paediatric asthma incidence attributable to ambient NO2 pollution: estimates from global datasets, Lancet Planet. Health, 3, e166–e178, 2019.

Adebiyi, A., Kok, J. F., Murray, B. J., Ryder, C. L., Stuut, J.-B. W., Kahn, R. A., Knippertz, P., Formenti, P., Mahowald, N. M., Pérez García-Pando, C., Klose, M., Ansmann, A., Samset, B. H., Ito, A., Balkanski, Y., Di Biagio, C., Romanias, M. N., Huang, Y., and Meng, J.: A review of coarse mineral dust in the Earth system, Aeolian Res., 60, 100 849, 2023.

Al-Abadleh, H. A.: Iron content in aerosol particles and its impact on atmospheric chemistry, Chem. Commun., 60, 1840–1855, 2024.

Al-Kindi, S. S., Pope, F. D., Beddows, D. C., Bloss, W. J., and Harrison, R. M.: Size-dependent chemical ageing of oleic acid aerosol under dry and humidified conditions, Atmos. Chem. Phys., 16, 15 561–15 579, 2016.

Alpert, P. A., Dou, J., Corral Arroyo, P., Schneider, F., Xto, J., Luo, B., Peter, T., Huthwelker, T., Borca, C. N., Henzler, K. D., Schaefer, T., Herrmann, H., Raabe, J., Watts, B., Krieger, U. K., and Ammann, M.: Photolytic radical persistence due to anoxia in viscous aerosol particles, Nat. Commun., 12, 1769, 2021.

Andreae, M. and Rosenfeld, D.: Aerosol–cloud–precipitation interactions. Part 1. The nature and sources of cloud-active aerosols, Earth-Sci. Rev., 89, 13–41, 2008.

Andreae, M. O.: Aerosols Before Pollution, Science, 315, 50–51, 2007.

Apte, J. S., Marshall, J. D., Cohen, A. J., and Brauer, M.: Addressing Global Mortality from Ambient $PM_{2.5}$, Environ. Sci. Technol., 49, 8057–8066, 2015.

Atkinson, R. and Arey, J.: Atmospheric Degradation of Volatile Organic Compounds, Chem. Rev., 103, 4605–4638, 2003.

Ayres, J. G., , Paul, B., , Flemming R., C., , Vincent, C., , Ken, D., , Andy, G., , Roy M., H., , Robert, H., , Frank, K., , Ingeborg M., K., , Francelyne, M., , Robert L., M., , Ian, M., , Andre, N., , Constantinos, S., , Steve, S., , Armelle, B.-S., , Art, C., , Sean, D., , and Froines, J.: Evaluating the Toxicity of Airborne Particulate Matter and Nanoparticles by Measuring Oxidative Stress Potential—A Workshop Report and Consensus Statement, Inhal. Toxicol., 20, 75–99, 2008.

Bachi, A., Dalle-Donne, I., and Scaloni, A.: Redox Proteomics: Chemical Principles, Methodological Approaches and Biological/Biomedical Promises, Chem. Rev., 113, 596–698, 2013.

Backes, A. T., Reinmuth-Selzle, K., Leifke, A. L., Ziegler, K., Krevert, C. S., Tscheuschner, G., Lucas, K., Weller, M. G., Berkemeier, T., Pöschl, U., and Fröhlich-Nowoisky, J.: Oligomerization and Nitration of the Grass Pollen Allergen Phl p 5 by Ozone, Nitrogen Dioxide, and Peroxynitrite: Reaction Products, Kinetics, and Health Effects, Int. J. Mol. Sci., 22, 2021.

Bandookwala, M., , and Sengupta, P.: 3-Nitrotyrosine: a versatile oxidative stress biomarker for major neurodegenerative diseases, Int. J. Neurosci., 130, 1047–1062, 2020.

Bates, J. T., Weber, R. J., Abrams, J., Verma, V., Fang, T., Klein, M., Strickland, M. J., Sarnat, S. E., Chang, H. H., Mulholland, J. A., Tolbert, P. E., and Russell, A. G.: Reactive Oxygen Species Generation Linked to Sources of Atmospheric Particulate Matter and Cardiorespiratory Effects, Environ. Sci. Technol., 49, 13 605–13 612, 2015.

Bates, J. T., Fang, T., Verma, V., Zeng, L., Weber, R. J., Tolbert, P. E., Abrams, J. Y., Sarnat, S. E., Klein, M., Mulholland, J. A., and Russell, A. G.: Review of Acellular Assays of Ambient Particulate Matter Oxidative Potential: Methods and Relationships with Composition, Sources, and Health Effects, Environ. Sci. Technol., 53, 4003–4019, 2019.

Berkemeier, T., Huisman, A. J., Ammann, M., Shiraiwa, M., Koop, T., and Pöschl, U.: Kinetic regimes and limiting cases of gas uptake and heterogeneous reactions in atmospheric aerosols and clouds: a general classification scheme, Atmos. Chem. Phys., 13, 6663–6686, 2013.

Berkemeier, T., Steimer, S. S., Krieger, U. K., Peter, T., Pöschl, U., Ammann, M., and Shiraiwa, M.: Ozone uptake on glassy, semi-solid and liquid organic matter and the role of reactive oxygen intermediates in atmospheric aerosol chemistry, Phys. Chem. Chem. Phys., 18, 12 662–12 674, 2016.

Berkemeier, T., Ammann, M., Krieger, U. K., Peter, T., Spichtinger, P., Pöschl, U., Shiraiwa, M., and Huisman, A. J.: Technical note: Monte Carlo genetic algorithm (MCGA) for model analysis of multiphase chemical kinetics to determine transport and reaction rate coefficients using multiple experimental data sets, Atmos. Chem. Phys., 17, 8021–8029, 2017.

Berkemeier, T., Takeuchi, M., Eris, G., and Ng, N. L.: Kinetic modeling of formation and evaporation of secondary organic aerosol from NO3 oxidation of pure and mixed monoterpenes, Atmos. Chem. Phys., 20, 15 513–15 535, 2020.

Bond, T. C., Doherty, S. J., Fahey, D. W., Forster, P. M., Berntsen, T., DeAngelo, B. J., Flanner, M. G., Ghan, S., Kärcher, B., Koch, D., Kinne, S., Kondo, Y., Quinn, P. K., Sarofim, M. C., Schultz, M. G., Schulz, M., Venkataraman, C., Zhang, H., Zhang, S., Bellouin, N., Guttikunda, S. K., Hopke, P. K., Jacobson, M. Z., Kaiser, J. W., Klimont, Z., Lohmann, U., Schwarz, J. P., Shindell, D., Storelvmo, T., Warren, S. G., and Zender, C. S.: Bounding the role of black carbon in the climate system: A scientific assessment, J. Geohys. Res., D, 118, 5380–5552, 2013.

Borm, P. J. A., Kelly, F., Künzli, N., Schins, R. P. F., and Donaldson, K.: Oxidant generation by particulate matter: from biologically effective dose to a promising, novel metric, Occup. Environ. Med., 64, 73, 2007.

Boucher, O.: Atmospheric Aerosols, in: Atmospheric Aerosols: Properties and Climate Impacts, edited by Boucher, O., pp. 9–24, Springer Netherlands, Dordrecht, ISBN 978-94-017-9649-1, 2015.

Brauer, M. et al.: Global burden and strength of evidence for 88 risk factors in 204 countries and 811 subnational locations, 1990–2021: a systematic analysis for the Global Burden of Disease Study 2021, Lancet, 403, 2162–2203, 2024.

Burnett, R., Chen, H., Szyszkowicz, M., Fann, N., Hubbell, B., Pope, C. A., Apte, J. S., Brauer, M., Cohen, A., Weichenthal, S., Coggins, J., Di, Q., Brunekreef, B., Frostad, J., Lim, S. S., Kan, H., Walker, K. D., Thurston, G. D., Hayes, R. B., Lim, C. C., Turner, M. C., Jerrett, M., Krewski, D., Gapstur, S. M., Diver, W. R., Ostro, B., Goldberg, D., Crouse, D. L., Martin, R. V., Peters, P., Pinault, L., Tjepkema, M., van Donkelaar, A., Villeneuve, P. J., Miller, A. B., Yin, P., Zhou, M., Wang, L., Janssen, N. A. H., Marra, M., Atkinson, R. W., Tsang, H., Quoc Thach, T., Cannon, J. B., Allen, R. T., Hart, J. E., Laden, F., Cesaroni, G., Forastiere, F., Weinmayr, G., Jaensch, A., Nagel, G., Concin, H., and Spadaro, J. V.: Global estimates of mortality associated with long-term exposure to outdoor fine particulate matter, Proc. Natl. Acad. Sci. USA, 115, 9592–9597, 2018.

Burnett, R. T., Stieb, D., Brook, J. R., Cakmak, S., Dales, R., Raizenne, M., Vincent, R., and Dann, T.: Associations between Short-Term Changes in Nitrogen Dioxide and Mortality in Canadian Cities, Arch. Environ. Occup. Health, 59, 228–236, 2004.

Burnett, R. T., Pope, C. A., Ezzati, M., Olives, C., Lim, S. S., Mehta, S., Shin, H. H., Singh, G., Hubbell, B., Brauer, M., Anderson, H. R., Smith, K. R., Balmes, J. R., Bruce, N. G., Kan, H., Laden, F., Prüss-Ustün, A., Turner, M. C., Gapstur, S. M., Diver, W. R., and Cohen, A.: An Integrated Risk Function for Estimating the Global Burden of Disease Attributable to Ambient Fine Particulate Matter Exposure, Environ. Health Perspect., 122, 397–403, 2014.

Calas, A., Uzu, G., Martins, J. M. F., Voisin, D., Spadini, L., Lacroix, T., and Jaffrezo, J.-L.: The importance of simulated lung fluid (SLF) extractions for a more relevant evaluation of the oxidative potential of particulate matter, Sci. Rep., 7, 11 617, 2017.

Calvin, K., Dasgupta, D., Krinner, G., Mukherji, A., Thorne, P. W., Trisos, C., Romero, J., Aldunce, P., Barrett, K., Blanco, G., Cheung, W. W., Connors, S., Denton, F., Diongue-Niang, A., Dodman, D., Garschagen, M., Geden, O., Hayward, B., Jones, C., Jotzo, F., Krug, T., Lasco, R., Lee, Y.-Y., Masson-Delmotte, V., Meinshausen, M., Mintenbeck, K., Mokssit, A., Otto, F. E., Pathak, M., Pirani, A., Poloczanska, E., Pörtner, H.-O., Revi, A., Roberts, D. C., Roy, J., Ruane, A. C., Skea, J., Shukla, P. R., Slade, R., Slangen, A., Sokona, Y., Sörensson, A. A., Tignor, M., Van Vuuren, D., Wei, Y.-M., Winkler, H., Zhai, P., Zommers, Z., Hourcade, J.-C., Johnson, F. X., Pachauri, S., Simpson, N. P., Singh, C., Thomas, A., Totin, E., Alegría, A., Armour, K., Bednar-Friedl, B., Blok, K., Cissé, G., Dentener, F., Eriksen, S., Fischer, E., Garner, G., Guivarch, C., Haasnoot, M., Hansen, G., Hauser, M., Hawkins, E., Hermans, T., Kopp, R., Leprince-Ringuet, N., Lewis, J., Ley, D., Ludden, C., Niamir, L., Nicholls, Z., Some, S., Szopa, S., Trewin, B., Van Der Wijst, K.-I., Winter, G., Witting, M., Birt, A., Ha, M., Arias, P., Bustamante, M., Elgizouli, I., Flato, G., Howden, M., Méndez-Vallejo, C., Pereira, J. J., Pichs-Madruga, R., Rose, S. K., Saheb, Y., Sánchez Rodríguez, R., Ürge Vorsatz, D., Xiao, C., Yassaa, N., Romero, J., Kim, J., Haites, E. F., Jung, Y., Stavins, R., Birt, A., Ha, M., Orendain, D. J. A., Ignon, L., Park, S., Park, Y., Reisinger, A., Cammaramo, D., Fischlin, A., Fuglestvedt, J. S., Hansen, G., Ludden, C., Masson-Delmotte, V., Matthews, J. R., Mintenbeck, K., Pirani, A., Poloczanska, E., Leprince-Ringuet, N., and Péan, C.: IPCC, 2023: Climate Change 2023: Synthesis Report. Contribution of Working Groups I, II and III to the Sixth Assessment Report of the Intergovernmental Panel on Climate Change [Core Writing Team, H. Lee and J. Romero (eds.)]. IPCC, Geneva, Switzerland., Tech. rep., Intergovernmental Panel on Climate Change, 2023.

Camman, J., Chazeau, B., Marchand, N., Durand, A., Gille, G., Lanzi, L., Jaffrezo, J.-L., Wortham, H., and Uzu, G.: Oxidative potential apportionment of atmospheric PM1: a new approach combining high-sensitive online analysers for chemical composition and offline OP measurement technique, Atmos. Chem. Phys., 24, 3257–3278, 2024.

Campbell, S. J., Utinger, B., Lienhard, D. M., Paulson, S. E., Shen, J., Griffiths, P. T., Stell, A. C., and Kalberer, M.: Development of a Physiologically Relevant Online Chemical Assay To Quantify Aerosol Oxidative Potential, Anal. Chem., 91, 13 088–13 095, 2019.

Campbell, S. J., Utinger, B., Barth, A., Paulson, S. E., and Kalberer, M.: Iron and Copper Alter the Oxidative Potential of Secondary Organic Aerosol: Insights from Online Measurements and Model Development, Environ. Sci. Technol., 57, 13 546–13 558, 2023.

Campbell, S. J., Barth, A., Chen, G. I., Tremper, A. H., Priestman, M., Ek, D., Gu, S., Kelly, F. J., Kalberer, M., and Green, D. C.: High time resolution quantification of PM2.5 oxidative potential at a Central London roadside supersite, Environ. Int., 193, 109 102, 2024.

Campbell, S. J., Utinger, B., Barth, A., Leni, Z., Zhang, Z.-H., Resch, J., Li, K., Steimer, S. S., Banach, C., Gfeller, B., Wragg, F. P. H., Westwood, J., Wolfer, K., Bukowiecki, N., Ihalainen, M., Yli-Pirilä, P., Somero, M., Kortelainen, M., Louhisalmi, J., Sklorz, M., Czech, H., di Bucchianico, S., Streibel, T., Delaval, M. N., Ruger, C., Baumlin, N., Salathe, M., Fang, Z., Pardo, M., D'Aronco, S., Giorio, C., Shi, Z., Harrison, R. M., Green, D. C., Kelly, F. J., Rudich, Y., Paulson, S. E., Sippula, O., Zimmermann, R., Geiser, M., and Kalberer, M.: Short-lived reactive components substantially contribute to particulate matter oxidative potential, Sci. Adv., 11, eadp8100, 2025.

Carslaw, K. S., Boucher, O., Spracklen, D. V., Mann, G. W., Rae, J. G. L., Woodward, S., and Kulmala, M.: A review of natural aerosol interactions and feedbacks within the Earth system, Atmos. Chem. Phys., 10, 1701–1737, 2010.

Charrier, J. G. and Anastasio, C.: Impacts of antioxidants on hydroxyl radical production from individual and mixed transition metals in a surrogate lung fluid, Atmos. Environ., 45, 7555–7562, 2011.

Charrier, J. G. and Anastasio, C.: On dithiothreitol (DTT) as a measure of oxidative potential for ambient particles: evidence for the importance of soluble transition metals, Atmos. Chem. Phys., 12, 9321–9333, 2012.

Charrier, J. G., McFall, A. S., Richards-Henderson, N. K., and Anastasio, C.: Hydrogen Peroxide Formation in a Surrogate Lung Fluid by Transition Metals and Quinones Present in Particulate Matter, Environ. Sci. Technol., 48, 7010–7017, 2014.

Chebbi, A. and Carlier, P.: Carboxylic acids in the troposphere, occurrence, sources, and sinks: A review, Atmos. Environ., 30, 4233–4249, 1996.

Cho, A. K., Sioutas, C., Miguel, A. H., Kumagai, Y., Schmitz, D. A., Singh, M., Eiguren-Fernandez, A., and Froines, J. R.: Redox activity of airborne particulate matter at different sites in the Los Angeles Basin, Environ. Res., 99, 40–47, 2005.

Choobari, O. A., Zawar-Reza, P., and Sturman, A.: The global distribution of mineral dust and its impacts on the climate system: A review, Atmos. Res., 138, 152–165, 2014.

Chow, J. C.: Measurement Methods to Determine Compliance with Ambient Air Quality Standards for Suspended Particles, J. Air Waste Manag. Assoc., 45, 320–382, 1995.

Cohen, A. J., Brauer, M., Burnett, R., Anderson, H. R., Frostad, J., Estep, K., Balakrishnan, K., Brunekreef, B., Dandona, L., Dandona, R., Feigin, V., Freedman, G., Hubbell, B., Jobling, A., Kan, H., Knibbs, L., Liu, Y., Martin, R., Morawska, L., Pope, C. A., Shin, H., Straif, K., Shaddick, G., Thomas, M., van Dingenen, R., van Donkelaar, A., Vos, T., Murray, C. J. L., and Forouzanfar, M. H.: Estimates and 25-year trends of the global burden of disease attributable to ambient air pollution: an analysis of data from the Global Burden of Diseases Study 2015, Lancet, 389, 1907–1918, 2017.

Deguillaume, L., Leriche, M., Desboeufs, K., Mailhot, G., George, C., and Chaumerliac, N.: Transition Metals in Atmospheric Liquid Phases: Sources, Reactivity, and Sensitive Parameters, Chem. Rev., 105, 3388–3431, 2005.

Dennis-Smither, B. J., Hanford, K. L., Kwamena, N. O., Miles, R. E., and Reid, J. P.: Phase, morphology, and hygroscopicity of mixed oleic acid/sodium chloride/water aerosol particles before and after ozonolysis, J. Phys. Chem. A, 116, 6159–68, 2012.

Després, V. R., Huffman, J. A., Burrows, S. M., Hoose, C., Safatov, A. S., Buryak, G., Fröhlich-Nowoisky, J., Elbert, W., Andreae, M. O., Pöschl, U., and Jaenicke, R.: Primary biological aerosol particles in the atmosphere: a review, Tellus B: B-Chem. Phys. Meteorol, 2012.

Dominutti, P. A., Jaffrezo, J.-L., Marsal, A., Mhadhbi, T., Elazzouzi, R., Rak, C., Cavalli, F., Putaud, J.-P., Bougiatioti, A., Mihalopoulos, N., Paraskevopoulou, D., Mudway, I., Nenes, A., Daellenbach, K. R., Banach, C., Campbell, S. J., Cigánková, H., Contini, D., Evans, G., Georgopoulou, M., Ghanem, M., Glencross, D. A., Guascito, M. R., Herrmann, H., Iram, S., Jovanović, M., Jovašević-Stojanović, M., Kalberer, M., Kooter, I. M., Paulson, S. E., Patel, A., Perdrix, E., Pietrogrande, M. C., Mikuška, P., Sauvain, J.-J., Seitanidi, K., Shahpoury, P., Souza, E. J. d. S., Steimer, S., Stevanovic, S., Suarez, G., Subramanian, P. S. G., Utinger, B., van Os, M. F., Verma, V., Wang, X., Weber, R. J., Yang, Y., Querol, X., Hoek, G., Harrison, R. M., and Uzu, G.: An interlaboratory comparison to quantify oxidative potential measurement in aerosol particles: challenges and recommendations for harmonisation, Atmos. Meas. Tech., 18, 177–195, 2025.

Dou, J., Alpert, P. A., Corral Arroyo, P., Luo, B., Schneider, F., Xto, J., Huthwelker, T., Borca, C. N., Henzler, K. D., Raabe, J., Watts, B., Herrmann, H., Peter, T., Ammann, M., and Krieger, U. K.: Photochemical degradation of iron(III) citrate/citric acid aerosol quantified with the combination of three complementary experimental techniques and a kinetic process model, Atmos. Chem. Phys., 21, 315–338, 2021.

El Haddad, I., Vienneau, D., Daellenbach, K. R., Modini, R., Slowik, J. G., Upadhyay, A., Vasilakos, P. N., Bell, D., de Hoogh, K., and Prevot, A. S. H.: Opinion: How will advances in aerosol science inform our understanding of the health impacts of outdoor particulate pollution?, Atmos. Chem. Phys., 24, 11 981–12 011, 2024.

Elbert, W., Taylor, P. E., Andreae, M. O., and Pöschl, U.: Contribution of fungi to primary biogenic aerosols in the atmosphere: wet and dry discharged spores, carbohydrates, and inorganic ions, Atmos. Chem. Phys., 7, 4569–4588, 2007.

Eleftheriadis, K., Vratolis, S., and Nyeki, S.: Aerosol black carbon in the European Arctic: Measurements at Zeppelin station, Ny-Ålesund, Svalbard from 1998–2007, Geophys. Res. Lett., 36, 2009.

Fang, T., Verma, V., Guo, H., King, L. E., Edgerton, E. S., and Weber, R. J.: A semi-automated system for quantifying the oxidative potential of ambient particles in aqueous extracts using the dithiothreitol (DTT) assay: results from the Southeastern Center for Air Pollution and Epidemiology (SCAPE), Atmos. Meas. Tech., 8, 471–482, 2015.

Faust, B. C. and Hoigné, J.: Photolysis of Fe (III)-hydroxy complexes as sources of OH radicals in clouds, fog and rain, Atmos. Environ., 24, 79–89, 1990.

Faustini, A., Rapp, R., and Forastiere, F.: Nitrogen dioxide and mortality: review and meta-analysis of long-term studies, Eur. Respir. J., 44, 744–753, 2014.

Franze, T., Weller, M. G., Niessner, R., and Pöschl, U.: Protein Nitration by Polluted Air, Environ. Sci. Technol., 39, 1673–1678, 2005.

Frezzini, M. A., De Francesco, N., Massimi, L., and Canepari, S.: Effects of operating conditions on PM oxidative potential assays, Atmos. Environ., 268, 118 802, 2022.

Fröhlich-Nowoisky, J., Kampf, C. J., Weber, B., Huffman, J. A., Pöhlker, C., Andreae, M. O., Lang-Yona, N., Burrows, S. M., Gunthe, S. S., Elbert, W., Su, H., Hoor, P., Thines, E., Hoffmann, T., Després, V. R., and Pöschl, U.: Bioaerosols in the Earth system: Climate, health, and ecosystem interactions, Atmos. Res., 182, 346–376, 2016.

Gallimore, P. J., Griffiths, P. T., Pope, F. D., Reid, J. P., and Kalberer, M.: Comprehensive modeling study of ozonolysis of oleic acid aerosol based on real-time, online measurements of aerosol composition, J. Geophys. Res. Atmos., 122, 4364–4377, 2017.

George, C., Ammann, M., D'Anna, B., Donaldson, D. J., and Nizkorodov, S. A.: Heterogeneous Photochemistry in the Atmosphere, Chem. Rev., 115, 4218–4258, 2015.

George, I. J. and Abbatt, J. P. D.: Heterogeneous oxidation of atmospheric aerosol particles by gas-phase radicals, Nat. Chem., 2, 713–722, 2010.

Goldstein, A. H. and Galbally, I. E.: Known and Unexplored Organic Constituents in the Earth's Atmosphere, Environ. Sci. Technol., 41, 1514–1521, 2007.

Gurgueira, S. A., Lawrence, J., Coull, B., Murthy, G. G. K., and González-Flecha, B.: Rapid increases in the steady-state concentration of reactive oxygen species in the lungs and heart after particulate air pollution inhalation., Environ. Health Perspect., 110, 749–755, 2002.

Hallquist, M., Wenger, J. C., Baltensperger, U., Rudich, Y., Simpson, D., Claeys, M., Dommen, J., Donahue, N. M., George, C., Goldstein, A. H., Hamilton, J. F., Herrmann, H., Hoffmann, T., Iinuma, Y., Jang, M., Jenkin, M. E., Jimenez, J. L., Kiendler-Scharr, A., Maenhaut, W., McFiggans, G., Mentel, T. F., Monod, A., Prévôt, A. S. H., Seinfeld, J. H., Surratt, J. D., Szmigielski, R., and Wildt, J.: The formation, properties and impact of secondary organic aerosol: current and emerging issues, Atmos. Chem. Phys., 9, 5155–5236, 2009.

Hamilton, D. S.: Natural aerosols and climate: Understanding the unpolluted atmosphere to better understand the impacts of pollution, Weather, 70, 264–268, 2015.

Harrison, R. M., Jones, A. M., Gietl, J., Yin, J., and Green, D. C.: Estimation of the Contributions of Brake Dust, Tire Wear, and Resuspension to Nonexhaust Traffic Particles Derived from Atmospheric Measurements, Environ. Sci. Technol., 46, 6523–6529, 2012.

Hearn, J. D. and Smith, G. D.: Kinetics and Product Studies for Ozonolysis Reactions of Organic Particles Using Aerosol CIMS, J. Phys. Chem. A, 108, 10 019–10 029, 2004.

Hearn, J. D., Lovett, A. J., and Smith, G. D.: Ozonolysis of oleic acid particles: evidence for a surface reaction and secondary reactions involving Criegee intermediates, Phys. Chem. Chem. Phys., 7, 501–11, 2005.

Heintzenberg, J.: Fine particles in the global troposphere A review, Tellus B, 41B, 149–160, 1989.

Hemming, B. L. and Seinfeld, J. H.: On the Hygroscopic Behavior of Atmospheric Organic Aerosols, Ind. Eng. Chem. Res., 40, 4162–4171, 2001.

Houle, F. A., Hinsberg, W. D., and Wilson, K. R.: Oxidation of a model alkane aerosol by OH radical: the emergent nature of reactive uptake, Phys. Chem. Chem. Phys., 17, 4412–4423, 2015.

Hung, H.-M. and Ariya, P.: Oxidation of Oleic Acid and Oleic Acid/Sodium Chloride(aq) Mixture Droplets with Ozone: Changes of Hygroscopicity and Role of Secondary Reactions, J. Phys. Chem. A, 111, 620–632, 2007.

Ischiropoulos, H.: Biological Tyrosine Nitration: A Pathophysiological Function of Nitric Oxide and Reactive Oxygen Species, Arch. Biochem. Biophys., 356, 1–11, 1998.

Ito, A.: Atmospheric Processing of Combustion Aerosols as a Source of Bioavailable Iron, Environ. Sci. Technol. Lett., 2, 70–75, 2015.

Jimenez, J. L., Canagaratna, M. R., Donahue, N. M., Prevot, A. S. H., Zhang, Q., Kroll, J. H., DeCarlo, P. F., Allan, J. D., Coe, H., Ng, N. L., Aiken, A. C., Docherty, K. S., Ulbrich, I. M., Grieshop, A. P., Robinson, A. L., Duplissy, J., Smith, J. D., Wilson, K. R., Lanz, V. A., Hueglin, C., Sun, Y. L., Tian, J., Laaksonen, A., Raatikainen, T., Rautiainen,

J., Vaattovaara, P., Ehn, M., Kulmala, M., Tomlinson, J. M., Collins, D. R., Cubison, M. J., E., Dunlea, J., Huffman, J. A., Onasch, T. B., Alfarra, M. R., Williams, P. I., Bower, K., Kondo, Y., Schneider, J., Drewnick, F., Borrmann, S., Weimer, S., Demerjian, K., Salcedo, D., Cottrell, L., Griffin, R., Takami, A., Miyoshi, T., Hatakeyama, S., Shimono, A., Sun, J. Y., Zhang, Y. M., Dzepina, K., Kimmel, J. R., Sueper, D., Jayne, J. T., Herndon, S. C., Trimborn, A. M., Williams, L. R., Wood, E. C., Middlebrook, A. M., Kolb, C. E., Baltensperger, U., and Worsnop, D. R.: Evolution of Organic Aerosols in the Atmosphere, Science, 326, 1525–1529, 2009.

Kanakidou, M., Seinfeld, J. H., Pandis, S. N., Barnes, I., Dentener, F. J., Facchini, M. C., Van Dingenen, R., Ervens, B., Nenes, A., Nielsen, C. J., Swietlicki, E., Putaud, J. P., Balkanski, Y., Fuzzi, S., Horth, J., Moortgat, G. K., Winterhalter, R., Myhre, C. E. L., Tsigaridis, K., Vignati, E., Stephanou, E. G., and Wilson, J.: Organic aerosol and global climate modelling: a review, Atmos. Chem. Phys., 5, 1053–1123, 2005.

King, M. D., Thompson, K. C., and Ward, A. D.: Laser Tweezers Raman Study of Optically Trapped Aerosol Droplets of Seawater and Oleic Acid Reacting with Ozone: Implications for Cloud-Droplet Properties, J. Am. Chem. Soc., 126, 16 710–16 711, 2004.

King, M. D., Jones, S. H., Lucas, C. O. M., Thompson, K. C., Rennie, A. R., Ward, A. D., Marks, A. A., Fisher, F. N., Pfrang, C., Hughes, A. V., and Campbell, R. A.: The reaction of oleic acid monolayers with gas-phase ozone at the air water interface: the effect of sub-phase viscosity, and inert secondary components, Phys. Chem. Chem. Phys., 22, 28 032–28 044, 2020.

Knopf, D. A., Anthony, L. M., and Bertram, A. K.: Reactive Uptake of O3 by Multicomponent and Multiphase Mixtures Containing Oleic Acid, J. Phys. Chem. A, 109, 5579–5589, 2005.

Kroll, J. H. and Seinfeld, J. H.: Chemistry of secondary organic aerosol: Formation and evolution of low-volatility organics in the atmosphere, Atmos. Environ., 42, 3593–3624, 2008.

Kroll, J. H., Smith, J. D., Che, D. L., Kessler, S. H., Worsnop, D. R., and Wilson, K. R.: Measurement of fragmentation and functionalization pathways in the heterogeneous oxidation of oxidized organic aerosol, Phys. Chem. Chem. Phys., 11, 8005–8014, 2009.

Kroll, J. H., Donahue, N. M., Jimenez, J. L., Kessler, S. H., Canagaratna, M. R., Wilson, K. R., Altieri, K. E., Mazzoleni, L. R., Wozniak, A. S., Bluhm, H., Mysak, E. R., Smith, J. D., Kolb, C. E., and Worsnop, D. R.: Carbon oxidation state as a metric for describing the chemistry of atmospheric organic aerosol, Nat. Chem., 3, 133–139, 2011.

Kroll, J. H., Lim, C. Y., Kessler, S. H., and Wilson, K. R.: Heterogeneous Oxidation of Atmospheric Organic Aerosol: Kinetics of Changes to the Amount and Oxidation State of Particle-Phase Organic Carbon, J. Phys. Chem. A, 119, 10 767–10 783, 2015.

Krüger, M., Mishra, A., Spichtinger, P., Pöschl, U., and Berkemeier, T.: A numerical compass for experiment design in chemical kinetics and molecular property estimation, J. Cheminform., 16, 34, 2024.

Kwon, H.-S., Ryu, M. H., and Carlsten, C.: Ultrafine particles: unique physicochemical properties relevant to health and disease, Exp. Mol. Med., 52, 318–328, 2020.

Lakey, P. S. J., Berkemeier, T., Tong, H., Arangio, A. M., Lucas, K., Pöschl, U., and Shiraiwa, M.: Chemical exposure-response relationship between air pollutants and reactive oxygen species in the human respiratory tract, Sci. Rep., 6, 32 916, 2016.

Landrigan, P. J., Fuller, R., Acosta, N. J. R., Adeyi, O., Arnold, R., Basu, N. N., Baldé, A. B., Bertollini, R., Bose-O'Reilly, S., Boufford, J. I., Breysse, P. N., Chiles, T., Mahidol, C., Coll-Seck, A. M., Cropper, M. L., Fobil, J., Fuster, V., Greenstone, M., Haines, A., Hanrahan, D., Hunter, D., Khare, M., Krupnick, A., Lanphear, B., Lohani, B., Martin, K., Mathiasen, K. V., McTeer, M. A., Murray, C. J. L., Ndahimananjara, J. D., Perera, F., Potočnik, J., Preker, A. S., Ramesh, J., Rockström, J., Salinas, C., Samson, L. D., Sandilya, K., Sly, P. D., Smith, K. R., Steiner, A., Stewart, R. B., Suk, W. A., van Schayck, O. C. P., Yadama, G. N., Yumkella, K., and Zhong, M.: The Lancet Commission on pollution and health, Lancet, 391, 462–512, 2018.

Lee, A. K. Y. and Chan, C. K.: Single particle Raman spectroscopy for investigating atmospheric heterogeneous reactions of organic aerosols, Atmos. Environ., 41, 4611–4621, 2007.

Lelieveld, J., Evans, J. S., Fnais, M., Giannadaki, D., and Pozzer, A.: The contribution of outdoor air pollution sources to premature mortality on a global scale, Nature, 525, 367–371, 2015.

Lelieveld, J., Klingmüller, K., Pozzer, A., Pöschl, U., Fnais, M., Daiber, A., and Münzel, T.: Cardiovascular disease burden from ambient air pollution in Europe reassessed using novel hazard ratio functions, Eur. Heart J., 40, 1590–1596, 2019.

Lelieveld, J., Pozzer, A., Pöschl, U., Fnais, M., Haines, A., and Münzel, T.: Loss of life expectancy from air pollution compared to other risk factors: a worldwide perspective, Cardiovasc. Res., 116, 1910–1917, 2020.

Lelieveld, S., Wilson, J., Dovrou, E., Mishra, A., Lakey, P. S. J., Shiraiwa, M., Pöschl, U., and Berkemeier, T.: Hydroxyl Radical Production by Air Pollutants in Epithelial Lining Fluid Governed by Interconversion and Scavenging of Reactive Oxygen Species, Environ. Sci. Technol., 55, 14 069–14 079, 2021.

Li, N., Georas, S., Alexis, N., Fritz, P., Xia, T., Williams, M. A., Horner, E., and Nel, A.: A work group report on ultrafine particles (American Academy of Allergy, Asthma & Immunology): Why ambient ultrafine and engineered nanoparticles should receive special attention for possible adverse health outcomes in human subjects, J. Allergy Clin. Immunol., 138, 386–396, 2016.

Lin, M. and Yu, J. Z.: Dithiothreitol (DTT) concentration effect and its implications on the applicability of DTT assay to evaluate the oxidative potential of atmospheric aerosol samples, Environ. Pollut., 251, 938–944, 2019.

Liu, F., Lakey, P. S. J., Berkemeier, T., Tong, H., Kunert, A. T., Meusel, H., Cheng, Y., Su, H., Fröhlich-Nowoisky, J., Lai, S., Weller, M. G., Shiraiwa, M., Pöschl, U., and Kampf, C. J.: Atmospheric protein chemistry influenced by anthropogenic air pollutants: nitration and oligomerization upon exposure to ozone and nitrogen dioxide, Faraday Discuss., 200, 413–427, 2017.

Liu, X., Zhang, X., Jin, B., Wang, T., Qian, S., Zou, J., Dinh, V. N. T., Jaffrezo, J.-L., Uzu, G., Dominutti, P., Darfeuil, S., Favez, O., Conil, S., Marchand, N., Castillo, S., de la Rosa, J. D., Grange, S., Hueglin, C., Eleftheriadis, K., Diapouli, E., Manousakas, M.-I., Gini, M., Nava, S., Calzolai, G., Alves, C., Monge, M., Reche, C., Harrison, R. M., Hopke, P. K., Alastuey, A., and Querol, X.: Source apportionment of PM10 based on offline chemical speciation data at 24 European sites, npj Clim. Atmos. Sci., 8, 255, 2025.

Lohmann, U. and Feichter, J.: Global indirect aerosol effects: a review, Atmos. Chem. Phys., 5, 715–737, 2005.

Lopez, B., Wang, X., Chen, L.-W. A., Ma, T., Mendez-Jimenez, D., Cobb, L. C., Frederickson, C., Fang, T., Hwang, B., Shiraiwa, M., Park, M., Park, K., Yao, Q., Yoon, S., and Jung, H.: Metal contents and size distributions of brake and tire wear particles dispersed in the near-road environment, Sci. Total Environ., 883, 163 561, 2023.

Mendez, M., Visez, N., Gosselin, S., Crenn, V., Riffault, V., and Petitprez, D.: Reactive and Nonreactive Ozone Uptake during Aging of Oleic Acid Particles, J. Phys. Chem. A, 118, 9471–9481, 2014.

Milsom, A., Lees, A., Squires, A. M., and Pfrang, C.: MultilayerPy (v1.0): a Python-based framework for building, running and optimising kinetic multi-layer models of aerosols and films, Geosci. Model Dev., 15, 7139–7151, 2022.

Morris, J. W., Davidovits, P., Jayne, J. T., Jimenez, J. L., Shi, Q., Kolb, C. E., Worsnop, D. R., Barney, W. S., and Cass, G.: Kinetics of submicron oleic acid aerosols with ozone: A novel aerosol mass spectrometric technique, Geophys. Res. Lett., 29, 71–1–71–4, 2002a.

Morris, J. W., Davidovits, P., Jayne, J. T., Jimenez, J. L., Shi, Q., Kolb, C. E., Worsnop, D. R., Barney, W. S., and Cass, G.: Kinetics of submicron oleic acid aerosols with ozone: A novel aerosol mass spectrometric technique, Geophys. Res. Lett., 29, 71–1–71–4, 2002b.

Mudway, I. S. and Kelly, F. J.: Ozone and the lung: a sensitive issue, Mol. Asp. Med., 21, 1–48, 2000.

Nemmar, A., Hoet, P., Vanquickenborne, B., Dinsdale, D., Thomeer, M., Hoylaerts, M., Vanbilloen, H., Mortelmans, L., and Nemery, B.: Passage of Inhaled Particles Into the Blood Circulation in Humans, Circulation, 105, 411–414, 2002.

Oberdörster, G., Sharp, Z., Atudorei, V., Elder, A., Gelein, R., Lunts, A., Kreyling, W., and Cox, C.: EXTRAPULMONARY TRANSLOCATION OF ULTRAFINE CARBON PARTICLES FOLLOWING WHOLE-BODY INHALATION EXPOSURE OF RATS, Journal of Toxicology and Environmental Health, Part A, 65, 1531–1543, 2002.

Palm, B. B., Campuzano-Jost, P., Day, D. A., Ortega, A. M., Fry, J. L., Brown, S. S., Zarzana, K. J., Dube, W., Wagner, N. L., Draper, D. C., Kaser, L., Jud, W., Karl, T., Hansel, A., Gutiérrez-Montes, C., and Jimenez, J. L.: Secondary organic aerosol formation from in situ OH, O3, and NO3 oxidation of ambient forest air in an oxidation flow reactor, Atmos. Chem. Phys., 17, 5331–5354, 2017.

Pfrang, C., Shiraiwa, M., and Pöschl, U.: Coupling aerosol surface and bulk chemistry with a kinetic double layer model (K2-SUB): oxidation of oleic acid by ozone, Atmos. Chem. Phys., 10, 4537–4557, 2010.

Pope, C. A., Coleman, N., Pond, Z. A., and Burnett, R. T.: Fine particulate air pollution and human mortality: 25+ years of cohort studies, Environ. Res., p. 108924, 2019.

Pope III, C. A., , and Dockery, D. W.: Health Effects of Fine Particulate Air Pollution: Lines that Connect, J. Air Waste Manag. Assoc., 56, 709–742, 2006.

Pöschl, U., Rudich, Y., and Ammann, M.: Kinetic model framework for aerosol and cloud surface chemistry and gas-particle interactions - Part 1: General equations, parameters, and terminology, Atmos. Chem. Phys., 7, 5989–6023, 2007.

Pozdnyakov, I. P., Melnikov, A. A., Tkachenko, N., Chekalin, S. V., Lemmetyinen, H., and Plyusnin, V. F.: Ultrafast photophysical processes for Fe(iii)-carboxylates, Dalton Trans., 43, 17 590–17 595, 2014.

Prospero, J. M., Charlson, R. J., Mohnen, V., Jaenicke, R., Delany, A. C., Moyers, J., Zoller, W., and Rahn, K.: The atmospheric aerosol system: An overview, Rev. Geophys., 21, 1607–1629, 1983.

Pryor, S., Crippa, P., and Sullivan, R.: Atmospheric Chemistry, in: Reference Module in Earth Systems and Environmental Sciences, Elsevier, ISBN 978-0-12-409548-9, 2015.

Pöhlker, C., Wiedemann, K. T., Sinha, B., Shiraiwa, M., Gunthe, S. S., Smith, M., Su, H., Artaxo, P., Chen, Q., Cheng, Y., Elbert, W., Gilles, M. K., Kilcoyne, A. L. D., Moffet, R. C., Weigand, M., Martin, S. T., Pöschl, U., and Andreae, M. O.: Biogenic Potassium Salt Particles as Seeds for Secondary Organic Aerosol in the Amazon, Science, 337, 1075–1078, 2012.

Pöschl, U.: Atmospheric Aerosols: Composition, Transformation, Climate and Health Effects, Angew. Chem. Int. Ed., 44, 7520–7540, 2005.

Pöschl, U. and Shiraiwa, M.: Multiphase Chemistry at the Atmosphere–Biosphere Interface Influencing Climate and Public Health in the Anthropocene, Chem. Rev., 115, 4440–4475, 2015.

Quinn, P. K., Collins, D. B., Grassian, V. H., Prather, K. A., and Bates, T. S.: Chemistry and Related Properties of Freshly Emitted Sea Spray Aerosol, Chem. Rev., 115, 4383–4399, 2015.

Ravishankara, A. R.: Heterogeneous and Multiphase Chemistry in the Troposphere, Science, 276, 1058–1065, 1997.

Reinmuth-Selzle, K., Ackaert, C., Kampf, C. J., Samonig, M., Shiraiwa, M., Kofler, S., Yang, H., Gadermaier, G., Brandstetter, H., Huber, C. G., Duschl, A., Oostingh, G. J., and Pöschl, U.: Nitration of the Birch Pollen Allergen Bet v 1.0101: Efficiency and Site-Selectivity of Liquid and Gaseous Nitrating Agents, J. Proteome Res., 13, 1570–1577, 2014.

Reinmuth-Selzle, K., Kampf, C. J., Lucas, K., Lang-Yona, N., Fröhlich-Nowoisky, J., Shiraiwa, M., Lakey, P. S. J., Lai, S., Liu, F., Kunert, A. T., Ziegler, K., Shen, F., Sgarbanti, R., Weber, B., Bellinghausen, I., Saloga, J., Weller, M. G., Duschl, A., Schuppan, D., and Pöschl, U.: Air Pollution and Climate Change Effects on Allergies in the Anthropocene: Abundance, Interaction, and Modification of Allergens and Adjuvants, Environ. Sci. Technol., 51, 4119–4141, 2017.

Rosenfeld, D., Lohmann, U., Raga, G. B., O'Dowd, C. D., Kulmala, M., Fuzzi, S., Reissell, A., and Andreae, M. O.: Flood or Drought: How Do Aerosols Affect Precipitation?, Science, 321, 1309–1313, 2008.

Schauer, J. J., Rogge, W. F., Hildemann, L. M., Mazurek, M. A., Cass, G. R., and Simoneit, B. R.: Source apportionment of airborne particulate matter using organic compounds as tracers, Atmos. Environ., 30, 3837–3855, 1996.

Schraufnagel, D. E., Balmes, J. R., Cowl, C. T., De Matteis, S., Jung, S.-H., Mortimer, K., Perez-Padilla, R., Rice, M. B., Riojas-Rodriguez, H., Sood, A., Thurston, G. D., To, T., Vanker, A., and Wuebbles, D. J.: Air Pollution and Noncommunicable Diseases: A Review by the Forum of International Respiratory Societies' Environmental Committee, Part 1: The Damaging Effects of Air Pollution, Chest, 155, 409–416, 2019.

Seinfeld, J. H. and Pandis, S. N.: Atmospheric Chemistry and Physics: From Air Pollution to Climate Change, Wiley, 3rd edn., ISBN 978-1-118-94740-1, 2016.

Shahpoury, P., Lelieveld, S., Johannessen, C., Berkemeier, T., Celo, V., Dabek-Zlotorzynska, E., Harner, T., Lammel, G., and Nenes, A.: Influence of aerosol acidity

and organic ligands on transition metal solubility and oxidative potential of fine particulate matter in urban environments, Sci. Total Environ., 906, 167 405, 2024.

Sharma, V. K. and Graham, N. J.: Oxidation of Amino Acids, Peptides and Proteins by Ozone: A Review, Ozone: Sci. Eng, 32, 81–90, 2010.

Shiraiwa, M., Garland, R. M., and Pöschl, U.: Kinetic double-layer model of aerosol surface chemistry and gas-particle interactions (K2-SURF): Degradation of polycyclic aromatic hydrocarbons exposed to O3, NO2, H2O, OH and NO3, Atmos. Chem. Phys., 9, 9571–9586, 2009.

Shiraiwa, M., Pfrang, C., and Pöschl, U.: Kinetic multi-layer model of aerosol surface and bulk chemistry (KM-SUB): the influence of interfacial transport and bulk diffusion on the oxidation of oleic acid by ozone, Atmos. Chem. Phys., 10, 3673–3691, 2010.

Shiraiwa, M., Ammann, M., Koop, T., and Pöschl, U.: Gas uptake and chemical aging of semisolid organic aerosol particles, Proc. Natl. Acad. Sci. U.S.A., 108, 11 003–11 008, 2011.

Shiraiwa, M., Selzle, K., Yang, H., Sosedova, Y., Ammann, M., and Pöschl, U.: Multiphase Chemical Kinetics of the Nitration of Aerosolized Protein by Ozone and Nitrogen Dioxide, Environ. Sci. Technol., 46, 6672–6680, 2012.

Shiraiwa, M., Zuend, A., Bertram, A. K., and Seinfeld, J. H.: Gas–particle partitioning of atmospheric aerosols: interplay of physical state, non-ideal mixing and morphology, Phys. Chem. Chem. Phys., 15, 11 441–11 453, 2013.

Shiraiwa, M., Ueda, K., Pozzer, A., Lammel, G., Kampf, C. J., Fushimi, A., Enami, S., Arangio, A. M., Fröhlich-Nowoisky, J., Fujitani, Y., Furuyama, A., Lakey, P. S. J., Lelieveld, J., Lucas, K., Morino, Y., Pöschl, U., Takahama, S., Takami, A., Tong, H., Weber, B., Yoshino, A., and Sato, K.: Aerosol Health Effects from Molecular to Global Scales, Environ. Sci. Technol., 51, 13 545–13 567, 2017.

Song, C. H. and Carmichael, G. R.: The aging process of naturally emitted aerosol (sea-salt and mineral aerosol) during long range transport, Atmos. Environ., 33, 2203–2218, 1999.

Tong, H., Arangio, A. M., Lakey, P. S. J., Berkemeier, T., Liu, F., Kampf, C. J., Brune, W. H., Pöschl, U., and Shiraiwa, M.: Hydroxyl radicals from secondary organic aerosol decomposition in water, Atmos. Chem. Phys., 16, 1761–1771, 2016.

Tong, H., Lakey, P. S. J., Arangio, A. M., Socorro, J., Shen, F., Lucas, K., Brune, W. H., Pöschl, U., and Shiraiwa, M.: Reactive Oxygen Species Formed by Secondary Organic Aerosols in Water and Surrogate Lung Fluid, Environ. Sci. Technol., p. acs.est.8b03695, 2018.

Tuet, W. Y., Chen, Y., Xu, L., Fok, S., Gao, D., Weber, R. J., and Ng, N. L.: Chemical oxidative potential of secondary organic aerosol (SOA) generated from the photooxidation of biogenic and anthropogenic volatile organic compounds, Atmos. Chem. Phys., 17, 839–853, 2017.

Turner, M. C., Jerrett, M., Pope, C. A., Krewski, D., Gapstur, S. M., Diver, W. R., Beckerman, B. S., Marshall, J. D., Su, J., Crouse, D. L., and Burnett, R. T.: Long-Term Ozone Exposure and Mortality in a Large Prospective Study, Am. J. Respir. Crit. Care Med, 193, 1134–1142, 2016.

Twomey, S.: Pollution and the planetary albedo, Atmos. Environ., 8, 1251–1256, 1974.

Twomey, S.: The Influence of Pollution on the Shortwave Albedo of Clouds, J. Atmos. Sci., 34, 1149–1152, 1977.

Utinger, B., Campbell, S. J., Bukowiecki, N., Barth, A., Gfeller, B., Freshwater, R., Rüegg, H.-R., and Kalberer, M.: An automated online field instrument to quantify the oxidative potential of aerosol particles via ascorbic acid oxidation, Atmos. Meas. Tech., 16, 2641–2654, 2023.

van der Vliet, A., O'Neill, C. A., Cross, C. E., Koostra, J. M., Volz, W. G., Halliwell, B., and Louie, S.: Determination of low-molecular-mass antioxidant concentrations in human respiratory tract lining fluids, Am. J. Physiol. Lung Cell Mol. Physiol., 276, 289–296, 1999.

Vesna, O., Sax, M., Kalberer, M., Gaschen, A., and Ammann, M.: Product study of oleic acid ozonolysis as function of humidity, Atmos. Env., 43, 3662–3669, 2009.

Wang, J., Huang, D., Chen, F., Chen, J., Jiang, H., Zhu, Y., Chen, C., and Zhao, J.: Rapid Redox Cycling of Fe(II)/Fe(III) in Microdroplets during Iron–Citric Acid Photochemistry, Environ. Sci. Technol., 57, 4434–4442, 2023.

Weichenthal, S., Crouse, D. L., Pinault, L., Godri-Pollitt, K., Lavigne, E., Evans, G., van Donkelaar, A., Martin, R. V., and Burnett, R. T.: Oxidative burden of fine particulate air pollution and risk of cause-specific mortality in the Canadian Census Health and Environment Cohort (CanCHEC), Environ. Res., 146, 92–99, 2016.

Weller, C., Horn, S., and Herrmann, H.: Photolysis of Fe(III) carboxylato complexes: Fe(II) quantum yields and reaction mechanisms, J. Photochem. Photobiol. A, 268, 24–36, 2013.

Weller, C., Tilgner, A., Bräuer, P., and Herrmann, H.: Modeling the Impact of Iron–Carboxylate Photochemistry on Radical Budget and Carboxylate Degradation in Cloud Droplets and Particles, Environ. Sci. Technol., 48, 5652–5659, 2014.

Zahardis, J. and Petrucci, G. A.: The oleic acid-ozone heterogeneous reaction system: products, kinetics, secondary chemistry, and atmospheric implications of a model system - a review, Atmos. Chem. Phys., 7, 1237–1274, 2007.

Zappoli, S., Andracchio, A., Fuzzi, S., Facchini, M., Gelencsér, A., Kiss, G., Krivácsy, Z., Molnár, , Mészáros, E., Hansson, H.-C., Rosman, K., and Zebühr, Y.: Inorganic, organic and macromolecular components of fine aerosol in different areas of Europe in relation to their water solubility, Atmos. Environ., 33, 2733–2743, 1999.

Ziemann, P. J.: Aerosol products, mechanisms, and kinetics of heterogeneous reactions of ozone with oleic acid in pure and mixed particles, Faraday Discuss., 130, 469–90; discussion 491–517, 519–24, 2005.

A. Personal List of Publications

Journal Articles

1. Mishra, A., Lelieveld S., Krüger M., Campbell C. J., Srivastava, D., Lanzafame, G. M., Tomaz, S., Favez, O., Bonnaire, N., Lucarelli, F., Alleman, L., Uzu, G., Jaffrezo, J-L., Green D. C., Priestman, M., Tremper, A. H., Barth, A., Kalberer, M., Bandowe, B. A. M., Lammel, G., Pöschl, U., Shahpoury, P., Albinet, A., Berkemeier, T.: Chemical kinetics and reaction mechanisms of reactive species production and antioxidant depletion in different assays measuring aerosol oxidative potential, *in preparation*.

2. Mishra, A., Kilchhofer, K., Iezzi, L., Pöschl, U., Alpert, P. A., Ammann, M., Berkemeier, T.: Photochemical degradation of iron citrate in anoxic viscous films enhanced by redox cascades, *ACS Earth Space Chem.* **9**, 689-698, (2025).

3. Tang, R., Sahu, R., Su, Y., Milsom, A., Mishra, A., Berkemeier, T., Pfrang, C.: Impact of Cooking Methods on Indoor Air Quality: A Comparative Study of Particulate Matter (PM) and Volatile Organic Compound (VOC) Emissions, *Indoor Air* **7**, 6355613, (2024).

4. Lelieveld, S., Lelieveld, J., Mishra, A., Daiber, A., Pozzer, A., Pöschl, U.,Berkemeier, T.,: Endogenous Nitric Oxide Can Enhance Oxidative Stress Caused by Air Pollutants and Explain Higher Susceptibility of Individuals with Inflammatory Disorders, *Environ. Sci. Technol.* **58**, 1823-1831, (2024).

5. Krüger, M. , Mishra, A., Spichtinger, P., Pöschl, U.,Berkemeier, T.,: A kinetic compass for the design of experiments to determine kinetic parameters, *J. Cheminform.* **16**, 34, (2024).

6. Milsom, A., Qi, S., Mishra, A., Berkemeier, Zhang, Z., Pfrang, C.,: In situ measurements and modelling of the oxidation kinetics in films of a cooking aerosol proxy using a quartz crystal microbalance with dissipation monitoring (QCM-D), *Atmos. Chem. Phys.* **23**, 10835-10843, (2023).

7. Mishra, A., Lelieveld, S., Pöschl, U., Berkemeier, T.: Multiphase Kinetic Modeling of Air Pollutant Effects on Protein Modification and Nitrotyrosine Formation in Epithelial Lining Fluid, *Environ. Sci. Technol.* **57**, 12642-12653, (2023).

8. Dovrou, E., Lelieveld, S., Mishra, A., Pöschl, U., Berkemeier, T.: Influence of ambient and endogenous H_2O_2 on reactive oxygen species concentrations and OH radical production in the respiratory tract, *Environ. Sci.: Atmos* **3**, 1066-1074, (2023).

9. Müller, M., Mishra, A., Berkemeier, T., Hausammann, E., Peter, T., Krieger, U. K.: Electrodynamic balance–mass spectrometry reveals impact of oxidant concentration on product composition in the ozonolysis of oleic acid *Phys. Chem. Chem. Phys.* **24**, 27086-27104 (2022).

10. Berkemeier, T., Mishra, A., Mattei, C., Huisman, A. J., Krieger, U. K., and Pöschl, U.: Ozonolysis of Oleic Acid Aerosol Revisited: Multiphase Chemical Kinetics and Reaction Mechanisms. *ACS. Earth. Space. Chem.* **5**, 3313-3323 (2021).

11. Lelieveld, S., Wilson, J., Dovrou, E., Mishra, A., Lakey, P. S. J., Shiraiwa, M.,Pöschl, U., Berkemeier, T.,: Hydroxyl radical production by air pollutants in epithelial lining fluid governed by interconversion and scavenging of reactive oxygen species *Environ. Sci. Technol.* **55**, 14069-14079, (2021).

Oral presentations

1. Mishra, A., Lelieveld S., Campbell C. J., Srivastava, D., Lanzafame, G. M., Tomaz, S., Favez, O., Bonnaire, N., Lucarelli, F., Alleman, L., Uzu, G., Jaffrezo, J-L., Chen G. I., Green D. C., Priestman, M., Tremper, A. H., Barth, A., Kalberer, M., Bandowe, B. A. M., Lammel, G., Pöschl, U., Shahpoury, P., Albinet, A., Berkemeier, T.: Chemical kinetics and reaction mechanisms of aerosol oxidative potential, European Aerosol Conference, Lecce, Italy, 31st August - 5th September 2025.

2. Mishra, A., Kilchhofer, K., Iezzi, L., Pöschl, U., Alpert, P. A., Ammann, M., Berkemeier, T.: Diffusion-limited Kinetics of Iron Citrate Photochemical Degradation in Organic Films, European Aerosol Conference, Tampere, Finland, 25th - 30th August 2024.

3. Mishra, A., Lelieveld, S., Pöschl, U., Berkemeier, T.: Multiphase Kinetic Modeling of Air Pollutant Effects on Protein Modification and Nitrotyrosine Formation in Epithelial Lining Fluid, European Aerosol Conference, Malaga, Spain, 3rd - 8th September 2023.

4. Mishra, A., Müller, M., Peter, T., Pöschl, U., Krieger, U. K., Berkemeier, T.: Multiphase chemical kinetics and reaction mechanisms of oleic acid ozonolysis: Evaporation and dimerization kinetics dictate the evolution of products, International Aerosol Conference, Athens, Greece, 4th - 9th September 2022.

5. Mishra, A., Dovrou, E., Lelieveld, S., Pöschl, U., Berkemeier, T.: Constraining the production rate of reactive oxygen species from air pollution in the human

lung with EPR spectroscopy and mechanisms in cloud chemistry models, General Assembly of the European Geosciences Union, Vienna, Austria, 23rd - 27th May 2022.

Poster presentations

1. Mishra, A., Lelieveld, S., Pöschl, U., Berkemeier, T. Modification of proteins by biological and atmospheric oxidants in the epithelial lining fluid, 782 WE-Heraeus-Seminar: Aerosols, Health and Climate: Gigacity and Future, Bad Honnef, Germany, 20th - 24th March 2023.

B. Supplement

B.1 Supplement of "Ozonolysis of Oleic Acid Aerosol Revisited: Multiphase Chemical Kinetics and Reaction Mechanisms"

Supplementary Information to:

Ozonolysis of oleic acid aerosol revisited: multiphase chemical kinetics and reaction mechanisms

Thomas Berkemeier[1,*], Ashmi Mishra[1], Coraline Mattei[1], Andrew J. Huisman[2,‡], Ulrich K. Krieger[2], Ulrich Pöschl[1,*]

[1] Multiphase Chemistry Department, Max Planck Institute for Chemistry, Hahn-Meitner-Weg 1, Mainz, Germany;
[2] ETH Zurich, Institute for Atmospheric and Climate Science, Universitätstrasse 16, 8092, Zurich, Switzerland;
[‡] now at: Gentex Corporation, Applied Engineering Department, 600 N Centennial St, 49464, Zeeland, Michigan, USA

Correspondence to:
Thomas Berkemeier (t.berkemeier@mpic.de),
Ulrich Pöschl (u.poschl@mpic.de)

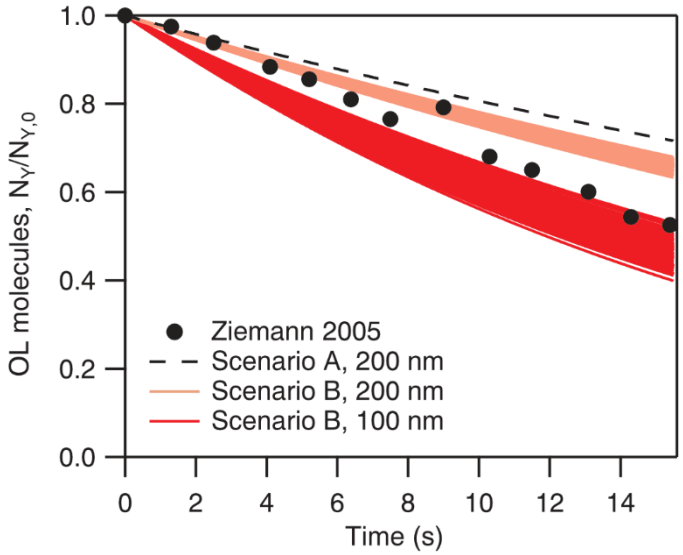

Figure S1: Model sensitivity towards different particle sizes in the EC1 experiment (black markers) in modelling scenario A (dashed line) and modelling scenario B (ensemble of colored lines).

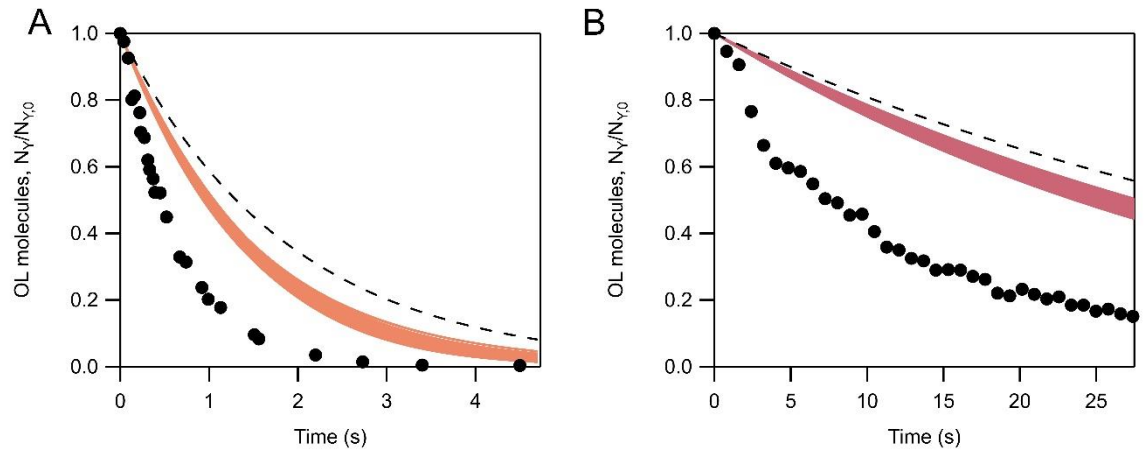

Figure S2: Model output according to modelling scenario A (dashed line) and modelling scenario B (ensemble of colored lines) for additional oleic acid ozonolysis data (black markers). (a) Data from Hearn et al. 2005[1], which was recorded under similar experimental conditions as experimental data set FT1 (Hearn and Smith 2004[2]). (b) Data provided in exchange with P. Ziemann, including additional data not shown in the original publication (Ziemann 2005[3]).

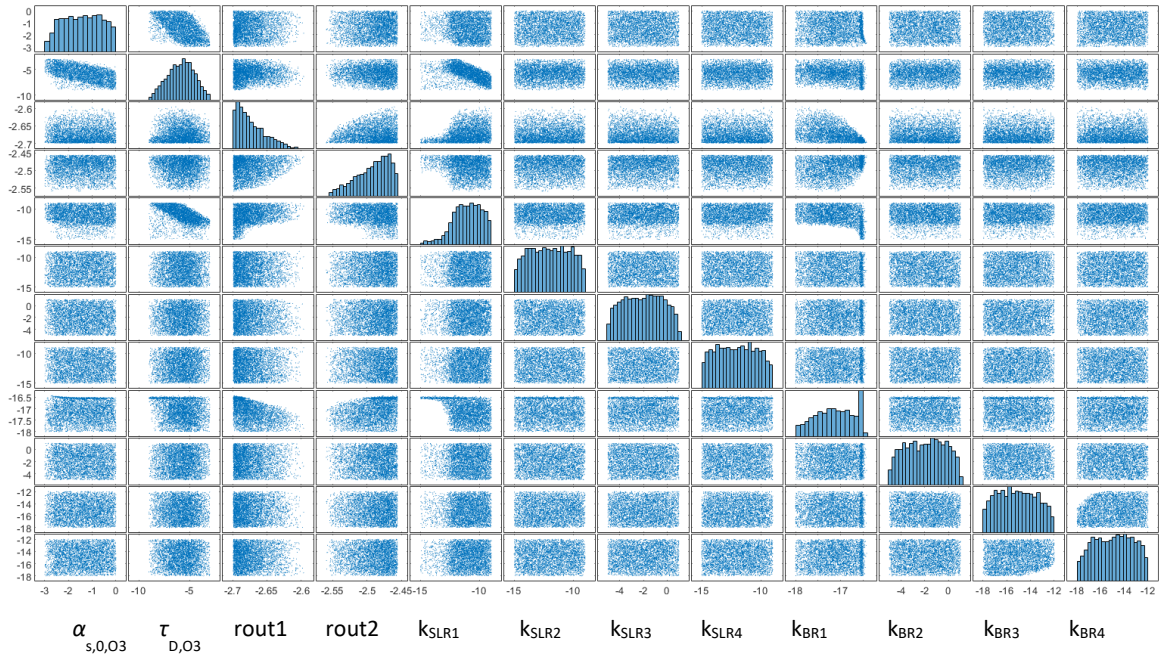

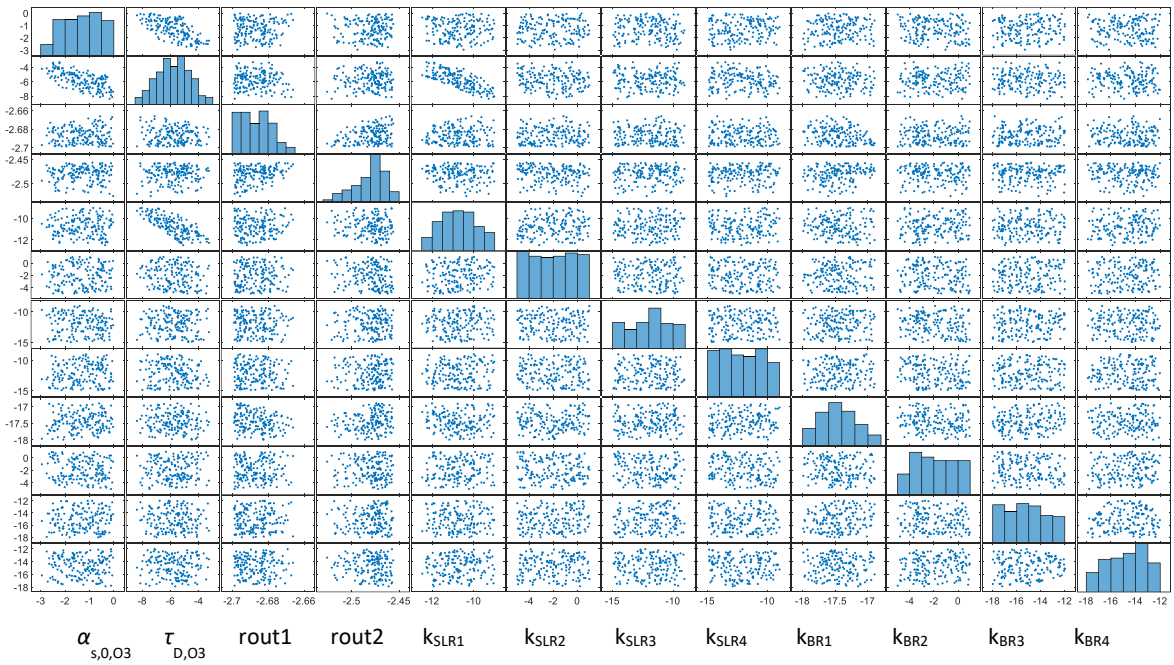

Figure S3: Scatter plot matrix of kinetic parameters of model fits according to modelling scenario B with (a) residual R<0.112 (N=3995) and (b) residual R<0.108 (N=167). Note that the boundaries of the individual plots do not correspond to the optimization boundaries but rather the minimal and maximal values returned upon optimization for each parameter.

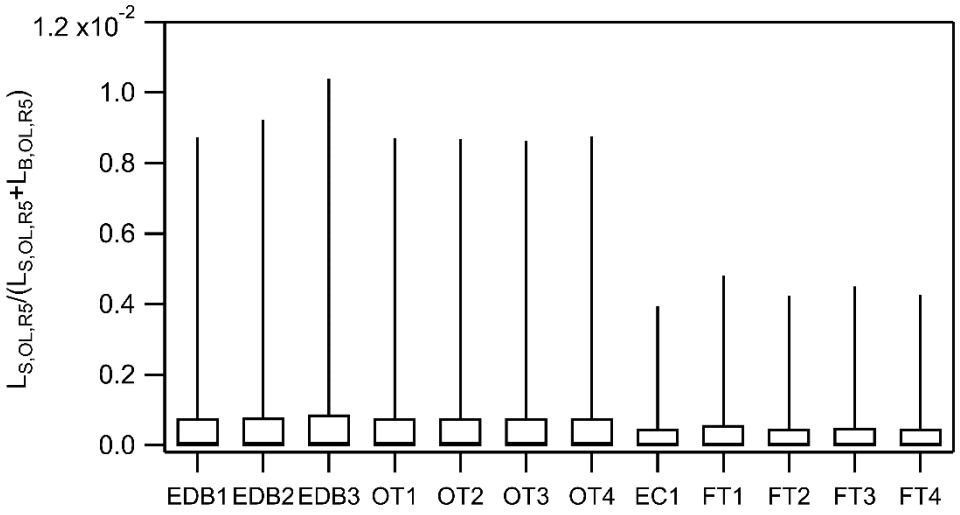

Figure S4: Surface-to-total OL loss ratio (STLR) for reaction R5 using KM-SUB model outputs for a host of N=167 fits to a range of 12 experimental data sets using modelling scenario B. The box-whisker plot shows the 10, 25, 50, 75 and 90 percentiles for each model output value.

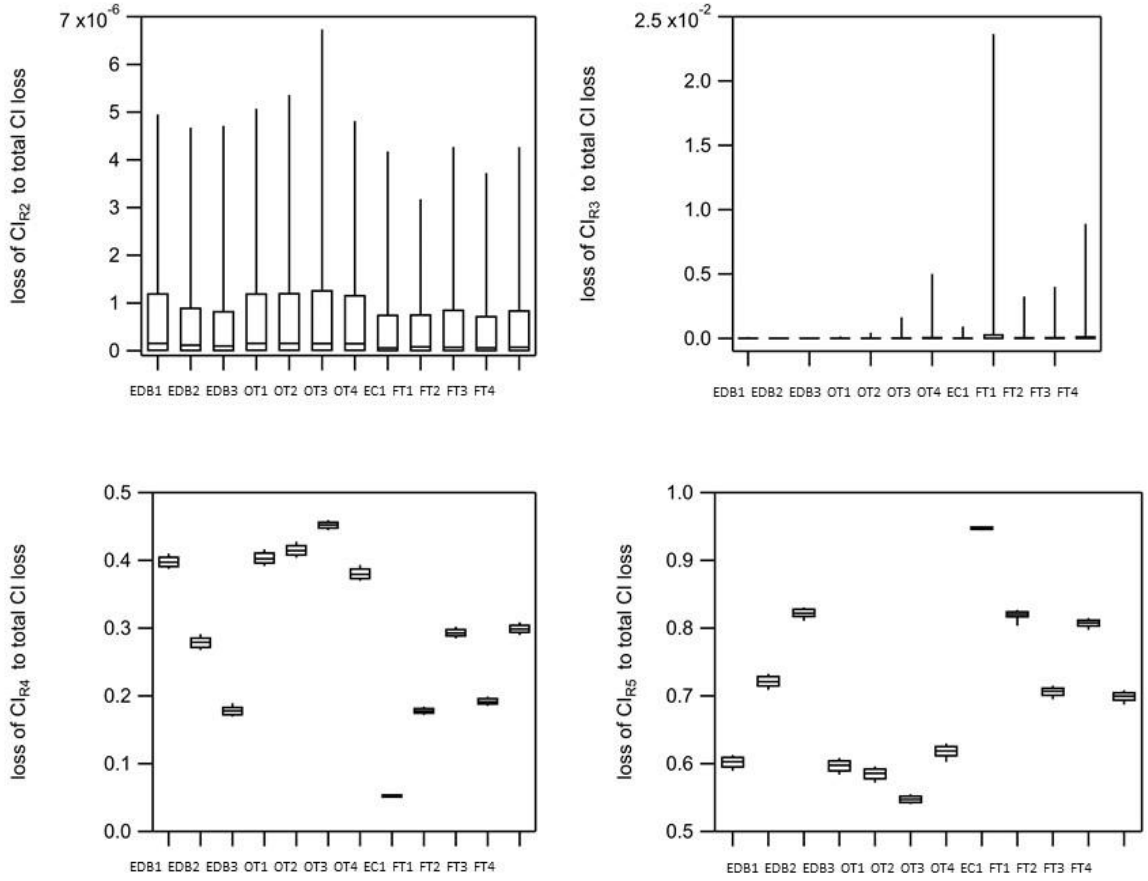

Figure S5: Relative CI fate for reactions (a) R2, (b) R3, (c) R4, and (d) R5 to total CI loss. The box-whisker plots show the 10, 25, 50, 75 and 90 percentiles for each model output value.

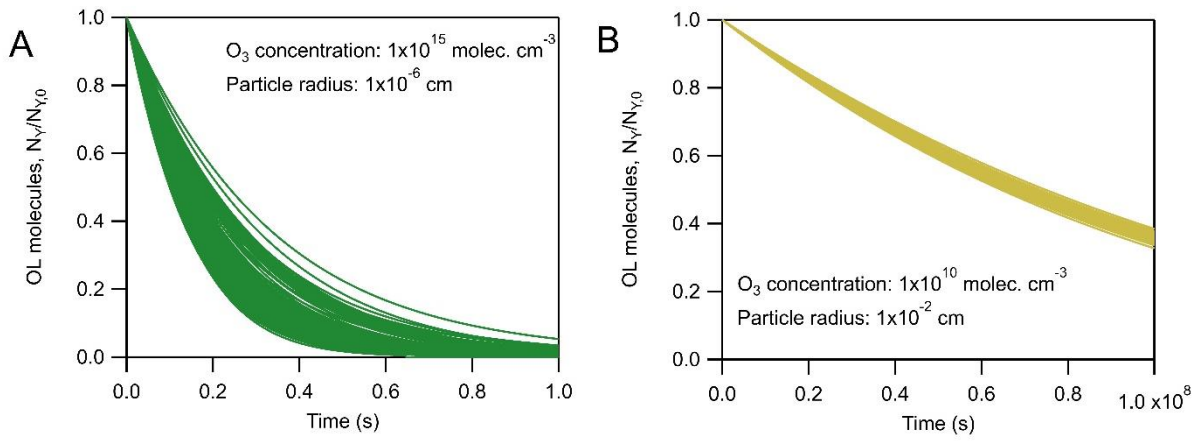

Figure S6: Model output for additional experimental conditions that have not been investigated experimentally.

Table S1: Reaction mechanism used for modelling scenario C, adapted from the template in Zeng and Wilson[4].

$O3 + OL \rightarrow CI + \frac{1}{2}$ C9-acid $+ \frac{1}{2}$ Nonanal	Fitted	(R1b)
$CI \rightarrow RO\bullet + OH\bullet$	Fitted	(R2b)
$CI + CI \rightarrow$ Peroxide	Fitted	(R3)
CI + C9-acid → Peroxide	Fitted	(R4)
CI + OL → OL*	Fitted	(R5)
$O3 + OL^* \rightarrow CI + \frac{1}{2}$ C9-acid	Fitted	(R6)
RO• → C9-acid	Fitted	(R7)
C9-acid + OH• → C9-acid•	2×10^{-11}, Ref [1]	(R8)
OL + OH• → OL•	2×10^{-11}, Ref [1]	(R9)
OL + OH• $\rightarrow CI + \frac{1}{2}$ C9-acid	6.6×10^{-11}, Ref [1]	(R10)
OL* + OH• → OL*•	2×10^{-11}, Ref [1]	(R11)
OL* + OH• $\rightarrow CI + \frac{1}{2}$ C9-acid	6.6×10^{-11}, Ref [1]	(R12)
Peroxide + OH → Peroxide•	2×10^{-11}, Ref [1]	(R13)
C9-acid + RO• → C9-acid + C9-acid•	1.66×10^{-15}, Ref [1]	(R14)
OL* + RO• → C9-acid + OL*•	1.66×10^{-15}, Ref [1]	(R15)
OL + RO• → C9-acid + OL*•	1.66×10^{-15}, Ref [1]	(R16)
Peroxide + RO• → C9-acid + Peroxide•	1.66×10^{-15}, Ref [1]	(R17)
C9-acid• + C9-acid• → C9-acid + C9-acid	4×10^{-15}, Ref [1]	(R18)
C9-acid• + OL*• → C9-acid + OL*	4×10^{-15}, Ref [1]	(R19)
OL*• + OL*• → OL* + OL*	4×10^{-15}, Ref [1]	(R20)
C9-acid• + Peroxide• → C9-acid + Peroxide	4×10^{-15}, Ref [1]	(R21)
Peroxide• + OL*• → Peroxide + OL*	4×10^{-15}, Ref [1]	(R22)
Peroxide• + Peroxide• → Peroxide + Peroxide	4×10^{-15}, Ref [1]	(R23)
C9-acid• + C9-acid• → RO• + RO•	1×10^{-16}, Ref [1]	(R24)
C9-acid• + OL*• → RO• + RO•	1×10^{-16}, Ref [1]	(R25)
OL*• + OL*• → RO• + RO•	1×10^{-16}, Ref [1]	(R26)
C9-acid• + Peroxide• → RO• + RO•	1×10^{-16}, Ref [1]	(R27)
OL*• + Peroxide• → RO• + RO•	1×10^{-16}, Ref [1]	(R28)
Peroxide• + Peroxide• → RO• + RO•	1×10^{-16}, Ref [1]	(R29)

References

(1) Hearn, J. D.; Lovett, A. J.; Smith, G. D. Ozonolysis of oleic acid particles: evidence for a surface reaction and secondary reactions involving Criegee intermediates. *Phys.Chem. Chem. Phys.* **2005**,7, 501–11.

(2) Hearn, J. D.; Smith, G. D. Kinetics and Product Studies for Ozonolysis Reactions of Organic Particles Using Aerosol CIMS. *J. Phys. Chem. A* **2004**,108, 10019–10029.

(3) Ziemann, P. J. Aerosol products, mechanisms, and kinetics of heterogeneous reac-tions of ozone with oleic acid in pure and mixed particles. *Faraday Discuss*. **2005**,130, 469–90; discussion 491–517, 519–24.

(4) Zeng, M.; Wilson, K. R. Efficient Coupling of Reaction Pathways of Criegee Intermediates and Free Radicals in the Heterogeneous Ozonolysis of Alkenes. *J. Phys. Chem. Lett.* 2020, *11*, 6580–6585.

B.2 Supplement of "Photochemical degradation of iron citrate in anoxic viscous films enhanced by redox cascades"

Supporting Information for: Photochemical degradation of iron citrate in anoxic viscous films enhanced by redox cascades

Ashmi Mishra[1], Kevin Kilchhofer[2,3], Lucia Iezzi[2,3], Ulrich Pöschl[1], Peter A. Alpert[2], Markus Ammann[2], and Thomas Berkemeier[1]

[1]Multiphase Chemistry Department, Max Planck Institute for Chemistry, 55128 Mainz, Germany
[2]PSI Center for Energy and Environmental Sciences, 5232 PSI Villigen, Switzerland
[3]Department of Environmental System Science, Institute for Atmospheric and Climate Science, ETH Zurich, 8092 Zurich, Switzerland

Correspondence: Thomas Berkemeier (t.berkemeier@mpic.de)

Fig. S1 CO_2 yield as a function of humidity

Fig. S2 Comparison of model results with 100% CO_2 yield

Fig. S3 Depth profile of O_2 at different humidities

Fig. S4 Depth profile of total Fe^{III} at different humidities

Fig. S5 Relative sinks of Fe^{II} as a fucntion of time and humidity

Fig. S6 Depth profile of HO_2 at different humidities

Fig. S7 Depth profile of H_2O_2 at different humidities

Fig. S8 Degree of oxygen saturation (S_{O_2}) as a function of particle size and relative humidity

Tab. S1 Acid-base equilibria

Tab. S2 Chemical reactions

Tab. S3 Input parameters for Vignes-type equation

Sect. S1 Layer sizing in the kinetic model

Sect. S2 Water activity parameterization

Sect. S3 Film Thickness calculation

1 Supplementary Figures

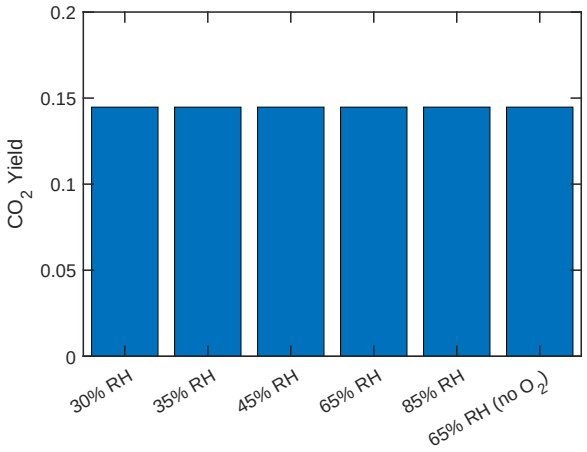

Figure S1. CO_2 yield as a function of humidity. The CO_2 yield is defined as the number of CO_2 molecules produced per loss of $Fe^{III}Cit$

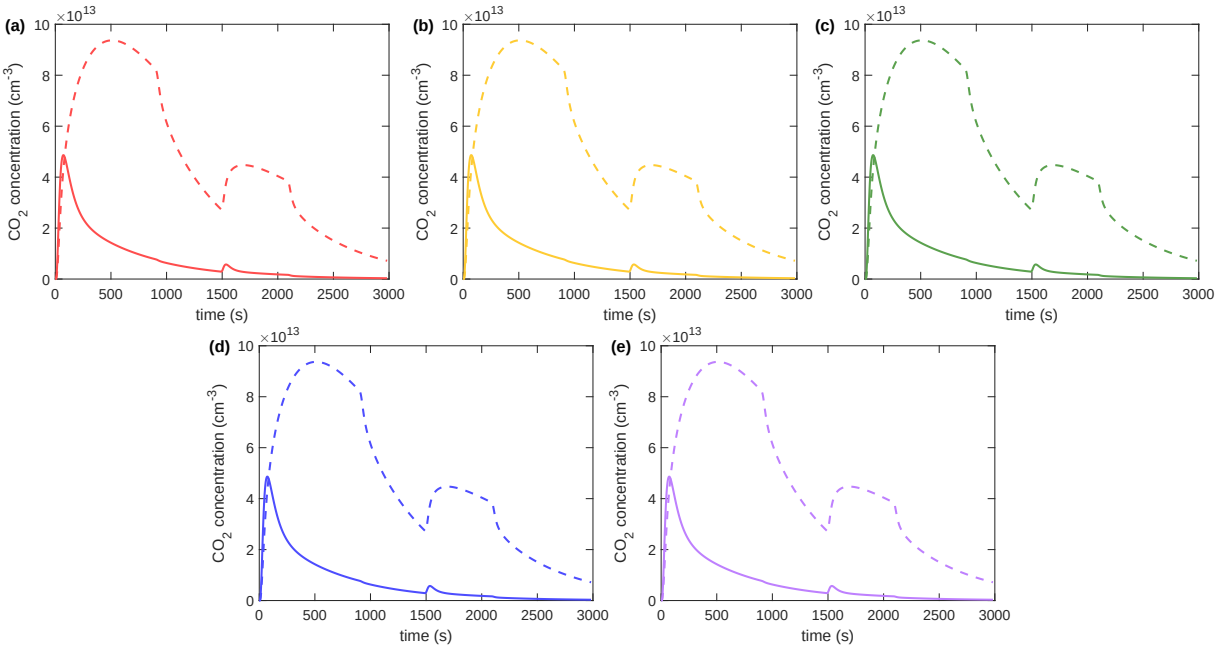

Figure S2. CO_2 concentration with best model fit parameters (solid lines) and a comparison with a model result assuming 100% CO_2 yield and a photolysis rate that is a factor of 15 lower than in the best model fit (dashed lines) to partially compensate for the higher CO_2 yield. Results are displayed as a function of time at different relative humidities (30 % RH (a), 35 % RH (b), 45 % RH (c), 65 % RH (d), 85 % RH (e)).

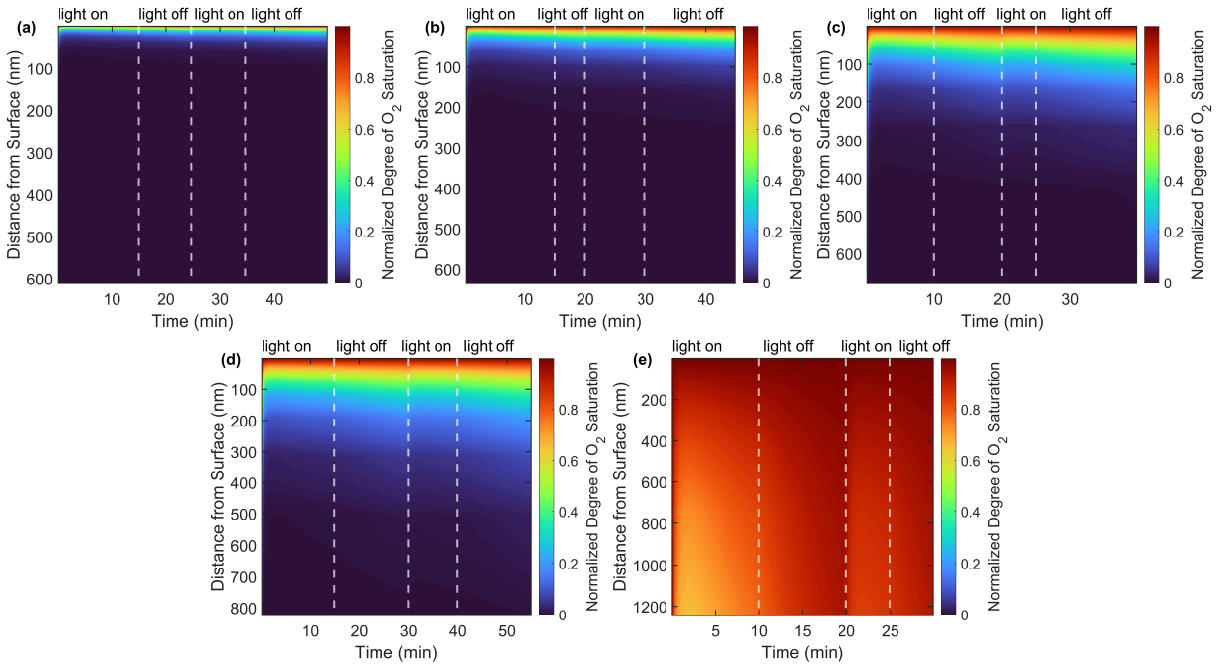

Figure S3. Model results for the depth profile of O_2 in the films as a function of time at different relative humidities (30 % RH (a), 35 % RH (b), 45 % RH (c), 65 % RH (d), 85 % RH (e)). The y-axis indicates the distance from the film surface.

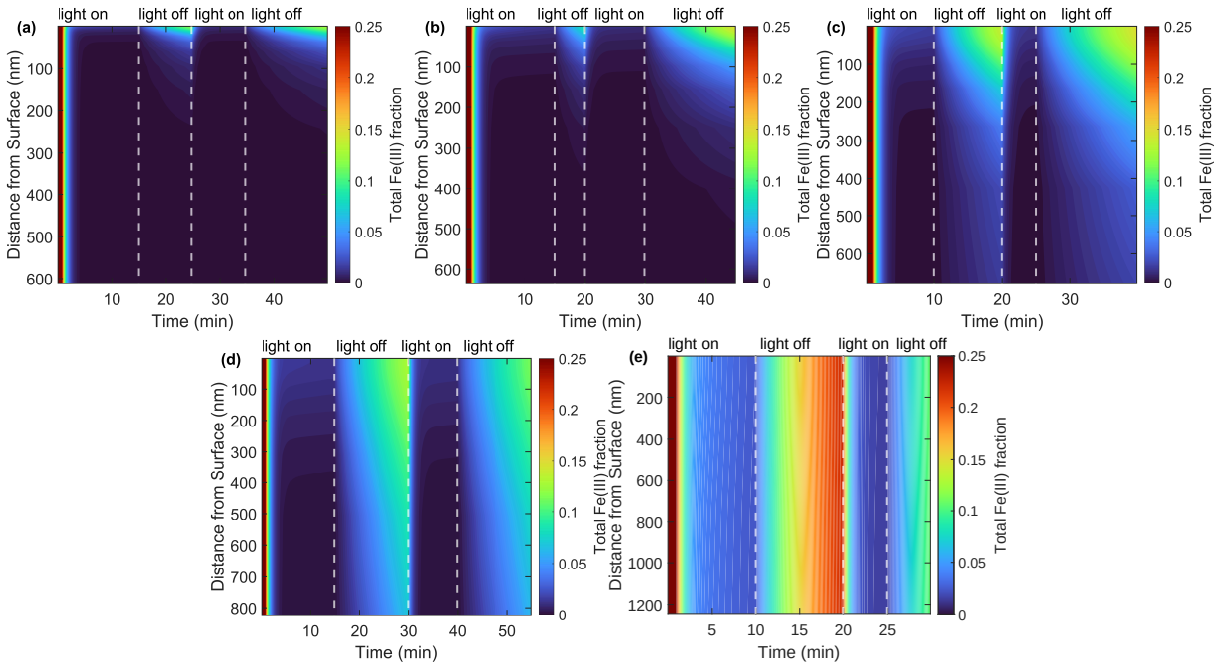

Figure S4. Model results for the depth profile of Fe^{III} fraction in the films as a function of time at different relative humidities (30 % RH (a), 35 % RH (b), 45 % RH (c), 65 % RH (d), 85 % RH (e)). The y-axis indicates the distance from the film surface.

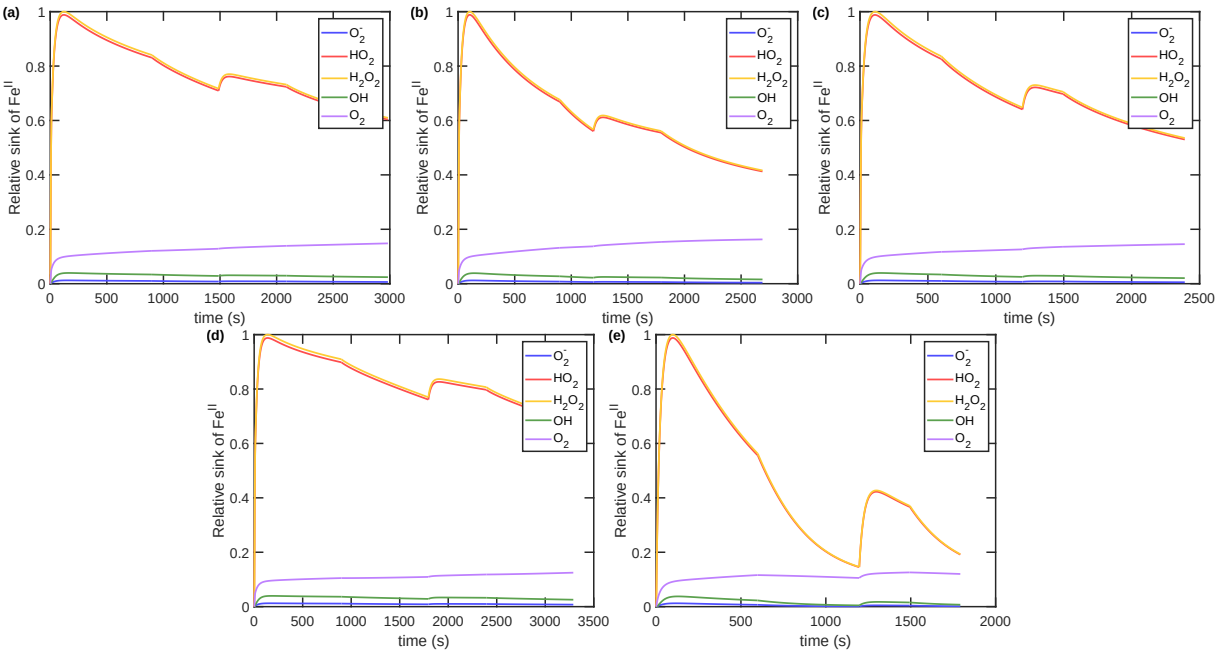

Figure S5. Relative Fe^{II}CitH sinks as a function of time at different relative humidities (30 % RH (a), 35 % RH (b), 45 % RH (c), 65 % RH (d), 85 % RH (e)).

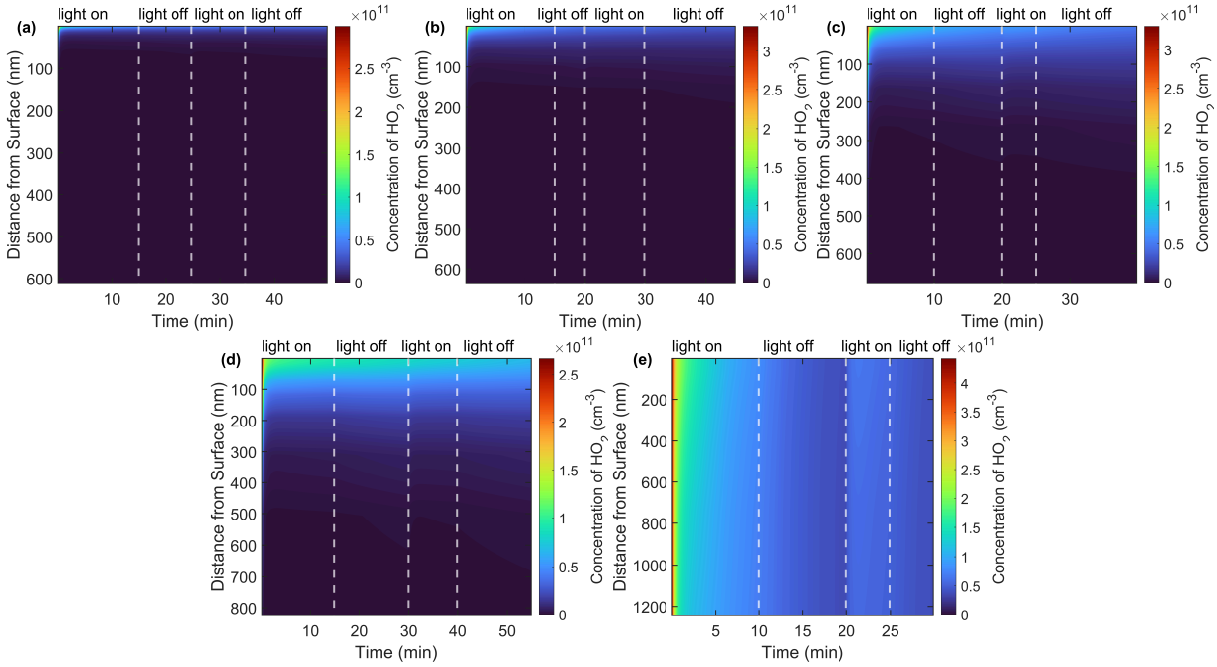

Figure S6. Model results for the depth profile of HO_2 in the films as a function of time at different relative humidities (30 % RH (a), 35 % RH (b), 45 % RH (c), 65 % RH (d), 85 % RH (e)). The y-axis indicates the distance from the film surface.

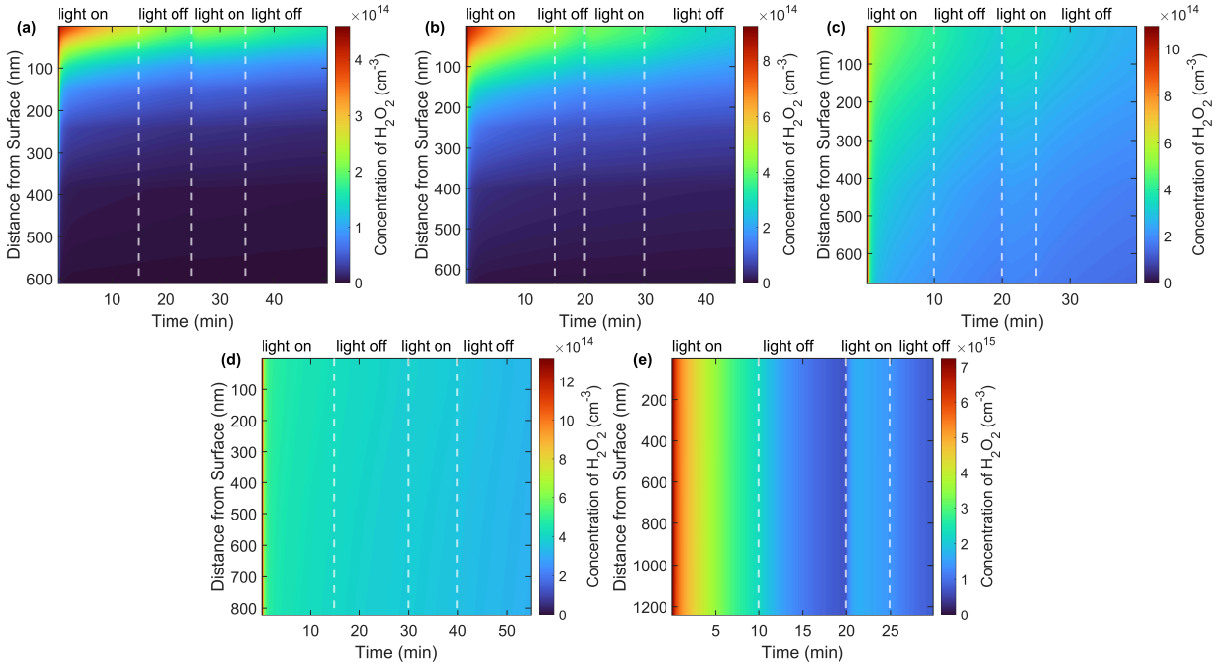

Figure S7. Model results for the depth profile of H_2O_2 in the films as a function of time at different relative humidities (30 % RH (a), 35 % RH (b), 45 % RH (c), 65 % RH (d), 85 % RH (e)). The y-axis indicates the distance from the film surface.

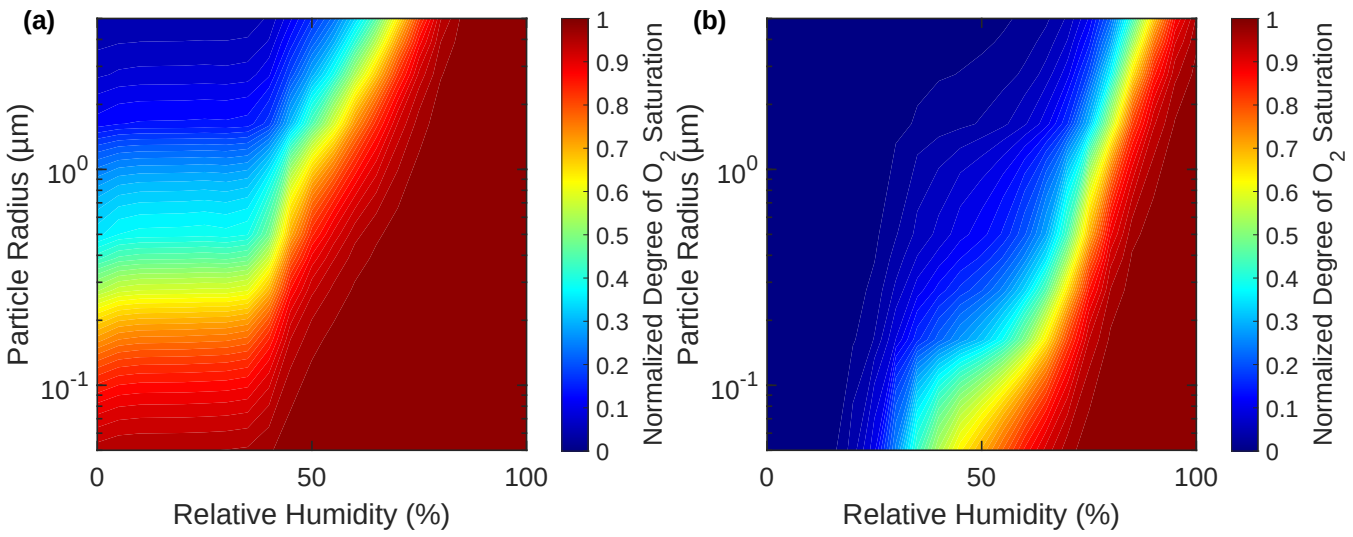

Figure S8. Normalized degree of oxygen saturation (S_{O_2} = $[O_2]_{bulk}/[O_2]_{bulk,sat}$) as a function of particle size and relative humidity at two different extremes of diffusion coefficients (panel a: $D_{b,CO2}$: 2.00 × 10^{-20} – 1.00 × 10^{-7} cm^2 s^{-1}, $D_{b,O2}$: 1.00 × 10^{-20} – 1.00 x 10^{-7} cm^2 s^{-1}, panel b: $D_{b,CO2}$: 6.90 × 10^{-12} – 9.80 × 10^{-6} cm^2 s^{-1}, $D_{b,O2}$: 1.90 × 10^{-11} – 1.00 × 10^{-5} cm^2 s^{-1}). The photon flux was set to solar irradiation at the Earth's surface at a zenith angle of 0°. The Fe^{III}Cit concentration was 0.41 M following Khaled et al. (2022) and citric acid was added to maintain a Fe^{III}Cit to organics mole ratio of 1:10.

2 Supplementary Tables

Table S1. Chemical reaction equilibria used in this study. In the KM-SUB model, the forward reaction rate is set to 1×10^8 M^{-1} s^{-1} and the backward reaction rate is derived from the equilibrium constant.

Number	Equilibrium reaction	Equilibrium constant	Reference
1	$OH^- + H^+ \rightleftharpoons H_2O$	1.80×10^{-16} M	
2	$CitH_2^- + H^+ \rightleftharpoons CitH_3$	1.33×10^3 M^{-1}	Martell and Smith (1982)
3	$CitH^{2-} + H^+ \rightleftharpoons CitH_2^-$	5.88×10^4 M^{-1}	Martell and Smith (1982)
4	$Cit^{3-} + H^+ \rightleftharpoons CitH^{2-}$	2.50×10^6 M^{-1}	Martell and Smith (1982)
5	$Fe^{3+} + Cit^{3-} \rightleftharpoons Fe^{III}Cit$	1.58×10^{13} M^{-1}	Dou et al. (2021)
6	$[Fe^{III}CitOH]^- + H^+ \rightleftharpoons Fe^{3+} + Cit^{3-} + H_2O$	1.20×10^{-8} M	Dou et al. (2021)
7	$Fe^{3+} + CitH^{2-} \rightleftharpoons [Fe^{III}CitH]^+$	2.51×10^7 M^{-1}	Dou et al. (2021)
8	$Fe^{2+} + CitH^{2-} \rightleftharpoons Fe^{II}CitH$	1.94×10^{10} M^{-1}	Dou et al. (2021)
9	$[Fe^{III}OH]^{2+} + H^+ \rightleftharpoons Fe^{3+} + H_2O$	4.57×10^{-3} M	Smith and Martell (1976)
10	$Fe^{2+} + O{=}C(CH_2COO)_2^{2-} \rightleftharpoons Fe^{II}[O{=}C(CH_2COO)_2]$	2.00×10^{-3} M^{-1}	Dou et al. (2021)
11	$2H^+ + O{=}C(CH_2COO)_2^{2-} \rightleftharpoons O{=}C(CH_2COOH)_2$	1.50×10^6 M^{-2}	Dou et al. (2021)
12	$2H^+ + OH{-}C(CH_2COO)_2^{2-} \rightleftharpoons OH{-}C(CH_2COOH)_2$	1.50×10^6 M^{-2}	Dou et al. (2021)
13	$O_2^- + H^+ \rightleftharpoons HO_2$	6.30×10^4 M^{-1}	Bielski et al. (1985)
14	$Fe^{3+} + CitH_3 \rightleftharpoons Fe^{III}Cit + 3H^+$	8.06×10^{-2} M^{-2}	Inferred from 2, 3, 4, 5
15	$[Fe^{III}OH]^{2+} + CitH^{2-} \rightleftharpoons Fe^{III}Cit + H_2O$	1.38×10^9	Inferred from 4, 5, 9
16	$[Fe^{III}CitOH]^- + CitH_3 \rightleftharpoons Fe^{III}Cit + CitH_3 + OH^-$	1.42×10^2 M	Inferred from 2, 5, 9
17	$[Fe^{III}CitH]^+ + CitH_2^- \rightleftharpoons Fe^{III}Cit + CitH_3$	3.35×10^2	Inferred from 2, 4, 5, 7
18	$[Fe^{III}CitH]^+ + Cit^{3-} \rightleftharpoons Fe^{III}Cit + CitH^{2-}$	6.29×10^5	Inferred from 5, 7
19	$[Fe^{III}CitOH]^- + CitH_2^- \rightleftharpoons Fe^{III}Cit + CitH^{2-} + H_2O$	3.22 M	Inferred from 3, 5, 6
20	$[Fe^{III}CitOH]^- + CitH^{2-} \rightleftharpoons Fe^{III}Cit + Cit^{3-} + H_2O$	7.57×10^{-2} M	Inferred from 4, 5, 6
21	$[Fe^{III}OH]^{2+} + CitH_2^- \rightleftharpoons Fe^{III}Cit + H^+ + H_2O$	2.35×10^4 M	Inferred from 3, 4, 5, 9
22	$[Fe^{III}OH]^{2+} + CitH_3 \rightleftharpoons Fe^{III}Cit + 2H^+ + H_2O$	1.76×10^1 M^2	Inferred from 2, 3, 4, 5, 9
23	$[Fe^{III}OH]^{2+} + Cit^{3-} \rightleftharpoons Fe^{III}Cit + OH^-$	3.46×10^1	Inferred from 1, 5, 9
24	$[Fe^{III}CitH]^+ + CitH^{2-} \rightleftharpoons Fe^{III}Cit + CitH_2^-$	1.48×10^4	Inferred from 3, 4, 5, 7
25	$Fe^{3+} + CitH_2^- \rightleftharpoons Fe^{III}Cit + 2H^+$	1.07×10^2 M	Inferred from 3, 4, 5

Table S2. Chemical reactions included in the KM-SUB model. The respective lower and upper boundaries indicate the initial constraints of the fit ensemble. Values that were fixed during the fitting procedure are indicated using square brackets. Species on top of the arrow in the chemical reaction refer to those that partake in the chemical reaction but that are not used to determine the reaction order.

Reaction	Range	Reference
$Fe^{III}Cit + h\nu \rightarrow Fe^{2+} + Cit^{\bullet}$	2.65×10^{-2} - 1.06×10^{-1} s^{-1}	This study
$Cit^{\bullet} \rightarrow OH-C(CH_2COO)_2^{2-} + CO_2$	[1.00×10^{9} s^{-1}]	Pozdnyakov et al. (2014)
$OH-C(CH_2COO)_2^{2-} + Fe^{III}Cit \rightarrow Fe^{2+} + O=C(CH_2COO)_2^{2-} + CitH^{2-}$	8.20×10^{-23} - 8.20×10^{-19} cm^3 s^{-1}	This study
$Cit^{\bullet} \rightarrow Cit^{3-}$	1.00×10^{8} - 1.00×10^{10} s^{-1}	This study
$HO_2 + HO_2 \rightarrow H_2O_2 + O_2$	[3.45×10^{-12} cm^3 s^{-1}]	Ervens et al. (2003)
$HO_2 + O_2^- \xrightarrow{H_2O} H_2O_2 + O_2 + OH^-$	[1.70×10^{-13} cm^3 s^{-1}]	Ervens et al. (2003)
$O_2^- + O_2^- \xrightarrow{2H+} H_2O_2$	[3.82×10^{-16} cm^3 s^{-1}]	Ervens et al. (2003)
$H_2O_2 + OH \rightarrow HO_2 + H_2O$	[5.50×10^{-14} cm^3 s^{-1}]	Ervens et al. (2003)
$OH + OH \rightarrow H_2O_2$	[8.60×10^{-12} cm^3 s^{-1}]	Ervens et al. (2003)
$OH + O_2^- \rightarrow O_2 + OH^-$	[1.30×10^{-11} cm^3 s^{-1}]	Ervens et al. (2003)
$OH + HO_2 \rightarrow O_2 + H_2O$	[1.20×10^{-11} cm^3 s^{-1}]	Ervens et al. (2003)
$H_2O_2 + HO_2 \rightarrow OH + O_2 + H_2O$	[4.98×10^{-21} cm^3 s^{-1}]	Ervens et al. (2003)
$Fe^{2+} + O_2 \rightarrow Fe^{3+} + O_2^-$	8.31×10^{-23} - 4.16×10^{-21} cm^3 s^{-1}	This study
$Fe^{2+} + O_2^- \xrightarrow{2H+} H_2O_2 + Fe^{3+}$	[1.66×10^{-14} cm^3 s^{-1}]	Rush and Bielski (1985)
$Fe^{2+} + HO_2 \xrightarrow{H+} H_2O_2 + Fe^{3+}$	[1.99×10^{-15} cm^3 s^{-1}]	Rush and Bielski (1985)
$Fe^{2+} + H_2O_2 \rightarrow Fe^{3+} + OH + OH^-$	[1.26×10^{-19} cm^3 s^{-1}]	Walling (1975)
$Fe^{2+} + OH \rightarrow Fe^{III}OH$	[7.14×10^{-13} cm^3 s^{-1}]	Christensen and Sehested (1981)
$Fe^{II}[O=C(CH_2COO)_2] + O_2 \rightarrow O_2^- + Fe^{3+} + O=C(CH_2COO)_2^{2-}$	8.31×10^{-23} - 4.16×10^{-21} cm^3 s^{-1}	This study
$Fe^{II}[O=C(CH_2COO)_2] + O_2^- \xrightarrow{2H+} H_2O_2 + Fe^{3+} + O=C(CH_2COO)_2^{2-}$	[1.66×10^{-14} cm^3 s^{-1}]	Rush and Bielski (1985)
$Fe^{II}[O=C(CH_2COO)_2] + HO_2 \xrightarrow{H+} H_2O_2 + Fe^{3+} + O=C(CH_2COO)_2^{2-}$	[1.99×10^{-15} cm^3 s^{-1}]	Rush and Bielski (1985)
$Fe^{II}[O=C(CH_2COO)_2] + H_2O_2 \rightarrow Fe^{3+} + OH + OH^- + O=C(CH_2COO)_2^{2-}$	[1.26×10^{-19} cm^3 s^{-1}]	Walling (1975)
$Fe^{II}[O=C(CH_2COO)_2] + OH \rightarrow Fe^{III}OH + O=C(CH_2COO)_2^{2-}$	[7.14×10^{-13} cm^3 s^{-1}]	Christensen and Sehested (1981)
$Fe^{II}CitH + O_2 \rightarrow Fe^{III}Cit + HO_2$	8.31×10^{-23} - 4.16×10^{-21} cm^3 s^{-1}	This study
$Fe^{II}CitH + HO_2 \rightarrow H_2O_2 + Fe^{III}Cit$	[1.99×10^{-15} cm^3 s^{-1}]	Rush and Bielski (1985)
$Fe^{II}CitH + H_2O_2 \rightarrow Fe^{III}Cit + OH + H_2O$	[1.26×10^{-19} cm^3 s^{-1}]	Walling (1975)
$Fe^{II}CitH + OH \rightarrow Fe^{III}Cit + H_2O$	[7.14×10^{-13} cm^3 s^{-1}]	Christensen and Sehested (1981)
$OH-C(CH_2COO)_2^{2-} + O_2 \rightarrow O=C(CH_2COO)_2^{2-} + O_2^- + H^+$	[1.66×10^{-15} cm^3 s^{-1}]	Dou et al. (2021)
Organics + $OH \rightarrow$ (1-α)product + (α)$Cit^{\bullet}$	[1.66×10^{-12} cm^3 s^{-1}]	This study

Table S3. Input parameters used in the correction factor α (Eq. 1) and Vignes-type equation (Eq. 2) and their optimization boundaries.

	C	D	$D_{\text{b,org}}$	$D_{\text{b,w}}$
O_2	-5 – 5	-5 – 5	1.0×10^{-20} – 1.0×10^{-11} cm^2 s^{-1}	1.0×10^{-7} – 1.0×10^{-5} cm^2 s^{-1}
CO_2	-5 – 5	-5 – 5	1.0×10^{-20} – 1.0×10^{-11} cm^2 s^{-1}	1.0×10^{-7} – 1.0×10^{-5} cm^2 s^{-1}

3 Supplementary Text

3.1 Layer sizing in the kinetic model

The thickness (d) of each bulk layer in the chemical model was altered such that each layer is not equally spaced but rather that the layers closer to the surface are thinner while those in the deep bulk are thicker.

$$d(i) = 3.46 \times 10^{-8} f^{(i-1)}; \tag{1}$$

where i is the layer number and f is a factor required such that the sum of d is equal to the total film thickness.

3.2 Water activity parameterization

The water activity (a_w) was parameterized using the mass fraction of citric acid, following Lienhard et al. (2012):

$$a_w = \frac{1 - mfs}{(1 + q \times mfs + r \times mfs^2)} \tag{2}$$

where,

$$q = -3.16761 + 0.01939T - 4.02725 \times 10^{-5} T^2 \tag{3}$$

$$r = 6.59108 - 0.05294T + 1.06028 \times 10^{-4} T^2 \tag{4}$$

Dou et al. (2021) showed that the water activity of an aqueous 1 M iron citrate solution corresponds to the water activity of a 0.81 M aqueous citric acid solution. Hence, following Dou et al. (2021), we further parameterize Fe^{III}Cit using a correction factor of 0.81, yielding the apparent citrate moles to be:

$$nCit = n\text{CitH}_3 + 0.81 \times nFe^{\text{III}}Cit \tag{5}$$

We consider that the citric acid and Fe^{III}Cit solution is a "pure" citric acid solution which has water activity a_w. We can then use equation 2 to calculate $mfs_{\mathrm{CitH_3}}$, and the correction factor 0.81 to calculate the moles of "citric acid" in the film. By using the molecular weight of citric acid, we get the mass fraction of the solutes in equation 2.

3.3 Film Thickness Calculation

The film thickness in the flow-tube is described by the volume of the film (V_{film}) divided by the inner surface of the flow-tube (A_{ft}):

$$h_{\mathrm{film}} = \frac{V_{\mathrm{film}}}{A_{\mathrm{ft}}} \tag{6}$$

where,

$$A_{\mathrm{ft}} = 2\pi \cdot r_{\mathrm{ft}} \cdot l_{\mathrm{ft}}, \tag{7}$$

and the volume with the mass of the film:

$$V_{\mathrm{film}} = \frac{m_{\mathrm{film}}}{\rho} \tag{8}$$

The mass of the film refers to the mass fractions of the solutes in the film, as calculated above in section 3.2. The density of the solution is calculated as a weighted mean of the density of the solutes.

$$\rho = \frac{n_{\mathrm{CitH_3}} \cdot \rho_{\mathrm{CitH_3}} + n_{Fe^{\mathrm{III}}Cit} \cdot \rho_{Fe^{\mathrm{III}}Cit}}{n_{tot}} \tag{9}$$

The density of citric acid is taken from Lienhard et al. (2012). $\rho_{Fe^{\mathrm{III}}Cit}$ is directly proportional to $\rho_{\mathrm{CitH_3}}$, where the proportional factor is the ratio between the densities of the pure solids (ρ°). Thus, equation 9 becomes:

$$\rho = \rho_{\mathrm{CitH_3}} \cdot \left(\frac{n_{\mathrm{CitH_3}} + n_{Fe^{\mathrm{III}}Cit} \cdot \frac{\rho^{\circ}_{Fe^{\mathrm{III}}Cit}}{\rho^{\circ}_{\mathrm{CitH_3}}}}{n_{\mathrm{CitH_3}} + n_{Fe^{\mathrm{III}}Cit}}\right) \tag{10}$$

References

Bielski, B. H. J., Cabelli, D. E., Arudi, R. L., and Ross, A. B.: Reactivity of HO2/O-2 Radicals in Aqueous Solution, J. Phys. Chem. Ref. Data, 14, 1041–1100, https://doi.org/10.1063/1.555739, 1985.

Christensen, H. and Sehested, K.: Pulse radiolysis at high temperatures and high pressures, Radiat. Phys. Chem., 18, 723–731, https://doi.org/10.1016/0146-5724(81)90195-3, 1981.

Dou, J., Alpert, P. A., Corral Arroyo, P., Luo, B., Schneider, F., Xto, J., Huthwelker, T., Borca, C. N., Henzler, K. D., Raabe, J., Watts, B., Herrmann, H., Peter, T., Ammann, M., and Krieger, U. K.: Photochemical degradation of iron(III) citrate/citric acid aerosol quantified with the combination of three complementary experimental techniques and a kinetic process model, Atmos. Chem. Phys., 21, 315–338, https://doi.org/10.5194/acp-21-315-2021, 2021.

Ervens, B., George, C., Williams, J. E., Buxton, G. V., Salmon, G. A., Bydder, M., Wilkinson, F., Dentener, F., Mirabel, P., Wolke, R., and Herrmann, H.: CAPRAM 2.4 (MODAC mechanism): An extended and condensed tropospheric aqueous phase mechanism and its application, J. Geophys. Res., 108, https://doi.org/10.1029/2002JD002202, 2003.

Khaled, A., Zhang, M., and Ervens, B.: The number fraction of iron-containing particles affects OH, HO_2 and H_2O_2 budgets in the atmospheric aqueous phase, Atmos. Chem. Phys., 22, 1989–2009, https://doi.org/10.5194/acp-22-1989-2022, 2022.

Lienhard, D. M., Bones, D. L., Zuend, A., Krieger, U. K., Reid, J. P., and Peter, T.: Measurements of Thermodynamic and Optical Properties of Selected Aqueous Organic and Organic–Inorganic Mixtures of Atmospheric Relevance, J. Phys. Chem. A, 116, 9954–9968, https://doi.org/10.1021/jp3055872, 2012.

Martell, A. E. and Smith, R. M.: Critical Stability Constants: First Supplement, Boston, MA, oCLC: 851794557, 1982.

Pozdnyakov, I. P., Melnikov, A. A., Tkachenko, N., Chekalin, S. V., Lemmetyinen, H., and Plyusnin, V. F.: Ultrafast photophysical processes for Fe(iii)-carboxylates, Dalton Trans., 43, 17 590–17 595, https://doi.org/10.1039/C4DT01419G, 2014.

Rush, J. D. and Bielski, B. H. J.: Pulse radiolytic studies of the reaction of perhydroxyl/superoxide O2- with iron(II)/iron(III) ions. The reactivity of HO2/O2- with ferric ions and its implication on the occurrence of the Haber-Weiss reaction, J. Phys. Chem., 89, 5062–5066, https://doi.org/10.1021/j100269a035, 1985.

Smith, R. M. and Martell, A. E.: Critical Stability Constants: Inorganic Complexes, Cham, oCLC: 1159214048, 1976.

Walling, C.: Fenton's reagent revisited, Acc. Chem. Res., 8, 125–131, https://doi.org/10.1021/ar50088a003, 1975.

B.3 Supplement of "Chemical kinetics and reaction mechanisms of reactive species production and antioxidant depletion in different assays measuring aerosol oxidative potential

1 Supplementary Figures

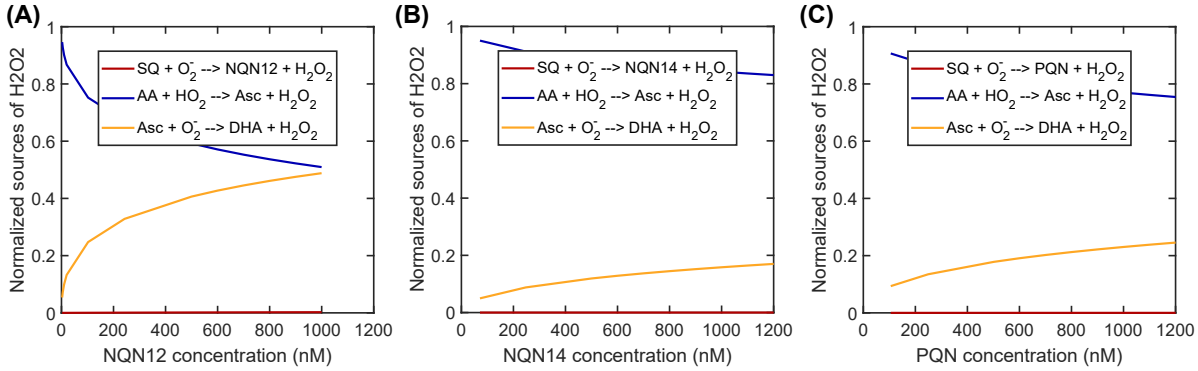

Figure 1: *Normalized sources of H_2O_2 as a function of 1,2-NQN (A), 1,2-NQN (B) and PQN (C) concentrations.*

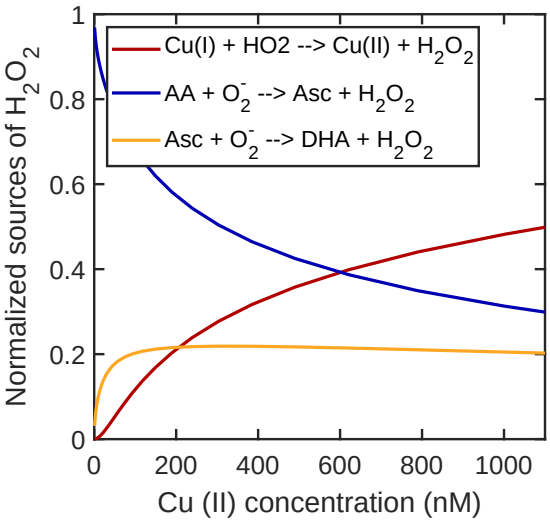

Figure 2: *Normalized sources of H_2O_2 as a function of Cu concentration.*

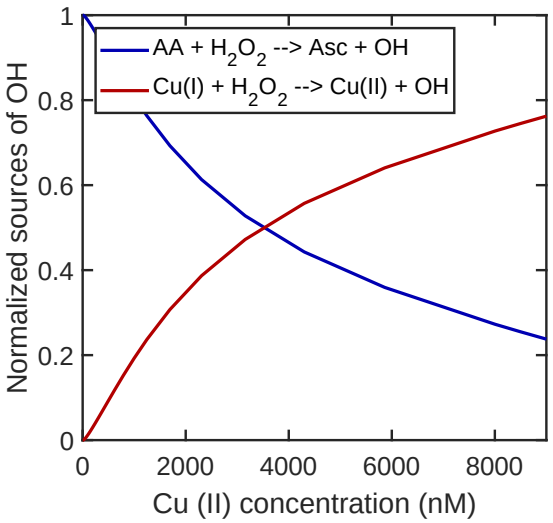

Figure 3: *Normalized sources of OH as a function of Cu concentration.*

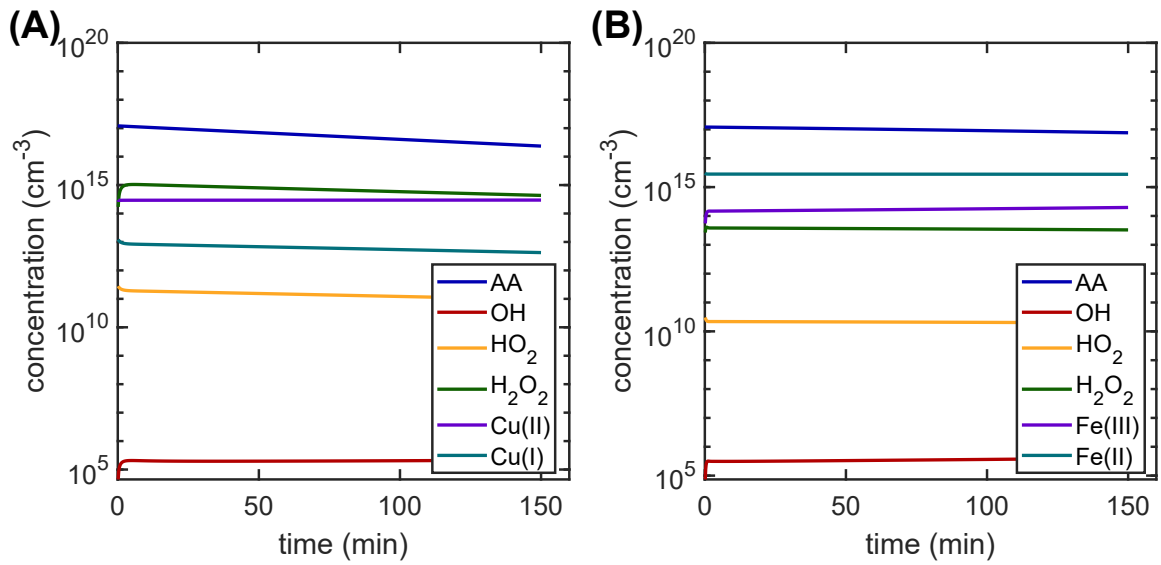

Figure 4: *Concentration of ROS and TMs (Cu (A), Fe (B)) over time.*

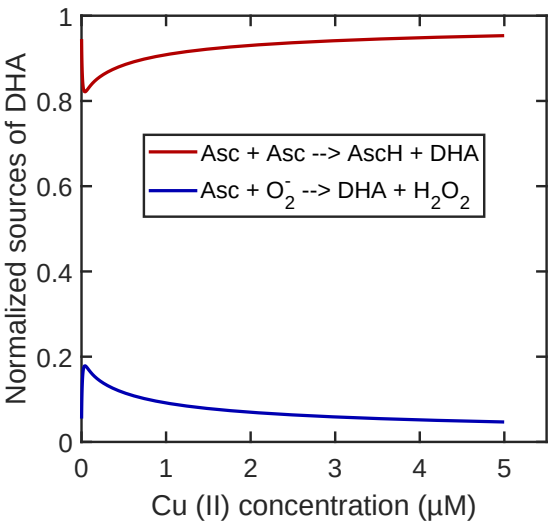

Figure 5: *Normalized sources of DHA as a function of Cu concentration.*

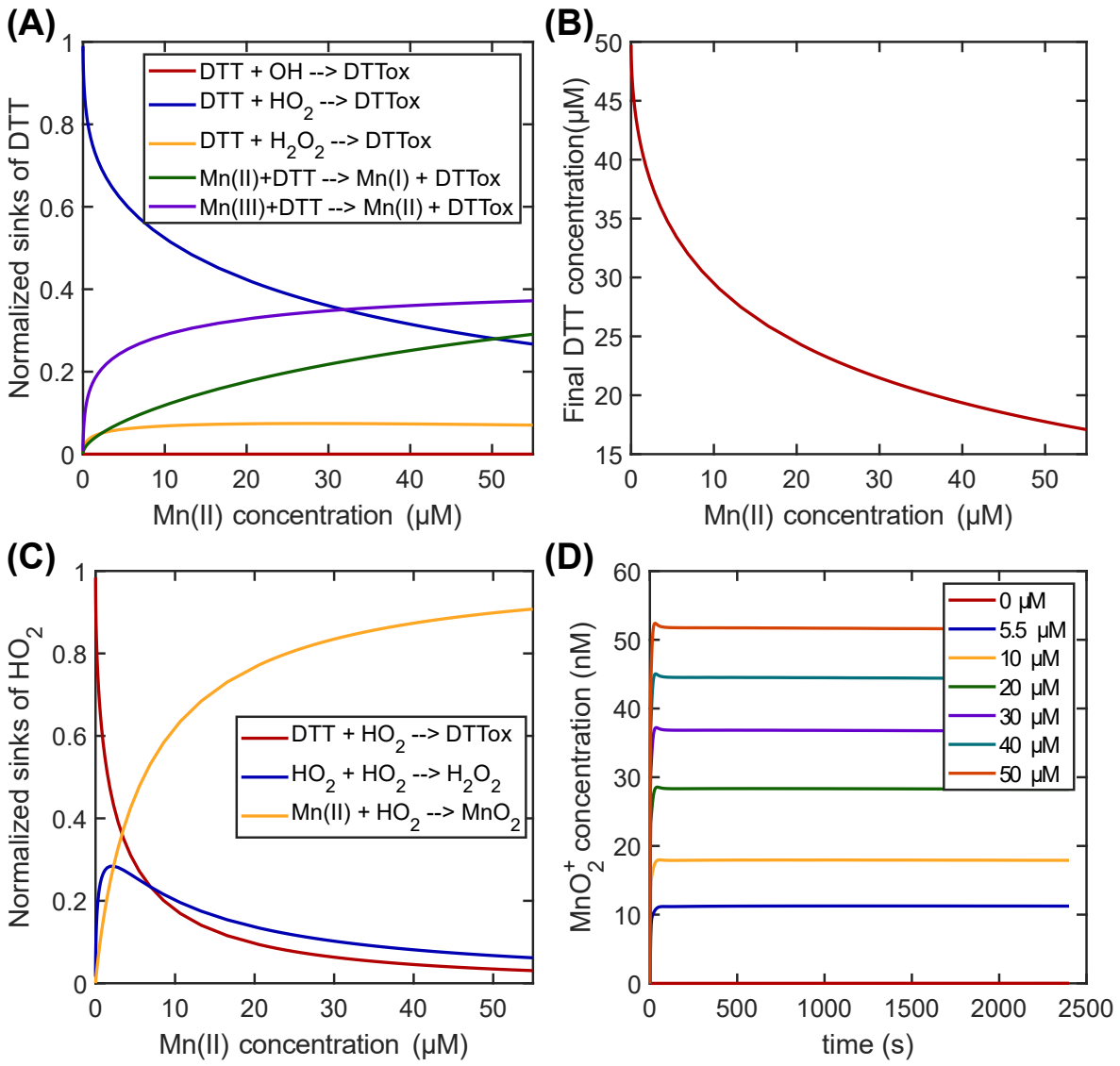

Figure 6: *Normalized sinks of DTT (A), final DTT concentration (B), and normalized sinks of HO_2 (C) as a function of Mn concentration. Panel D shows the MnO_2^+ concentration over time.*

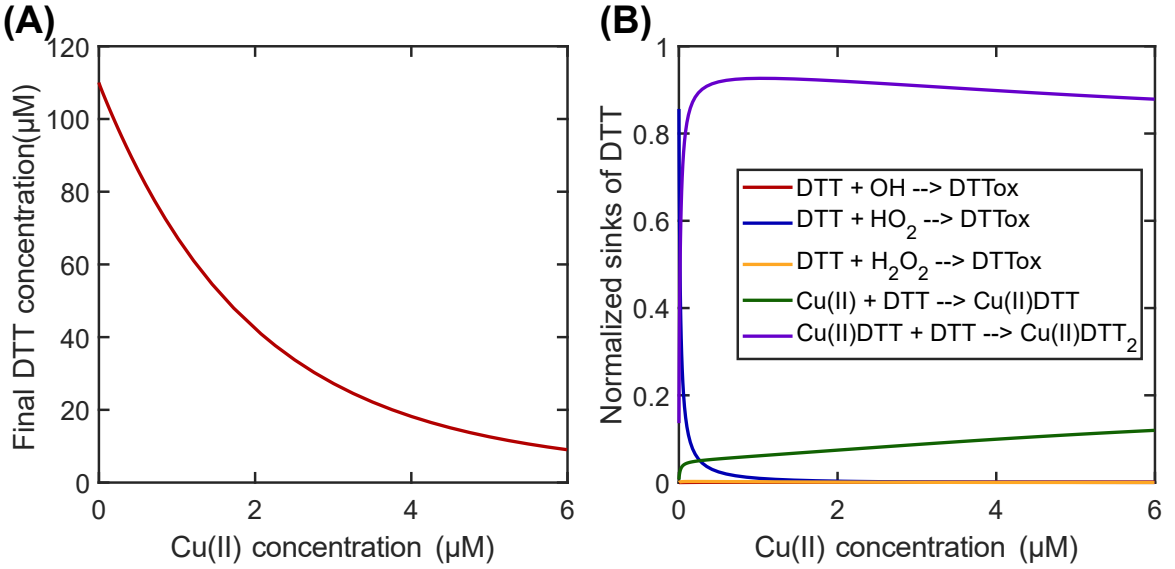

Figure 7: *End concentration of DTT (A) and normalized sinks of DTT as a function of Cu concentration (B).*

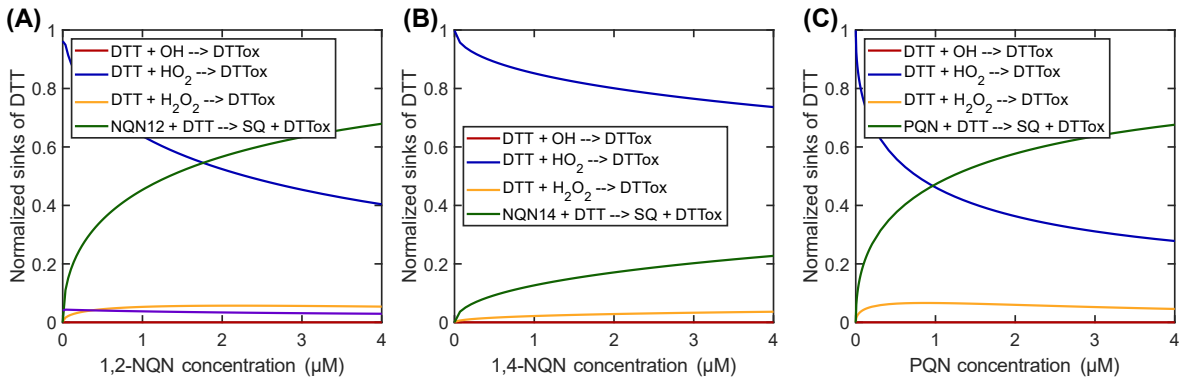

Figure 8: *Normalized sinks of DTT as a function of 1,2-NQN (A), 1,4-NQN (B) and PQN (C) concentrations.*

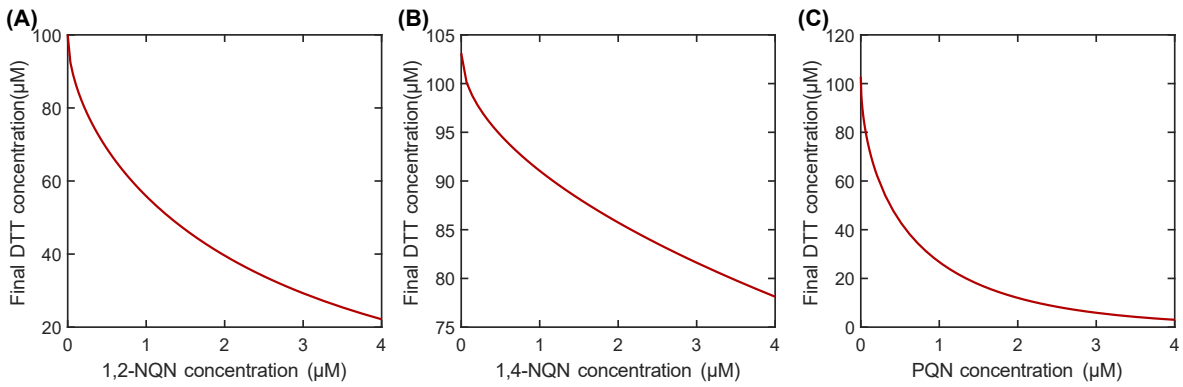

Figure 9: *End concentration of DTT as a function of 1,2-NQN (A), 1,4-NQN (B) and PQN (C) concentrations.*

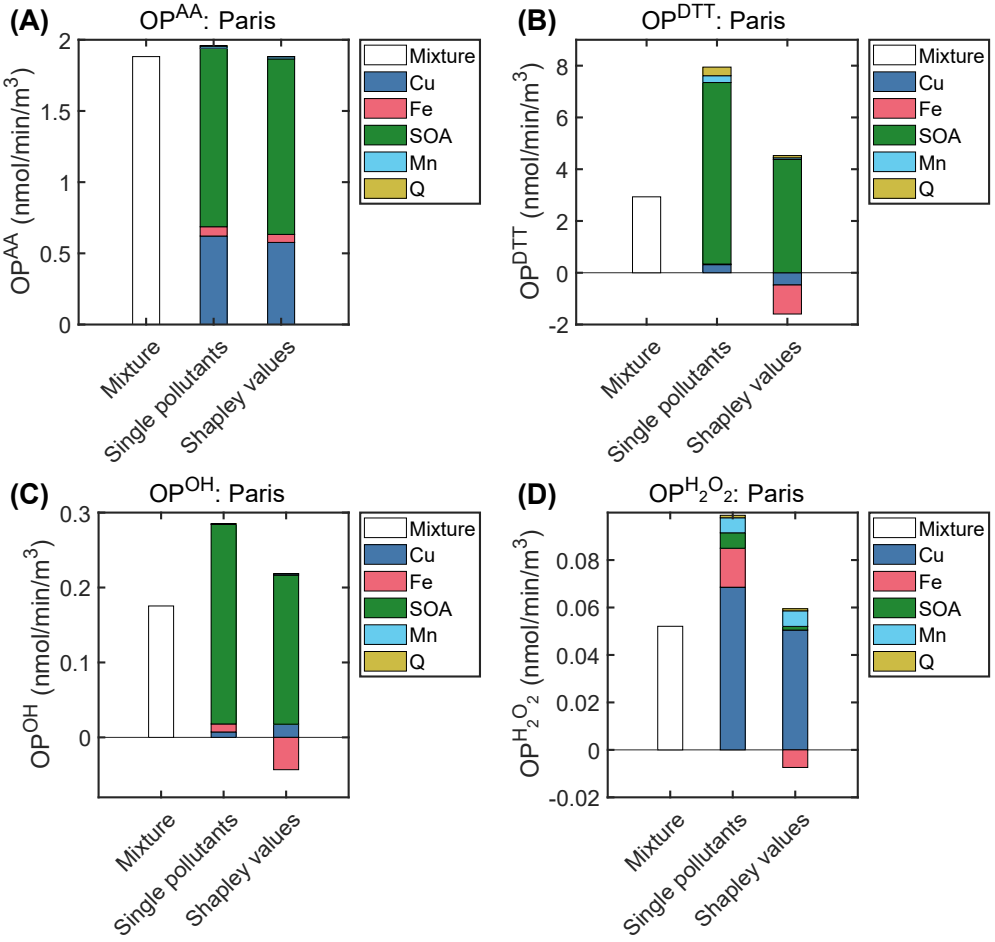

Figure 10: *Contributions of different PM2.5 constituents to OP^{AA} (A), OP^{DTT} (B), OP^{OH} (C), and $OP^{H_2O_2}$ (D) in Paris. The "Mixture" bar shows the model result when all species are included in the model. The "Single pollutants" bar indicates a scenario where only one specific species was included. The "Shapley values" bar is calculated using the Shapley analysis.*

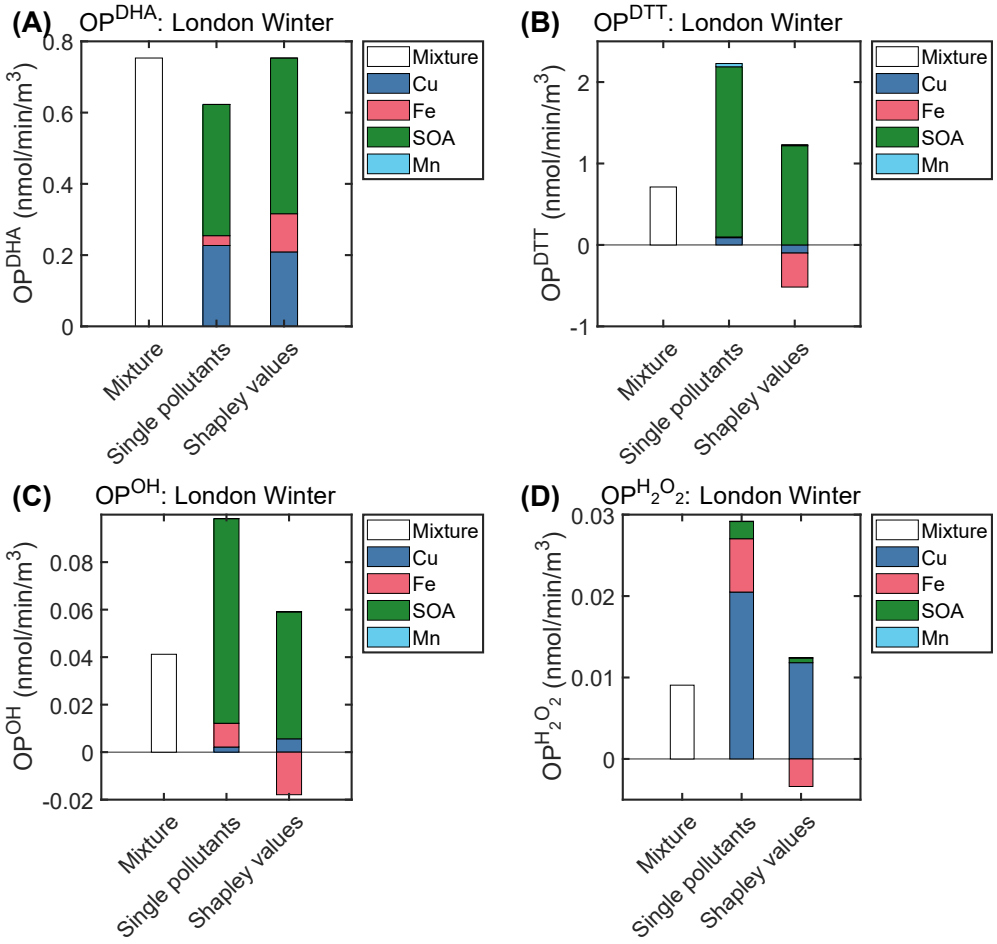

Figure 11: *Contributions of different PM2.5 constituents to OP^{AA} (A), OP^{DTT} (B), OP^{OH} (C), and $OP^{H_2O_2}$ (D) in London during winter. The "Mixture" bar shows the model result when all species are inclmuded in the model. The "Single pollutants" bar indicates a scenario where only one specific species was included. The "Shapley values" bar is calculated using the Shapley analysis.*

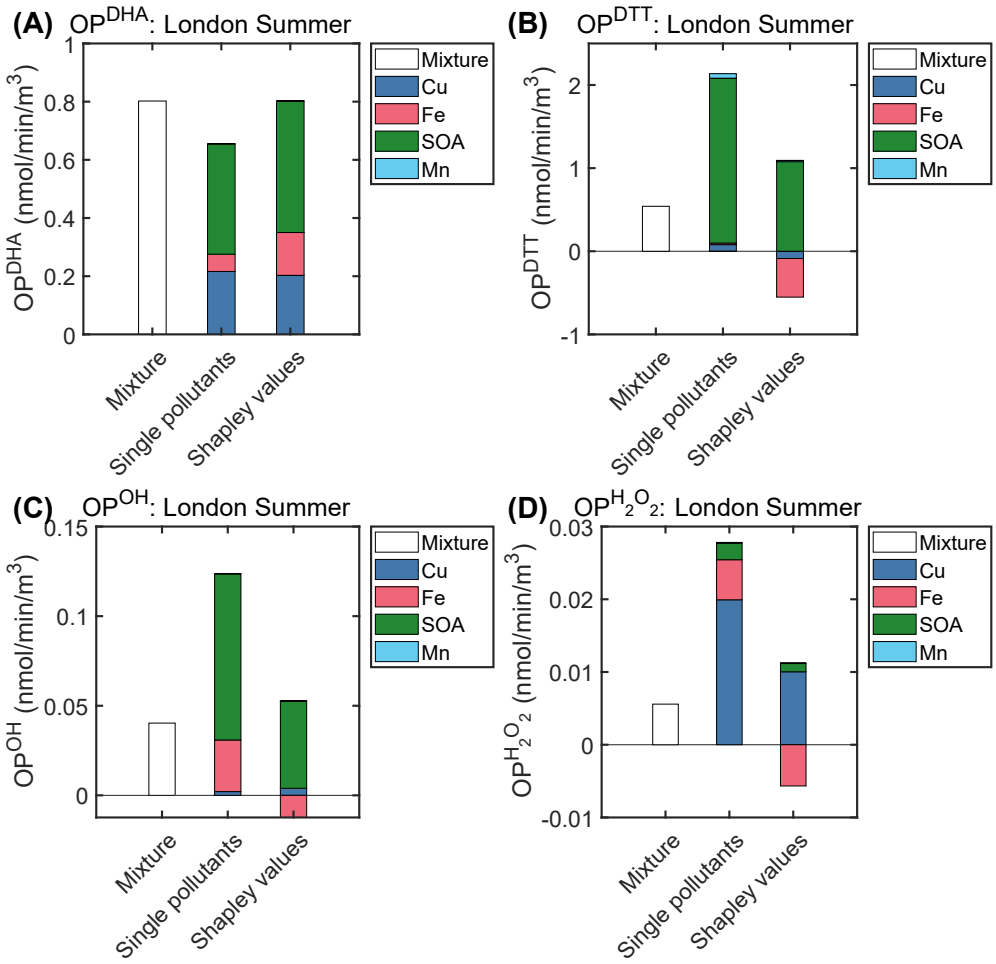

Figure 12: *Contributions of different PM2.5 constituents to OP^{AA} (A), OP^{DTT} (B), OP^{OH} (C), and $OP^{H_2O_2}$ (D) in London during summer. The "Mixture" bar shows the model result when all species are included in the model. The "Single pollutants" bar indicates a scenario where only one specific species was included. The "Shapley values" bar is calculated using the Shapley analysis.*

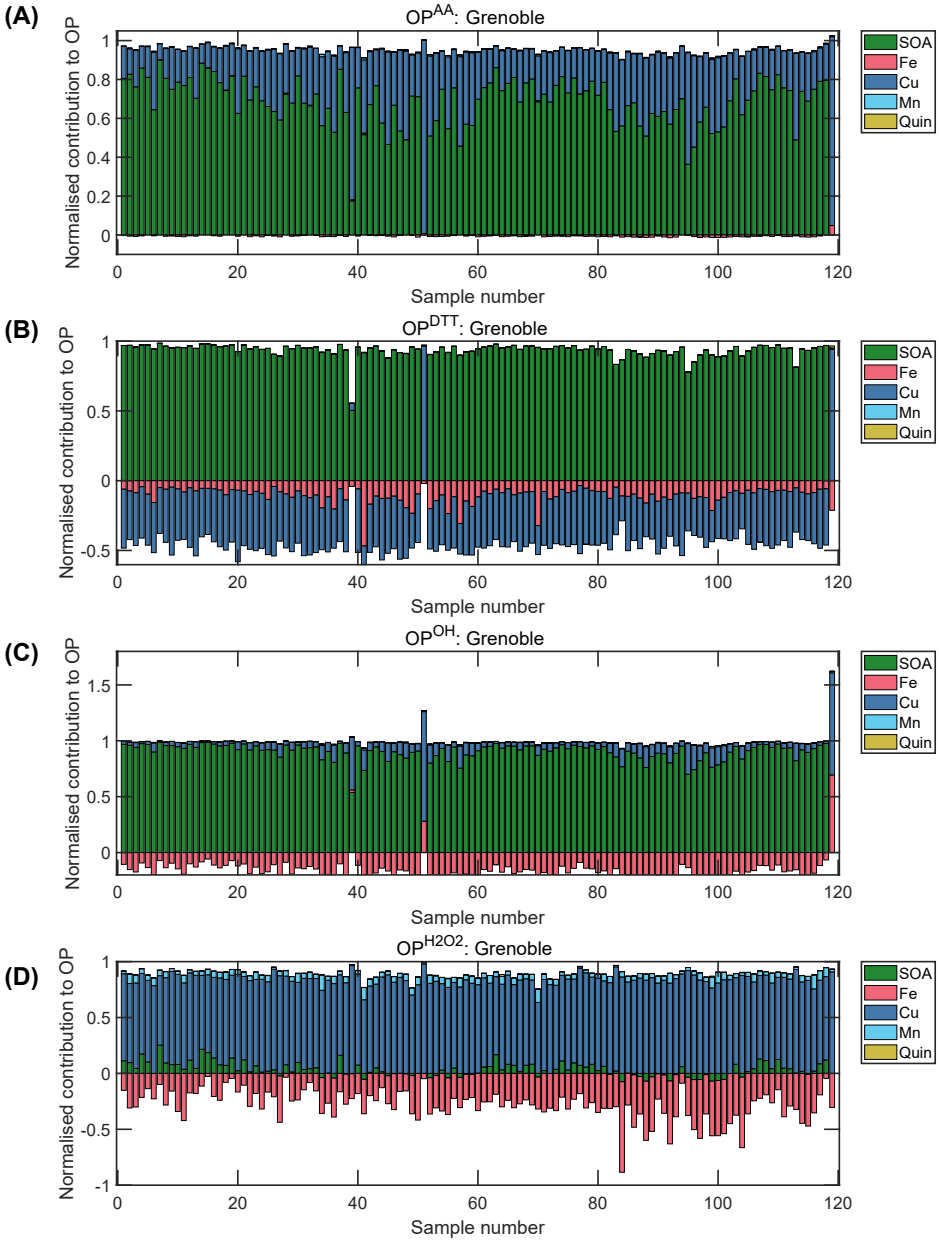

Figure 13: *Relative contributions of different PM2.5 constituents to OP^{AA} (A), OP^{DTT} (B), OP^{OH} (C), and $OP^{H_2O_2}$ (D) in Grenoble.*

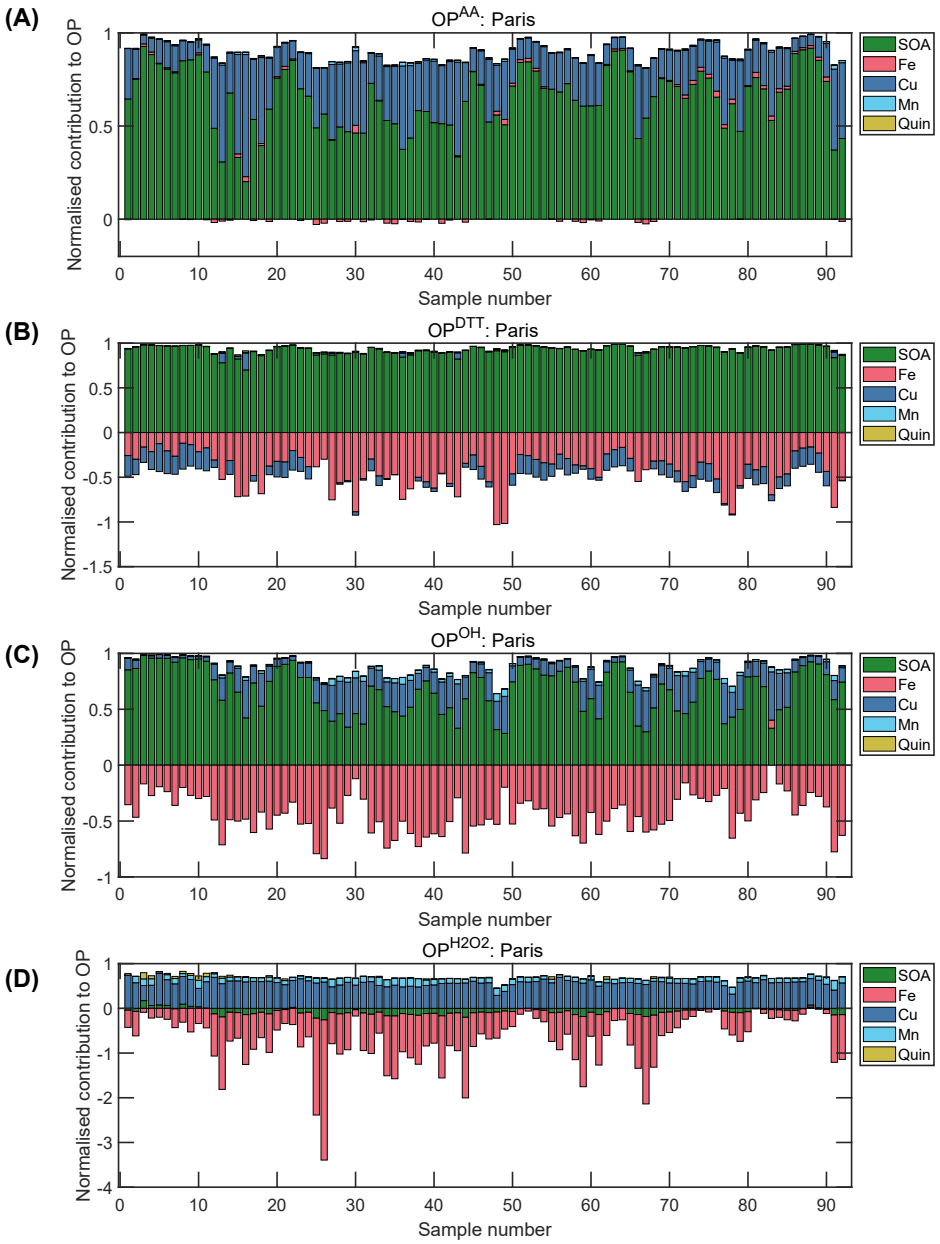

Figure 14: *Relative contributions of different PM2.5 constituents to OP^{AA} (A), OP^{DTT} (B), OP^{OH} (C), and $OP^{H_2O_2}$ (D) in Paris.*

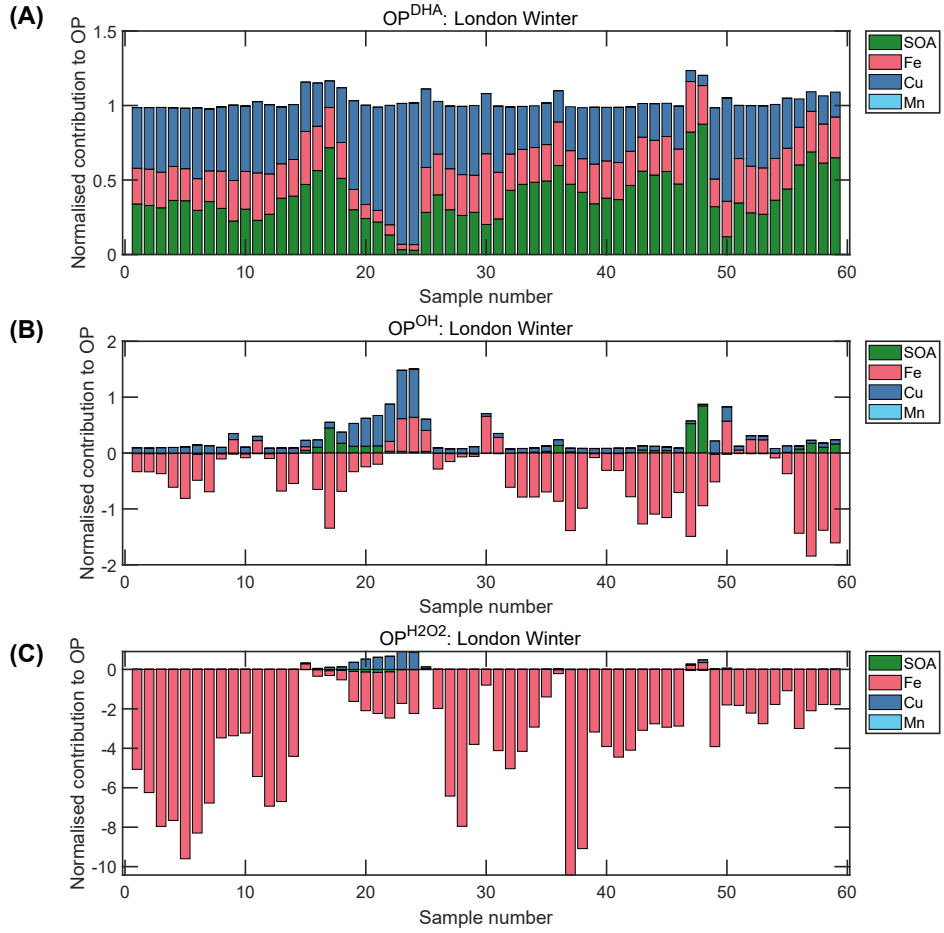

Figure 15: *Relative contributions of different PM2.5 constituents to OP^{AA} (A), OP^{DTT} (B), OP^{OH} (C), and $OP^{H_2O_2}$ (D) in London (during Winter).*

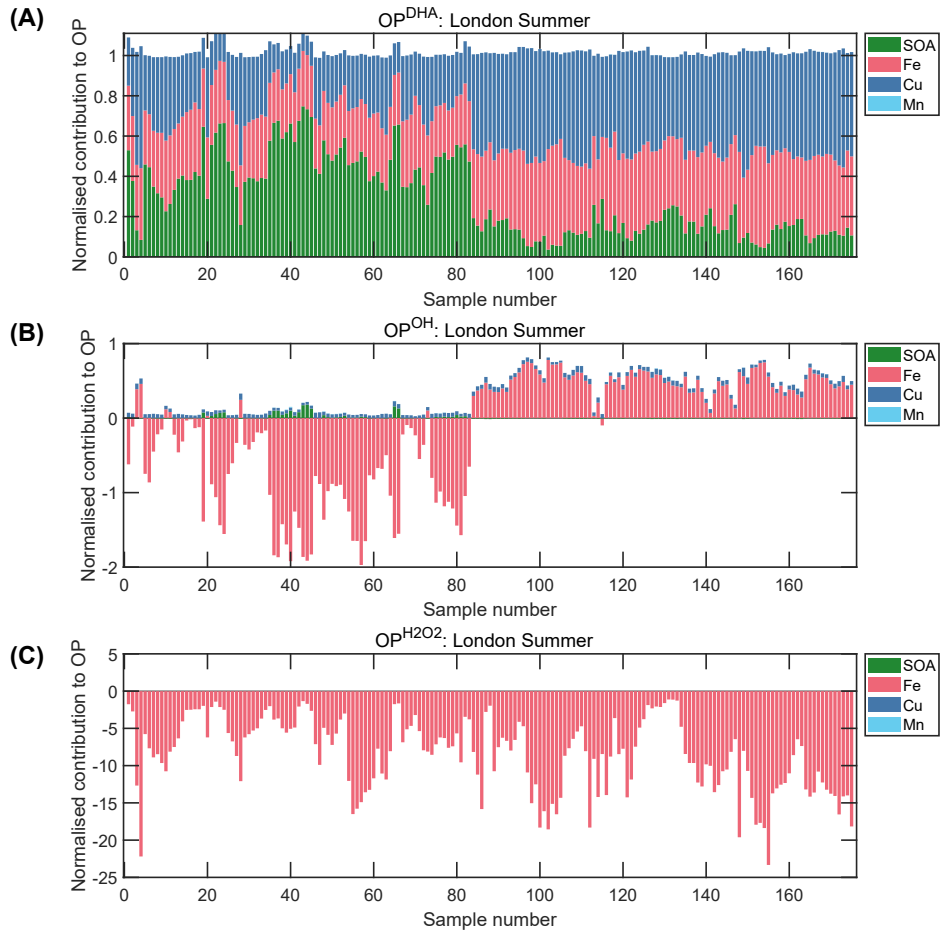

Figure 16: *Relative contributions of different PM2.5 constituents to OP^{AA} (A), OP^{DTT} (B), OP^{OH} (C), and $OP^{H_2O_2}$ (D) in London (during Summer).*

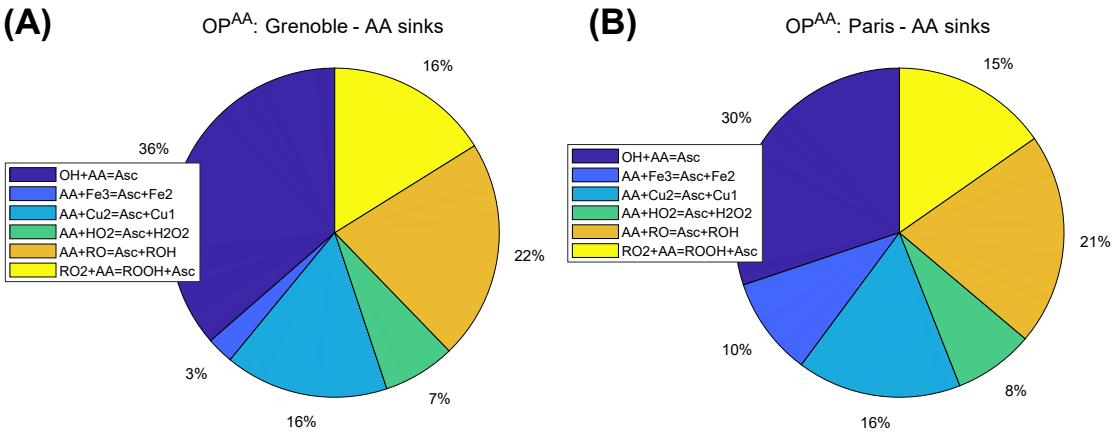

Figure 17: *Main sinks of ascorbic acid for Grenoble (A) and Paris (B).*

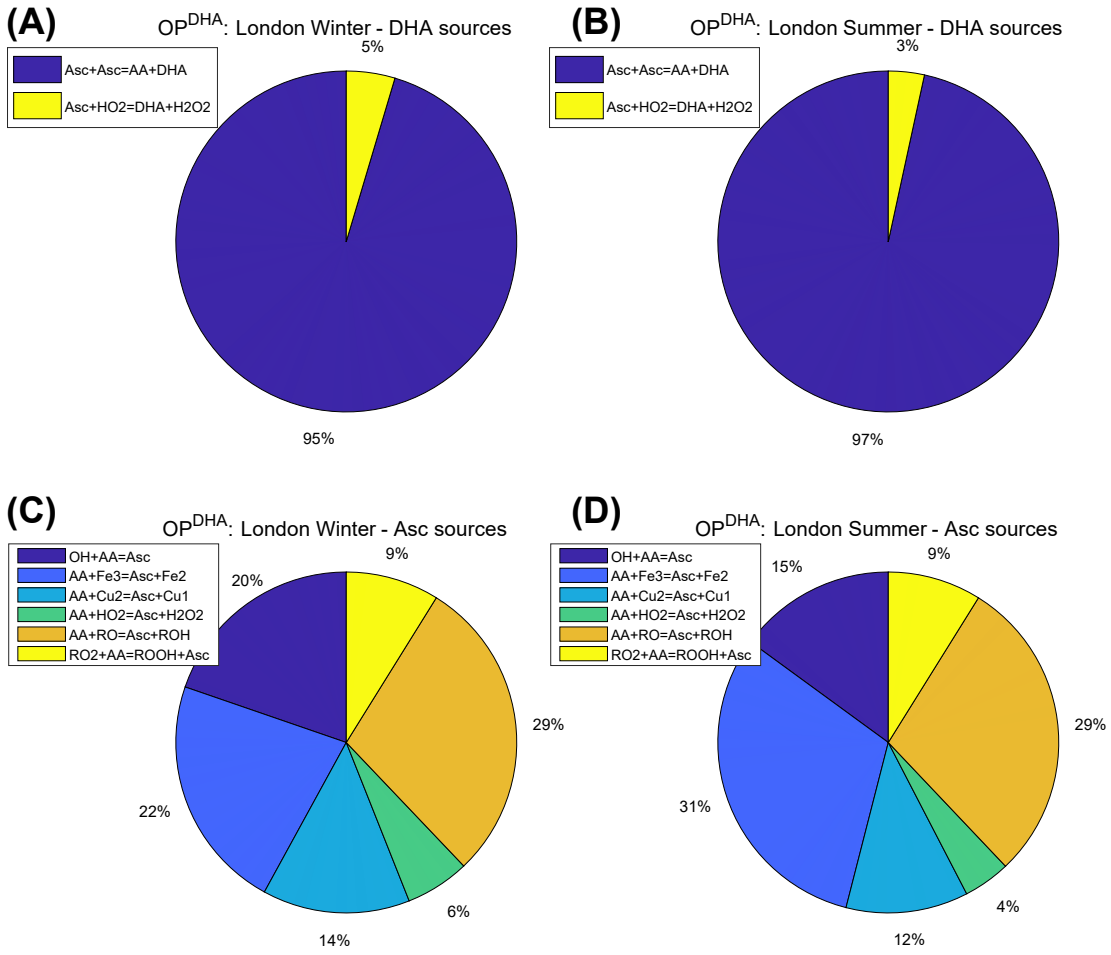

Figure 18: *Main sources of dehydroascorbic acid for London winter (A) and London summer (B). Main sources of ascorbyl radical for London winter (C) and London summer (D).*

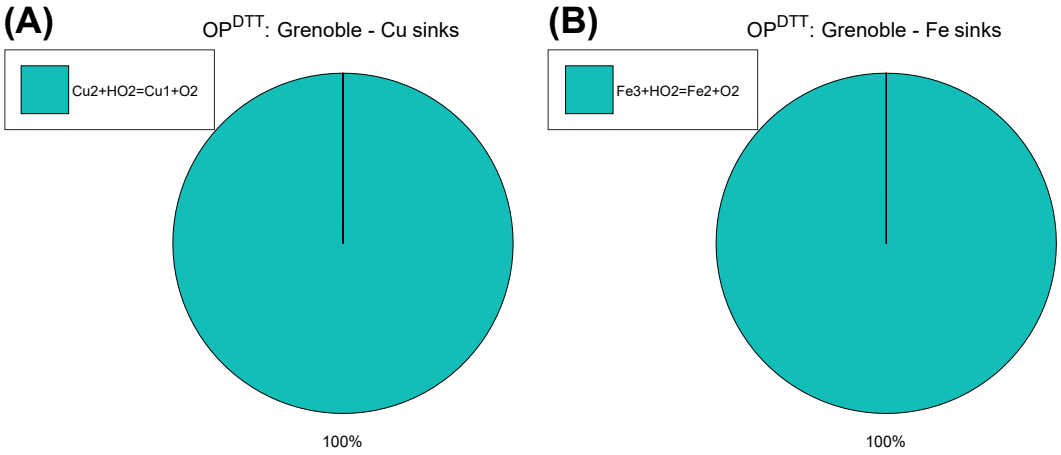

Figure 19: *Main sinks of Cu(II) and Fe(III) in the DTT assay for Grenoble data.*

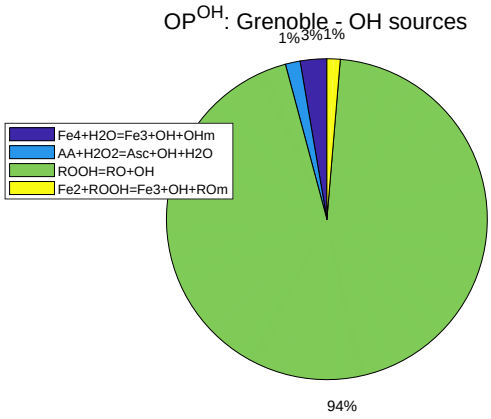

Figure 20: *Main sources of OH for Grenoble data.*

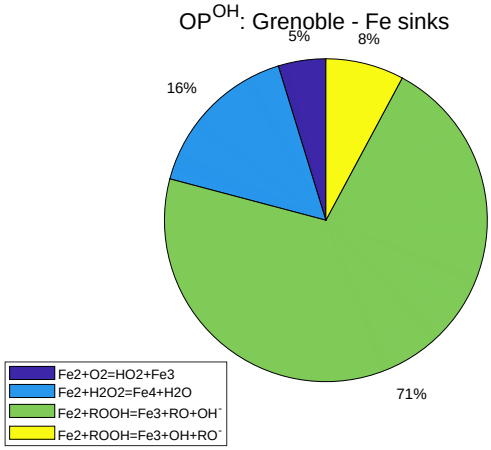

Figure 21: *Main sinks of Fe(II) in the OH assay for Grenoble data.*

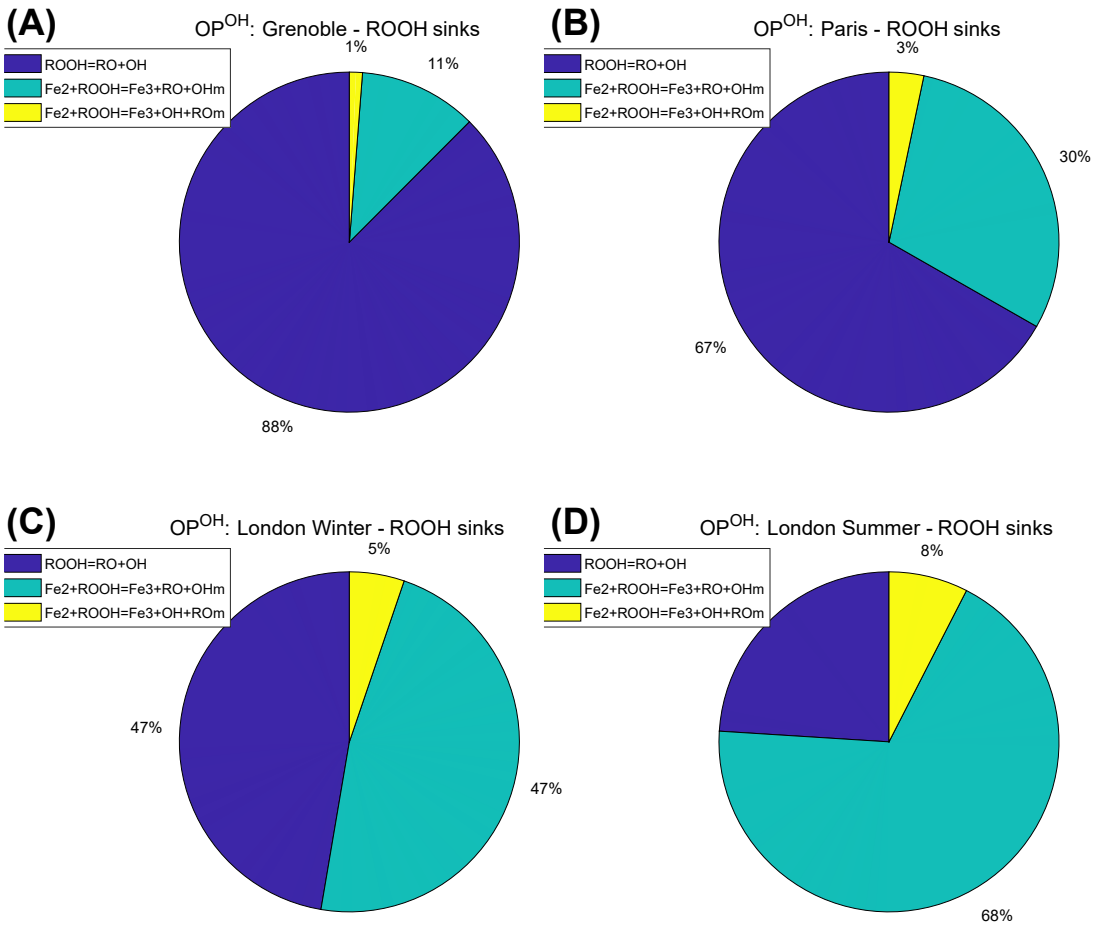

Figure 22: *Main sinks of ROOH in the OH assay for Grenoble (A), Paris (B), London in winter (C) and London in summer (D).*

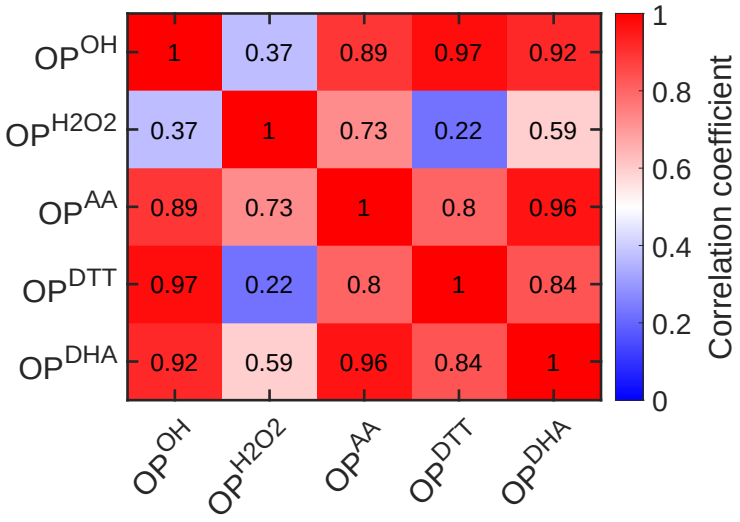

Figure 23: *Correlation matrix between intrinsic OP assays in Grenoble.*

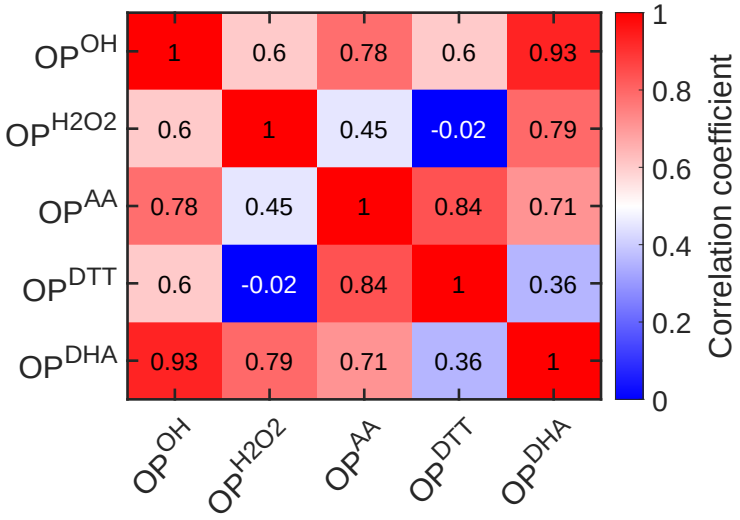

Figure 24: *Correlation matrix between intrinsic OP assays in Paris.*

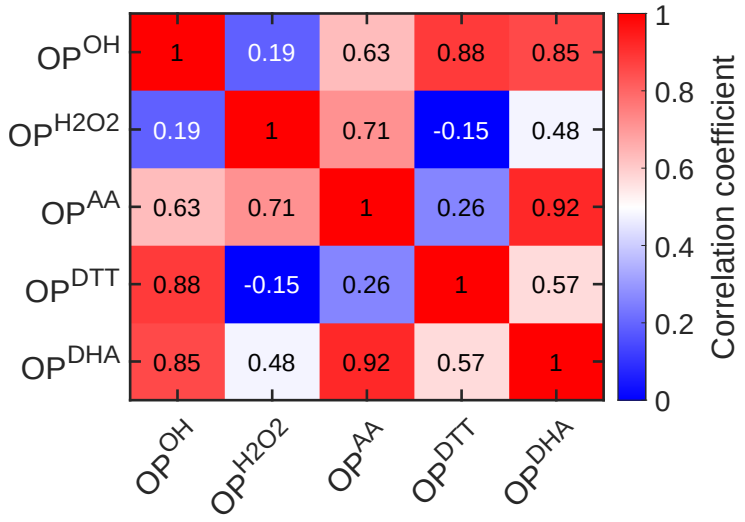

Figure 25: *Correlation matrix between intrinsic OP assays in London during Winter.*

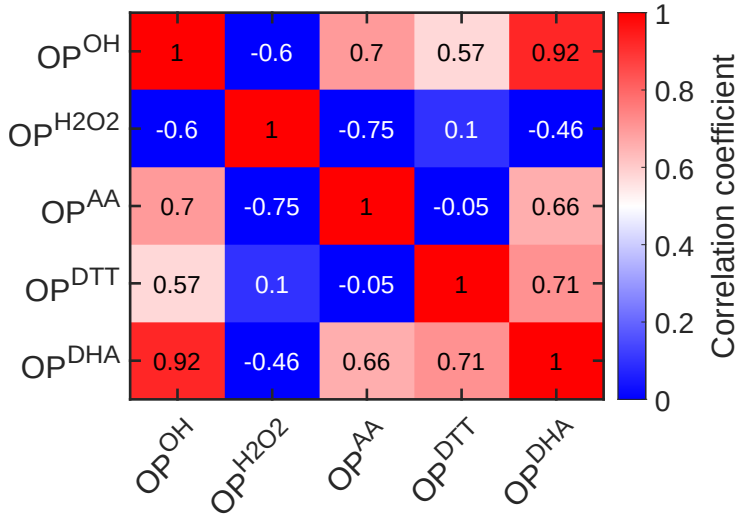

Figure 26: *Correlation matrix between intrinsic OP assays in London during Summer.*

2 Supplementary Tables

Table 1: *Chemical reactions included in the KM-OP model. The respective lower and upper boundaries indicate the initial constraints of the fit ensemble. Values that were fixed during the fitting procedure are indicated using square brackets. Species in parenthesis in the chemical reaction refer to those that partake in the chemical reaction but that are not used to determine the reaction order. The rate coefficients are for 298 K in units of $cm^3\ s^{-1}$, unless otherwise noted. All reactions were assumed to have an activation energy (Ea) of 50 kJ mol^{-1}.*

Reaction number	Reaction	Range	Reference
1	$OH + AA \rightarrow AA^{\bullet} + OH^-$	$[1.20 \times 10^{-11}]$	Shen et al. (2021)
2	$OH + UAH \rightarrow UA + OH^-$	$[1.20 \times 10^{-11}]$	Lakey et al. (2016)
3	$OH + GSH \rightarrow GS + OH^-$	$[1.70 \times 10^{-11}]$	Lakey et al. (2016)
4	$OH + GSSG \rightarrow GSSG^+ + OH^-$	$[1.20 \times 10^{-11}]$	Assumed to be fast
5	$OH + Cit \rightarrow NRP + \ + OH^-$	$[9.7 \times 10^{-14}]$	Liu et al. (2017)
6	$1,2-NQN + AA \rightarrow 1,2-NQN^{\bullet} + AA^{\bullet}$	$1.50 \times 10^{-22} - 1.50 \times 10^{-16}$	This study
7	$1,2-NQN^{\bullet} + O_2 \rightarrow 1,2-NQN + O_2^-$	$[1.35 \times 10^{-14}]$	This study
8	$1,2-NQN^{\bullet} + O_2^- (+ 2H^+) \rightarrow 1,2-NQN + H_2O_2$	$3.3 \times 10^{-15} - 3.3 \times 10^{-11}$	This study
9	$1,2-NQN^{\bullet} + Fe(III) \rightarrow 1,2-NQN + Fe(II)$	$1.00 \times 10^{-19} - 1.00 \times 10^{-13}$	This study
10	$1,4-NQN + AA \rightarrow 1,4-NQN^{\bullet} + AA^{\bullet}$	$1.50 \times 10^{-22} - 1.50 \times 10^{-16}$	This study
11	$1,4-NQN^{\bullet} + O_2 \rightarrow 1,4-NQN + O_2^-$	$[3.06 \times 10^{-14}]$	This study
12	$1,4-NQN^{\bullet} + O_2^- \ (+ 2H^+) \rightarrow 1,4-NQN + H_2O_2$	$3.3 \times 10^{-15} - 3.3 \times 10^{-11}$	This study
13	$PQN + AA \rightarrow PQN^{\bullet} + AA^{\bullet}$	$1.50 \times 10^{-22} - 1.50 \times 10^{-16}$	This study
14	$PQN^{\bullet} + O_2 \rightarrow PQN + O_2^-$	$[2.31 \times 10^{-14}]$	This study
15	$PQN^{\bullet} + O_2^- (+ 2H^+) \rightarrow PQN + H_2O_2$	$3.30 \times 10^{-15} - 3.30 \times 10^{-11}$	This study
16	$Fe(III) + AA \rightarrow Fe(II) + AA^{\bullet}$	$6.97 \times 10^{-21} - 6.97 \times 10^{-19}$	This study
17	$Fe(II) + O_2 \rightarrow Fe(III) + O_2^-$	$[4.48 \times 10^{-21}]$	Gonzalez et al. (2021)
18	$Fe(II) + O_2^- (+ 2H^+) \rightarrow Fe(III) + H_2O_2$	$[1.66 \times 10^{-14}]$	Ervens et al. (2003)
19	$Fe(II) + OH \rightarrow Fe(III) + OH^-$	$[5.81 \times 10^{-13}]$	Halliwell and Gutteridge (2015)
20	$Fe(III) + HO_2 \rightarrow Fe(II) + O_2 + H^+$	$[2.16 \times 10^{-16}]$	Ervens et al. (2003)
21	$Fe(III) + O_2^- \rightarrow Fe(II) + O_2$	$[2.49 \times 10^{-13}]$	Ervens et al. (2003)
22	$Fe(II) + H_2O_2 \rightarrow Fe(IV) + H_2O$	$8.14 \times 10^{-19} - 8.14 \times 10^{-17}$	This study
23	$Fe(II) + H_2O_2 \rightarrow Fe(III) + OH + OH^-$	$1.26 \times 10^{-20} - 1.26 \times 10^{-18}$	This study
24	$Fe(II) + Fe(IV) \rightarrow Fe(III) + Fe(III)$	$[6.60 \times 10^{-18}]$	Lakey et al. (2016)
25	$Fe(IV) \ (+ H_2O) \rightarrow Fe(III) + OH + OH^-$	$1.30 \times 10^{-4} - 1.30\ s^{-1}$	This study
26	$H_2O_2 + OH \rightarrow HO_2 + H_2O$	$[5.50 \times 10^{-14}]$	Lakey et al. (2016)
27	$OH + OH \rightarrow H_2O_2$	$[8.60 \times 10^{-12}]$	Lakey et al. (2016)
28	$OH + HO_2 \rightarrow O_2 + H_2O$	$[1.66 \times 10^{-11}]$	Ervens et al. (2003)
29	$HO_2 + HO_2 \rightarrow H_2O_2 + O_2$	$[1.40 \times 10^{-15}]$	Lakey et al. (2016)
30	$H_2O_2 + HO_2 \rightarrow H_2O_2 + O_2$	$[5.00 \times 10^{-21}]$	Lakey et al. (2016)
31	$HO_2 + O_2^- (+ H_2O) \rightarrow H_2O_2 + O_2 + OH^-$	$[1.70 \times 10^{-13}]$	Ervens et al. (2003)
32	$OH + O_2^- \rightarrow O_2 + OH^-$	$[1.83 \times 10^{-11}]$	Ervens et al. (2003)
33	$Cu(II) + AA \rightarrow Cu(I) + AA^{\bullet}$	$1.46 \times 10^{-19} - 1.46 \times 10^{-17}$	This study
34	$Cu(I) + O_2 \rightarrow Cu(II) + O_2^-$	$[7.64 \times 10^{-16}]$	Ervens et al. (2003)
35	$Cu(I) + O_2^- (+ 2H^+) \rightarrow Cu(II) + H_2O_2$	$1.56 \times 10^{-12} - 1.56 \times 10^{-10}$	This study
36	$Cu(I) + OH \rightarrow Cu(II) + OH^-$	$[4.98 \times 10^{-12}]$	Ervens et al. (2003)
37	$Cu(I) + H_2O_2 \rightarrow Cu(III) + OH^- + OH^-$	$1.16 \times 10^{-19} - 1.16 \times 10^{-14}$	This study
38	$Cu(I) + Cu(III) \rightarrow Cu(II) + Cu(II)$	$[5.80 \times 10^{-12}]$	Lakey et al. (2016)
39	$Cu(II) + H_2O_2 \rightarrow Cu(I) + HO_2$	7.64×10^{-19}	Pham et al. (2013)
40	$Cu(II) + O_2^- \rightarrow Cu(I) + O_2$	$[1.83 \times 10^{-11}]$	Ervens et al. (2003)

Continued.

Reaction number	Reaction	Range	Reference
41	$Cu(II) + HO_2 \rightarrow Cu(I) + O_2$	$[1.66 \times 10^{-13}]$	Ervens et al. (2003)
42	$Cu(I) + HO_2 \rightarrow Cu(II) + O_2$	$[4.98 \times 10^{-12}]$	Ervens et al. (2003)
43	$Cu(III)\ (+ H_2O) \rightarrow Cu(II) + OH + OH^-$	$2.32 \times 10^{-3} - 2.32\ s^{-1}$	This study
44	$AA^\bullet + AA^\bullet \rightarrow AA + DHA$	$[5.00 \times 10^{-16}]$	Lakey et al. (2016)
45	$AA + GS \rightarrow AA^\bullet + GSH$	$[1.00 \times 10^{-12}]$	Lelieveld et al. (2021)
46	$AA + UA \rightarrow AA^\bullet + UAH$	$[1.70 \times 10^{-15}]$	Lelieveld et al. (2021)
47	$UAH + GS \rightarrow UA + GSH$	$[5.00 \times 10^{-14}]$	Lelieveld et al. (2021)
48	$AA + H_2O_2 \rightarrow AA^\bullet + OH + OH^-$	$2.19 \times 10^{-23} - 2.19 \times 10^{-19}$	This study
49	$AA + HO_2\ (+ H^+) \rightarrow AA^\bullet + H_2O_2$	$[2.65 \times 10^{-17}]$	Lelieveld et al. (2021)
50	$AA + O_2^-\ (+ 2H^+) \rightarrow AA^\bullet + H_2O_2$	$[5.10 \times 10^{-17}]$	Lelieveld et al. (2021)
51	$OH + Benzoate \rightarrow BenzOH$	$[1.00 \times 10^{-11}]$	Lakey et al. (2016)
52	$O_2^- + O_2^-\ (+ 2H^+) \rightarrow H_2O_2 + O_2$	$[2.49 \times 10^{-14}]$	Kohen and Nyska (2002)
53	$GSH + H_2O_2 \rightarrow GSSG + O_2$	$[1.44 \times 10^{-21}]$	Lelieveld et al. (2021)
54	$GS^- + H_2O_2 \rightarrow GSOH + O_2$	$[1.60 \times 10^{-21}]$	Lelieveld et al. (2021)
55	$HO_2 + GSH \rightarrow GS + H_2O_2$	$[3.32 \times 10^{-19}]$	Lelieveld et al. (2021)
56	$Cu(I) + H_2O_2 \rightarrow Cu(II) + OH + OH^-$	$1.16 \times 10^{-19} - 1.16 \times 10^{-15}$	This study
57	$DTT + OH \rightarrow DTT^\bullet + H_2O$	$[1.66 \times 10^{-11}]$	Netto and Stadtman (1996)
58	$DTT + HO_2 \rightarrow DTT^\bullet + 2OH^-$	$2.65 \times 10^{-17} - 2.65 \times 10^{-13}$	This study
59	$DTT + H_2O_2 \rightarrow DTT^\bullet + H_2O + OH^-$	$[3.04 \times 10^{-21}]$	Netto and Stadtman (1996)
60	$Fe(III) + DTT \rightarrow DTT^\bullet + Fe(II)$	4.65×10^{-21}	Netto and Stadtman (1996)
61	$Cu(II) + DTT \rightarrow [Cu^{2+}(DTT^{2-})]$	$2.00 \times 10^{-21} - 2.00 \times 10^{-17}$	This study
62	$[Cu^{2+}(DTT^{2-})] + DTT \rightarrow [Cu_2{}^{+}(DTT^{2-})_2]^{2-}$	$2.00 \times 10^{-19} - 2.00 \times 10^{-15}$	This study
63	$[Cu_2{}^{+}(DTT_2-)_2]^{2-} \rightarrow [Cu^{+}(DTT^{2-})(DTT^{\bullet-})]^{2-}$	$2.00 \times 10^{-3} - 2.00 \times 10^{1}\ s^{-1}$	This study
64	$[Cu^{+}(DTT^{2-})(DTT^{\bullet-})]^{2-} + O_2 \rightarrow [Cu^{+}(DTT^{2-})(DTTOO^{\bullet-})]^{2-}$	$2.00 \times 10^{-19} - 2.00 \times 10^{-15}$	This study
65	$[Cu^{+}(DTT^{2-})(DTTOO^{\bullet-})]^{2-} + DTT \rightarrow [Cu^{2+}(DTT^{2-})] + 2\,RSSR$	$2.00 \times 10^{-18} - 2.00 \times 10^{-14}$	This study
66	$[Cu^{2+}(DTT^{2-})] \rightarrow [Cu^{+}(DTT^{\bullet}-)]$	$2.00 \times 10^{-3} - 2.00 \times 10^{1}\ s^{-1}$	This study
67	$[Cu^{+}(DTT^{\bullet}-)] + O_2 \rightarrow [Cu^{+}(DTTOO^{\bullet-})]$	$2.00 \times 10^{-23} - 2.00 \times 10^{-19}$	This study
68	$[Cu^{+}(DTTOO^{\bullet}-)] \rightarrow Cu(I) + RSSR$	$2.00 \times 10^{-6} - 2.00 \times 10^{-2}\ s^{-1}$	This study
69	$Fe(IV) + DTT \rightarrow Fe(III) + DTT^\bullet$	$5.00 \times 10^{-19} - 5.00 \times 10^{-15}$	This study
70	$DTT^\bullet + DTT \rightarrow RSSR^{\bullet-}$	$1.00 \times 10^{-14} - 1.00 \times 10^{-11}$	This study
71	$DTT^\bullet + O_2 \rightarrow RSS + HO_2$	$[1.18 \times 10^{-12}]$	This study
72	$1,2-NQN + DTT \rightarrow 1,2-NQN^\bullet + DTT^\bullet$	$8.00 \times 10^{-23} - 8.00 \times 10^{-17}$	This study
73	$RSSR^{\bullet-} + 1,2-NQN \rightarrow RSSR + 1,2-NQN^\bullet$	$1.00 \times 10^{-19} - 1.00 \times 10^{-13}$	This study
74	$DTT^\bullet + 1,2-NQN \rightarrow RS-1,2-NQN$	$1.00 \times 10^{-18} - 1.00 \times 10^{-12}$	This study
75	$1,4-NQN + DTT \rightarrow 1,4-NQN^\bullet + DTT^\bullet$	$5.00 \times 10^{-24} - 5.00 \times 10^{-18}$	This study
76	$RSSR^{\bullet-} + 1,4-NQN \rightarrow RSSR + 1,4-NQN^\bullet$	$1.00 \times 10^{-19} - 1.00 \times 10^{-13}$	This study
77	$DTT^\bullet + 1,4-NQN \rightarrow RS-1,4-NQN$	$1.00 \times 10^{-18} - 1.00 \times 10^{-12}$	This study
78	$PQN + DTT \rightarrow PQN^\bullet + DTT^\bullet$	$6.00 \times 10^{-22} - 6.00 \times 10^{-16}$	This study
79	$RSSR^{\bullet-} + PQN \rightarrow RSSR + PQN^\bullet$	$1.00 \times 10^{-19} - 1.00 \times 10^{-13}$	This study
80	$DTT^\bullet + PQN \rightarrow RS-PQN$	$10^{-18} - 1.00 \times 10^{-12}$	This study
81	$AA^\bullet + O_2^-\ (+ 2H^+) \rightarrow DHA + H_2O_2$	$1.00 \times 10^{-16} - 1.00 \times 10^{-12}$	This study
82	$DHA + OH\ (+ 2H^+) \rightarrow NRP$	$[1.66 \times 10^{-11}]$	Shen et al. (2021)
83	$DHA + H_2O_2 \rightarrow NRP$	$[6.97 \times 10^{-23}]$	Shen et al. (2021)
84	$DHA\ (+ H_2O) \rightarrow DKG$	$4.8 \times 10^{-6} - 4.8 \times 10^{-2}\ s^{-1}$	This study
85	$Mn(II) + DTT \rightarrow Mn(I) + DTT^\bullet$	$5.00 \times 10^{-23} - 5.00 \times 10^{-19}$	This study
86	$RSSR^{\bullet-} + O_2 \rightarrow RSSR + HO_2$	$[1.00 \times 10^{-12}]$	Kumagai et al. (2002)
87	$Mn(II) + OH \rightarrow Mn(III) + OH^-$	$[3.32 \times 10^{-14}]$	Jacobsen et al. (1998)
88	$Mn(II) + HO_2 \rightarrow MnO_2{}^{+}$	$1.00 \times 10^{-17} - 1.00 \times 10^{-13}$	Jacobsen et al. (1998)
89	$MnO_2{}^{+} + MnO_2{}^{+}\ (+ 2H^+) \rightarrow 2\,Mn(II) + H_2O_2$	$[9.96 \times 10^{-15}]$	Morgan (2005)
90	$Mn(III) + H_2O_2 \rightarrow Mn(II) + HO_2 + H^+$	$[1.21 \times 10^{-16}]$	Jacobsen et al. (1998)
91	$Mn(III) + H_2O_2 \rightarrow MnO_2{}^{+}$	$[4.65 \times 10^{-18}]$	Jacobsen et al. (1998)
92	$MnO_2{}^{+} + HO_2 \rightarrow Mn(II) + H_2O_2$	$[1.66 \times 10^{-14}]$	Halliwell and Gutteridge (2015)

Continued.

Reaction number	Reaction	Range	Reference
93	$Mn(III) + DTT \rightarrow Mn(II) + DTT^{\bullet}$	$5.00 \times 10^{-17} - 5.00 \times 10^{-15}$	This study
94	$Mn(II) + O_2 \rightarrow Mn(III) + HO_2$	$[3.98 \times 10^{-21}]$	Halliwell and Gutteridge (2015)
95	$PQN + DTT \rightarrow RSSR + PQN^{\bullet}$	$1.00 \times 10^{-21} - 1.00 \times 10^{-17}$	This study
96	$RS-1,4-NQN + DTT \rightarrow RSSR + 1,4-NQN^{\bullet}$	$1.00 \times 10^{-21} - 1.00 \times 10^{-17}$	This study
97	$RS-1,2-NQN + DTT \rightarrow RSSR + 1,2-NQN^{\bullet}$	$1.00 \times 10^{-21} - 1.00 \times 10^{-17}$	This study
98	$GSOO + GSOO \rightarrow 0.56\,HO_2$	$[6.79 \times 10^{-13}]$	Lelieveld et al. (2021)
99	$GSOO + GSH \rightarrow GSO + GSOH$	$[3.32 \times 10^{-15}]$	Lelieveld et al. (2021)
100	$GS + GSH \rightarrow GSSG^{-}$	$[1.59 \times 10^{-14}]$	Lelieveld et al. (2021)
101	$GSSG^{-} \rightarrow GS$	$[1.60 \times 10^{5}\ s^{-}1]$	Lelieveld et al. (2021)
102	$GSSG^{-} + O_2\ (+ H_2O) \rightarrow GSSG + O_2{}^{-}$	$[8.30 \times 10^{-12}]$	Lelieveld et al. (2021)
103	$GS + GS \rightarrow GSSG$	$[8.30 \times 10^{-12}]$	Lelieveld et al. (2021)
104	$GSOH + GSH \rightarrow GSSG + H_2O$	$[1.20 \times 10^{-18}]$	Lelieveld et al. (2021)
105	$GSO + GSO \rightarrow NRP$	$[9.96 \times 10^{-14}]$	Lelieveld et al. (2021)
106	$GSH + Cu(II) \rightarrow [Cu_2{}^{+}(GSH)]$	$1.00 \times 10^{-20} - 1.00 \times 10^{-16}$	This study
107	$Cu_2{}^{+}(GSH) + GSH \rightarrow [Cu_2{}^{+}(GSH)(GSH)]$	$1.00 \times 10^{-19} - 1.00 \times 10^{-15}$	This study
108	$2[Cu_2{}^{+}(GSH)_2] + O_2 \rightarrow 2[Cu_2{}^{+}(GS)(GSH)] + H_2O_2$	$2.00 \times 10^{-36} - 2.00 \times 10^{-32}\ cm^6\ s^{-1}$	This study
109	$2[Cu_2{}^{+}(GS)(GSH)] + O_2 \rightarrow 2[Cu_2{}^{+}(GS)(GS)] + H_2O_2$	$2.00 \times 10^{-41} - 2.00 \times 10^{-37}\ cm^6\ s^{-1}$	This study
110	$[Cu_2{}^{+}(GS)(GS)] \rightarrow Cu(II) + GSSG$	$2.00 \times 10^{-4}\ s^{-1}$	This study
111	$ROOH \rightarrow RO + OH$	$[1.50 \times 10^{-3}\ s^{-1}]$	Campbell et al. (2023)
112	$OH + ROOH \rightarrow ROH + HO_2$	$[1.00 \times 10^{-16}]$	Campbell et al. (2023)
113	$RO \rightarrow R$	$[5.00 \times 10^{5}\ s^{-1}]$	Campbell et al. (2023)
114	$R + O_2 \rightarrow RO_2$	$[7.97 \times 10^{-12}]$	Campbell et al. (2023)
115	$AA + RO \rightarrow AA^{\bullet} + ROH$	$[2.01 \times 10^{-17}]$	Campbell et al. (2023)
116	$Fe(II) + ROOH \rightarrow Fe(III) + RO + OH^{-}$	$[6.64 \times 10^{-17}]$	Campbell et al. (2023)
117	$Fe(II) + ROOH \rightarrow Fe(III) + OH + RO^{-}$	$[7.31 \times 10^{-18}]$	Campbell et al. (2023)
118	$DTT + RO \rightarrow DTT^{\bullet} + ROH$	$[1.66 \times 10^{-17}]$	Assumed to be the same as 116
119	$SOA + OH \rightarrow H_2O + R$	$[1.66 \times 10^{-13}]$	Campbell et al. (2023)
120	$SOA + RO \rightarrow ROH + R$	$[1.33 \times 10^{-16}]$	Walling (1967)
121	$ROOH + RO \rightarrow ROH + RO_2$	$[5.48 \times 10^{-16}]$	Assumed to be the same as 112
122	$R + R \rightarrow product$	$[2.00 \times 10^{-14}]$	Wei et al. (2022)
123	$RO + RO \rightarrow ROOR$	$[2.32\times 10^{-12}]$	Walling (1967)
124	$RO_2 + RO_2 \rightarrow RO + RO + O_2$	$[2.16 \times 10^{-13}]$	Mouchel-Vallon et al. (2017)
125	$RO_2 + RO_2 \rightarrow carbonyl + carbonyl + H_2O_2$	$[4.98 \times 10^{-14}]$	Mouchel-Vallon et al. (2017)
126	$Fe(II) + ROOR \rightarrow Fe(III) + RO + RO^{-}$	$[5.00 \times 10^{-23}]$	Wei et al. (2022)
127	$R + O_2 \rightarrow RO_2$	$[7.64 \times 10^{-12}]$	Chevallier et al. (2004)
128	$RO_2 + HO_2 \rightarrow ROOH + O_2$	$[6.97 \times 10^{-16}]$	Mouchel-Vallon et al. (2017)
129	$RO + O_2 \rightarrow carbonyl + O_2{}^{-}$	$[9.96 \times 10^{-15}]$	Wei et al. (2022)
130	$RO \rightarrow R$	$[1.00 \times 10^{5}\ s^{-1}]$	Campbell et al. (2023)
131	$RO_2 + AA \rightarrow ROOH + AA^{\bullet}$	$[2.49 \times 10^{-15}]$	Buettner and Jurkiewicz (1996)
132	$RO_2 + DTT \rightarrow ROOH + DTT^{\bullet}$	$[1.74 \times 10^{-16}]$	Campbell et al. (2023)
133	$RO_2 \rightarrow O_2{}^{-} + carbonyl$	$[10\ s^{-1}]$	Chevallier et al. (2004)
134	$spin-trap + RO \rightarrow spin-trap-RO$	$[2.11 \times 10^{-18}]$	Sueishi et al. (2014)
135	$spin-trap + OH \rightarrow spin-trap-OH$	$[1.66 \times 10^{-12}]$	Halliwell and Gutteridge (2015)
136	$spin-trap + O_2{}^{-} \rightarrow spin-trap-O_2{}^{-}$	$[1.99 \times 10^{-21}]$	Halliwell and Gutteridge (2015)
137	$spin-trap + R \rightarrow spin-trap-R$	$[3.98 \times 10^{-15}]$	Kemp (1999)

Table 2: *Environmental input parameters for the different laboratory experiments*

Experiment number	Temperature (K)	Citric acid (μM)	AA (μM)	UAH (μM)	GSH (μM)	DTT (μM)	Benzoate (mM)	Reference
1 – 10 (Fig. 3A, B)	298	300	200	100	100	0	0	Charrier et al. (2014)
11 – 12 (Fig. 3C)	298	300	200	100	100	0	10	Charrier and Anastasio (2015)
13 – 15 (Fig. 4A)	310	0	200	0	0	0	0	Expósito et al. (2024)
16 – 17 (Fig. 4B)	310	0	200	0	0	0	0	Shen et al. (2021)
18 – 21, 26 – 29 (Fig. 5A, D)	310	0	0	0	0	100	0	Charrier and Anastasio (2012)
22 – 23 (Fig. 5A, B)	310	0	0	0	0	50	0	Expósito et al. (2024)
24 – 25, 30 – 32 (Fig. 5C, E)	310	0	0	0	0	100	0	Xiong et al. (2017)

3 Supplementary Text

3.1 H_2O_2 production experiments

In order to reproduce the experimental data of Charrier et al. (2014), in addition to the transition metals and quinones, the model includes 300 μM of citric acid, 200 μM ascorbic acid, 100 μM uric acid and 100 μM GSH. The final output is calculated by diving the H_2O_2 concentration at 3600 seconds by 3600, resulting in a production rate of H_2O_2.

3.2 OH production experiments

In order to reproduce the experimental data of Charrier and Anastasio (2015), in addition to the transition metals and quinones, the model includes 300 μM of citric acid, 200 μM ascorbic acid, 100 μM uric acid, 100 μM GSH and 10 mM of Benzoate. The rate of OH production is calculated by taking the linear slope between 0 and 4 hrs.

3.3 Ascorbic acid experiments

In order to reproduce the experimental data of Expósito et al. (2024), in addition to the transition metals and quinones, the model includes an initial concentration of 200 μM ascorbic acid. The simulations are conducted at 310 K.

3.4 DHA production experiments

In order to reproduce the experimental data of Shen et al. (2021), the model include 200 μM of ascorbic acid, and varying concentrations of transition metals. These are allowed to react for 20 mins. The simulations are conducted at 310 K. The oxidation of ascorbic acid is determined by quantifying the oxidation product dehydroascorbic acid (DHA) at the end of the 20 mins.

3.5 DTT experiments with transition metals and quinones

In order to reproduce the experimental data of Charrier and Anastasio (2012) and Xiong et al. (2017), the model includes an initial DTT concentration of 100 μM and varying concentrations of transition metals and quinones. The simulations are conducted at 310 K. To reproduce the data of Expósito et al. (2024), the initial DTT concentration is set to 50 μM, as used in their study. The rate of DTT loss is calculated by taking the linear slope between 0 and 15 mins.

3.6 DTT experiments with SOA

In order to reproduce the experimental data of Tuet et al. (2017), we follow the experimental protocol from Fang et al. (2015). An initial DTT concentration of 0.1 mM is included in the model. The simulations are conducted at 310 K. The rate of DTT loss was determined by taking the linear slope at 0, 4, 13, 23, 30, and 41 mins.

3.7 EPR experiments with SOA

In order to reproduce the experimental data of Tong et al. (2018), we include an initial spin trap concentration of 10 mM, and an SOA concentration between 0 and 4 mM. As the SOA was freshly produced, we assume a low degree of aging, and perform the simulations with 10% and 3% peroxide content Wang et al. (2018).

4 References

Buettner, G. R. and Jurkiewicz, B. A.: Catalytic Metals, Ascorbate and Free Radicals: Combinations to Avoid, Radiation Research, 145, 532–541, 1996.

Campbell, S. J., Utinger, B., Barth, A., Paulson, S. E., and Kalberer, M.: Iron and Copper Alter the Oxidative Potential of Secondary Organic Aerosol: Insights from Online Measurements and Model Development, Environ. Sci. Technol., 57, 13 546–13 558, 2023.

Charrier, J. G. and Anastasio, C.: On dithiothreitol (DTT) as a measure of oxidative potential for ambient particles: evidence for the importance of soluble transition metals, Atmos. Chem. Phys., 12, 9321–9333, 2012.

Charrier, J. G. and Anastasio, C.: Rates of Hydroxyl Radical Production from Transition Metals and Quinones in a Surrogate Lung Fluid, Environ. Sci. Technol., 49, 9317–9325, 2015.

Charrier, J. G., McFall, A. S., Richards-Henderson, N. K., and Anastasio, C.: Hydrogen Peroxide Formation in a Surrogate Lung Fluid by Transition Metals and Quinones Present in Particulate Matter, Environ. Sci. Technol., 48, 7010–7017, 2014.

Chevallier, E., Jolibois, R., Meunier, N., Carlier, P., and Monod, A.: "Fenton-like" reactions of methylhydroperoxide and ethylhydroperoxide with Fe2+ in liquid aerosols under tropospheric conditions, Atmospheric Environment, 38, 921–933, 2004.

Ervens, B., George, C., Williams, J. E., Buxton, G. V., Salmon, G. A., Bydder, M., Wilkinson, F., Dentener, F., Mirabel, P., Wolke, R., and Herrmann, H.: CAPRAM 2.4 (MODAC mechanism): An extended and condensed tropospheric aqueous phase mechanism and its application, Journal of Geophysical Research: Atmospheres, 108, 2003.

Expósito, A., Maillo, J., Uriarte, I., Santibáñez, M., and Fernández-Olmo, I.: Kinetics of ascorbate and dithiothreitol oxidation by soluble copper, iron, and manganese, and 1,4-naphthoquinone: Influence of the species concentration and the type of fluid, Chemosphere, 361, 142 435, 2024.

Fang, T., Verma, V., Guo, H., King, L. E., Edgerton, E. S., and Weber, R. J.: A semi-automated system for quantifying the oxidative potential of ambient particles in aqueous extracts using the dithiothreitol (DTT) assay: results from the Southeastern Center for Air Pollution and Epidemiology (SCAPE), Atmos. Meas. Tech., 8, 471–482, 2015.

Gonzalez, D. H., Diaz, D. A., Baumann, J. P., Ghio, A. J., and Paulson, S. E.: Effects of albumin, transferrin and humic-like substances on iron-mediated OH radical formation in human lung fluids, Free Radical Biology and Medicine, 165, 79–87, 2021.

Halliwell, B. and Gutteridge, J. M. C.: Free Radicals in Biology and Medicine, OUP Oxford, Oxford, ISBN 978-0-19-871748-5, 2015.

Jacobsen, F., Holcman, J., and Sehested, K.: Oxidation of manganese(II) by ozone and reduction of manganese(III) by hydrogen peroxide in acidic solution, International Journal of Chemical Kinetics, 30, 207–214, 1998.

Kemp, T. J.: Kinetic Aspects of Spin Trapping, Progress in Reaction Kinetics, 24, 287–358, 1999.

Kohen, R. and Nyska, A.: Invited Review: Oxidation of Biological Systems: Oxidative Stress Phenomena, Antioxidants, Redox Reactions, and Methods for Their Quantification, Toxicol Pathol, 30, 620–650, 2002.

Kumagai, Y., Koide, S., Taguchi, K., Endo, A., Nakai, Y., Yoshikawa, T., and Shimojo, N.: Oxidation of Proximal Protein Sulfhydryls by Phenanthraquinone, a Component of Diesel Exhaust Particles, Chem. Res. Toxicol., 15, 483–489, 2002.

Lakey, P. S. J., Berkemeier, T., Tong, H., Arangio, A. M., Lucas, K., Pöschl, U., and Shiraiwa, M.: Chemical exposure-response relationship between air pollutants and reactive oxygen species in the human respiratory tract, Sci. Rep., 6, 32 916, 2016.

Lelieveld, S., Wilson, J., Dovrou, E., Mishra, A., Lakey, P. S. J., Shiraiwa, M., Pöschl, U., and Berkemeier, T.: Hydroxyl Radical Production by Air Pollutants in Epithelial Lining Fluid Governed by Interconversion and Scavenging of Reactive Oxygen Species, Environ. Sci. Technol., 55, 14 069–14 079, 2021.

Liu, M. J., Wiegel, A. A., Wilson, K. R., and Houle, F. A.: Aerosol Fragmentation Driven by Coupling of Acid–Base and Free-Radical Chemistry in the Heterogeneous Oxidation of Aqueous Citric Acid by OH Radicals, J. Phys. Chem. A, 121, 5856–5870, 2017.

Morgan, J. J.: Kinetics of reaction between O2 and Mn(II) species in aqueous solutions, Geochimica et Cosmochimica Acta, 69, 35–48, 2005.

Mouchel-Vallon, C., Deguillaume, L., Monod, A., Perroux, H., Rose, C., Ghigo, G., Long, Y., Leriche, M., Aumont, B., Patryl, L., Armand, P., and Chaumerliac, N.: CLEPS 1.0: A new protocol for cloud aqueous phase oxidation of VOC mechanisms, Geosci. Model Dev., 10, 1339–1362, 2017.

Netto, L. E. and Stadtman, E. R.: The Iron-Catalyzed Oxidation of Dithiothreitol Is a Biphasic Process: Hydrogen Peroxide Is Involved in the Initiation of a Free Radical Chain of Reactions, Archives of Biochemistry and Biophysics, 333, 233–242, 1996.

Pham, A. N., Xing, G., Miller, C. J., and Waite, T. D.: Fenton-like copper redox chemistry revisited: Hydrogen peroxide and superoxide mediation of copper-catalyzed oxidant production, Journal of Catalysis, 301, 54–64, 2013.

Shen, J., Griffiths, P. T., Campbell, S. J., Utinger, B., Kalberer, M., and Paulson, S. E.: Ascorbate oxidation by iron, copper and reactive oxygen species: review, model development, and derivation of key rate constants, Scientific Reports, 11, 7417, 2021.

Sueishi, Y., Hori, M., Ishikawa, M., Matsu-ura, K., Kamogawa, E., Honda, Y., Kita, M., and Ohara, K.: Scavenging rate constants of hydrophilic antioxidants against multiple reactive oxygen species, Journal of Clinical Biochemistry and Nutrition, 54, 67–74, 2014.

Tong, H., Lakey, P. S. J., Arangio, A. M., Socorro, J., Shen, F., Lucas, K., Brune, W. H., Pöschl, U., and Shiraiwa, M.: Reactive Oxygen Species Formed by Secondary Organic Aerosols in Water and Surrogate Lung Fluid, Environ. Sci. Technol., 52, 11 642–11 651, 2018.

Tuet, W. Y., Chen, Y., Xu, L., Fok, S., Gao, D., Weber, R. J., and Ng, N. L.: Chemical oxidative potential of secondary organic aerosol (SOA) generated from the photooxidation of biogenic and anthropogenic volatile organic compounds, Atmos. Chem. Phys., 17, 839–853, 2017.

Walling, C.: Some aspects of the chemistry of alkoxy radicals, 15, 69–80, 1967.

Wang, S., Ye, J., Soong, R., Wu, B., Yu, L., Simpson, A. J., and Chan, A. W. H.: Relationship between chemical composition and oxidative potential of secondary organic aerosol from polycyclic aromatic hydrocarbons, Atmos. Chem. Phys., 18, 3987–4003, 2018.

Wei, J., Fang, T., Lakey, P. S. J., and Shiraiwa, M.: Iron-Facilitated Organic Radical Formation from Secondary Organic Aerosols in Surrogate Lung Fluid, Environ. Sci. Technol., 56, 7234–7243, 2022.

Xiong, Q., Yu, H., Wang, R., Wei, J., and Verma, V.: Rethinking Dithiothreitol-Based Particulate Matter Oxidative Potential: Measuring Dithiothreitol Consumption versus Reactive Oxygen Species Generation, Environ. Sci. Technol., 51, 6507–6514, 2017.

B.4 Supplement of "Multiphase Kinetic Modeling of Air Pollutant Effects on Protein Modification and Nitrotyrosine Formation in Epithelial Lining Fluid"

Supplementary Materials for

Multiphase kinetic modelling of air pollutant effects on protein modification and nitrotyrosine formation in epithelial lining fluid

Ashmi Mishra[1], Steven Lelieveld[1], Ulrich Pöschl[1], Thomas Berkemeier[1,*]

Affiliations:

[1]Multiphase Chemistry Department, Max Planck Institute for Chemistry; Mainz, Germany.

*Correspondence to: Thomas Berkemeier (t.berkemeier@mpic.de)

Contents of Supporting Information

Additional information

S1: Overview KM-SUB-ELF 2.0

S2: Particulate pollutant concentrations in the ELF

S3: Enzyme concentrations and reactions

S4: Parameterization of ROS formation from secondary organic aerosol

S5: Endogenous superoxide production from macrophages

S6: Synergistic effect of $^{\bullet}NO_2$ and $PM_{2.5}$

Tables

Table S1: Chemical reactions

Table S2: Input parameters of the KM-SUB-ELF 2.0 model

Table S3: Concentrations of pollutants used in the pollution scenarios

Figures

Figure S1: Schematic overview of KM-SUB-ELF 2.0

Figure S2: Biological vs. atmospheric contribution of various oxidants explored in the study

Figure S3: Contribution of different sources to $^{\bullet}OH$ production in the model as a function of endogenous superoxide production

Figure S4: Modified tyrosine concentration in the ELF as a function of the concentration of three distinct pollutants

Figure S5: Fraction of modified tyrosine attributed to different tyrosyl radicals

Figure S6: Nitrotyrosine concentration in the epithelial lining fluid as a function of $PM_{2.5}$ and $^{\bullet}NO_2$ levels

Figure S7: Sensitivity of tyrosine peroxide concentration to decomposition reaction with catalase

Figure S8: Concentration of nitrotyrosine and dityrosine as a function of antioxidant concentrations

Figure S9: Sensitivity of $PM_{2.5}$ deposition fractions to concentration of Ntyr after 2 h exposure to air pollution under different pollution scenarios

Figure S10: Concentration of nitrotyrosine in the gas phase of the upper and lower respiratory tract

Supplementary Text

S1. Overview KM-SUB-ELF 2.0

The kinetic multi-layer model of surface and bulk chemistry in the epithelial lining fluid (KM-SUB-ELF 2.0)[1] describes chemical reactions and mass transport in the respiratory tract, linking atmospheric and physiological chemistry, with the goal of understanding chemical mechanism behind the adverse health effects or air pollution. Table S1 shows the chemical mechanism used in this study, which includes redox chemistry of transition metals, HO_x and NO_x radical chemistry, antioxidant redox reaction as well as oxidation reactions of proteins in a total of 201 reactions. Of these, 23 are gas-phase chemical reactions adopted from the Master Chemical Mechanism (MCM),[2,3] and 178 are aqueous-phase reactions within the ELF, of which six occur in the surfactant layer, and two in the cellular layer.

S2. Particulate pollutant concentrations in the ELF

The concentrations of redox-active $PM_{2.5}$ constituents in the ELF are calculated as described previously,[4] using Eq. S1.

$$C_{\mathrm{ELF,Y}} = \frac{C_{\mathrm{gas,PM2.5}} \times Q \times t_{\mathrm{acc}} \times f_{\mathrm{dep,PM2.5}} \times w_{\mathrm{Y}} \times s_{\mathrm{Y}}}{M_{\mathrm{Y}} \times V_{\mathrm{ELF}}} \qquad \text{(Eq. S1)}$$

The initial concentrations of redox-active $PM_{2.5}$ constituents in the ELF ($C_{ELF,Y}$) are calculated based on ventilation rate (Q), deposition fraction ($f_{dep,PM2.5}$), accumulation time in the ELF (t_{acc}), fractional solubilities (s_Y), and their mass fractions in $PM_{2.5}$ (w_Y). The mass fractions are median values from field observations across 70 different sites across the globe. The median mass fractions of Fe, Cu, SOA and the three quinone species are 8.14×10^{-3}, 3.07×10^{-4}, 0.333, 6.28×10^{-6}, 3.43×10^{-6} and, 6.64×10^{-6}, respectively. As fractional solubilities, s_Y, we use 0.4 and 0.1 for copper and iron ions, respectively. For the lung ventilation rate, we assume 1.5 $m^3\ h^{-1}$, for $f_{dep,PM2.5}$ we assume 0.45 of all the inhaled $PM_{2.5}$, and the model simulates a 2-hour exposure episode (t_{acc}). The total ELF volume, V_{ELF}, is set to 20 mL.

S3. Enzyme concentrations and reactions

The enzyme activity in the ELF is applied as previously described.[4] Briefly, the molar concentrations of enzymes are calculated from enzyme activity in enzyme units (*U*), the catalytic constant, k_{cat}, and Eq. S2.

$$[\text{Enzyme}] = \frac{v_{max}}{k_{cat}} \quad \text{(Eq. S2)}$$

One *U* is defined as the amount of enzyme needed to catalyze 1 micromole of substrate per minute. Catalase (CAT) is an important endogenous H_2O_2 scavenger in the ELF.[9] $U_{cat,ELF}$ is 3.7 ± 0.6 *U* mL^{-1},[9] and $k_{cat,CAT}$ is reported to range between 10^5 – 10^6 s^{-1}. These values translate into a molar concentration ranging from 1.3 – 24 pM (~5 pM) in the ELF. The glutathione peroxidase (GPx) concentration in the model ELF is 50 nM based on a molar mass of 2.19×10^4 g mol^{-1} and a mass concentration of 1 µg mL^{-1} in ELF.[10] In cells, the catalytic activity of catalase is reported to be an order of magnitude higher compared to ELF, which equates to 50 pM.[11,12] Peroxiredoxins are thiol proteins that are present in the cells at much higher concentrations than catalase, with concentrations of tens of micromolar.[13] Hence, peroxiredoxins are probably the predominant sink of H_2O_2 in lung cells. For simplicity, we choose a conservative estimate of 10 µM for the sum of all H_2O_2-scavenging enzymes in this work, and assume a common reaction rate of 3.3×10^{-14} cm^3 s^{-1} for the enzymes.[13] Two superoxide ($^{\bullet}O_2^-$) molecules are converted into H_2O_2 and O_2 by superoxide dismutase (SOD; Tab. S1, Reaction No. 127). SOD exists in cells in micromolar levels hence, using the same scaling factor as for H_2O_2 between cells and ELF, we have an ELF SOD concentration of 0.1 uM. We note that *U* and k_{cat} are difficult to determine because the ELF is very difficult to sample. We therefore note that the enzyme concentrations used in this study are subject to uncertainty.

S4. Parameterization of ROS formation from secondary organic aerosol

Secondary organic aerosol (SOA) has been shown to form reactive oxygen species (ROS) in aqueous solutions and the process is included in the model.[5–7] Because the exact reaction mechanism is unclear, ROS formation by SOA in the ELF is parameterized using formation rates

of ˙OH based on experimental observations.[5,6,8] Tong et al. (2016) quantified ˙OH production of SOA, from which we infer first- and second-order rate coefficients that reproduce a molar yield in the experimental data of 0.1% in the absence of iron (R137; Tab. S1), and a 1% yield of ˙OH in the presence of iron (R138; Tab. S1), respectively.

S5. Endogenous superoxide production from macrophages

A recent study shows that macrophages contribute to formation of ROS in the ELF, by releasing superoxide.[14] Fang et al. show a baseline production superoxide rate of about 0.06 µM min-1 in experiments using 4×10^4 cells cm^{-3}.[14] A macrophage concentration in the ELF of 1.5×10^7 cm^{-3} has been reported [9], which is used to linearly scale the observed superoxide production rate.

$$P_{O_2^{\bullet-}} = 0.06\ \mu M\ min^{-1} \cdot \frac{1.5 \cdot 10^7\ cm^{-3}}{4 \cdot 10^4\ cm^{-3}} = 22.5\ \mu M\ min^{-1} = 2.26 \cdot 10^{14}\ cm^{-3}\ s^{-1}$$

We use a rounded value of $2.0 \cdot 10^{14}$ cm^{-3} s^{-1} as endogenous superoxide production rate from macrophages in the aqueous epithelial lining fluid layer in the model.

S6. Synergistic effect of ˙NO_2 and $PM_{2.5}$

To illustrate the synergistic effect of ˙NO_2 and $PM_{2.5}$, we calculate the concentration of nitrotyrosine as a function of ˙NO_2 and $PM_{2.5}$ (Fig. S8a) and determine the percentage increase due to synergy (i.e. exceeding the expected linear additive behavior) according to Eq. S3.

$$\text{synergy} = \frac{[\text{Ntyr}]_{PM_{2.5}\&NO_2} - [\text{Ntyr}]_{PM_{2.5}\ only} - [\text{Ntyr}]_{NO_2\ only}}{[\text{Ntyr}]_{PM_{2.5}\ only} + [\text{Ntyr}]_{NO_2\ only}} \cdot 100 \qquad \text{(Eq. S3)}$$

Here, $[\text{Ntyr}]_{PM_{2.5}\&NO_2}$ means the concentration of nitrotyrosine in a calculation containing both $PM_{2.5}$ and ˙NO_2. $[\text{Ntyr}]_{PM_{2.5}\ only}$ is the nitrotyrosine concentration at ˙NO_2 = 0 ppb, and vice versa.

The results are shown in Fig. S8b. We find a substantial synergistic effect that is mostly a function of $PM_{2.5}$ concentration. At a $PM_{2.5}$ concentration > 10 µg/m^3, the synergistic effect always exceeds 20 %. At very high pollutant concentrations, however, it can reach up to 3000 %, i.e. the synergistic effect is 30x bigger than the linear effect.

Supplementary Tables

Table S1. Chemical reactions used in the KM-SUB-ELF 2.0 model, with reference.

#	Reaction	Rate constant ($cm^3\ s^{-1}$ or s^{-1})	Ref.
	Gas-phase reactions		
1	$^{\bullet}NO + O_3 \rightarrow {}^{\bullet}NO_2 + O_2$	2.05×10^{-14}	2,3
2	$^{\bullet}NO_2 + O_3 \rightarrow NO_3^{\bullet} + O_2$	4.85×10^{-17}	2,3
3	$^{\bullet}NO + {}^{\bullet}NO + O_2 \rightarrow {}^{\bullet}NO_2 + {}^{\bullet}NO_2$	8.93×10^{-20}	2,3
4	$^{\bullet}NO + NO_3^{\bullet} \rightarrow {}^{\bullet}NO_2 + {}^{\bullet}NO_2$	2.57×10^{-11}	2,3
5	$^{\bullet}NO_2 + NO_3^{\bullet} \rightarrow {}^{\bullet}NO + {}^{\bullet}NO_2 + O_2$	7.73×10^{-16}	2,3
6	$^{\bullet}NO_2 + NO_3^{\bullet} \rightarrow N_2O_5$	1.21×10^{-12}	2,3
7	$^{\bullet}OH + O_3 \rightarrow HO_2^{\bullet} + O_2$	8.20×10^{-14}	2,3
8	$^{\bullet}OH + H_2O_2 \rightarrow HO_2^{\bullet} + H_2O$	1.73×10^{-12}	2,3
9	$HO_2^{\bullet} + O_3 \rightarrow {}^{\bullet}OH + O_2 + O_2$	8.24×10^{-16}	2,3
10	$^{\bullet}OH + HO_2^{\bullet} \rightarrow H_2O + O_2$	1.08×10^{-10}	2,3
11	$HO_2^{\bullet} + HO_2^{\bullet} \rightarrow H_2O_2 + O_2$	5.09×10^{-12}	2,3
12	$HO_2^{\bullet} + O_2^{\bullet-} + H^+ \rightarrow H_2O_2 + O_2$	3.50×10^{-12}	2,3
13	$^{\bullet}OH + {}^{\bullet}NO \rightarrow HONO$	8.91×10^{-12}	2,3
14	$^{\bullet}OH + NO_2^{\bullet} \rightarrow HNO_3$	8.91×10^{-12}	2,3
15	$^{\bullet}OH + NO_3^{\bullet} \rightarrow HO_2^{\bullet} + {}^{\bullet}NO_2$	2.00×10^{-11}	2,3
16	$HO_2^{\bullet} + {}^{\bullet}NO \rightarrow {}^{\bullet}OH + {}^{\bullet}NO_2$	8.24×10^{-12}	2,3
17	$HO_2^{\bullet} + {}^{\bullet}NO_2 \rightarrow HO_2NO_2$	6.87×10^{-13}	2,3
18	$HO_2NO_2 \rightarrow HO_2^{\bullet} + {}^{\bullet}NO_2$	2.49×10^{-1}	2,3
19	$^{\bullet}OH + HO_2NO_2 \rightarrow {}^{\bullet}NO_2 + H_2O + O_2$	2.96×10^{-12}	2,3
20	$HO_2^{\bullet} + {}^{\bullet}NO_3^{\bullet} \rightarrow {}^{\bullet}OH + {}^{\bullet}NO_2 + O_2$	4.00×10^{-12}	2,3
21	$^{\bullet}OH + HONO \rightarrow {}^{\bullet}NO_2 + H_2O$	5.78×10^{-12}	2,3
22	$^{\bullet}OH + HNO_3 \rightarrow NO_3^{\bullet} + H_2O$	1.37×10^{-13}	2,3
23	$N_2O_5 \rightarrow {}^{\bullet}NO_2 + NO_3^{\bullet}$	1.83×10^{-1}	2,3
	Surfactant reactions		
24	SPB + $^{\bullet}OH \rightarrow$ SPB-ox	1.70×10^{-11}	15–17
25	POG + $^{\bullet}OH \rightarrow$ POG-ox	1.70×10^{-11}	8
26	SPB + $O_3 \rightarrow$ SPB-ox	1.00×10^{-14}	18,19
27	POG + $O_3 \rightarrow$ POG-ox + 0.17 H_2O_2	1.66×10^{-16}	20–23
28	aToc + OH → aToc-ox	4.50×10^{-13}	24
29	aToc + $O_3 \rightarrow$ aToc-ox	1.20×10^{-18}	25
	Aqueous ELF reactions		
30	$O_2^{\bullet-} + HO_2 + H_2O \rightarrow H_2O_2 + OH^- + O_2$	1.70×10^{-13}	8,26
31	$HO_2 + HO_2 \rightarrow H_2O_2 + O_2$	1.40×10^{-15}	26
32	$O_2^{\bullet-} + O_2^{\bullet-} + 2H^+ \rightarrow H_2O_2 + O_2$	3.82×10^{-16}	26
33	$H_2O_2 + {}^{\bullet}OH \rightarrow HO_2 + H_2O$	5.50×10^{-14}	27

34	$^{\bullet}OH + {}^{\bullet}OH \rightarrow H_2O_2$	8.60×10^{-12}	28
35	$^{\bullet}OH + O_2^{\bullet-} \rightarrow O_2 + OH^-$	1.30×10^{-11}	15
36	$^{\bullet}OH + HO_2 \rightarrow H_2O + O_2$	1.20×10^{-11}	28
37	$H_2O_2 + HO_2 \rightarrow {}^{\bullet}OH + O_2 + H_2O$	4.98×10^{-21}	29
38	$Fe^{2+} + O_2^{\bullet-} + 2H^+ \rightarrow Fe^{3+} + H_2O_2$	3.10×10^{-14}	8,26
39	$Fe^{2+} + HO_2 + H^+ \rightarrow Fe^{3+} + H_2O_2$	1.99×10^{-15}	30
40	$Fe^{2+} + H_2O_2 \rightarrow Fe^{3+} + {}^{\bullet}OH + OH^-$	4.30×10^{-18}	31
41	$Fe^{2+} + {}^{\bullet}OH \rightarrow Fe^{3+} + OH^-$	5.30×10^{-13}	32
42	$Fe^{2+} + H_2O_2 \rightarrow Fe^{4+} + H_2O$	9.50×10^{-18}	8
43	$Fe^{3+} + H_2O_2 \rightarrow Fe^{2+} + HO_2 + H^+$	3.32×10^{-24}	31
44	$Fe^{3+} + HO_2 \rightarrow Fe^{2+} + O_2 + H^+$	3.30×10^{-18}	26
45	$Fe^{3+} + O_2^{\bullet-} \rightarrow Fe^{2+} + O_2 + H^+$	3.30×10^{-18}	26
46	$Fe^{4+} + Fe^{2+} \rightarrow Fe^{3+} + Fe^{3+}$	6.60×10^{-18}	33
47	$Fe^{3+} + AscH \rightarrow Fe^{2+} + Asc^{\bullet}$	1.10×10^{-19}	8
48	$Fe^{4+} + AscH \rightarrow Fe^{3+} + Asc^{\bullet}$	7.60×10^{-19}	8
49	$Fe^{2+} + O_2 \rightarrow O_2^{\bullet-} + Fe^{3+}$	5.20×10^{-21}	8
50	$Cu^+ + HO_2 + H^+ \rightarrow Cu^{2+} + H_2O_2$	2.30×10^{-12}	8
51	$Cu^+ + O_2^{\bullet-} + H_2O \rightarrow Cu^{2+} + H_2O_2 + OH^-$	5.80×10^{-15}	8
52	$Cu^{2+} + HO_2 \rightarrow Cu^+ + O_2 + H^+$	1.60×10^{-11}	8
53	$Cu^{2+} + O_2^{\bullet-} \rightarrow Cu^+ + O_2$	8.30×10^{-12}	8
54	$Cu^{2+} + AscH \rightarrow Cu^+ + Asc^{\bullet}$	1.40×10^{-18}	8
55	$Cu^+ + O_2 \rightarrow Cu^{2+} + O_2^{\bullet-}$	6.90×10^{-20}	8
56	$Cu^+ + H_2O_2 \rightarrow Cu^{2+} + {}^{\bullet}OH + OH^-$	2.40×10^{-20}	8
57	$Cu^+ + H_2O_2 \rightarrow Cu^{3+} + OH^- + OH^-$	5.00×10^{-19}	8
58	$Cu^+ + Cu^{3+} \rightarrow Cu^{2+} + Cu^{2+}$	5.80×10^{-12}	8
59	$Cu^{2+} + H_2O_2 \rightarrow Cu^+ + O_2^{\bullet-} + H^+$	3.80×10^{-24}	8
60	$PQN + AscH \rightarrow PQN^{\bullet} + Asc^{\bullet}$	1.20×10^{-20}	34
61	$PQN^{\bullet} + O_2 \rightarrow PQN + O_2^{\bullet-}$	4.60×10^{-13}	8
62	$PQN^{\bullet} + O_2^{\bullet-} + 2H^+ \rightarrow PQN + H_2O_2$	3.30×10^{-12}	8
63	$NQN12 + AscH \rightarrow NQN12^{\bullet} + Asc^{\bullet}$	1.50×10^{-19}	34
64	$NQN12^{\bullet} + O_2 \rightarrow NQN12 + O_2^{\bullet-}$	4.60×10^{-13}	8
65	$NQN12^{\bullet} + O_2^{\bullet-} + 2H^+ \rightarrow NQN12 + H_2O_2$	3.30×10^{-12}	8
66	$NQN14 + AscH \rightarrow NQN14^{\bullet} + Asc^{\bullet}$	6.30×10^{-21}	34
67	$NQN14^{\bullet} + O_2 \rightarrow NQN14 + O_2^{\bullet-}$	4.60×10^{-13}	8
68	$NQN14^{\bullet} + O_2^{\bullet-} + 2H^+ \rightarrow NQN14 + H_2O_2$	3.30×10^{-12}	8
69	$UAH + O_3 \rightarrow Products$	2.35×10^{-15}	35
70	$UAH + {}^{\bullet}OH \rightarrow Products + OH^-$	1.20×10^{-11}	36
71	$GSH + {}^{\bullet}OH \rightarrow Products + OH^-$	1.50×10^{-11}	37
72	$GSSG + {}^{\bullet}OH \rightarrow Products + OH^-$	1.50×10^{-11}	4
73	$Asc^{\bullet} + Asc^{\bullet} + H^+ \rightarrow AscH + DHA$	5.00×10^{-16}	38
74	$AscH + O_2^{\bullet-} + H^+ \rightarrow Asc^{\bullet} + H_2O_2$	5.10×10^{-17}	8

75	$AscH + HO_2 \rightarrow Asc^{\bullet} + H_2O_2$	2.65×10^{-17}	39
76	$AscH + {}^{\bullet}OH \rightarrow Products + OH^-$	1.80×10^{-11}	40
77	$AscH + O_3 \rightarrow Products$	9.97×10^{-14}	35
78	$GS^- + O_3 \rightarrow Products$	1.33×10^{-12}	35
79	$GSH + O_3 \rightarrow Products$	1.33×10^{-12}	35
80	$GSOO^{\bullet} + GSOO^{\bullet} \rightarrow 0.56\ O_2^{\bullet-} + Products$	6.79×10^{-13}	41
81	$O_2^{\bullet-} + GSH \rightarrow GSO^{\bullet} + OH^-$	3.32×10^{-19}	42–44
82	$^{\bullet}NO_2 + GS^{\bullet} \rightarrow GSNO_2$	4.98×10^{-12}	45
83	$GSOO^{\bullet} + {}^{\bullet}NO_2 \rightarrow GSOONO_2$	2.49×10^{-12}	41
84	$GSOONO_2 \rightarrow GSOO^{\bullet} + {}^{\bullet}NO_2$	7.5×10^{-1}	41
85	$^{\bullet}NO_2 + GS^- \rightarrow NO_2^- + GS^{\bullet}$	4.00×10^{-13}	45
86	$^{\bullet}NO_2 + GSH \rightarrow NO_2^- + GS^{\bullet} + H^+$	1.66×10^{-14}	46
87	$GSOO^{\bullet} + GSH \rightarrow GSO^{\bullet} + GSOH$	3.32×10^{-15}	45
88	$GSO + NO_2 \rightarrow GSOONO$	7.47×10^{-12}	45
89	$GSOONO \rightarrow Products$	7.00×10^{2}	45
90	$GS^{\bullet} + GS^- \rightarrow GSSG^{\bullet-}$	1.59×10^{-14}	45,47
91	$GS^{\bullet} + O_2 \rightarrow GSOO^{\bullet}$	3.20×10^{-12}	47
92	$GSOO^{\bullet} \rightarrow GS^{\bullet} + O_2$	6.00×10^{5}	47
93	$GSSG^{\bullet-} \rightarrow GS^{\bullet} + GS^-$	1.60×10^{5}	45,47
94	$GSSG^{\bullet-} + O_2 \rightarrow GSSG + O_2^{\bullet-}$	8.30×10^{-12}	45,47
95	$GS^{\bullet} + GS^{\bullet} \rightarrow GSSG$	8.30×10^{-12}	47
96	$GSOH + GSH \rightarrow GSSG + H_2O$	1.20×10^{-18}	48
97	$GSO^{\bullet} + GSO^{\bullet} \rightarrow Products$	9.96×10^{-14}	45
98	$GS^- + H_2O_2 \rightarrow GSOH + OH^-$	1.60×10^{-21}	48
99	$GS^{\bullet} + AscH \rightarrow GSH + Asc^{\bullet}$	1.00×10^{-12}	49,50
100	$UA + {}^{\bullet}NO_2 \rightarrow UA^{\bullet} + NO_2^-$	3.00×10^{-14}	51,52
101	$AscH + {}^{\bullet}NO_2 \rightarrow Asc^{\bullet} + NO_2^-$	5.80×10^{-14}	51,52
102	$UA^{\bullet} + AscH \rightarrow UA + Asc^{\bullet}$	1.70×10^{-15}	50
103	$GS^{\bullet} + UA \rightarrow GSH + UA^{\bullet}$	5.00×10^{-14}	46
104	$O_2^{\bullet-} + {}^{\bullet}NO_2 \rightarrow O_2NOOm$	7.50×10^{-12}	45,53
105	$O_2NOO^- \rightarrow NO_2^- + O_2$	7.00×10^{-1}	45
106	$O_2NOO^- \rightarrow O_2^{\bullet-} + {}^{\bullet}NO_2$	1.10×10^{0}	45
107	$^{\bullet}NO_2 + {}^{\bullet}NO_2 \rightarrow N_2O_4$	7.50×10^{-13}	54
108	$N_2O_4 \rightarrow {}^{\bullet}NO_2 + {}^{\bullet}NO_2$	6.90×10^{3}	54
109	$N_2O_4 + H_2O \rightarrow NO_2^- + NO_3^- + 2H^+$	1.00×10^{3}	45
110	$O_2^{\bullet-} + O_3 + H_2O \rightarrow {}^{\bullet}OH + 2O_2 + OH^-$	2.50×10^{-12}	55
111	$HO_2 + O_3 \rightarrow {}^{\bullet}OH + 2O_2$	1.66×10^{-17}	55
112	$NO_2^- + {}^{\bullet}OH \rightarrow {}^{\bullet}NO_2 + OH^-$	8.80×10^{-12}	53
113	$^{\bullet}OH + {}^{\bullet}NO_2 \rightarrow NO_3^- + H^+$	7.50×10^{-12}	45
114	$^{\bullet}OH + {}^{\bullet}NO_2 \rightarrow ONOOH$	7.50×10^{-12}	45
115	$ONOOH \rightarrow {}^{\bullet}NO_2 + {}^{\bullet}OH$	3.00×10^{-1}	45

116	$ONOOH \rightarrow NO_3^- + H^+$	7.00×10^{-1}	45
117	$ONOO^- + GSH \rightarrow NO_2^- + GSOH$	1.10×10^{-18}	56
118	$GSO^{\bullet} + {}^{\bullet}NO_2 \rightarrow GSOONO$	7.50×10^{-12}	45
119	$GSOONO + H_2O \rightarrow$ Products	7.00×10^{2}	45
120	$ONOOH + AscH \rightarrow Im_1$	1.66×10^{-15}	57
121	$Im_1 \rightarrow ONOOH + AscH$	5.00×10^{2}	57
122	$Im_1 \rightarrow Im_2$	4.00×10^{1}	57
123	$Im_2 \rightarrow Im_1$	5.00×10^{0}	57
124	$Im_2 + AscH \rightarrow Asc + DHA + NO_2^- + H_2O$	1.66×10^{-19}	57
125	$Im_2 \rightarrow Asc + NO_3^- + H^+$	8.50×10^{-1}	57
126	$ONOOH + UA \rightarrow UA^{rad} + NO_2 +$ Products	2.60×10^{-19}	58
127	$O_2^{\bullet-} + SOD \xrightarrow{2H^+} H_2O_2 + SOD$	2.65×10^{-12}	4
128	$H_2O_2 +$ catalase $\rightarrow H_2O + 0.5\ O_2 +$ catalase	3.20×10^{-14}	4
129	$ONOOH +$ Glutathione peroxidase $\rightarrow NO_2^-$	1.33×10^{-14}	59
131	$O_2^{\bullet-} + {}^{\bullet}NO \rightarrow ONOO^-$	3.16×10^{-11}	60
132	$ONOO^- + CO_2 \rightarrow ONOOCO_2^-$	4.98×10^{-17}	61
133	$ONOOCO_2^- \rightarrow {}^{\bullet}NO_2 + CO_3^{\bullet-}$	3.3×10^{5}	45,61
134	$ONOOCO_2^- \rightarrow NO_3^- + CO_2$	6.7×10^{5}	45,61
135	$ONOO^- + GSH \rightarrow NO_2^- + GSOH$	2.24×10^{-18}	62
136	${}^{\bullet}NO_2 + {}^{\bullet}NO \rightarrow N_2O_3$	1.83×10^{-12}	61
137	$SOA \rightarrow {}^{\bullet}OH$	5.56×10^{-7}	*See SI text*
138	$SOA + Fe^{2+} \rightarrow {}^{\bullet}OH + Fe^{3+}$	7.90×10^{-23}	*See SI text*
139	$Ala + O_3 \rightarrow$ products	1.66×10^{-18}	63
140	$Arg + O_3 \rightarrow$ products	8.80×10^{-18}	63
141	$Asp + O_3 \rightarrow$ products	1.03×10^{-18}	63
142	$Cys + O_3 \rightarrow$ products	3.32×10^{-17}	63
143	$Glu + O_3 \rightarrow$ products	1.46×10^{-18}	63
144	$Gly + O_3 \rightarrow$ products	5.81×10^{-18}	63
145	$His + O_3 \rightarrow$ products	2.82×10^{-17}	63
146	$Ile + O_3 \rightarrow$ products	1.63×10^{-18}	63
147	$Leu + O_3 \rightarrow$ products	1.59×10^{-18}	63
148	$Lys + O_3 \rightarrow$ products	5.81×10^{-18}	63
149	$Met + O_3 \rightarrow$ products	6.31×10^{-15}	63
150	$Phe + O_3 \rightarrow$ products	3.16×10^{-17}	63
151	$Pro + O_3 \rightarrow$ products	1.83×10^{-17}	63
152	$Ser + O_3 \rightarrow$ products	1.33×10^{-17}	63
153	$Thr + O_3 \rightarrow$ products	5.98×10^{-18}	63
154	$Trp + O_3 \rightarrow$ products	1.16×10^{-14}	63
155	$Val + O_3 \rightarrow$ products	1.99×10^{-18}	63
156	$Ala + {}^{\bullet}OH \rightarrow$ products	1.28×10^{-13}	64
157	$Arg + {}^{\bullet}OH \rightarrow$ products	5.81×10^{-12}	64

158	Asp + $^{\bullet}OH \rightarrow$ products	1.25×10^{-13}	64
159	Cys + $^{\bullet}OH \rightarrow$ products	5.65×10^{-11}	64
160	Glu + $^{\bullet}OH \rightarrow$ products	3.82×10^{-13}	64
161	Gly + $^{\bullet}OH \rightarrow$ products	2.82×10^{-14}	64
162	His + $^{\bullet}OH \rightarrow$ products	2.16×10^{-11}	64
163	Ile + $^{\bullet}OH \rightarrow$ products	2.99×10^{-12}	64
164	Leu + $^{\bullet}OH \rightarrow$ products	2.82×10^{-12}	64
165	Lys + $^{\bullet}OH \rightarrow$ products	5.65×10^{-13}	64
166	Met + $^{\bullet}OH \rightarrow$ products	1.38×10^{-11}	64
167	Phe + $^{\bullet}OH \rightarrow$ products	1.08×10^{-11}	64
168	Pro + $^{\bullet}OH \rightarrow$ products	7.97×10^{-13}	64
169	Ser + $^{\bullet}OH \rightarrow$ products	5.31×10^{-13}	64
170	Thr + $^{\bullet}OH \rightarrow$ products	8.47×10^{-13}	64
171	Trp + $^{\bullet}OH \rightarrow$ products	2.16×10^{-11}	64
172	Val + $^{\bullet}OH \rightarrow$ products	1.26×10^{-12}	64
173	Cys + $CO_3^{\bullet-} \rightarrow$ products	1.99×10^{-13}	65
174	Met + $CO_3^{\bullet-} \rightarrow$ products	1.99×10^{-13}	66
175	Cys + $ONOO^- \rightarrow$ products	6.31×10^{-18}	66
176	Met + $ONOO^- \rightarrow$ products	5.98×10^{-19}	66
177	Trp + $ONOO^- \rightarrow$ products	6.64×10^{-20}	120
178	Cys + $H_2O_2 \rightarrow$ products	3.82×10^{-21}	66
179	Met + $H_2O_2 \rightarrow$ products	3.32×10^{-23}	66
180	Met + $O_2^{\bullet-} \rightarrow$ products	4.98×10^{-22}	66
181	Tyrosine + O3 → $TyrO^{\bullet}$	4.65×10^{-15}	19
182	Tyrosine + $^{\bullet}OH \rightarrow TyrO^{\bullet}$	9.96×10^{-13}	67
183	Tyrosine + $^{\bullet}NO_2 \rightarrow TyrO^{\bullet}$	7.47×10^{-14}	68
184	Tyrosine + $CO_3^{\bullet-} \rightarrow TyrO^{\bullet}$	5.31×10^{-16}	68
185	Tyrosine + $^{\bullet}OH \rightarrow {}^{\bullet}TyrOH$	2.00×10^{-11}	67
186	$TyrO^{\bullet} + {}^{\bullet}NO_2 \rightarrow$ Ntyr	4.98×10^{-12}	68
187	$^{\bullet}TyrOH + {}^{\bullet}NO_2 \rightarrow$ Ntyr	4.98×10^{-12}	*Same as 186*
188	$TyrO^{\bullet} + {}^{\bullet}NO \rightarrow$ NOtyr	1.66×10^{-12}	68
189	$^{\bullet}TyrOH + {}^{\bullet}NO \rightarrow$ NOtyr	1.66×10^{-12}	*Same as 188*

190	$TyrO^{\bullet} + TyrO^{\bullet} \rightarrow$ Dityr	3.82×10^{-13}	67
191	$^{\bullet}TyrOH + {}^{\bullet}TyrOH \rightarrow$ Dityr	4.98×10^{-13}	67
192	$^{\bullet}TyrOH + TyrO^{\bullet} \rightarrow$ Dityr	3.82×10^{-13}	67
193	$TyrO^{\bullet} + O_2^{\bullet-} \rightarrow TyrOOH$	2.49×10^{-12}	68
194	$TyrO^{\bullet} + AscH \rightarrow Tyr$	7.31×10^{-13}	69
195	$TyrO^{\bullet} + GSH \rightarrow Tyr$	3.32×10^{-15}	70
196	$TyrO^{\bullet} + UAH \rightarrow Tyr$	3.99×10^{-13}	68
197	$^{\bullet}TyrOH + O_2 \rightarrow TyrOO^{\bullet}$	1.66×10^{-18}	71
198	$TyrOO^{\bullet} + AscH \rightarrow TyrOOH$	1.16×10^{-14}	72
199	$TyrOO^{\bullet} + UAH \rightarrow TyrOOH$	3.16×10^{-15}	72
	Cell reactions		
200	H_2O_2 + enzymes $\rightarrow H_2O + 0.5\ O_2$ + enzymes	3.32×10^{-14}	4
201	$O_2^{\bullet-} + SOD \xrightarrow{2H^+} H_2O_2 + SOD$	2.65×10^{-12}	4

190

Table S2. Input parameters used in the KM-SUB-ELF 2.0

Parameter	Value	Unit	References
Henry's law equilibrium constant of O_3	$1.0 \cdot 10^{-2}$	M atm^{-1}	4
Henry's law equilibrium constant of H_2O_2	$9.1 \cdot 10^{4}$	M atm^{-1}	4
Henry's law equilibrium constant of $^{\bullet}OH$	29	M atm^{-1}	4
Henry's law equilibrium constant of $HO_2^{\bullet}$	$6.8 \cdot 10^{2}$	M atm^{-1}	4
Particulate mass fraction of Cu^{2+}	$3.1 \cdot 10^{-4}$	-	4
Particulate mass fraction of Fe^{2+}	$8.1 \cdot 10^{-3}$	-	4
Particulate mass fraction of quinones	$1.9 \cdot 10^{-5}$	-	4
Particulate mass fraction of SOA	0.33	-	4
Water soluble fraction of Cu^{2+}	0.40	-	4
Water soluble fraction of Fe^{2+}	0.10	-	4
Water soluble fraction of quinones	0.10	-	4
Water soluble fraction of SOA	0.10	-	4
Particulate exposure time	2	h	4
ELF catalase concentration	5	pM	4
ELF superoxide dismutase concentration	0.1	μM	See SI text
ELF glutathione concentration	108	μM	4
ELF ascorbate concentration	40	μM	4
ELF uric acid concentration	200	μM	4
ELF α-Tocopherol concentration	0.7	μM	4
ELF SP-B_{1-25} concentration	$3.76 \cdot 10^{-2}$	M	8
ELF POG concentration	4.55	M	8
Lung PM accumulation time	2	h	4
PM deposition factor	0.45	-	4
Lung functional residual capacity	2750	cm^3	4
Tidal volume	1500	cm^3	4
Duration of breath	3.6	sec	4
ELF pH	7	-	4
ELF volume	20	cm^3	4
ELF surface area	$8.9 \cdot 10^{5}$	cm^2	4
ELF temperature	310	K	4
ELF O_2 concentration	$1.6 \cdot 10^{17}$	cm^3	4
Cellular concentration of H_2O_2-scavenging enzymes	1	μM	1
H_2O_2 effective membrane permeability coefficient	$1.0 \cdot 10^{-6}$	cm s^{-1}	90
H_2O_2 production in the cell layer	$1.0 \cdot 10^{14}$	cm^{-3} s^{-1}	1
$O_2^{\bullet-}$ production in the ELF layer	$2.0 \cdot 10^{14}$	cm^{-3} s^{-1}	See SI text
Thickness of cell membrane	$1.0 \cdot 10^{-4}$	cm	1
Ambient H_2O_2 concentration	1	ppb	1
Blood H_2O_2 concentration	5	μM	1
ELF alanine concentration	2531	μM	See main text
ELF arginine concentration	650	μM	See main text
ELF aspartic acid concentration	863	μM	See main text
ELF aspartate concentration	1250	μM	See main text
ELF glutamate concentration	399	μM	See main text
ELF glutamic acid concentration	1180	μM	See main text

ELF glycine concentration	2455	μM	See main text
ELF histidine concentration	219	μM	See main text
ELF isoleucine concentration	463	μM	See main text
ELF leucine concentration	92	μM	See main text
ELF lysine concentration	718	μM	See main text
ELF methionine concentration	3546	μM	See main text
ELF phenylalanine concentration	151	μM	See main text
ELF proline concentration	248	μM	See main text
ELF serine concentration	1062	μM	See main text
ELF threonine concentration	801	μM	See main text
ELF tryptophan concentration	1296	μM	See main text
ELF tyrosine concentration	49	μM	See main text
ELF valine concentration	183	μM	See main text

Table S3. Concentrations of gas-phase pollutants considered in the examined pollution scenarios (Fig. 7). The $^{\bullet}NO_2$ levels represent a 1:1 mass ratio with $PM_{2.5}$ levels[4] except for the indoor gas stove scenario, where high levels of $^{\bullet}NO_2$ have been observed.[73] Note, $PM_{2.5}$ levels are also high from cooking emissions, however, these are likely dominated by organics rather than the redox active transition metals, therefore, we use the same $PM_{2.5}$ concentration in gas stove scenario as with the indoor scenario.

	Remote	**Rural**	**Indoor**	**urban**	**Polluted urban**	**Indoor gas stove**
O_3 (ppb)	15 [74]	20 [75]	10 [76]	30 [75]	75 [77]	10 [76]
H_2O_2 (ppb)	0.2 [78]	0.5 [79]	0.9 [80,81]	1 [82]	2 [83]	0.9 [80,81]
$^{\bullet}NO_2$ (ppb)	2.1	4.2	5.3	15.9	31.9	100[73]
$PM_{2.5}$ ($\mu g \cdot m^{-3}$)	4 [84]	8 [85,86]	10 [87]	30 [75]	60 [88,89]	10 [87]

Supplementary Figures

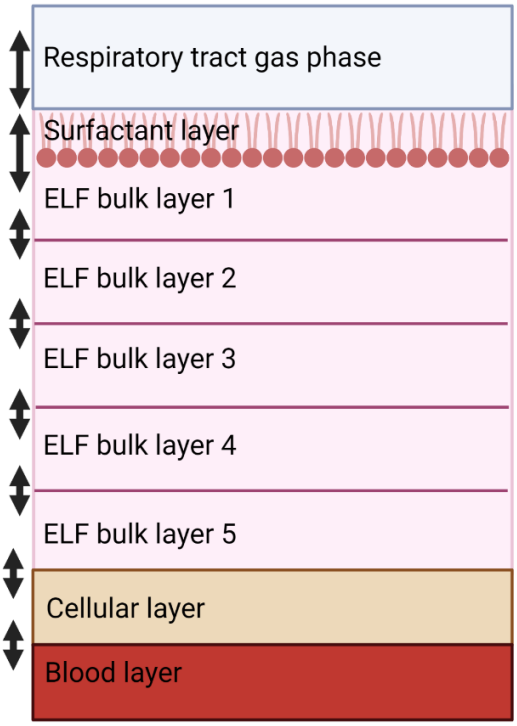

Figure S1: Schematic overview of KM-SUB-ELF 2.0. Arrows indicate mass transport between two model layers. In each layer, chemical reactions occur. Created with BioRender.com

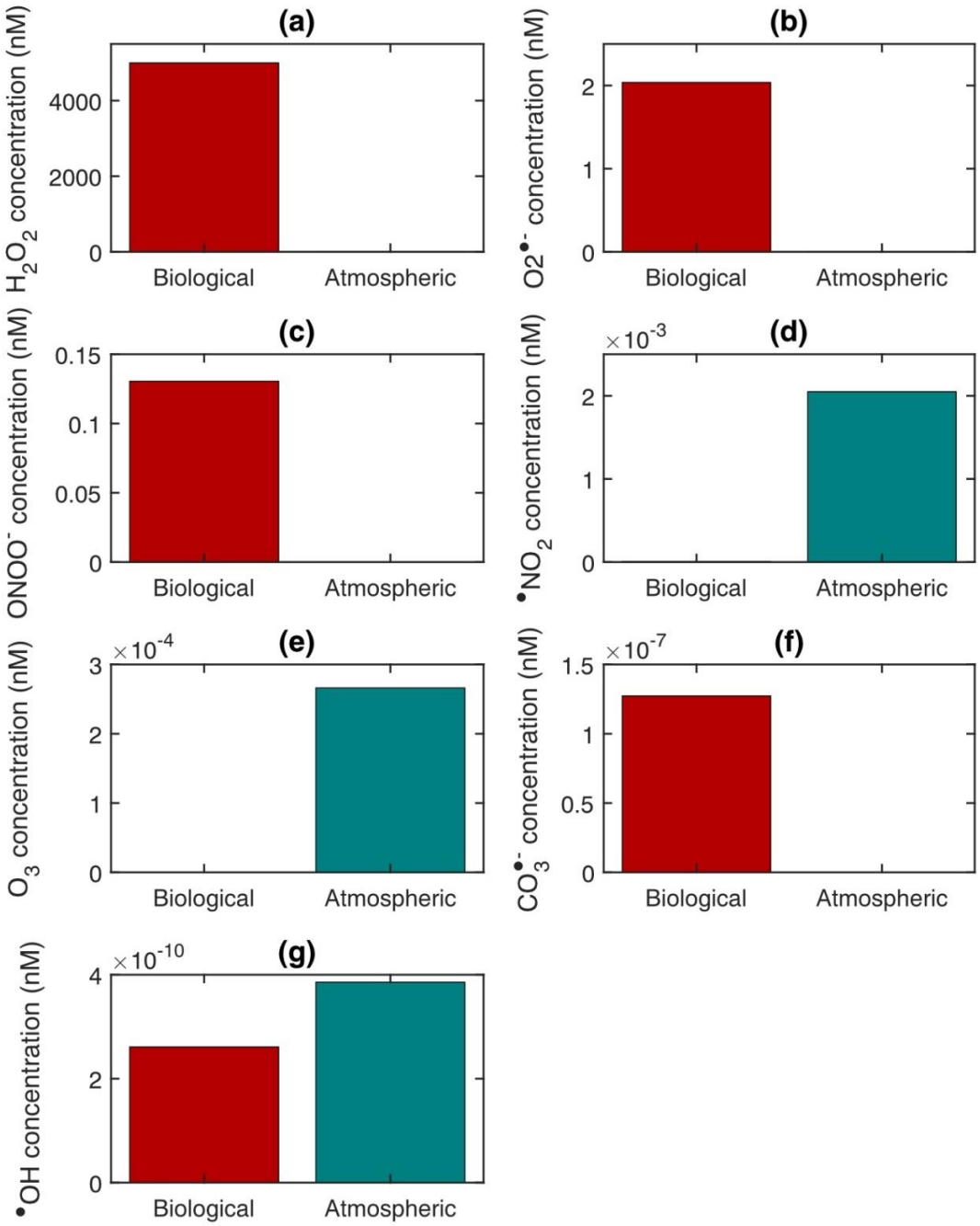

Figure S2: Biological vs. atmospheric contribution of various oxidants (a: H_2O_2, b: $O_2^{\bullet-}$, c: $ONOO^-$, d: $^{\bullet}NO_2$, e: O_3, f: $CO_3^{\bullet-}$, g: $^{\bullet}OH$) explored in the study. The biological concentrations were calculated in a model scenario where no air pollutants were present, while for the atmospheric concentrations, we use urban scenario with 30 µg m^{-3} $PM_{2.5}$ and $^{\bullet}NO_2$, as well as 30 ppb O_3.

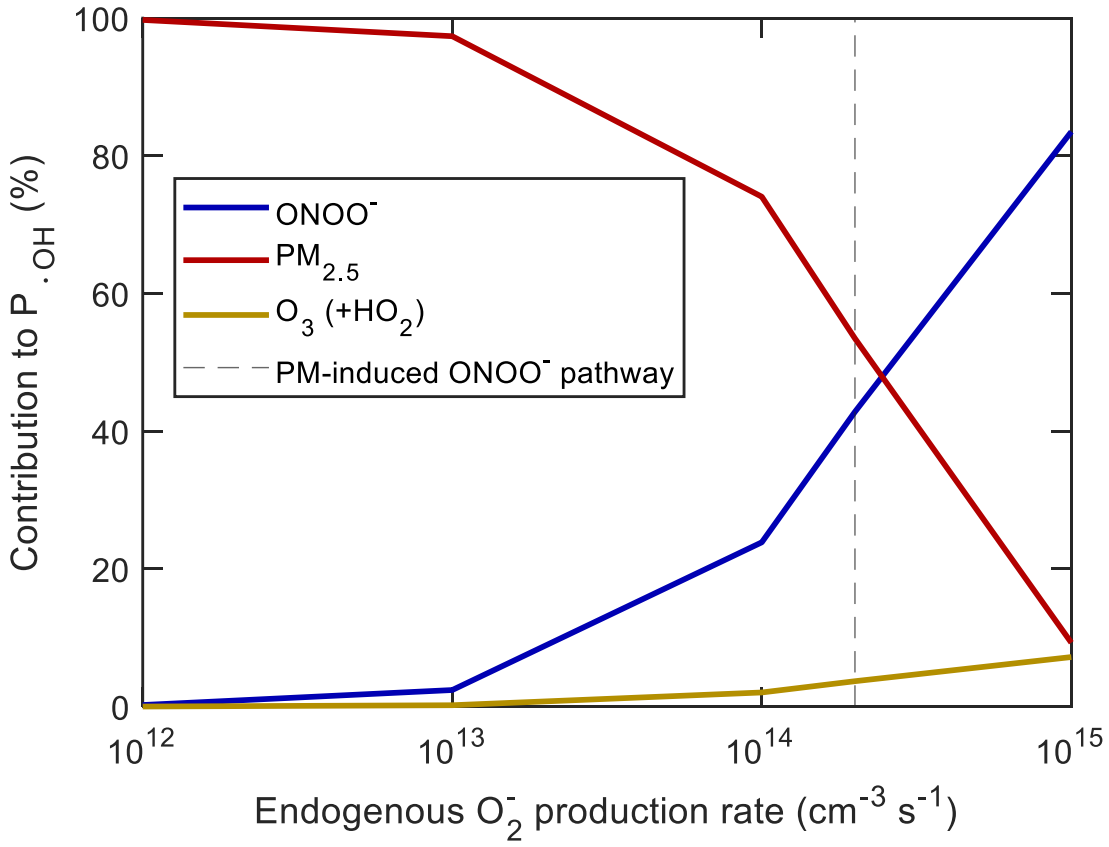

Figure S3: Contribution of different sources to •OH production in the model as a function of endogenous superoxide production. Grey dashed line indicates the production value of unstimulated macrophages. Beyond the dashed line, the production of superoxide is emerging from PM-stimulated macrophages.

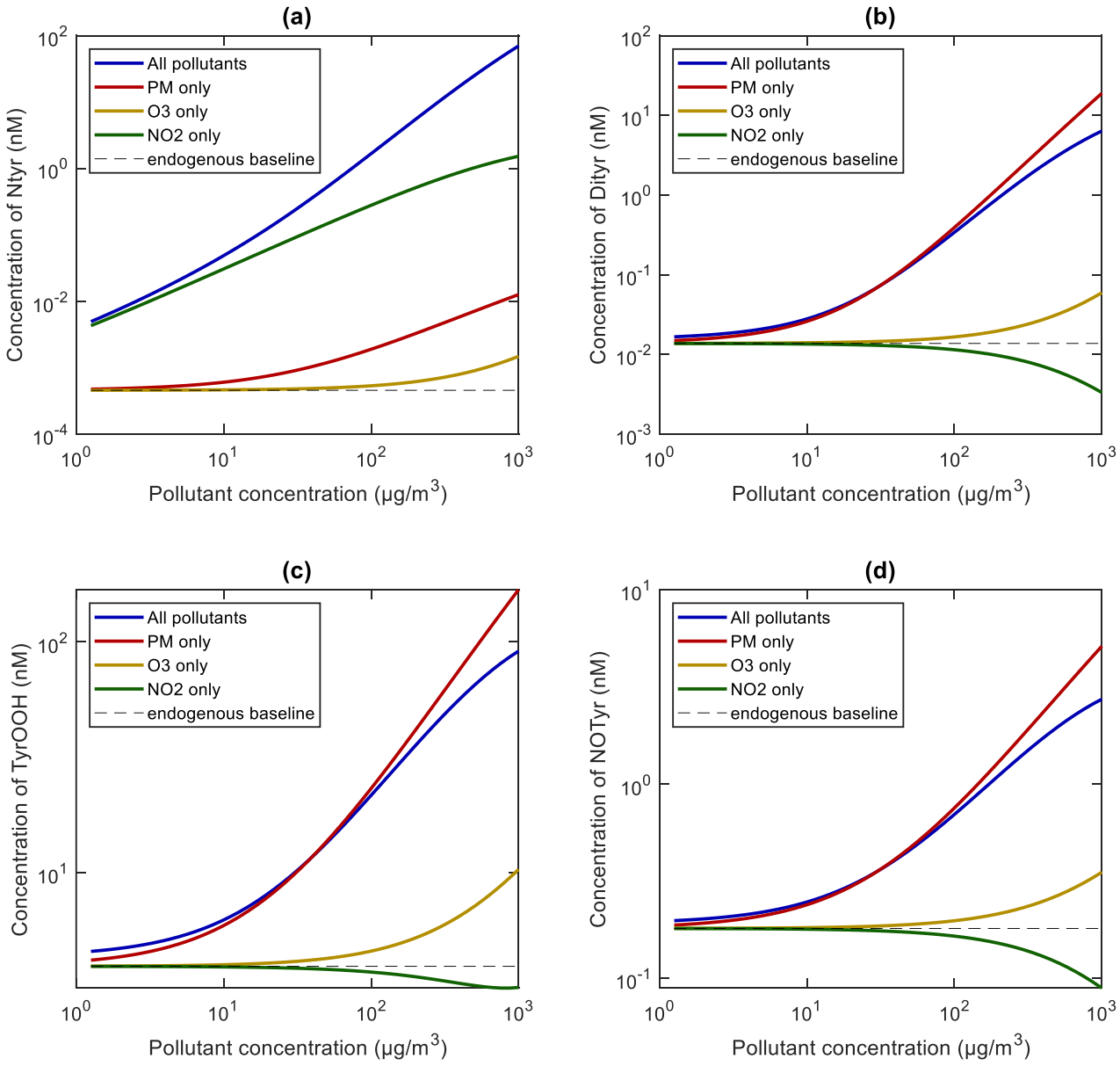

Figure S4: Concentration of modified tyrosine (a: nitrotyrosine (Ntyr), b: dityrosine (Dityr), c: tyrosine peroxide (TyrOOH), d: nitrosotyrosine (NOTyr)) in the ELF as a function of the concentration of three distinct pollutants.

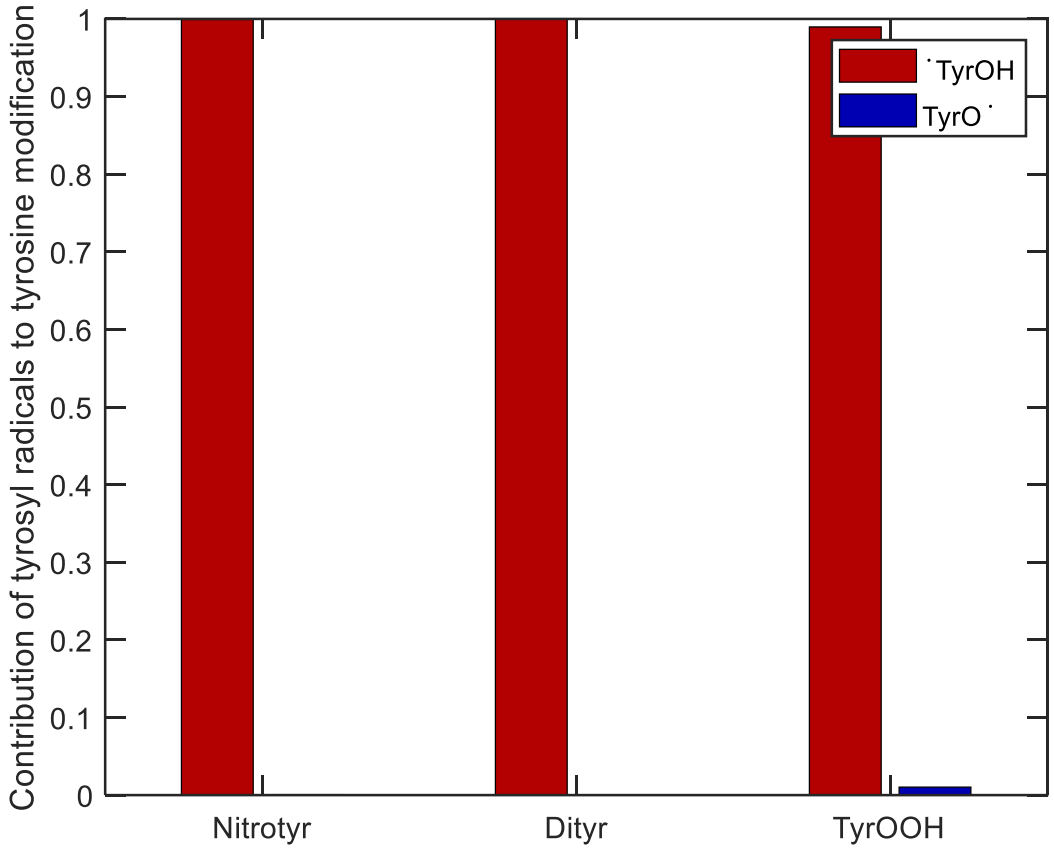

Figure S5: Fraction contribution of tyrosyl radicals to modified tyrosine considered in this study at an urban pollution scenario, of 30 µg m^{-3} $PM_{2.5}$ and $^{\bullet}NO_2$, as well as 30 ppb O_3.

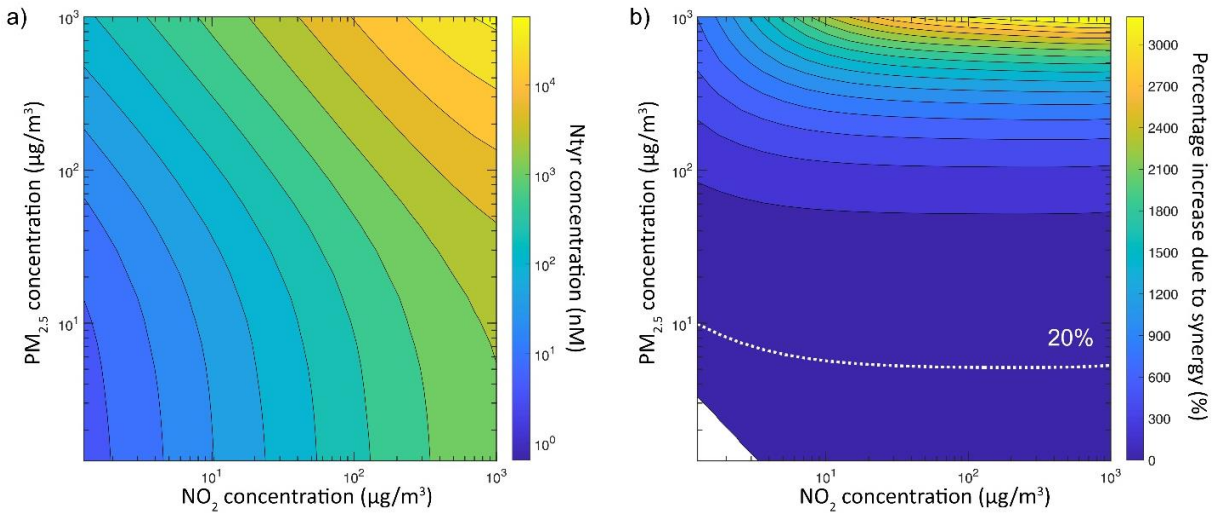

Figure S6: Nitrotyrosine concentration (a) and percentage increase in nitrotyrosine due to synergistic effects (b) in the epithelial lining fluid (ELF) after 2 h exposure as a function of $PM_{2.5}$ and $^{\bullet}NO_2$ levels. White dotted line represents the 20 % increase in synergy.

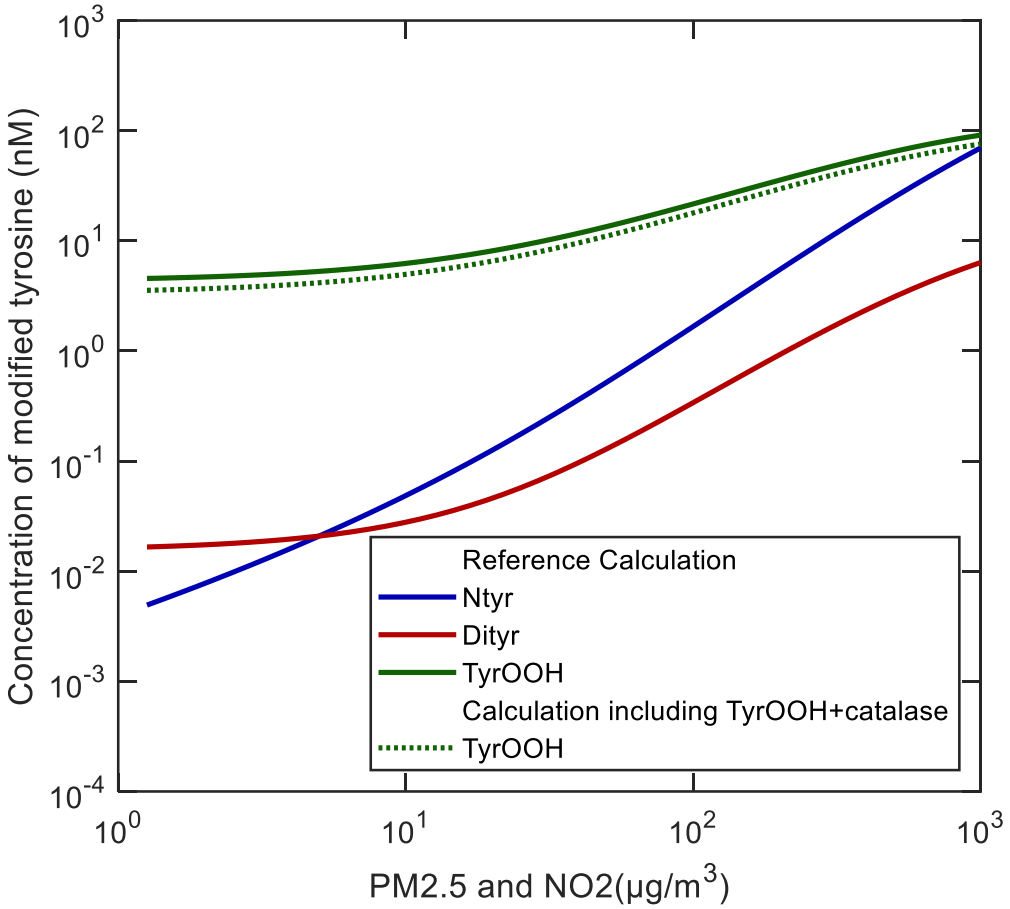

Figure S7: Concentration of modified tyrosine as a function of $PM_{2.5}$ and $^{\bullet}NO_2$. Solid lines show reference calculation results. Dotted line includes calculation where tyrosine peroxide reacts with catalase, with same reactivity as H_2O_2 to show the sensitivity of tyrosine peroxide concentration to decomposition reaction with catalase.

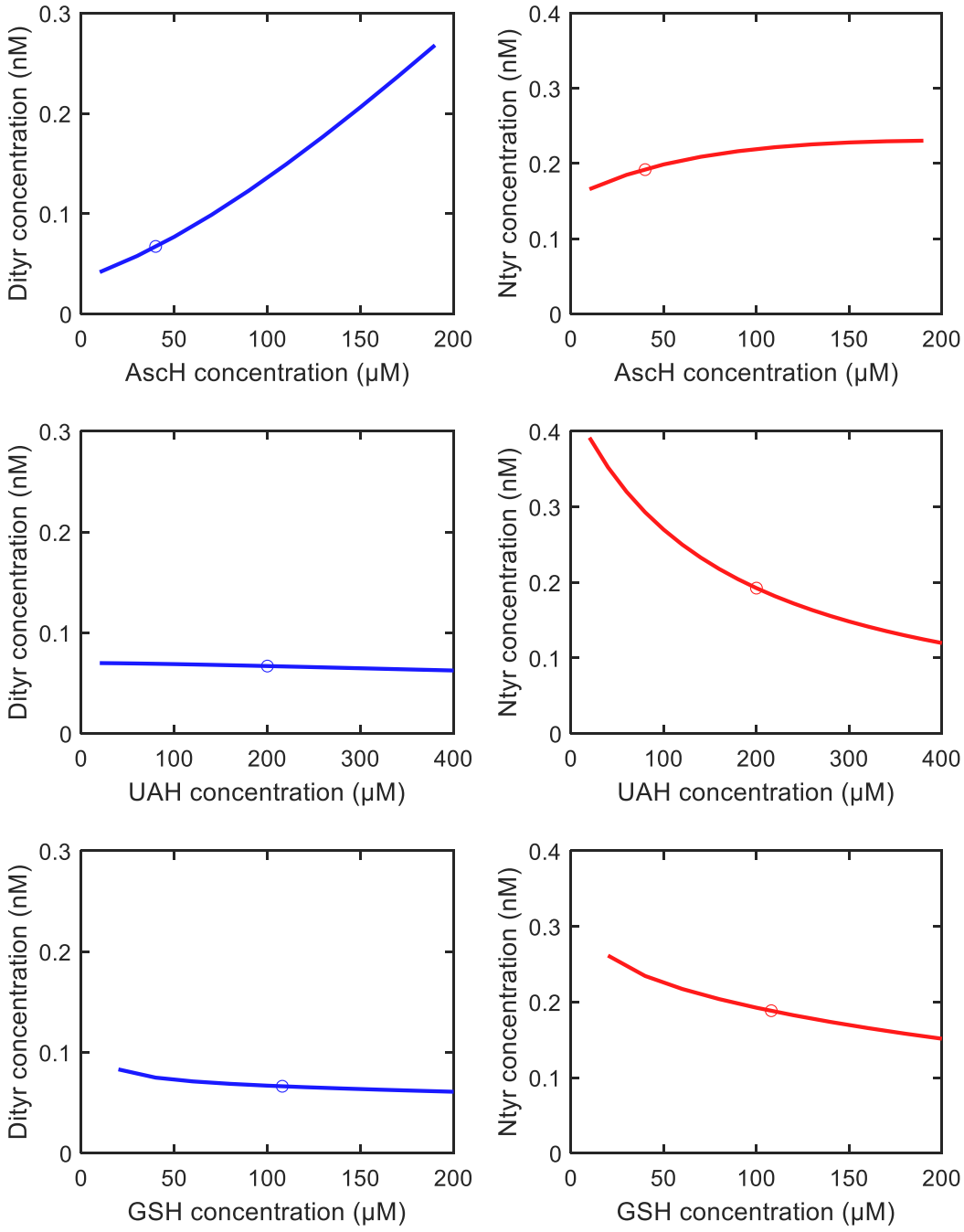

Figure S8: Concentration of Ntyr and Dityr as a function of antioxidant concentrations in a standard pollution scenario ($PM_{2.5}$ and $^{\bullet}NO_2$: 25 μg/m^3 and 30 ppb O_3). Markers represent the values that were used in the study.

.

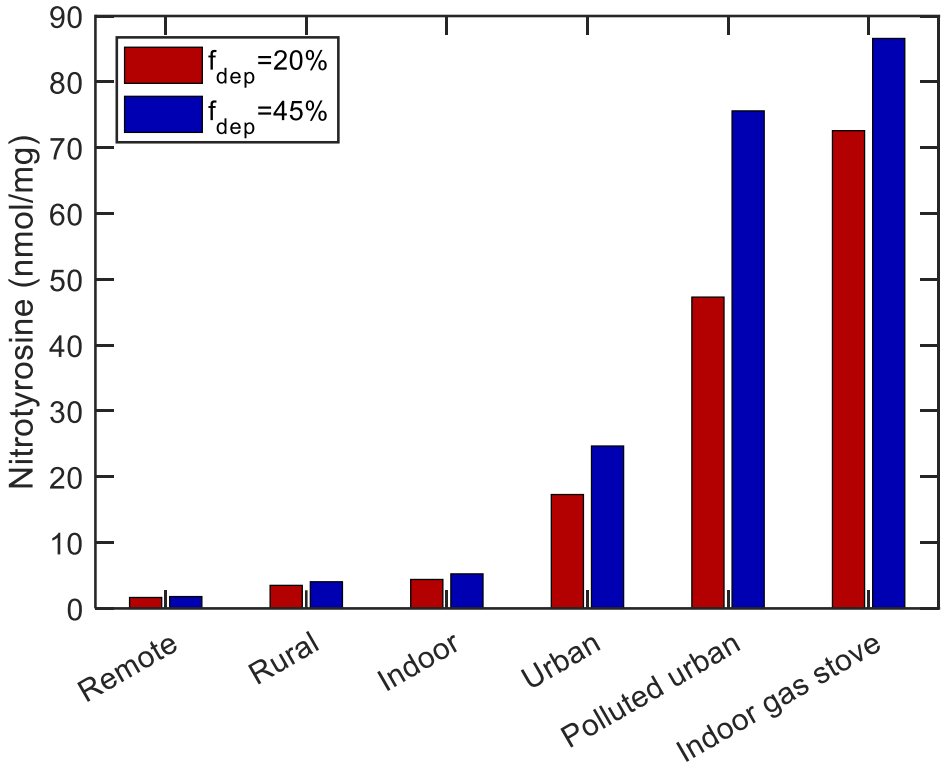

Figure S9: Sensitivity of $PM_{2.5}$ deposition fractions to concentration of Ntyr after 2 h exposure to air pollution under different pollution scenarios.

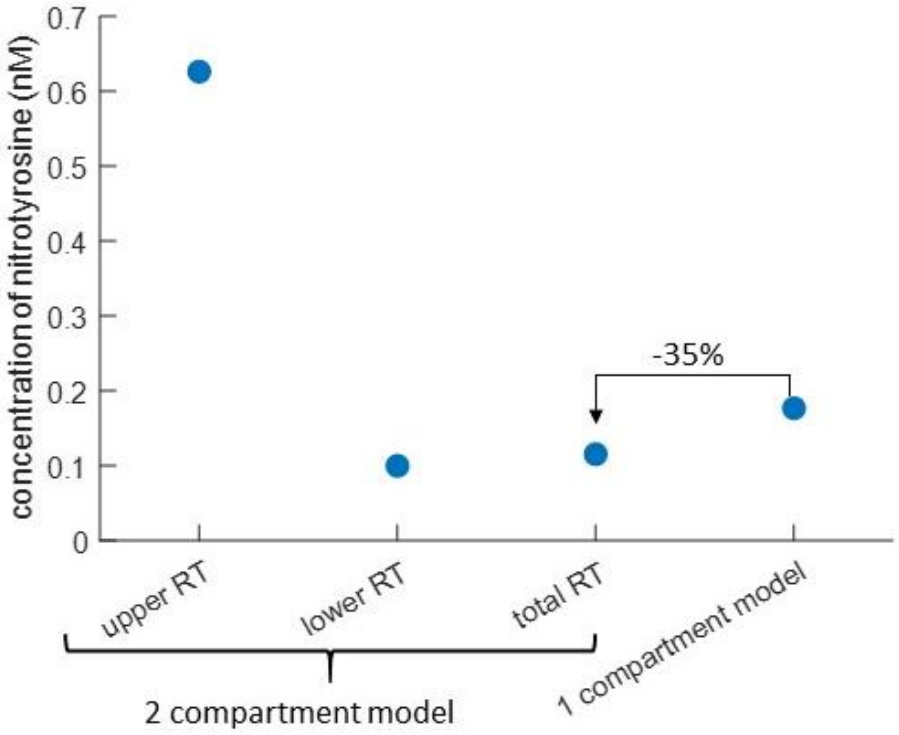

Figure S10: Concentration of Ntyr in the gas phase of the upper and lower respiratory tract (RT).

References

(1) Dovrou, E.; Lelieveld, S.; Mishra, A.; Pöschl, U.; Berkemeier, T. Influence of Ambient and Endogenous H2O2 on Reactive Oxygen Species Concentrations and OH Radical Production in the Respiratory Tract. *Environ. Sci. Atmospheres* **2023**. https://doi.org/10.1039/D2EA00179A.

(2) Saunders, S. M.; Jenkin, M. E.; Derwent, R. G.; Pilling, M. J. Protocol for the Development of the Master Chemical Mechanism, MCM v3 (Part A): Tropospheric Degradation of Non-Aromatic Volatile Organic Compounds. *Atmos. Chem. Phys.* **2003**, *3* (1), 161–180. https://doi.org/10.5194/acp-3-161-2003.

(3) Jenkin, M. E.; Saunders, S. M.; Wagner, V.; Pilling, M. J. Protocol for the Development of the Master Chemical Mechanism, MCM v3 (Part B): Tropospheric Degradation of Aromatic Volatile Organic Compounds. *Part B* **2003**, *3* (1), 181–193. https://doi.org/10.5194/acp-3-181-2003.

(4) Lelieveld, S.; Wilson, J.; Dovrou, E.; Mishra, A.; Lakey, P. S. J.; Shiraiwa, M.; Pöschl, U.; Berkemeier, T. Hydroxyl Radical Production by Air Pollutants in Epithelial Lining Fluid Governed by Interconversion and Scavenging of Reactive Oxygen Species. *Environ. Sci.* **2021**, *55* (20), 14069–14079. https://doi.org/10.1021/acs.est.1c03875.

(5) Wang, Y.; Kim, H.; Paulson, S. E. Hydrogen Peroxide Generation from α- and β-Pinene and Toluene Secondary Organic Aerosols. *Atmos. Environ.* **2011**, *45* (18), 3149–3156. https://doi.org/10.1016/j.atmosenv.2011.02.060.

(6) Tong, H.; Arangio, A. M.; Lakey, P. S. J.; Berkemeier, T.; Liu, F.; Kampf, C. J.; Brune, W. H.; Pöschl, U.; Shiraiwa, M. Hydroxyl Radicals from Secondary Organic Aerosol Decomposition in Water. *Atmos. Chem. Phys.* **2016**, *16* (3), 1761–1771. https://doi.org/10.5194/acp-16-1761-2016.

(7) Tong, H.; Lakey, P. S. J.; Arangio, A. M.; Socorro, J.; Kampf, C. J.; Berkemeier, T.; Brune, W. H.; Pöschl, U.; Shiraiwa, M. Reactive Oxygen Species Formed in Aqueous Mixtures of Secondary Organic Aerosols and Mineral Dust Influencing Cloud Chemistry and Public Health in the Anthropocene. *Faraday Discuss.* **2017**, *200*, 251–270. https://doi.org/10.1039/C7FD00023E.

(8) Lakey, P. S. J.; Berkemeier, T.; Tong, H.; Arangio, A. M.; Lucas, K.; Pöschl, U.; Shiraiwa, M. Chemical Exposure-Response Relationship between Air Pollutants and Reactive Oxygen Species in the Human Respiratory Tract. *Sci. Rep.* **2016**, *6* (1), 32916. https://doi.org/10.1038/srep32916.

(9) Cantin, A. M.; Fells, G. A.; Hubbard, R. C.; Crystal, R. G. Antioxidant Macromolecules in the Epithelial Lining Fluid of the Normal Human Lower Respiratory Tract. *J. Clin. Invest.* **1990**, *86* (3), 962–971. https://doi.org/10.1172/JCI114798.

(10) Comhair, S. A. A.; Lewis, M. J.; Bhathena, P. R.; Hammel, J. P.; Erzurum, S. C. Increased Glutathione and Glutathione Peroxidase in Lungs of Individuals with Chronic Beryllium Disease. *Am. J. Respir. Crit. Care Med.* **1999**, *159* (6), 1824–1829. https://doi.org/10.1164/ajrccm.159.6.9810044.

(11) Andreoli, S. P.; Mallett, C.; McAteer, J. A.; Williams, L. V. Antioxidant Defense Mechanisms of Endothelial Cells and Renal Tubular Epithelial Cells In Vitro: Role of the Glutathione Redox Cycle and Catalase. *Pediatr. Res.* **1992**, *32* (3), 360–365. https://doi.org/10.1203/00006450-199209000-00023.

(12) Bracaglia. HHS Public Access. *Physiol. Behav.* **2017**, *176* (3), 139–148. https://doi.org/10.1016/j.bbrc.2016.01.026.Direct.
(13) Winterbourn, C. C.; Hampton, M. B. Thiol Chemistry and Specificity in Redox Signaling. *Free Radic. Biol. Med.* **2008**, *45* (5), 549–561. https://doi.org/10.1016/j.freeradbiomed.2008.05.004.
(14) Fang, T.; Huang, Y.-K.; Wei, J.; Monterrosa Mena, J. E.; Lakey, P. S. J.; Kleinman, M. T.; Digman, M. A.; Shiraiwa, M. Superoxide Release by Macrophages through NADPH Oxidase Activation Dominating Chemistry by Isoprene Secondary Organic Aerosols and Quinones to Cause Oxidative Damage on Membranes. *Environ. Sci. Technol.* **2022**, *56* (23), 17029–17038. https://doi.org/10.1021/acs.est.2c03987.
(15) Buxton, G. V.; Greenstock, C. L.; Helman, W. P.; Ross, A. B. Critical Review of Rate Constants for Reactions of Hydrated Electrons, Hydrogen Atoms and Hydroxyl Radicals (·OH/·O⁻) in Aqueous Solution. *J. Phys. Chem.* **1988**, *17* (2), 513–886. https://doi.org/10.1063/1.555805.
(16) Hoffman, M. Z.; Hayon, E. Pulse Radiolysis Study of Sulfhydryl Compounds in Aqueous Solution. *J. Phys. Chem.* **1973**, *77* (8), 990–996. https://doi.org/10.1021/j100627a005.
(17) Zhao, M. J.; Jung, L.; Tanielian, C.; Mechin, R. Kinetics of the Competitive Degradation of Deoxyribose and Other Biomolecules by Hydroxyl Radicals Produced by the Fenton Reaction. *Free Radic. Res.* **1994**, *20* (6), 345–363. https://doi.org/10.3109/10715769409145635.
(18) Kanofsky, J. R.; Sima, P. D. Reactive Absorption of Ozone by Aqueous Biomolecule Solutions: Implications for the Role of Sulfhydryl Compounds as Targets for Ozone. *Arch. Biochem. Biophys.* **1995**, *316* (1), 52–62. https://doi.org/10.1006/abbi.1995.1009.
(19) Pryor, W. A.; Giamalva, D. H.; Church, D. F. Kinetics of Ozonation. 2. Amino Acids and Model Compounds in Water and Comparisons to Rates in Nonpolar Solvents. *J. Am. Chem. Soc.* **1984**, *106* (23), 7094–7100. https://doi.org/10.1021/ja00335a038.
(20) Kim, H. I.; Kim, H.; Shin, Y. S.; Beegle, L. W.; Jang, S. S.; Neidholdt, E. L.; Goddard, W. A.; Heath, J. R.; Kanik, I.; Beauchamp, J. L. Interfacial Reactions of Ozone with Surfactant Protein B in a Model Lung Surfactant System. *J. Am. Chem. Soc.* **2010**, *132* (7), 2254–2263. https://doi.org/10.1021/ja908477w.
(21) Hasson, A. S.; Ho, A. W.; Kuwata, K. T.; Paulson, S. E. Production of Stabilized Criegee Intermediates and Peroxides in the Gas Phase Ozonolysis of Alkenes: 2. Asymmetric and Biogenic Alkenes. *J. Geophys. Res. Atmospheres* **2001**, *106* (D24), 34143–34153. https://doi.org/10.1029/2001JD000598.
(22) Hewitt, C. N.; Kok, G. L. Formation and Occurrence of Organic Hydroperoxides in the Troposphere: Laboratory and Field Observations. *J. Atmos. Chem.* **1991**, *12* (2), 181–194. https://doi.org/10.1007/BF00115779.
(23) Zhou, Z.; Abbatt, J. P. D. Formation of Gas-Phase Hydrogen Peroxide via Multiphase Ozonolysis of Unsaturated Lipids. *Environ. Sci. Technol. Lett.* **2021**, *8* (2), 114–120. https://doi.org/10.1021/acs.estlett.0c00757.
(24) Navarrete, M.; Rangel, C.; Corchado, J. C.; Espinosa-García, J. Trapping of the OH Radical by α-Tocopherol: A Theoretical Study. *J. Phys. Chem. A* **2005**, *109* (21), 4777–4784. https://doi.org/10.1021/jp050717e.
(25) Kermani, S.; Ben-Jebria, A.; Ultman, J. S. Kinetics of Ozone Reaction with Uric Acid, Ascorbic Acid, and Glutathione at Physiologically Relevant Conditions. *Arch. Biochem. Biophys.* **2006**, *451* (1), 8–16. https://doi.org/10.1016/j.abb.2006.04.015.

(26) Rush, J. D.; Bielski, B. H. J. Pulse Radiolytic Studies of the Reaction of Perhydroxyl/Superoxide O2- with Iron(II)/Iron(III) Ions. The Reactivity of HO2/O2- with Ferric Ions and Its Implication on the Occurrence of the Haber-Weiss Reaction. *J. Phys. Chem.* **1985**, *89* (23), 5062–5066. https://doi.org/10.1021/j100269a035.
(27) Christensen, H.; Sehested, K.; Corfitzen, H. Reactions of Hydroxyl Radicals with Hydrogen Peroxide at Ambient and Elevated Temperatures. *J. Phys. Chem.* **1982**, *86* (9), 1588–1590. https://doi.org/10.1021/j100206a023.
(28) Sehested, K.; Rasmussen, O. L.; Fricke, H. Rate Constants of OH with HO2,O2-, and H2O2+ from Hydrogen Peroxide Formation in Pulse-Irradiated Oxygenated Water. *J. Phys. Chem.* **1968**, *72* (2), 626–631. https://doi.org/10.1021/j100848a040.
(29) Koppenol, W. H. The Haber-Weiss Cycle – 70 Years Later. *Redox Rep.* **2001**, *6* (4), 229–234. https://doi.org/10.1179/135100001101536373.
(30) Jayson, G. G.; Parsons, B. J.; Swallow, A. J. Oxidation of Ferrous Ions by Perhydroxyl Radicals. *J. Chem. Soc. Faraday Trans. 1 Phys. Chem. Condens. Phases* **1973**, *69*, 236–242. https://doi.org/10.1039/f19736900236.
(31) Lewis, S.; Lynch, A.; Bachas, L.; Hampson, S.; Ormsbee, L.; Bhattacharyya, D. Chelate-Modified Fenton Reaction for the Degradation of Trichloroethylene in Aqueous and Two-Phase Systems. *Environ. Eng. Sci.* **2009**, *26* (4), 849–859. https://doi.org/10.1089/ees.2008.0277.
(32) Stuglik, Z.; PawełZagórski, Z. Pulse Radiolysis of Neutral Iron(II) Solutions: Oxidation of Ferrous Ions by OH Radicals. *Radiat. Phys. Chem. 1977* **1981**, *17* (4), 229–233. https://doi.org/10.1016/0146-5724(81)90336-8.
(33) Hug, S. J.; Leupin, O. Iron-Catalyzed Oxidation of Arsenic(III) by Oxygen and by Hydrogen Peroxide: PH-Dependent Formation of Oxidants in the Fenton Reaction. *Environ. Sci. Technol.* **2003**, *37* (12), 2734–2742. https://doi.org/10.1021/es026208x.
(34) Charrier, J. G.; McFall, A. S.; Richards-Henderson, N. K.; Anastasio, C. Hydrogen Peroxide Formation in a Surrogate Lung Fluid by Transition Metals and Quinones Present in Particulate Matter. *Environ. Sci. Technol.* **2014**, *48* (12), 7010–7017. https://doi.org/10.1021/es501011w.
(35) Mudway, I. S.; Kelly, F. J. Ozone and the Lung: A Sensitive Issue. *Mol. Aspects Med.* **2000**, *21* (1), 1–48. https://doi.org/10.1016/S0098-2997(00)00003-0.
(36) Masuda, T.; Shinohara, H.; Kondo, M. Reactions of Hydroxyl Radicals with Nucleic Acid Bases and the Related Compounds in Gamma-Irradiated Aqueous Solution. *J. Radiat. Res. (Tokyo)* **1978**, *16* (3), 153–161. https://doi.org/10.1269/jrr.16.153.
(37) Liphard, M.; Bothe, E.; Schulte-Frohlinde, D. The Influence of Glutathione on Single-Strand Breakage in Single-Stranded DNA Irradiated in Aqueous Solution in the Absence and Presence of Oxygen. *Int. J. Radiat. Biol.* **1990**, *58* (4), 589–602. https://doi.org/10.1080/09553009014551951.
(38) Carr, A.; Lykkesfeldt, J. *Vitamin C in Health and Disease*; MDPI-Multidisciplinary Digital Publishing Institute, 2018.
(39) Shen, J.; Griffiths, P. T.; Campbell, S. J.; Utinger, B.; Kalberer, M.; Paulson, S. E. Ascorbate Oxidation by Iron, Copper and Reactive Oxygen Species: Review, Model Development, and Derivation of Key Rate Constants. *Sci. Rep.* **2021**, *11* (1), 7417. https://doi.org/10.1038/s41598-021-86477-8.
(40) Adams, G. E.; Boag, J. W.; Currant, J.; Michael, B. D. *Absolute Rate Constants for the Reaction of the Hydroxyl Radical with Organic Compounds*; Pulse Radiolysis, 1965.

(41) Goldstein, S.; Lind, J.; Merenyi, G. Reaction of Organic Peroxyl Radicals with $^{\bullet}NO_2$ and $^{\bullet}NO$ in Aqueous Solution: Intermediacy of Organic Peroxynitrate and Peroxynitrite Species. *J. Phys. Chem. A* **2004**, *108* (10), 1719–1725. https://doi.org/10.1021/jp037431z.
(42) Jones, C. M.; Lawrence, A.; Wardman, P.; Burkitt, M. J. Electron Paramagnetic Resonance Spin Trapping Investigation into the Kinetics of Glutathione Oxidation by the Superoxide Radical: Re-Evaluation of the Rate Constant. *Free Radic. Biol. Med.* **2002**, *32* (10), 982–990. https://doi.org/10.1016/S0891-5849(02)00791-8.
(43) Winterbourn, C. C.; Metodiewa, D. The Reaction of Superoxide with Reduced Glutathione. *Arch. Biochem. Biophys.* **1994**, *314* (2), 284–290. https://doi.org/10.1006/abbi.1994.1444.
(44) Wefers, H.; Sies, H. Oxidation of Glutathione by the Superoxide Radical to the Disulfide and the Sulfonate Yielding Singlet Oxygen. *Eur. J. Biochem.* **1983**, *137* (1–2), 29–36. https://doi.org/10.1111/j.1432-1033.1983.tb07791.x.
(45) Kirsch, M.; Lehnig, M.; Korth, H.-G.; Sustmann, R.; de Groot, H. Inhibition of Peroxynitrite-Induced Nitration of Tyrosine by Glutathione in the Presence of Carbon Dioxide through Both Radical Repair and Peroxynitrate Formation. *Chem. Eur. J.* **2001**, *7* (15), 3313–3320. https://doi.org/10.1002/1521-3765(20010803)
(46) Ford, E.; Hughes, M. N.; Wardman, P. Kinetics of the Reactions of Nitrogen Dioxide with Glutathione, Cysteine, and Uric Acid at Physiological PH. *Free Radic. Biol. Med.* **2002**, *32* (12), 1314–1323. https://doi.org/10.1016/S0891-5849(02)00850-X.
(47) Wardman, P.; Sonntag, C. [3] Kinetic factors that control the fate of thiyl radicals in cells. In *Methods in Enzymology*; Elsevier: gr, 1995; Vol. 251, pp 31–45. https://doi.org/10.1016/0076-6879(95)51108-3.
(48) Luo, D.; Smith, S. W.; Anderson, B. D. Kinetics and Mechanism of the Reaction of Cysteine and Hydrogen Peroxide in Aqueous Solution. *J. Pharm. Sci.* **2005**, *94* (2), 304–316. https://doi.org/10.1002/jps.20253.
(49) Winkler, B. S.; Orselli, S. M.; Rex, T. S. The Redox Couple between Glutathione and Ascorbic Acid: A Chemical and Physiological Perspective. *Free Radic. Biol. Med.* **1994**, *17* (4), 333–349. https://doi.org/10.1016/0891-5849(94)90019-1.
(50) Buettner, G. R.; Jurkiewicz, B. A. Catalytic Metals, Ascorbate and Free Radicals: Combinations to Avoid. *Radiat. Res.* **1996**, *145* (5), 532. https://doi.org/10.2307/3579271.
(51) Alfassi, Z. B.; Huie, R. E.; Neta, P.; Shoute, L. C. T. Temperature Dependence of the Rate Constants for Reaction of Inorganic Radicals with Organic Reductants. *J. Phys. Chem.* **1990**, *94* (25), 8800–8805. https://doi.org/10.1021/j100388a011.
(52) Augusto, O.; Bonini, M. G.; Amanso, A. M.; Linares, E.; Santos, C. C. X.; De Menezes, S. L. Nitrogen Dioxide and Carbonate Radical Anion: Two Emerging Radicals in Biology. *Free Radic. Biol. Med.* **2002**, *32* (9), 841–859. https://doi.org/10.1016/S0891-5849(02)00786-4.
(53) Goldstein, S.; Czapski, G. Reactivity of Peroxynitrite versus Simultaneous Generation of $^{\bullet}NO$ and $O_2^{\bullet-}$ toward NADH. *Chem. Res. Toxicol.* **2000**, *13* (8), 736–741. https://doi.org/10.1021/tx000099n.
(54) Graetzel, M. Pulsradiolytische Untersuchung einiger Elementarprozesse der Oxydation und Reduktion des Nitritions. *Berichte Bunsenges. Fuer Phys. Chem.* **1969**, *73* (7), 646–653. https://doi.org/10.1002/bbpc.19690730707.
(55) Jacob, D. Heterogeneous Chemistry and Tropospheric Ozone. *Atmos. Environ.* **2000**, *34* (12–14), 2131–2159. https://doi.org/10.1016/S1352-2310(99)00462-8.

(56) Bonini, M. G.; Augusto, O. Carbon Dioxide Stimulates the Production of Thiyl, Sulfinyl, and Disulfide Radical Anion from Thiol Oxidation by Peroxynitrite. *J. Biol. Chem.* **2001**, *276* (13), 9749–9754. https://doi.org/10.1074/jbc.M008456200.
(57) Kurz, C. R.; Kissner, R.; Nauser, T.; Perrin, D.; Koppenol, W. H. Rapid Scavenging of Peroxynitrous Acid by Monohydroascorbate. *Free Radic. Biol. Med.* **2003**, *35* (12), 1529–1537. https://doi.org/10.1016/j.freeradbiomed.2003.08.012.
(58) Squadrito, G. L.; Cueto, R.; Splenser, A. E.; Valavanidis, A.; Zhang, H.; Uppu, R. M.; Pryor, W. A. Reaction of Uric Acid with Peroxynitrite and Implications for the Mechanism of Neuroprotection by Uric Acid. *Arch. Biochem. Biophys.* **2000**, *376* (2), 333–337. https://doi.org/10.1006/abbi.2000.1721.
(59) Briviba, K.; Kissner, R.; Koppenol, W. H.; Sies, H. Kinetic Study of the Reaction of Glutathione Peroxidase with Peroxynitrite. *Chem. Res. Toxicol.* **1998**, *11* (12), 1398–1401. https://doi.org/10.1021/tx980086y.
(60) Nauser, T.; Koppenol, W. H. The Rate Constant of the Reaction of Superoxide with Nitrogen Monoxide: Approaching the Diffusion Limit. *J. Phys. Chem. A* **2002**, *106* (16), 4084–4086. https://doi.org/10.1021/jp025518z.
(61) Lancaster, J. R. Nitroxidative, Nitrosative, and Nitrative Stress: Kinetic Predictions of Reactive Nitrogen Species Chemistry Under Biological Conditions. *Chem. Res. Toxicol.* **2006**, *19* (9), 1160–1174. https://doi.org/10.1021/tx060061w.
(62) Radi, R. Oxygen Radicals, Nitric Oxide, and Peroxynitrite: Redox Pathways in Molecular Medicine. *Proc. Natl. Acad. Sci.* **2018**, *115* (23), 5839–5848. https://doi.org/10.1073/pnas.1804932115.
(63) Sharma, V. K.; Graham, N. J. D. Oxidation of Amino Acids, Peptides and Proteins by Ozone: A Review. *Ozone Sci. Eng.* **2010**, *32* (2), 81–90. https://doi.org/10.1080/01919510903510507.
(64) Davies, M. J. The Oxidative Environment and Protein Damage. *Methionine Oxid. Methionine Sulfoxide Reductases* **2005**, *1703* (2), 93–109. https://doi.org/10.1016/j.bbapap.2004.08.007.
(65) Huie, R. E.; Shoute, L. C. T.; Neta, P. Temperature Dependence of the Rate Constants for Reactions of the Carbonate Radical with Organic and Inorganic Reductants. *Int. J. Chem. Kinet.* **1991**, *23* (6), 541–552. https://doi.org/10.1002/kin.550230606.
(66) Davies, M. J. Protein Oxidation and Peroxidation. *Biochem. J.* **2016**, *473* (Pt 7), 805–825. https://doi.org/10.1042/BJ20151227.
(67) Solar, S.; Solar, W.; Getoff, N. Reactivity of Hydroxyl with Tyrosine in Aqueous Solution Studied by Pulse Radiolysis. *J. Phys. Chem.* **1984**, *88* (10), 2091–2095. https://doi.org/10.1021/j150654a030.
(68) *Biochemistry of Peroxynitrite and Protein Tyrosine Nitration | Chemical Reviews*. https://pubs.acs.org/doi/full/10.1021/acs.chemrev.7b00568 (accessed 2023-02-03).
(69) Hunter, E. P. L.; Desrosiers, M. F.; Simic, M. G. The Effect of Oxygen, Antioxidants, and Superoxide Radical on Tyrosine Phenoxyl Radical Dimerization. *Free Radic. Biol. Med.* **1989**, *6* (6), 581–585. https://doi.org/10.1016/0891-5849(89)90064-6.
(70) Folkes, L. K.; Trujillo, M.; Bartesaghi, S.; Radi, R.; Wardman, P. Kinetics of Reduction of Tyrosine Phenoxyl Radicals by Glutathione. *Arch. Biochem. Biophys.* **2011**, *506* (2), 242–249. https://doi.org/10.1016/j.abb.2010.12.006.

(71) Candeias, L. P.; Wardman, P.; Mason, R. P. The Reaction of Oxygen with Radicals from Oxidation of Tryptophan and Indole-3-Acetic Acid. *Biophys. Chem.* **1997**, *67* (1), 229–237. https://doi.org/10.1016/S0301-4622(97)00052-5.
(72) Alfassi, Z. B.; Huie, R. E.; Kumar, M.; Neta, P. Temperature Dependence of the Rate Constants for Oxidation of Organic Compounds by Peroxyl Radicals in Aqueous Alcohol Solutions. *J. Phys. Chem.* **1992**, *96* (2), 767–770. https://doi.org/10.1021/j100181a045.
(73) Farmer, D. K.; Vance, M. E.; Abbatt, J. P. D.; Abeleira, A.; Alves, M. R.; Arata, C.; Boedicker, E.; Bourne, S.; Cardoso-Saldaña, F.; Corsi, R.; DeCarlo, P. F.; Goldstein, A. H.; Grassian, V. H.; Hildebrandt Ruiz, L.; Jimenez, J. L.; Kahan, T. F.; Katz, E. F.; Mattila, J. M.; Nazaroff, W. W.; Novoselac, A.; O'Brien, R. E.; Or, V. W.; Patel, S.; Sankhyan, S.; Stevens, P. S.; Tian, Y.; Wade, M.; Wang, C.; Zhou, S.; Zhou, Y. Overview of HOMEChem: House Observations of Microbial and Environmental Chemistry. *Environ. Sci. Process. Impacts* **2019**, *21* (8), 1280–1300. https://doi.org/10.1039/C9EM00228F.
(74) Williams, J.; Keßel, S. U.; Nölscher, A. C.; Yang, Y.; Lee, Y.; Yáñez-Serrano, A. M.; Wolff, S.; Kesselmeier, J.; Klüpfel, T.; Lelieveld, J.; Shao, M. Opposite OH Reactivity and Ozone Cycles in the Amazon Rainforest and Megacity Beijing: Subversion of Biospheric Oxidant Control by Anthropogenic Emissions. *Atmos. Environ.* **2016**, *125*, 112–118. https://doi.org/10.1016/j.atmosenv.2015.11.007.
(75) Seinfeld, J. H.; Pandis, S. N.; Noone, K. *Atmospheric Chemistry and Physics: From Air Pollution to Climate Change* ; 1998; Vol. 51. https://doi.org/10.1063/1.882420.
(76) Salonen, H.; Salthammer, T.; Morawska, L. Human Exposure to Ozone in School and Office Indoor Environments. *Environ. Int.* **2018**, *119* (May), 503–514. https://doi.org/10.1016/j.envint.2018.07.012.
(77) Yang, G.; Liu, Y.; Li, X. Spatiotemporal Distribution of Ground-Level Ozone in China at a City Level. *Sci. Rep.* **2020**, *10* (1), 1–12. https://doi.org/10.1038/s41598-020-64111-3.
(78) O'Sullivan, D. W.; Heikes, B. G.; Snow, J.; Burrow, P.; Avery, M.; Blake, D. R.; Sachse, G. W.; Talbot, R. W.; Thornton, D. C.; Bandy, A. R. Long-Term and Seasonal Variations in the Levels of Hydrogen Peroxide, Methylhydroperoxide, and Selected Compounds over the Pacific Ocean. *J. Geophys. Res. Atmospheres* **2004**, *109* (15), 1–21. https://doi.org/10.1029/2003JD003689.
(79) Aneja, V. P. Analysis of Gaseous Hydrogen Peroxide Concentrations in Raleigh, North Carolina. *Air Waste* **1994**, *44* (2), 176–183. https://doi.org/10.1080/1073161X.1994.10467247.
(80) Li, T. H.; Turpin, B. J.; Shields, H. C.; Weschler, C. J. Indoor Hydrogen Peroxide Derived from Ozone/d-Limonene Reactions. *Environ. Sci. Technol.* **2002**, *36* (15), 3295–3302. https://doi.org/10.1021/es015842s.
(81) Zhou, Z.; Abbatt, J. P. D. Formation of Gas-Phase Hydrogen Peroxide via Multiphase Ozonolysis of Unsaturated Lipids. *Environ. Sci. Technol. Lett.* **2021**. https://doi.org/10.1021/acs.estlett.0c00757.
(82) Kok, G. L.; Darnall, K. R.; Winer, A. M.; Pitts, J. N.; Gay, B. W. Ambient Air Measurements of Hydrogen Peroxide in the California South Coast Air Basin. *Environ. Sci. Technol.* **1978**, *12* (9), 1077–1080. https://doi.org/10.1021/es60145a011.
(83) He, S. Z.; Chen, Z. M.; Zhang, X.; Zhao, Y.; Huang, D. M.; Zhao, J. N.; Zhu, T.; Hu, M.; Zeng, L. M. Measurement of Atmospheric Hydrogen Peroxide and Organic Peroxides in Beijing before and during the 2008 Olympic Games: Chemical and Physical Factors

Influencing Their Concentrations. *J. Geophys. Res. Atmospheres* **2010**, *115* (17). https://doi.org/10.1029/2009JD013544.
(84) Artaxo, P.; Rizzo, L. V.; Brito, J. F.; Barbosa, H. M. J.; Arana, A.; Sena, E. T.; Cirino, G. G.; Bastos, W.; Martin, S. T.; Andreae, M. O. Atmospheric Aerosols in Amazonia and Land Use Change: From Natural Biogenic to Biomass Burning Conditions. *Faraday Discuss.* **2013**, *165*, 203–235. https://doi.org/10.1039/c3fd00052d.
(85) Clements, N.; Hannigan, M. P.; Miller, S. L.; Peel, J. L.; Milford, J. B. Comparisons of Urban and Rural PM10-2.5 and PM2.5 Mass Concentrations and Semi-Volatile Fractions in Northeastern Colorado. *Atmospheric Chem. Phys.* **2016**, *16* (11), 7469–7484. https://doi.org/10.5194/acp-16-7469-2016.
(86) Kundu, S.; Stone, Elizabeth. A. 基因的改变NIH Public Access. *Bone* **2011**, *23* (1), 1–7. https://doi.org/10.1039/c3em00719g.Composition.
(87) Patel, S.; Sankhyan, S.; Boedicker, E. K.; Decarlo, P. F.; Farmer, D. K.; Goldstein, A. H.; Katz, E. F.; Nazaroff, W. W.; Tian, Y.; Vanhanen, J.; Vance, M. E. Indoor Particulate Matter during HOMEChem: Concentrations, Size Distributions, and Exposures. *Environ. Sci. Technol.* **2020**, *54* (12), 7107–7116. https://doi.org/10.1021/acs.est.0c00740.
(88) Karambelas, A.; Holloway, T.; Kinney, P. L.; Fiore, A. M.; Defries, R.; Kiesewetter, G.; Heyes, C. Urban versus Rural Health Impacts Attributable to PM2.5 and O3 in Northern India. *Environ. Res. Lett.* **2018**, *13* (6). https://doi.org/10.1088/1748-9326/aac24d.
(89) Liu, T.; Meng, H.; Yu, M.; Xiao, Y.; Huang, B.; Lin, L.; Zhang, H.; Hu, R.; Hou, Z.; Xu, Y.; Yuan, L.; Qin, M.; Zhao, Q.; Xu, X.; Gong, W.; Hu, J.; Xiao, J.; Chen, S.; Zeng, W.; Li, X.; He, G.; Rong, Z.; Huang, C.; Du, Y.; Ma, W. Urban-Rural Disparity of the Short-Term Association of PM2.5 with Mortality and Its Attributable Burden. *The Innovation* **2021**, *2* (4), 100171. https://doi.org/10.1016/j.xinn.2021.100171.
(90) Wragg, D.; Leoni, S.; Casini, A. Aquaporin-Driven Hydrogen Peroxide Transport: A Case of Molecular Mimicry? *RSC Chem. Biol.* **2020**, *1* (5), 390–394. https://doi.org/10.1039/D0CB00160K.

B.5 Supplement of "Influence of ambient and endogenous H_2O_2 on reactive oxygen species concentrations and OH radical production in the respiratory tract"

Supplementary Information for

Influence of ambient and endogenous H_2O_2 on reactive oxygen species concentrations and OH radical production in the respiratory tract

Eleni Dovrou[a,£,*], Steven Lelieveld[a], Ashmi Mishra[a], Ulrich Pöschl[a], Thomas Berkemeier[a*]

[a]Multiphase Chemistry Department, Max Planck Institute for Chemistry, Mainz 55128, Germany

[£]Now at: Institute of Chemical Engineering Sciences, Foundation for Research and Technology Hellas, Patra 26504, Greece

*Corresponding authors. Email: dovrouel@gmail.com, t.berkemeier@mpic.de

Supplementary Text

Section S1: Typical ambient and endogenous H_2O_2 concentrations

Gas-phase H_2O_2 is mainly produced via dismutation of the hydroperoxyl radical ($HO_2^{\bullet}$), which is formed by atmospheric photochemical processes. $HO_2^{\bullet}$is generated by the photolysis of formaldehyde and by reactions between hydroxyl radicals ($^{\bullet}OH$) and hydrocarbons. The formation of $^{\bullet}OH$ is triggered by photolysis of ozone, producing molecular and atomic oxygen, with the latter reacting with water vapor yielding $^{\bullet}OH$. Subsequently, $^{\bullet}OH$ reacts with hydrocarbons acting as a final source of $HO_2^{\bullet}$and H_2O_2. Anthropogenic sources, such as biomass burning, fire plumes, combustion facilities and vehicle exhausts yield both $HO_2^{\bullet}$and formaldehyde, contributing to H_2O_2 formation. An important source of high concentrations of H_2O_2 is thunderstorms, which produce H_2O_2 via electrical discharges during high electric field conditions. Thus, gas-phase H_2O_2 is continuously produced in the atmosphere via both natural and anthropogenic sources and constitutes the most abundant peroxide.[1,2]

In urban areas, typical ambient H_2O_2 levels are 0.5-1.5 ppb , while higher levels ≥2 ppb have been reported under polluted conditions in both urban and rural areas (Table S5).[3–7] Urban regions are typically characterized by elevated $^{\bullet}NO_x$ levels compared to rural areas, which, due to higher consumption of HO_2, may in some cases limit H_2O_2 production.

H_2O_2 has been investigated previously for its potential to trigger oxidative stress in the lung.[8–18] The chemical stability of H_2O_2 allows it to permeate biomembranes.[19] It is also produced endogenously via cellular sources. Cellular enzymes such as NADPH oxidase produce H_2O_2 via superoxide, which is subsequently converted to H_2O_2.[20–23] Cellular levels of H_2O_2 typically range from 1 to 100 nM.[12] Under oxidative signaling events, H_2O_2 levels reach up to 500-700 nM.[8,11] At high H_2O_2 levels, the cell can go into a state of oxidative stress, which can lead to inflammatory signaling and cell death.[12] H_2O_2 is also observed in blood with concentrations ranging from 0.8 to 6 μM for healthy individuals; individuals with diabetes or other health conditions can have H_2O_2 levels of 10-82 μM in their blood.[16,21,24,25] Measuring the H_2O_2 concentration in the ELF is challenging due to the difficulty in extracting lung lining fluid from a living organism.

Section S2: Kinetic multi-layer model

We investigate the effects and interactions of ambient and endogenous H_2O_2 and other air pollutants in the epithelial lining fluid (ELF) using a multiphase kinetic model, which builds on an existing kinetic modeling framework[26,27] and describe chemical mechanisms and transport of reactive oxygen species (ROS) influencing oxidative stress. In the model, the respiratory tract is divided into: (a) the gas phase of the respiratory tract, (b) the surfactant layer, (c) the aqueous ELF, (d) a cellular layer, and (e) a blood layer.

The kinetic multi-layer model of surface and bulk chemistry in the epithelial lining fluid (KM-SUB-ELF) described by Lakey et al.[26] and Lelieveld et al.[27] was extended to simulate the production rate and concentration of ROS in the ELF considering effects of underlying cells and blood vessels. The newly developed model (KM-SUB-ELF 2.0) treats inhalation and exhalation from and to the ambient gas phase, adsorption and desorption to and from the ELF, diffusion in the ELF, mass transport between the ELF, cells and blood, as well as 131 chemical reactions are represented in the model. The model considers particulate pollution from fine particulate matter smaller than 2.5 μm (PM2.5) and gas-phase pollution from $^{\bullet}NO_2$, O_3, and H_2O_2. The model generates a system of ordinary differential equations, which is solved using the stiff differential equation solver *ode23tb* in Matlab, and calculates the evolution of reactant concentrations over time. An explicit Jacobian matrix is provided to aid in computation. Model parameters are listed in Tables S1-S4.

The surfactant layer consists of a surfactant lipid, 1-palmitoyl-2-oleoyl-*sn*-glycerol (POG), a surfactant protein ($SP\text{-}B_{1\text{-}25}$), and the antioxidant α-tocopherol (α-Toc), following Lelieveld et al. [27]. Chemical reactions of POG and $SP\text{-}B_{1\text{-}25}$ with $^{\bullet}OH$ and O_3 occur in this compartment. The ozonolysis of POG yields Criegee intermediates, which are assumed to hydrolyze to H_2O_2 according to reaction R1 with an experimentally-determined yield of 0.17.[27] Diffusion of ROS between the surfactant layer and the ELF can increase ROS concentrations in the ELF.

$$\mathrm{POG} + \mathrm{O_3} \rightarrow \mathrm{HCHO} + (0.17)\mathrm{H_2O_2} \qquad 1.66 \times 10^{-16}\ \mathrm{cm^3\ s^{-1}} \qquad (1)$$

The low molecular mass antioxidants ascorbate (Asc), glutathione (GSH), uric acid (UA), and α-Toc) are included in the model. In addition, the model considers three quinones as part of PM2.5, phenanthrenequinone, 1,2-naphthoquinone and 1,4-naphthoquinone, and their reaction with oxygen, $HO_2^{\bullet}$, and Asc. Ambient and endogenous contributions, Fenton chemistry involving iron and copper, as well as HO_x ($\equiv ^{\bullet}OH$, $HO_2^{\bullet}$) chemistry are main pathways leading to formation and consumption of H_2O_2 and thus ROS. The rate coefficients follow the work of Lakey et al.[26]. All reactions included in the model are listed in Table S1. Partitioning from gas phase into the surfactant layer is calculated according to Henry's law for aqueous solutions. Accordingly, equal partitioning is assumed between surfactant and aqueous ELF layer for all volatile species.

The composition of PM2.5 in the atmosphere varies strongly depending on location, source, season, weather, and time of day. We use a standardized PM2.5 composition that was established previously using the median mass fractions of redox-active PM2.5 constituents from a large set of atmospheric field measurements.[27] The mass fractions are 3.1×10^{-4} for copper, 8.1×10^{-3} for iron, 1.6×10^{-5} for quinones, and 0.33 for secondary organic aerosol (SOA).

The most influential model parameters are varied for sensitivity analyses in this study (Figs. 2 and 3, Figs. S1-S7). However, if not noted otherwise, these parameters are kept at their default values. The default effective membrane permeability of H_2O_2 is 1×10^{-5} cm s^{-1}, the default blood

concentration of H_2O_2 is 5 μM, the default ambient concentration of H_2O_2 is 1 ppb, the default cellular production rate of H_2O_2 is 1×10^{14} cm^{-3} s^{-1}, and the default concentration of H_2O_2-scavenging enzymes in the cell layer is 10 μM (Table S4).

Section S3: Antioxidant concentrations and enzymatic reactions

In the model, the antioxidants Asc, GSH, and UA are present in the ELF at concentrations of 40 μM, 108 μM, and 200 μM, respectively.[26–29] α-Toc is considered to be in the surfactant layer with concentration of 200 μM.[27] In line with previous models, antioxidants are considered constant within the two-hour simulation time to prevent the significant changes in redox chemistry in the unlikely event of full antioxidant depletion.[27]

Enzymatic reactions are considered within ELF and cellular compartments. Superoxide dismutase (SOD) and catalase are included in ELF, while in cells, a range of H_2O_2-scavenging enzymes (peroxiredoxins, catalase, GSH peroxidase) are considered as outlined below and in Table S2. The reaction of SOD with $O_2^{\bullet-}$ results in the production of H_2O_2 and O_2, each with 50% yield.[27] Catalase has been experimentally determined to be the main defense of ELF against H_2O_2, following a two-step reaction mechanism.[30–32] In the first step H_2O_2 reacts with catalase forming a catalase-H_2O_2 complex, which, in the second step, reacts with another H_2O_2 molecule forming water and oxygen. In this work, the two steps are combined, producing water and oxygen with a 50% yield, respectively.

The catalytic activity of enzymes is typically reported in enzyme units (U), defined as the amount of enzyme required to catalyze one micromole of substrate per minute. In the substrate-limited regime, the enzyme concentration can be calculated as the ratio of the catalytic activity v_{max}, given in U mL^{-1}, and the catalytic constant, k_{cat}.

$$[\text{enzyme}] = \frac{v_{\max}}{k_{\text{cat}}} \tag{8}$$

For SOD, k_{cat} has been reported between 10^5-10^6 s^{-1} and v_{max} at 36.8±2.0 U mL^{-1}.[27,30,33,34] Using Eq. 8, the SOD concentration can be estimated between 0.61 and 6.1 nM. Similarly, k_{cat} for catalase is reported in the range of 3×10^6-4×10^7 s^{-1} with a v_{max} of 3.7±0.6 U mL^{-1}, resulting in an estimated catalase concentration range of 1.6-16 pM.[30,35] From these concentration ranges, 1 nM of SOD and 5 pM of catalase are chosen as an order of magnitude estimate, respectively, following the work of Lelieveld et al.[27]. In the cellular layer, the catalytic activity of catalase is reported to be an order of magnitude higher compared to ELF, which equates to 50 pM.[36,37] In contrast, peroxiredoxins are thiol proteins that are present in the cells at much higher concentrations of tens of micromolar.[38] Hence, peroxiredoxins are likely the predominant sink of H_2O_2 in lung cells. Thus, for simplicity, we choose a conservative estimate of 10 μM for the sum of all H_2O_2-scavenging enzymes in this work, and assume a common reaction rate of 3.3×10^{-14} cm^3 s^{-1} for the enzymes.[38] Note that H_2O_2 is scavenged only by the reduced forms of peroxiredoxins, yielding peroxiredoxins in an oxidized form. The reduced form must be regenerated in a NADPH-dependent reaction.[39] Here, we assume that the concentration of the reduced form of peroxiredoxins is constant during the calculation.

Section S4: Production of H_2O_2 in the cellular layer

Respiratory cells are known ROS producers, among them type II alveolar cells and endothelial cells. Type II alveolar cells constitute about 4 % of the alveolar surface area and 10-15 % of all

lung cells.[40] Kinnula et al.[41] find a production rate of 0.7 nmol H_2O_2 min^{-1} mg $protein^{-1}$ for type II alveolar cells and 0.06 nmol H_2O_2 min^{-1} mg $protein^{-1}$ for endothelial cells. Piotrowski et al.[42] find a baseline production of type II alveolar cells of 0.15 nmol H_2O_2 min^{-1} mg $protein^{-1}$. We estimate from literature that the protein mass density is in the range of 150 – 300 mg cm^{-3}.[43] Using these numbers, we can derive a best estimate for the cellular H_2O_2 production rate in the range of 2×10^{13} – 5×10^{14} cm^{-3} s^{-1} as detailed below. Note, however, that these measurements stem from *in vitro* experiments using rat alveolar cells and can only be regarded as order of magnitude estimates for the human lung. We thus choose a central value of 1×10^{14} cm^{-3} s^{-1} from this range for the calculations in this study.

Upper Estimate - 15 % of cells are type II alveolar cells (0.7 nmol mg $protein^{-1}$ min^{-1}) and the rest behave like endothelial cells (0.06 nmol mg $protein^{-1}$ min^{-1}) at a protein mass density of 300 mg cm^{-3}

$$(0.15 \cdot 0.7\ \text{nmol mg}^{-1}\ \text{min}^{-1} + 0.85 \cdot 0.06\ \text{nmol mg}^{-1}\ \text{min}^{-1}) \cdot 300\ \text{mg cm}^{-3} \cdot 6.022 \cdot 10^{23}\ \text{mol}^{-1} \cdot \frac{1}{60}\text{min s}^{-1} \approx 5 \cdot 10^{14}\ \text{cm}^{-3}\ \text{s}^{-1}$$

Lower Estimate - 10 % of cells are type II cells (0.15 nmol mg $protein^{-1}$ min^{-1}) at a protein mass density of 150 mg cm^{-3} and the remaining cells do not produce significant amounts of H_2O_2

$$(0.1 \cdot 0.15\ \text{nmol mg}^{-1}\ \text{min}^{-1}) \cdot 150\ \text{mg cm}^{-3} \cdot 6.022 \cdot 10^{23}\ \text{mol}^{-1} \cdot \frac{1}{60}\text{min s}^{-1} \approx 2 \cdot 10^{13}\ \text{cm}^{-3}\ \text{s}^{-1}$$

Section S5: Secondary Organic Aerosol (SOA)

Secondary organic aerosol (SOA) is a major component of ambient PM2.5[44,45] and contains highly oxidized organic compounds such as organic (hydro)peroxides.[46] These peroxides may be labile and decay with a short half-life[47] or follow a similar chemistry to H_2O_2 by forming $^{\bullet}OH$ radicals in reactions with transition metals and water.[48] SOA has been shown to produce superoxide and H_2O_2 in aqueous solution and to contribute to the oxidative potential and cytotoxicity of PM2.5.[49–52]

SOA may contribute to $^{\bullet}OH$ production in an iron-dependent and an iron-independent process.[47,48] Following the work of Tong et al. [48] and Lakey et al. [26], we consider a relative $^{\bullet}OH$ yield from SOA of 1% within the 2-hour calculation window. However, expanding the parameterization in Lakey et al.,[26] we attribute a tenth, i.e. 0.1 % of SOA, to iron-independent SOA sources (Fig. S8), which is in line with the observations in Tong et al.[48].

Note that the contribution of SOA to $^{\bullet}OH$ production in epithelial lining fluid is not well established. Interpreting experimental results that contain a multitude of chemical components is very challenging. Furthermore, experiments are often performed using electron paramagnetic resonance (EPR) spectroscopy and radical detection with spin trapping agents. These techniques are affected by radical-spin trap-adduct half-lives and yields, which further hamper experimental interpretation. As an example, recent studies find differences in the type and amount of radical species formed in pure water or in surrogate lung fluid (SLF).[48,51,53,54] While $^{\bullet}OH$ and superoxide have been observed in experiments performed in pure water,[48,53] $R^{\bullet}$ radicals have been found as the major product in SLF.[51,54] These observations indicate either a different decomposition mechanism of SOA, or altered radical-spin trap-adduct half-lives and yields under the different

experimental conditions. It remains open whether •OH is formed initially, but reacts with other SLF constituents before reaction with the spin trapping agent. Furthermore, organic peroxides inhaled through SOA may also be scavenged by enzymes such as peroxiredoxins and peroxidases before significant conversion to •OH occurs. Comprehensive experimental and modelling analyses are required to unravel the exact mechanism and extent of radical formation from SOA in epithelial lining fluid. However, this is out of the scope of the present work. For these reasons, the contribution of SOA to •OH production in this work may constitute an upper estimate.

Section S6: H_2O_2 and •OH source apportionment in ELF

In this study, the source apportionment of H_2O_2 in the ELF could not be achieved with traditional flux analyses, i.e. comparing chemical and diffusion fluxes, due to the inherit coupling of chemical reaction and diffusion in multiple compartments. Instead, we performed a sensitivity analysis and compared five scenarios (endogenous transport of H_2O_2, inhalation of ambient H_2O_2, •NO_2, O_3, and PM2.5), in which only a single source was present in the model at a time, to the scenario with all sources. For instance, to estimate the H_2O_2 concentration attributed to endogenous transport of H_2O_2, the sources from ambient H_2O_2, O_3, NO_2 and PM2.5 were turned off. We followed the same approach for each of the five sources. Note that this approach was only possible because non-linear effects were almost non-existent, i.e. the total H_2O_2 concentration was very close to the sum of the H_2O_2 generated in each single-source scenario. Thus, dividing the H_2O_2 concentration in each single-source scenario over the H_2O_2 concentration considering all sources gives a good approximation of the apportionment of sources.

For source apportionment of the hydroxyl radical (•OH), a traditional flux analysis could be performed due to negligible diffusion of the reactive radical across compartment boundaries. The production of •OH is mainly attributed to Fenton(-like) reactions of H_2O_2 and SOA with iron in the model.

The H_2O_2 consumption by enzymes in the cell layer affects the source apportionment of •OH production and H_2O_2 concentration (Fig. S7b). Increase of the enzyme concentration leads to a decrease in contribution of Fenton chemistry (H_2O_2/Fe) to •OH production, shifting the contribution towards the Fenton-like reactions involving SOA (SOA/Fe). Figure S4b shows a stronger influence of endogenous H_2O_2 in the H_2O_2 concentration in the ELF at low enzyme concentrations. The endogenous and gas-phase H_2O_2 contributions converge with increasing enzyme availability.

Section S7: Discussion of model sensitivity and limitations

The model presented in this work, KM-SUB-ELF 2.0, describes chemical mechanisms and transport of ROS within the respiratory tract, aiming to investigate the influence of ambient and endogenous H_2O_2 as well as main air pollutants in ROS production. Due to the complexity of the respiratory tract, KM-SUB-ELF 2.0 outlines the essential processes to provide a first estimate on evaluating the parameters influencing ROS production. A key model parameter is the effective membrane permeability of H_2O_2 (μ_{eff}. Figures 2a and S1a show the concentrations of H_2O_2 in all model compartments as a function of μ_{eff}. The concentrations in atmosphere and blood in the model are not affected, but the ELF and cellular concentrations are strongly influenced by μ_{eff}. The reported range of cellular H_2O_2 (1-10 nM) constrains this important model parameter. The value of μ_{eff} also affects the •OH source (Fig. S7a): at the best guess value for μ_{eff}, •OH production is

mainly due to Fenton chemistry of peroxides contained in SOA, while at very high or very low μ_{eff}, Fenton chemistry of H_2O_2 is the dominant •OH source.

It is important to note that the •OH yield from SOA is a challenging topic, requiring further investigation and thus contributing to the uncertainty of the calculations. This topic is discussed in detail in Sect. S5, but a more in-depth investigation is out of the scope of this study.

Another important parameter influencing the ROS levels in the respiratory tract is the cellular concentration of H_2O_2-scavenging enzymes. Figure S1b shows a linear dependence of H_2O_2 concentration in the cells and a similarly strong dependence of H_2O_2 concentration in the LLF, which levels off towards very high enzyme concentrations.

The concentration of PM2.5 determines the production of •OH in the ELF, as shown in Figure 3B and D. The concentrations of H_2O_2 in ELF and respiratory tract gas phase, however, are not affected by PM2.5 concentrations (Figs. S1c, S3c). PM2.5 becomes a significant source of H_2O_2 only at the highest concentrations investigated in this study (1000 µg/m3; Fig. S4c), which are exceedingly high even for the most polluted cities on Earth.

We finally note that the biological mechanisms contributing to ROS production and consumption are strongly simplified in the model. Future work is needed to include biological sources of superoxide and their stimulation with PM2.5.[55] The model structure of the respiratory tract could be further subdivided, for example into extrathoracic, bronchial, and alveolar space (Fig. S9), which likely experience different concentrations of deposited PM2.5 and inhaled water-soluble trace gases such as H_2O_2, NO_2 and O_3. Preliminary calculations separating upper and lower respiratory tract show that between 10-90 % of ambient gas-phase H_2O_2 will be consumed in the extrathoracic space (nasal cavity to trachea) alone, depending on factors such as geometry, ELF volume, H_2O_2-scavenging enzyme concentrations, and membrane permeability in the upper respiratory tract. The exhaled H_2O_2 concentrations in this early test simulation were strongly increased, due to a higher saturation of the extrathoracic ELF with H_2O_2, coming much closer to values reported for exhaled breath condensate. We expect that the upgraded model structure and inclusion of macrophages as additional endogenous ROS sources will reconcile the agreement with these measurements, and decrease the importance of ambient H_2O_2 for the deep lung. However, this model upgrade is still in development, outside the scope of this work, and will be addressed in future publications. Nevertheless, this work provides important insights in the evaluation of toxicity of the main air pollutants and the effect of endogenous processes to ROS levels in the respiratory tract.

Section S8: Contribution of ambient and endogenous H_2O_2 to ROS in the ELF

In the model KM-SUB-ELF 2.0, the concentration of H_2O_2 in ELF can be either determined by transport of endogenous H_2O_2 (endogenous H_2O_2 regime), inhalation of ambient H_2O_2 (ambient H_2O_2 regime) or both (transition regime). Which regime is active depends on the effective membrane permeability μ_{eff}, with the ambient H_2O_2 regime dominating the H_2O_2 concentration in ELF when $\mu_{eff} < 1 \cdot 10^{-5}$ cm s^{-1}, while the endogenous H_2O_2 regime dominates the H_2O_2 concentration in the ELF when $\mu_{eff} > 1 \times 10^{-5}$ cm s^{-1} (Figs. 2 and S3). At 1×10^{-5} cm s^{-1}, the best guess for membrane permeability in this study, we observe a transition between both regimes. Figure S5 illustrates the regimes of H_2O_2 supply: in the ambient-H_2O_2 regime, only changes in ambient H_2O_2 concentrations change the H_2O_2 concentrations in the ELF. Likewise, in the endogenous H_2O_2 regime, only changes in blood H_2O_2 concentrations change the H_2O_2

concentrations in the ELF. In the transition range between both regimes, both concentrations are important. Note that, while membrane permeability of H_2O_2 affects the regime of H_2O_2 supply, $^{\bullet}OH$ production in the ELF is dominated by PM2.5 constituents regardless of μ_{eff} in the model. Note also that additional endogenous sources of ROS, such as superoxide production by macrophages in the ELF or a larger production rate of H_2O_2 by epithelial cells, may tip the scales fully in favor of endogenous sources of H_2O_2.

Supplementary Figures

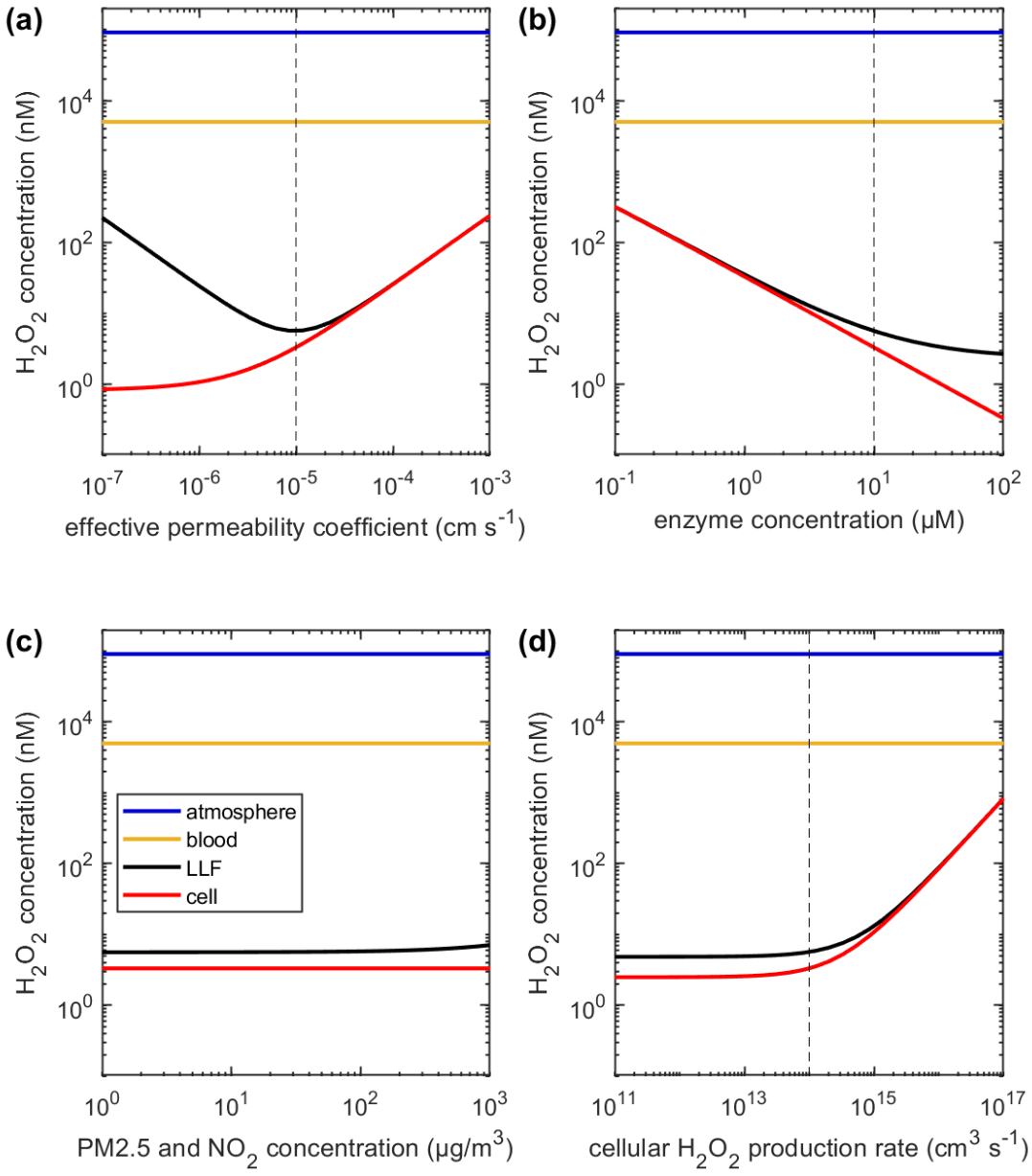

Fig. S1. H_2O_2 concentrations in respiratory tract compartments. H_2O_2 concentration in blood (red line), epithelial lining fluid (ELF; black line), and cells (orange line) as a function of various model parameters: (a) effective membrane permeability coefficient of H_2O_2, (b) H_2O_2-scavenging enzyme concentration in cells, (c) ambient PM2.5 and NO_2 concentration, and (d) cellular H_2O_2 production rate in a standard pollution scenario (PM2.5=30 μg m^{-3}, NO2=30 μg m-3, O3=30 ppb, H_2O_2=1 ppb) unless otherwise indicated. Effective permeability and enzyme concentration are the parameters with the strongest sensitivity, while cellular H_2O_2 production rate only becomes sensitive at large values. The parameters used in the standard scenario in this study are marked with a vertical dashed line.

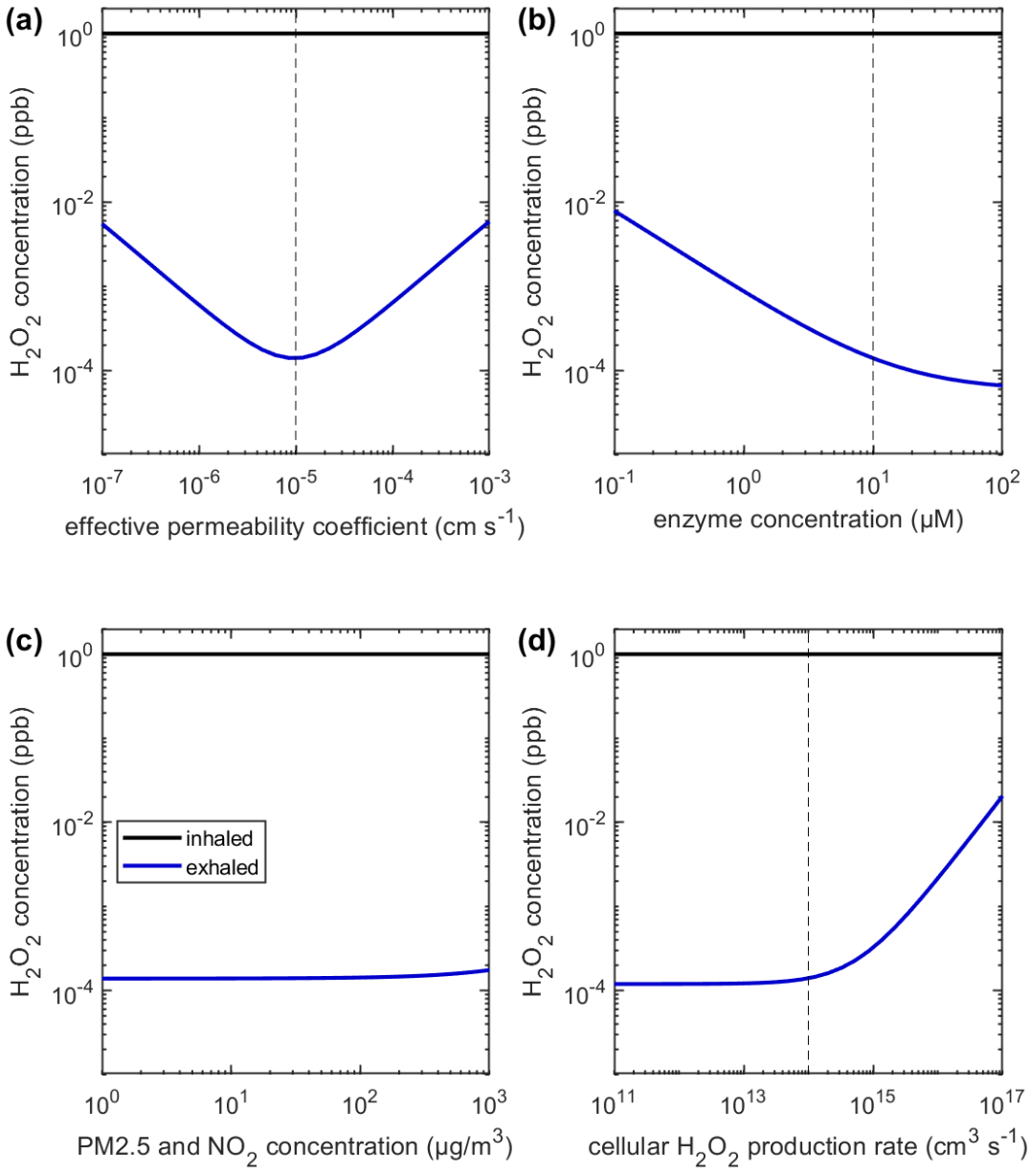

Fig. S2. Comparison of inhaled and exhaled H_2O_2 concentrations. Inhaled and exhaled H_2O_2 concentrations as a function of various model parameters: (a) effective membrane permeability coefficient of H_2O_2, (b) H_2O_2-scavenging enzyme concentration in cells, (c) ambient PM2.5 and NO_2 concentration, and (d) cellular H_2O_2 production rate in a standard pollution scenario (PM2.5=30 μg m^{-3}, NO_2=30 μg m^{-3}, O_3=30 ppb, H_2O_2=1 ppb) unless otherwise indicated. Inhaled H_2O_2 concentrations are always larger than exhaled concentrations. The parameters used in the standard scenario in this study are marked with a vertical dashed line.

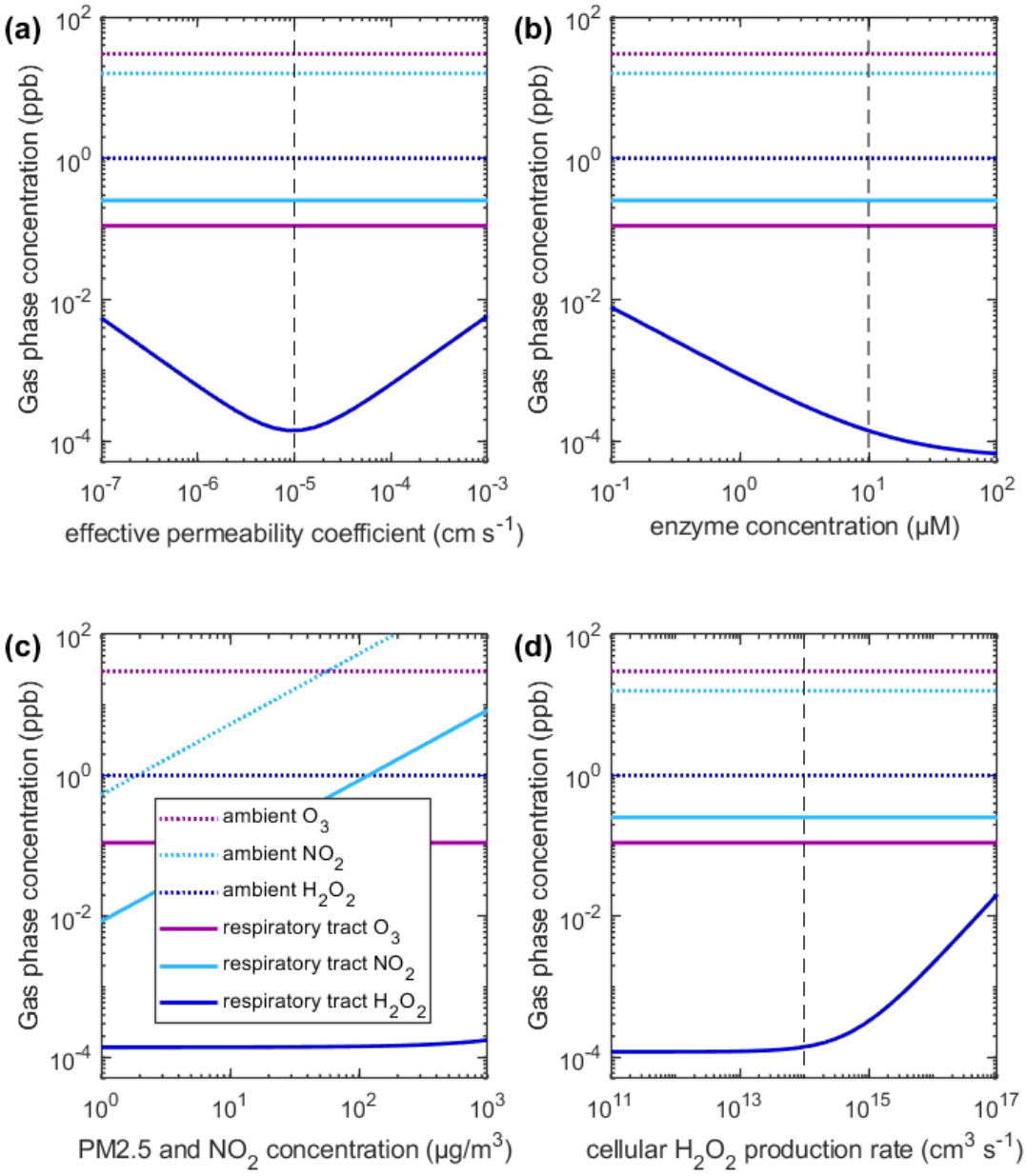

Fig. S3. Comparison of ambient and respiratory tract gas-phase concentrations. The ambient (dotted lines) and respiratory tract (solid lines) gas-phase concentrations of H_2O_2 (blue), O_3 (purple), and NO_2 (black line) as a function of various model parameters: (a) effective membrane permeability coefficient of H_2O_2, (b) H_2O_2-scavenging enzyme concentration in cells, (c) ambient PM2.5 and NO_2 concentration, and (d) cellular H_2O_2 production rate in a standard pollution scenario (PM2.5=30 μg m^{-3}, NO_2=30 μg m^{-3}, O_3=30 ppb, H_2O_2=1 ppb) unless otherwise indicated. All respiratory tract / exhaled concentrations are significantly below their ambient / inhaled concentrations due to reactive uptake to the epithelial lining fluid. The parameters used in the standard scenario in this study are marked with a vertical dashed line.

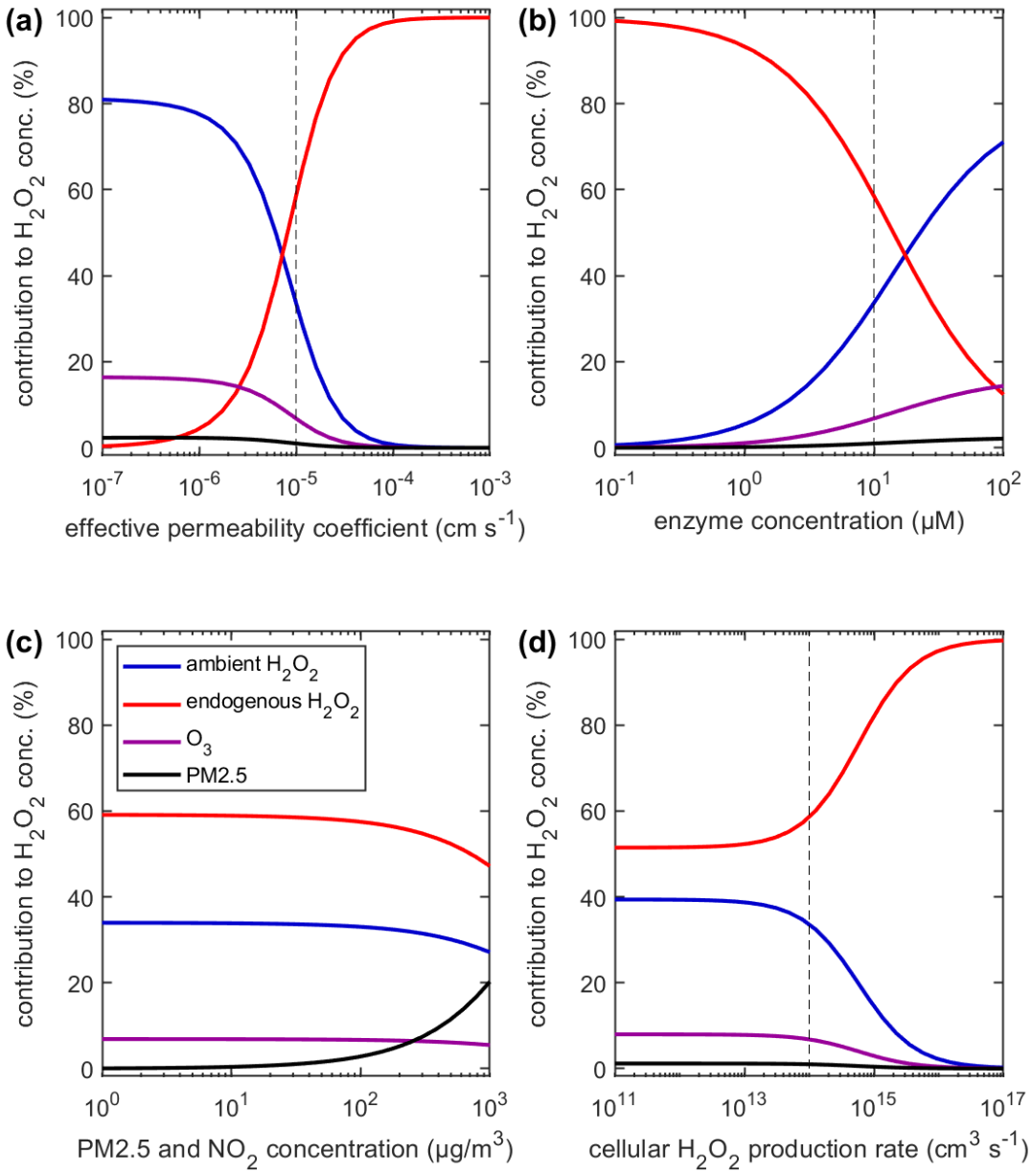

Fig. S4. Source apportionment of H_2O_2 sources in the ELF. The contribution of ambient H_2O_2 (blue line), endogenous transport of H_2O_2 (red line), ozone (purple line), and PM2.5 (black line) as a function of various model parameters: (a) effective membrane permeability coefficient of H_2O_2, (b) H_2O_2-scavenging enzyme concentration in cells, (c) ambient PM2.5 concentration, and (d) cellular H_2O_2 production rate in a standard pollution scenario (PM2.5=30 μg m^{-3}, NO_2=30 μg m^{-3}, O_3=30 ppb, H_2O_2=1 ppb) unless otherwise indicated. The dominant sources are ambient H_2O_2 and endogenous transport of H_2O_2, but the contributions are strongly influenced by the effective membrane permeability and H_2O_2-scavenging enzyme concentration in cells. The parameters used in the standard scenario in this study are marked with a vertical dashed line.

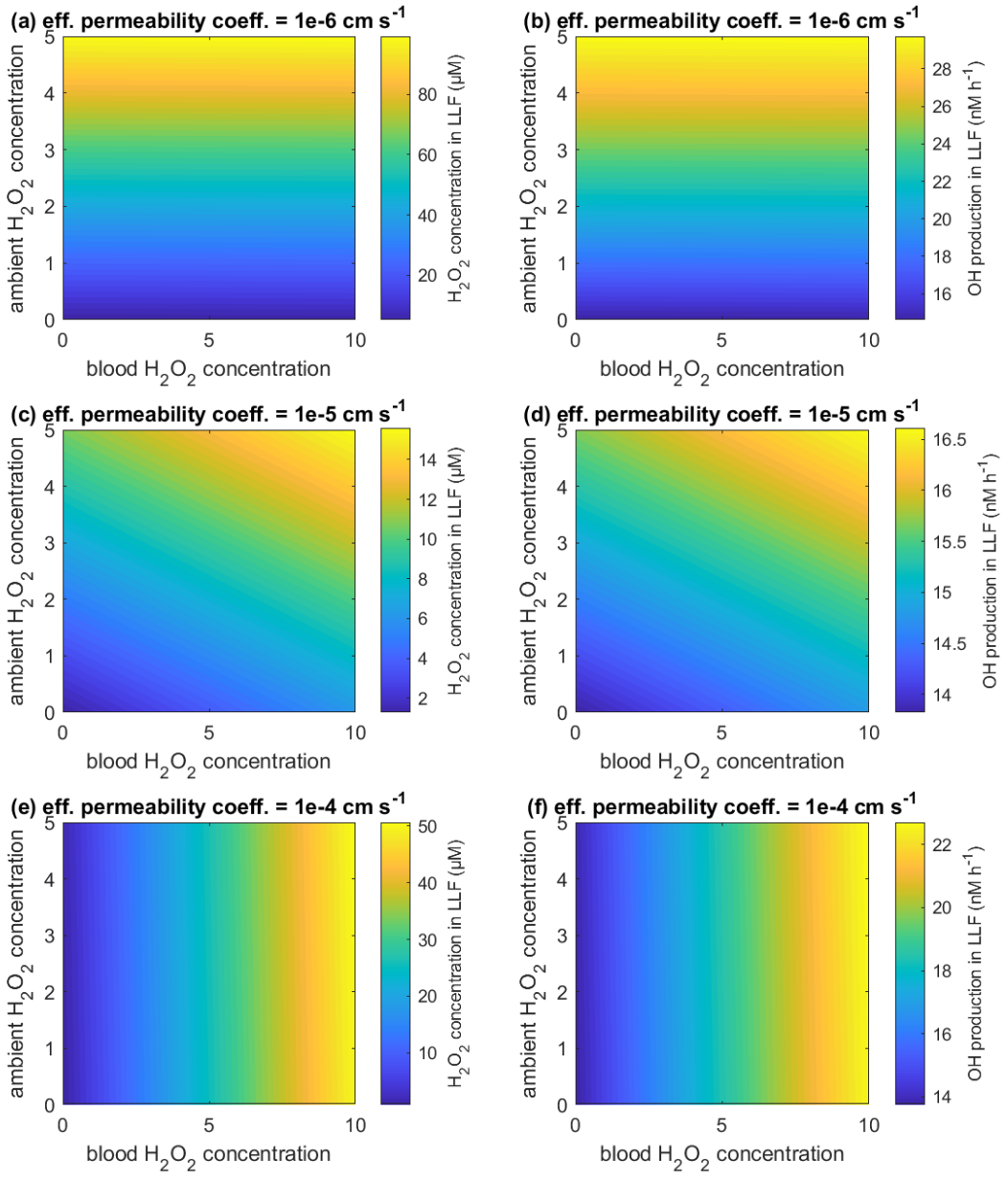

Fig. S5. Comparison of the influence of inhalation of ambient H_2O_2 and transport of endogenous H_2O_2. H_2O_2 concentration (panels a, c, e) and $^{\bullet}OH$ production (panels b, d, f) in ELF are displayed as a function of ambient and blood H_2O_2 concentrations and for three different values of the effective membrane permeability coefficient of H_2O_2. A higher effective membrane permeability of H_2O_2 enhances the influence of endogenous transport of H_2O_2, which is evident from the increasingly vertical contour lines. While the system is clearly in the *ambient-H_2O_2 regime* in panels (a) and (b), it is fully in the *endogenous-H_2O_2 regime* in panels (e) and (f).

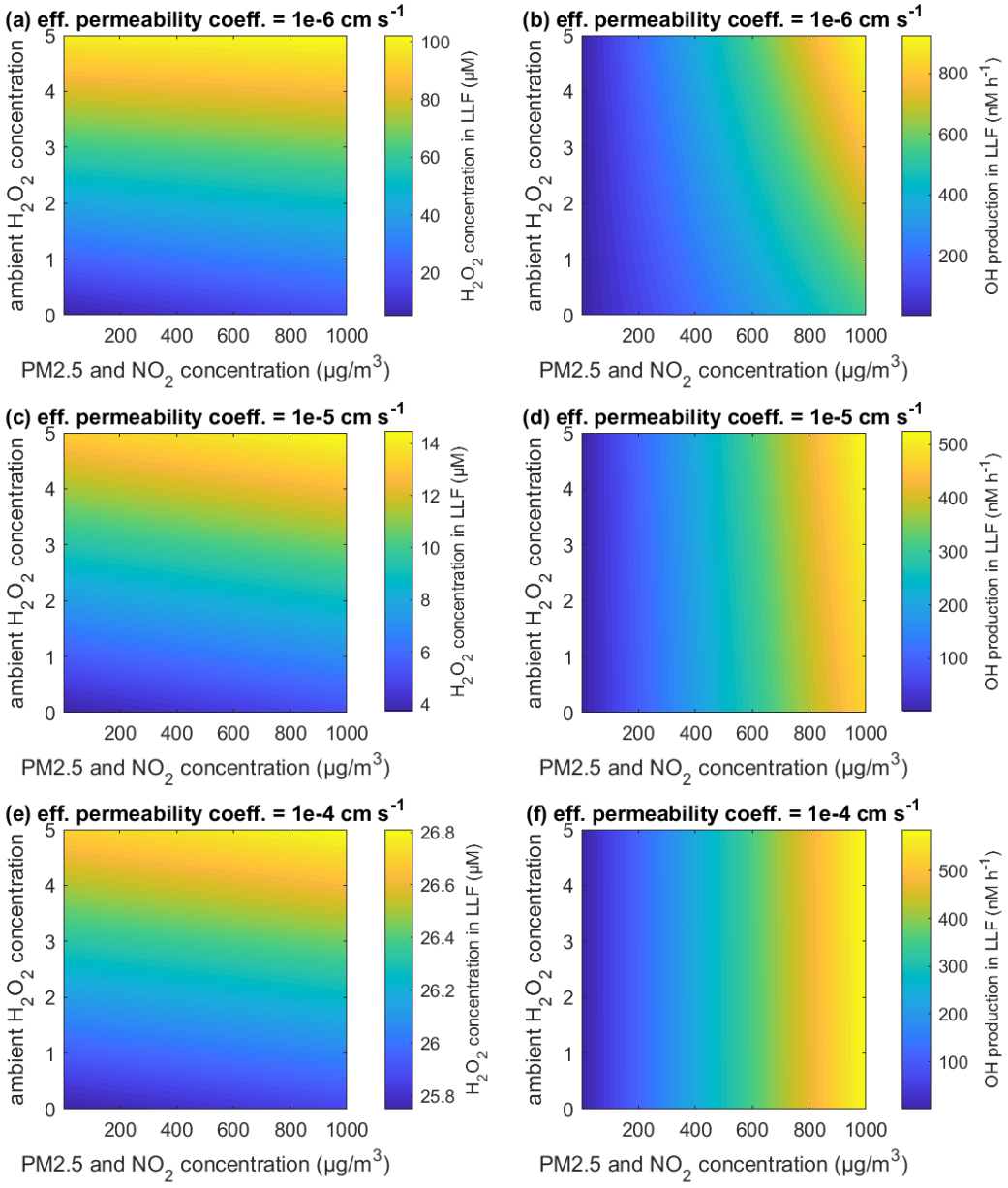

Fig. S6. Comparison of the influence of inhalation of ambient H_2O_2 and PM2.5 concentration. H_2O_2 concentration (panels a, c, e) and $^{\bullet}OH$ production (panels b, d, f) in ELF as a function of ambient and PM2.5 concentrations and for three different values of the effective membrane permeability coefficient of H_2O_2. The value of the effective permeability coefficient has only very little effect on the general result that $^{\bullet}OH$ production is dominated by PM2.5 concentrations, while H_2O_2 concentration is hardly affected by PM2.5 concentrations.

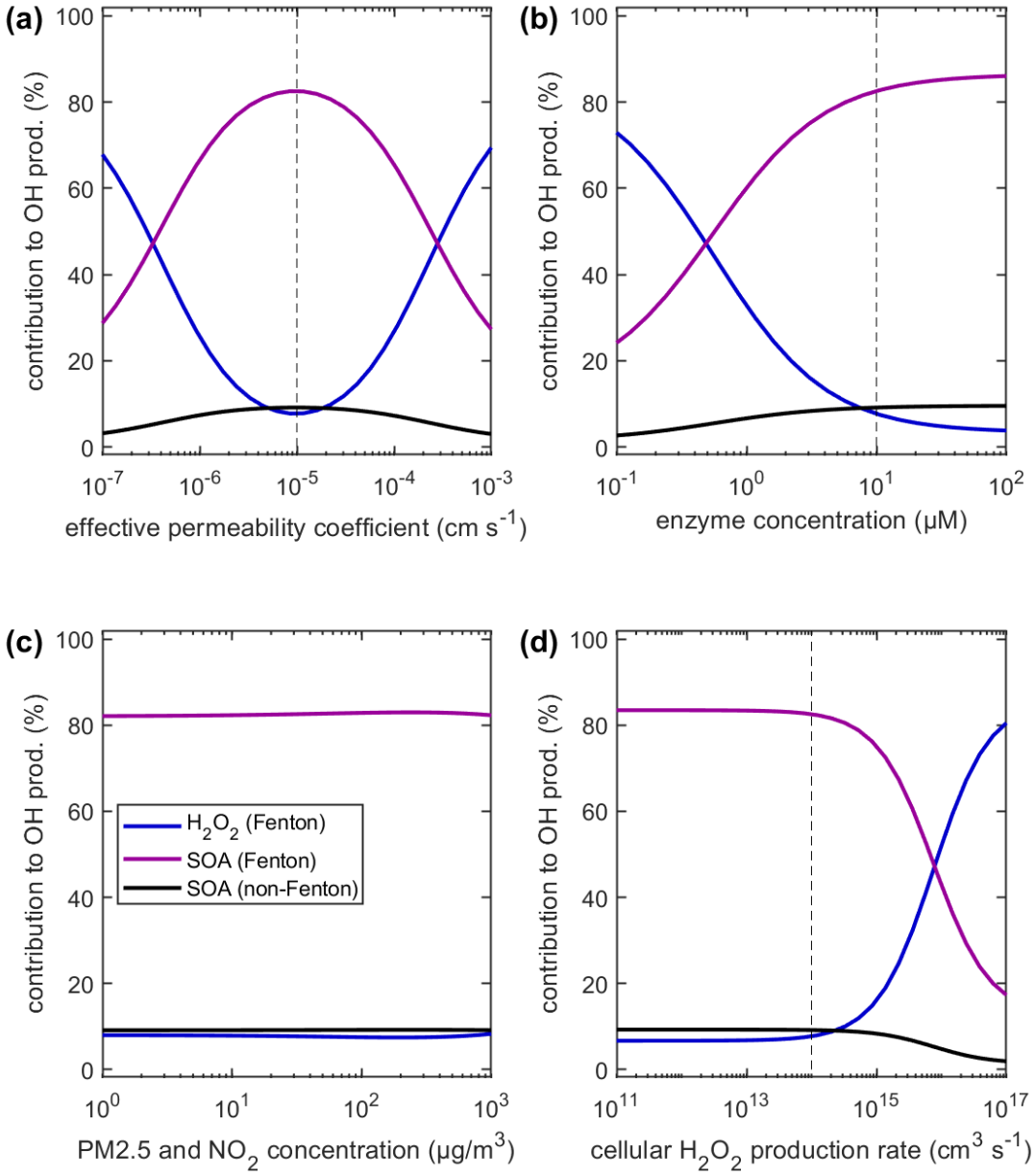

Fig. S7. Source apportionment of ˙OH sources in the ELF. The contribution of Fenton chemistry of H_2O_2 (blue line), Fenton chemistry of SOA (purple line), and non-Fenton chemistry of SOA (black line) as a function of various model parameters: (a) effective membrane permeability coefficient of H_2O_2, (b) H_2O_2-scavenging enzyme concentration in cells, (c) ambient PM2.5 concentration, and (d) cellular H_2O_2 production rate in a standard pollution scenario (PM2.5=30 μg m^{-3}, NO_2=30 μg m^{-3}, O_3=30 ppb, H_2O_2=1 ppb) unless otherwise indicated. The dominant sources are Fenton chemistry of H_2O_2 and SOA, but the contributions are strongly influenced by the effective membrane permeability and H_2O_2-scavenging enzyme concentration in cells. The parameters used in the standard scenario in this study are marked with a vertical dashed line.

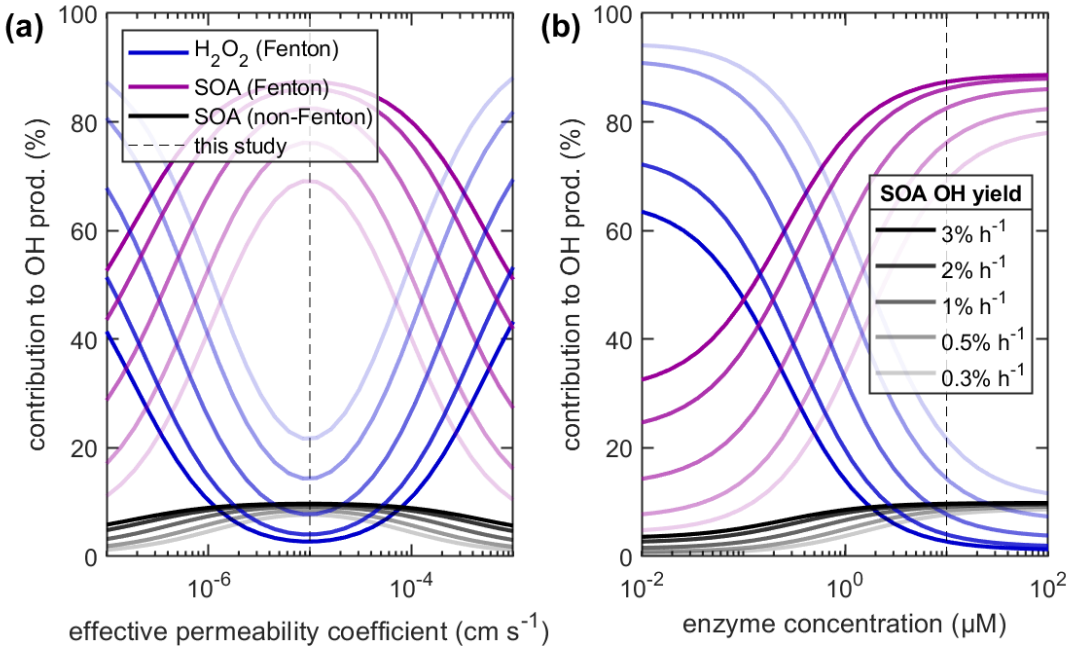

Fig. S8. Source apportionment of ˙OH sources in the ELF as a function of aqueous SOA chemistry. Effect of effective permeability and H_2O_2-scavenging enzyme concentration in cells on ˙OH production. The contribution of Fenton chemistry of H_2O_2 (blue line), Fenton chemistry of SOA (purple line), and non-Fenton chemistry of SOA (black line) as a function of various model parameters: (a) effective membrane permeability coefficient of H_2O_2, (b) H_2O_2-scavenging enzyme concentration in cells. The results are given for a range of ˙OH yield of SOA (0.3-3 % h^{-1}).

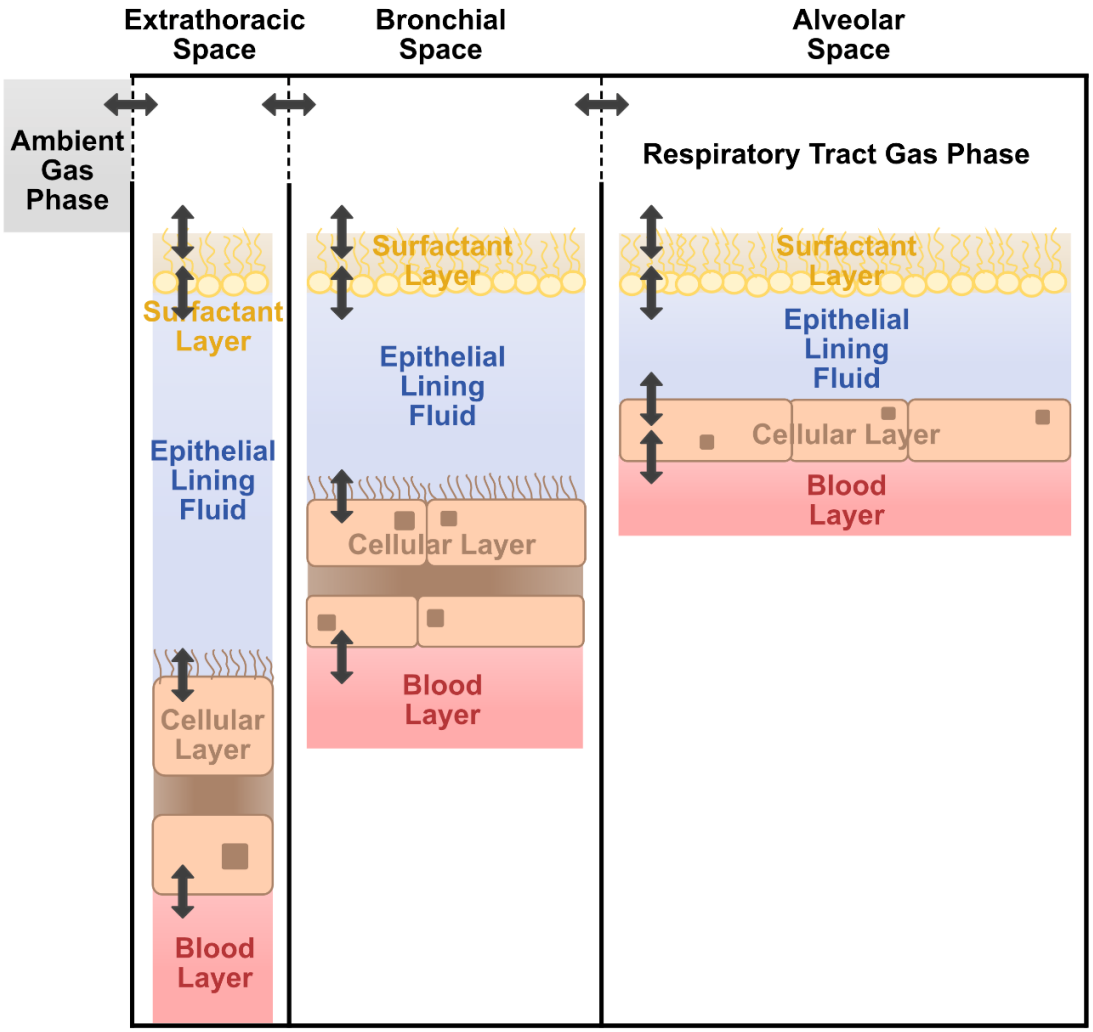

Fig. S9. Proposed model structure for follow-up study. To improve the model, we suggest a sub-division of the respiratory tract. Shown here is a schematic representation of the respiratory tract in three parts: extrathoracic, bronchial and alveolar space. Geometry of those three spaces will be different with the extrathoracic space having the largest layer thicknesses but least overall surface area, and the alveolar space the smallest layer thicknesses but largest surface area, respectively (schematic not to scale). The gas-phase compartments will be connected through a fast flux according to the breathing rate.

Supplementary Tables

Table S1. Chemical reactions included in the model.

Reaction	Compartment	Rate constant	Unit	Reference	#
$^{\bullet}NO + O_3 \rightarrow {}^{\bullet}NO_2 + O_2$	Gas	$2.05 \cdot 10^{-14}$	$cm^3\ s^{-1}$	[56,57]	1
$^{\bullet}NO_2 + O_3 \rightarrow {}^{\bullet}NO_3 + O_2$	Gas	$4.85 \cdot 10^{-17}$	$cm^3\ s^{-1}$	[56,57]	2
$^{\bullet}NO + {}^{\bullet}NO \xrightarrow{O_2} {}^{\bullet}NO_2 + {}^{\bullet}NO_2$	Gas	$8.93 \cdot 10^{-20}$	$cm^3\ s^{-1}$	[56,57]	3
$^{\bullet}NO + {}^{\bullet}NO_3 \rightarrow {}^{\bullet}NO_2 + {}^{\bullet}NO_2$	Gas	$2.57 \cdot 10^{-11}$	$cm^3\ s^{-1}$	[56,57]	4
$^{\bullet}NO_2 + {}^{\bullet}NO_3 \rightarrow {}^{\bullet}NO + {}^{\bullet}NO_2 + O_2$	Gas	$7.73 \cdot 10^{-16}$	$cm^3\ s^{-1}$	[56,57]	5
$^{\bullet}NO_2 + {}^{\bullet}NO_3 \rightarrow N_2O_5$	Gas	$1.21 \cdot 10^{-12}$	$cm^3\ s^{-1}$	[56,57]	6
$^{\bullet}OH + O_3 \rightarrow HO_2^{\bullet} + O_2$	Gas	$8.20 \cdot 10^{-14}$	$cm^3\ s^{-1}$	[56,57]	7
$^{\bullet}OH + H_2O_2 \rightarrow HO_2^{\bullet} + H_2O$	Gas	$1.73 \cdot 10^{-12}$	$cm^3\ s^{-1}$	[56,57]	8
$HO_2^{\bullet} + O_3 \rightarrow {}^{\bullet}OH + O_2 + O_2$	Gas	$8.24 \cdot 10^{-16}$	$cm^3\ s^{-1}$	[56,57]	9
$^{\bullet}OH + HO_2^{\bullet} \rightarrow H_2O + O_2$	Gas	$1.08 \cdot 10^{-10}$	$cm^3\ s^{-1}$	[56,57]	10
$HO_2^{\bullet} + HO_2^{\bullet} \rightarrow H_2O_2 + O_2$	Gas	$5.09 \cdot 10^{-12}$	$cm^3\ s^{-1}$	[56,57]	11
$HO_2^{\bullet} + HO_2^{\bullet} \rightarrow H_2O_2$	Gas	$3.50 \cdot 10^{-12}$	$cm^3\ s^{-1}$	[56,57]	12
$^{\bullet}OH + {}^{\bullet}NO \rightarrow HONO$	Gas	$8.91 \cdot 10^{-12}$	$cm^3\ s^{-1}$	[56,57]	13
$^{\bullet}OH + {}^{\bullet}NO_2 \rightarrow HNO_3$	Gas	$8.91 \cdot 10^{-12}$	$cm^3\ s^{-1}$	[56,57]	14
$^{\bullet}OH + NO_3^{\bullet} \rightarrow HO_2^{\bullet} + {}^{\bullet}NO_2$	Gas	$2.00 \cdot 10^{-11}$	$cm^3\ s^{-1}$	[56,57]	15
$HO_2^{\bullet} + {}^{\bullet}NO \rightarrow {}^{\bullet}OH + {}^{\bullet}NO_2$	Gas	$8.24 \cdot 10^{-12}$	$cm^3\ s^{-1}$	[56,57]	16
$HO_2^{\bullet} + {}^{\bullet}NO_2 \rightarrow HO_2NO_2$	Gas	$6.87 \cdot 10^{-13}$	$cm^3\ s^{-1}$	[56,57]	17
$HO_2NO_2 \rightarrow HO_2^{\bullet} + {}^{\bullet}NO_2$	Gas	$2.49 \cdot 10^{-1}$	s^{-1}	[56,57]	18
$^{\bullet}OH + HO_2NO_2 \rightarrow NO_2^{\bullet} + H_2O + O_2$	Gas	$2.96 \cdot 10^{-12}$	$cm^3\ s^{-1}$	[56,57]	19
$HO_2^{\bullet} + {}^{\bullet}NO_3 \rightarrow {}^{\bullet}OH + {}^{\bullet}NO_2$	Gas	$4.00 \cdot 10^{-12}$	$cm^3\ s^{-1}$	[56,57]	20
$^{\bullet}OH + HONO \rightarrow {}^{\bullet}NO_2 + H_2O$	Gas	$5.78 \cdot 10^{-12}$	$cm^3\ s^{-1}$	[56,57]	21
$^{\bullet}OH + HNO_3 \rightarrow {}^{\bullet}NO_3 + H_2O$	Gas	$1.37 \cdot 10^{-13}$	$cm^3\ s^{-1}$	[56,57]	22
$N_2O_5 \rightarrow {}^{\bullet}NO_2 + {}^{\bullet}NO_3$	Gas	$1.83 \cdot 10^{-1}$	s^{-1}	[56,57]	23
$HO_2NO_2 \rightarrow {}^{\bullet}NO_2 + HO_2^{\bullet}$	Gas	$2.49 \cdot 10^{-1}$	s^{-1}	[56,57]	24
$CI + O_3 \rightarrow$ products	Gas	$1.00 \cdot 10^{-13}$	$cm^3\ s^{-1}$	[58]	25
$SPB + {}^{\bullet}OH \rightarrow SPB\text{-}ox$	Surfactant	$1.70 \cdot 10^{-11}$	$cm^3\ s^{-1}$	[59–61]	26
$POG + {}^{\bullet}OH \rightarrow POG\text{-}ox$	Surfactant	$1.70 \cdot 10^{-11}$	$cm^3\ s^{-1}$	[26]	27
$SPB + O_3 \rightarrow SPB\text{-}ox$	Surfactant	$1.00 \cdot 10^{-14}$	$cm^3\ s^{-1}$	[62,63]	28
$POG + O_3 \rightarrow 0.17\ H_2O_2$	Surfactant	$1.66 \cdot 10^{-16}$	$cm^3\ s^{-1}$	[64,65]	29
$\alpha\text{-Toc} + {}^{\bullet}OH \rightarrow \alpha\text{-Toc-ox}$	Surfactant	$4.50 \cdot 10^{-13}$	$cm^3\ s^{-1}$	[66]	30
$\alpha\text{-Toc} + O_3 \rightarrow \alpha\text{-Toc-ox}$	Surfactant	$1.20 \cdot 10^{-18}$	$cm^3\ s^{-1}$	[67]	31

$O_2^{\bullet-} + HO_2 \xrightarrow{H_2O} H_2O_2 + OH^- + O_2$	ELF	$1.70 \cdot 10^{-13}$	$cm^3\ s^{-1}$	[26,68]	32
$HO_2 + HO_2 \rightarrow H_2O_2 + O_2$	ELF	$1.40 \cdot 10^{-15}$	$cm^3\ s^{-1}$	[68]	33
$O_2^{\bullet-} + O_2^{\bullet-} + 2H^+ \rightarrow H_2O_2 + O_2$	ELF	$3.82 \cdot 10^{-16}$	$cm^3\ s^{-1}$	[68]	34
$H_2O_2 + {}^{\bullet}OH \rightarrow HO_2 + H_2O$	ELF	$5.50 \cdot 10^{-14}$	$cm^3\ s^{-1}$	[69]	35
${}^{\bullet}OH + {}^{\bullet}OH \rightarrow H_2O_2$	ELF	$8.60 \cdot 10^{-12}$	$cm^3\ s^{-1}$	[70]	36
${}^{\bullet}OH + O_2^{\bullet-} \rightarrow O_2 + OH^-$	ELF	$1.30 \cdot 10^{-11}$	$cm^3\ s^{-1}$	[59]	37
${}^{\bullet}OH + HO_2 \rightarrow H_2O + O_2$	ELF	$1.20 \cdot 10^{-11}$	$cm^3\ s^{-1}$	[70]	38
$H_2O_2 + HO_2 \rightarrow {}^{\bullet}OH + O_2 + H_2O$	ELF	$4.98 \cdot 10^{-21}$	$cm^3\ s^{-1}$	[71]	39
$Fe^{2+} + O_2^- + 2H^+ \rightarrow Fe^{3+} + H_2O_2$	ELF	$3.10 \cdot 10^{-14}$	$cm^3\ s^{-1}$	[26,68]	40
$Fe^{2+} + HO_2 + H^+ \rightarrow Fe^{3+} + H_2O_2$	ELF	$1.99 \cdot 10^{-15}$	$cm^3\ s^{-1}$	[72]	41
$Fe^{2+} + H_2O_2 \rightarrow Fe^{3+} + {}^{\bullet}OH + OH^-$	ELF	$4.30 \cdot 10^{-18}$	$cm^3\ s^{-1}$	[73]	42
$Fe^{2+} + {}^{\bullet}OH \rightarrow Fe^{3+} + OH^-$	ELF	$5.30 \cdot 10^{-13}$	$cm^3\ s^{-1}$	[74]	43
$Fe^{2+} + H_2O_2 \rightarrow Fe^{4+} + H_2O$	ELF	$9.50 \cdot 10^{-18}$	$cm^3\ s^{-1}$	[26]	44
$Fe^{3+} + H_2O_2 \rightarrow Fe^{2+} + HO_2 + H^+$	ELF	$3.32 \cdot 10^{-24}$	$cm^3\ s^{-1}$	[73]	45
$Fe^{3+} + HO_2 \rightarrow Fe^{2+} + O_2 + H^+$	ELF	$3.30 \cdot 10^{-18}$	$cm^3\ s^{-1}$	[68]	46
$Fe^{4+} + Fe^{2+} \rightarrow Fe^{3+} + Fe^{3+}$	ELF	$6.60 \cdot 10^{-18}$	$cm^3\ s^{-1}$	[75]	47
$Fe^{3+} + Asc \rightarrow Fe^{2+} + Asc^{\bullet}$	ELF	$1.10 \cdot 10^{-19}$	$cm^3\ s^{-1}$	[26]	48
$Fe^{4+} + Asc \rightarrow Fe^{3+} + Asc^{\bullet}$	ELF	$7.60 \cdot 10^{-19}$	$cm^3\ s^{-1}$	[26]	49
$Fe^{2+} + O_2 \rightarrow O_2^{\bullet-} + Fe^{3+}$	ELF	$5.20 \cdot 10^{-21}$	$cm^3\ s^{-1}$	[26]	50
$Cu^+ + HO_2 \xrightarrow{H^+} Cu^{2+} + H_2O_2$	ELF	$2.30 \cdot 10^{-12}$	$cm^3\ s^{-1}$	[26]	51
$Cu^+ + O_2^{\bullet-} \xrightarrow{H_2O} Cu^{2+} + H_2O_2 + OH^-$	ELF	$5.80 \cdot 10^{-15}$	$cm^3\ s^{-1}$	[26]	52
$Cu^{2+} + HO_2 \rightarrow Cu^+ + O_2 + H^+$	ELF	$1.60 \cdot 10^{-11}$	$cm^3\ s^{-1}$	[26]	53
$Cu^{2+} + O_2^{\bullet-} \rightarrow Cu^+ + O_2$	ELF	$8.30 \cdot 10^{-12}$	$cm^3\ s^{-1}$	[26]	54
$Cu^{2+} + Asc \rightarrow Cu^+ + Asc^{\bullet}$	ELF	$1.40 \cdot 10^{-18}$	$cm^3\ s^{-1}$	[26]	55
$Cu^+ + O_2 \rightarrow Cu^{2+} + O_2^{\bullet-}$	ELF	$6.90 \cdot 10^{-20}$	$cm^3\ s^{-1}$	[26]	56
$Cu^+ + H_2O_2 \rightarrow Cu^{2+} + {}^{\bullet}OH + OH^-$	ELF	$2.40 \cdot 10^{-20}$	$cm^3\ s^{-1}$	[26]	57
$Cu^+ + H_2O_2 \rightarrow Cu^{3+} + OH^- + OH^-$	ELF	$5.00 \cdot 10^{-19}$	$cm^3\ s^{-1}$	[26]	58
$Cu^+ + Cu^{3+} \rightarrow Cu^{2+} + Cu^{2+}$	ELF	$5.80 \cdot 10^{-12}$	$cm^3\ s^{-1}$	[26]	59
$Cu^{2+} + H_2O_2 \rightarrow Cu^+ + O_2^{\bullet-} + H^+$	ELF	$3.80 \cdot 10^{-24}$	$cm^3\ s^{-1}$	[26]	60
$PQN + Asc \rightarrow PQN^{\bullet} + Asc^{\bullet}$	ELF	$1.20 \cdot 10^{-20}$	$cm^3\ s^{-1}$	[76]	61
$PQN^{\bullet} + O_2 \rightarrow PQN + O_2^{\bullet-}$	ELF	$4.60 \cdot 10^{-13}$	$cm^3\ s^{-1}$	[26]	62
$PQN^{\bullet} + O_2^{\bullet-} \xrightarrow{2H^+} PQN + H_2O_2$	ELF	$3.30 \cdot 10^{-12}$	$cm^3\ s^{-1}$	[26]	63
$NQN12 + Asc \rightarrow NQN12^{\bullet} + Asc^{\bullet}$	ELF	$1.50 \cdot 10^{-19}$	$cm^3\ s^{-1}$	[76]	64
$NQN12^{\bullet} + O_2 \rightarrow NQN12 + O_2^{\bullet-}$	ELF	$4.60 \cdot 10^{-13}$	$cm^3\ s^{-1}$	[26]	65
$NQN12^{\bullet} + O_2^{\bullet-} \xrightarrow{2H^+} NQN12 + H_2O_2$	ELF	$3.30 \cdot 10^{-12}$	$cm^3\ s^{-1}$	[26]	66

$NQN14 + Asc \rightarrow NQN14^{\bullet} + Asc^{\bullet}$	ELF	$6.30 \cdot 10^{-21}$	$cm^3\ s^{-1}$	76	67
$NQN14^{\bullet} + O_2 \rightarrow NQN14 + O_2^{\bullet-}$	ELF	$4.60 \cdot 10^{-13}$	$cm^3\ s^{-1}$	26	68
$NQN14^{\bullet} + O_2^{\bullet-} \xrightarrow{2H^+} NQN14 + H_2O_2$	ELF	$3.30 \cdot 10^{-12}$	$cm^3\ s^{-1}$	26	69
$UA + O_3 \rightarrow Products$	ELF	$9.60 \cdot 10^{-17}$	$cm^3\ s^{-1}$	67	70
$UA + {}^{\bullet}OH \rightarrow Products + OH^-$	ELF	1.20×10^{-11}	$cm^3\ s^{-1}$	77	71
$GSH + {}^{\bullet}OH \rightarrow Products + OH^-$	ELF	$1.50 \cdot 10^{-11}$	$cm^3\ s^{-1}$	78	72
$GSSG + {}^{\bullet}OH \rightarrow Products + OH^-$	ELF	$1.50 \cdot 10^{-11}$	$cm^3\ s^{-1}$	27	73
$Asc^{\bullet} + Asc^{\bullet} \xrightarrow{H^+} Asc + DHA$	ELF	$5.00 \cdot 10^{-16}$	$cm^3\ s^{-1}$	79	74
$Asc + O_2^{\bullet-} \xrightarrow{H^+} Asc^{\bullet} + H_2O_2$	ELF	$5.10 \cdot 10^{-17}$	$cm^3\ s^{-1}$	26	75
$Asc + HO_2 \rightarrow Asc^{\bullet} + H_2O_2$	ELF	$2.65 \cdot 10^{-17}$	$cm^3\ s^{-1}$	80	76
$Asc + {}^{\bullet}OH \rightarrow Products + OH^-$	ELF	$1.80 \cdot 10^{-11}$	$cm^3\ s^{-1}$	81	77
$Asc + {}^{\bullet}O_3 \rightarrow Products$	ELF	$9.10 \cdot 10^{-17}$	$cm^3\ s^{-1}$	67	78
$1.25\ GS^{\bullet} + 0.5\ O_3 \rightarrow Products$	ELF	$9.60 \cdot 10^{-20}$	$cm^3\ s^{-1}$	67	79
$1.25\ GSH + 0.5\ O_3 \rightarrow Products$	ELF	$9.60 \cdot 10^{-20}$	$cm^3\ s^{-1}$	67	80
$GSOO + GSOO \rightarrow 0.56\ O_2^{\bullet-} + Products$	ELF	$6.79 \cdot 10^{-13}$	$cm^3\ s^{-1}$	82	81
$O_2^{\bullet-} + GSH \rightarrow GSO^{\bullet} + OH^-$	ELF	$3.32 \cdot 10^{-19}$	$cm^3\ s^{-1}$	83–85	82
$NO_2^{\bullet} + GS^{\bullet} \rightarrow GSNO_2$	ELF	$4.98 \cdot 10^{-12}$	$cm^3\ s^{-1}$	86	83
$GSOO^{\bullet} + NO_2^{\bullet} \rightarrow GSOONO_2$	ELF	$2.49 \cdot 10^{-12}$	$cm^3\ s^{-1}$	82	84
$GSOONO_2 \rightarrow GSOO^{\bullet} + NO_2^{\bullet}$	ELF	$7.50 \cdot 10^{-1}$	s^{-1}	82	85
$NO_2^{\bullet} + GS^- \rightarrow NO_2^- + GS^{\bullet}$	ELF	$4.00 \cdot 10^{-13}$	$cm^3\ s^{-1}$	86	86
$NO_2^{\bullet} + GSH \rightarrow NO_2^- + GS^{\bullet} + H^+$	ELF	$1.66 \cdot 10^{-14}$	$cm^3\ s^{-1}$	87	87
$GSOO^{\bullet} + GSH \rightarrow GSO^{\bullet} + GSOH$	ELF	$3.32 \cdot 10^{-15}$	$cm^3\ s^{-1}$	86	88
$GSO + NO_2 \rightarrow GSOONO$	ELF	$7.47 \cdot 10^{-12}$	$cm^3\ s^{-1}$	86	89
$GSOONO \rightarrow Products$	ELF	$7.00 \cdot 10^{2}$	s^{-1}	86	90
$GS^{\bullet} + GS^- \rightarrow GSSG^{\bullet-}$	ELF	$1.59 \cdot 10^{-14}$	$cm^3\ s^{-1}$	86,88	91
$GSSG^{\bullet-} \rightarrow GS^{\bullet} + GS^-$	ELF	$1.60 \cdot 10^{5}$	s^{-1}	86,88	92
$GSSG^{\bullet-} + O_2 \rightarrow GSSG + O_2^{\bullet-}$	ELF	$8.30 \cdot 10^{-12}$	$cm^3\ s^{-1}$	86,88	93
$GS^{\bullet} + GS^{\bullet} \rightarrow GSSG$	ELF	$8.30 \cdot 10^{-12}$	$cm^3\ s^{-1}$	88	94
$GSOH + GSH \rightarrow GSSG + H_2O$	ELF	$1.20 \cdot 10^{-18}$	$cm^3\ s^{-1}$	89	95
$GSO^{\bullet} + GSO^{\bullet} \rightarrow Products$	ELF	$9.96 \cdot 10^{-14}$	$cm^3\ s^{-1}$	86	96
$GS^- + H_2O_2 \rightarrow GSOH + OH^-$	ELF	$1.60 \cdot 10^{-21}$	$cm^3\ s^{-1}$	89	97
$GS^{\bullet} + Asc \rightarrow GSH + Asc^{\bullet}$	ELF	$1.00 \cdot 10^{-12}$	$cm^3\ s^{-1}$	90,91	98
$UA + NO_2^{\bullet} \rightarrow UA^{\bullet} + NO_2^-$	ELF	$3.00 \cdot 10^{-14}$	$cm^3\ s^{-1}$	92,93	99
$Asc + NO_2^{\bullet} \rightarrow Asc^{\bullet} + NO_2^-$	ELF	$5.80 \cdot 10^{-14}$	$cm^3\ s^{-1}$	92,93	100
$UA^{\bullet} + Asc \rightarrow UA + Asc^{\bullet}$	ELF	$1.70 \cdot 10^{-15}$	$cm^3\ s^{-1}$	91	101

$GS^{\bullet} + UA \rightarrow GSH + UA^{\bullet}$	ELF	$5.00 \cdot 10^{-14}$	$cm^3\ s^{-1}$	[87]	102
$O_2^{\bullet-} + NO_2^{\bullet} \rightarrow O_2NOO^-$	ELF	$7.50 \cdot 10^{-12}$	$cm^3\ s^{-1}$	[86,94]	103
$O_2NOO^- \rightarrow NO_2^- + O_2$	ELF	$7.00 \cdot 10^{-1}$	s^{-1}	[86]	104
$O_2NOO^- \rightarrow O_2^{\bullet-} + NO_2^{\bullet}$	ELF	1.10	s^{-1}	[86]	105
$NO_2^{\bullet} + NO_2^{\bullet} \rightarrow N_2O_4$	ELF	$7.50 \cdot 10^{-13}$	$cm^3\ s^{-1}$	[27]	106
$N_2O_4 \rightarrow NO_2^{\bullet} + NO_2^{\bullet}$	ELF	$6.90 \cdot 10^{3}$	s^{-1}	[27]	107
$N_2O_4 \xrightarrow{H_2O} NO_2^- + NO_3^- + 2H^+$	ELF	$1.00 \cdot 10^{3}$	s^{-1}	[86]	108
$O_2^{\bullet-} + O_3 \xrightarrow{H_2O} {}^{\bullet}OH + 2O_2 + OH^-$	ELF	$2.50 \cdot 10^{-12}$	$cm^3\ s^{-1}$	[95]	109
$HO_2 + O_3 \rightarrow {}^{\bullet}OH + 2O_2$	ELF	$1.66 \cdot 10^{-17}$	$cm^3\ s^{-1}$	[95]	110
$NO_2^- + {}^{\bullet}OH \rightarrow NO_2^{\bullet} + OH^-$	ELF	$8.80 \cdot 10^{-12}$	$cm^3\ s^{-1}$	[94]	111
${}^{\bullet}OH + NO_2^{\bullet} \rightarrow NO_3^- + H^+$	ELF	$7.50 \cdot 10^{-12}$	$cm^3\ s^{-1}$	[86]	112
${}^{\bullet}OH + NO_2^{\bullet} \rightarrow ONOOH$	ELF	$7.50 \cdot 10^{-12}$	$cm^3\ s^{-1}$	[86]	113
$ONOOH \rightarrow NO_2^{\bullet} + {}^{\bullet}OH$	ELF	$3.00 \cdot 10^{-1}$	s^{-1}	[86]	114
$ONOOH \rightarrow NO_3^- + H^+$	ELF	$7.00 \cdot 10^{-1}$	s^{-1}	[86]	115
$ONOO^- + GSH \rightarrow NO_2^- + GSOH$	ELF	$1.10 \cdot 10^{-18}$	$cm^3\ s^{-1}$	[96]	116
$GSO^{\bullet} + NO_2^{\bullet} \rightarrow GSOONO$	ELF	$7.50 \cdot 10^{-12}$	$cm^3\ s^{-1}$	[86]	117
$GSOONO \xrightarrow{H_2O} Products$	ELF	$7.00 \cdot 10^{2}$	s^{-1}	[86]	118
$ONOOH + Asc \rightarrow Im_1$	ELF	$1.66 \cdot 10^{-15}$	$cm^3\ s^{-1}$	[97]	119
$Im_1 \rightarrow ONOOH + Asc$	ELF	$5.00 \cdot 10^{2}$	s^{-1}	[97]	120
$Im_1 \rightarrow Im_2$	ELF	$4.00 \cdot 10^{1}$	s^{-1}	[97]	121
$Im_2 \rightarrow Im_1$	ELF	5.00	s^{-1}	[97]	122
$Im_2 + Asc \rightarrow Asc + DHA + NO_2^- + H_2O$	ELF	$1.66 \cdot 10^{-19}$	$cm^3\ s^{-1}$	[97]	123
$Im_2 \rightarrow Asc + NO_3^- + H^+$	ELF	$8.50 \cdot 10^{-1}$	$cm^3\ s^{-1}$	[97]	124
$ONOOH + UA \rightarrow UA^{rad} + NO_2 +$ Products	ELF	$2.60 \cdot 10^{-19}$	$cm^3\ s^{-1}$	[97]	125
$O_2^{\bullet-} + SOD \xrightarrow{H^+} 0.5\ H_2O_2 + SOD$	ELF	$2.65 \cdot 10^{-12}$	$cm^3\ s^{-1}$	[27]	126
$H_2O_2 +$ catalase $\rightarrow H_2O + 0.5\ O_2 +$ catalase	ELF	$3.20 \cdot 10^{-14}$	$cm^3\ s^{-1}$	[27]	127
${}^{\bullet}OH +$ organic matter $\rightarrow$ oxidized organic matter	ELF	$1.66 \cdot 10^{-12}$	$cm^3\ s^{-1}$	[77,98]	128
$\rightarrow H_2O_2$	Cells	$1 \cdot 10^{14}$	$cm^{-3}\ s^{-1}$	this study	129
$H_2O_2 +$ enzymes $\rightarrow H_2O + O_2 +$ enzymes	Cells	$3.32 \cdot 10^{-14}$	$cm^3\ s^{-1}$	[27]	130
$O_2^{\bullet-} + SOD \xrightarrow{H^+} 0.5\ H_2O_2 + SOD$	Cells	$2.65 \cdot 10^{-12}$	$cm^3\ s^{-1}$	[27]	131

Table S2. Concentrations of gas-phase pollutants considered in the examined pollution scenarios (Fig. 3). The NO_2 levels represent a 1:1 mass ratio with PM2.5 levels[27].

	Remote	**Rural**	**Indoor**	**Heavily cleaned indoor**	**Clean urban**	**Polluted urban**
O_3 (ppb)	15 [99]	20 [2]	10 [100]	10 [100]	30 [2]	75 [101]
H_2O_2 (ppb)	0.2 [102]	0.5 [4]	0.9 [103,104]	280 [105]	1 [3]	2 [5]
NO_2 (ppb)	2.1	4.2	5.3	5.3	15.9	31.9
PM2.5 ($\mu g \cdot m^{-3}$)	4 [106]	8 [107,108]	10 [109]	10 [109]	30 [2]	60 [110,111]

Table S3. Overview of important and default input parameters for KM-SUB-ELF 2.0 in the standard pollution scenario.

Parameter	**Value**	**Unit**
PM2.5 concentration	30	$\mu g\ m^{-3}$
NO_2 concentration	30	$\mu g\ m^{-3}$
O_3 concentration	30	ppb
Concentration of ambient H_2O_2	1	ppb
Concentration of blood H_2O_2	5	μM
Effective membrane permeability of H_2O_2	1×10^{-5}	$cm\ s^{-1}$
H_2O_2 production in the cell layer	1×10^{14}	$cm^{-3}\ s^{-1}$
Concentration of H_2O_2-scavenging enzymes in cells	10	μM

Table S4. Input parameters of the model KM-SUB-ELF 2.0.

Parameter	Value	Unit
Henry's law equilibrium constant of O_3	$1.0 \cdot 10^{-2}$	M atm^{-1}
Henry's law equilibrium constant of H_2O_2	$9.1 \cdot 10^{4}$	M atm^{-1}
Henry's law equilibrium constant of $^{\bullet}OH$	29	M atm^{-1}
Henry's law equilibrium constant of $HO_2^{\bullet}$	$6.8 \cdot 10^{2}$	M atm^{-1}
Particulate mass fraction of Cu^{2+}	$3.1 \cdot 10^{-4}$	-
Particulate mass fraction of Fe^{2+}	$8.1 \cdot 10^{-3}$	-
Particulate mass fraction of quinones	$1.9 \cdot 10^{-5}$	-
Particulate mass fraction of SOA	0.33	-
Water soluble fraction of Cu^{2+}	0.40	-
Water soluble fraction of Fe^{2+}	0.10	-
Water soluble fraction of quinones	0.10	-
Water soluble fraction of SOA	0.10	-
Particulate exposure time	2	h
ELF catalase concentration	5	pM
ELF superoxide dismutase concentration	1000	pM
ELF glutathione concentration	108	µM
ELF ascorbate concentration	40	µM
ELF uric acid concentration	200	µM
ELF α-Tocopherol concentration	0.7	µM
ELF SP-$B_{1\text{-}25}$ concentration	5000	µM
ELF POG concentration	13000	µM
ELF organic matter concentration	40000	µM
PM2.5 accumulation time	2	h
PM2.5 deposition factor	0.45	-
Functional residual capacity of respiratory tract	2750	cm^3
Tidal volume	1500	cm^3
Duration of breath	3.67	sec
ELF pH	7	-
ELF volume	20	cm^3
Respiratory tract surface area	$8.9 \cdot 10^{5}$	cm^2
Respiratory tract temperature	310	K
Cellular concentration of H_2O_2-scavenging enzymes	10	µM
H_2O_2 effective membrane permeability coefficient	$1 \cdot 10^{-5}$ $(4 \cdot 10^{-6} - 40 \cdot 10^{-5})$	cm s^{-1}
H_2O_2 production in the cell layer	$1 \cdot 10^{14}$	cm^{-3} s^{-1}
Thickness of cell membrane	$1 \cdot 10^{-4}$	cm
Ambient H_2O_2 concentration	1	ppb
Blood H_2O_2 concentration	5	µM

Table S5. Literature values for H_2O_2 ambient and indoor concentrations.

Concentration (ppb)	Region	Reference
1.0	Indoor	Li et al., 2002 [103]
0.1-1.5	Workplace	Christensen et al., 2000 [112]
0.1-5	California	Kok et al., 1978 [3]
0.5	North Carolina	Das & Anjela, 1994 [4]
2.0	Beijing	He et al., 2010 [5]
≤1.5	Nagoya	Watanabe & Tanaka, 1995 [6]
0.5-4.5	Remote Beijing	Weihan et al., 1998 [7]

References

1 D. Vione, V. Maurino, C. Minero and E. Pelizzetti, The atmospheric chemistry of hydrogen peroxide: A review, *Ann. Chim.*, 2003, **93**, 477–488.

2 J. H. Seinfeld, S. N. Pandis, *Atmospheric Chemistry and Physics: From Air Pollution to Climate Change*, 3rd Edition, 2016.

3 G. L. Kok, K. R. Darnall, A. M. Winer, J. N. Pitts and B. W. Gay, Ambient Air Measurements of Hydrogen Peroxide in the California South Coast Air Basin, *Environ. Sci. Technol.*, 1978, **12**, 1077–1080.

4 V. P. Aneja, Analysis of gaseous hydrogen peroxide concentrations in raleigh, north carolina, *Air Waste*, 1994, **44**, 176–183.

5 S. Z. He, Z. M. Chen, X. Zhang, Y. Zhao, D. M. Huang, J. N. Zhao, T. Zhu, M. Hu and L. M. Zeng, Measurement of atmospheric hydrogen peroxide and organic peroxides in Beijing before and during the 2008 Olympic Games: Chemical and physical factors influencing their concentrations, *J. Geophys. Res*, 2010, **115**, 1-12.

6 K. Watanabe, H. Tanaka Measurement of gaseous hydrogen peroxide (H2O2) concentrations in the urban atmosphere. *J. Meteo. Soc. Japan.*, 1995, **73**, 839-847.

7 S. Weihan, L. Wei, D. Guoan and W. E. Wilson, A study on hydrogen peroxide in the atmosphere, *Adv. Atmos. Sci.*, 1989, **6**, 509–515.

8 D. Ezeriņa, B. Morgan and T. P. Dick, Imaging dynamic redox processes with genetically encoded probes, *J. Mol. Cell. Cardiol.*, 2014, **73**, 43–49.

9 O. Lyublinskaya and F. Antunes, Measuring intracellular concentration of hydrogen peroxide with the use of genetically encoded H 2 O 2 biosensor HyPer, *Redox Biol.*, 2019, **24**, 101200.

10 M. B. Schleiss, O. Holz, M. Behnke, K. Richter, H. Magnussen and R. A. Jörres, The concentration of hydrogen peroxide in exhaled air depends on expiratory flow rate, *Eur. Respir. J.*, 2000, **16**, 1115–1118.

11 J. R. Stone, S. Yang, Hydrogen Peroxide: A Signaling Messenger. *Antiox. Red. Sign.*, 2006, **8**, 243-271.

12 H. Sies, Hydrogen peroxide as a central redox signaling molecule in physiological oxidative stress: Oxidative eustress, *Redox Biol.*, 2017, **11**, 613–619.

13 W. J. C. Van Beurden, G. A. Harff, P. N. R. Dekhuijzen, M. J. A. Van Den Bosch, J. P. H. M. Creemers and F. W. J. M. Smeenk, An efficient and reproducible method for measuring hydrogen peroxide in exhaled breath condensate, *Respir. Med.*, 2002, **96**, 197–203.

14 C. Caffarelli, E. Calcinai, L. Rinaldi, C. Povesi Dascola, L. Terracciano and M. Corradi, Hydrogen peroxide in exhaled breath condensate in asthmatic children during acute exacerbation and after treatment, *Respiration*, 2012, **84**, 291–298.

15 W. B. Gerritsen, P. Zanen, A. A. Bauwens, J. M. van den Bosch and F. J. Haas, Validation of a new method to measure hydrogen peroxide in exhaled breath condensate, *Respir. Med.*, 2005, **99**, 1132–1137.

16 H. Knobloch, G. Becher, M. Decker and P. Reinhold, Evaluation of H2O2 and pH in exhaled breath condensate samples: Methodical and physiological aspects, *Biomarkers*, 2008, **13**, 319–341.

17 C. Nagaraja, B. L. Shashibhushan, Sagar, M. Asif and P. H. Manjunath, Hydrogen peroxide in exhaled breath condensate: A clinical study, *Lung India*, 2012, **29**, 123–127.

18 M. E. Quimbar, S. Q. Davis, S. T. Al-Farra, A. Hayes, V. Jovic, M. Masuda and A. R. Lippert, Chemiluminescent Measurement of Hydrogen Peroxide in the Exhaled Breath Condensate of Healthy and Asthmatic Adults, *Anal. Chem.*, 2020, **92**, 14594–14600.

19 M. R. Branco, H. S. Marinho, L. Cyrne and F. Antunes, Decrease of H 2O 2 Plasma Membrane Permeability during Adaptation to H 2O 2 in Saccharomyces cerevisiae, *J. Biol. Chem.*, 2004, **279**, 6501–6506.

20 F. Antunes and P. M. Brito, Quantitative biology of hydrogen peroxide signaling, *Redox Biol.*, 2017, **13**, 1–7.

21 R. Gaikwad, P. R. Thangaraj and A. K. Sen, Direct and rapid measurement of hydrogen peroxide in human blood using a microfluidic device, *Sci. Rep.*, 2021, **11**, 1–10.

22 R. Bretón-Romero and S. Lamas, Hydrogen peroxide signaling in vascular endothelial cells, *Redox Biol.*, 2014, **2**, 529–534.

23 E. Dicker and A. I. Cederbaum, Increased NADH-dependent production of reactive oxygen intermediates by microsomes after chronic ethanol consumption: Comparisons with NADPH, *Arch. Biochem. Biophys.*, 1992, **293**, 274–280.

24 H. J. Forman, A. Bernardo and K. J. A. Davies, What is the concentration of hydrogen

peroxide in blood and plasma?, *Arch. Biochem. Biophys.*, 2016, **603**, 48–53.

25 B. Halliwell, M. V. Clement, J. Ramalingam and Lee Hua Long, Hydrogen peroxide. Ubiquitous in cell culture and in vivo?, *IUBMB Life*, 2000, **50**, 251–257.

26 P. S. J. Lakey, T. Berkemeier, H. Tong, A. M. Arangio, K. Lucas, U. Pöschl and M. Shiraiwa, Chemical exposure-response relationship between air pollutants and reactive oxygen species in the human respiratory tract, *Sci. Rep.*, 2016, **6**, 1–6.

27 S. Lelieveld, J. Wilson, E. Dovrou, A. Mishra, P. S. J. Lakey, M. Shiraiwa, U. Pöschl and T. Berkemeier, Hydroxyl Radical Production by Air Pollutants in Epithelial Lining Fluid Governed by Interconversion and Scavenging of Reactive Oxygen Species, *Environ. Sci. Technol.*, 2021, **55**. 14069-14079.

28 I. S. Mudway and F. J. Kelly, Ozone and the lung: A sensitive issue, *Mol. Aspects Med.*, 2000, **21**, 1–48.

29 A. Van Der Vliet, C. A. O'Neill, C. E. Cross, J. M. Koostra, W. G. Volz, B. Halliwell and S. Louie, Determination of low-molecular-mass antioxidant concentrations in human respiratory tract lining fluids, *Am. J. Physiol. - Lung Cell. Mol. Physiol.*, 1999, **276**, 289–296.

30 A. M. Cantin, G. A. Fells, R. C. Hubbard and R. G. Crystal, Antioxidant macromolecules in the epithelial lining fluid of the normal human lower respiratory tract, *J. Clin. Invest.*, 1990, **86**, 962–971.

31 H. Aebi, [13] Catalase in Vitro, *Methods Enzymol.*, 1984, **105**, 121–126.

32 B. P. Jones and A. Suggett, The Catalase-Hydrogen Peroxide System, *Biochem. J.*, 1968, **110**, 621–629.

33 J. A. Fee and C. Bull, Steady-state kinetic studies of superoxide dismutases. Saturative behavior of the copper- and zinc-containing protein, *J. Biol. Chem.*, 1986, **261**, 13000–13004.

34 A. Bar-Even, E. Noor, Y. Savir, W. Liebermeister, D. Davidi, D. S. Tawfik and R. Milo, The moderately efficient enzyme: Evolutionary and physicochemical trends shaping enzyme parameters, *Biochemistry*, 2011, **50**, 4402–4410.

35 G. B. Smejkal and S. Kakumanu, Enzymes and their turnover numbers, *Expert Rev. Proteomics*, 2019, **16**, 543–544.

36 S. P. Andreoli, C. Mallett, J. A. McAteer and L. V. Williams, Antioxidant defense mechanisms of endothelial cells and renal tubular epithelial cells In Vitro: Role of the glutathione redox cycle and catalase, *Pediatr. Res.*, 1992, **32**, 360–365.

37 C. N. Scaglione, Q. Xu, V. K. Ramanujan, Direct measurement of catalase activity in living cells and tissue biopsies. *Biochem. Biophys. Res. Commun.*. **470**, 191-196 (2017).

38 C. C. Winterbourn and M. B. Hampton, Thiol chemistry and specificity in redox signaling, *Free Radic. Biol. Med.*, 2008, **45**, 549–561.

39 A. Tovar-Méndez, M. A. Matamoros, P. Bustos-Sanmamed, K. J. Dietz, F. J. Cejudo, N. Rouhier, S. Sato, S. Tabata and M. Becana, Peroxiredoxins and NADPH-dependent thioredoxin systems in the model legume lotus japonicus, *Plant Physiol.*, 2011, **156**, 1535–1547.

40 V. Castranova, J. Rabovsky, J. H. Tucker and P. R. Miles, The alveolar type II epithelial cell: A multifunctional pneumocyte, *Toxicol. Appl. Pharmacol.*, 1988, **93**, 472–483.

41 V. L. Kinnula, J. I. Everitt, A. R. Whorton and J. D. Crapo, Hydrogen peroxide production by alveolar type II cells, alveolar macrophages, and endothelial cells, *Am. J. Physiol. - Lung Cell. Mol. Physiol.*, 1991, **261**, L84-L91.

42 W. J. Piotrowski, J. Marczak, D. Dinsdale, Z. Kurmanowska, Y. Tarasow, J. Komos and D. Nowak, Release of hydrogen peroxide by rat type II pneumocytes in the prolonged culture, *Toxicol. Vitr.*, 2000, **14**, 85–93.

43 K. R. Albe, M. H. Butler and B. E. Wright, Cellular concentrations of enzymes and their substrates, *J. Theor. Biol.*, 1990, **143**, 163–195.

44 J. L. Jimenez, M. R. Canagaratna, N. M. Donahue, A. S. H. Prevot, Q. Zhang, J. H. Kroll, P. F. DeCarlo, J. D. Allan, H. Coe, N. L. Ng, A. C. Aiken, K. S. Docherty, I. M. Ulbrich, A. P. Grieshop, A. L. Robinson, J. Duplissy, J. D. Smith, K. R. Wilson, V. A. Lanz, C. Hueglin, Y. L. Sun, J. Tian, A. Laaksonen, T. Raatikainen, J. Rautiainen, P. Vaattovaara, M. Ehn, M. Kulmala, J. M. Tomlinson, D. R. Collins, M. J. Cubison, E. J. Dunlea, J. A. Huffman, T. B. Onasch, M. R. Alfarra, P. I. Williams, K. Bower, Y. Kondo, J. Schneider, F. Drewnick, S. Borrmann, S. Weimer, K. Demerjian, D. Salcedo, L. Cottrell, R. Griffin, A. Takami, T. Miyoshi, S. Hatakeyama, A. Shimono, J. Y. Sun, Y. M. Zhang, K. Dzepina, J. R. Kimmel, D. Sueper, J. T. Jayne, S. C. Herndon, A. M. Trimborn, L. R. Williams, E. C. Wood, A. M. Middlebrook, C. E. Kolb, U. Baltensperger and D. R. Worsnop, Evolution of organic aerosols in the atmosphere, *Science*, 2009, **326**, 1525–1529.

45 M. Hallquist, J. C. Wenger, U. Baltensperger, Y. Rudich, D. Simpson, M. Claeys, J. Dommen, N. M. Donahue, C. George, A. H. Goldstein, J. F. Hamilton, H. Herrmann, T. Hoffmann, Y. Iinuma, M. Jang, M. E. Jenkin, J. L. Jimenez, A. Kiendler-Scharr, W. Maenhaut, G. McFiggans, T. F. Mentel, A. Monod, A. S. H. Prévôt, J. H. Seinfeld, J. D. Surratt, R. Szmigielski and J. Wildt, The formation, properties and impact of secondary organic aerosol: Current and emerging issues, *Atmos. Chem. Phys.*, 2009, **9**, 5155–5236.

46 K. S. Docherty, W. Wu, Y. Bin Lim and P. J. Ziemann, Contributions of organic peroxides to secondary aerosol formed from reactions of monoterpenes with O 3, *Environ. Sci. Technol.*, 2005, **39**, 4049–4059.

47 M. Krapf, I. El Haddad, E. A. Bruns, U. Molteni, K. R. Daellenbach, A. S. H. Prévôt, U. Baltensperger and J. Dommen, Labile Peroxides in Secondary Organic Aerosol, *Chem*, 2016, **1**, 603–616.

48 H. Tong, A. M. Arangio, P. S. J. Lakey, T. Berkemeier, F. Liu, C. J. Kampf, W. H. Brune, U. Poschl and M. Shiraiwa, Hydroxyl radicals from secondary organic aerosol decomposition in water, *Atmos. Chem. Phys.*, 2016, **16**, 1761–1771.

49 Y. Wang, H. Kim and S. E. Paulson, Hydrogen peroxide generation from α- and β-pinene and toluene secondary organic aerosols, *Atmos. Environ.*, 2011, **45**, 3149–3156.

50 P. H. Chowdhury, Q. He, R. Carmieli, C. Li, Y. Rudich and M. Pardo, Connecting the Oxidative Potential of Secondary Organic Aerosols with Reactive Oxygen Species in Exposed Lung Cells, *Environ. Sci. Technol.*, 2019, **53**, 13949–13958.

51 J. Wei, T. Fang, P. S. J. Lakey and M. Shiraiwa, Iron-Facilitated Organic Radical Formation from Secondary Organic Aerosols in Surrogate Lung Fluid, *Environ. Sci. Technol.*, 2022, **56(11)**, 7234-7243.

52 Z. H. Zhang, E. Hartner, B. Utinger, B. Gfeller, A. Paul, M. Sklorz, H. Czech, B. X. Yang, X. Y. Su, G. Jakobi, J. Orasche, J. Schnelle-Kreis, S. Jeong, T. Gröger, M. Pardo, T. Hohaus, T. Adam, A. Kiendler-Scharr, Y. Rudich, R. Zimmermann and M. Kalberer, Are reactive oxygen species (ROS) a suitable metric to predict toxicity of carbonaceous aerosol particles?, *Atmos. Chem. Phys.*, 2022, **22**, 1793–1809.

53 J. Wei, T. Fang, C. Wong, P. S. J. Lakey, S. A. Nizkorodov and M. Shiraiwa, Superoxide Formation from Aqueous Reactions of Biogenic Secondary Organic Aerosols, *Environ. Sci. Technol.*, 2021, **55**, 260–270.

54 H. Tong, P. S. J. Lakey, A. M. Arangio, J. Socorro, F. Shen, K. Lucas, W. H. Brune, U. Pöschl and M. Shiraiwa, Reactive Oxygen Species Formed by Secondary Organic Aerosols in Water and Surrogate Lung Fluid, *Environ. Sci. Technol.*, 2018, **52**, 11642–11651.

55 T. Fang, Y. Huang, J. Wei, J. E. M. Mena, P. S. J. Lakey, M. T. Kleinman, M. A. Digman and M. Shiraiwa, Superoxide Release by Macrophages through NADPH Oxidase Activation Dominating Chemistry by Isoprene Secondary Organic Aerosols and Quinones to Cause Oxidative Damage on Membranes, 2022, **56(23)**, 17029-17038.

56 S. M. Saunders, M. E. Jenkin, R. G. Derwent and M. J. Pilling, Protocol for the development of the Master Chemical Mechanism, MCM v3 (Part A): Tropospheric degradation of non-aromatic volatile organic compounds, *Atmos. Chem. Phys.*, 2003, **3**, 161–180.

57 M. E. Jenkin, S. M. Saunders, V. Wagner and M. J. Pilling, Protocol for the development of the Master Chemical Mechanism, MCM v3 (Part B): Tropospheric degradation of aromatic volatile organic compounds, *Atmos. Chem. Phys.*, 2003, **3**, 181–193.

58 Y. P. Chang, H. H. Chang and J. J. M. Lin, Kinetics of the simplest Criegee intermediate reaction with ozone studied using a mid-infrared quantum cascade laser spectrometer, *Phys. Chem. Chem. Phys.*, 2017, **20**, 97–102.

59 G. V. Buxton, C. L. Greenstock, W. P. Helman and A. B. Ross, Critical Review of rate constants for reactions of hydrated electrons, hydrogen atoms and hydroxyl radicals (·OH/·O− in Aqueous Solution, *J. Phys. Chem. Ref. Data*, 1988, **17**, 513–886.

60 M. Simic, P. Neta and E. Hayon, Pulse radiolysis study of alcohols in aqueous solution, *J. Phys. Chem.*, 1969, **73**, 3794–3800.

61 M. J. Zhao, L. Jung, C. Tanielian and R. Mechin, Kinetics of the competitive degradation of deoxyribose and other biomolecules by hydroxyl radicals produced by the fenton reaction, *Free Radic. Res.*, 1994, **20**, 345–363.

62 Kanofsky, J. R. & Sima, P. D. Reactive absorption of ozone by aqueous biomolecule solutions: Implications for the role of sulfhydryl compounds as targets for ozone. *Arch Biochem Biophys.*, 1995, **316**, 52-62.

63 W. A. Pryor, D. H. Giamalva and D. F. Church, Kinetics of Ozonation. 2. Amino Acids and Model Compounds in Water and Comparisons to Rates in Nonpolar Solvents, *J. Am. Chem. Soc.*, 1984, **106**, 7094–7100.

64 P. Neeb, F. Sauer, O. Horie and G. K. Moortgat, Formation of hydroxymethyl hydroperoxide and formic acid in alkene ozonolysis in the presence of water vapour, *Atmos. Environ.*, 1997, **31**, 1417–1423.

65 M. Zeng, N. Heine and K. R. Wilson, Evidence that criegee intermediates drive autoxidation in unsaturated lipids, *Proc. Natl. Acad. Sci. U. S. A.*, 2020, **117**, 4486–4490.

66 M. Navarrete, C. Rangel, J. C. Corchado and J. Espinosa-García, Trapping of the OH radical by α-tocopherol: A theoretical study, *J. Phys. Chem. A*, 2005, **109**, 4777–4784.

67 S. Kermani, A. Ben-Jebria and J. S. Ultman, Kinetics of ozone reaction with uric acid, ascorbic acid, and glutathione at physiologically relevant conditions, *Arch. Biochem. Biophys.*, 2006, **451**, 8–16.

68 J. D. Rush and B. H. J. Bielski, Pulse radiolytic studies of the reactions of HO2/O2- with Fe(II)/Fe(III) ions. The reactivity of HO2/O2- with ferric ions and its implication on the occurrence of the Haber-Weiss reaction, *J. Phys. Chem.*, 1985, **89**, 5062–5066.

69 H. Christensen, K. Sehested and H. Corfitzen, Reactions of hydroxyl radicals with hydrogen peroxide at ambient and elevated temperatures, *J. Phys. Chem.*, 1982, **86**, 1588–1590.

70 K. Sehested, O. L. Rasmussen and H. Fricke, Rate constants of OH with HO2, O2-, and H2O2+ from hydrogen peroxide formation in pulse-irradiated oxygenated water, *J. Phys. Chem.*, 1968, **72**, 626–631.

71 W. H. Koppenol, The Haber-Weiss cycle - 70 years later, *Redox Rep.*, 2001, **6**, 229–234.

72 G. G. Jayson, B. J. Parsons and A. J. Swallow, Oxidation of ferrous ions by hydroxyl

radicals, *J. Chem. Soc. Faraday Trans. 1 Phys. Chem. Condens. Phases*, 1972, **68**, 2053–2058.

73 S. Lewis, A. Lynch, L. Bachas, S. Hampson, L. Ormsbee and D. Bhattacharyya, Chelate-modified fenton reaction for the degradation of trichloroethylene in aqueous and two-phase systems, *Environ. Eng. Sci.*, 2009, **26**, 849–859.

74 Z. Stuglik and Z. PawełZagórski, Pulse radiolysis of neutral iron(II) solutions: oxidation of ferrous ions by OH radicals, *Radiat. Phys. Chem.*, 1981, **17**, 229–233.

75 S. J. Hug and O. Leupin, Iron-catalyzed oxidation of Arsenic(III) by oxygen and by hydrogen peroxide: pH-dependent formation of oxidants in the Fenton reaction, *Environ. Sci. Technol.*, 2003, **37**, 2734–2742.

76 J. G. Charrier, A. S. McFall, N. K. Richards-Henderson and C. Anastasio, Hydrogen peroxide formation in a surrogate lung fluid by transition metals and quinones present in particulate matter, *Environ. Sci. Technol.*, 2014, **48**, 7010–7017.

77 Masuda, T., Shinohara, H. & Kondo, M. Reactions of hydroxyl radicals with nucleic acid bases and the related compounds in gamma-irradiated aqueous solution. *J. Radiat. Res.*, 1975, **16**, 153-161.

78 M. Liphard, E. Bothe and D. Schulte-Frohlinde, The influence of glutathione on single-Strand breakage in single-stranded DNA irradiated in aqueous solution in the absence and presence of oxygen, *Int. J. Radiat. Biol.*, 1990, **58**, 589–602.

79 W. V. Drigalski, Vitamin C in urine in health and disease., *Klin. Wochenschr.*, 1935, **14**, 338–339.

80 J. Shen, P. T. Griffiths, S. J. Campbell, B. Utinger, M. Kalberer and S. E. Paulson, Ascorbate oxidation by iron, copper and reactive oxygen species: review, model development, and derivation of key rate constants, *Sci. Rep.*, 2021, **11**, 1–14.

81 B. D. Adams, G.E., Boag, J.W., Currant, J. and Michael, Absolute rate constants for the reaction of the hydroxyl radical with organic compounds, *Pulse radiolysis*, 1965, 131–143.

82 S. Goldstein, J. Lind and G. Merenyi, Reaction of Organic Peroxyl Radicals with ·NO2 and ·NO in Aqueous Solution: Intermediacy of Organic Peroxynitrate and Peroxynitrite Species, *J. Phys. Chem. A*, 2004, **108**, 1719–1725.

83 C. M. Jones, A. Lawrence, P. Wardman and M. J. Burkitt, Electron paramagnetic resonance spin trapping investigation into the kinetics of glutathione oxidation by the superoxide radical: Re-evaluation of the rate constant, *Free Radic. Biol. Med.*, 2002, **32**, 982–990.

84 C. C. Winterbourn, Revisiting the reactions of superoxide with glutathione and other thiols, *Arch. Biochem. Biophys.*, 2016, **595**, 68–71.

85 H. Wefers and H. Sies, Oxidation of glutathione by the superoxide radical to the disulfide and the sulfonate yielding singlet oxygen, *Eur. J. Biochem.*, 1983, **137**, 29–36.

86 M. Kirsch, M. Lehnig, H. G. Korth, R. Sustmann and H. De Groot, Inhibition of peroxynitrite-induced nitration of tyrosine by glutathione in the presence of carbon dioxide through both radical repair and peroxynitrate formation, *Chem. - A Eur. J.*, 2001, **7**, 3313–3320.

87 E. Ford, M. N. Hughes and P. Wardman, Kinetics of the reactions of nitrogen dioxide with glutathione, cysteine, and uric acid at physiological pH, *Free Radic. Biol. Med.*, 2002, **32**, 1314–1323.

88 P. Wardman and C. von Sonntag, Kinetic factors that control the fate of thiyl radicals in cells, *Methods Enzymol.*, 1995, **251**, 31–45.

89 D. Luo, S. W. Smith and B. D. Anderson, Kinetics and mechanism of the reaction of cysteine and hydrogen peroxide in aqueous solution, *J. Pharm. Sci.*, 2005, **94**, 304–316.

90 B. S. Winkler, S. M. Orselli and T. S. Rex, The redox couple between glutathione and ascorbic acid: A chemical and physiological perspective, *Free Radic. Biol. Med.*, 1994, **17**, 333–349.

91 G. R. Buettner, B. A. Jurkiewicz, N. May, G. R. Buettner and B. A. Jurkiewicz, Catalytic Metals , Ascorbate and Free Radicals : Combinations to Avoid Linked references are available on JSTOR for this article : Catalytic Metals , Ascorbate and Free Radicals : Combinations to Avoid ’, 2018, **145**, 532–541.

92 Z. B. Alfassi, R. E., Huie, P. Neta, P., L. C. T. Shoute, Temperature dependence of the rate constats for reaction of inorganic radicals with organic reductants. *J. Phys. Chem.*, 1990, **94**, 8800–8805.

93 O. Augusto, M. G. Bonini, A. M. Amanso, E. Linares, C. C. X. Santos and S. L. De Menezes, Nitrogen dioxide and carbonate radical anion: Two emerging radicals in biology, *Free Radic. Biol. Med.*, 2002, **32**, 841–859.

94 S. Goldstein and G. Czapski, Reactivity of peroxynitrite versus simultaneous generation of ·NO and O2·- toward NADH, *Chem. Res. Toxicol.*, 2000, **13**, 736–741.

95 D. J. Jacob, Heterogeneous chemistry and tropospheric ozone, *Atmos. Environ.*, 2000, **34**, 2131–2159.

96 M. G. Bonini and O. Augusto, Carbon Dioxide Stimulates the Production of Thiyl, Sulfinyl, and Disulfide Radical Anion from Thiol Oxidation by Peroxynitrite, *J. Biol. Chem.*, 2001, **276**, 9749–9754.

97 C. R. Kurz, R. Kissner, T. Nauser, D. Perrin and W. H. Koppenol, Rapid scavenging of peroxynitrous acid by monohydroascorbate, *Free Radic. Biol. Med.*, 2003, **35**, 1529–1537.

98 W. A. Pryor Oxy-radicals and related and reactions: Their formation, lifetimes, and reactions. *Annu. Rev. Physiol.*, 1986, **48**, 657–667.

99 J. Williams, S. U. Keßel, A. C. Nölscher, Y. Yang, Y. Lee, A. M. Yáñez-Serrano, S. Wolff, J. Kesselmeier, T. Klüpfel, J. Lelieveld and M. Shao, Opposite OH reactivity and ozone cycles in the Amazon rainforest and megacity Beijing: Subversion of biospheric oxidant control by anthropogenic emissions, *Atmos. Environ.*, 2016, **125**, 112–118.

100 H. Salonen, T. Salthammer and L. Morawska, Human exposure to ozone in school and office indoor environments, *Environ. Int.*, 2018, **119**, 503–514.

101 G. Yang, Y. Liu and X. Li, Spatiotemporal distribution of ground-level ozone in China at a city level, *Sci. Rep.*, 2020, **10**, 1–12.

102 D. W. O'Sullivan, B. G. Heikes, J. Snow, P. Burrow, M. Avery, D. R. Blake, G. W. Sachse, R. W. Talbot, D. C. Thornton and A. R. Bandy, Long-term and seasonal variations in the levels of hydrogen peroxide, methylhydroperoxide, and selected compounds over the Pacific Ocean, *J. Geophys. Res. D Atmos.*, 2004, **109**, 1–21.

103 T. H. Li, B. J. Turpin, H. C. Shields and C. J. Weschler, Indoor hydrogen peroxide derived from ozone/d-limonene reactions, *Environ. Sci. Technol.*, 2002, **36**, 3295–3302.

104 Z. Zhou and J. P. D. Abbatt, Formation of Gas-Phase Hydrogen Peroxide via Multiphase Ozonolysis of Unsaturated Lipids, *Environ. Sci. Technol. Lett.*, 2021, **8(2)**, 114-120.

105 S. Zhou, Z. Liu, Z. Wang, C. J. Young, T. C. Vandenboer, B. B. Guo, J. Zhang, N. Carslaw and T. F. Kahan, Hydrogen Peroxide Emission and Fate Indoors during Non-bleach Cleaning: A Chamber and Modeling Study, *Environ. Sci. Technol.*, 2020, **54**, 15643–15651.

106 P. Artaxo, L. V. Rizzo, J. F. Brito, H. M. J. Barbosa, A. Arana, E. T. Sena, G. G. Cirino, W. Bastos, S. T. Martin and M. O. Andreae, Atmospheric aerosols in Amazonia and land use change: From natural biogenic to biomass burning conditions, *Faraday Discuss.*, 2013, **165**, 203–235.

107 N. Clements, M. P. Hannigan, S. L. Miller, J. L. Peel and J. B. Milford, Comparisons of urban and rural PM10-2.5 and PM2.5 mass concentrations and semi-volatile fractions in northeastern Colorado, *Atmos. Chem. Phys.*, 2016, **16**, 7469–7484.

108 S. Kundu, E. A. Stone, Composition and sources of fine particulate matter across urban and rural sites in the Midwestern United States. *Environ. Sci. Process Impacts*., 2014, **16**, 1360–1370.

109 S. Patel, S. Sankhyan, E. K. Boedicker, P. F. Decarlo, D. K. Farmer, A. H. Goldstein, E. F. Katz, W. W. Nazaroff, Y. Tian, J. Vanhanen and M. E. Vance, Indoor Particulate Matter during HOMEChem: Concentrations, Size Distributions, and Exposures, *Environ. Sci. Technol.*, 2020, **54**, 7107–7116.

110 A. Karambelas, T. Holloway, P. L. Kinney, A. M. Fiore, R. Defries, G. Kiesewetter, C. Heyes, Urban versus rural health impacts attributable to PM2.5 and O3 in northern India. *Environ. Res. Lett.*, 2018, **13**, 1-10.

111 T. Liu, H. Meng, M. Yu, Y. Xiao, B. Huang, L. Lin, H. Zhang, R. Hu, Z. Hou, Y. Xu, L. Yuan, M. Qin, Q. Zhao, X. Xu, W. Gong, J. Hu, J. Xiao, S. Chen, W. Zeng, X. Li, G. He, Z. Rong, C. Huang, Y. Du and W. Ma, Urban-rural disparity of the short-term association of PM2.5 with mortality and its attributable burden, *Innov.*, 2021, **2**, 100171.

112 C. S. Christensen, S. Brodsgaard, P. Mortensen, K. Egmose and S. A. Linde, Determination of hydrogen peroxide in workplace air: Interferences and method validation, *J. Environ. Monit.*, 2000, **2**, 339–343.